

# Advancements in Design and Analysis of Protective Structures 2019

Special Issue Editor in Chief: Chiara Bedon

Guest Editors: Michel Arrigoni, Filipe Santos, and Lucia Figuli



---

# **Advancements in Design and Analysis of Protective Structures 2019**

Advances in Civil Engineering

---

## **Advancements in Design and Analysis of Protective Structures 2019**

Special Issue Editor in Chief: Chiara Bedon

Guest Editors: Michel Arrigoni, Filipe Santos, and Lucia Figuli



Copyright © 2019 Hindawi. All rights reserved.

This is a special issue published in "Advances in Civil Engineering." All articles are open access articles distributed under the Creative Commons Attribution License, which permits unrestricted use, distribution, and reproduction in any medium, provided the original work is properly cited.

## Editorial Board

Khalid Abdel-Rahman, Germany	Giulio Dondi, Italy	Shazim A. Memon, Kazakhstan
José Aguiar, Portugal	Mohamed ElGawady, USA	Giovanni Minafò, Italy
Reza Akhavian, USA	Ahmed Elghazouli, UK	Hossein Moayedi, Vietnam
Maria Cruz Alonso, Spain	Behzad Esmaeili, USA	Abbas Mohajerani, Australia
Serji N. Amirkhanian, USA	Flora Faleschini, Italy	Fabrizio Mollaioli, Italy
P. Ch. Anastopoulos, USA	Harry Far, Australia	Rosario Montuori, Italy
Venu G. M. Annamdas, Singapore	Antonio Formisano, Italy	Ayman S. Mosallam, USA
Mehrdad Arashpour, Australia	Giovanni Garcea, Italy	Roberto Nascimbene, Italy
Pedro Arias-Sánchez, Spain	Emilio García-Taengua, UK	Behzad Nematollahi, Australia
Farhad Aslani, Australia	Elhem Ghorbel, France	Luís C. Neves, UK
Daniele Baraldi, Italy	Agathoklis Giaralis, UK	Trung Ngo, Australia
Emilio Bastidas-Arteaga, France	Rodrigo Gonçalves, Portugal	Sanjay Nimbalkar, Australia
Chiara Bedon, Italy	Arturo Gonzalez, Ireland	Giuseppe Oliveto, Italy
Rafik Belarbi, France	Belén González-Fonteboa, Spain	Alejandro Orfila, Spain
Rafael J. Bergillos, Spain	Salvatore Grasso, Italy	Togay Ozbakkaloglu, UK
Giovanni Biondi, Italy	Fan Gu, UK	Hayri Baytan Ozmen, Turkey
Hugo C. Biscaia, Portugal	Kirk Hatfield, USA	Alessandro Palmeri, UK
Giosuè Boscato, Italy	Khandaker Hossain, Canada	Fabrizio Paolacci, Italy
Melina Bosco, Italy	Zahid Hossain, USA	Fulvio Parisi, Italy
Jorge Branco, Portugal	Mohammad R. Hosseini, Australia	Arnaud Perrot, France
Emanuele Brunesi, Italy	Bon-Gang Hwang, Singapore	Christophe Petit, France
Alberto Campisano, Italy	Dong-Sheng Jeng, Australia	Giuseppe Piccardo, Italy
Francesco Canestrari, Italy	Jian Ji, China	Prodromos Psarropoulos, Greece
Paolo Castaldo, Italy	Jiang Jin, China	Giuseppe Quaranta, Italy
Giulio Castori, Italy	Andreas Lampropoulos, UK	Carlo Rainieri, Italy
Robert Černý, Czech Republic	Raffaele Landolfo, Italy	Damien Rangeard, France
Constantin Chalioris, Greece	Eul-Bum Lee, Republic of Korea	Dimitris Rizos, USA
Noel Challamel, France	Chun-Qing Li, Australia	Geoffrey W. Rodgers, New Zealand
Daniel W.M. Chan, Hong Kong	Dongsheng Li, China	Hugo Rodrigues, Portugal
Carlos Chastre, Portugal	Li Li, Canada	Hamid Reza Ronagh, Australia
Ghassan Chehab, Lebanon	Xuemei Liu, Australia	Pier Paolo Rossi, Italy
Wensu Chen, Australia	Zaobao Liu, China	Lukasz Sadowski, Poland
Nicholas Chileshe, Australia	Davide Lo Presti, UK	Anna Saetta, Italy
Heap-Yih (John) Chong, Australia	Cristiano Loss, Canada	Timo Saksala, Finland
Francesco Colangelo, Italy	Lyan-Ywan Lu, Taiwan	Evangelos J. Sapountzakis, Greece
Ottavia Corbi, Italy	Eric Lui, USA	Vassilis Sarhosis, UK
Marco Corradi, Italy	Zhongguo John Ma, USA	Halil Sezen, USA
Mario D'Aniello, Italy	Lorenzo Macorini, UK	M. Shahria Alam, Canada
Jorge de Brito, Portugal	Yann Malecot, France	Faiz U.A. Shaikh, Australia
Gianmarco de Felice, Italy	John Mander, USA	Mostafa Sharifzadeh, Australia
Stefano de Miranda, Italy	Giuseppe Carlo Marano, Italy	Sanjay Kumar Shukla, Australia
Tayfun Dede, Turkey	Fabio Mazza, Italy	Amir Si Larbi, France
Angelo Di Egidio, Italy	Claudio Mazzotti, Italy	Stefano Sorace, Italy
Luigi Di Sarno, Italy	Ahmed Mebarki, France	Flavio Stochino, Italy

Claudio Tamagnini, Italy

Yaya Tan, China

Patrick W.C. Tang, Australia

Yinshan Tang, UK

Huu-Tai Thai, Australia

Filippo Ubertini, Italy

Humberto Varum, Portugal

Castorina S. Vieira, Portugal

Valeria Vignali, Italy

Claudia Vitone, Italy

Hao Wang, USA

Lei Wang, USA

Linbing Wang, USA

Wayne Yu Wang, UK

Roman Wan-Wendner, Austria

Bo Xia, Australia

Wei-Chau Xie, Canada

Michael Yam, Hong Kong

Libo Yan, Germany

Jian Yang, China

Xu Yang, Australia

Hui Yao, China

Victor Yepes, Spain

Gürol Yildirim, Turkey

Qingliang Yu, Netherlands

Mariano Angelo Zanini, Italy

Xiong Zhang, USA

Yuqing Zhang, UK

Dong Zhao, USA

Xianbo Zhao, Australia

Annan Zhou, Australia

Abdul Aziz bin Abdul Samad, Malaysia

# Contents

## **Advancements in Design and Analysis of Protective Structures 2019**

Chiara Bedon , Michel Arrigoni, Filipe Santos , and Lucia Figuli  
Editorial (2 pages), Article ID 2450561, Volume 2019 (2019)

## **A Predictive Model for Damage Assessment and Deformation in Blast Walls Resulted by Hydrocarbon Explosions**

Majid Aleyaasin   
Research Article (13 pages), Article ID 5129274, Volume 2019 (2019)

## **Experimental Study on the Seismic Behaviour of Reinforced Concrete Bridge Piers Strengthened by BFRP Sheets**

Yong Li, Meng-Fei Xie , and Jing-Bo Liu  
Research Article (11 pages), Article ID 4169421, Volume 2019 (2019)

## **Comparative Study of Wellhole Surrounding Rock under Nonuniform Ground Stress**

Zhongyu Jiang  and Guoqing Zhou  
Research Article (9 pages), Article ID 7424123, Volume 2019 (2019)

## **Research on the Obstruction Process of Rigid Netting Barriers toward Granular Flow**

Yunyun Fan  and Fengyuan Wu  
Research Article (18 pages), Article ID 9542129, Volume 2019 (2019)

## **Repairing and Strengthening of Damaged RC Columns Using Thin Concrete Jacketing**

Bassam A. Tayeh, Mohammed Abu Naja, Samir Shihada, and Mohammed Arafa   
Research Article (16 pages), Article ID 2987412, Volume 2019 (2019)

## **Numerical and Experimental Investigation of the Mechanical Behavior of Cable-Supported Barrel Vault Structures with Varying Temperature**

Guojun Sun , Mingze Wu, Zhihua Chen, and Suduo Xue  
Research Article (16 pages), Article ID 4572196, Volume 2019 (2019)

## **Robustness and Resilience of Structures under Extreme Loads**

Flavio Stochino , Chiara Bedon , Juan Sagaseta, and Daniel Honfi  
Review Article (14 pages), Article ID 4291703, Volume 2019 (2019)

## **Comparison of Uplift Capacity and Nonlinear Failure Surfaces of Single-Belled Anchor in Homogeneous and Layered Sand Deposits**

Tanaya Deb  and Sujit Kumar Pal  
Research Article (23 pages), Article ID 4672615, Volume 2019 (2019)

## **Effect of Selected Nanospheres on the Mechanical Strength of Lime-Stabilized High-Plasticity Clay Soils**

Ali Ghorbani , Hadi Hasanzadehshooiili , Mostafa Mohammadi, Fariborz Sianati, Mahdi Salimi, Lukasz Sadowski , and Jacek Szymanowski  
Research Article (11 pages), Article ID 4257530, Volume 2019 (2019)

---

## **Mechanical Properties of High-Strength High-Performance Reinforced Concrete Shaft Lining Structures in Deep Freezing Wells**

Shilong Peng, Chuanxin Rong , Hua Cheng , Xiaojian Wang, Mingjing Li, Bin Tang, and Xuemei Li  
Research Article (14 pages), Article ID 2430652, Volume 2019 (2019)

## **Research on Improved Equivalent Diagonal Strut Model for Masonry-Infilled RC Frame with Flexible Connection**

Guang Yang , Erfeng Zhao , Xiaoya Li, Emad Norouzzadeh Tochaei, Kan Kan , and Wei Zhang   
Research Article (18 pages), Article ID 3725373, Volume 2019 (2019)

## **Buckling Analysis of Sandwich Plate Systems with Stiffening Ribs: Theoretical, Numerical, and Experimental Approaches**

Guangping Zou , Yuyang Wang, Qichao Xue , and Chunwei Zhang  
Research Article (14 pages), Article ID 8737561, Volume 2019 (2019)

## **Improved SDOF Approach to Incorporate the Effects of Axial Loads on the Dynamic Responses of Steel Columns Subjected to Blast Loads**

Junbo Yan , Yan Liu , and Fenglei Huang   
Research Article (9 pages), Article ID 7810542, Volume 2019 (2019)

## **Shear Storage Capacity of Vertical Stiffener Joints between Concrete-Filled Double Steel Tubular Columns and Steel Beams**

Zhijun Zhou , Yufen Zhang , Miao Wang, and Krushar Demoha  
Research Article (9 pages), Article ID 3587982, Volume 2019 (2019)

## **Generation of Uniform Hazard Spectrum Based on the Stochastic Method of Simulating Ground Motion and Its Use in Nuclear Power Plants**

Xueming Zhang , Weiming Yan, Haoxiang He , Yunlun Sun, and Shicai Chen   
Research Article (12 pages), Article ID 6037863, Volume 2018 (2019)

## Editorial

# Advancements in Design and Analysis of Protective Structures 2019

**Chiara Bedon<sup>1</sup>, Michel Arrigoni,<sup>2</sup> Filipe Santos<sup>1,3</sup>, and Lucia Figuli<sup>4</sup>**

<sup>1</sup>*University of Trieste, Trieste, Italy*

<sup>2</sup>*ENSTA Bretagne, Brest, France*

<sup>3</sup>*New University Lisbon, Lisbon, Portugal*

<sup>4</sup>*University of Žilina, Žilina, Slovakia*

Correspondence should be addressed to Chiara Bedon; chiara.bedon@dia.units.it

Received 17 July 2019; Accepted 17 July 2019; Published 28 July 2019

Copyright © 2019 Chiara Bedon et al. This is an open access article distributed under the Creative Commons Attribution License, which permits unrestricted use, distribution, and reproduction in any medium, provided the original work is properly cited.

This ADAP 2019 Annual Issue follows and extends the ADAP Special Volume of 2018 and aims at providing a further insight into current trends and recent advancements in design and analysis, experimental testing, and modelling of protective structures.

From a structural point of view, such a definition includes multiple loading and boundary conditions that designers should properly take into account when ensuring appropriate safety levels to people. In fact, protective structures and facilities are expected to optimally perform their function under severe loads, even when associated with mostly different threats. Extreme events like earthquakes, fire accidents, explosions (even nuclear), and high-rise natural hazards are primary reasons of severe damages in constructed facilities and causalities. Impacts due to collisions of transportation means, on the other hand, should also be properly accounted for when designing bridges or containment structures in general. A key role, in all the mentioned cases, is given to design optimization and mitigation of input forces/effects. Such a result can be achieved by both reducing the magnitude of applied loads on structures, that is, via active, passive, and semiactive additional devices, and enhancing the structural resistance and capacity, that is, via efficient materials and structural components.

With a more general definition of protection and protective tools to improve security, different means are indeed accepted, being possible to achieve the final protective goal at the emergency management level rather than at the material/

structural level only, thus suggesting a cooperation of multiple aspects and expertise.

The revised papers included in the final ADAP Annual Issue booklet are related to various topics, including studies at the management, material, and assembly levels, under a multitude of loads.

Blast loads and explosions still represent one of the major attractions for research studies (M. Aleyasin; J. Yan et al.). Accurate predictive models for damage assessment of several structural typologies are mandatory for calculation, towards the fulfilment of safe design purposes. This is especially the case of strategic buildings, requiring even more conservative and reliable calculations. Also, in presence of seismic events, however, both structural systems, bridges and infrastructures (Y. Li et al.; G. Yang et al.), should be properly investigated, with a special care for soils (X. Zhang et al.; Z. Jiang and G. Zhou; T. Deb and S. K. Pal; A. Ghorbani et al.) or other geological issues (Y. Fan and F. Wu). Extreme loading conditions can also include—for certain structural typologies—deep temperature gradients to properly assess and mitigate via enhanced material properties and retrofit approaches (G. Sun et al.; S. Peng et al.; B. A. Tayeh et al.) or the potential risk of buckling phenomena to prevent via appropriate stiffeners (G. Zou et al.). As a common aspect of these major challenges, design processes should in any case maximize the well-known concepts of robustness, redundancy, and resilience under exceptional loads (F. Stochino et al.).

In conclusion, let us have some final considerations on this ADAP Annual Issue project.

All the contributing authors are warmly acknowledged for their active support. The hope is that—like for the 2018 ADAP version—the readers could renovate their interest, on the topic and find fruitful research outcomes in the published papers.

The involved peer reviewers are also gratefully acknowledged for their continuous and hard work and special efforts for ensuring the publication of high-quality scholarly articles, towards the success of the ADAP 2019 annual edition.

A final dedicated acknowledgement is also extended by the Lead Guest Editor towards the team of Guest Editors for the support they provided for the overall project.

## **Conflicts of Interest**

The editors declare no conflicts of interest.

*Chiara Bedon  
Michel Arrigoni  
Filipe Santos  
Lucia Figuli*

## Research Article

# A Predictive Model for Damage Assessment and Deformation in Blast Walls Resulted by Hydrocarbon Explosions

Majid Aleyasin 

Lecturer School of Engineering, University of Aberdeen, Aberdeen AB24 3UE, UK

Correspondence should be addressed to Majid Aleyasin; eng780@abdn.ac.uk

Received 18 February 2019; Revised 7 May 2019; Accepted 10 June 2019; Published 4 July 2019

Academic Editor: Chiara Bedon

Copyright © 2019 Majid Aleyasin. This is an open access article distributed under the Creative Commons Attribution License, which permits unrestricted use, distribution, and reproduction in any medium, provided the original work is properly cited.

In this paper, a new method is developed to find the ductility ratio in blast walls, resulted by hydrocarbon explosions. In this method, only the explosion energy and distance from the centre of explosion are required to find the damage by using simple predictive models in terms of empirical-type formulas. The explosion model herein is a TNO multiphysics method. This provides the maximum overpressure and pulse duration in terms of the explosion length and distance from explosion centre. Thereafter, the obtained results are combined with the SDOF model of the blast wall to determine the ductility ratio and the damage. By using advanced optimisation techniques, two types of predictive models are found. In the first model, the formula is found in terms of 2 parameters of explosion length and distance from explosion centre. However, the 2<sup>nd</sup> model has 3 parameters of explosion length, distance, and also the natural period of the blast wall. These predictive models are then used to find explosion damages and ductility ratio. The results are compared with FEM analysis and pressure-impulse (P-I) method. It is shown that both types of models fit well with the outputs of the simulation. Moreover, results of both models are close to FEM analysis. The comparison tables provided in this paper show that, in the asymptotic region of P-I diagrams, results are not accurate. Therefore, this new method is superior to classical pressure-impulse (P-I) diagrams in the literature. Advantage of the new method is the easy damage assessment by using simple empirical-type formulas. Therefore, the researchers can use the method in this paper, for damage assessment in other types of blast resistive structures.

## 1. Introduction

Blast walls are sacrificial barriers to protect offshore structures when subjected to hydrocarbon explosions. Substantial research has been performed to develop a code of practice for design of such structures [1]. The theoretical foundations for designing blast-resistive structures and blast walls can be found in [2, 3].

An analytical method based on plate theory for blast wall design [4] is rarely used in the literature since the results of those studies cannot be used directly as a design code. However, linear and nonlinear finite elements have been used significantly (for example, [5, 6]). They are applicable in cases where batch simulations enable cost-benefit analysis [7].

Presently, the dominant approach is a single degree of freedom (SDOF) method [1–3] and leads to some design curves known as Bigg's chart. They appeared first in a

well-known book [8] but originated from the initial attempt by Newmark [9]. This SDOF method enables the famous pressure-impulse (P-I) diagrams which was first introduced in [9] to be constructed [1–3].

These P-I diagrams strongly depend on pressure versus time expression (pulse shape) of the explosion [10], and together with SDOF modelling, they are used to find the blast response of complex of structures, such as cable-supported facades [11]. Both SDOF-type model [12] and continuous beam model [13] are used for developing P-I diagrams. Recently, it is shown that batch finite element simulations [14] cannot lead to P-I diagram unless preliminary information regarding SDOF parameters is available.

Regardless of importance of the P-I diagrams in the damage assessment, they are not straightforward and the designer needs substantial information about the calculation of the explosive loads and pulse shape to be able to use P-I

diagrams in damage assessment. There is not any attempt (or new method) that directly connects intensity of explosion to the resulted damage and deflection in the blast walls. Recently, the author looked at this important issue where, in the vicinity of box girders [15], TNT explosions may occur. Since the possibility of hydrocarbon explosions are much higher than any terrorist activities, blast walls are used in many offshore structures. Therefore, any research regarding this topic is justifiable.

In this article, the explosive physics known as the multienergy method known as TNO [16], and further models fitted into it [17], is combined with the SDOF method for deformation of the blast walls. Thereafter, the deformation and ductility, for both rigid plastic models and elastic-plastic models, are determined in each distance and explosion length. Then outcomes of the batch simulations are exported to advanced optimisation programs to develop two types of predictive models expressed by using simple empirical-type formulas.

Using any of the models in this paper, the designer can find the deformation (or ductility) from the intensity of explosions (explosion length), distance of the blast wall from explosion centre, and natural period of the blast wall. As far as the author is aware, this new method is the easiest one for predicting the damage in the blast wall, thereby declaring the explosion resistance. The knowledge about explosion physics is embedded in the formulas. Therefore, it is an excellent tool for preliminary analysis of the blast wall.

In a case study, in the asymptotic region of the P-I diagram, it is shown that, while P-I provides inaccurate results, this method leads to accurate results, when it is compared with FEM simulation of the blast wall. Therefore, the approach herein can be extended to other types of structures in future to replace P-I diagrams (or FEM) for predicting the damage.

## 2. Overpressure History in Explosions

When hydrocarbon mass  $m_c$  (in kg) with heat energy  $\Delta H_c$  (Joule/kg) causes an explosion with efficiency  $\eta$ , the resulted explosive energy  $E_0$  will be

$$E_0 = \eta m_c \Delta H_c. \quad (1)$$

In the TNO multienergy method [16], an explosion length is defined by

$$R_0 = \left( \frac{E_0}{P_0} \right)^{1/3}, \quad (2a)$$

where  $P_0$  is the atmospheric pressure (in Pa); therefore,  $R_0$  truly has units of the length (m). If  $R_s$  is the distance from the explosion centre (m), dimensionless  $\bar{R}$  will be defined by

$$\bar{R} = \frac{R_s}{R_0} = \left( \frac{E_0}{P_0} \right)^{-1/3} R_s. \quad (2b)$$

Then, the overpressure  $p_{\max}$  (in bar, i.e., dimensionless) and explosion pulse duration  $\bar{t}_+$  (dimensionless) can be found from TNO charts [16]. In those charts, the overpressure and duration can be found from the curves

designated by the level of the explosion. The charts are developed from computer simulations performed in eighties and are strongly applicable to hydrocarbon explosions. Due to the importance of the TNO charts, researchers produced curve fitted formulas for the data in those charts. These formulas are given in [17] via the following equation:

$$\begin{aligned} 0.6 \leq \bar{R} \leq 30 & \quad p_{\max} = 0.0605 \bar{R}^{-0.99} & p_{\max} \bar{t}_+ = 0.0605 \bar{R}^{-0.99} & \text{Level 3,} \\ 0.6 \leq \bar{R} \leq 100 & \quad p_{\max} = 0.301 \bar{R}^{-1.11} & p_{\max} \bar{t}_+ = 0.114 \bar{R}^{-1.03} & \text{Level 6,} \\ 2 \leq \bar{R} \leq 100 & \quad p_{\max} = 0.318 \bar{R}^{-1.13} & p_{\max} \bar{t}_+ = 0.114 \bar{R}^{-1.03} & \text{Level 9.} \end{aligned} \quad (3)$$

It should be reminded that another valuable software is provided for blast waves (for example, [18, 19]) but not reformulated for designers yet (such as (3)). In the above expressions,  $\bar{t}_+$  is dimensionless overpressure pulse duration given in [16]:

$$\bar{t}_+ = \frac{t_d C_0}{R_0}, \quad (4)$$

where  $t_d$  is the overpressure duration in sec and  $C_0$  is the sound velocity at atmospheric conditions in m/sec. Majority of explosions will fall into all of the three levels in (3). It is recommended that the overpressure and duration should be computed in each level and the average value should be taken into consideration [17].

The author herein produced the overpressure contours in terms of  $R_0$  and  $R_s$  which are two important parameters in any explosions. They are shown in Figure 1 and are used in the next part of the paper, for developing the new method.

## 3. SDOF Model for Blast Walls

The typical geometry of the cross section of a blast wall [1] is similar to (a) in Figure 2.

The finite element analysis shows [5] the deformation pattern resulted by an explosion by using shell elements which is similar to Figure 3.

The front view of a typical blast wall [1] is shown in (b) in Figure 2. The main parameter is the pitch  $\bar{p}$  that is shown in (a). The wall is connected to the structure by upper and lower supports shown in (c). When overpressure  $p_{\max}$  is applied to the wall with uniform distribution, the upper and lower supports with thicknesses  $t_U$  and  $t_L$  (in m) (see (c) in Figure 2) have equivalent lengths  $L_U$  and  $L_L$  shown in (Figure 15). They will yield since they have limited yield stress  $f_y^*$  (Pa). The total length is  $L$  (in m), and  $(M_{c,Rd})_U$  and  $(M_{c,Rd})_L$  are the yield moments (per length, i.e., in N) of the upper and lower supports and are given by the following equations [1-3]:

$$\begin{aligned} (M_{c,Rd})_U &= \frac{t_U^2 f_y^*}{4}, \\ (M_{c,Rd})_L &= \frac{t_L^2 f_y^*}{4}. \end{aligned} \quad (5)$$

$M_{c,Rd}$  or the plastic bending moment (per unit length) of the main wall is given by (6). It depends on the details of the

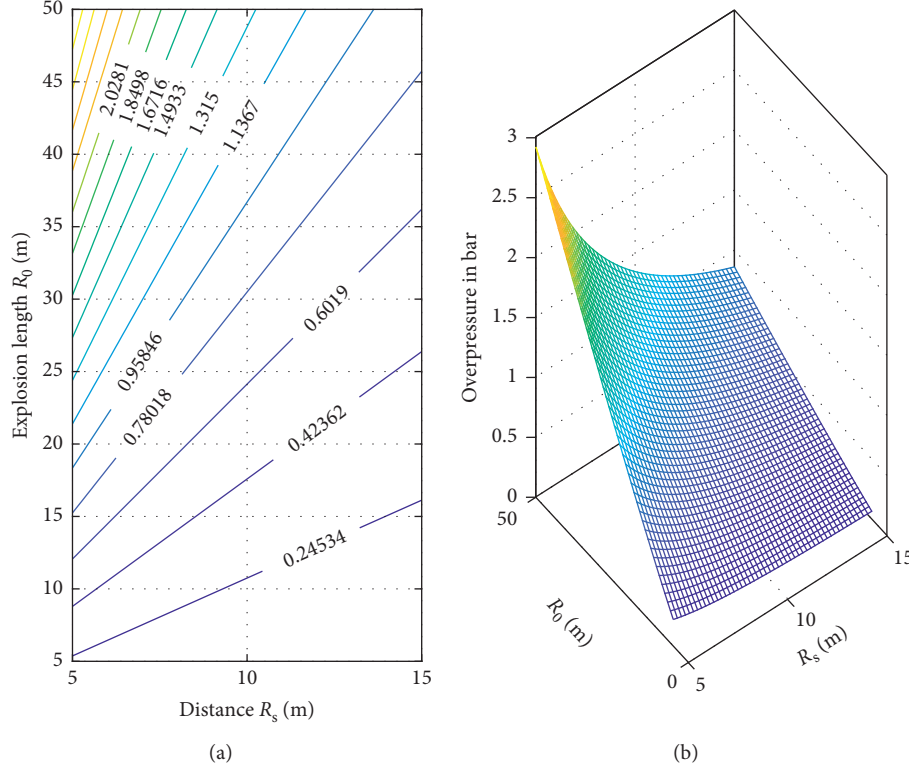


FIGURE 1: Overpressure in the TNO model for explosion. (a) Overpressure contours in bar. (b) Average value of levels 3, 6, and 9.

cross section in (a) in Figure 2, which are designated by two parameters,  $W_{\text{pl},y}$  (plastic section modulus) and  $f_y^*$  (material yield stress) of the cross section:

$$M_{c,Rd} = \frac{W_{\text{pl},y} f_y^* K_F K_{VM}}{\bar{p}}. \quad (6)$$

$K_F$  and  $K_{VM}$  in (6) are flattening and shear correction factors described in [1]. The equivalent length of the blast wall  $L_E$  is less than the total length  $L$  and can be found by

$$L_E = \frac{2L}{\sqrt{1 + ((M_{c,Rd})_L/M_{c,Rd})} + \sqrt{1 + ((M_{c,Rd})_U/M_{c,Rd})}}. \quad (7)$$

Derivation of (7) is shown in Appendix A, and instead of total length,  $L_E$  will be used in all calculations, regarding the blast wall. For example, the stiffness per unit length will be given as shown in [1–3] as follows:

$$k = \frac{384EI}{5L_E^3\bar{p}}. \quad (8)$$

The corrected stiffness of wall  $k_R$  is recommended in [1] to correct (8) resulted from beam theory which is

$$k_R = \frac{kL_E}{1.6L - 0.6L_E}. \quad (9)$$

Equations (8), (9), and others that follow are true when the SDOF method is chosen as a route of the analysis, where the beam simplification and can be justified. This is also current practice for the preliminary design of blast walls

[1–3]. However, for the detail of the buckling pattern similar to Figure 3, the beam model simplification is not appropriate. According to rigid plastic theory in structures, the maximum resistance of a beam cross section  $R_m$  [2, 3] is given by

$$R_m = \frac{8M_{c,Rd}}{L_E}. \quad (10)$$

This  $R_m$  is defined for finding maximum elastic deformation of the wall  $\gamma_{el}$  [1–3] by using the following formula:

$$\gamma_{el} = \frac{8M_{c,Rd}}{k_R L_E}. \quad (11)$$

However, if the maximum blast load  $F_1$  given by the following equation exceeds  $R_m$ , the wall deforms plastically:

$$F_1 = A_s p_{\max}. \quad (12)$$

In (12),  $A_s$  is the projected blast area per pitch in Figure 4. For further clarification, this area with the pressure  $p_{\max}$  applied to it is shown in Figure 4.

The deformation is allowed up to the ductility limit. The ductility  $\mu$  is very important in design of structures under extreme and blast loading [2, 3, 8] and is the ratio of maximum plastic deformation to the elastic limit  $\gamma_{el}$  given by

$$\mu = \frac{\gamma_{\max}}{\gamma_{el}}. \quad (13)$$

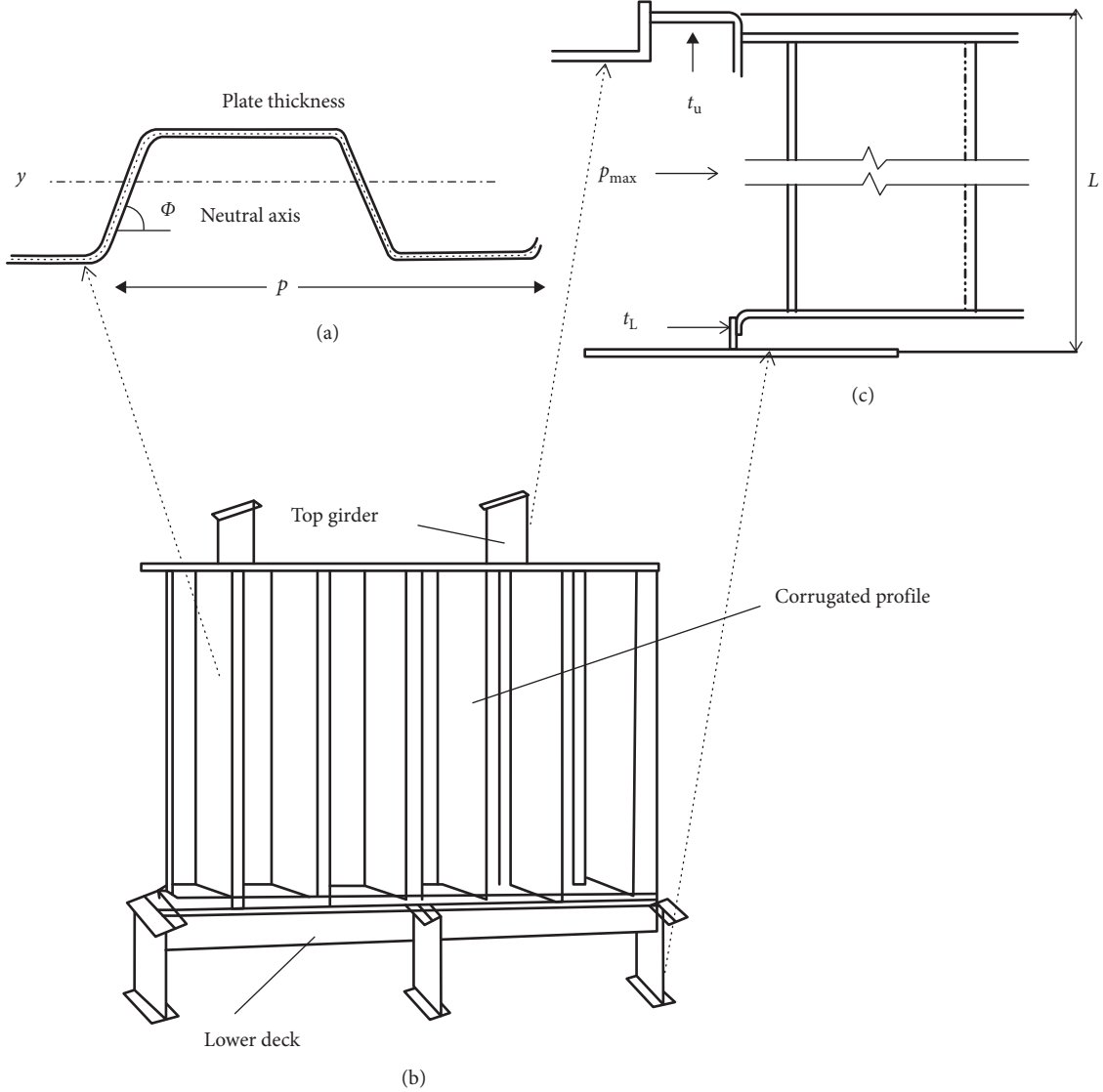


FIGURE 2: (a) Cross section of the (b) blast wall (front view) and (c) upper and lower supports.

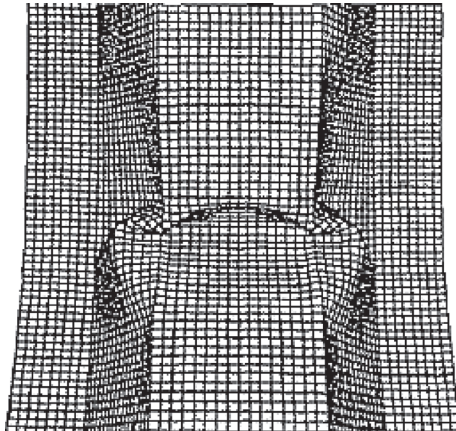


FIGURE 3: Deformation pattern from FEM analysis.

The backbone of the SDOF model relies on the natural period of free structural vibration  $T$ , [2, 3, 8] of the blast wall which will be given by

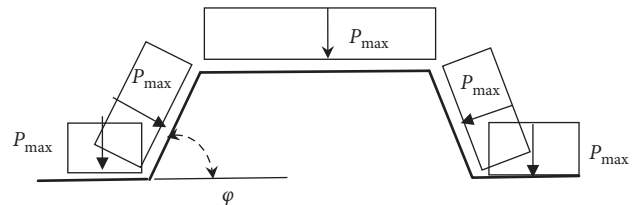


FIGURE 4: Applied pressure on the wall surface.

$$T = 2\pi \sqrt{\frac{MK_{LM}}{\bar{p}k_R}} \quad (14)$$

In (14),  $M$  is the blast wall mass (for one pitch) and  $K_{LM}$  is the correction factor for the distributed mass. In Appendix B, it shows that for rigid plastic theory based on plastic hinge assumption [2, 3], we find that  $K_{LM} = 0.333$ . However, in the current practice [1], designers use higher values without any justification. Part of this article

investigates how this apparent inconsistency can affect the ductility results.

The SDOF modelling is well known by Biggs' chart since it appeared in a famous book [8]. However, the initial research is done by Newmark who is one of the pioneers in structural dynamic. He summarised Biggs' chart a decade before it is seen in [8], in his famous paper [9] by using the following formula:

$$\frac{F_1}{R_m} \cong \frac{\sqrt{2\mu - 1}}{(t_d/T)\pi} + \frac{(1 - (1/2\mu))(t_d/T)}{(t_d/T) + 0.7}. \quad (15)$$

All the parameters in (15) are described in previous formulas. When an explosion with length  $R_0$  occurs at distance  $R_s$ , one can find the preliminary ductility curves. For a particular blast wall that is designed by a manufacturer, geometrical and material details are available. Therefore, the ductility contour can be constructed easily from (15), without using the pressure-impulse diagram of the blast wall.

#### 4. Numerical Example

For a steel blast wall with pitch  $\bar{p} = 1.2$  meter, the cross-sectional dimensions are shown in Figure 5. It is one of the existing profiles of the blast wall that is described in [1].

The second moment of the cross section  $I = 8.767 \times 10^{-5} \text{ m}^4$ , the section modulus  $W_{\text{ply}} = 4.37 \times 10^{-4} \text{ m}^3$ , mass per pitch  $M = 410 \text{ kg}$ , thicknesses of the upper and lower supports  $t_U = 12 \text{ mm}$  and  $t_L = 10 \text{ mm}$ , and Young's modulus  $E = 210 \text{ GPa}$ , and yield stress  $f_y^* = 400 \text{ MPa}$ , the length  $L = 3 \text{ m}$ , and the correction factors [1]  $K_F = 0.9$  and  $K_{VM} = 0.95$ . In Figure 6, the ductility is shown, which is the result of substantial simulations of the SDOF model for this blast wall.

Figure 6 is prepared for  $K_{LM} = 0.85$  as recommended in [1] and is not the result of rigid plastic theory. Figure 6 is drawn in range  $15 < R_0 < 25$  and  $5 < R_s < 10$ , and the contours seem linear and visible. However, for higher ranges, visibility and linearity cannot be observed.

#### 5. Model with Two Parameters

A nonlinear predictive model of Figure 6 with two parameters  $R_0$  and  $R_s$  (both explosion related) can be suggested in this form:

$$\mu \cong C_{\mu 2} R_0^\alpha R_s^\beta. \quad (16)$$

For example, the higher range estimation of ductility for can be replaced by the following approximate expression:

$$\mu \cong 1.0008 R_0^{4.2434} R_s^{-6.2520}, \quad 20 < R_0 < 50, 10 < R_s < 15. \quad (17)$$

In Figure 7, the computed ductility ratio and the estimated ductility ratio in (17) are drawn together. It can be concluded that, in higher ductility ratios, where severe plastic deformation occurs, the estimated ductility is very close to the computed ductility. In (17), only explosion-

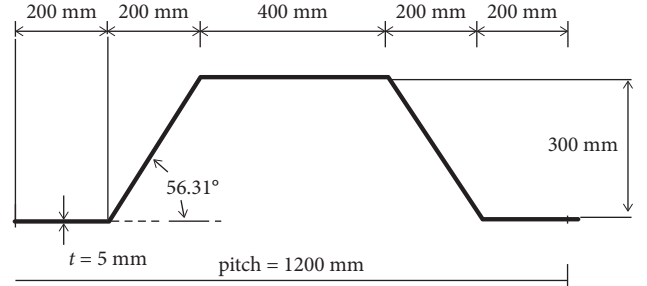


FIGURE 5: A typical cross section (one pitch) of a blast wall [1].

related parameters are used. Three parameter models will be discussed as well.

#### 6. Rigid Plastic Modelling

Rigid plastic theory [2, 3] assumes plastic hinge at the midlength of the blast wall. In appendix B, it is shown that, in such situation, the equivalent mass  $M_e = M/3$  and  $K_{LM} = 0.333$ . The damage calculation will be straightforward because the calculations regarding overpressure and duration remain the same as the ones used for producing Figure 7. Obviously if we assume  $K_{LM} = 0.333$ , the results will change which is shown in Figure 8. The region in which ductility ratio is below 1 remains elastic, and by producing such contour maps, the pressure-impulse diagram is not required. If we compare Figure 6 in which peak deformation  $y_{\max} = 3.75 y_{el}$  with Figure 8 in which  $y_{\max} = 5.03 y_{el}$ , we can conclude that considering  $K_{LM} = 0.333$  (rigid plastic model) provides conservative estimation for ductility.

#### 7. Model with Three Parameters

A nonlinear predictive model with three parameters  $R_0$ ,  $R_s$  (explosion related), and  $T$  in (14) which are blast wall related can be suggested as in the following form:

$$\mu \cong C_{\mu 3} R_0^\alpha R_s^\beta T^\gamma. \quad (18)$$

The parameters  $C_{\mu 3}$ ,  $\alpha$ ,  $\beta$ , and  $\gamma$  in (18) can be found by taking the logarithm for that expression that will change it into

$$\log(\mu) \cong \log(C_{\mu 3}) + \alpha \log(R_0) + \beta \log(R_s) + \gamma \log(T). \quad (19)$$

The above expression enables the linear regression techniques to be implemented for finding the parameters  $C_{\mu 3}$ ,  $\alpha$ ,  $\beta$ , and  $\gamma$ . These parameters can be found by using nonlinear regression analysis. Moreover, the powerful Nelder–Mead algorithm [20] which is built in MATLAB is also used, to find the fractional powers  $\alpha$ ,  $\beta$ , and  $\gamma$  in (18). Finally, the numerical expression of (18) when  $K_{LM} = 0.333$  (rigid plastic modelling) will be in the following form:

$$\mu \cong 1.0008 R_0^{4.4483} R_s^{-6.1082} T^{0.2698}, \quad 20 < R_0 < 50, 10 < R_s < 15. \quad (20)$$

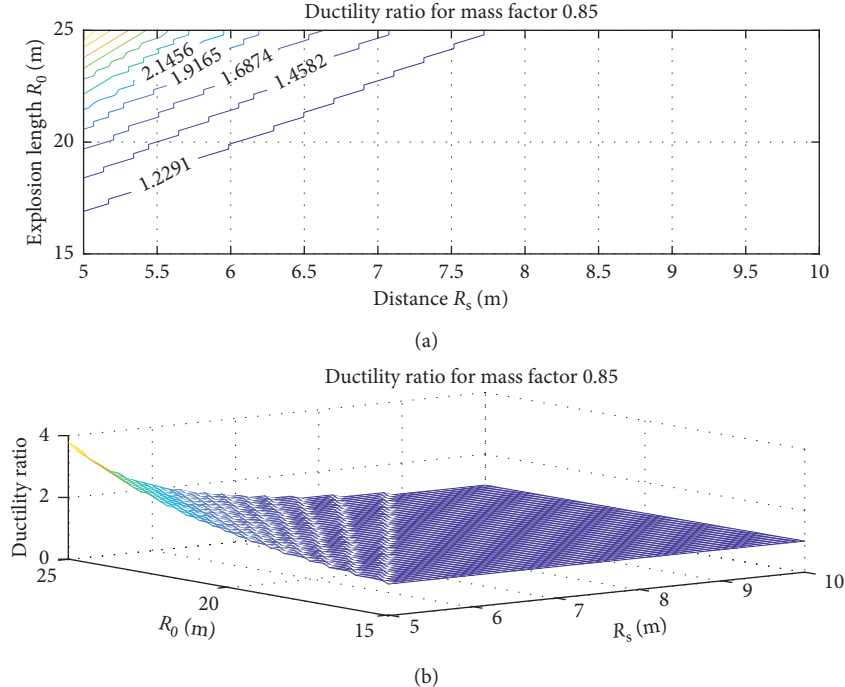


FIGURE 6: Contours for the ductility ratio.

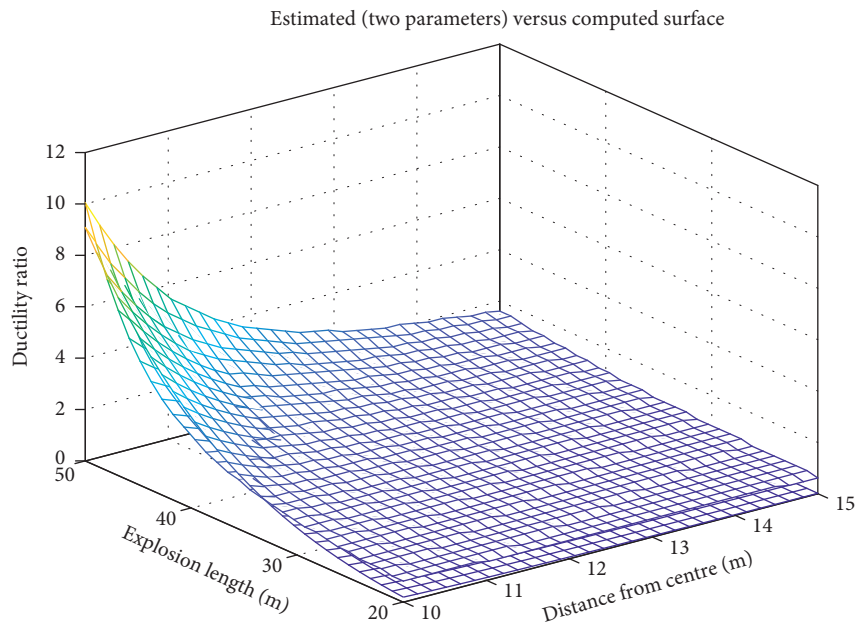


FIGURE 7: Computed versus estimated ductility ratio.

In Figure 9, the computed ductility ratio and the estimated ductility ratio in (20) are drawn together. It can be concluded that, in higher ductility ratios, where severe plastic deformation occurs, the estimated ductility is very close to the computed ductility. In (20), explosion-related parameters plus blast wall natural period are used. Three-parameter models use  $K_{LM} = 0.333$  (rigid plastic modelling) because of its conservativeness in estimation of the maximum ductility.

The author has suggested many other forms for the regression analysis, using advanced optimisation techniques

[20], and so far, he has not found better forms than (20) for the 3-parameter-type model and (17) for the 2-parameter-type model. It is quite possible that some other forms with closest fit may be found by further research.

## 8. Comparison of the Results

Consider that an explosion with effective energy  $E_0 = 9500 \text{ MJ}$  occurs at distance  $R_s = 12 \text{ m}$  from the explosion centre. According to parameters (2a), (2b) and (3).

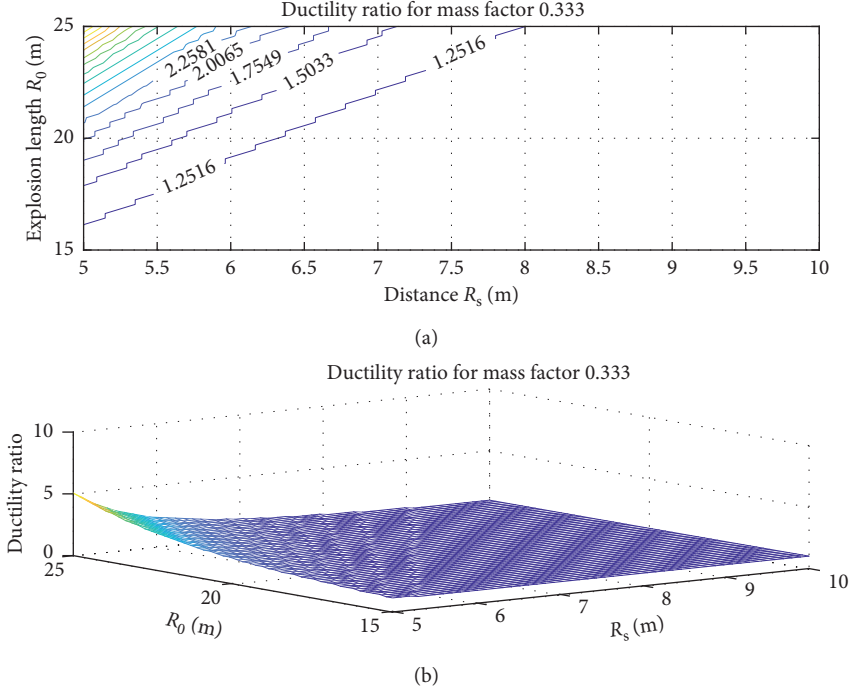


FIGURE 8: Contours for the ductility ratio in the rigid plastic model.

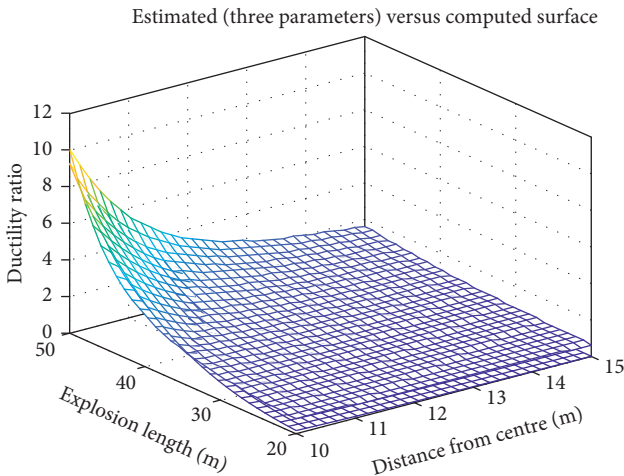


FIGURE 9: Computed versus estimated ductility ratio.

The overpressure is the average value of the explosion levels 3 and 9 and 6, in (3).

$$\begin{aligned} R_0 &= 45.629 \text{ m}, \\ \bar{R} &= 0.263, \\ P_{\max} &= 0.997 \text{ bar}. \end{aligned} \quad (21)$$

The elastic deformation from (11) is  $y_{\text{el}} = 7.8 \text{ mm}$ , whereas the maximum deflection at the middle section,  $y_{\max}$ , in (12) can be found by knowing about the ductility ratio.

Since the velocity of sound in the room temperature condition is  $C_0 = 340 \text{ m/sec}$ , from formula (4), we have duration of the explosion pulse  $t_d = 74 \text{ msec}$ , whereas the

natural period of the blast wall herein which is given by using (14) is  $T = 16.1 \text{ msec}$ .

The pressure-impulse curve that introduced before is still used for damage assessment for many structures. They are a series of the asymptotic curves inscribed in the vertical and horizontal asymptotes. To find the points on the curves, either we use analytical methods [21, 22] or numerical methods [23] and sometimes FEM analysis [24]. In the  $x$ - $y$  plane, the vertical axis displays  $F_{\max}/K_e y_{\text{el}}$ , whereas horizontal axis displays  $x = I/y_{\text{el}} \sqrt{K_e M_e}$ ,  $I$  is the impulse, and  $F_{\max}$  is the maximum explosion forces. With uniform overpressure, they are

$$\begin{aligned} F_{\max} &= A_{\text{eff}} P_{\max}, \\ I &= 0.5 F_{\max} t_d. \end{aligned} \quad (22)$$

In [2, 3], it can be shown that the equations of the vertical and horizontal asymptotes are in terms of the ductility ratio  $\mu$  that is defined in (13), i.e.,

$$\begin{aligned} \frac{I}{y_{\text{el}} \sqrt{K_e M_e}} &= \sqrt{2\mu - 1}, \\ \frac{F_{\max}}{K_e y_{\text{el}}} &= \frac{2\mu - 1}{2\mu}. \end{aligned} \quad (23)$$

Typical curves for elastic-plastic structures are shown in Figure 10 in which the ductility ratio can be found via interpolation. The snapshot designated by the point shows the coordinates  $I/y_{\text{el}} \sqrt{K_e M_e} = 13.622$  and  $F_{\max}/K_e y_{\text{el}} = 1.03$  that correspond to this particular explosion, and we can find the ductility  $\mu \approx 7.24$  as a result of this explosion.

However, the direct simulation in this paper shows that  $\mu \approx 2.414$ . It shows that the P-I method particularly in asymptotic ends are significantly inaccurate. The two

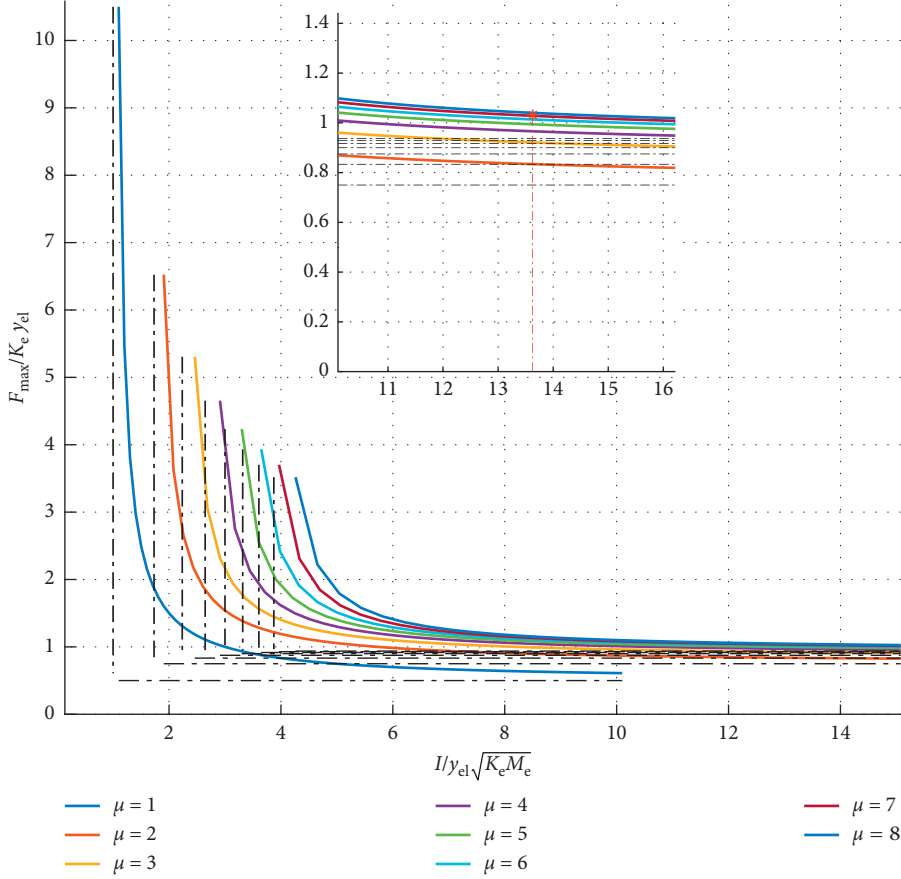


FIGURE 10: Pressure-impulse diagram for elastic-plastic structures.

approximated models in this paper that are expressed by (17) and (20) to replace the P-I method give much closer results. The comparison is shown in Table 1.

Further comparison can be done by using FEM technique via ABAQUS modelling [25] of the blast wall in this example. The meshing is shown by a snapshot in Figure 11. In this model 6500-shell-type S4R elements, each with nine internal integration point are used. Obviously substantial FEM outputs, including the local buckling details in bottom flanges are available. However, the one that can be compared with  $y_{\max}$  in (12) has been extracted. Since ductility ratio is not defined in ABAQUS, Table 2 is provided to compare the  $y_{\max}$  (maximum deflection) in each approach.

The last row of Table 2 is found from history of the displacement of the middle of the top flange of the blast wall. This history for  $U$ ,  $V$ , and  $A$  is shown in Figure 12. It is obvious that velocity in mm/s and acceleration in m/s<sup>2</sup> are big numbers since  $T$  in (14) is very low.

Figure 12 is prepared by using history of nodes. However, the history of stress and strain in any location of the blast wall can be prepared by element output files. Similar to Figure 11, Figure 13 shows the Mises stress map that is scaled in Pa.

Obviously, the yield stress is  $f_y^* = 400$  MPa, and the material is assumed elastic-perfectly plastic (E-P-P); all similar to the SDOF model. Since the blast wall is modelled with shell elements, Poisson's ratio of the material  $\nu = 0.3$  is

TABLE 1: Comparison of the results (ductility ratio).

The method used	Ductility ratio
TNO + SDOF simulation	$\mu \geq 2.414$
Pressure-impulse curves	$\mu \geq 7.24$
Two-parameter empirical formula (17)	$\mu \geq 1.968$
Three-parameter empirical formula (20)	$\mu \geq 2.019$

also required. The history of the Mises stress and also the maximum principal strain can be found from the element file. To do this, the shell element corresponding to middle of the top flange of the blast wall is chosen. The history file for stress and stain for that location is shown in Figure 14. It is obvious that stress does not exceed 400 MPa. However, for strain after quick jump at the beginning of the explosion, the fluctuations are not significant. From the model in this paper, we can check and verify the displacement as shown in Table 2. This suits the purpose of this paper in developing a simple and accurate model for checking high-fidelity FEM analysis.

In Table 3, the material properties and also maximum velocity, acceleration, and stress and strain are shown. The maximum displacement is shown in Table 2 for the comparison purposes. The maximum stress in Table 3 exceeded slightly above 400 MPa because the E-P-P material model is ABAQUS, which is expressed via a very low plastic Young's modulus (not zero).

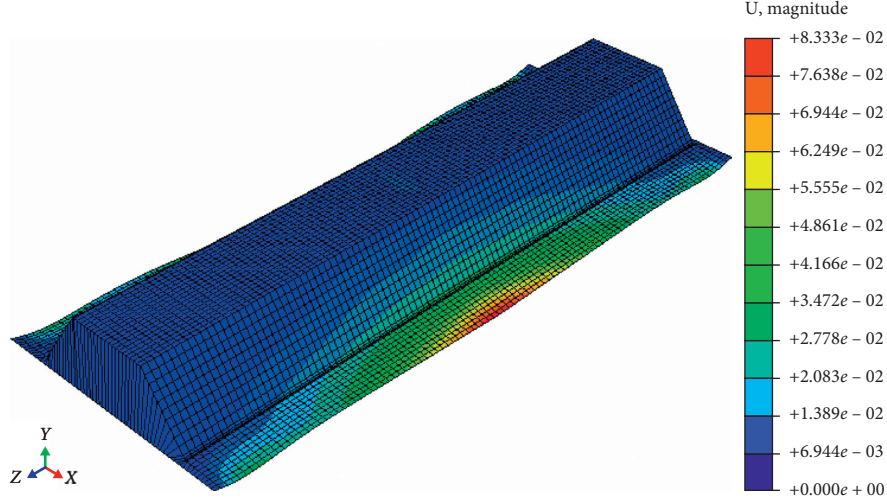


FIGURE 11: FEM meshing of the blast wall (displacement map in m).

TABLE 2: Comparison of the results (maximum deflection).

The method used	Maximum deflection
TNO + SDOF simulation	$y_{\max} \cong 18.9$ mm
Pressure-impulse curves	$y_{\max} \cong 56.7$ mm
Empirical formula (17)	$y_{\max} \cong 13.2$ mm
Empirical formula (20)	$y_{\max} \cong 15.8$ mm
FEM analysis via ABAQUS	$y_{\max} \cong 19.5$ mm

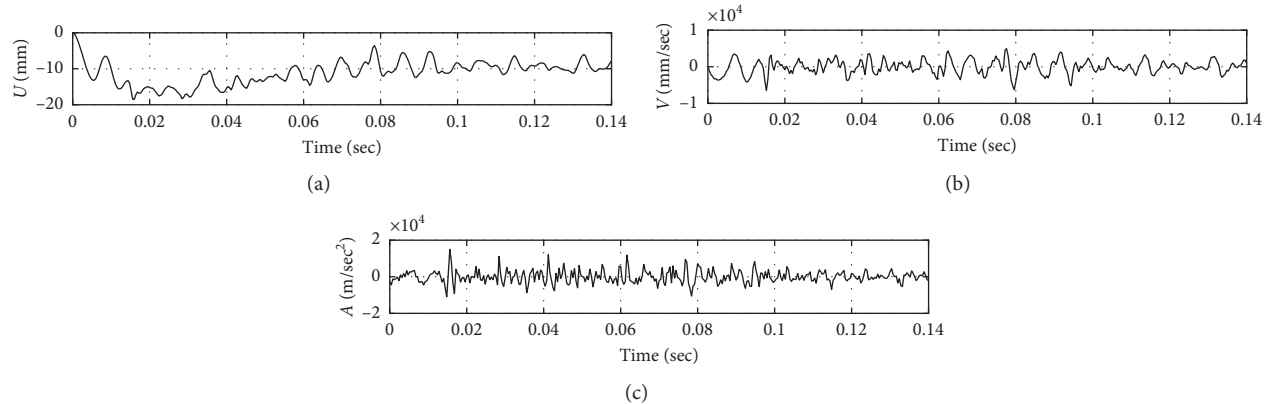


FIGURE 12: (a) Displacement (deflection), (b) velocity, and (c) acceleration history of the top flange.

The outcomes of this section are shown in Table 4. This table compares the advantages and disadvantage of each method that is discussed. It can be seen that there are many advantages of using the method in this paper, particularly when we compare with the pressure-impulse diagram. However, it should be used together with high-fidelity FEM analysis to achieve more details about the response of the blast wall to the explosion.

## 9. Conclusions and Remarks

In this paper, a new method for damage assessments in blast walls are developed. It is much easier than the classical method of the pressure-impulse diagram and FEM analysis. As shown in [21–24], and also in this paper, the high-fidelity analytical or FEM models cannot predict explosion response without knowledge about explosion overpressure and pulse duration.

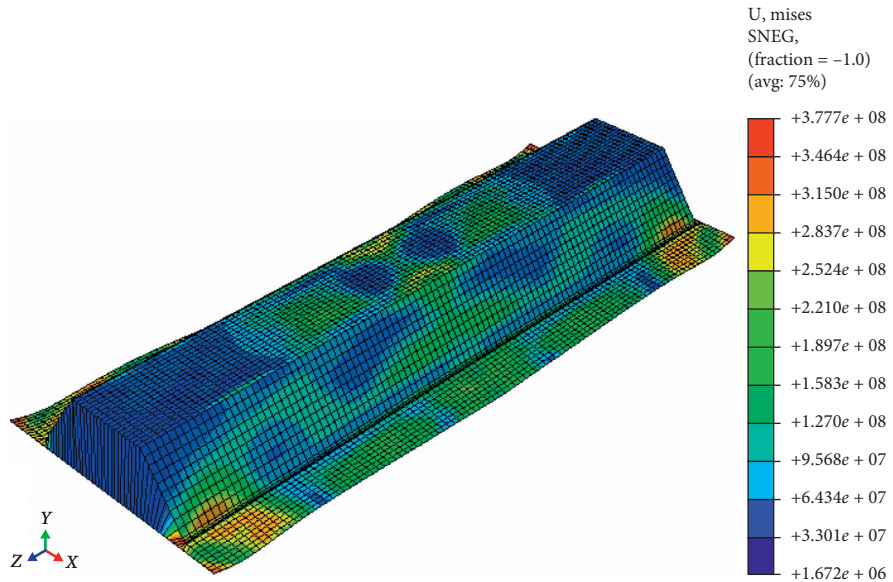


FIGURE 13: Mises stress map scaled in Pa.

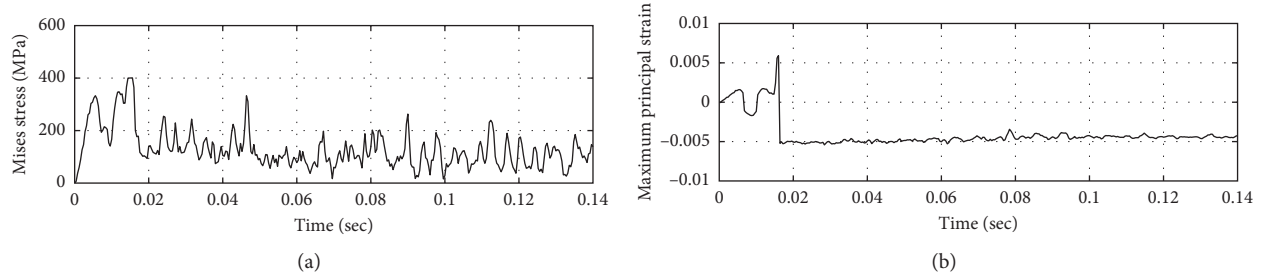


FIGURE 14: History of (a) Mises stress and (b) maximum plastic strain of the middle of top flange.

TABLE 3: Summary of FEM analysis (results are for middle of the top flange).

Young's modulus for E-P-P steel	$E = 210 \text{ GPa}$
Poisson's ratio	$\nu = 0.3$
Maximum velocity	$v_{\max} = 6456 \text{ mm/s}$
Maximum acceleration	$a_{\max} \cong 15001 \text{ m/s}^2$
Maximum Mises stress	$\sigma_{\max} \cong 400810000 \text{ Pa}$
Maximum principal strain	$\varepsilon_p = 00059$

TABLE 4: Comparison table for methods discussed.

The method used	Advantages	Disadvantages
TNO + SDOF simulation	(1) Reliable source for checking FEM (deflection) (2) Simple compared to FEM	(1) Low fidelity compared to FEM analysis (2) Includes the model for history of overpressure
Pressure-impulse curves	(1) Simple to find the ductility and displacement	(1) Inaccuracy in asymptotic region (2) Needs overpressure history (3) Low fidelity compared to FEM analysis
Empirical formulas (17) and (20) in this paper	(1) No need for history of overpressure (2) Simple to find the ductility and displacement (3) Reliable source for checking FEM (deflection)	(1) Low fidelity compared to FEM analysis
FEM analysis via ABAQUS	(1) High fidelity of the model (2) Availability of results in any location (3) Local buckling details	(1) Needs overpressure history (2) Meshing difficulties and model complexity (3) Verification of the results by another method

The inaccuracy of the P-I diagram in the asymptotic region is clearly shown in this paper via Tables 1 and 2. Regardless of that, the P-I diagram is an active field of research

for blast-resistive structure as seen in recent publications [22–24]. Therefore, an alternative method is required to replace the P-I diagram in asymptotic region. This approach

should be much easier than FEM analysis and can produce a result accurate enough to be compared with FEM. The author believes that he has found an alternative in this paper.

When overpressure-time history is not available, both of the SDOF and FEM cannot predict the damage. The advantage of this new method is the combination of SDOF method and overpressure-time history of explosion. Herein the TNO method (that provides overpressure history) with SDOF (that provides deflection) has been combined together. Thereafter approximate formulas have been produced that easily predicts the ductility ratio without using P-I diagrams or doing SDOF calculations or FEM analysis. Therefore, it will be very useful for preliminary design applications.

## Symbols

$A_s:$	Cross-sectional area
$A, B, C:$	Constants of the parabolic function
$A_{\text{eff}}:$	Effective overpressured area
$C_0:$	Velocity of sound
$E_0, E:$	Explosive energy and modulus of elasticity
$f_y^*, F_1:$	Steel yield stress and total applied force
$F_{\max}:$	The maximum explosion force
$I:$	Second moment of cross section (in bending)
$I:$	Impulse of the explosion pulse
$k, k_R:$	Stiffness and reduced stiffness (in bending)
$K_F, K_{VM}:$	Flattening and shear correction factors
$K_{LM}:$	Mass correction factor
$L, L_E:$	Total length and equivalent length
$L_U, L_L:$	Lengths of the upper and lower supports
$M, M_e:$	Mass and equivalent mass of the blast wall
$m_c:$	Hydrocarbon mass
$(M_{c,Rd})_U,$	Yield bending moment in the upper and
$(M_{c,Rd})_L:$	lower supports
$M_{c,Rd}:$	Yield bending moment in the blast wall
$p_{\max}:$	Maximum overpressure
$\bar{p}, p_0:$	Projected blast area per pitch and atmospheric pressure
$R_0, \bar{R}:$	Explosion length and dimensionless explosion length
$R_m:$	Maximum elastic resistance of beam cross section
$R_s:$	Distance from explosion centre
$\bar{t}_+, t_d:$	Dimensionless pulse duration and pulse duration
$t_U$ and $t_L:$	Thicknesses of the upper and lower supports
$T:$	Natural period of the structure
$W_{\text{pl,y}}:$	Plastic section modulus
$W_0:$	Maximum deflection of the midspan
$y_{el}, y_{\max}:$	Maximum elastic and maximum plastic deformation
$\Delta H_c:$	Heat energy
$\alpha, \beta, \gamma:$	Constants in the predictive model
$\mu:$	Ductility ratio
$\eta:$	Efficiency of explosion.

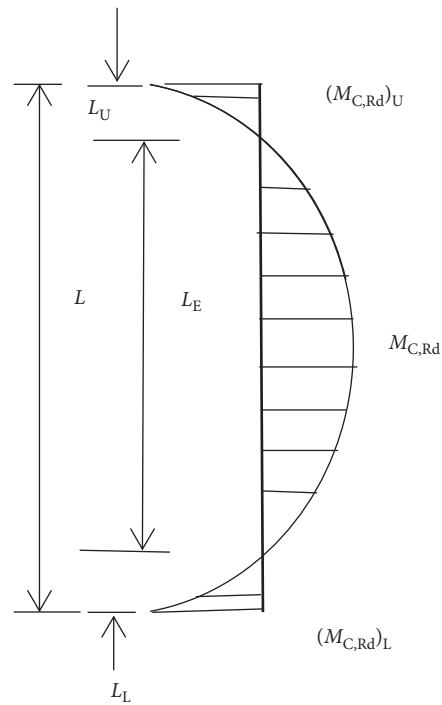


FIGURE 15: Parabolic bending moment distribution.

## Appendix

### A. Equivalent Lengths and Bending Moment Distribution

According to Figure 15, the total length of the blast wall consist of 3 parts:

$$L = L_E + L_U + L_L. \quad (\text{A.1})$$

The overpressure as a result of explosion produces a uniform load that results a parabolic type of bending moment as follows:

$$M(x) = Ax^2 + Bx + C. \quad (\text{A.2})$$

When we place the origin of the coordinate system at the middle of the wall, then we have

$$M(0) = A \times 0^2 + B \times 0x + C = M_{c,Rd} \implies C = M_{c,Rd}. \quad (\text{A.3})$$

Moreover, the shear force at maximum bending moment is zero, i.e.,

$$\begin{aligned} \frac{dM}{dx} &= 2Ax + B, \\ \frac{dM}{dx}(0) &= 2A \times 0 + B = 0 \implies B = 0. \end{aligned} \quad (\text{A.4})$$

The segment with length  $L_E < L$  acts as the simply supported beam such that, in its two ends, the bending moment is zero such that

$$\left(\frac{L_E}{2}\right) = A \times \left(\frac{L_E}{2}\right)^2 + 0 \times \frac{L_E}{2} + M_{c,Rd} = 0 \implies A = \frac{-4M_{c,Rd}}{L_E^2}. \quad (\text{A.5})$$

Then, (A.2) can simplified into

$$M(x) = M_{c,Rd} \left( 1 - \frac{4x^2}{L_E^2} \right). \quad (\text{A.6})$$

The upper and lower supports of the blast wall act as cantilevers such that maximum bending moments of the supports occur at the corners such that

$$\begin{aligned} M(0.5L_E + L_U) &= M_{c,Rd} \left( 1 - \frac{4(0.5L_E + L_U)^2}{L_E^2} \right) \\ &= -(M_{c,Rd})_U \implies \frac{4(0.5L_E + L_U)^2}{L_E^2} \\ &= 1 + \frac{(M_{c,Rd})_U}{M_{c,Rd}}, \end{aligned} \quad (\text{A.7})$$

$$\begin{aligned} M(0.5L_E + L_L) &= M_{c,Rd} \left( 1 - \frac{4(0.5L_E + L_L)^2}{L_E^2} \right) \\ &= -(M_{c,Rd})_L \implies \frac{4(0.5L_E + L_L)^2}{L_E^2} \\ &= 1 + \frac{(M_{c,Rd})_L}{M_{c,Rd}}. \end{aligned} \quad (\text{A.8})$$

The expressions (A.7) and (A.8) can be simplified into

$$\begin{aligned} L_U &= \frac{L_E}{2} \left( \sqrt{1 + \frac{(M_{c,Rd})_U}{M_{c,Rd}}} - 1 \right), \\ L_L &= \frac{L_E}{2} \left( \sqrt{1 + \frac{(M_{c,Rd})_L}{M_{c,Rd}}} - 1 \right). \end{aligned} \quad (\text{A.9})$$

Substituting (A.9) into (A.1), and after simplification, we have equation (7):

$$L_E = \frac{2L}{\sqrt{1 + ((M_{c,Rd})_U/M_{c,Rd})} + \sqrt{1 + ((M_{c,Rd})_L/M_{c,Rd})}}. \quad (\text{A.10})$$

## B. Rigid-Plastic Beam Model

In rigid plastic type of modelling, the plastic hinge occurs at the middle of the beam where the maximum lateral deflection  $W_0$  will occur (Figure 16).

Obviously, the lateral deformation and velocity pattern will be linear and are given by

$$W = \frac{W_0}{(L/2)} x \implies \dot{W} = \frac{W_0}{(L/2)} \dot{x}. \quad (\text{B.1})$$

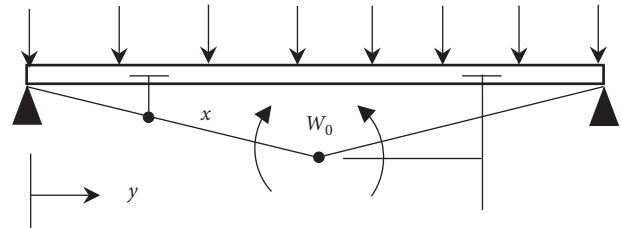


FIGURE 16: Plastic hinge in the simply supported beam.

Then, considering the form in (B.1), the overall kinetic energy of the beam will be

$$\begin{aligned} KE &= 2 \int_0^L \frac{1}{2} \rho A (\dot{W}(x))^2 dx = \rho A \int_0^L \left( \frac{x}{L/2} \dot{W}_0 \right)^2 dx \\ &= \frac{4\rho A \dot{W}_0^2}{L^2} \int_0^{L/2} x^2 dx = \frac{4\rho A \dot{W}_0^2 L^3}{24L^2} = \frac{1}{6} M \dot{W}_0^2. \end{aligned} \quad (\text{B.2})$$

The equivalent mass  $M_e$  located at the plastic hinge position should possess the same kinetic energy in (B.2), i.e.,

$$KE = \frac{1}{2} M_e \dot{W}_0^2. \quad (\text{B.3})$$

Comparing (B.2) with (B.3) will result

$$\frac{1}{2} M_e \dot{W}_0^2 = \frac{1}{6} M \dot{W}_0^2 \implies M_e = \frac{1}{3} M. \quad (\text{B.4})$$

## Data Availability

The data used to support the findings of this study are available from the corresponding author upon request.

## Conflicts of Interest

The author declares no conflicts of interest.

## Acknowledgments

The author appreciates Aberdeen University for the time provided to him for doing independent research as part of his duties of an academic post.

## References

- [1] Fire and Blast Information Group (FABIG), "Design guide for stainless steel blast walls," Technical Note 5, Fire and Blast Information Group Berkshire (UK), Berkshire, UK, 1999.
- [2] M. Y. H. Bangash and T. Bangash, *Explosion-Resistant Buildings: Design, Analysis, and Case Studies*, Springer, New York, NY, USA, 2006.
- [3] T. Krauthammer, *Modern Protective Structures*, CRC Press, Boca Raton, FL, USA, 2008.
- [4] J. Q. Fang, P. Chung, and R. W. Wolfe, "Analysis of a blast-loaded protective wall for bridge columns," *Bridge Structures*, vol. 4, no. 3-4, pp. 135–141, 2008.
- [5] L. A. Louca, M. Punjani, and J. E. Harding, "Non-linear analysis of blast walls and stiffened panels subjected to hydrocarbon explosions," *Journal of Constructional Steel Research*, vol. 37, no. 2, pp. 93–113, 1996.

- [6] G. K. Schleyer, T. H. Kewaisy, J. W. Wesevich, and G. S. Langdon, "Validated finite element analysis model of blast wall panels under shock pressure loading," *Ships and Offshore Structures*, vol. 1, no. 3, pp. 257–271, 2006.
- [7] H. Y. Lei, J. C. Lee, C. B. Lia et al., "Cost–benefit analysis of corrugated blast walls," *Ships and Offshore Structures*, vol. 10, no. 5, pp. 565–574, 2015.
- [8] J. M. Biggs, *Introduction to Structural Dynamics*, McGraw-Hill, New York, NY, USA, 1964.
- [9] N. M. Newmark, *An Engineering Approach to Blast Resistance Design*, Vol. 121, University of Illinois, Champaign, IL, USA, 1956.
- [10] Q. M. Li and H. Meng, "Pulse loading shape effects on pressure-impulse diagram of an elastic-plastic, single-degree-of-freedom structural model," *International Journal of Mechanical Sciences*, vol. 44, no. 9, pp. 1985–1998, 2002.
- [11] C. Amadio and C. Bedon, "Viscoelastic spider connectors for the mitigation of cable-supported façades subjected to air blast loading," *Engineering Structures*, vol. 42, pp. 190–200, 2012.
- [12] J. Dragos, C. Wu, and K. Vugts, "Pressure-impulse diagrams for an elastic-plastic member under confined blasts," *International Journal of Protective Structures*, vol. 4, no. 2, pp. 143–162, 2013.
- [13] A. S. Fallah, E. Nwankwo, and L. A. Louca, "Pressure-impulse diagrams for blast loaded continuous beams based on dimensional analysis," *Journal of Applied Mechanics*, vol. 80, no. 5, article 051011, 2013.
- [14] M. H. Hedayati, S. Sriramula, and R. D. Neilson, "Dynamic behaviour of unstiffened stainless steel profiled barrier blast walls," *Ships and Offshore Structures*, vol. 13, no. 4, pp. 403–411, 2018.
- [15] M. Aleyasin, "Protective and blast resistive design of post-tensioned box girders using computational geometry," *Advances in Civil Engineering*, vol. 2018, Article ID 4932987, 7 pages, 2018.
- [16] A. C. Van den Berg, "The multi-energy method: a framework for vapour cloud explosion blast prediction," *Journal of Hazardous Materials*, vol. 12, no. 1, pp. 1–10, 1985.
- [17] F. D. Alonso, E. G. Ferradás, J. F. S. Pérez, A. M. Aznar, J. R. Gimeno, and J. M. Alonso, "Characteristic overpressure-impulse-distance curves for vapour cloud explosions using the TNO multi-energy model," *Journal of Hazardous Materials*, vol. 137, no. 2, pp. 734–741, 2006.
- [18] P. W. Sielicki and M. Stachowski, "Implementation of sapper-blast-module, a rapid prediction software for blast wave properties," *Central European Journal of Energetic Materials*, vol. 12, no. 3, pp. 473–486, 2015.
- [19] A. Alia and M. Souli, "High explosive simulation using multi-material formulations," *Applied Thermal Engineering*, vol. 26, no. 10, pp. 1032–1042, 2006.
- [20] J. C. Lagarias, J. A. Reeds, M. H. Wright, and P. E. Wright, "Convergence properties of the nelder–mead simplex method in low dimensions," *SIAM Journal on Optimization*, vol. 9, no. 1, pp. 112–147, 1998.
- [21] V. R. Feldgun, D. Z. Yankelevsky, and Y. S. Karinski, "A nonlinear SDOF model for blast response simulation of elastic thin rectangular plates," *International Journal of Impact Engineering*, vol. 88, pp. 172–188, 2016.
- [22] Y. Ye, L. Zhu, X. Bai, T. X. Yu, Y. Li, and P. J. Tan, "Pressure-impulse diagrams for elastoplastic beams subjected to pulse-pressure loading," *International Journal of Solids and Structures*, vol. 160, pp. 148–157, 2019.
- [23] R. Yu, D. Zhang, L. Chen, and H. Yan, "Non-dimensional pressure-impulse diagrams for blast-loaded reinforced concrete beam columns referred to different failure modes," *Advances in Structural Engineering*, vol. 21, no. 14, pp. 2114–2129, 2018.
- [24] S. Chen, X. Xing Chen, G. Q. Li, and Y. Lu, "Development of pressure-impulse diagrams for framed PVB-laminated glass windows," *Journal of Structural Engineering*, vol. 145, no. 3, article 04018263, 2019.
- [25] A. Khennane, *Introduction to Finite Element Analysis Using MATLAB and ABAQUS*, CRC Press, Boca Raton, FL, USA, 2013.

## Research Article

# Experimental Study on the Seismic Behaviour of Reinforced Concrete Bridge Piers Strengthened by BFRP Sheets

**Yong Li,<sup>1,2</sup> Meng-Fei Xie<sup>ID,1</sup> and Jing-Bo Liu<sup>2</sup>**

<sup>1</sup>The Key Laboratory of Roads and Railway Engineering Safety Control, Shijiazhuang Tiedao University, Shijiazhuang 050043, China

<sup>2</sup>Department of Civil Engineering, Tsinghua University, Beijing 100084, China

Correspondence should be addressed to Meng-Fei Xie; xiemengfei@126.com

Received 7 January 2019; Revised 11 May 2019; Accepted 18 June 2019; Published 1 July 2019

Academic Editor: Chiara Bedon

Copyright © 2019 Yong Li et al. This is an open access article distributed under the Creative Commons Attribution License, which permits unrestricted use, distribution, and reproduction in any medium, provided the original work is properly cited.

With the continuous development of the ductility capacity concept for seismic design of bridges, the ductility capacity of many existing bridges does not meet the requirements of the current code for seismic performance because of the low reinforcement ratio and reinforcement corrosion of reinforced concrete (RC) piers. Because of their superior mechanical properties and low price, basalt fibre-reinforced polymer (BFRP) sheets have potential application in the seismic retrofits field of existing bridges. To study the seismic strengthening effect of RC pier columns, scaled specimens with standard reinforcement ratios, with low reinforcement ratios according to the past code and with corroded reinforcements, were designed and manufactured and then wrapped and pasted with BFRP sheets on the plastic hinge areas. Pseudostatic tests were conducted to verify the seismic performance of the strengthened and unstrengthened specimens. Experimental results showed that the ultimate flexural capacity, deformation capacity, and energy dissipation capacity of strengthened RC pier columns were superior. Especially for strengthened specimens with low reinforcement ratios or corrosion reinforcement, their seismic performance could rival than that of columns with standard reinforcement ratios, which showed the advantage of BFRP sheets in the seismic retrofitting of existing bridge piers.

## 1. Introduction

Bridge damage in earthquakes leads to traffic interruption and economic losses [1]. At present, there are a large number of viaducts designed according to the elastic seismic design method adopted by the previous seismic design code for highway bridges [2]. After Wenchuan earthquake of 2008, the seismic design code for bridges [3] adopted the ductility seismic design concept which recommends two-stage design and two-level fortification. Additionally, the newest Seismic Ground Motion Parameter Zonation Map of China (GB 18306-2015) increased the areas of seismic fortification intensity of 7° and above and put forward the concept of very rare ground motion [4]. Therefore, bridges in service designed according to the previous seismic design code cannot meet the seismic performance objects of the current seismic design code.

Reinforced concrete (RC) piers of existing viaducts would bear various loads and might also be subjected to the marine environment or severe atmospheric conditions. Chemical

erosion always causes corrosion and mechanical degradation of reinforcements, which affects the usability and safety of the structures. When corroded RC piers are subjected to earthquakes, serious damage or even collapse may occur. Aseismic design is adopted to prevent bridge collapse and control seismic damage to a certain extent. At present, the seismic concept design combining elastic superstructure and ductile substructure is used mostly in the seismic design of bridges [5, 6]. Plastic hinges can appear in certain positions of RC pier columns to realize the ductility seismic design [7, 8]. Therefore, reinforced concrete piers with insufficient flexural ability or ductility ability, unclear plastic hinge positions, or clear positions that are hard to repair need to be retrofitted.

Many studies have been carried out on the seismic reinforcement of viaduct piers with fibre-reinforced polymer (FRP) sheets [9, 10]. At present, commonly used fibres include aramid fibre-reinforced polymer (AFRP), glass fibre-reinforced polymer (GFRP), and carbon fibre-reinforced polymer (CFRP), and CFRP is the most widely used material

because of its excellent properties [11, 12]. However, CFRP is largely imported in China, and its high cost restricts the application. Compared with other FRPs, basalt fibre-reinforced polymer (BFRP) shows a series of good mechanics performance, as shown in Table 1. More importantly, BFRP is derived from natural minerals and worthy to be spread, with advantages of low cost and nonpollution [13, 14].

There are few studies on the application of BFRP sheets in the seismic strengthening of building and bridge structures. Lu et al. [15–17] conducted a study on the seismic performance of earthquake-damaged concrete frame joints reinforced by BFRP sheets. The results showed that the seismic performance of strengthened joints was greatly improved, and all 3-dimensional reinforced concrete frame joints strengthened by BFRP sheets achieved the design object of strong-column and weak-beam. Wu et al. [18] conducted a contrastive study of strengthened short RC columns with BFRP bundles (not BFRP sheets) and CFRP sheets. It was recommended that BFRP bundles can significantly improve the shear capacity and change the failure mode of short RC columns. Because there is less research on BFRP sheets used in seismic strengthening of viaduct piers, quasistatic loading tests of 1:5 scaled pier columns were conducted under low-cycle reciprocating loading to obtain the hysteresis performance curve, and then stiffness, flexural capacity, equivalent viscous damping coefficient, and energy dissipation parameters were analysed to reveal the improvement efficiency of BFRP sheets in seismic strengthening.

## 2. Experimental Design

**2.1. Specimen Design and Fabrication.** Five scaled specimens of circular RC pier columns, 2100 mm high and 240 mm diameter, were designed and fabricated. Two specimens were designed with standard reinforcement ratios and one of them was strengthened; one specimen was designed with lower reinforcement ratio and strengthened; and two specimens were designed with standard reinforcement ratios and corroded and one of them was strengthened. The geometric dimensions and reinforcement details of specimens are shown in Figure 1. The tested cubic compressive strength of concrete was 43.2 MPa. Longitudinal reinforcement included hot-rolled ribbed steel bars 10 mm in diameter, and the tested yield strength was 498.3 MPa. Stirrup bars adopted hot-rolled plain steel bars 8 mm in diameter, and the tested yield strength was 358.3 MPa.

**2.2. Corrosion and Strength of Specimens.** A flume filled with NaCl solution at a concentration of 3.5% was set up in the plastic hinge area of two specimens. Stainless steel tubes were placed in the flume as electrochemical cathodes, and one longitudinal steel bar extending through the top of specimens served as electrochemical anodes. The concentration and volume of the NaCl solution remained unchanged during the electrifying process [19, 20]. The designed density was determined to be 0.6 mA/cm<sup>2</sup> according to Faraday's formula. Details of the corrosion specimens are listed in Table 2, and the electrification process is shown in Figure 2. At the end of corrosion process, both the corroded longitudinal and stirrup steel bars showed

pitting corrosion. The actual corrosion rate was evaluated by the cross-section method. The tested diameters of longitudinal and stirrup steel bars were 9.8 mm and 7.1 mm, respectively. The yield strengths of longitudinal and stirrup steel bars were 309.2 MPa and 281.4 MPa, respectively.

Mechanical properties of the BFRP sheets used for strengthening are shown in Table 3. First, the surface of specimens was polished and smoothed, and then the BFRP sheets coated with adhesive were wrapped and adhered to the specimens. The adhesive was XW-500-A carbon fibre, and the colloidal properties are listed in Table 4. To avoid damage in the lap areas, the lap length was set at 100 mm. One layer of the BFRP sheet was wrapped vertically in the tensile direction, and two layers were wrapped laterally. The adhesion height of each layer was set at 400 mm.

**2.3. Measuring Points Arrangement and Loading System.** Four strain gauges were symmetrically pasted on longitudinal steel bars located on both sides of each specimen. Two strain gauges were pasted on two stirrup bars on one side of the specimen. Four concrete strain gauges were pasted on both sides of each specimen. Four displacement sensors were laterally installed on both sides of the specimen. Another displacement sensor was set up at the top of specimen to measure the lateral deformation of the specimen top. The details of measuring points are shown in Figure 3.

According to the seismic design code [3], the axial compression ratio of regular viaducts should not exceed 0.3. Therefore, the axial compression ratio was set 0.2 during tests. Throughout tests, the vertical load of 146.0 kN was applied at the top of specimens and kept constant. Lateral reciprocating loads were applied to the specimen top, as shown in Figure 4(a). A loading rule of variable amplitude displacement control was adopted to conduct the pseudostatic tests (Figure 4(b)). Testing ended when the lateral bearing capacity of the specimen decreased by 85% of the maximum value or when the specimen was destroyed [21].

The dynamic response of the structural components under seismic loads is partly different from the pseudostatic tests, because of the different Young's Moduli of concrete when it is exposed to quasistatic loads rather than dynamic excitation [22]. However, quasistatic tests can effectively obtain the mechanical properties of structural members, thus providing technical support for the research of the structural resilience model and structural failure mechanism and mode.

## 3. Experimental Results

**3.1. Failure Characteristics of Columns.** As shown in Figure 5, failure characteristics of the strengthened and unstrengthened specimens under quasistatic loading were different. At the initial loading stage, lateral cracks appeared at the plastic hinge area of unstrengthened columns. With the increase in loading, lateral cracks gradually extended and widened. Finally, concrete at the plastic hinge area crushed and the column failed. For the corroded specimen, there were vertical and lateral corrosion cracks with a width of 0.05–0.15 mm before loading (Figure 2(d)). In the initial

TABLE 1: Comparison of different FRPs.

Type	Tensile strength (MPa)	Elastic modulus (GPa)	Maximum elongation (%)	Suitable temperature (°C)
BFRP	3000–4800	80–110	3.30	-200–650
GFRP	3100–4650	73–86	5.20	-60–350
CFRP	3500–6000	230–250	2.20	-100–500
AFRP	2900–3400	70–140	3.60	-60–250

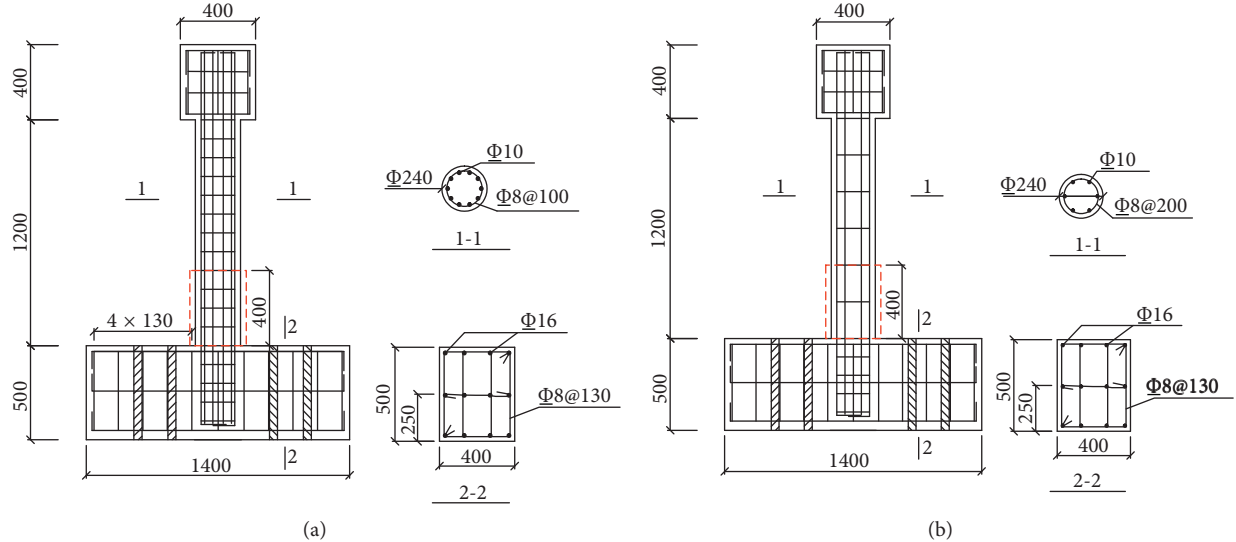


FIGURE 1: Details of specimens: (a) standard reinforcement ratio; (b) low reinforcement ratio (unit: mm).

TABLE 2: Design parameters of specimens.

Numbering	Theoretical corrosion rate (%)	Actual corrosion rate (%)	Longitudinal reinforcement ratio (%)	Volume stirrup ratio (%)	Strengthened by BFRP sheets	Axial pressure ratio
NU-1	—	—	1.7	1.0	No	0.2
NU-2	—	—	1.7	1.0	Yes	0.2
LU-2	—	—	1.1	0.5	Yes	0.2
NC-1	8.0	7.3	1.7	1.0	No	0.2
NC-2	8.0	7.2	1.7	1.0	Yes	0.2

1, unstrengthened; 2, strengthened; C, low reinforcement ratio; N, standard reinforcement ratio; U, uncorroded.

stage of lateral loading, corrosion cracks extended and new cracks appeared gradually. As the lateral load continued to increase, corrosion cracks elongated and widened and more lateral cracks developed. Finally, concrete in the plastic hinge area was crushed, concrete between the corrosion cracks fell off, and the column specimen failed.

For specimens strengthened by BFRP sheets, a slight crackling sound could be heard from the surface of the BFRP sheets in the initial stage of lateral loading, which was caused by a slight fracture between the sheets and the colloid. At the same time, lateral cracks appeared above the reinforced area. As the lateral load continued to increase, lateral cracks in the unstrengthened area above the strengthened area gradually extended and then cracks appeared in the connection between the column bottom and the base. Finally, the cracking failure appeared at the connection between the column and the cap, whereas the plastic hinge area strengthened by BFRP sheets remained in a good condition.

**3.2. Hysteresis Curve.** The load displacement curves of reinforced concrete columns are drawn according to the lateral load and displacement of the specimen top, as shown in Figure 6.

It can be seen in Figure 6 that the reinforcement ratio, steel corrosion, and BFRP sheets all affect the energy dissipation of specimens. The hysteresis loop area, flexural capacity, and ultimate displacement of the unstrengthened specimen NU-1 were smaller than those of the strengthened specimen NU-2. Under multidirectional forces including lateral loads and axial pressure, BFRP sheets delayed the creation and expansion of cracks in the plastic hinge area and thus delayed concrete failure. In addition, the strengthened specimen LU-2, with a low reinforcement ratio, showed an equivalent hysteresis loop area and flexural capacity with the unreinforced column NU-1, with a standard reinforcement ratio.

When the steel bars in specimen NC-1 were corroded, the flexural capacity and ductility of the specimen were



FIGURE 2: Corrosion of specimens: (a) beginning; (b) during corrosion; (c) after corrosion; (d) corroded crack.

TABLE 3: Mechanical properties of BFRP sheets.

Mass density ( $\text{kg}/\text{m}^3$ )	Tensile strength (MPa)	Elastic modulus (GPa)	Elongation at break (%)
3000	3200	105	2.6

TABLE 4: Colloidal properties of carbon fibre adhesive.

Tensile strength (MPa)	Elastic modulus (MPa)	Elongation at break (%)	Bending strength (MPa)	Compressive strength (MPa)
$\geq 40$	$\geq 2500$	$\geq 1.5$	$\geq 50$	$\geq 70$

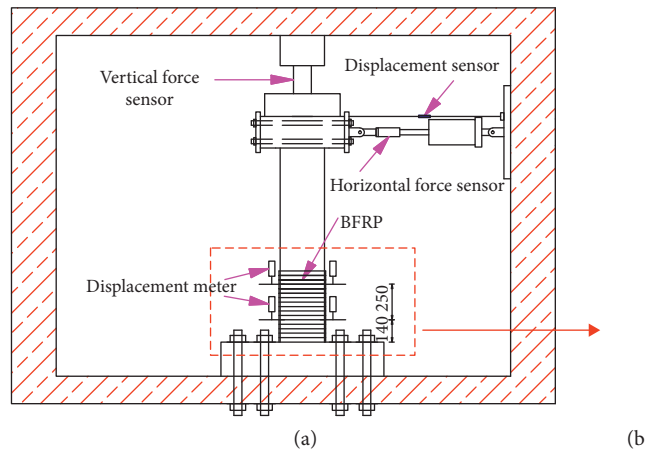


FIGURE 3: Measuring points arrangement: (a) deformation measuring points; (b) strain measuring points (unit: mm).

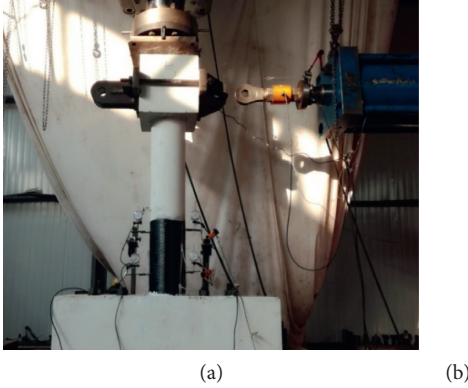


FIGURE 4: Loading system: (a) test devices; (b) actual lateral displacement applied.

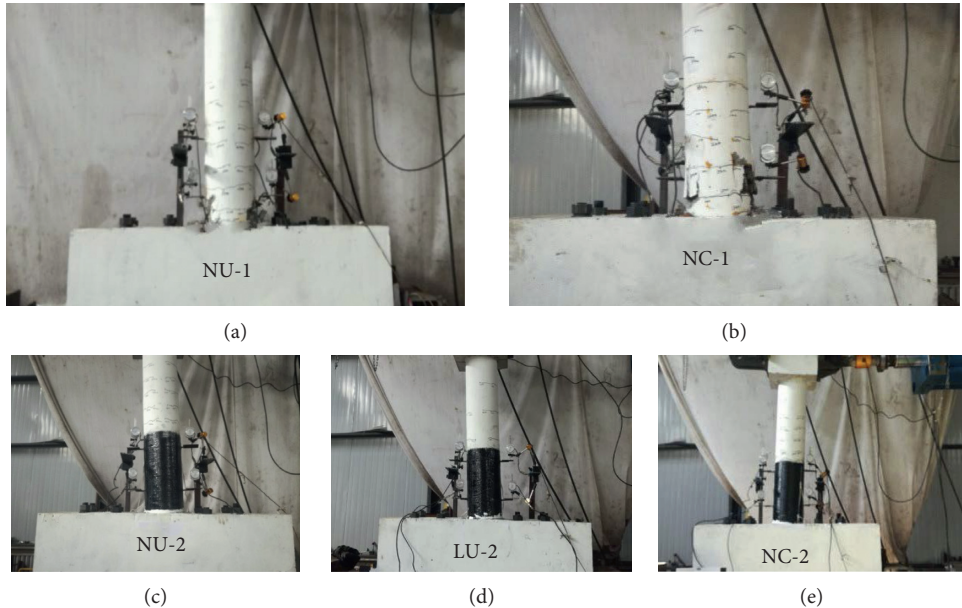


FIGURE 5: Failure characteristics of specimens: (a) NU-1; (b) NC-1 (c) NU-2; (d) LU-2; (e) NC-2.

reduced to a certain extent (Figure 6(d)). After the BFRP sheet strengthened the corroded column, it restrained the lateral expansion of concrete, limited the extension and widening of corrosion cracks, and delayed concrete failure. As a result, the ultimate flexural capacity of the corroded specimen NC-2 was higher than that of unstrengthed specimen NC-1, and the ultimate displacement also greatly increased.

**3.3. Strain Analysis.** The strain of the longitudinal steel bars, stirrups, and BFRP sheets of specimens are shown in Figure 7.

As can be seen in Figure 7, under the same conditions, the reinforcement strain of the strengthened specimen is lower than that of the unstrengthed specimen. At the same time, the yield strain and ultimate strain of the strengthened specimen are both delayed compared with those of the unstrengthed specimen. In Figure 7(c), S-1 and S-2, respectively, represent the vertical strain on the basalt fibre sheet surface 140 mm and 390 mm from the bottom of

specimen. It can be seen in the figure that the vertical strain of the BFRP sheet increases rapidly after the steel reaches yield no matter where it is.

**3.4. Skeleton Curves.** The skeleton curves of specimens were obtained according to the tested hysteretic performance curves, as shown in Figure 8. Furthermore, yield load  $F_y$ , peak load  $F_p$ , ultimate load  $F_u$ , and corresponding drift ratios  $\theta_y$ ,  $\theta_p$ , and  $\theta_u$  as well as ductility coefficient  $\mu$  can be obtained and are shown in Table 5. Ductility coefficient  $\mu$  reflects the ductility of reinforced concrete columns and can be calculated according to the following formula:

$$\begin{cases} \mu = \theta_u / \theta_y, \\ \theta_u = \Delta_u / l, \\ \theta_y = \Delta_y / l, \end{cases} \quad (1)$$

where  $\Delta_y$  and  $\Delta_u$  represent the top displacement of columns at the stage of longitudinal bars yielding and the stage when

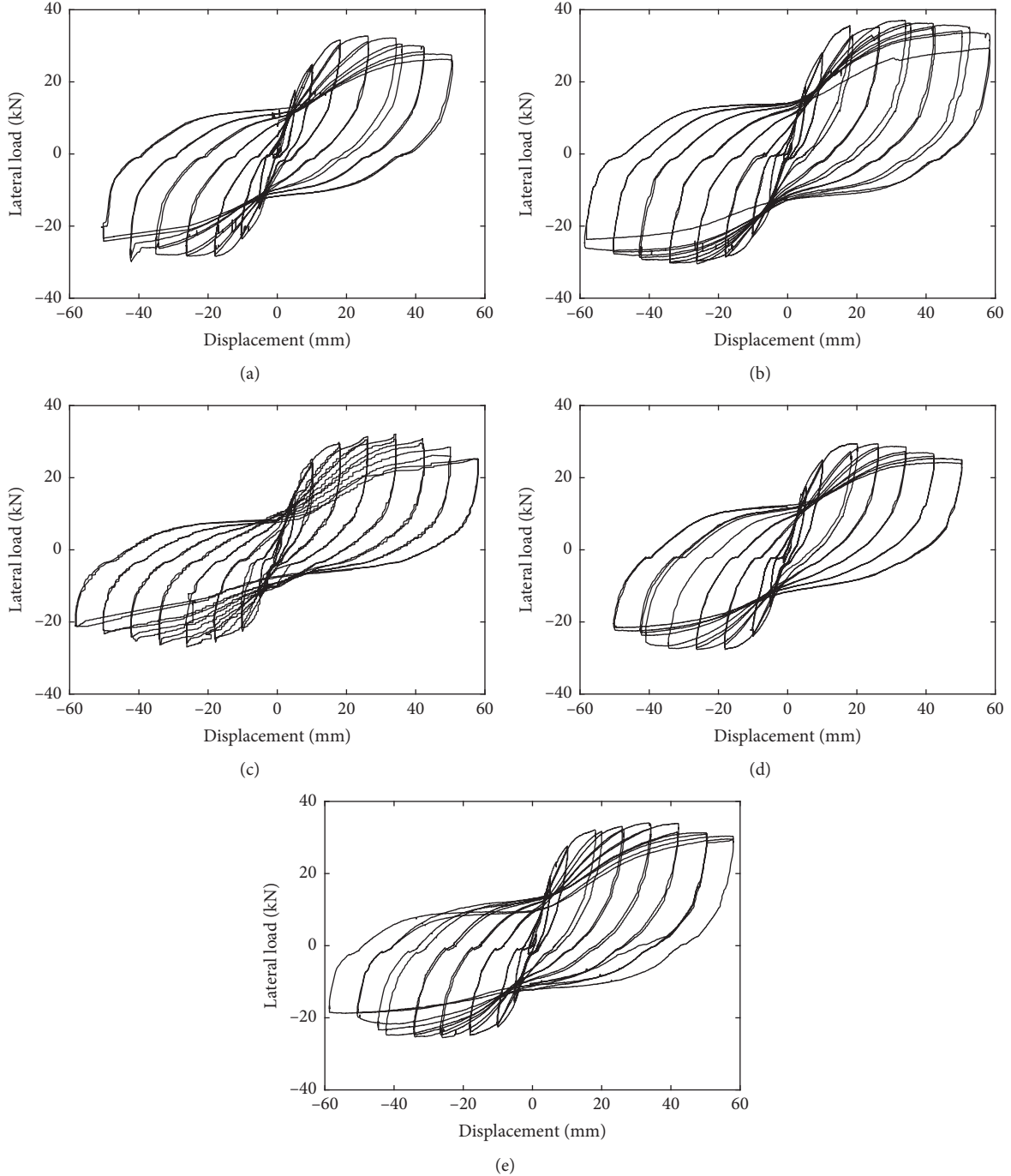


FIGURE 6: Tested hysteresis curve of columns: (a) NU-1; (b) NU-2; (c) LU-2; (d) NC-1; (e) NC-2.

the flexural capacity decreases to 85% of the maximum value, respectively;  $l$  is the height of the circular column and equals 1200 mm.

As can be seen in Figure 8 and Table 5, after the steel bars were corroded, the flexural capacity and ductility of the specimen were significantly reduced. It also can be inferred that when the reinforcement ratio decreased, flexural capacity and ductility of columns would decrease too. However, the ultimate flexural capacity and deformation capacity of columns strengthened by BFRP sheets were higher than

those of unstrengthened columns. The ultimate flexural capacity and lateral displacement rate of NU-2 were 13.46% and 38.04% higher than those of NU-1, respectively. The flexural capacity of LU-2 was strengthened to the flexural capacity level of NU-1, and its ultimate lateral displacement was 22.77% higher than that of NU-1. The ultimate flexural capacity of NC-2 was increased by 18.71% compared with NC-1 and recovered to the flexural capacity level of NU-1. The corresponding lateral displacement ratio was increased by 37.25% compared with NC-1 and 28.07% compared with

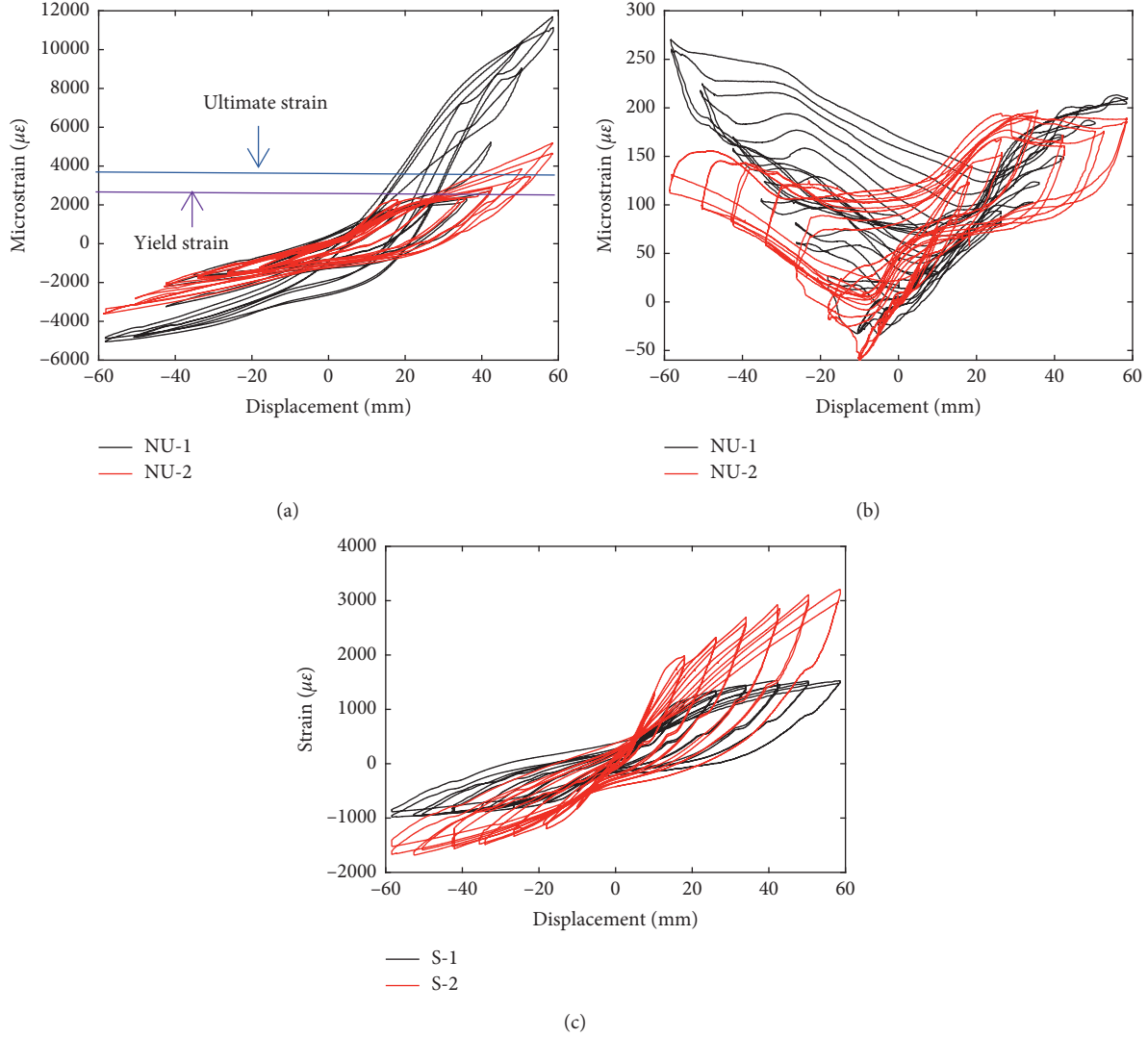


FIGURE 7: Strain analysis: (a) longitudinal reinforcement; (b) stirrup; (c) BFRP sheet of NU-2.

NU-1. It can be concluded that compared with the unstrengthened columns, BFRP sheets can significantly improve the ductility performance of reinforced concrete columns.

**3.5. Energy Dissipation and Equivalent Viscous Damping Coefficient.** Figure 9(a) shows the energy dissipation process of specimens during cyclic loading. The energy dissipation parameter  $E_D$  represents the area of each hysteretic loop of cyclic loading. The cumulative energy dissipation  $E_s$  of specimens from initial loading to failure can be predicted by using the following formula and is shown in Figure 9(b):

$$E_s = \sum_{i=1}^n E_{D_i}, \quad (2)$$

where  $E_{D_i}$  is the energy dissipation of specimens during cyclic loading.

According to Figure 9, reinforcement corrosion reduced the energy dissipation capacity of columns and so did a low

reinforcement ratio inevitably. Compared with the specimen NU-1 with a standard reinforcement ratio, the energy dissipation of NU-2 and LU-2 strengthened by BFRP sheets increased by 46.41% and 16.59%, respectively. Compared with the specimen NC-1, the cumulative energy dissipation of specimen NC-2 increased by 41.82%.

The equivalent viscous damping coefficient  $\xi_{eq}$  also reflects the energy dissipation capacity of columns, which can be calculated by using the following formulas:

$$(E_e)_i = \frac{|+F_i| + |\Delta_i| + |-F_i| - |\Delta_i|}{2}, \quad (3)$$

$$\xi_{eq} = \frac{(E_{D_i})}{2\pi(E_e)_i}, \quad (4)$$

where  $E_e$  is the elastic energy dissipation, and it is the sum of the area of ABO and OCD in the triangle in Figure 10;  $+F_i$  and  $-F_i$  are the maximum and minimum loading values of the first hysteresis loop during the level of  $i$  cyclic loading;  $+\Delta_i$  and  $-\Delta_i$  are corresponding displacement values.

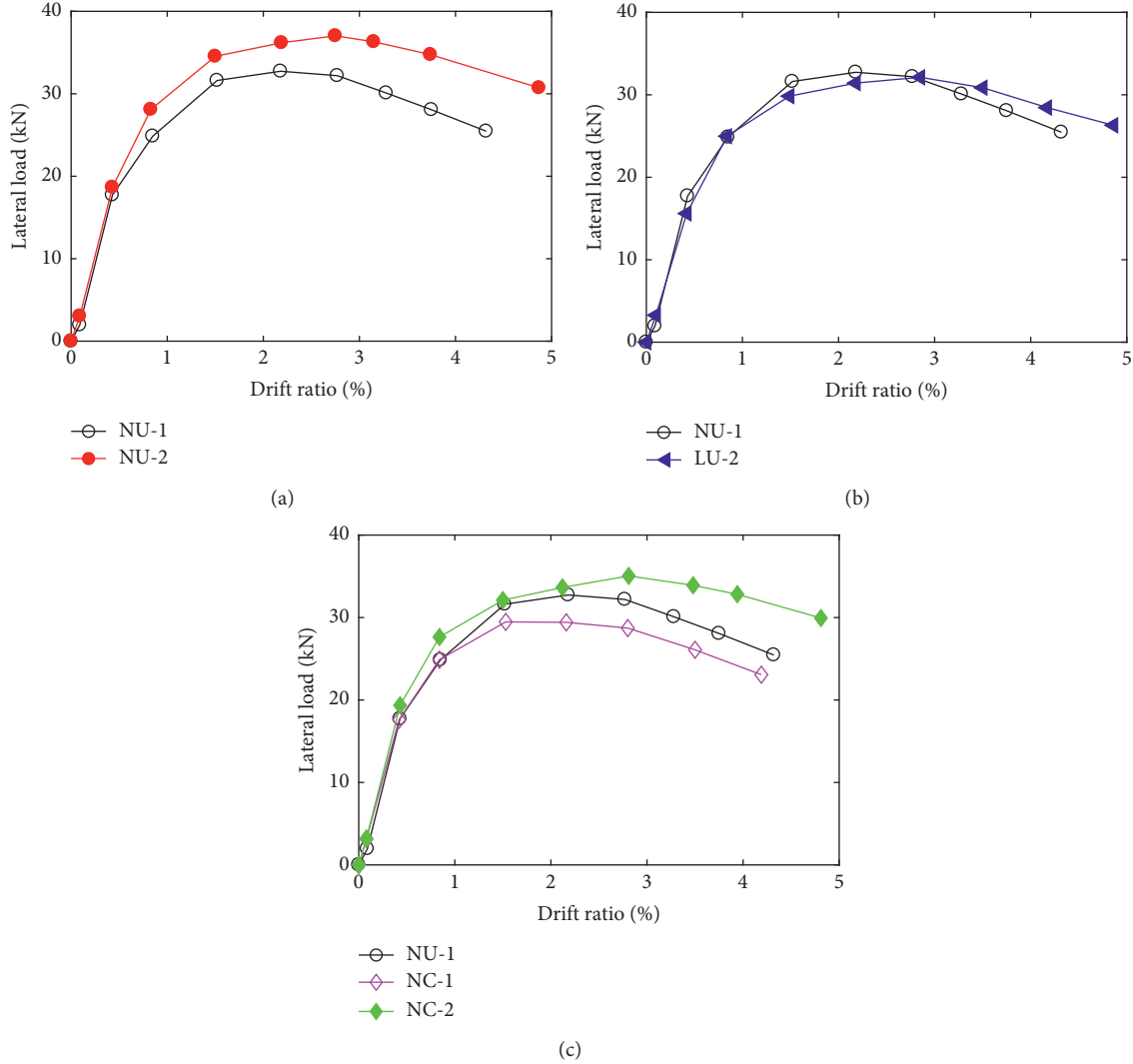


FIGURE 8: Column skeleton curve: (a) NU-1 and NU-2; (b) NU-1 and LU-2; (c) NU-1, NC-1, and NC-2.

TABLE 5: Test result of specimens.

Specimen	Yield		Peak		Ultimate		Ductility parameter $\mu$
	$F_y$ (kN)	$\theta_y$ (%)	$F_p$ (kN)	$\theta_p$ (%)	$F_u$ (kN)	$\theta_u$ (%)	
NU-1	26.71	1.08	32.72	2.18	27.78	3.74	3.47
NU-2	32.14	1.09	37.01	2.75	31.52	4.79	4.38
LU-2	27.01	1.03	32.13	2.85	27.31	4.36	4.26
NC-1	24.49	0.84	29.48	1.53	25.12	3.49	4.16
NC-2	28.92	0.99	35.14	2.81	29.82	4.79	4.87

Here, the equivalent viscous damping coefficient  $\xi_{eq}$  is calculated by taking the first hysteresis loop of the last loading cycle before column failure, as shown in Table 6.

The equivalent viscous damping coefficient of NU-2 was 20.00% higher than that of NU-1, and the equivalent viscous damping coefficient of NC-2 was 9.68% higher than that of NC-1. BFRP sheets slowed the development of cracks and increased the energy dissipation capacity of columns. At the same time, BFRP sheets also dissipated part of the energy. The equivalent viscous damping coefficients of NC-1 and NC-2 were 3.33% and 13.33% higher than those of NU-1,

perhaps because rust filled the pores and cracks of concrete and increased the friction between rust and concrete. The equivalent viscous damping coefficient of LU-2 was close to that of NU-1, which indicated that BFRP sheets can improve the equivalent viscous damping coefficient of columns with low reinforcement ratios to the level of columns with standard reinforcement ratios.

**3.6. Stiffness Degradation Rule.** Because stiffness varies in the loading process, secant stiffness  $K_{gi}$  is usually used to

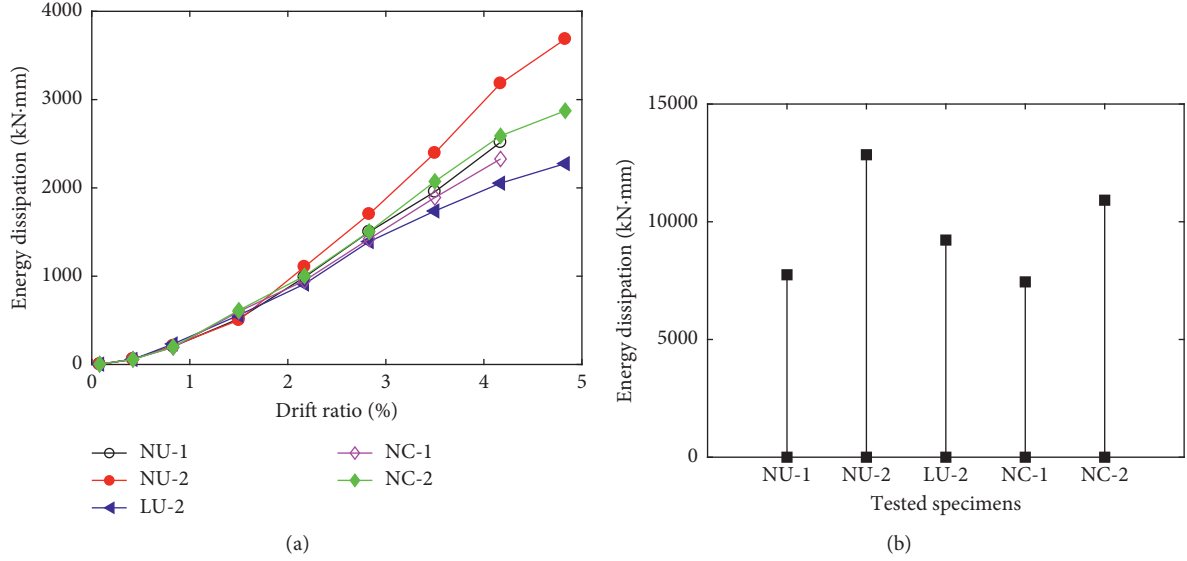
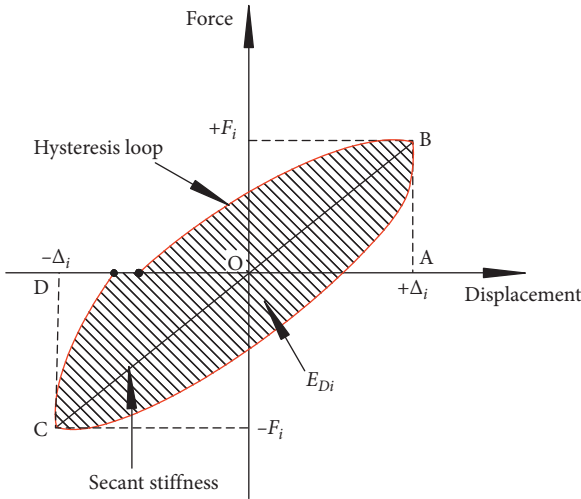
FIGURE 9: Energy dissipation analysis: (a) energy dissipation  $E_D$ ; (b) cumulative energy dissipation  $E_S$ .

FIGURE 10: Schematic diagram of energy dissipation and secant stiffness.

TABLE 6: Equivalent viscous damping coefficient of specimens.

Specimen	Energy dissipation $E_D$ ( $\text{kN}\cdot\text{mm}$ )	Elastic energy dissipation $E_e$ ( $\text{kN}\cdot\text{mm}$ )	Equivalent viscous damping ratio $\xi_{eq}$
NU-1	2517.30	1327.42	0.30
NU-2	3685.23	1646.62	0.36
LU-2	2275.50	1248.82	0.29
NC-1	2327.78	1178.45	0.31
NC-2	2973.72	1416.84	0.34

represent stiffness during seismic response analysis. Secant stiffness can be calculated according to the following formula, and the schematic diagram is shown in Figure 10:

$$K_{gi} = \frac{|+F_i| + |-F_i|}{|+\Delta_i| + |-\Delta_i|}. \quad (5)$$

The stiffness degradation curves of tested specimens are shown in Figure 11.

The stiffness of all specimens decreased along with the increase in lateral displacement. The stiffness degradation rate of NC-1 was higher than that of NU-1, which indicated that reinforcement corrosion would accelerate stiffness degradation. The stiffness degradation curves of LU-2 and NU-1 were basically the same. The stiffness degradation rates of strengthened specimens were lower than those of strengthened ones. Because of the restraining effect of BFRP

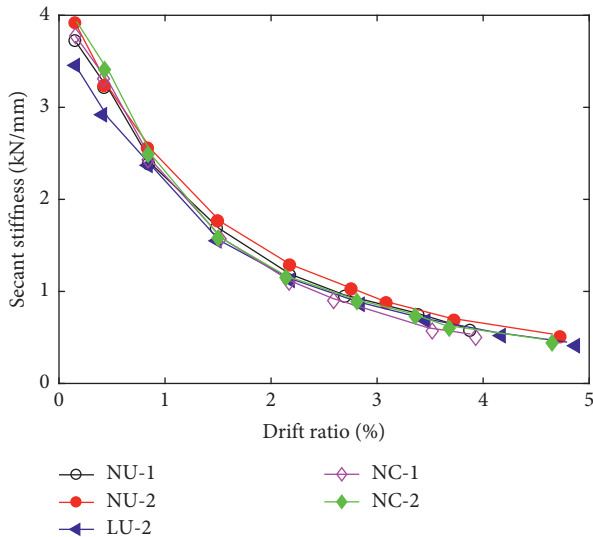


FIGURE 11: Stiffness degradation curves.

sheets, stiffness degradation was delayed and ductility was increased, so that the strengthened columns could still maintain a marginally higher flexural capacity in the case of high deformation and low stiffness in the later loading stage of the tests.

#### 4. Conclusions

Comparative quasistatic tests of scaled reinforced concrete pier columns strengthened by BFRP sheets and unstrengthened ones were carried out under constant axial pressure load and lateral reciprocating load. The failure characteristics, hysteretic performance, skeleton curves, energy dissipation, equivalent viscous damping coefficients, and stiffness degradation are compared and analysed.

- (1) When the unstrengthened reinforced concrete column was damaged, the concrete on both sides of the plastic hinge area fell off in large quantities, whereas BFRP sheets effectively restrained cracks and crush of concrete in the plastic hinge area.
- (2) Under the same conditions, the yield strain and ultimate strain of the strengthened column appeared later than that of the unstrengthened column. Moreover, under the same lateral displacement, the stirrup strain of the strengthened column was lower than that of the unstrengthened column.
- (3) Reinforcement ratio and corrosion rate both affected the energy dissipation of reinforced concrete columns. The flexural capacity and ultimate displacement of strengthened specimens were higher than those of the unstrengthened ones. The strengthened specimen with a low reinforcement ratio showed significantly higher ductility and ultimate flexural capacity than the column with standard reinforcement ratio. When the reinforced concrete column was corroded, its flexural capacity and ductility were reduced to a certain extent. However,

the lateral load capacity and ductility of the strengthened corroded column were close to those of the uncorroded column.

- (4) The ultimate lateral deformation capacity and ductility coefficient of the strengthened columns with standard or low reinforcement ratios and the strengthened corroded specimen were all higher than those of the unstrengthened column with a standard reinforcement ratio.
- (5) The energy dissipation capacity of the strengthened corroded column and the column with a low reinforcement ratio was restored to that of the uncorroded column with a standard reinforcement ratio. The stiffness of the column decreased gradually with the increase in lateral displacement, but stiffness degradation rates of strengthened columns were lower than that of unstrengthened ones.

#### Data Availability

The data used to support the findings of this study are available from the corresponding author upon request.

#### Conflicts of Interest

The authors declare no conflicts of interest.

#### Acknowledgments

This study was supported by the Natural Science Foundation of Hebei Education Department in China (Grant No: BJ2018048), Natural Science Foundation of China (Grant No: 51508350 and 51508351), Natural Science Foundation of Hebei Province in China (Grant No: E2016210087), and Graduate Innovation Funding Project of Shijiazhuang Tiedao University in China (Grant No. YC2019008).

#### References

- [1] X. Li, Z. X. Li, and A. N. Crewe, "Sismic analysis of a high-pier, long-span, continuous RC frame bridge under spatially variable ground motions," *Soil Dynamics and Earthquake Engineering*, vol. 3, pp. 154–196, 2018.
- [2] Ministry of Transport of China, *Specification of Seismic Design Highway Engineering*, (JTJ 044-89), China Communications Press, Beijing, China, 1990.
- [3] Ministry of Transport of China, *Guidelines Seismic Design of Highway Bridges*, (JTJ 044-89), China Communications Press, Beijing, China, 2008.
- [4] National Standardization Administration of China, *China Earthquake Parameter Zoning Map (GB 18306-2001)*, Standard Press of China, Beijing, China, 2002.
- [5] P. Zhu, M. Abe, and Y. Fujino, "Modelling three-dimensional non-linear seismic performance of elevated bridges with emphasis on pounding of girders," *Earthquake Engineering & Structural Dynamics*, vol. 31, no. 11, pp. 1891–1913, 2002.
- [6] J. Hoshikuma, G. F. Zhang, and J. Sakai, "Seismic behavior of retrofit bridges during the 2011 great east Japan earthquake," in *Proceedings of the International Symposium on Engineering Lessons Learned from the 2011 Great East Japan Earthquake*, Tokyo, Japan, March 2012.

- [7] M. B. Ding, X. C. Chen, and X. Y. Zhang, "Study on seismic strengthening of railway bridge pier with CFRP and concrete jackets," *Earthquakes and Structures*, vol. 15, pp. 275–283, 2018.
- [8] B. Guliz, O. Alpay, and A. Enver, "Seismic performance evaluation and strengthening of a curved bridge having concrete piers and composite deck," *Teknik Dergi*, vol. 23, pp. 6203–6209, 2012.
- [9] J. W. Chen, X. Y. Guo, and X. H. Zheng, "Quasi static experimental study of seismic performance of damaged RC column strengthened with AFL," *Journal of Experimental Mechanics*, vol. 31, pp. 341–351, 2016.
- [10] Y. H. Mugahed Amran, R. Alyousef, R. S. M. Rashid, H. Alabduljabbar, and C.-C. Hung, "Properties and applications of FRP in strengthening RC structures: a review," *Structures*, vol. 16, pp. 208–238, 2018.
- [11] Y. Z. Lin and S. Z. Tian, "Study on influence of CFRP strengthening mode on seismic performance of RC bridge pier," *World Earthquake Engineering*, vol. 31, pp. 250–259, 2015.
- [12] Z. H. Dong, Q. Han, X. L. Du et al., "Experimental study on seismic performance of CFRP confined RC rectangular hollow section bridge piers," in *Proceedings of the International Efforts in Lifeline Earthquake Engineering—6th China-Japan-US Trilateral Symposium on Lifeline Earthquake Engineering*, Sichuan, China, December 2014.
- [13] A. I. Ibrahim, G. Wu, and Z.-Y. Sun, "Experimental study of cyclic behavior of concrete bridge columns reinforced by steel basalt-fiber composite bars and hybrid stirrups," *Journal of Composites for Construction*, vol. 21, no. 2, article 04016091, 2017.
- [14] S. Zhang, L. H. Xu, and X. B. Hu, "Seismic performance of masonry walls strengthened with BFRP," *Engineering Journal of Wuhan University*, vol. 48, pp. 294–299, 2015.
- [15] Y. Y. Zhou, J. T. Yu, and Z. D. Lu, "Seismic behavior of BFRP-reinforced pre-damaged concrete beam-column joints," *Journal of Central South University of Science and Technology*, vol. 41, pp. 1514–1521, 2010.
- [16] Y. Y. Zhou, Z. D. Lu, and K. C. Zhang, "Experimental study on seismic behavior of strengthened RC column-beam joints damaged by simulated earthquake," *Journal of Building Structures*, vol. 31, pp. 64–73, 2010.
- [17] J. T. Yu, L. Su, and Z. D. Lu, "Experimental study on BFRP damaged concrete beam-column joints by simulated earthquake," *Journal of Tongji University (Natural Science)*, vol. 39, pp. 18–24, 2011.
- [18] G. Wu, Y. Wei, and Z. S. Wu, "Comparative study on seismic performance of rectangular concrete columns strengthened with BFRP and CFRP composites," *Industrial Construction*, vol. 37, pp. 14–18, 2007.
- [19] J. Li, J. Gong, and L. Wang, "Seismic behavior of corrosion-damaged reinforced concrete columns strengthened using combined carbon fiber-reinforced polymer and steel jacket," *Construction and Building Materials*, vol. 23, no. 7, pp. 2653–2663, 2009.
- [20] J. X. Gong and J. B. Li, "Seismic behavior of strengthened corrosion-damaged circular reinforced concrete columns," *China Journal of Highway and Transport*, vol. 23, pp. 41–48, 2010.
- [21] D. Anggawidjaja, T. Ueda, J. Dai, and H. Nakai, "Deformation capacity of RC piers wrapped by new fiber-reinforced polymer with large fracture strain," *Cement and Concrete Composites*, vol. 28, no. 10, pp. 914–927, 2006.
- [22] C. Chisari, C. Bedon, and C. Amadio, "Dynamic and static identification of base-isolated bridges using genetic algorithms," *Engineering Structures*, vol. 102, no. 11, pp. 80–92, 2015.

## Research Article

# Comparative Study of Wellhole Surrounding Rock under Nonuniform Ground Stress

Zhongyu Jiang<sup>1,2</sup> and Guoqing Zhou<sup>1</sup>

<sup>1</sup>State Key Lab for Geomechanics and Deep Underground Engineering, China University of Mining and Technology, Xuzhou 221116, China

<sup>2</sup>School of Architecture and Civil Engineering, Anhui Polytechnic University, Wuhu 241000, China

Correspondence should be addressed to Zhongyu Jiang; [westwind@ahpu.edu.cn](mailto:westwind@ahpu.edu.cn)

Received 25 February 2019; Accepted 28 May 2019; Published 25 June 2019

Academic Editor: Timo Saksala

Copyright © 2019 Zhongyu Jiang and Guoqing Zhou. This is an open access article distributed under the Creative Commons Attribution License, which permits unrestricted use, distribution, and reproduction in any medium, provided the original work is properly cited.

The stress analysis of the wellhole surrounding rock and the regular failure of the wellhole has always been a concern for the well builders. Firstly, the Hamilton canonical equations are obtained by using the Hamiltonian variational principle in the sector domain, and the zero eigensolution and nonzero eigensolutions of the homogeneous equation are solved. According to the Hamiltonian operator matrix with the orthogonal eigenfunction system, the special solution form of the nonhomogeneous boundary condition equation is obtained. Then, according to the principle of the same coefficient being equal, the relationship equation between the direction eigenvalue and the angle coefficient is obtained, from which the specific expression of the special solution of the equation can be determined. Furthermore, the analytical solution of the wellhole surrounding rock problem under nonuniform ground stress is obtained by using the linear elastic accumulative principle. Finally, a concrete example is given to compare the finite element method and the symplectic algorithm. The results are consistent, which ensures the accuracy and the reliability of the symplectic algorithm. The relationship between the circumferential stress distribution around the hole and the lateral pressure coefficient is further analyzed.

## 1. Introduction

In the mine construction, the stress analysis of the wellhole surrounding rock and the regular failure of the wellhole are always been a concern for the well builders [1]. This has not only important theoretical significance but also practical application value. In the past, the axisymmetric plane strain analysis of a circular wellhole subjected to two-dimensional isobaric original ground stress field in the distance is familiar to all [2]. However, the nonaxisymmetric problem under the two-dimensional unequal pressure condition is more common in engineering. Because of the complexity of boundary conditions, it is more difficult to solve these kinds of problems.

At present, although there are many accurate and easy-to-use finite element calculation programs, these methods make it easier to analyze the stress and deformation of the wellhole surrounding rock [3]. However, the pursuit of basic theoretical solutions is still the goal of engineers and

technicians unremitting efforts. This is because the theoretical solution can provide a valuable means for design engineers to evaluate the results of numerical analysis. Moreover, the theoretical solution can reveal the relationship between variables more intuitively. Verruijt mapped the half-plane problem of a circular tunnel to a circular ring using complex variables and gave a detailed analytical solution to the case of a uniform radial displacement of the circular tunnel boundary [4]. Exadaktylos and Stavropoulou gave the closed-form plane strain solution of stresses and displacements around a semicircular or “D” shaped cross-sectional tunnel periphery based on complex potential function and conformal mapping representation [5]. Zhu used the theory of complex variable function to analyze the surrounding rock stress of the underground excavation tunnel. By conformal transformation, the original boundary problem of the excavated section is mapped to a new problem with a unit circle as its boundary. Then, two analytic

functions are used to express the surrounding rock stress of the excavated tunnel [6]. However, it is difficult to determine the analytic function in the derivation process, and it needs to be recalculated for different external boundary conditions, lacking generality.

Zhong [7] and Yao et al. [8] developed symplectic elasticity theory in the Hamilton system. It shows great advantages in revealing the physical essence of elastic solutions and calculating local mechanical properties. Hamilton state space [6–9] breaks through the limitations of the traditional separating variable method [5] and provides a broad prospect for solving existing problems of elasticity. In state space, according to the expansion theorem of eigenfunction, the arbitrary integrable state vector can be represented by orthogonal eigenvectors. The determination of eigensolution is very important for the explicit solution of a problem.

Leung applied the Hamiltonian method to study the two-dimensional elastic plane problems. It is a method of separable variables for partial differential equations using displacements and their conjugate stresses as unknowns. The analytical solution of stress distribution under arbitrary boundary and without considering the assumption of the beam is obtained [9]. Tseng and Tarn based on the Hamiltonian state space method, by means of variable separation and symplectic eigenfunction expansion, discussed the theoretical solution of stress field around a circular hole in an elastic plate with a hole subjected to unidirectional tension [10]. Tseng and Tarn used the state space method to analyze the deformation and stress distribution of circular elastic plates under axisymmetric loads. Based on this, the effect of thickness on the bending of circular plates was evaluated [11].

## 2. Description of the Problem

Consider the wellhole with radius  $R_0$  in the  $x$  and  $y$  direction at infinity is being affected by nonuniform ground stress  $\sigma_x$  and  $\sigma_y$  (Figure 1). The lateral pressure coefficient is given by the relation  $m = \sigma_y/\sigma_x$ , where assume  $|\sigma_x| \geq |\sigma_y|$ , then  $0 \leq m \leq 1$ .

Basic assumptions are as follows:

- (1) The entire stress state is in the elastic zone, and the wellhole and surrounding rock wall are isotropic linear elastic materials
- (2) The stress boundary conditions at infinity remain constant along the axial direction of the wellhole, and this problem is reduced to the plane strain problem in the infinite domain

For the square boundary conditions of this problem, it is advisable to use Cartesian coordinates. But here the stress near the wellhole is mainly discussed, so it is more appropriate to use polar coordinates. Firstly, the square boundary is transformed into a circular boundary. The center of the wellhole is taken as the center of the circle, a length  $R_\infty$  is taken which is much larger than radius  $R_0$  of the wellbore as the radius, and great circle (shown in the dotted line in Figure 1) is drawn. Considering that the radius of the great circle is much larger than the radius of the wellhole, the stress of point A at the great circle is the same as that without hole. According to the stress state formula of a point, the

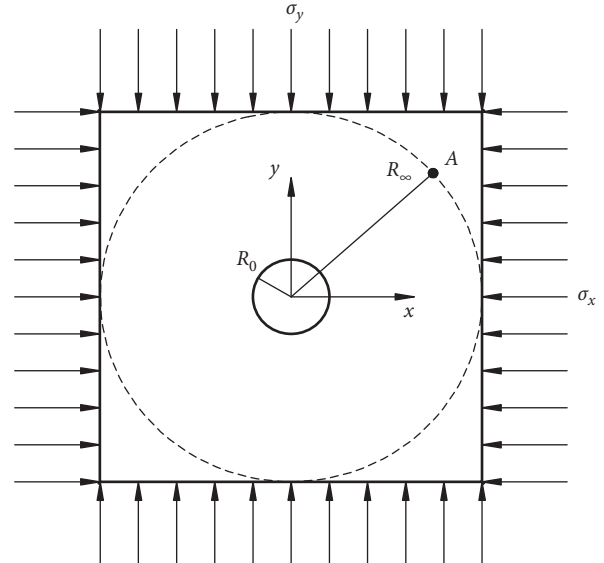


FIGURE 1: Force diagram of the surrounding rock wall of non-uniform pressure.

stress components in the polar coordinates of that point can be obtained. Thus, the original problem is transformed into a ring with an inner diameter of  $R_0$  and outer diameter of  $R_\infty$ . The boundary conditions are as follows.

When  $\rho = R_0$ ,

$$\begin{aligned} \sigma_\rho &= 0, \\ \tau_{\rho\varphi} &= 0. \end{aligned} \quad (1)$$

When  $\rho = R_\infty$ ,

$$\begin{cases} \sigma_\rho = \frac{1+m}{2}\sigma_x + \frac{1-m}{2}\sigma_x \cos 2\varphi, \\ \tau_{\rho\varphi} = \frac{1-m}{2}\sigma_x \sin 2\varphi. \end{cases} \quad (2)$$

## 3. Hamiltonian Variational Principle of the Polar Coordinate System

Define new variables:  $S_\rho = \rho\sigma_\rho$ ,  $S_\varphi = \rho\sigma_\varphi$ , and  $S_{\rho\varphi} = \rho\tau_{\rho\varphi}$ , in a typical sector region (Figure 2)  $R_1 \leq \rho \leq R_2$ ,  $\alpha \leq \varphi \leq \beta$ . Then, perform variable substitution  $\xi = \ln \rho$ , that is,  $\rho = e^\xi$ , and  $\xi_1 = \ln R_1$  and  $\xi_2 = \ln R_2$ . In the variational principle,  $\varphi$  is simulated as time coordinates,  $\xi$  is horizontal, and  $S_\rho$  lateral force factors are eliminated. Then, the mixed energy variational principle of the Hamiltonian system under polar coordinates is obtained:

$$\delta \int_\alpha^\beta \int_{\xi_1}^{\xi_2} \left\{ S_{\rho\varphi} \frac{\partial u_\rho}{\partial \varphi} + S_\varphi \frac{\partial u_\rho}{\partial \varphi} + S_\varphi \left( u_\rho + v \frac{\partial u_\rho}{\partial \xi} \right) - S_{\rho\varphi} \left( u_\varphi - \frac{\partial u_\varphi}{\partial \xi} \right) + \frac{1}{2} E \left( \frac{\partial u_\rho}{\partial \xi} \right)^2 - \frac{1}{2E} \left[ (1-v^2) S_\varphi^2 + 2(1+v) S_{\rho\varphi}^2 \right] \right\} d\xi d\varphi = 0. \quad (3)$$

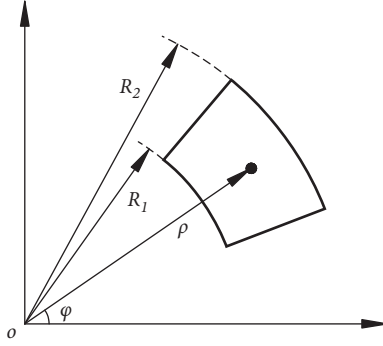


FIGURE 2: Polar coordinates sector region.

Introducing  $\mathbf{q}^T = (u_\rho \ u_\varphi)$  for the displacement vector,  $\mathbf{p}^T = (S_{\rho\rho} \ S_\varphi)$  for the dual vector of  $\mathbf{q}$ , and  $(\cdot) = \partial/\partial\varphi$  for the derivative of  $\varphi$ , equation (3) can be rewritten as follows:

$$\delta \int_a^\beta \int_{\xi_1}^{\xi_2} [\mathbf{p}^T \dot{\mathbf{q}} - \mathcal{H}(\mathbf{q}, \mathbf{p})] d\xi d\varphi = 0, \quad (4)$$

where the Hamiltonian density function  $\mathcal{H}$  is

$$\begin{aligned} \mathcal{H}(\mathbf{q}, \mathbf{p}) &= S_{\rho\varphi} \left( u_\varphi - \frac{\partial u_\rho}{\partial \xi} \right) - S_\varphi \left( u_\rho + v \frac{\partial u_\rho}{\partial \xi} \right) - \frac{1}{2} E \left( \frac{\partial u_\rho}{\partial \xi} \right)^2 \\ &\quad - \frac{1}{2E} [(1-v^2) S_\varphi^2 + 2(1+v) S_{\rho\varphi}^2]. \end{aligned} \quad (5)$$

The variational principle is developed to obtain the Hamiltonian regular equations:

$$\begin{Bmatrix} \dot{\mathbf{q}} \\ \dot{\mathbf{p}} \end{Bmatrix} = \begin{bmatrix} \mathbf{A} & \mathbf{D} \\ \mathbf{B} & -\mathbf{A}^* \end{bmatrix} \begin{Bmatrix} \mathbf{q} \\ \mathbf{p} \end{Bmatrix}, \quad (6)$$

where

$$\begin{aligned} \mathbf{A} &= \begin{bmatrix} 0 & 1 - \frac{\partial}{\partial \xi} \\ -1 - v \frac{\partial}{\partial \xi} & 0 \end{bmatrix}, \\ \mathbf{B} &= \begin{bmatrix} -E \frac{\partial^2}{\partial \xi^2} & 0 \\ 0 & 0 \end{bmatrix}, \\ \mathbf{D} &= \begin{bmatrix} \frac{2(1+v)}{E} & 0 \\ 0 & \frac{1-v^2}{E} \end{bmatrix}, \\ \mathbf{A}^* &= \begin{bmatrix} 0 & -1 + v \frac{\partial}{\partial \xi} \\ 1 + \frac{\partial}{\partial \xi} & 0 \end{bmatrix}. \end{aligned} \quad (7)$$

The mutual adjoint operator matrix with  $\mathbf{A}^*$  is  $\mathbf{A}$ , and the total-state vector  $\mathbf{v}$  and the matrix  $\mathbf{H}$  are introduced; Hamilton's regular equations (6) become

$$\dot{\mathbf{v}} = \mathbf{H}\mathbf{v}, \quad (8)$$

where

$$\begin{aligned} \mathbf{v} &= \begin{pmatrix} \mathbf{q} \\ \mathbf{p} \end{pmatrix} = (u_\rho \ u_\varphi \ S_{\rho\varphi} \ S_\varphi)^T, \\ \mathbf{H} &= \begin{bmatrix} \mathbf{A} & \mathbf{D} \\ \mathbf{B} & -\mathbf{A}^* \end{bmatrix}. \end{aligned} \quad (9)$$

It is not difficult to prove [8] that the matrix  $\mathbf{H}$  is a Hamilton operator matrix of symplectic geometric space.

The homogeneous boundary conditions for the sides  $\xi = \xi_1$  and  $\xi = \xi_2$  are

$$\begin{aligned} E \frac{\partial u_\rho}{\partial \xi} + v S_\varphi &= 0, \\ S_{\rho\varphi} &= 0. \end{aligned} \quad (10)$$

Separate the variable to solve the homogeneous equation, and let  $\mathbf{v}(\varphi, \xi) = e^{\mu\varphi} \psi(\xi)$ ; substituting it into the Hamiltonian dual equation, obtain the following eigenequation:

$$\mathbf{H}\psi(\xi) = \mu\psi(\xi), \quad (11)$$

where  $\mu$  is the eigenvalue and  $\psi(\xi)$  is the eigenfunction vector.

#### 4. General Solution of Homogeneous Boundary Conditions

First, the eigenequation (11) is expanded:

$$\begin{cases} -\mu u_\rho + u_\varphi - \frac{du_\varphi}{d\xi} + \frac{2(1+v)}{E} S_{\rho\varphi} + 0 = 0, \\ -u_\rho - v \frac{du_\rho}{d\xi} - \mu u_\varphi + 0 + \frac{1-v^2}{E} S_\varphi = 0, \\ -E \frac{d^2 u_\rho}{d\xi^2} + 0 - \mu S_{\rho\varphi} + S_\varphi - v \frac{dS_\varphi}{d\xi} = 0, \\ 0 + 0 - S_{\rho\varphi} - \frac{dS_{\rho\varphi}}{d\xi} - \mu S_\varphi = 0. \end{cases} \quad (12)$$

This is the simultaneous ordinary differential equations for  $\xi$ . The solution should first find the direction eigenvalue  $\lambda$  of  $\xi$ . The characteristic equation is

$$\det \begin{vmatrix} -\mu & 1 - \lambda & \frac{2(1+v)}{E} & 0 \\ -1 - v\lambda & -\mu & 0 & \frac{(1-v^2)}{E} \\ -E\lambda^2 & 0 & -\mu & 1 - v\lambda \\ 0 & 0 & 1 - \lambda & -\mu \end{vmatrix} = 0. \quad (13)$$

Expand its determinant, and solve

$$\begin{aligned}\lambda_{1,2} &= \pm(1+\mu i), \\ \lambda_{3,4} &= \pm(1-\mu i).\end{aligned}\quad (14)$$

The general expression of equation (12) is

$$\left\{ \begin{array}{l} u_\rho = A_1 e^{\lambda_1 \xi} + A_2 e^{\lambda_2 \xi} + A_3 e^{\lambda_3 \xi} + A_4 e^{\lambda_4 \xi}, \\ u_\varphi = B_1 e^{\lambda_1 \xi} + B_2 e^{\lambda_2 \xi} + B_3 e^{\lambda_3 \xi} + B_4 e^{\lambda_4 \xi}, \\ S_{\rho\varphi} = C_1 e^{\lambda_1 \xi} + C_2 e^{\lambda_2 \xi} + C_3 e^{\lambda_3 \xi} + C_4 e^{\lambda_4 \xi}, \\ S_\varphi = D_1 e^{\lambda_1 \xi} + D_2 e^{\lambda_2 \xi} + D_3 e^{\lambda_3 \xi} + D_4 e^{\lambda_4 \xi}. \end{array} \right. \quad (15)$$

According to the difference in eigenvalues of  $\mu$ , the expression of the general solution has changed. When the eigenvalues  $\mu = 0$  and  $\pm i$ , the direction eigenvalue  $\lambda$  has multiple roots, which means that the eigenvalue  $\mu$  has Jordan-type eigensolutions and has its special physical meaning. The eigensolution does not decay with the increase or decrease of the ordinate  $\varphi$  and is the basic eigensolution.

When  $\mu = 0$ , the eigensolution and its Jordan-type eigensolution are expressed as

$$\Psi_0^0 = \begin{pmatrix} 0 \\ e^\xi \\ 0 \\ 0 \end{pmatrix}, \quad (16)$$

$$\Psi_0^1 = \begin{pmatrix} c_1 e^\xi + c_2 e^{-\xi} + \frac{1-\nu}{2} \xi e^\xi \\ 0 \\ 0 \\ \frac{E}{1-\nu} c_1 e^\xi + \frac{E}{1+\nu} c_2 e^{-\xi} + \frac{E}{2} e^\xi \left( \xi + \frac{2-\nu}{1-\nu} \right) \end{pmatrix},$$

where

$$\begin{aligned}c_1 &= -\frac{1}{2} - \frac{1-\nu}{2} \frac{R_2^2 \ln R_2 - R_1^2 \ln R_1}{R_2^2 - R_1^2}, \\ c_2 &= -\frac{1+\nu}{2} \frac{R_2^2 R_1^2}{R_2^2 - R_1^2} \ln \left( \frac{R_2}{R_1} \right).\end{aligned}\quad (17)$$

When  $\mu = \pm i$ , the eigensolution and its Jordan-type eigensolution are expressed as

$$\begin{aligned}\Psi_i^0 &= (1 \ i \ 0 \ 0)^T, \\ \Psi_{-i}^0 &= (1 \ -i \ 0 \ 0)^T, \\ \Psi_i^1 &= (u_\rho^1 i \ u_\varphi^1 \ S_{\rho\varphi}^1 \ S_\varphi^1 i)^T, \\ \Psi_{-i}^1 &= (-u_\rho^1 i \ u_\varphi^1 \ S_{\rho\varphi}^1 \ -S_\varphi^1 i)^T,\end{aligned}\quad (18)$$

where

$$\left. \begin{aligned}u_\rho^1 &= \frac{1}{2} (1-\nu) \xi + \alpha (1-3\nu) e^{2\xi} + \beta (1+\nu) e^{-2\xi} \\ u_\varphi^1 &= -\frac{1}{2} [1+\nu+(1-\nu)\xi] + \alpha (5+\nu) e^{2\xi} + \beta (1+\nu) e^{-2\xi} \\ S_{\rho\varphi}^1 &= E \left( \frac{1}{2} + 2\alpha e^{2\xi} - 2\beta e^{-2\xi} \right) \\ S_\varphi^1 &= E \left( \frac{1}{2} + 6\alpha e^{2\xi} + 2\beta e^{-2\xi} \right) \\ \alpha &= \frac{-1}{4(R_1^2 + R_2^2)}, \\ \beta &= -\alpha R_1^2 R_2^2\end{aligned} \right\}, \quad (19)$$

The original problem corresponding to the eigensolution and its Jordan eigensolution is solved as follows:

$$\mathbf{v}_\mu^n = \sum_{m=0}^n \frac{1}{m!} \varphi^m \Psi_\mu^{n-m}, \quad (n = 0, 1). \quad (20)$$

Since the eigenvalues of the current problem are complex numbers, the corresponding eigenvectors are also complex forms. The emergence of complex numbers has brought great trouble to operation. The original problem was of the real type, so the complex eigensolution can be converted into a real type. According to the properties of symplectic orthogonal conjugation of the Hamiltonian matrix [8], the real and imaginary parts of the complex eigenvectors correspond to the symplectic conjugate eigenvalue solution of the original problem, respectively. It can be seen that  $\mathbf{v}_i^0$  and  $\mathbf{v}_{-i}^0$  are a pair of complex conjugate eigensolutions with each other. The real part and imaginary part are written as follows:

$$\begin{aligned}\mathbf{v}_{iR}^0 &= (\cos \varphi \ -\sin \varphi \ 0 \ 0)^T, \\ \mathbf{v}_{iI}^0 &= (\sin \varphi \ \cos \varphi \ 0 \ 0)^T,\end{aligned}\quad (21)$$

$\mathbf{v}_i^1$  and  $\mathbf{v}_{-i}^1$  are another pair of complex conjugate eigensolutions. The real part and imaginary part are written as follows:

$$\begin{aligned}\mathbf{v}_{iR}^1 &= \begin{pmatrix} \varphi \cos \varphi - u_\rho^1 \sin \varphi \\ -\varphi \sin \varphi + u_\varphi^1 \cos \varphi \\ S_{\rho\varphi}^1 \cos \varphi \\ -S_\varphi^1 \sin \varphi \end{pmatrix}, \\ \mathbf{v}_{iI}^1 &= \begin{pmatrix} \varphi \sin \varphi + u_\rho^1 \cos \varphi \\ \varphi \cos \varphi + u_\varphi^1 \sin \varphi \\ S_{\rho\varphi}^1 \sin \varphi \\ S_\varphi^1 \cos \varphi \end{pmatrix}.\end{aligned}\quad (22)$$

These real solutions are all solutions of the original problem.

The general solution of homogeneous boundary conditions for the original problem equation (8) can be expressed as

$$\begin{aligned} \mathbf{v}_h = & a_1 \mathbf{v}_0^0 + a_2 \mathbf{v}_0^1 + a_3 \operatorname{Re}(\mathbf{v}_i^0) + a_4 \operatorname{Im}(\mathbf{v}_i^0) + a_5 \operatorname{Re}(\mathbf{v}_i^1) \\ & + a_6 \operatorname{Im}(\mathbf{v}_i^1), \end{aligned} \quad (23)$$

where the coefficients  $a_1 \sim a_6$  are determined by the boundary conditions at both ends.

## 5. Special Solution for Nonhomogeneous Boundary Conditions

Above all, the general solution of the eigenequation under the homogeneous boundary conditions is solved, but the special solution under the nonhomogeneous boundary condition is much more complicated. According to the Hamiltonian matrix property [12, 13], block operator  $\mathbf{A}$  has orthogonal eigenfunction systems in Hilbert space  $\mathbf{X} \times \mathbf{X}$  and the eigenvalues and eigenfunction systems of  $\mathbf{A}$  can be expressed as follows:

$$U_k = \begin{pmatrix} \cos k\varphi \\ \sin k\varphi \end{pmatrix}, \quad (K = 0, \pm 1, \pm 2, \dots). \quad (24)$$

Block operator  $-\mathbf{A}^*$  has orthogonal eigenfunction systems in Hilbert space  $\mathbf{X} \times \mathbf{X}$ , and the eigenvalues and eigenfunction systems of  $-\mathbf{A}^*$  can be expressed as follows:

$$\hat{U}_k = \begin{pmatrix} \sin k\varphi \\ \cos k\varphi \end{pmatrix}, \quad (K = 0, \pm 1, \pm 2, \dots). \quad (25)$$

The boundary conditions of the original problem are relatively complex, so it is difficult to solve it directly. Since the rock deformation is small elastic deformation, the linear elastic accumulative theory is applicable. Therefore, the complex boundary conditions can be decomposed into a plurality of simple stress situations. The problem can be solved by accumulating each simple stress situation result [14]. Any one complicated boundary function can be decomposed into a simple regular trigonometric function system by Fourier decomposition. Therefore, the two sides only subjected to the boundary load of normal cosine angle should be taken into consideration firstly. The specific form is as follows.

When  $\xi = \xi_1$ ,

$$\begin{aligned} E \frac{\partial u_\rho}{\partial \xi} + v S_\varphi &= 0, \\ S_{\rho\varphi} &= 0. \end{aligned} \quad (26)$$

When  $\xi = \xi_2$ ,

$$\begin{aligned} E \frac{\partial u_\rho}{\partial \xi} + v S_\varphi &= P_0 \cos k\varphi, \\ S_{\rho\varphi} &= 0, \end{aligned} \quad (27)$$

where  $P_0$  is the normal load coefficient and  $k$  is the angle coefficient, taking an integer. Especially when  $k = 0$ , the boundary load is a constant term.

According to the general solution of the homogeneous equation (15) and the eigenfunction equations (24) and (25) of the block operators  $\mathbf{A}$  and  $-\mathbf{A}^*$ , the special solution of the equation satisfying the nonhomogeneous boundary conditions equation (26) can be written as

$$\begin{cases} \tilde{u}_\rho = P_0 (A_1 e^{\lambda_1 \xi} + A_2 e^{\lambda_2 \xi} + A_3 e^{\lambda_3 \xi} + A_4 e^{\lambda_4 \xi}) \cos k\varphi, \\ \tilde{u}_\varphi = P_0 (B_1 e^{\lambda_1 \xi} + B_2 e^{\lambda_2 \xi} + B_3 e^{\lambda_3 \xi} + B_4 e^{\lambda_4 \xi}) \sin k\varphi, \\ \tilde{S}_{\rho\varphi} = P_0 (C_1 e^{\lambda_1 \xi} + C_2 e^{\lambda_2 \xi} + C_3 e^{\lambda_3 \xi} + C_4 e^{\lambda_4 \xi}) \sin k\varphi, \\ \tilde{S}_\varphi = P_0 (D_1 e^{\lambda_1 \xi} + D_2 e^{\lambda_2 \xi} + D_3 e^{\lambda_3 \xi} + D_4 e^{\lambda_4 \xi}) \cos k\varphi. \end{cases} \quad (28)$$

These constants in the above formula are not completely independent, and they should also satisfy equation (8) so that the relationship between these constants can be obtained:

$$\begin{cases} A_i = \frac{[(1 - v\lambda_i)(1 + \lambda_i) - k^2]}{Ek\lambda_i^2} C_i, \\ B_i = \frac{\lambda_i^3 + \lambda_i^2 + (\nu k^2 - 1)\lambda_i + k^2 - 1}{Ek^2\lambda_i^2} C_i, \\ B_i = \frac{(1 - k^2) + (1 - \nu)\lambda_i + (2 + \nu)\lambda_i^2}{E(\lambda_i - 1)\lambda_i^2} C_i, \\ D_i = \frac{1 + \lambda_i}{k} C_i. \end{cases} \quad (29)$$

According to the principle that the same coefficient must be equal, a quartic equation about the direction eigenvalue  $\lambda$  and the angle coefficient  $k$  is obtained.

$$\lambda^4 - 2(k^2 + 1)\lambda^2 + (k^2 - 1)^2 = 0. \quad (30)$$

Thus, the direction eigenvalue  $\lambda$  can be calculated according to the angle coefficient  $k$ , and the specific expression of the special solution of the nonhomogeneous equation can be determined. The values of the integral constants  $A_i$ ,  $B_i$ ,  $C_i$ , and  $D_i$  are then determined according to the boundary conditions equation (26).

Similarly, the boundary loads in the form of tangential direction sine multiple times angle on both sides are considered. The specific form is

When  $\xi = \xi_1$ ,

$$\begin{aligned} E \frac{\partial u_\rho}{\partial \xi} + v S_\varphi &= 0, \\ S_{\rho\varphi} &= 0. \end{aligned} \quad (31)$$

$$S_{\rho\varphi} = 0.$$

When  $\xi = \xi_2$ ,

$$\begin{aligned} E \frac{\partial u_\rho}{\partial \xi} + v S_\varphi &= 0, \\ S_{\rho\varphi} &= T_0 \sin k\varphi, \end{aligned} \quad (32)$$

where  $T_0$  is the tangential load coefficient and  $k$  is the angle coefficient, taking an integer.

By the same method, a special solution of the equation that satisfies the boundary condition equation (31) and (32) can be calculated. Finally, according to the linear elastic accumulative theory, the theoretical solution which satisfies the boundary condition equations (1) and (2) of the original problem can finally be obtained.

## 6. Examples

In order to verify the correctness of the results obtained by the symplectic elastic method, the finite element software was used for the comparative calculation. The relevant data used in the calculation are as follows: the wellhole radius  $R_0 = 5$  m, calculating boundary radius at a distance  $R_\infty = 50$  m, elastic modulus of surrounding rock  $E = 30$  GPa, Poisson's ratio  $\nu = 0.2$ , nonuniform ground stress conditions:  $\sigma_x = -50$  MPa and  $\sigma_y = -30$  MPa, and the lateral pressure coefficient  $m = 0.6$ . According to the boundary condition equations (1) and (2) of the original problem, the boundary condition can be divided into three parts: (1) the normal direction is affected by the uniform load; (2) the normal direction is affected by the 2 times cosine load; and (3) the tangential direction is affected by the 2 times sinusoidal load.

Firstly, the boundary is subjected to normal uniform load, that is, the normal load coefficient  $P_0 = -40$  MPa and the angle coefficient  $k = 0$ , and substituting them into the formula equation (30), the direction eigenvalue  $\lambda_{1,2,3,4} = \pm 1$  can be obtained. Then, the special solution equation (28) is substituted into the boundary condition to obtain the undetermined coefficients, and a special solution of corresponding boundary conditions is obtained. In the same method, special solutions of corresponding other boundary conditions can be obtained. Finally, by accumulating the special solutions under various boundary conditions, we can get the displacement and stress cloud diagram of the surrounding rock of the wellhole under nonuniform ground stress.

By comparing and analyzing the result cloud diagrams in Figures 3 to 7, it can be seen that the distribution of each result cloud diagrams obtained by the two methods is consistent, and there is little difference in the value of extreme points. These show the correctness and reliability of the symplectic method. The difference between the two methods is that the symplectic method is an analytical method, while the finite element method is a numerical method.

Comparing the stress extremum in Figures 5 and 6, it can be seen that the circumferential stress extremum around the hole is much larger than the radial stress extremum, which is consistent with the engineering practice. In Figure 6, the circumferential stresses are all compressive stresses, and the distribution is extremely inhomogeneous at the edge of the hole. The value of circumferential stress in the horizontal position is relatively small, and it reaches the maximum value in the vertical direction. Tensile stress may occur in the horizontal direction under certain conditions. Considering

the brittleness of geotechnical materials, tensile failure should be avoided as far as possible.

The influence of different lateral pressure coefficients  $m$  on the circumferential stress value around the hole is detailed in Table 1. From the data, it can be seen that the circumferential stress around the hole changes periodically along the azimuth angle. Especially when the azimuth angle is equal to  $0^\circ$ ,  $90^\circ$ ,  $180^\circ$ ,  $270^\circ$ , and  $360^\circ$ , the circumferential stress reaches the extreme value. The maximum occurs at  $0^\circ$ ,  $180^\circ$ , and  $360^\circ$ , and the minimum occurs at  $90^\circ$  and  $270^\circ$ . The data show that when the azimuth angle is  $0^\circ$ ,  $180^\circ$ , and  $360^\circ$ , the maximum circumferential stress around the hole gradually changes from compressive stress to tensile stress with the decrease of the lateral pressure coefficient. When the lateral pressure coefficient  $m$  is between 0.3 and 0.4, the circumferential stress will appear on the inflection point; that is, the circumferential stress is zero.

Figure 8 depicts the influence of different lateral pressure coefficients  $m$  on the circumferential stress around the hole. When the value of  $m$  changes from 1 to 0, the stress distribution around the hole changes from circular to dumbbell-shaped, then to "8" shape, and finally to double "8" shape (where the vertical "8" shape is much larger than the horizontal "8" shape). The circumferential stress around the hole in the horizontal direction gradually changes from compressive stress to tensile stress with the decrease of the  $m$  value. Especially when the value of  $m$  is near 0.3, the stress critical point appears. When the value of  $m$  is less than 0.3, the tensile stress will appear in the horizontal direction of the hole edge. This is consistent with the data in Table 1. The circumferential stress around the hole in the vertical direction increases slowly with the decrease of the  $m$  value. Especially when  $m=0$ , the maximum tensile stress appears in the horizontal direction and the maximum compressive stress appears in the vertical direction. According to the properties of wellhole materials, the circumferential stress of the sidewall should be avoided as far as possible in engineering practice, which is particularly important.

## 7. Conclusion

The symplectic method realizes the conversion from Euclidean space to Hilbert space, breaking through the limitations of the traditional variable separation method. In this paper, the eigenvalues and eigenfunctions of Hamiltonian block operators are written according to the symplectic elastic mechanics method in the polar coordinate system. According to the characteristics of Hamiltonian block operators, the problem of nonhomogeneous boundary conditions is solved. And the relationship equation (30) between the direction eigenvalue  $\lambda$  and the angle factor  $k$  is found, which provides a theoretical foundation for further calculation of arbitrary boundary conditions.

The symplectic elastic mechanics method is used to accurately analyze the wellhole surrounding rock under nonuniform ground stress. By comparing the results of the symplectic algorithm and finite element method, we can see

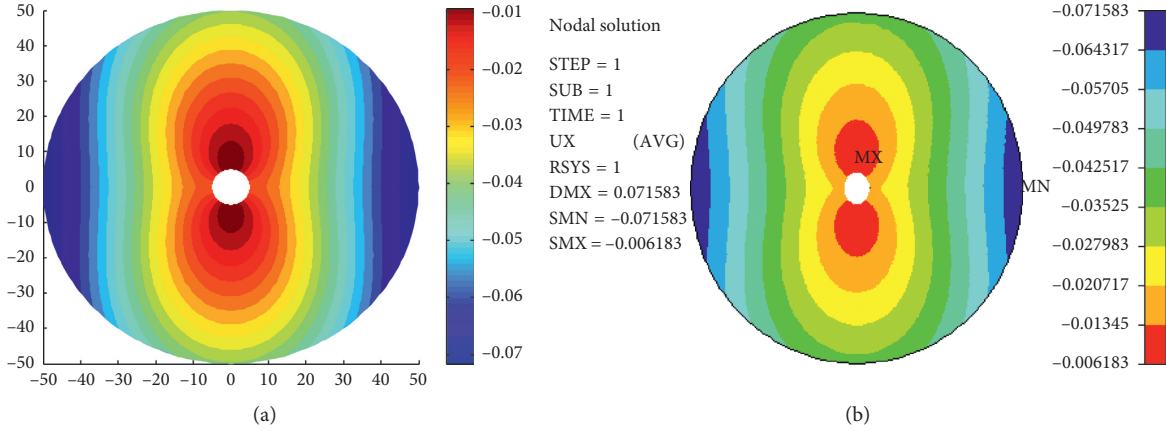


FIGURE 3: Cloud diagram of the radial displacement  $u_\rho$ .

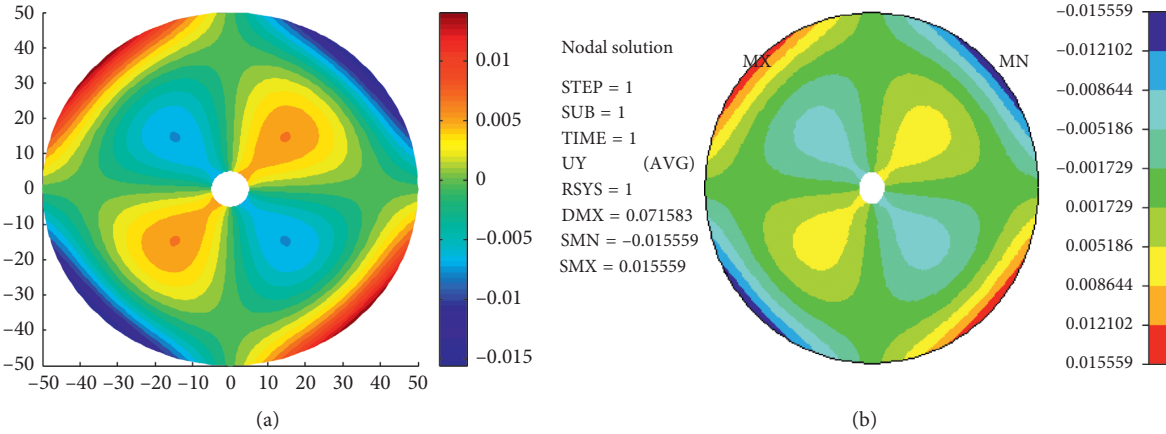


FIGURE 4: Cloud diagram of the circumferential displacements  $u_\phi$ .

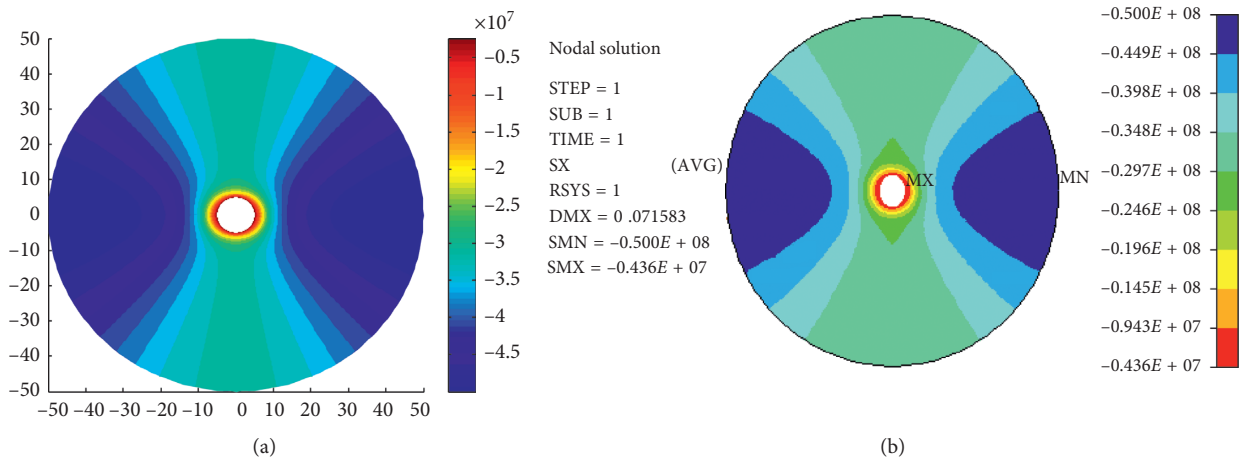
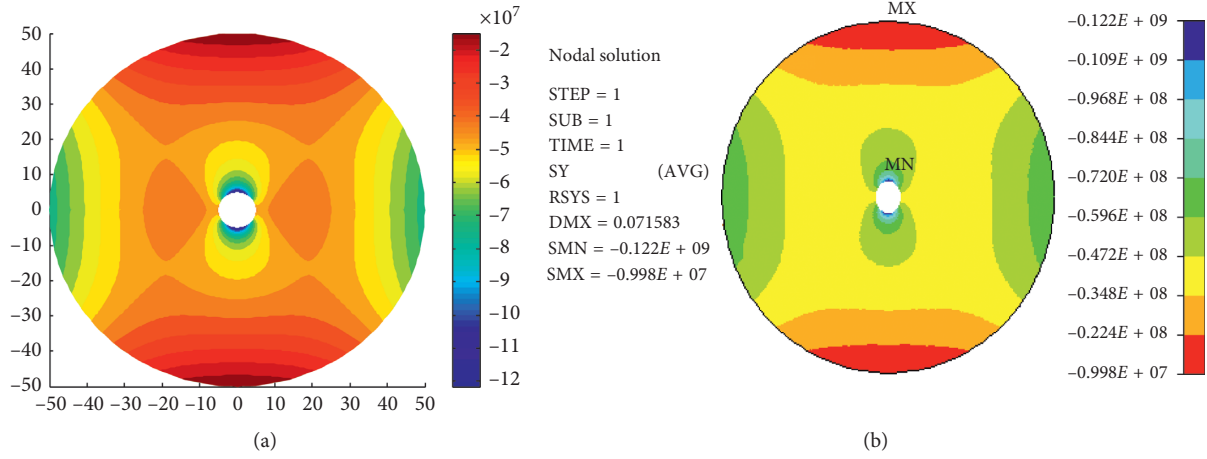
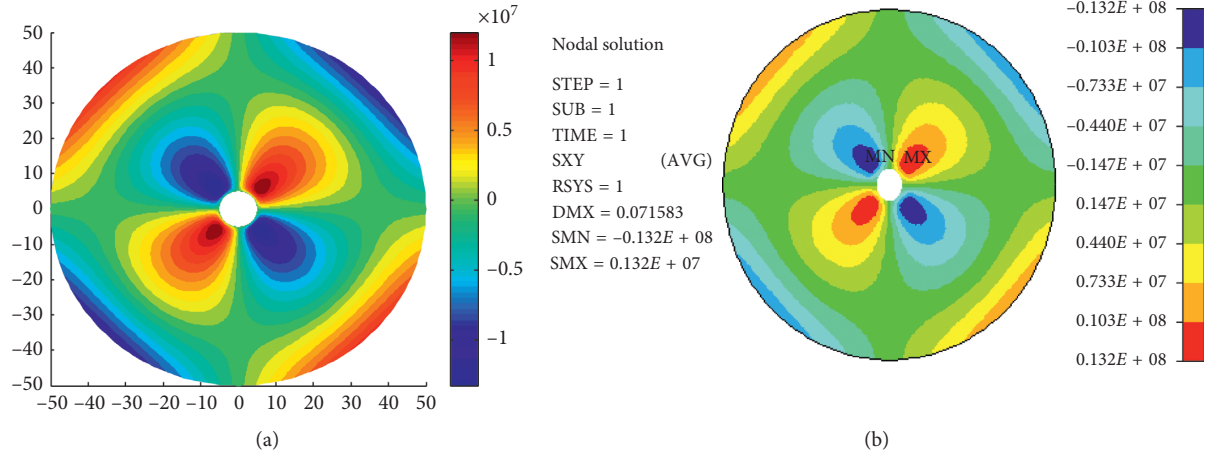


FIGURE 5: Cloud diagram of the radial stresses  $\sigma_r$ .

that the distribute regulation of the two methods is completely consistent, and the numerical values are almost the same. The results show that the circumferential stress

distribution of the wellhole rock is closely related to the lateral pressure coefficient  $m$ . With the change of the lateral pressure coefficient  $m$  from 1 to 0, the circumferential stress

FIGURE 6: Cloud diagram of the circumferential stresses  $\sigma_\varphi$ .FIGURE 7: Cloud diagram of the shear stress  $\tau_{\rho\varphi}$ .TABLE 1: Circumferential stress  $\sigma_\varphi$  around the hole corresponding to different  $m$  values (unit: MPa).

Angle	$m$										
	1	0.9	0.8	0.7	0.6	0.5	0.4	0.3	0.2	0.1	0
0°	-101.01	-85.76	-70.5	-55.25	-40	-24.74	-9.49	5.76	21.02	36.27	51.53
30°	-101.01	-90.86	-80.71	-70.55	-60.4	-50.25	-40.1	-29.95	-19.79	-9.64	0.51
60°	-101.01	-101.06	-101.11	-101.16	-101.21	-101.27	-101.32	-101.37	-101.42	-101.47	-101.52
90°	-101.01	-106.16	-111.32	-116.47	-121.62	-126.77	-131.93	-137.08	-142.23	-147.38	-152.54
120°	-101.01	-101.06	-101.11	-101.16	-101.21	-101.27	-101.32	-101.37	-101.42	-101.47	-101.52
150°	-101.01	-90.86	-80.71	-70.55	-60.4	-50.25	-40.1	-29.95	-19.79	-9.64	0.51
180°	-101.01	-85.76	-70.5	-55.25	-40	-24.74	-9.49	5.76	21.02	36.27	51.53
210°	-101.01	-90.86	-80.71	-70.55	-60.4	-50.25	-40.1	-29.95	-19.79	-9.64	0.51
240°	-101.01	-101.06	-101.11	-101.16	-101.21	-101.27	-101.32	-101.37	-101.42	-101.47	-101.52
270°	-101.01	-106.16	-111.32	-116.47	-121.62	-126.77	-131.93	-137.08	-142.23	-147.38	-152.54
300°	-101.01	-101.06	-101.11	-101.16	-101.21	-101.27	-101.32	-101.37	-101.42	-101.47	-101.52
330°	-101.01	-90.86	-80.71	-70.55	-60.4	-50.25	-40.1	-29.95	-19.79	-9.64	0.51
360°	-101.01	-85.76	-70.5	-55.25	-40	-24.74	-9.49	5.76	21.02	36.27	51.53

of the wellhole rock changes differently in horizontal and vertical directions. In the horizontal position, the circumferential compressive stress gradually decreases with the

decrease of the  $m$  value until it becomes tensile stress and finally reaches the maximum of tensile stress. In the vertical direction, the circumferential compressive stress increases

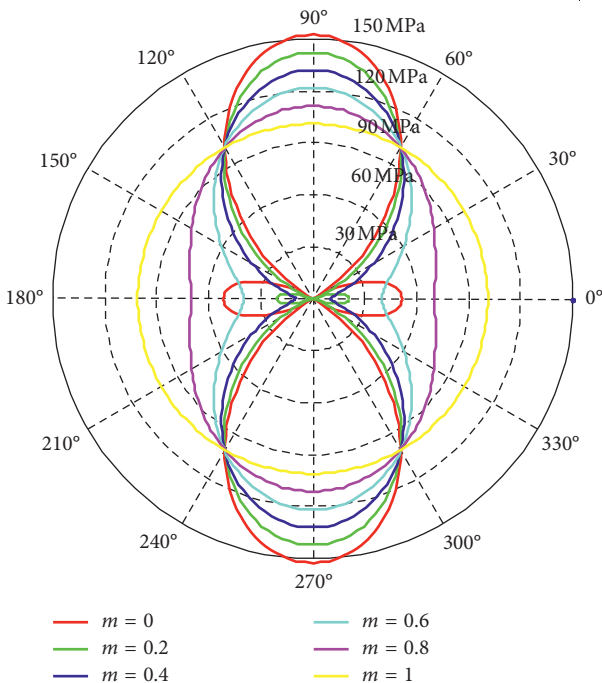


FIGURE 8: Circumferential stress curves around the hole corresponding to different  $m$  values.

slowly with the decrease of the  $m$  value and finally reaches the maximum of compressive stress. The research results not only provide theoretical guidance for wellhole design but also provide technical support for preventing wellhole fracture.

## Data Availability

The data used to support the findings of this study are available from the corresponding author upon request.

## Conflicts of Interest

The authors declare that there are no conflicts of interest regarding the publication of this paper.

## Acknowledgments

This work was supported by the National Natural Science Foundation of China (41772338).

## References

- [1] X. F. Chen, M. L. Shen, Y. Zhang et al., “Numerical model research of super deep shaft sidewall destruction,” *Chinese Journal of Underground Space and Engineering*, vol. 6, no. 5, pp. 926–931, 2010.
- [2] S. P. Timoshenko and J. N. Goodier, *Theory of Elasticity*, McGraw-Hill, New York, NY, USA, 3rd edition, 1970.
- [3] Y. Zhou and G. Q. Zhou, “Strict axisymmetric deformation analysis of shaft linings considering shaft-curing load,” *Chinese Journal of Geotechnical Engineering*, vol. 30, no. 7, pp. 999–1004, 2008.
- [4] A. Verruijt, “A complex variable solution for a deforming circular tunnel in an elastic half-plane,” *International Journal for Numerical and Analytical Methods in Geomechanics*, vol. 21, no. 2, pp. 77–89, 1997.
- [5] G. E. Exadaktylos and M. C. Stavropoulou, “A closed-form elastic solution for stresses and displacements around tunnels,” *International Journal of Rock Mechanics and Mining Sciences*, vol. 39, no. 7, pp. 905–916, 2002.
- [6] J. H. Zhu, “Analytic functions in stress analysis of the surrounding rock for caverns with the complex variable theory,” *Applied Mathematics and Mechanics*, vol. 34, no. 4, pp. 345–354, 2013.
- [7] W. X. Zhong, *New Solution System for Theory of Elasticity*, Dalian University of Technology Press, Dalian, China, 1995.
- [8] W. A. Yao, W. X. Zhong, and C. W. Lim, *Symplectic Elasticity*, World Scientific, Singapore, 2009.
- [9] A. Y. T. Leung and J. J. Zheng, “Closed form stress distribution in 2D elasticity for all boundary conditions,” *Applied Mathematics and Mechanics*, vol. 28, no. 12, pp. 1455–1467, 2007.
- [10] W.-D. Tseng and J.-Q. Tarn, “Three-dimensional solution for the stress field around a circular hole in a plate,” *Journal of Mechanics*, vol. 30, no. 6, pp. 611–624, 2014.
- [11] W.-D. Tseng and J.-Q. Tarn, “Exact elasticity solution for axisymmetric deformation of circular plates,” *Journal of Mechanics*, vol. 31, no. 6, pp. 617–629, 2015.
- [12] Eburlitu, *Completeness of the Eigenfunction Systems of Infinite Dimensional Hamiltonian Operators and its Applications in Elasticity*, Inner Mongolia University, Hohhot, China, 2011.
- [13] X. Guo and G. Hou, “On the block basis property of the off-diagonal Hamiltonian operators and its application to symplectic elasticity,” *European Physical Journal Plus*, vol. 131, no. 10, pp. 368–376, 2016.
- [14] W.-D. Tseng and J.-Q. Tarn, “A state space solution approach for problems of cylindrical tubes and circular plates,” *Journal of Mechanics*, vol. 31, no. 5, pp. 557–572, 2015.

## Research Article

# Research on the Obstruction Process of Rigid Netting Barriers toward Granular Flow

**Yunyun Fan<sup>1</sup> and Fengyuan Wu<sup>2</sup>**

<sup>1</sup>*Key Laboratory of Ministry of Education on Safe Mining of Deep Metal Mines, Northeastern University, Shenyang 110004, China*

<sup>2</sup>*School of Civil Engineering, Shenyang Jianzhu University, Shenyang 110168, China*

Correspondence should be addressed to Yunyun Fan; [yunyunfan@126.com](mailto:yunyunfan@126.com)

Received 11 February 2019; Revised 29 April 2019; Accepted 8 May 2019; Published 19 June 2019

Academic Editor: Sanjay Nimbalkar

Copyright © 2019 Yunyun Fan and Fengyuan Wu. This is an open access article distributed under the Creative Commons Attribution License, which permits unrestricted use, distribution, and reproduction in any medium, provided the original work is properly cited.

With the advantages of a simple structure and rapid construction, the rigid netting barrier (RNB) exerts a good obstruction effect on granular flow and is a common engineering measure used to prevent geological disasters in the form of granular flows. However, due to the limitations of current measuring and testing techniques, it is difficult to obtain an accurate measurement of the granular flow velocity and the impact force of granular flow on the mesh structures that are of primary concern in the design of protective structures. To study the characteristics of the obstruction process of RNBs toward granular flow, a typical impact experiment involving granular flow was numerically simulated by the discrete element method, and the correctness and effectiveness of the calculation method were also verified. On this basis, the discrete element method was applied to simulate the obstruction process affecting granular flow under different RNB setting conditions, and the calculation results clearly present the phenomena that occur during the obstruction process of RNBs toward granular flow, such as “run-up,” “overflow,” “passing-through,” and “grain-size segregation.” By analyzing the effects of these phenomena on the obstruction efficiency and the time history of the forces acting on the RNB, the rational setting of an RNB was further discussed. This study can provide a reference for the engineering application of RNB.

## 1. Introduction

There are many physical phenomena included in granular flows with highly mobile natures, such as avalanches, landslides, rockfalls, and debris flows, which cause human casualties and damage to infrastructure [1–3]. Over the years, various engineering measures have been used to mitigate or prevent natural granular flow disasters. Common prevention and control measures generally include civil engineering works such as check dams, grid-type dams, lateral walls, deflection and terminal walls, and berms or barriers that control debris flows [4, 5]. However, if the prevention and control engineering measures fail due to unreasonable engineering layout or insufficient project argument, they may cause more serious damage and loss [6, 7]. Therefore, it is necessary to study in depth the impact of

granular flows, the obstruction effect of barriers, and the structural design and rational layout of prevention and control measures.

The barriers are commonly used as control measures in engineering to reduce the mobility of granular flow and slow the granular flow movement [8, 9]. Furthermore, the interaction between the grains and the structure can promote energy dissipation from the granular flow [10]. The barriers are often designed using empirical methods, and existing research on the interaction mechanism between granular flows and barriers is not deep enough [11]. Therefore, the study of the interaction between granular materials and the barriers under different barrier setting conditions is of great significance for more effective control structure design [12–14].

In recent years, several large-scale experiments [15] have been carried out to monitor the impact of granular flows

with different material properties on barriers under different environmental conditions [16–18]. These research results provide valuable basic data and a solid foundation for the study of the obstruction process of barriers toward granular flows. However, due to the limitations of measuring and testing methods, field investigations and large-scale testing cannot clarify the complex interaction mechanism between granular flows and barriers [19]. Flume experiments indicate that the barriers can greatly reduce the flow velocity [20]. This reduction can be estimated empirically on the basis of the cross-sectional blockage over the channel area, but it only takes into account geometric effects, without any consideration of the interaction between granular flows and barriers [21]. Then, the dynamic behavior of dry granular flows toward barriers has been further studied [9, 13, 22–24]. In the studies, some more critical influence mechanisms were revealed, such as the formation of dead zones [21, 25] and run-ups [26, 27]. The dead zones allow momentum to run-up vertically along the barrier [28], and the run-ups reduce the load on the top of the barrier and increase the impact pressure. The granular material gradually accumulates at the base of the barriers and rapidly attenuates energy by shearing of the grains to suppress the run-up height against the barriers. Further studies have shown that grain size and gradation both exert a great influence on the impact process, thus resulting in larger run-up heights and peak impact forces [29, 30].

With the rapid development of scientific computing technologies and modern mechanics theories, numerical simulations have become an important means to study the interaction process between granular flows and barriers. So far, the continuous model used for granular flow simulation is primarily based on the depth-averaged theory [21, 29, 31–34] and is similar to the shallow water model. The main differences of the continuous model are that different bottom resistance terms were used for the corresponding granular material types [2, 29, 33] and that the lateral pressure coefficient related to the motion state was introduced [21, 29, 31, 35]. Although the continuous model has been widely applied in large-scale granular flow simulations using different numerical methods, the depth-averaged theory is essentially a planar two-dimensional model, which can neither yield more information about the mechanical behavior of the granular material against structures [36, 37] nor supply the concerned barrier peak impact forces when applied in the simulation of granular flows with vertical momentum [30, 38]. Therefore, the discrete element method is more suitable for simulations of the physical process of granular flows impacting barriers [24, 39–42]. Numerical simulation by the discrete element method can reproduce the processes of experiments or actual disasters, and the simulation results can be verified by comparison with experimental results. Furthermore, the complex interactions between granular flows and barriers and the main pathways of energy dissipation can also be better understood through analysis [10, 11]. However, the discrete element method has higher requirements for calculation, so it is only appropriate for use to analyze the

interaction between small-scale granular flows and barriers and to study the corresponding mechanisms [14].

Obviously, the current limited understanding of the obstruction process of barriers toward granular flow has hindered the development of protective barrier designs [43]. This study focused on the widely used rigid netting barriers with a simple structure (for convenience in the text, the rigid netting barrier is abbreviated as RNB). The discrete element method was used to simulate the obstruction process of RNB toward granular flow under different setting conditions. At the same time, the mechanisms of some special phenomena, the impact of granular flow on barriers, and the deceleration and obstruction effects exerted on granular flow by barriers were also studied. Furthermore, the numerical simulation can compensate for the insufficiency of the current test technology in measuring granular flow velocity and its impact on the RNB. Finally, the discrete element method can provide suggestions for the rational design and optimization of barrier layouts.

## 2. Numerical Methods

The software PFC3D based on the discrete element method was used for numerical calculations. According to the characteristics of this study, the linear contact model and the slip model were selected, and quartz sand was simulated by clumps.

**2.1. Contact Model.** In the contact-stiffness models shown in Figure 1, the force between two entities in contact is decomposed into normal force and shear force [44].

The normal force and the increment of the shear force can be, respectively, expressed as follows:

$$\begin{aligned} F_i^n &= K^n U^n n_i, \\ \Delta F_i^s &= K^s \Delta U_i^s, \end{aligned} \quad (1)$$

where  $F_i^n$  is the normal force,  $K^n$  is the normal stiffness at the contact,  $U^n$  is the normal overlap of discrete elements,  $n_i$  is the unit normal vector,  $\Delta F_i^s$  is the increment of shear force,  $K^s$  is the shear stiffness at the contact, and  $\Delta U_i^s$  is the relative displacement increment in the shear direction.

It can be seen from Equation (1) that the relationship between the contact force and the relative displacement can be expressed by the contact stiffness, including the normal stiffness and shear stiffness. The linear contact model is the most commonly used contact model, which assumes that the stiffness is a continuous variable.

The normal contact stiffness and the shear contact stiffness between contact entities A and B (which could be a ball, a clump, a wall, a line wall, or other elements) are, respectively, expressed as follows:

$$\begin{aligned} K^n &= \frac{k_n^{[A]} k_n^{[B]}}{k_n^{[A]} + k_n^{[B]}}, \\ K^s &= \frac{k_s^{[A]} k_s^{[B]}}{k_s^{[A]} + k_s^{[B]}}, \end{aligned} \quad (2)$$

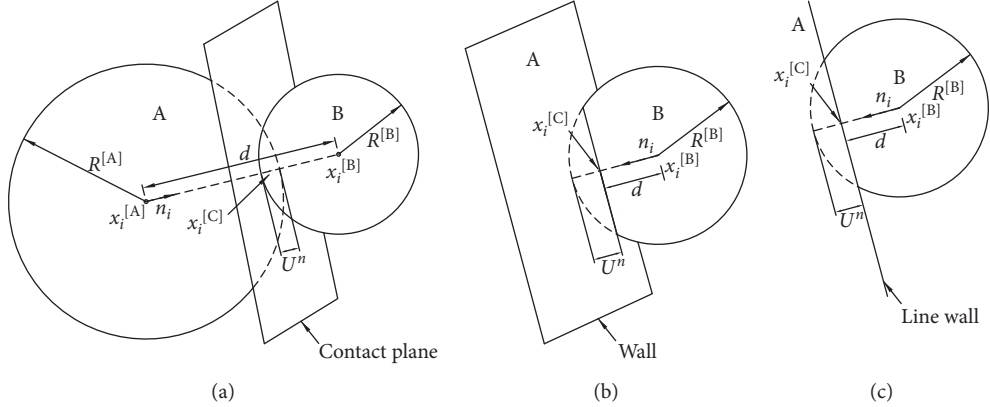


FIGURE 1: Sketch of the contact: (a) the contact between balls; (b) the contact between a ball and a wall; (c) the contact between a ball and a line wall.

where  $k_n$  and  $k_s$  represent the normal stiffness and shear stiffness of the two entities, respectively.

Furthermore, when the absolute value of the shear force at the contact  $|F_i^s|$  is greater than the maximum allowable shear contact force  $F_{\max}^s = \mu|F_i^n|$  (where the friction coefficient at the contact  $\mu$  is equal to the minimum of the friction coefficient of the two contact entities), relative sliding occurs between the entities, and  $F_i^s = \text{sgn}(F_i^s)F_{\max}^s$ .

**2.2. Equations of Motion for a Clump.** To simulate discrete elements with complex shapes, balls can be clumped together. The clump can generally be regarded as a rigid body and allows the existence of overlap between the balls. The contact force inside the clump was not taken into account in the calculation, and only the external contact force was considered [44].

In addition to the total mass  $m$  and the location of the centroid  $x_i^{[G]}$ , the basic properties of a clump model are the inertia moment  $I_{ii}$  and the inertia products  $I_{ij}$ . These properties can be expressed in the following equation:

$$\begin{aligned} I_{ii} &= \sum_{p=1}^{N_p} \left\{ m^{[p]} (x_j^{[p]} - x_j^{[G]}) (x_j^{[p]} - x_j^{[G]}) + \frac{(2m^{[p]} R^{[p]} R^{[p]})}{5} \right\}, \\ I_{ij} &= \sum_{p=1}^{N_p} \left\{ m^{[p]} (x_i^{[p]} - x_i^{[G]}) (x_j^{[p]} - x_j^{[G]}) \right\}, \quad j \neq i. \end{aligned} \quad (3)$$

The clump model moves like a rigid body. The centroid moment  $M_i$  can be calculated as follows:

$$M_i = \sum_{p=1}^{N_p} \left( \tilde{M}_i^{[p]} + \varepsilon_{ijk} (x_j^{[p]} - x_j^{[G]}) F_k^{[p]} + \sum_{c=1}^{N_c} \varepsilon_{ijk} (x_j^{[c]} - x_j^{[p]}) F_k^{[p,c]} \right), \quad (4)$$

where the centroid moment  $\tilde{M}_i^{[p]}$  is the applied moment of the grain,  $F_k^{[p]}$  is the resultant force acting on the grain, and  $F_k^{[p,c]}$  is the contact force acting on the grain.

The rate of change of the angular momentum  $\dot{H}_i$  can be calculated as follows:

$$\dot{H}_i = \dot{\omega}_i I_{ii} + \dot{\omega}_j I_{ij} + \varepsilon_{ijk} \omega_j (w_k I_{kk} - \omega_l I_{kl}), \quad j \neq i, l \neq k. \quad (5)$$

Since  $M_i = \dot{H}_i$ , the rotational motion of a clump can be found by simultaneously solving Equations (4) and (5).

The equation for translational motion can be written in the following form:

$$F_i = \sum_{p=1}^{N_p} \left( \tilde{F}_i^{[p]} + \sum_{c=1}^{N_c} F_i^{[p,c]} \right) = m(\ddot{x}_i - g_i), \quad (6)$$

where  $F_i$  is the resultant force,  $\tilde{F}_i^{[p]}$  is the externally applied force acting on the grain,  $F_i^{[p,c]}$  is the force acting on the grain at the contact, and  $g_i$  is the body force acceleration vector.

By solving Equation (6), the position of the clump center of mass at moment  $t$  can be expressed by as follows:

$$x_i^{(t+\Delta t)} = x_i^{(t)} + \dot{x}_i^{(t+\Delta t/2)} \Delta t. \quad (7)$$

After determining the translational and rotational velocities of the clump, the velocity of each ball in the clump can be expressed as follows:

$$\dot{x}_i^{[p]} = \dot{x}_i^{[G]} + \varepsilon_{ijk} \omega_j (x_k^{[p]} - x_k^{[G]}). \quad (8)$$

The above iterative calculations were continuously performed on all elements so that the dynamic simulation of the studied object can be finally realized.

**2.3. Numerical Verification.** The correctness and availability of the numerical simulations need to be verified before performing systematic studies of the obstruction process of RNB toward granular flow. Numerical simulations were performed on the basis of the experiments conducted by Jiang and Towhata [45]. These experiments were mainly carried out using the setup shown in Figure 2. A flow flume with a length, width, and height of 2.93 m, 0.30 m, and 0.35 m, respectively, was used to provide an experimental environment for dry granular flow movement, and the angle between the bottom of the flow flume and the horizontal plane was adjusted by rotation around the bottom fixed

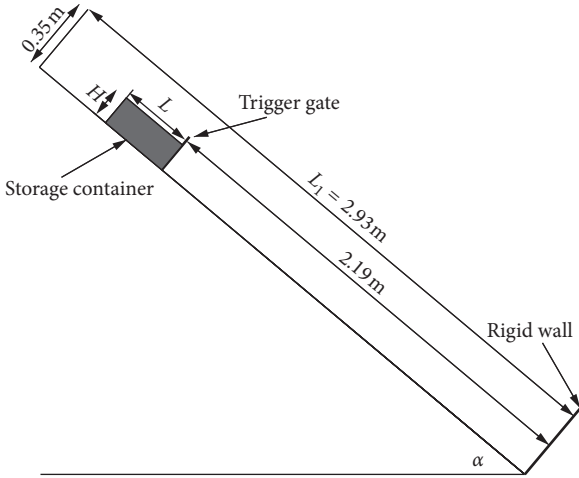


FIGURE 2: Sketch of the experimental equipment.

point. At the downstream end of the flow flume, a rigid wall was placed perpendicular to the bottom. The normal force on the wall could be measured by the sensor. At the initial moment, the dry granular material was placed in a square box of the upper flow flume. The dry granular material was limestone gravel with a grain size of 20 mm.  $L$  and  $H$  are the length and height of the box, respectively. During the experiment, the start of the granular material was controlled by momentarily opening the trigger gate perpendicular to the flow flume, and the distance  $L_1$  between the control gate and the rigid wall was 2.19 m. The friction angles of the flume bottom, flume sides, and rigid wall were  $25^\circ$ ,  $15^\circ$ , and  $21^\circ$ , respectively, which were obtained from experiments [45]. Based on these friction angles, the corresponding friction coefficients were determined.

The downstream rigid wall was divided into 6 segments, with each having the same width of 0.3 m as the bottom board of the flow flume. The height of segment nos. 1–5 was 5 cm, and the height of segment no. 6 was 15 cm, as shown in Figure 3. Although granular flow can run up after reaching the rigid wall, the grains that can reach the height of segment 6 under the experimental conditions may be quite few, which will lead to a quite limited impact of the grains at this height. Therefore, the height of segment 6 being set to 3 times that of the other segments can facilitate the collection of the impact force of these scattered grains so that the sensor can effectively work within its measuring range. The unit-width normal force of the six segments from the bottom to the top is denoted by  $F_i$ , where  $i$  is the number of each horizontal segment, and segments were numbered from the bottom to the top in the order of 1–6.  $h_i$  represents the distance between the center of each horizontal segment and the bottom.

As the actual grain shape is generally irregular, the simulation of the movement process of granular flow using only spherical grain element sometimes does not achieve good results [24, 30]. To provide a more realistic effect, an irregular shape of limestone gravel comprising four balls of the same size was used in the experiments. The four balls formed a clump element, and the distance between any two

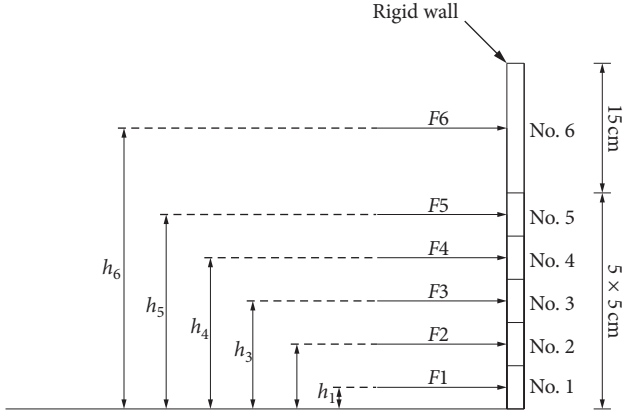


FIGURE 3: Sketch of the force acting on the rigid wall.

of the four balls was equal. After using the test data for numerical calibration and optimization, it was determined that when the distance  $D$  between the centers of the balls is 1.5 times the radius  $R$  of the balls (i.e.,  $D = 1.5 R$ ), the simulation effect is the best [30], as shown in Figure 4. To make the clump element and the limestone gravel with a diameter of approximately 20 mm equivalent in volume and density, the radii and densities of the balls were calibrated. It should be specially noted that the equivalent volume method was chosen here instead of the equivalent size method because when the clump mass is the same as the grain mass, the equivalent volume method enables the clump to achieve a density consistent with limestone gravel for a realistic and efficient numerical simulation. The radius of the balls was finally determined to be 6.6 mm, and the density was  $2.34 \text{ kg/m}^3$ .

According to the physical property parameters of reference [45], the mesoparameters shown in Table 1 were used in the calculation.

To make the number of clump elements in the simulation approximately equal to the number of gravel grains in the experiment, the number of clumps  $n_p$  was calculated using equation  $n_p = V_t \rho_t / V_s \rho_s$ , where  $V_t$  and  $\rho_t$  are, respectively, the total volume and density of the limestone gravel and  $V_s$  and  $\rho_s$  are the volume and density of the clumps, respectively.

The experiment numbered L44-H15- $\alpha 40^\circ$  in the literature [45] was selected for numerical calculation and verification. This experiment requires  $L = 44 \text{ cm}$ ,  $H = 15 \text{ cm}$ , and  $\alpha = 40^\circ$  in Figure 2.

Before the numerical verification, the mesoscopic parameters were calibrated by means of calculation and adjustment to correspond to the macroparameters used in the literature [45], such as the density and contact friction angle. In addition, to establish the calculation model, the size of the flow flume and the initial position and shape of the granular material (including the length and height) were calibrated before the numerical verification to ensure that the calculation corresponded to the experimental conditions of the geometric model. After the calibration work was done, the variation of the normal forces acting on the six rigid walls in the experiment was calculated using the discrete element

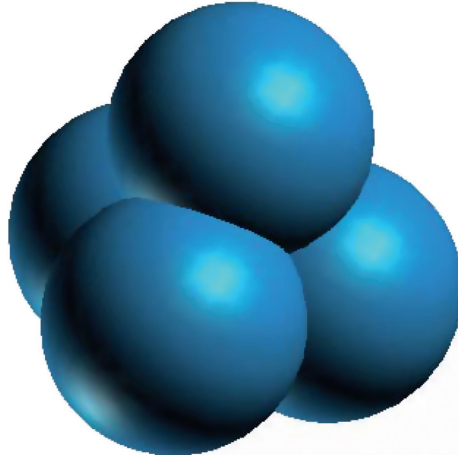


FIGURE 4: Clump discrete element.

TABLE 1: Mesoparameters used in the simulation.

Clump normal stiffness kn ( $\text{N}\cdot\text{m}^{-1}$ )	Clump shear stiffness ks ( $\text{N}\cdot\text{m}^{-1}$ )	Density of the balls forming a clump ( $\text{kg}\cdot\text{m}^{-3}$ )	Clump friction coefficient	Wall normal stiffness kn ( $\text{N}\cdot\text{m}^{-1}$ )	Wall shear stiffness ks ( $\text{N}\cdot\text{m}^{-1}$ )	Bottom friction coefficient	Friction coefficient of the sidewall	Friction coefficient of the rigid wall
1e4	1e4	2.34e3	0.47	1e8	1e8	0.47	0.27	0.38

method, and the calculation results were compared with the experimental results, as shown in Figure 5. Since the raw data calculated based on the discrete element method are relatively fluctuating, noise reduction measures were taken to better compare and analyze the raw data and the experimental data.

In addition to the unit-width normal forces of each barrier, the total force and moment acting on the rigid wall could be further obtained, as shown in Figure 6, which includes the experimental [45] and simulated results of the total unit-width normal force  $F$  and moment  $M$  of the test  $L44-H15-\alpha40^\circ$ .

By comparing the numerical results with the experimental data, it can be seen that although there are certain differences in some details, the overall calculation results agree well with the experimental data. Numerical simulations can reflect the effect of granular flow on rigid walls [30]. Therefore, more in-depth research and discussion can be carried out on this basis.

### 3. Numerical Results

After verification of the numerical calculation, more information was also obtained, such as the force acting on the barrier from granular flow during the obstruction process. This also suggests that the numerical simulation can be used to study the obstruction of granular flow by some barriers that are difficult to examine using modern technology testing (such as RNB). In this study, the obstruction process of RNB toward granular flow was mainly analyzed. For the sake of comparison, the following numerical calculation studies were carried out with the calculation parameters and

relevant conditions of the test  $L44-H15-\alpha40^\circ$ , and the selected grains had the same size as in the verification experiment. At the same time, considering the direct and important influence of the masses of grains that have not been obstructed by the RNB in the downstream, the obstruction efficiency is defined in this study as the ratio of the mass of the grains obstructed by the RNB relative to the total mass of the grains sliding from the source area.

On the basis of the verification examples, the RNB was placed at different positions of the flow flume to obstruct the granular flow to allow study of the force characteristics and the obstruction efficiency of the RNB under different setting conditions, as shown in Figure 7. For easy comparative analysis, the calculation parameters used for the numerical verification were still adopted in the following study. In particular, the RNB was simulated by line-wall elements. The linear contact model and slip model were used for the line wall elements as well as the wall elements, and the material property setting of the line wall elements was the same as that of the sidewall (Table 1).

The RNB shown in Figure 7 has a width of 0.3 m, which is the same as the width of the flow flume. In the following experiments, the obstruction effect of the RNB under different conditions (such as different positions, heights, and mesh sizes) and the force characteristics of the RNB were studied and analyzed.

**3.1. Influence of RNB Position.** To study the influence of the RNB position on the dynamic process, the RNB was placed 0.55 m, 1.10 m, and 1.64 m away from the downstream rigid wall, respectively. At the same time, to obtain good

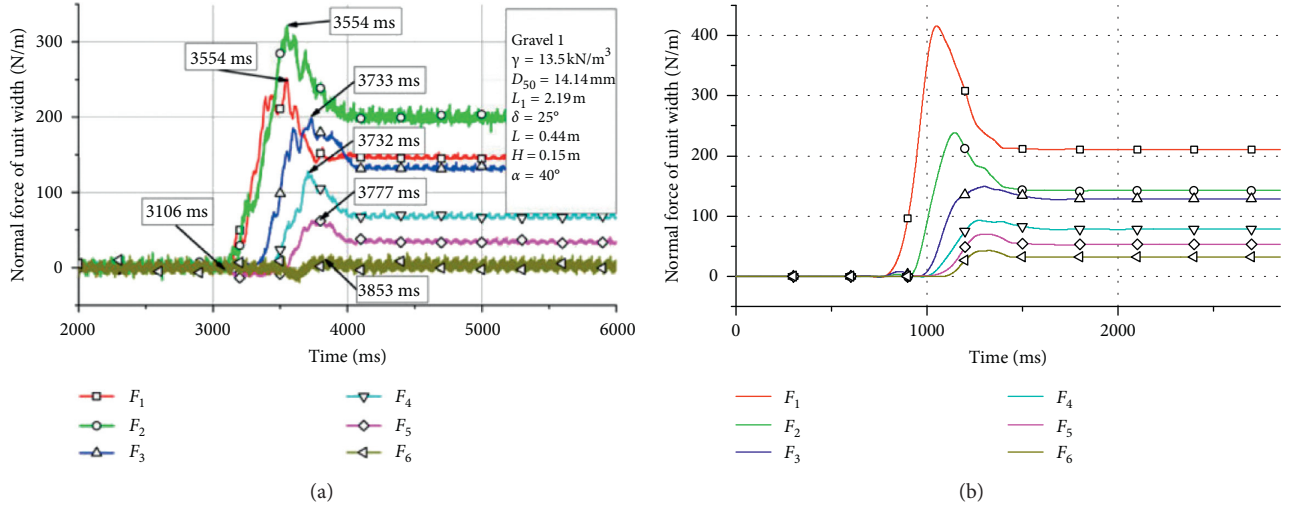


FIGURE 5: Time history of the unit-width normal force ( $L44-H15-\alpha 40^\circ$ ): (a) the experimental data [45]; (b) the numerical results [30].

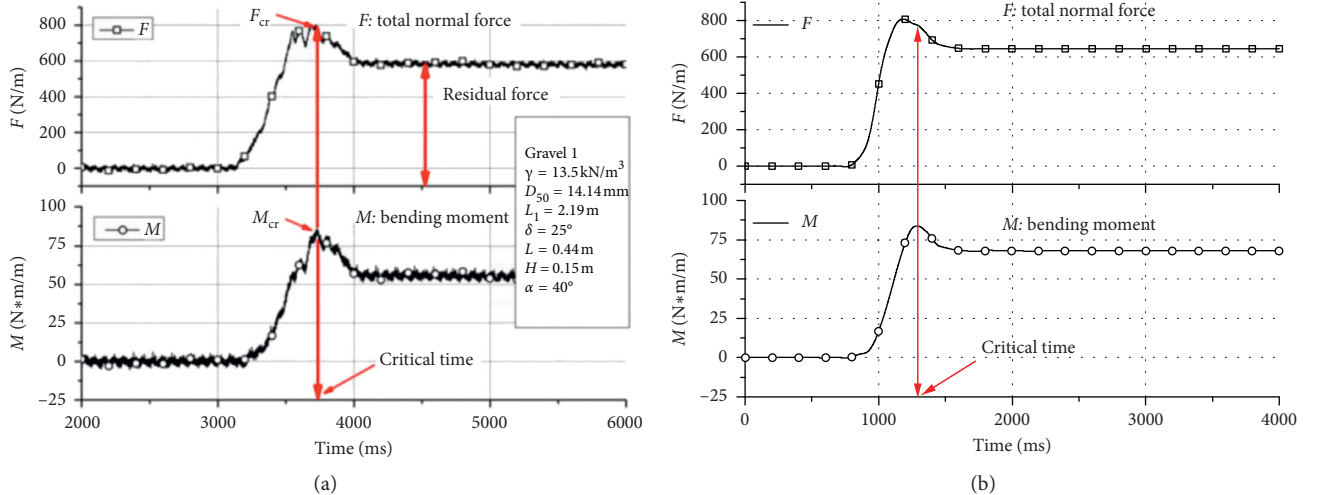


FIGURE 6: Time history of the total unit-width normal force and moment ( $L44-H15-\alpha 40^\circ$ ): (a) the experimental data [45]; (b) the numerical results [30].

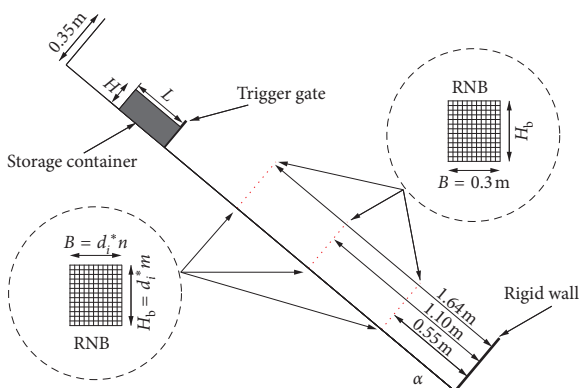


FIGURE 7: Setting of RNB in the flow flume.

obstruction efficiency, the RNB dimensions were set to  $0.30\text{ m} \times 0.35\text{ m}$ , which was consistent with the cross-sectional dimension of the flow flume, and the mesh size

was 20 mm. During the numerical verification of the test for  $L44\text{-}H15\text{-}40^\circ$ , 2408 clumps matched with the test granular material were generated in the source area. These clumps were used in the following analysis of the uniform-size grains. The obstruction efficiency of the RNB toward the granular flow was calculated at different positions, as shown in Table 2.

It can be seen from Table 2 that, owing to the reasonable height and mesh size, the obstruction efficiency was over 98%, which could basically achieve effective obstruction of the granular flow. The grains which were not effectively obstructed may have passed over the RNB by colliding with each other during the movement. When the RNB was placed at the relatively downstream position (in Case A1), the velocity of the grains was larger and the collision between the grains was more frequent, so the obstruction was less efficient than that when the RNB was placed upstream. Since each grain has its own velocity, to describe the overall

TABLE 2: Obstruction efficiency of RNB at different positions.

	Distance from the rigid wall (m)	Mesh size (m)	Height (m)	Obstruction efficiency (%)
Case A1	0.55	0.02	0.35	98.01
Case A2	1.10	0.02	0.35	98.48
Case A3	1.64	0.02	0.35	98.88

movement of the granular flow, the velocities of all grains were weighted and averaged, and then the granular flow velocity was obtained, which can be expressed as follows:

$$v_f = \frac{\sum_{c=1}^{N_c} m_i v_i}{\sum_{c=1}^{N_c} m_i}, \quad (9)$$

where  $v_f$  is the granular flow velocity and  $m_i$  and  $v_i$  are the mass and velocity of the  $i^{\text{th}}$  clump, respectively.

The time history of the granular flow velocity when the RNB was placed at different positions was calculated, as shown in Figure 8.

The time history of the impact of the granular flow on the RNB when placed at different positions was calculated, as shown in Figure 9.

From the time history of the velocity when the RNB was placed at different positions, it can be seen that when the grains moved toward the RNB, the velocity decreased significantly due to the obstruction from the RNB, and the maximum velocity appeared accordingly. The maximum velocity is an important indicator to characterize the hazard of granular flow and is one of the significant control factors in engineering design. Compared with the case in which the RNB was placed upstream, the granular flow had a higher velocity (the maximum velocity) when it reached a downstream RNB, and its deceleration process was faster, which may cause a stronger impact on the downstream RNB. This deduction was also confirmed in Figure 9, where it can be clearly seen that when the RNB was placed upstream, the peak and stable values of the unit-width normal force and moment acting on the RNB were smaller, and the ratios between the two values were also smaller. When the RNB was placed downstream, the impact of the granular flow was stronger due to the greater velocity (the maximum velocity), so the peak and stable values of the unit-width normal force and moment acting on the RNB, as well as the ratio of the two values, were larger, and at this time, the impact on the RNB was more fluctuating.

To analyze the typical process of a granular flow under obstruction by an RNB and to understand the characteristics of the forces acting on the RNB more deeply, the Case A1 working condition with a large impact on the RNB was studied. The velocity and shape of the granular flow at different moments are shown in Figure 10.

As seen from Figure 10, when the grains reached the RNB, a reverse rebound motion occurred. With the arrival and accumulation of the grains, a “dead zone” with a granular velocity of zero was formed in front of the RNB. This region actually reshaped the bottom boundary of the granular flow movement, and the following grains began to “run-up.” As the dead zone progressively expanded and the grains continued to run up on the dead zone, the final

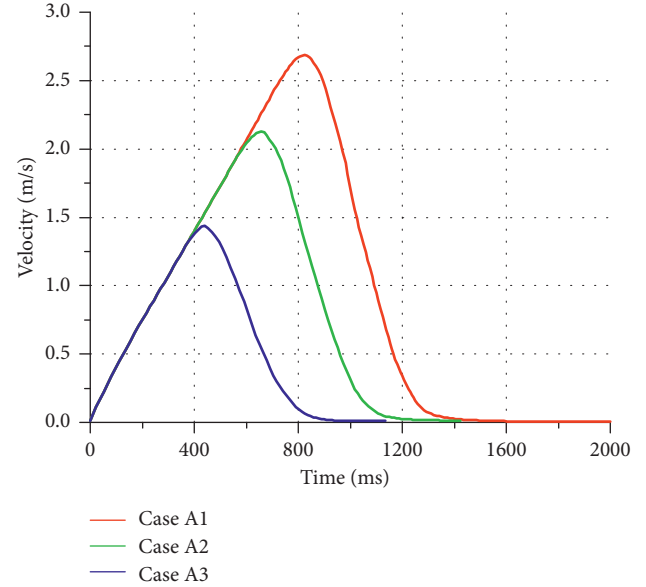


FIGURE 8: Time history of the granular flow velocity when the RNB was placed at different positions.

accumulation formed in front of the RNB. It has also been found that several grains passed over the RNB due to an upward velocity generated by the strong collision and then impacted the downstream rigid wall. The downstream RNB obstructed the grains that had larger velocities and stronger collisions, and these grains also had higher run-up heights and final stack heights, with more significant run-up motion. This is a good explanation for the fact that the peak and stable values of the unit-width normal force and moment acting on the RNB were larger and that the time history was more fluctuating.

In actual protection engineering, it is often impossible to determine the source of the failure rock and soil material. For example, the location of an unstable landslide on the side of a gully is difficult to determine effectively. Moreover, an RNB in a higher position has a large potential energy after obstructing a granular flow multiple times, and once destroyed, it will pose a greater threat downstream. Therefore, to obtain a greater range of protection, the RNB is generally placed as close to the downstream as possible to more reliably protect the buildings and facilities. Therefore, the following calculations were based on the setting of a downstream RNB.

**3.2. Influence of RNB Height.** To study the influence of the height setting of the RNB on the dynamic process, RNB with heights of 0.10 m, 0.20 m, 0.30 m, and 0.35 m was placed 0.55 m away from the rigid wall, respectively. The width of

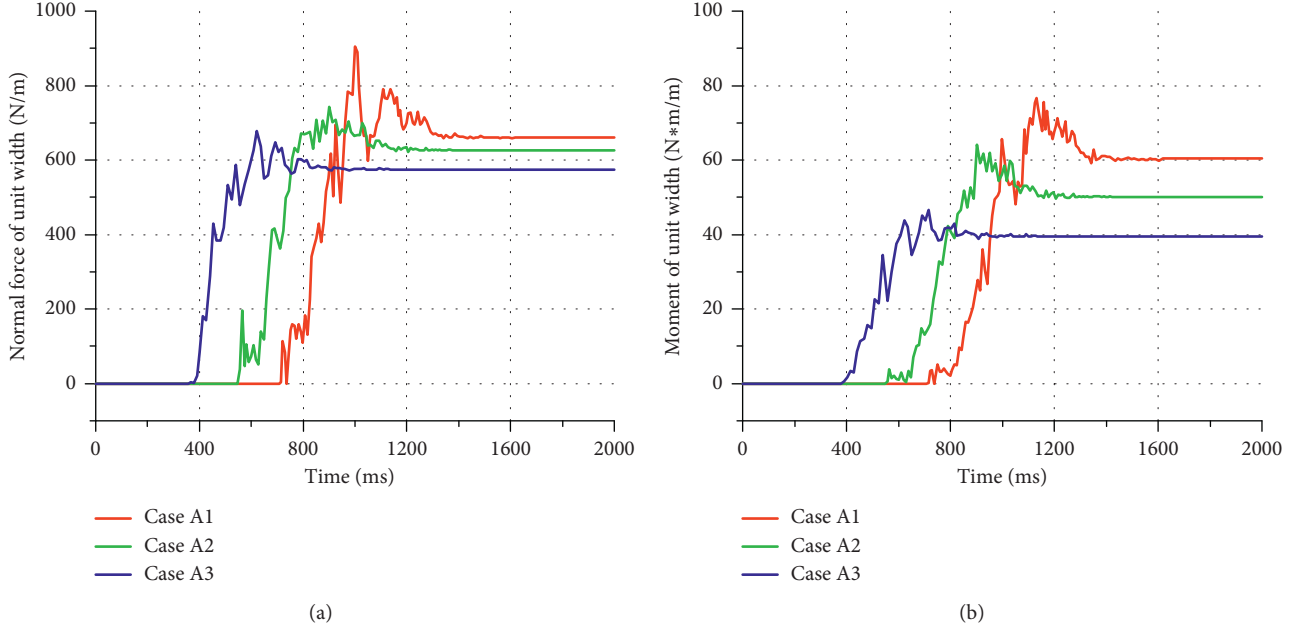


FIGURE 9: Time history of the impact of the granular flow on the RNB when placed at different positions: (a) time history of the unit-width normal force; (b) time history of the unit-width moment.

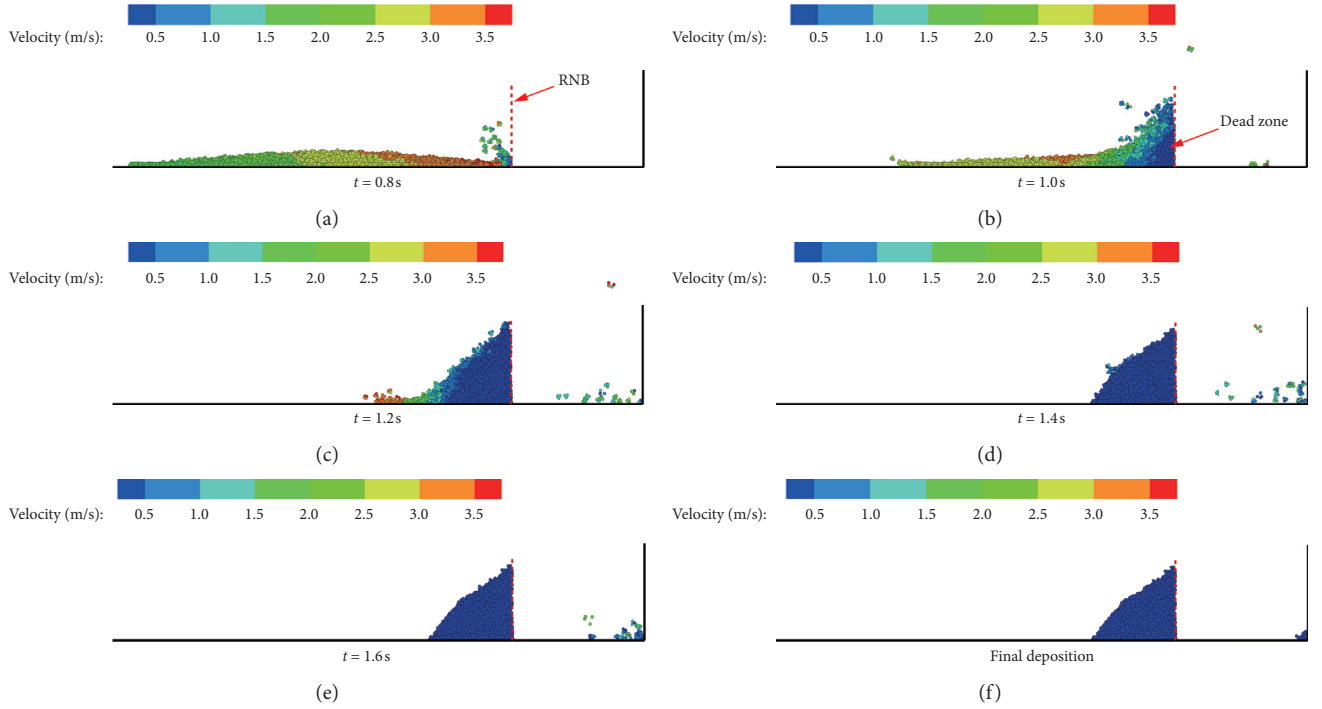


FIGURE 10: Granular flow process in Case A1.

the RNB was set to 0.30 m, which was the same as the section width of the flow flume. The mesh size was also set to 20 mm, and the obstruction efficiency of the RNB toward granular flow was calculated for different heights, as shown in Table 3.

It can be seen from Table 3 that the height of the RNB has a great influence on the obstruction efficiency. If a higher obstruction efficiency is desired, a sufficient RNB height is

necessary, in addition to a reasonable mesh size. If the RNB is not high enough, a space sufficient to accommodate the granular material cannot be formed so that a high obstruction efficiency cannot be achieved. Meanwhile, since the grains run up after reaching the RNB, an “overflow” phenomenon may occur when the run-up height exceeds the RNB height, resulting in a low obstruction efficiency.

TABLE 3: Obstruction efficiency of RNB with different heights.

	Distance from the rigid wall (m)	Mesh size (m)	Height (m)	Obstruction efficiency (%)
Case B1	0.55	0.02	0.10	37.04
Case B2	0.55	0.02	0.20	83.86
Case B3	0.55	0.02	0.30	97.82
Case B4	0.55	0.02	0.35	98.01

The time history of the granular flow velocity when RNB with different heights was placed was calculated, as shown in Figure 11.

The time history of the impact of the granular flow on the placed RNB with different heights was calculated, as shown in Figure 12.

It can be seen from Figure 11 that, under the obstruction of the RNB, the velocity began to decrease. Each case has the same maximum granular flow velocity, and the granular flow has the same deceleration process before running up to the RNB height. Interestingly, however, when the RNB height was insufficient, an obvious “platform” appeared in the falling section of the velocity curve, which means that the decrease of the velocity slowed, which was related to the overflow. During the run-up, once the grains reached the maximum height of the RNB, they passed over the RNB and continued to accelerate downstream. If the RNB height exceeded the maximum run-up height of the granular flow, overflow could be avoided. The increase of the RNB height above this maximum run-up height had little effect on the dynamic process. In this case, increasing the RNB height can only obstruct a very small number of grains splashed by the collision, and the influence on the obstruction efficiency was extremely small.

It can be seen from Figure 12 that when the RNB height exceeded the maximum run-up height of the granular flow, the time history of the impact on the RNB did not substantially change. When the RNB height was relatively small, although the granular flow had the same maximum velocity as in the cases in which the RNB was higher, a large number of grains passed over the RNB in an overflow manner, thereby reducing the impact on the RNB. During the overflow, the ratios of the peak and stable values of the unit-width normal force and moment acting on the RNB were relatively large. By comparing the time histories of Case B1 and Case B2, when overflow occurs, the peak and stable values of the unit-width normal force and moment acting on the RNB are not simply proportional to the RNB height. At the same time, as the RNB height increases, the run-up height of the grains is larger, and the force arm increases so that the growing rate of the unit-width moment acting on the RNB is greater than that of the unit-width normal force.

To analyze the kinetic characteristics of a granular flow with an insufficient RNB height, the Case B2 working condition with typical overflow characteristics was studied in detail, and the velocity and shape of the granular flow at different moments are shown in Figure 13.

As seen from Figure 13, the rebound of the grains when they first reached the RNB and the formation of the dead zone in front of the RNB showed no difference relative to the discussed Case A1. After the subsequent grains ran up to the

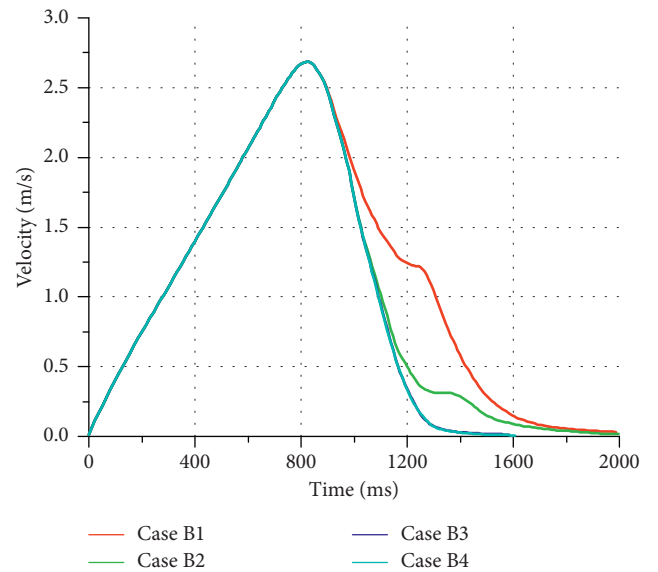


FIGURE 11: Time history of the granular flow velocity when RNB with different heights was placed.

maximum height of the RNB, they passed over the RNB in an overflow manner due to the lack of sufficient constraints. A stable dead zone was also gradually formed during the overflow process, and the dead zone was continuously developed and formed a final accumulation. After the overflow, the discharged grains moved downstream in the form of a projectile, which caused a large impact on the downstream bottom area of the flow flume. In actual engineering, this area may eventually form an impact crater, so it needs to be an item of focus. The calculation results show that, under the condition of an insufficient RNB height, the grains pass the RNB in the manner of overflow, thereby causing damage to the downstream. Due to the complexity of the granular flow movement and application conditions, the design height of the RNB cannot be obtained by simple calculation. The most effective method is to obtain the maximum run-up height of the granular flow under the corresponding conditions by numerical calculation.

According to the above analysis, the granular flow runs up when obstructed by the RNB, and overflow occurs when the RNB height cannot reach the maximum run-up height. Therefore, only if the design height of the RNB exceeds the maximum run-up height of the granular flows, the overflow can be avoided, and then the RNB can play its due role. Under the conditions of the examples in this study, to achieve better obstruction efficiency, the RNB height should be at least 0.3 m. Combined with the size of the actual flow flume, the following calculations and discussion will all be based on an RNB height of 0.35 m.

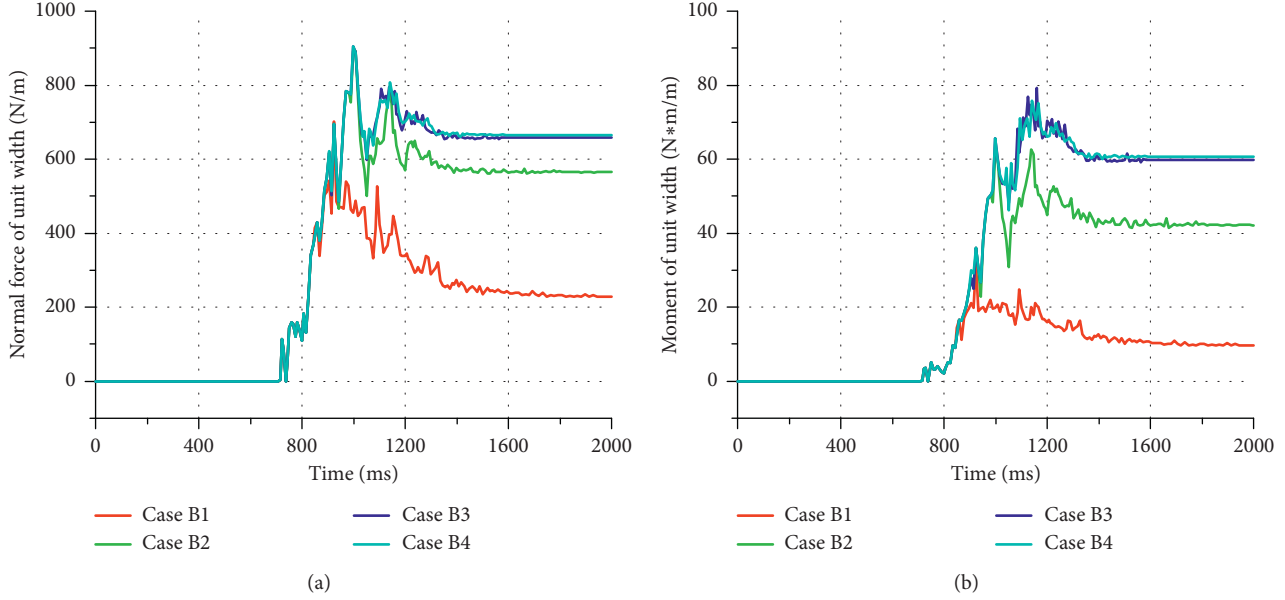


FIGURE 12: Time history of the impact of the granular flow on RNB with different heights: (a) time history of the unit-width normal force; (b) time history of the unit-width moment.

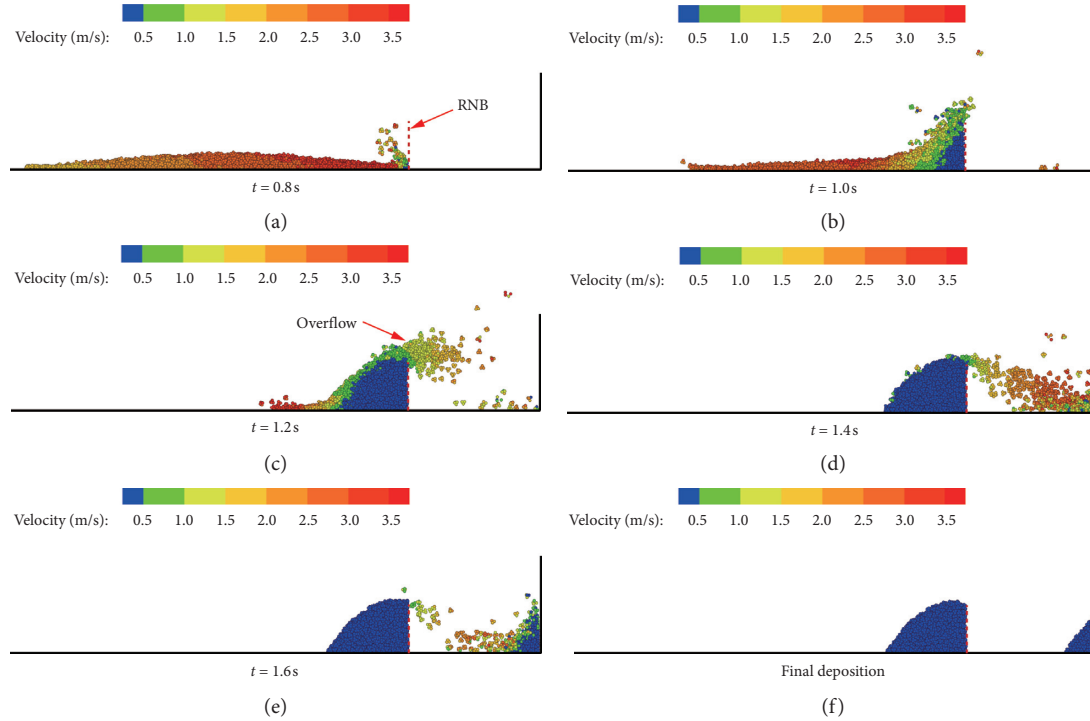


FIGURE 13: Granular flow process in Case B2.

**3.3. Influence of the RNB Mesh Size.** To study the influence of the RNB mesh size on the dynamic process, an RNB with a size of  $0.30\text{ m} \times 0.35\text{ m}$  was placed  $0.55\text{ m}$  away from the rigid wall. The mesh size was set to  $10\text{ mm}$ ,  $20\text{ mm}$ ,  $30\text{ mm}$ , and  $40\text{ mm}$ , respectively. The obstruction efficiency of the RNB toward granular flow was calculated for different mesh sizes, as shown in Table 4.

Table 4 shows a high obstruction efficiency of the RNB for the set mesh sizes. Even when the mesh size reached nearly 2 times the grain size, the obstruction efficiency was still relatively high, reaching 78.70%, which seems to be different from our intuitive experience. For deeper understanding of this phenomenon, a further analysis is necessary. In the case in which the mesh size is larger than

TABLE 4: Obstruction efficiency of the RNB with different mesh sizes.

	Distance from the rigid wall (m)	Mesh size (m)	Height (m)	Obstruction efficiency (%)
Case C1	1.10	0.01	0.35	99.90
Case C2	1.10	0.02	0.35	98.00
Case C3	1.10	0.03	0.35	90.20
Case C4	1.10	0.04	0.35	78.70

the grain size, although the grains that first reach the RNB may pass through the RNB due to their smaller size, the subsequently arriving grains form a force chain by contacting each other in front of the RNB. The force chain can effectively prevent the continuous passage of the grains, thereby achieving effective obstruction of grains smaller than the mesh size and forming the mechanism through which an RNB with a large-mesh size can still effectively obstruct fine grains. When the mesh size is relatively small, unobstructed grains mainly pass over the RNB by collision, which is sometimes difficult to avoid in actual engineering. When the mesh size reaches 0.02 m, continuing to reduce the mesh size provides stronger constraints and hindrance to the grains and, thus, can slightly improve the obstruction efficiency.

The time history of the granular flow velocity when RNB with different mesh sizes was placed was calculated, as shown in Figure 14.

The time history of the impact of the granular flow on RNB with different mesh sizes was calculated, as shown in Figure 15.

It can be seen from Figure 14 that the granular flow has different velocity curves after reaching RNB with different mesh sizes. When the mesh size is relatively large, the velocity deceleration is slow, and even the peak of the velocity curve is slightly increased because more grains passed through the RNB with a larger mesh size to continue the acceleration downstream. Obviously, the maximum granular flow velocity before reaching the RNB should be adopted for structural design. This value is the same in these cases because the increase in velocity caused by the accelerated motion of the grains that passed through the mesh to the downstream is not related to the force acting on the RNB. When the mesh size reached the grain size, the influence of reducing the mesh size on the velocity was not obvious.

It can be seen from Figure 15 that as the mesh size increased, part of the grains passed through the larger mesh, so the unit-width normal force and moment acting on the RNB were greatly reduced. Although this phenomenon reduced the load on the RNB, the grains passing through the mesh may also harm the downstream. When the mesh size reached 0.02 m, which was equivalent to the grain size, continuing to reduce the mesh size hardly changed the time history of the impact on the RNB, and this was because when the mesh size was small enough, the grains could no longer pass through the RNB. When the mesh size was small enough, the granular flow had a higher run-up and, thus, a larger force arm, resulting in a larger difference between the unit-width moments acting on the RNB with different mesh sizes.

To analyze the kinetic characteristics of the granular flow under the condition of a larger mesh size RNB, Case C3 with grain passing-through characteristics was studied in detail,

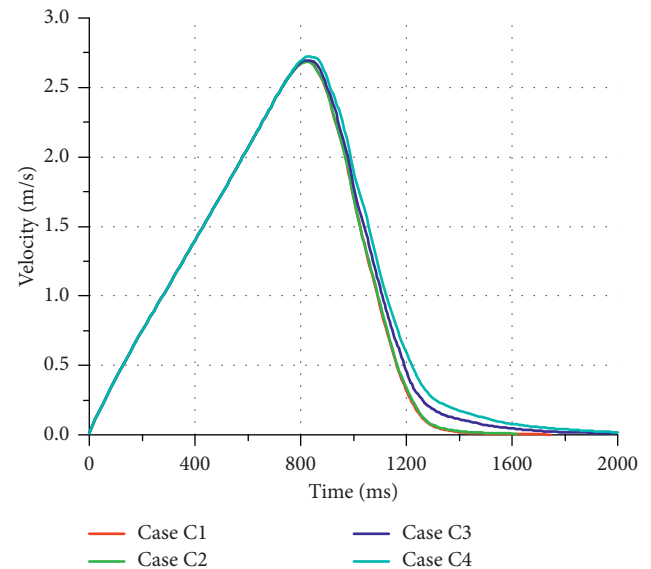


FIGURE 14: Time history of the granular flow velocity when RNB with different mesh sizes was placed.

and the velocity and shape of the granular flow at different moments are shown in Figure 16.

It can be seen from Figure 16 that when the grains reached the RNB, since the grain size was smaller than the mesh size, part of the grains moved downstream through the RNB, and the grains that had not passed through the RNB contacted and supported each other to form a relatively stable force chain, which in turn formed a dead zone with an obstruction effect, after which the subsequent grains ran up in the dead zone. When the granular flow reached a new height, some of the grains moved downstream through the RNB, so the grains could be seen to pass through the RNB from the bottom to the top. The grains that passed through the RNB from a higher position moved downstream in the form of projectile motion. Similar to the overflow, the grains passing through the RNB from a higher position impacted the downstream bottom, and thus, the area of the impacted bottom should be given sufficient attention. Although the grain passing-through phenomenon exists when the mesh size is larger than the grain size, the force chain formed by the grains in front of the RNB can effectively obstruct the subsequent grains, thereby achieving better obstruction efficiency. However, due to the complexity of granular flow movement, it is impossible to obtain the obstruction efficiency under large-mesh size conditions by simple methods. Therefore, numerical simulations may be the most effective method when experimental conditions are limited.

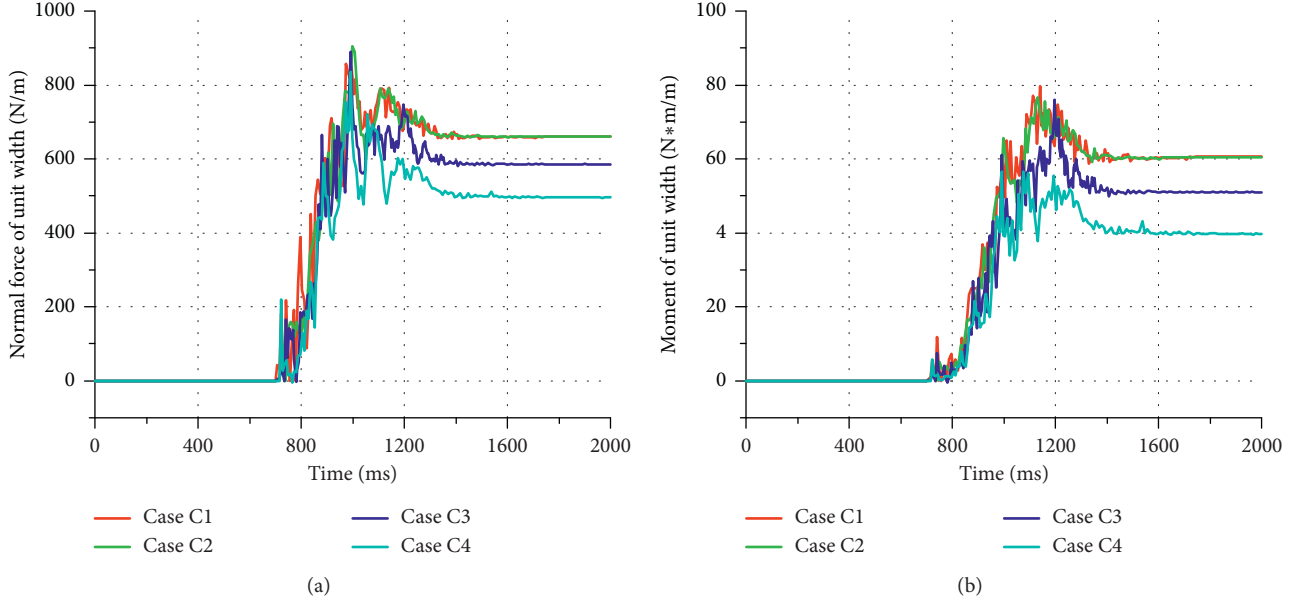


FIGURE 15: Time history of the impact of the granular flow on RNB with different mesh sizes: (a) time history of the unit-width normal force; (b) time history of the unit-width moment.

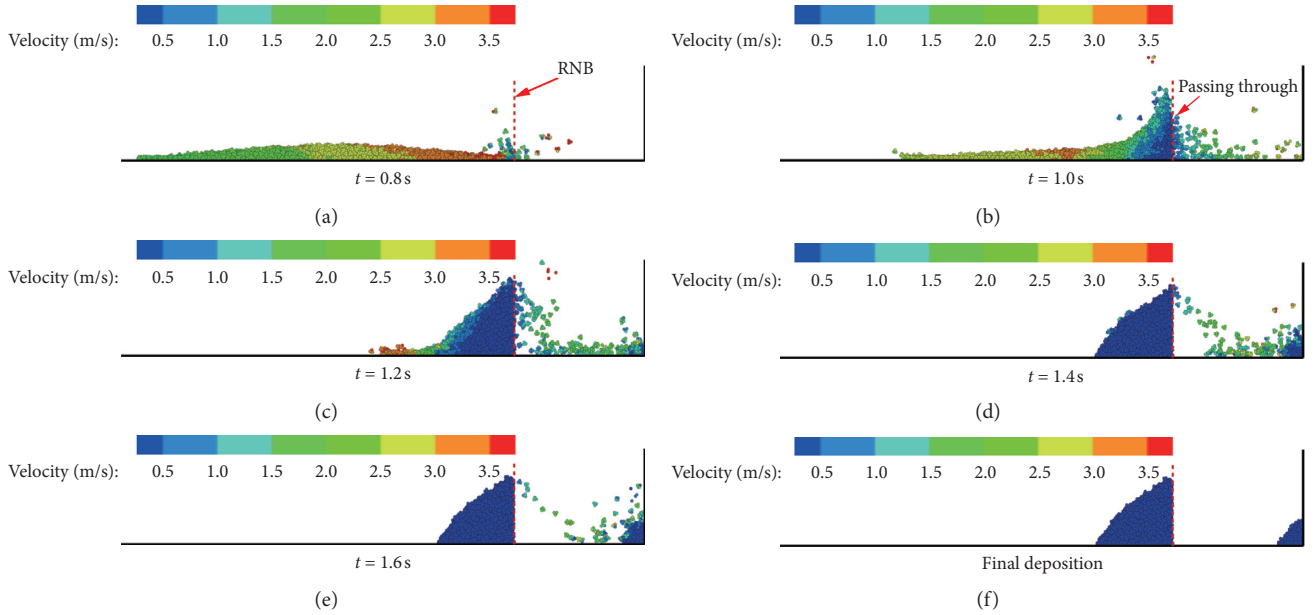


FIGURE 16: Granular flow process in Case C3.

The above analysis shows that, to improve the obstruction efficiency and avoid the grain passing-through phenomenon, it is necessary to set the mesh size small enough. In the case of uniform-size grains, if the mesh size used is smaller than the grain size, the passing-through phenomenon can be avoided, on the basis of which continuing to reduce the mesh size has little effect on improving the obstruction efficiency. However, grains in nature generally do not have the same size but instead have a wide gradation distribution, so further research is needed on the obstruction of the RNB toward graded grains.

**3.4. Influence of Grain Size Gradation.** To study the influence of the grain size gradation on the dynamic process, an RNB with a size of  $0.30\text{ m} \times 0.35\text{ m}$  was placed  $0.55\text{ m}$  away from the rigid wall to avoid the occurrence of overflow. The grains used in the calculations have a grain size gradation distribution, as shown in Table 5. Under the condition of test L44-H15- $\alpha 40^\circ$ , a total of 13988 clumps were generated in the source area according to the grain size gradation distribution. These clumps used the same calculation parameters as those used for the uniform-sized grains. The mesh size of the RNB was set to 10 mm, 20 mm, 30 mm, and 40 mm,

TABLE 5: Grain size gradation distribution.

Grain size (m)	Mass percentage	Cumulative mass percentage
0.010	5	5
0.015	20	25
0.020	50	75
0.030	20	95
0.040	5	100

respectively. The obstruction efficiency of the RNB toward the granular flow was calculated under different mesh size conditions, as shown in Table 5.

Table 6 shows that although some grains were still able to pass through the RNB, RNB with larger mesh sizes can still obstruct smaller grains and obtain a higher obstruction efficiency. The formation mechanism of this result is similar to that by which RNB obstructs uniform-size grains. By comparing the results of Case C with those of Case D, it can be found that, under the same mesh size conditions, when the mesh size was larger, the obstruction efficiency of the RNB toward the graded grains was higher, and when the mesh size was less, the obstruction efficiency was relatively low. This is because although the median size of the graded grains was the same as the grain size of the uniform-sized grains, when the mesh size was large, the RNB could ensure the obstruction of grains larger than the median size to improve the obstruction efficiency, but when the mesh size was small, the RNB could not effectively obstruct grains smaller than the median size, thereby reducing the obstruction efficiency. This indicates that the obstruction of an RNB toward the graded grains is quite different from that toward uniform-sized grains. Since the obstruction of graded grains mainly comes from the force chain formed by the mutual contact and support between the grains in front of the RNB, the obstruction efficiency of the RNB toward graded grains cannot be obtained by simple calculation.

The time history of the graded granular flow velocity when RNB with different mesh sizes was placed was calculated, as shown in Figure 17.

The time history of the impact of the graded granular flow on the placed RNB with different mesh sizes was calculated, as shown in Figure 18.

As seen from Figure 17, the time history of the graded granular flow velocity has similar characteristics to that of the uniform-sized grains. For example, when the mesh size was relatively large, the fine grains continued to move forward through the mesh and slowed the deceleration of velocity and caused a weak increase in the peak of the velocity curve, but the curve trends were not obvious. For this reason, although coarse grains exist as shown in Table 5, the larger mesh size was not discussed in this study. The fine grains that need to follow a more complex path to eventually pass through the RNB consume more energy, so the increased frequency collisions between the grading grains consume more energy too. Similar to the analysis of the cases with uniform-sized grains, although the peak of the velocity curve was obtained when studying the time history of the graded granular flow velocity under different RNB settings, it was affected by the accelerated motion of the grains that

TABLE 6: The obstruction efficiency of RNB with different mesh sizes toward graded grains.

	Distance from the rigid wall (m)	Mesh size (m)	Height (m)	Obstruction efficiency (%)
Case D1	0.55	0.01	0.35	99.73
Case D2	0.55	0.02	0.35	97.32
Case D3	0.55	0.03	0.35	89.26
Case D4	0.55	0.04	0.35	82.02

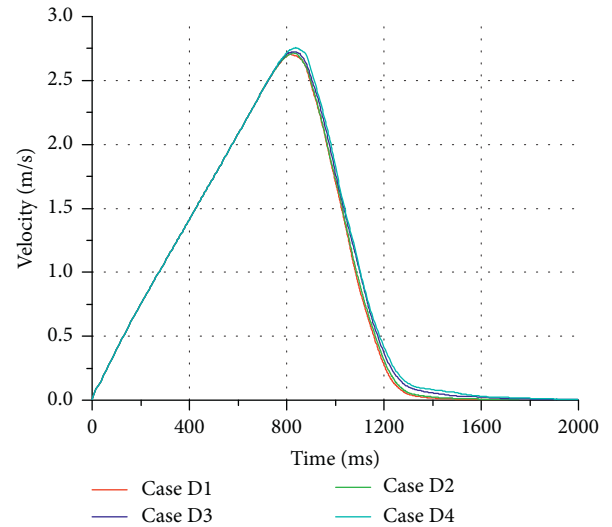


FIGURE 17: Time history of the graded granular flow velocity when RNB with different mesh sizes was placed.

passed through the RNB. Therefore, structural designs should be developed with reference to the maximum granular flow velocity before reaching the RNB but without consideration of the peak of the velocity curve, despite the quite small difference between these two velocity values in cases with graded grains.

It can be seen from the results shown in Figure 18 that the time histories of the impact of graded grains and uniform-sized grains on the RNB have similar characteristics. For example, the RNB with a larger mesh size under the impact of the graded grains was subject to a lesser unit-width normal force and moment. The difference between the unit-width normal force and moment acting on the RNB is gradually reduced as the mesh size decreases. There are also some significant differences; for example, due to the greater density of the graded grains, the peak and stable values of the unit-width normal force and moment acting on the RNB were larger. Meanwhile, under the impact of graded grains, the unit-width normal force and moment acting on the RNB were more fluctuating. This strong fluctuation made it difficult to distinguish the local curves under different mesh size conditions. This is because under the impact of graded grains, the collisions between the grains were more complicated and frequent, so this strong fluctuation must also be paid attention in actual engineering.

During the flow process, the graded grains showed a regular grain size distribution through complex interactions

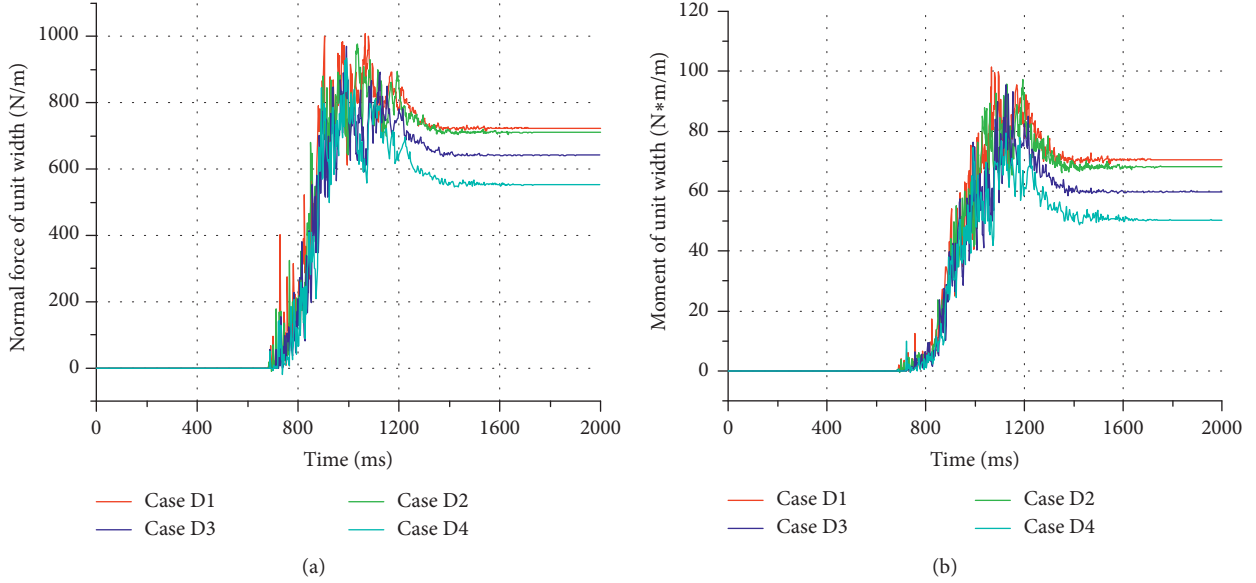


FIGURE 18: Time history of the impact of the graded granular flow on RNB with different mesh sizes: (a) time history of the unit-width normal force; (b) time history of the unit-width moment.

such as collisions and friction, which is called grain-size segregation [46, 47]. To analyze the characteristics of grain-size segregation in front of the RNB, the grain distributions under different mesh size conditions were compared, as shown in Figure 19.

As seen from the distribution diagram shown in Figure 19, the graded granular flow stopped and accumulated under the obstruction of the RNB and showed a certain grain size distribution characteristic. When the mesh size was relatively large, the grain size gradually decreased along the flume in the upstream direction due to the passing-through phenomenon, while the distribution along the height of the RNB exhibited more large grains in the upper part and more small grains in the lower part. The reason for this grain size distribution may be that the larger grains had more chance to be subjected to the upward impact force during the collision, and the small grains were more likely to be deposited through intergranular pore spaces to the bottom. The movement and accumulation processes of graded grains are complicated. At present, the understanding of the mechanism of grain-size segregation is not deep enough, so it still needs constant study [48, 49]. The grain size distribution determines the partitioning of the physicomechanical properties of the deposits in front of the RNB including the density, porosity, and permeability, which is the premise for the study of the forces on the RNB and for the stability analysis and cleanup of deposits. The discrete element method can effectively simulate the obstruction process of an RNB toward a complex graded granular flow, thus providing a reliable reference for the optimal design of RNB structures.

In actual engineering, natural grains usually have a wide gradation distribution, and it is almost inevitable that fine grains pass through the RNB; thus, it is not necessary to obstruct all grains. When a sufficiently small mesh size is set, the force chain formed between the grains can still effectively

obstruct most of the grains. At the same time, graded grains with more complex flow characteristics than those of uniform-size grains have a strong fluctuating impact on the RNB through more frequent collisions and form a special grain size distribution in front of the RNB. The discrete element numerical simulation can capture this information and provide a reference for reasonable RNB setting to achieve the expected protection effect.

#### 4. Discussion

RNB is a common engineering structure that can effectively obstruct granular flow disasters. Since it is difficult to obtain information such as the granular flow velocity and the time history of the forces acting on an RNB during the obstruction process using existing measurement technology, numerical simulations become an inevitable choice for use in the design and optimization of RNB structures.

In this study, a typical granular flow experiment was numerically simulated. Based on the verification of the correctness of the numerical simulation, the numerical analysis method was used to compare the protective effect of different RNBs on granular flows and the time history of the forces and moments acting on the RNB, and some useful conclusions were obtained. However, the simplified experiments and calculation models still have some ineluctable differences relative to actual protection engineering. For example, an actual RNB may have deformability, and the deformation of the structure will cause a new structural stress distribution. At the same time, whether the material of the mesh structure has sufficient strength and whether the RNB and the boundary have a reliable connection also become primary factors in maintaining the safety of the protective structure. These factors have not been considered in this study, so they are the direction in which the numerical

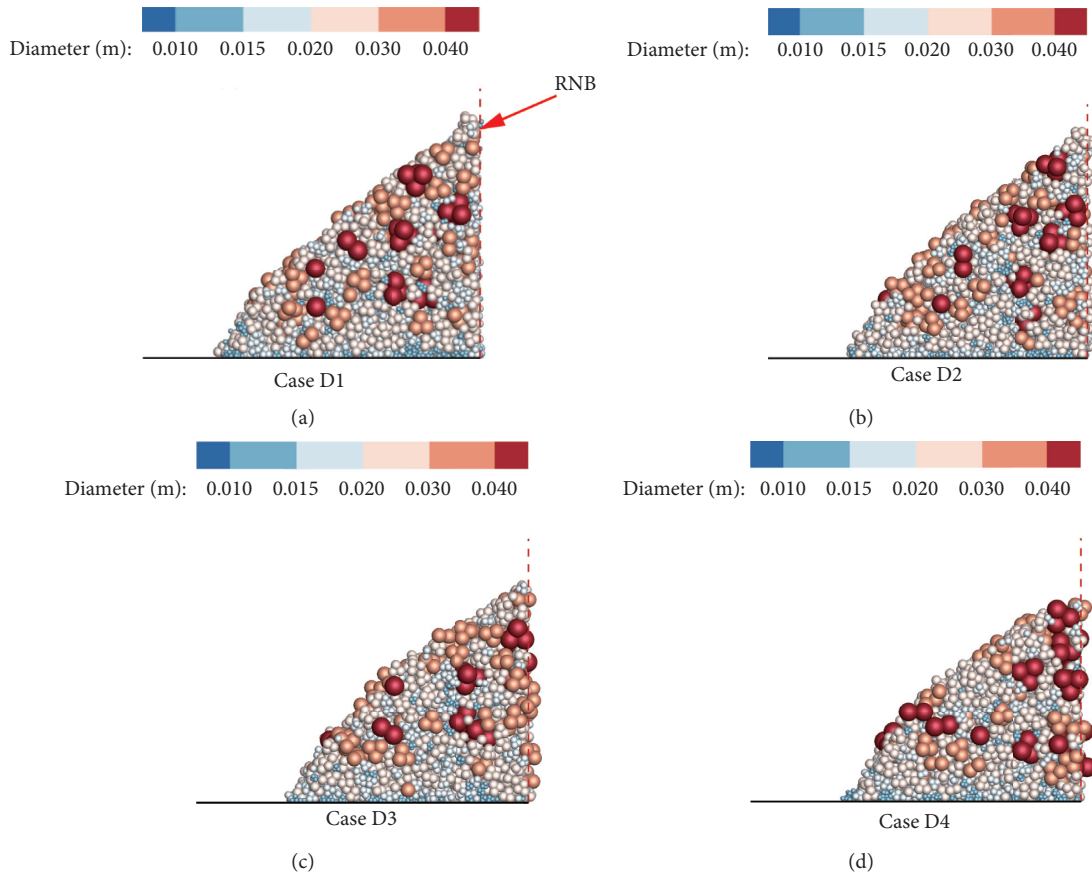


FIGURE 19: Distribution diagram of the grain size.

model needs to be further improved and developed. Although the influences of several factors, such as the RNB stiffness and deformation, were neglected in the calculation of the obstruction by the RNB, the results can still show the influence of the structural form and arrangement of the RNB on the main aspects, such as the forces acting on the RNB and the obstruction efficiency toward grains under the condition that the structural rigidity and strength are sufficient. Therefore, these studies apply to RNB with high stiffness and strength. However, if the RNB stiffness is insufficient, or even if the structure is flexible in actual engineering, the conclusions of this study will no longer be valid, and further research must be conducted to dynamically couple the calculations of the RNB and granular flow so that the numerical simulation can fully present the influence of the deformation or even damage of the mesh structure on the dynamic process.

In nature, grains have a wide gradation distribution, so the phenomenon in which fine grains pass through the RNB is almost inevitable in the prevention of actual disasters. At this point, combined with the grading characteristics of the protected rock and soil, the granular flow can be obstructed by setting multiple layers of RNB. As this method helps achieve grading obstruction and reduce the forces acting on the single-layer RNB, the failure risk of the single-layer RNB due to excessive force is reduced, thus providing a reliable solution to a complex engineering problem. Due to limited

space, this study did not undertake more in-depth optimization analysis for multilayer RNB settings. Nevertheless, the calculations for the single-layer RNB presented in this study can still reflect some fundamental obstruction characteristics of RNB toward graded granular flow. These studies are useful for further designing multilayer RNB and comprehensive protective measures.

Although the optimization analysis of RNB herein is not combined with specific engineering, the numerical simulation can be used to obtain dynamics data that are difficult to acquire using existing measuring equipment during the obstruction process of granular flow, such as the time history of the granular flow velocity, the time history of the unit-width normal force and moment acting on the RNB, and the size distribution of the graded grains in front of the RNB. Based on these data, it is possible to place an RNB to avoid harmful phenomena such as overflow, withstand the designed impact load, and achieve the desired obstruction efficiency. Therefore, this study can provide a reference for the optimization of RNB structures and layouts in practical engineering.

## 5. Conclusions

With the characteristics of a simple structure and quick construction, the RNB is an excellent and economical form of a protective structure. Based on the correctness

verification of the numerical simulation, the obstruction process of an RNB toward granular flows under different setting conditions was analyzed in this study.

It was found that there are several points that should be given attention when designing an RNB. (i) The position setting affects the time history of the forces acting on the RNB and the obstruction efficiency. Under the condition under which the source of the granular flow has been determined, the RNB should be placed upstream to improve the obstruction efficiency and reduce the forces on the RNB; otherwise, the RNB should be placed downstream to provide more reliable protection. (ii) Under effective obstruction from an RNB, the granular flow runs up in front of the RNB, so it is necessary to set an RNB high enough to avoid the overflow phenomenon. (iii) When the mesh size of the RNB is larger than the grain size, although the force chain formed between the grains in front of the RNB can support and obstruct fine grains, it is almost inevitable that small grains will pass through the mesh before the reliable force chain is formed, especially for naturally graded grains. Therefore, to obtain the desired protective effect, it is necessary to set a suitable mesh size. (iv) Under the condition of graded grains, the time history of the forces acting on the RNB and the obstruction efficiency are more complicated. Due to the higher density of the graded grains, the RNB withstands a greater force. Through the collision and action of differently sized grains, the time history of the forces acting on the RNB is more fluctuating.

The abovementioned points can provide a reference for RNB design, but more specific optimization designs (such as the RNB position, height, and mesh size) still need to be obtained through numerical simulations and comparative studies. The numerical simulation can provide not only the obstruction efficiency and the granular flow movement but also the maximum granular flow velocity, the time history of the forces acting on the RNB, and the grain size distribution. In the case of limited measurement techniques for details, the numerical simulation has become an important means to study the obstruction process of RNB structures toward granular flow. Although this study did not take into account the more complex influences of RNB deformation and strength, the analysis has fully demonstrated the main characteristics of granular flow movement and its impact on the RNB, and the obtained results are applicable to RNB with sufficient stiffness and strength. The obstruction efficiency, maximum granular flow velocity, and peak and stable forces obtained by numerical calculations are important indicators for use in RNB design. Through numerical simulation and structural optimization, the RNB can be made more reasonable and effective.

## Data Availability

The numerical calculation data used to support the findings of this study are included within the article and supplementary information files. Previously reported experimental data were used to support this study and are available at doi: 10.1007/s00603-012-0293-3. These prior studies are cited at relevant places within the text as references (Jiang and Towhata [45]).

## Conflicts of Interest

The authors declare that there are no conflicts of interest regarding the publication of this paper.

## Acknowledgments

This work was supported by the National Key Research and Development Program of China (Grant nos. 2016YFC0801603 and 2017YFC1503101), the National Natural Science Foundation of China (Grant nos. 41201007 and 51474048), the Fundamental Research Funds for the Central Universities of China (Grant no. N170108029), and the Research Fund for General Science Project of Department of Education of Liaoning Province (Grant no. L2013103).

## Supplementary Materials

The information on calculation data is as follows: The S1.xlsx is data of Figure 5. The S2.xlsx is data of Figure 6. The S3.xlsx is data of Figure 8. The S4.xlsx is data of Figure 9. The S5.xlsx is data of Figure 11. The S6.xlsx is data of Figure 12. The S7.xlsx is data of Figure 14. The S8.xlsx is data of Figure 15. The S9.xlsx is data of Figure 17. The S10.xlsx is data of Figure 18. These supplementary material files including calculation data are stored in the form of an excel file. The name of the sheet in the file indicates the calculation case. The title line of each sheet (the first line) indicates the name of the variable. Based on these descriptions, all the data supporting the manuscript can be easily found. (*Supplementary Materials*)

## References

- [1] J. E. Costa, *Physical Geomorphology of Debris Flows: Developments and Applications of Geomorphology*, Springer, Berlin, Germany, 1984.
- [2] T. Takahashi, *Debris Flow*, A A Balkema Publishers, Atlanta, GA, USA, 1991.
- [3] D. Rickenmann, “Empirical relationships for debris flows,” *Natural Hazards*, vol. 19, no. 1, pp. 47–77, 1999.
- [4] D. F. Van Dine, *Debris Flow Control Structures for Forest Engineering*, Victoria British Columbia, Ministry of Forests, Victoria, BC, Canada, 1996.
- [5] X. Yu, X. Chen, W. Zhao, and J. Chen, “The influence of an EPS concrete buffer layer thickness on debris dams impacted by massive stones in the debris flow,” *Shock and Vibration*, vol. 2015, Article ID 463640, 11 pages, 2015.
- [6] X. Chen, P. Cui, Y. You, J. Chen, and D. Li, “Engineering measures for debris flow hazard mitigation in the Wenchuan earthquake area,” *Engineering Geology*, vol. 194, pp. 73–85, 2015.
- [7] M. Xiong, X. Meng, S. Wang et al., “Effectiveness of debris flow mitigation strategies in mountainous regions,” *Progress in Physical Geography: Earth and Environment*, vol. 40, no. 6, pp. 768–793, 2016.
- [8] T. Mizuyama, “Structural countermeasures for debris flow disasters,” *International Journal of Erosion Control Engineering*, vol. 1, no. 2, pp. 38–43, 2008.
- [9] R. Brighenti, A. Segalini, and A. M. Ferrero, “Debris flow hazard mitigation: a simplified analytical model for the design

- of flexible barriers,” *Computers and Geotechnics*, vol. 54, pp. 1–15, 2013.
- [10] C. E. Choi, C. W. W. Ng, D. Song et al., “Flume investigation of landslide debris resisting baffles,” *Canadian Geotechnical Journal*, vol. 51, no. 5, pp. 540–553, 2013.
- [11] C. W. W. Ng, C. E. Choi, D. Song et al., “Physical modeling of baffles influence on landslide debris mobility,” *Landslides*, vol. 12, no. 1, pp. 1–18, 2015.
- [12] Y. C. Tai, Y. Wang, J. M. N. T. Gray, and K. Hutter, “Methods of similitude in granular avalanche flows,” *Advances in Cold-Region Thermal Engineering and Sciences*, vol. 533, pp. 415–428, 1999.
- [13] S. Hauksson, M. Pagliardi, M. Barbolini, and T. Jóhannesson, “Laboratory measurements of impact forces of supercritical granular flow against mast-like obstacles,” *Cold Regions Science and Technology*, vol. 49, no. 1, pp. 54–63, 2007.
- [14] A. M. Abdelrazek, I. Kimura, and Y. Shimizu, “Simulation of three-dimensional rapid free-surface granular flow past different types of obstructions using the SPH method,” *Journal of Glaciology*, vol. 62, no. 232, pp. 335–347, 2016.
- [15] L. Bugnion, B. W. McArdell, P. Bartelt, and C. Wendeler, “Measurements of hillslope debris flow impact pressure on obstacles,” *Landslides*, vol. 9, no. 2, pp. 179–187, 2012.
- [16] M. Hürlimann, D. Rickenmann, and C. Graf, “Field and monitoring data of debris-flow events in the Swiss Alps,” *Canadian Geotechnical Journal*, vol. 40, no. 1, pp. 161–175, 2003.
- [17] C. Berger, B. W. McArdell, and F. Schlunegger, “Sediment transfer patterns at the Illgraben catchment, Switzerland: implications for the time scales of debris flow activities,” *Geomorphology*, vol. 125, no. 3, pp. 421–432, 2011.
- [18] K. Hu, F. Wei, and Y. Li, “Real-time measurement and preliminary analysis of debris-flow impact force at Jiangjia Ravine, China,” *Earth Surface Processes and Landforms*, vol. 36, no. 9, pp. 1268–1278, 2011.
- [19] Y. Cui, C. E. Choi, L. H. D. Liu, and C. W. W. Ng, “Effects of particle size of mono-disperse granular flows impacting a rigid barrier,” *Natural Hazards*, vol. 91, no. 3, pp. 1179–1201, 2018.
- [20] K. M. Hákonardóttir, A. J. Hogg, T. Jóhannesson, and G. G. Tómasson, “A laboratory study of the retarding effects of braking mounds on snow avalanches,” *Journal of Glaciology*, vol. 49, no. 165, pp. 191–200, 2003.
- [21] J. M. N. T. Gray, Y.-C. Tai, and S. Noelle, “Shock waves, dead zones and particle-free regions in rapid granular free-surface flows,” *Journal of Fluid Mechanics*, vol. 491, pp. 161–181, 2003.
- [22] S. Moriguchi, R. I. Borja, A. Yashima, and K. Sawada, “Estimating the impact force generated by granular flow on a rigid obstruction,” *Acta Geotechnica*, vol. 4, no. 1, pp. 57–71, 2009.
- [23] W. Ashwood and O. Hungr, “Estimating total resisting force in flexible barrier impacted by a granular avalanche using physical and numerical modeling,” *Canadian Geotechnical Journal*, vol. 53, no. 10, pp. 1700–1717, 2016.
- [24] G. Gao and M. A. Meguid, “Modeling the impact of a falling rock cluster on rigid structures,” *International Journal of Geomechanics*, vol. 18, no. 2, article 04017141, 2018.
- [25] T. Faug, P. Lachamp, and M. Naaim, “Experimental investigation on steady granular flows interacting with an obstacle down an inclined channel: study of the dead zone upstream from the obstacle. Application to interaction between dense snow avalanches and defence structures,” *Natural Hazards and Earth System Science*, vol. 2, no. 3/4, pp. 187–191, 2002.
- [26] D. Mancarella and O. Hungr, “Analysis of run-up of granular avalanches against steep, adverse slopes and protective barriers,” *Canadian Geotechnical Journal*, vol. 47, no. 8, pp. 827–841, 2010.
- [27] C. W. W. Ng, C. E. Choi, A. Y. Su, J. S. H. Kwan, and C. Lam, “Large-scale successive boulder impacts on a rigid barrier shielded by gabions,” *Canadian Geotechnical Journal*, vol. 53, no. 10, pp. 1688–1699, 2016.
- [28] D. Song, C. W. W. Ng, C. E. Choi, G. G. D. Zhou, J. S. H. Kwan, and R. C. H. Koo, “Influence of debris flow solid fraction on rigid barrier impact,” *Canadian Geotechnical Journal*, vol. 54, no. 10, pp. 1421–1434, 2017.
- [29] S. B. Savage and K. Hutter, “The motion of a finite mass of granular material down a rough incline,” *Journal of Fluid Mechanics*, vol. 199, no. -1, pp. 177–215, 1989.
- [30] F. Wu, Y. Fan, L. Liang, and C. Wang, “Numerical Simulation of dry granular flow impacting a rigid wall using the discrete element method,” *PLoS One*, vol. 11, no. 8, Article ID e0160756, 2016.
- [31] O. Hungr, “A model for the runout analysis of rapid flow slides, debris flows, and avalanches,” *Canadian Geotechnical Journal*, vol. 32, no. 4, pp. 610–623, 1995.
- [32] A. Mangeney-Castelnau, J. P. Vilotte, M. O. Bristeau et al., “Numerical modeling of avalanches based on Saint Venant equations using a kinetic scheme,” *Journal of Geophysical Research Solid Earth*, vol. 108, no. B11, article 2527, 2013.
- [33] R. M. Iverson and D. L. George, “A depth-averaged debris-flow model that includes the effects of evolving dilatancy. I. Physical basis,” *Proceedings of The Royal Society A: Mathematical, Physical and Engineering Sciences*, vol. 470, no. 2170, article 20130819, 2014.
- [34] M. Brunet, L. Moretti, A. Le Friant, A. Mangeney, E. D. Fernández Nieto, and F. Bouchut, “Numerical simulation of the 30–45 ka debris avalanche flow of Montagne Pelée volcano, Martinique: from volcano flank collapse to submarine emplacement,” *Natural Hazards*, vol. 87, no. 2, pp. 1189–1222, 2017.
- [35] J.-b. Fei, T.-l. Chen, Y.-x. Jie, B.-y. Zhang, and X.-d. Fu, “A three-dimensional yield-criterion-based flow model for avalanches,” *Mechanics Research Communications*, vol. 73, pp. 25–30, 2016.
- [36] J. DeBruyn, “Viewpoint: unifying liquid and granular flow,” *Physics*, vol. 4, article 86, 2011.
- [37] Y. Forterre and O. Pouliquen, *Granular Flows. Glasses and Grains*, Springer, Basel, Switzerland, 2011.
- [38] Y.-J. Jiang, Y. Zhao, I. Towhata, and D.-X. Liu, “Influence of particle characteristics on impact event of dry granular flow,” *Powder Technology*, vol. 270, pp. 53–67, 2015.
- [39] T. Faug, R. Beguin, and C. Benoit, “Mean steady granular force on a wall over-flowed by free-surface gravity-driven dense flows,” *Physical Review E*, vol. 80, article 021305, 2009.
- [40] C. E. Choi, C. W. W. Ng, D. Song, R. P. H. Law, J. S. H. Kwan, and K. K. S. Ho, “A computational investigation of baffle configuration on the impedance of channelized debris flow,” *Canadian Geotechnical Journal*, vol. 52, no. 2, pp. 182–197, 2014.
- [41] A. Leonardi, F. K. Wittel, M. Mendoza, R. Vetter, and H. J. Herrmann, “Particle-fluid-structure interaction for debris flow impact on flexible barriers,” *Computer-Aided Civil and Infrastructure Engineering*, vol. 31, no. 5, pp. 323–333, 2014.
- [42] R. P. H. Law, C. E. Choi, and C. W. W. Ng, “Discrete element investigation of the influence of debris flow baffles on rigid

- barrier impact," *Canadian Geotechnical Journal*, vol. 53, no. 2, pp. 179–185, 2015.
- [43] M. Jakob and O. Hungr, *Debris-Flow Hazards and Related Phenomena*, Springer, Berlin, Germany, 2007.
- [44] Itasca Consulting Group Inc, *PFC Particle Flow Code, Ver. 5.0 Manual*, Itasca, Minneapolis, MN, USA, 2014.
- [45] Y.-J. Jiang and I. Towhata, "Experimental study of dry granular flow and impact behavior against a rigid retaining wall," *Rock Mechanics and Rock Engineering*, vol. 46, no. 4, pp. 713–729, 2013.
- [46] R. A. Bagnold, "Experiments on a gravity-free dispersion of large solid spheres in a Newtonian fluid under shear," *Proceedings of the Royal Society of London. Series A. Mathematical and Physical Sciences*, vol. 225, pp. 49–63, 1954.
- [47] S. B. Savage and C. K. K. Lun, "Particle size segregation in inclined chute flow of dry cohesionless granular solids," *Journal of Fluid Mechanics*, vol. 189, no. 189, pp. 311–335, 1988.
- [48] W. Zhou, Z. Lai, and G. Ma, "Effect of base roughness on size segregation in dry granular flows," *Granular Matter*, vol. 18, no. 4, article 83, 2016.
- [49] K. van der Vaart, A. R. Thornton, and C. G. Johnson, "Breaking size-segregation waves and mobility feedback in dense granular avalanches," *Granular Matter*, vol. 20, no. 3, article UNSP46, 2018.

## Research Article

# Repairing and Strengthening of Damaged RC Columns Using Thin Concrete Jacketing

Bassam A. Tayeh, Mohammed Abu Naja, Samir Shihada, and Mohammed Arafa 

Civil Engineering Department, Islamic University of Gaza, Gaza, State of Palestine

Correspondence should be addressed to Mohammed Arafa; marafa@iugaza.edu.ps

Received 28 January 2019; Revised 29 April 2019; Accepted 8 May 2019; Published 11 June 2019

Academic Editor: Chiara Bedon

Copyright © 2019 Bassam A. Tayeh et al. This is an open access article distributed under the Creative Commons Attribution License, which permits unrestricted use, distribution, and reproduction in any medium, provided the original work is properly cited.

This research aims to investigate the efficiency of repairing damaged concrete columns using thin concrete jacketing. The experimental program included casting of nine reference 300 mm long reinforced concrete column specimens: three specimens had a cross-sectional dimension of 100 mm × 100 mm, three specimens had a cross-sectional dimension of 150 mm × 150 mm, and three specimens had a cross-sectional dimension of 170 mm × 170 mm. A total of 36 identical column cores were cast with similar cross sections of 100 mm × 100 mm and a height of 300 mm. These cores were damaged by loading them with approximately 90% of their actual ultimate axial load capacities. Then, the columns were repaired and strengthened by applying two jacketing materials, which were 25 and 35 mm thick, on all four sides. Group 1 consisted of 18 column cores jacketed by normal strength concrete with a maximum aggregate size of 4.75 mm and steel reinforcement, whereas Group 2 consisted of 18 column cores jacketed using ultrahigh-performance fibre-reinforced self-compacting concrete with steel reinforcement. The experimental program showed that the Group 1 specimens had ultimate load capacities more than twice those of the unjacketed reference columns and the same axial capacity as the monolithically cast reference columns. The Group 2 specimens showed a significant increase in ultimate load capacity, which was approximately 3 times that of the unjacketed reference column and 1.86 times that of the monolithically cast reference columns. Moreover, using the shear studs was found to be the most effective among the three surface preparation techniques.

## 1. Introduction

The repair and rehabilitation of existing structures are major construction activities. Meanwhile, reinforced concrete (RC) is used widely as a construction material in most parts of the world. Structures made with this material often suffer damages due to overloading, natural disasters (e.g., earthquake and flood), fire, environmental effects (e.g., corrosion), or changes in building usage before reaching their intended design life. These damages may cause the structural elements to fail to meet the functional requirements within their designed service life. If proper attention is not paid in this regard, structures could fail to carry their design load and disasters could occur [1].

The failure of the most important structural elements, i.e., columns, may lead to the total collapse of frame-

structured buildings because they are the only structural elements that convey the total vertical loads of buildings to the soil. These members can lose their strength and stiffness due to damages during their service lives. Therefore, repair or reconstruction is necessary in case of noticeable cracks to ensure that loads are further carried and transmitted to the soil [2].

Strengthening methods depend on the type of structure and loading. Regarding structures subjected primarily to static loads, increasing flexural and axial compressive strength is essential. Regarding structures subjected primarily to dynamic loads, increasing flexural and shear strength is crucial. Improving column ductility and rearranging column stiffness can also be achieved with strengthening methods. Damages to RC columns may include slight cracks without damage to reinforcement,

superficial damage in concrete without damage to reinforcement, concrete crushing, reinforcement buckling, or tie rupture. On the basis of the degree of damages, techniques such as injections, removal and replacement, or jacketing can be applied [3–8]. Three principal techniques are available for strengthening RC columns: concrete jacketing, steel jacketing, and composite jacketing (FRP) [1].

The susceptibility of existing buildings to structural damages largely depends on the quality of the design, detailing, and construction. Engineers in many cases can extend the life span of buildings by utilising simple repairing or strengthening techniques. The choice of repairing or strengthening techniques becomes, therefore, the decisive factor because high costs may prevent many building owners from executing essential repair works [9–13].

Experimental investigations into strengthened or repaired columns are generally conducted on unloaded original columns, although having unloaded strengthened columns in the field presents a challenge. In studying the behaviour of strengthened columns with preloading, the original column is important but difficult to apply experimentally [3, 14–16].

Ersoy et al. [17] studied the repairing and strengthening of columns by jacketing. They tested four basic columns with identical dimensions and reinforcement under monotonic axial loading. After the test, they jacketed and retested these basic columns. They called the intervention either a repairing or strengthening jacket depending on whether the basic specimens had been loaded to a damaged level.

Fukuyama et al. [2] investigated jacketing with RC steel plates and carbon fibre sheets. This method has been widely used to repair or strengthen the RC columns damaged by the Hyogoken-Nanbu earthquake in 1995. To investigate the shear strength and ductility of RC columns repaired or strengthened by jacketing, they tested eight column specimens under constant axial compressive load and cyclic shear forces.

Meda et al. [7] studied the possibility of strengthening existing RC columns with a technique based on the application of a high-performance fibre-reinforced concrete jacket with 170 MPa compressive strength.

The ultrahigh-performance fibre concrete with a compressive strength of more than 100 MPa and improved durability marks an advancement in the concrete industry. This high-performance material offers various interesting applications. It allows the construction of sustainable and economic buildings with an extraordinary slim design. Its high strength and ductility make it the ultimate building material, e.g., for bridge decks, storage halls, thin-walled shell structures, and highly loaded columns. Aside from its improved strength properties, its outstanding resistance against all kinds of corosions is an additional milestone on the way towards zero-maintenance construction [18–21].

Many researchers have investigated the bond strength between two concrete layers and different techniques for increasing the roughness of the substrate surface [22–28].

Nowadays, repairing techniques suitable in terms of low cost and fast execution time should be identified. Hence, the

current research studied the repairing and strengthening of square RC columns by applying two concrete jacketing types: using ultrahigh-performance fibre-reinforced self-compacting concrete (UHPFRSCC) and normal strength concrete (NSC) as jacketing materials with three methods of surface roughening, i.e., mechanical wire brushing, mechanical scarification, and using shear studs. Moreover, the effects of jacket thickness on ultimate load-carrying capacity and axial displacement were studied. The obtained results were compared with those of the reference columns. The bonding among the column cores with their jacketing was investigated to decide on the best surface preparation technique.

## 2. Experimental Program

The experimental work herein aims to investigate the bonding among the column cores and their jacketing and the ultimate load-carrying capacity and axial displacement of uniaxial loaded square RC columns repaired and strengthened using two jacketing types with three methods of surface roughening. The obtained results are compared with those of the reference columns. Figure 1 presents the experimental plan of column specimens' fabrication.

**2.1. Fabrication of Column Specimens.** The current study includes the fabrication of 45 column specimens: 9 column specimens are reference columns, whereas 36 column cores are repaired and strengthened by applying two jacketing types using NSC-4.75 and UHPFRSCC with three methods of surface roughening. All column specimens are designed according to ACI 318 code requirements [25]. The longitudinal reinforcement ratio of all column specimens is not less than 1%. The details of the fabricated column specimens are as follows:

- (1) Three square column specimens (UC) are cast monolithically to act as unjacketed reference columns (similar to the column core). These reference columns have cross-sectional dimensions of 100 mm × 100 mm and a height of 300 mm with 4Ø8 mm longitudinal steel reinforcement and 3Ø2.5 mm steel reinforcement ties, as shown in Figure 2.
- (2) Six square column specimens (MC1 and MC2) are cast monolithically as reference columns. These reference columns have cross-sectional dimensions of 150 mm × 150 mm and 170 mm × 170 mm and a height of 300 mm with 4Ø8 mm longitudinal steel reinforcement and 3Ø2.5 mm steel reinforcement ties (Figure 3).
- (3) All the column specimens which are jacketed are loaded with approximately 90% of their actual axial capacity and are associated with appearing hairline cracks without reaching failure.
- (4) Two jacketing types are applied to two groups of column cores (A-B and X-Y). The first group (A-B) consists of 18 column cores jacketed with NSC-4.75

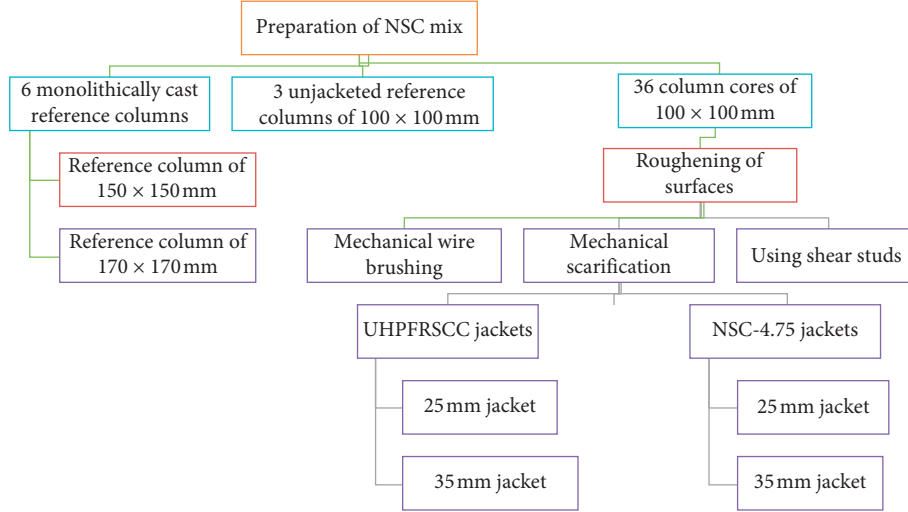


FIGURE 1: Experimental program.

using additional longitudinal and transverse steel reinforcement. The contact surfaces between the old and new concrete are roughened by three methods, i.e., mechanical wire brushing, mechanical scarification, and using shear studs. The second group (X-Y) consists of 18 column cores jacketed with UHPFRSCC using additional steel reinforcement. The surfaces are roughened in a similar way to the first group.

- (5) Two jacket thicknesses of 25 and 35 mm are applied to the two groups of column cores (A-B and X-Y).
- (6) The overall cross-sectional dimensions of the A-B and X-Y jacketed column specimens become 150 mm × 150 mm and 170 mm × 170 mm with jacket thicknesses of 25 and 35 mm, respectively, and fixed heights of 300 mm.
- (7) The test result for the column specimens is considered the average of the three samples (S1, S2, and S3). Table 1 shows the details of the 45 column specimens considered in the experimental program.

**2.2. Types of Concrete Mixes.** In this research, the following concrete mixes are designed on the basis of the targeted concrete compressive strength.

**2.2.1. NSC.** The NSC mix is prepared and used to cast the UC reference columns, MC reference columns, and the column cores of the two groups A-B and X-Y. Table 2 shows the NSC mixing proportions.

**2.2.2. NSC-4.75.** The NSC mix with a maximum aggregate size of 4.75 mm (NSC-4.75) is prepared and used to cast the jackets of the A-B column specimens. The absolute volume method recommended in [29, 30] is used to compute the quantities of concrete materials required for the NSC-4.75 mix. Table 3 shows the mixing proportions of NSC-4.75.

**2.2.3. UHPFRSCC.** The UHPFRSCC mix is used to cast the jacket of the X-Y column specimens. It is prepared using the ingredients detailed in Table 4 [31]. The UHPFRSCC mix is designed to obtain a target standard cylinder compressive strength of approximately 120 MPa. The UHPFRSCC mix is prepared at IUG Soil and Materials Laboratory. All required amounts of constituent materials are weighed accurately and mixed properly using a tilting revolving drum mixer to produce homogeneous concrete. The mixing procedures are based on the study in [32].

**2.3. Preparation of UC and MC Reference Columns and Column Cores.** The NSC mix is prepared to obtain a targeted standard cylinder compressive strength of approximately 25 MPa. The low targeted strength represents the real status of most damaged RC columns. The absolute volume method recommended in [29] is used to compute the quantities of concrete materials required for the NSC mix.

The UC and MC reference columns and A-B and X-Y column cores are reinforced with two types of steel-reinforcing bars. High tensile strength steel with a yield stress of 360 MPa is used for longitudinal steel reinforcement, whereas steel reinforcement ties with a yield stress of 240 MPa are used. Tests are carried out for each bar size: three steel specimens with a diameter of 8 mm and length of 300 mm and another three steel specimens with a diameter of 2.5 mm and length of 280 mm. All steel samples are obtained from randomly chosen bars. Table 5 shows the testing results of the main longitudinal and transverse steel reinforcements.

**2.4. Preparation of Jackets.** Two jacketing types are applied to the two groups of column cores, i.e., A-B and X-Y. The A-B group represents the 18 column cores jacketed by NSC with a maximum aggregate size of 4.75 mm (NSC-4.75); the steel reinforcement cage is placed in the jacket. The X-Y group represents the 18 column cores jacketed by UHPFRSCC; the steel reinforcement cage is placed in the jacket.

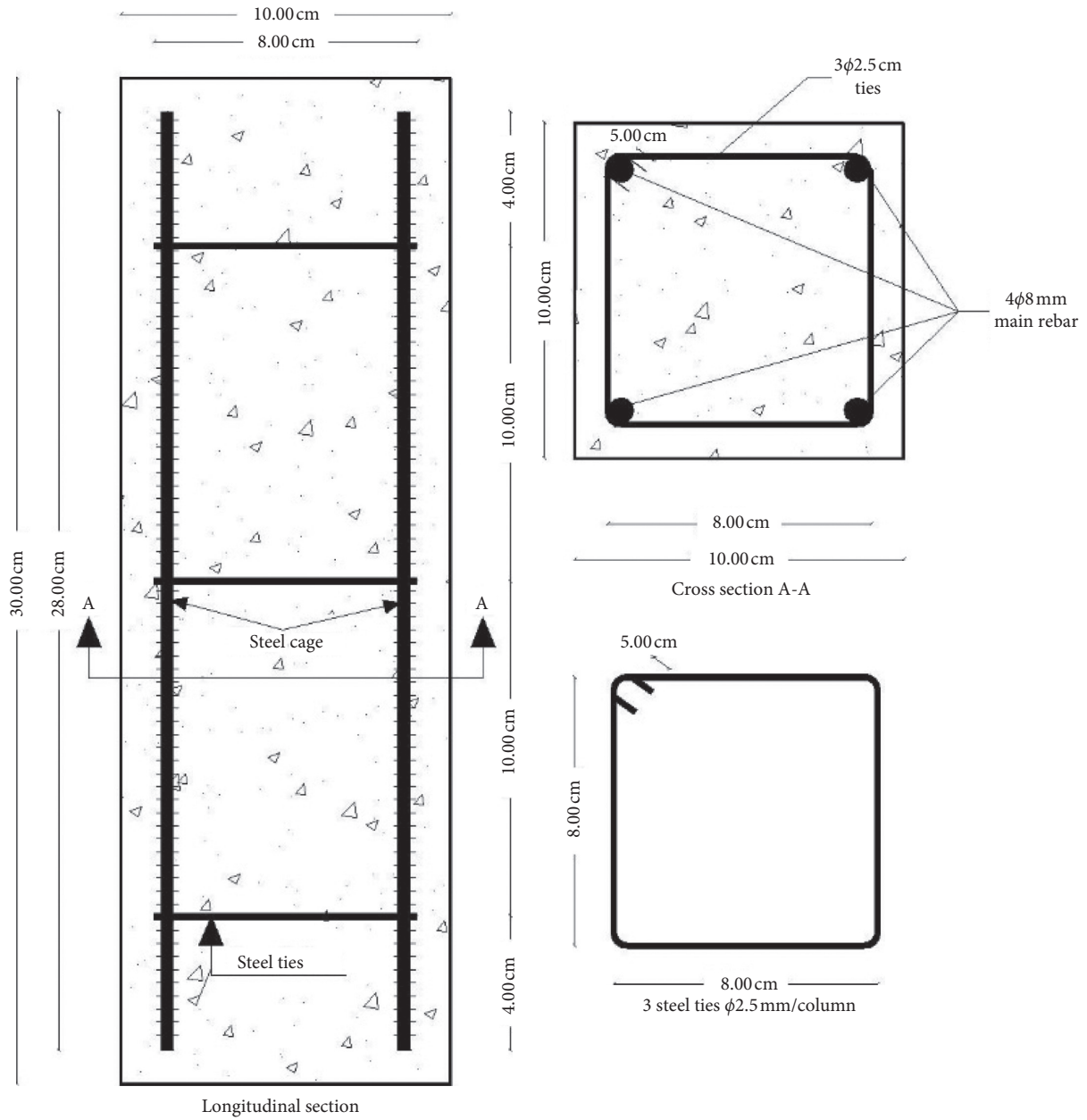


FIGURE 2: Geometry and reinforcement details of UC unjacketed reference columns.

**2.4.1. Preparation of Core Surfaces.** Three methods are used to roughen the surfaces of column cores to investigate the method which can provide the best bond between column cores and their jacketing.

**(1) Preparation of A-B-W and X-Y-W Groups.** Using mechanical wire brushing, the specimens' surfaces are cleaned to remove the dust and ensure their roughness. Figure 4 shows the preparation of the A-B-W and X-Y-W groups [33]. 4 $\varnothing$ 8 mm main steel-reinforcing bars with a length of 280 mm and a diameter of 8 mm are used at the four corners of the column cores. 3 $\varnothing$ 2.5 mm transverse steel reinforcement ties are used and fixed to the longitudinal steel bars (not welded) with a vertical spacing of 90 mm.

**(2) Preparation of A-B-C and X-Y-C Groups.** In preparing the core surfaces of the A-B-C and X-Y-C groups, a concrete cutting diskette is used to scarify the specimens' surfaces. The scarification is approximately 3–6 mm wide and 5–7 mm deep for good roughening. Figure 5 shows the preparation of the A-B-C and X-Y-C groups [33]. 4 $\varnothing$ 8 mm main steel-reinforcing bars with a length of 280 mm and a diameter of 8 mm are used at the four corners of the column cores. Figures 6 and 7 show the geometry and reinforcement detailing of the A-C and B-C groups, respectively. The geometry and steel detailing of the Y-W, B-C, and Y-C groups are discussed later. 3 $\varnothing$ 2.5 mm transverse steel reinforcement ties are used and fixed to the longitudinal steel bars (not welded) with a vertical spacing of 90 mm.

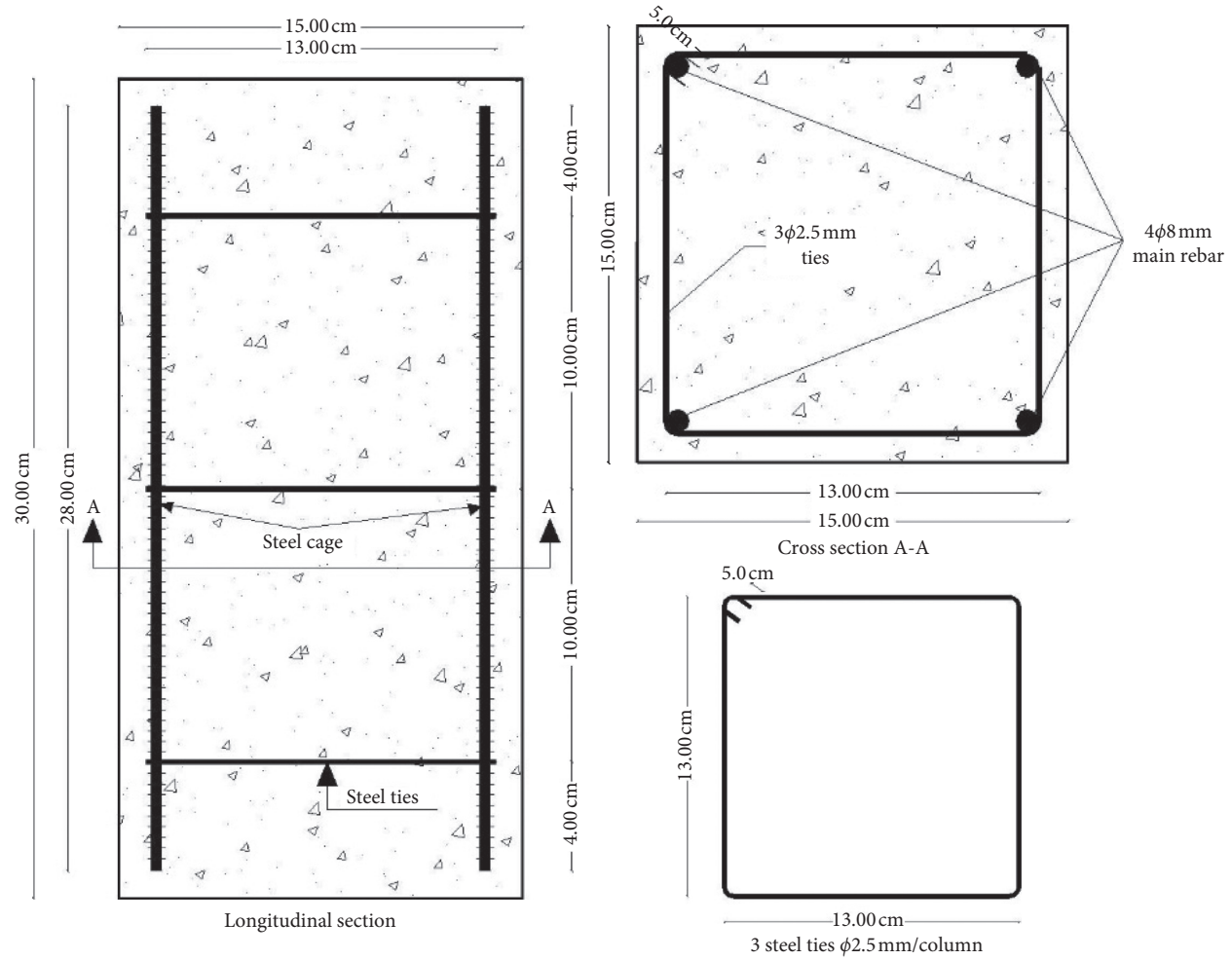


FIGURE 3: Geometry and reinforcement details of MC1 unjacketed reference columns.

TABLE 1: Details of column specimens.

#	Description	Notation	Column core (mm)	Overall cross section (mm)	Jacket thickness (mm)	Number of samples
1	UC unjacketed reference column	UC	100 × 100	Cross-sectional dimensions of UC and MC reference columns are fixed	25	3
2	MC monolithically cast reference columns	MC1	150 × 150		35	3
3		MC2	170 × 170		35	3
4	Roughening surface by mechanical wire brushing	A-W	100 × 100	150 × 150	25	3
5		B-W	100 × 100	170 × 170	35	3
6	NSC-4.75 jacket, [A-B]	A-C	100 × 100	150 × 150	25	3
7	Roughening surface by mechanical scarification	B-C	100 × 100	170 × 170	35	3
8		A-S	100 × 100	150 × 150	25	3
9	Bonding by using shear studs	B-S	100 × 100	170 × 170	35	3
10	Roughening surface by mechanical wire brushing	X-W	100 × 100	150 × 150	25	3
11		Y-W	100 × 100	170 × 170	35	3
12	UHPFRSCC jacket, [X-Y]	X-C	100 × 100	150 × 150	25	3
13	Roughening surface by mechanical scarification	Y-C	100 × 100	170 × 170	35	3
14		X-S	100 × 100	150 × 150	25	3
15	Bonding by using shear studs	Y-S	100 × 100	170 × 170	35	3

(3) Preparation of A-B-S and X-Y-S Groups. Mechanical drilling with a 6 mm diameter drilling bit is conducted to perforate a hole with a diameter of 6 mm and a depth of

25 mm in accordance with the ASTM A307 standards. The drilled holes are filled with the Sikadur-31 CF bonding material (SIKA Company) to ensure a good bond between

TABLE 2: NSC mixing proportions.

Material	kg/m <sup>3</sup>
Coarse aggregate	1317
Fine aggregate (sand)	658
Cement	300
Water	165

TABLE 3: NSC-4.75 mixing proportions.

Material	kg/m <sup>3</sup>
Coarse aggregate	1316.8
Fine aggregate (sand)	658.4
Cement	300
Water	165
Superplasticizer	9

TABLE 4: UHPFRSCC mixing proportions [31].

Material	kg/m <sup>3</sup>
Cement CEM I 42.5 R	900
Water	216
Silica fume	90
Quartz sand	1125
Superplasticizer	27
Steel fibres	36

the shear connectors and old concrete. L-shaped shear connectors with a diameter of 4 mm and a total length of 40 mm are used. The 25 mm straight portion of the shear connector is inserted in the drilled hole. Figure 8 shows the preparation of the A-B-S and X-Y-S groups. 4Ø8 mm main steel-reinforcing bars with a length of 280 mm and a diameter of 8 mm are used at the four corners of the column cores. Figures 9 and 10 show the geometry and reinforcement detailing of the A-S and B-S groups, respectively. The geometry and steel detailing of the X-S and Y-S groups are discussed later. 3Ø2.5 mm transverse reinforcement ties are used and fixed to the longitudinal steel bars (not welded) with a vertical spacing of 90 mm.

**2.4.2. Jacketing Using NSC-4.75.** The mixing procedure comprises the following steps [34]: The NSC-4.75 concrete is placed in timber moulds. Three standard test cylinders with a height of 300 mm and a diameter of 150 mm are used in compliance with the ASTM C470 standards. They are cast from the same batch of NSC-4.75 mix and compacted mechanically using a hand tamping rod to prevent segregation and honeycombing. The sides of the moulds are stripped away after being left for 24 h. All the specimens, i.e., UC and MC reference columns and A-B and X-Y column cores, are submerged in a curing water basin for 28 days. Figure 11 shows the A-B jacketed column specimens after curing, at which point they are ready to be tested.

**2.4.3. Jacketing Using UHPFRSCC.** After the UHPFRSCC is cast in the timber moulds, the surfaces are smoothed by trowelling. Three standard test cylinders with a height of

300 mm and a diameter of 150 mm are used in compliance with the ASTM C470 standards. They are cast from the same batch of UHPFRSCC mix without manual compaction (as it is self-compacting concrete). The sides of the moulds are stripped away after being left for 24 h. The X-Y jacketed column specimens are submerged in a curing water basin for 28 days. Three other standard test cylinders are cast with UHPFRSCC and submerged in a curing water basin for 28 days. Figure 12 shows the X-Y jacketed column specimens after curing, at which point they are ready to be tested.

**2.5. Testing of Column Specimens.** The UC and MC reference columns and the A-B and X-Y jacketed column specimens are tested using a high-capacity compression testing machine (with code number C109N and supplied by Matest Company for material testing). The machine configuration is changed to an elastic system to enable the testing of compressive strength versus the axial displacement in compliance with the ASTM C470 standards, as discussed in the following section.

**2.5.1. Ultimate Load-Carrying Capacity of Column Specimens.** After ending the curing period, the UC and MC reference columns and A-B and X-Y jacketed column specimens are kept in a dry place for 10–15 min to attain the surface dry condition. Loose sand grains or incrustations are removed from the contact faces with testing machine platens.

The column specimens are then located carefully in the testing machine to ensure the vertical concentricity (uniaxial) of the applied compressive load. Then, the test is performed by the hydraulic machine with 3000 kN compression testing capacity.

All column specimens are tested under a monotonically small loading rate of approximately 6 kN/s and a starting load of approximately 20 kN. The load is applied vertically at the top and bottom of the column specimens until failure and compression readings are recorded.

**2.5.2. Axial Displacement of Column Specimens.** The axial displacement of the UC and MC reference columns and A-B and X-Y jacketed column specimens is measured using the same compression testing machine. Three strain dial gauges with an accuracy of approximately 0.00254 mm are fixed at the midheight of the column (three faces) prior to testing. At each increment of 6 kN axial compression load, the readings of axial displacement are recorded using the machine data acquisition system.

### 3. Results and Discussion

**3.1. Compressive Strength of Reference Specimens.** The compressive strength of the NSC is obtained by testing three standard test cylinders (300 mm in height and 150 mm in diameter) at 28 days. Table 6 shows the average compressive strength of the three tested standard cylinders; the value is

TABLE 5: Steel reinforcement testing results.

Bar type	Diameter (mm)	Actual diameter (mm)	Yield stress (MPa)	Ultimate tensile strength (MPa)	% of elongation
Transverse steel reinforcement	2.5	2.5	240	276.8	31
Main rebar	8	8	360	414	20



FIGURE 4: Preparation of the A-B-W and X-Y-W groups.



FIGURE 5: Preparation of the A-B-C and X-Y-C groups.

almost equal to the targeted NSC cylinder compressive strength of 25 MPa.

The compressive strength of the UHPFRSCC is obtained by testing three standard test cylinders (300 mm in height and 150 mm in diameter) at 28 days. Table 6 shows the average compressive strength of the three tested standard cylinders. The value is close to the targeted UHPFRSCC cubic compressive strength of 120 MPa.

Figure 13 presents the obtained load-displacement diagrams of the UC, MC1, and MC2 column specimens. The UC, MC1, and MC2 reference columns reach their ultimate load-carrying capacities at an axial displacement of approximately 0.66 mm; they have almost equal axial displacements at rupture points of 0.972, 0.99, and 1.02 mm, respectively, possibly because they have similar steel reinforcement ratios and the same NSC mix.

**3.2. A-B Jacketed Column Specimens (NSC-4.75 Jacket).** The two jacket thicknesses of 25 and 35 mm result in a noticeable increase in the ultimate load-carrying capacity. The overall composite cross sections of the A-B jacketed column specimens are made of two different concrete mixes: the column cores are made of the NSC mix, whereas the outer jackets are made of the NSC-4.75 mix. Table 7 shows the effect of jacket thickness on the ultimate load-carrying capacity of the A-B group. The column cores are cast using the NSC mix with an unchanged cross section of 100 mm × 100 mm. Thus, the increase in cross-sectional area is obtained by applying the two jacket thicknesses.

The ratio of the jacket area of B-W/A-W is 1.51, whereas the corresponding ratio of ultimate load-carrying capacity is 1.38. This result shows a nearly direct proportional relation between jacket thickness and the ultimate load-carrying

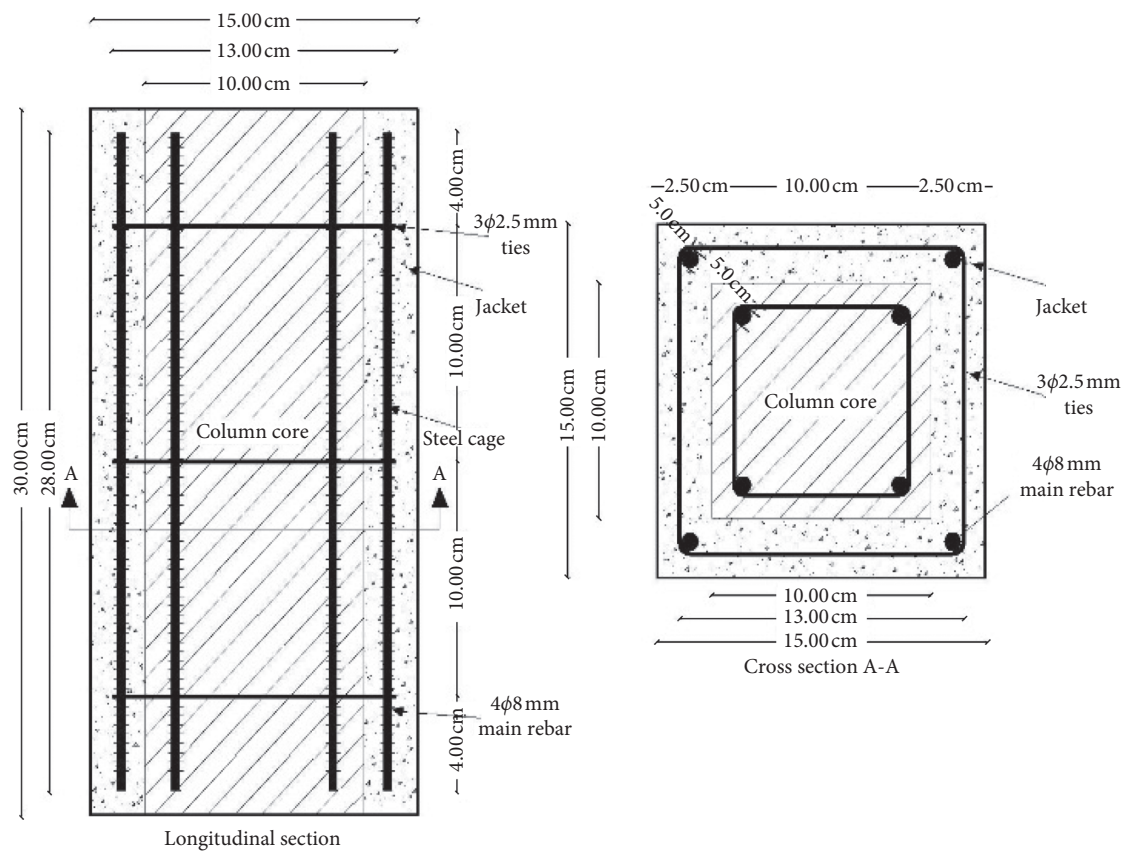


FIGURE 6: Geometry and reinforcement details of the A-W, X-W, A-C, and X-C groups.

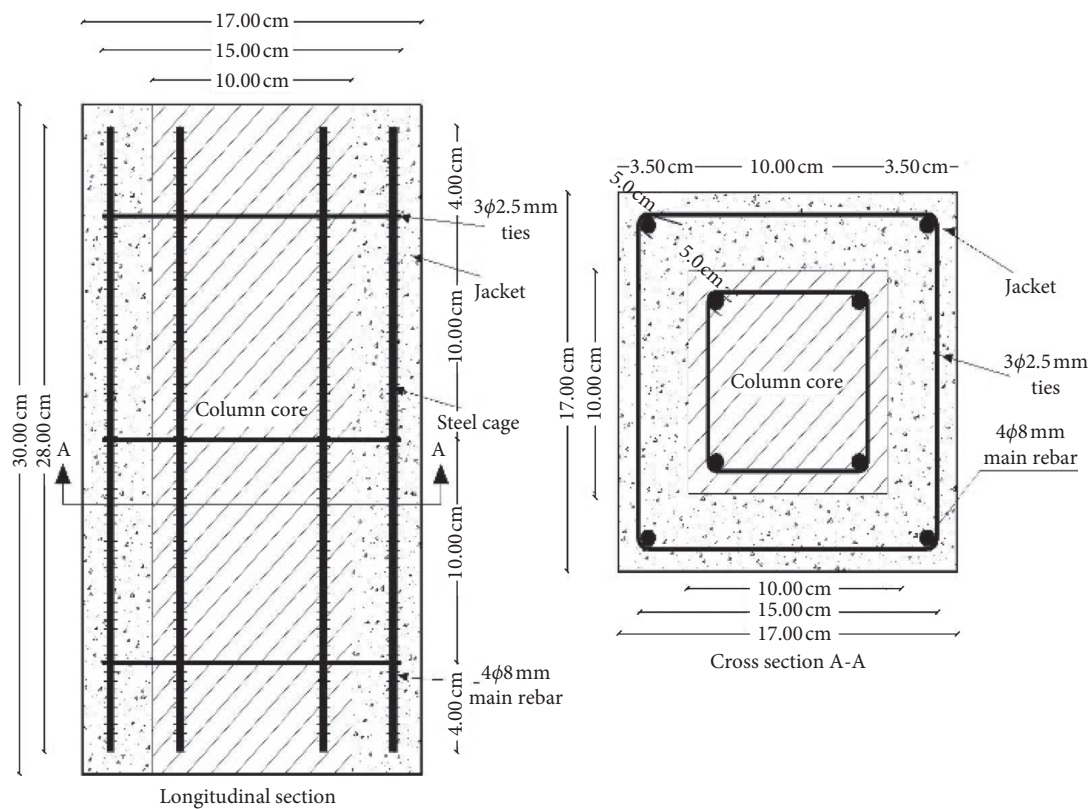


FIGURE 7: Geometry and reinforcement details of the B-W, Y-W, B-C, and Y-C groups.



FIGURE 8: Preparation of the A-B-S and X-Y-S groups.

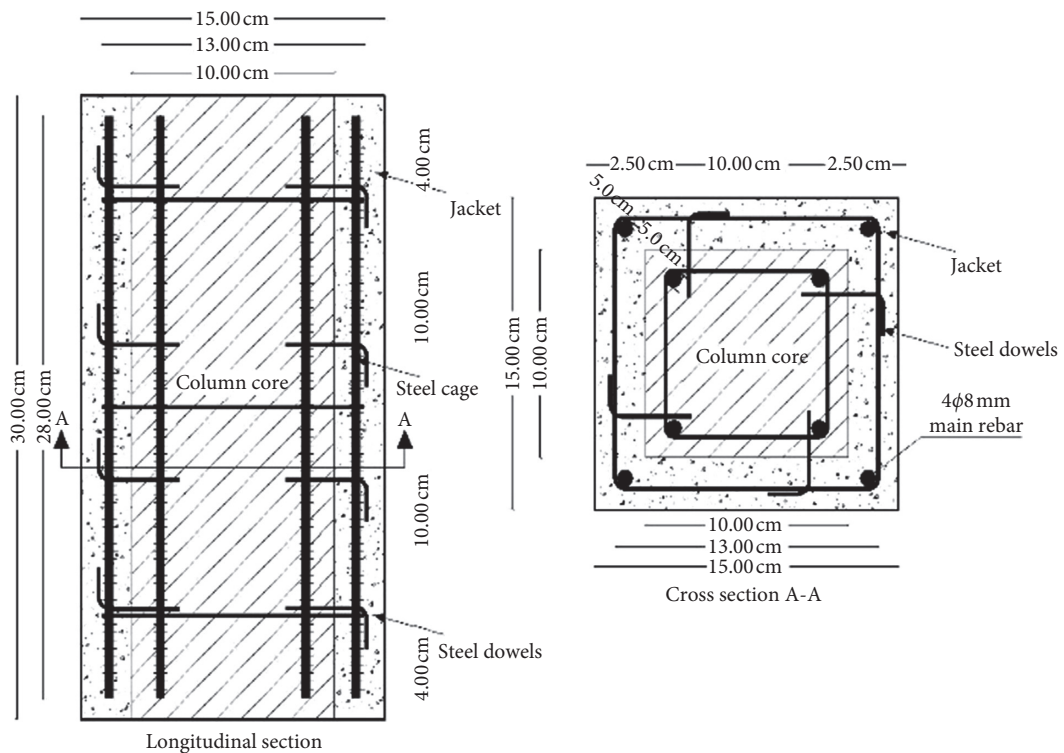


FIGURE 9: Geometry and reinforcement details of the A-S and X-S groups.

capacity of the A-B-W jacketed column specimens. The ratio of the jacket area of B-C/A-C is 1.51, whereas the corresponding ratio of ultimate load-carrying capacity is 1.26. This result shows a nearly direct proportional relation between jacket thickness and the ultimate load-carrying capacity of the A-B-C jacketed column specimens. The ratio of the jacket area of B-S/A-S is 1.51, whereas the corresponding ratio of ultimate load-carrying capacity is 1.32. This result shows an almost direct proportional relation between jacket thickness and the ultimate load-carrying capacity of the A-B-C jacketed column specimens.

Table 8 indicates that the A-W and B-W jacketed column specimens show an increase in ultimate load-carrying capacities of approximately 1.56 and 2.15 times those of the UC

reference columns, respectively. Table 8 also shows that A-W and B-W have an increase in ultimate load-carrying capacities of 1.08 and 0.95 times those of the corresponding MC reference columns, respectively. The results obtained are less than those obtained by Meda et al. [7], who strengthened a concrete column of cross section (300 mm × 300 mm) with normal strength RC jacket that is 60 mm thick. Their results also showed that the ultimate capacities of the jacketed columns are more than 2.5 times those of the unjacketed columns. However, the results obtained are in good agreement with those obtained by Mourad and Shannag [16], who strengthened a concrete column of cross section (150 mm × 150 mm) with ferrocement jackets of 20 mm jacket thickness after preloading one of them to 100% of

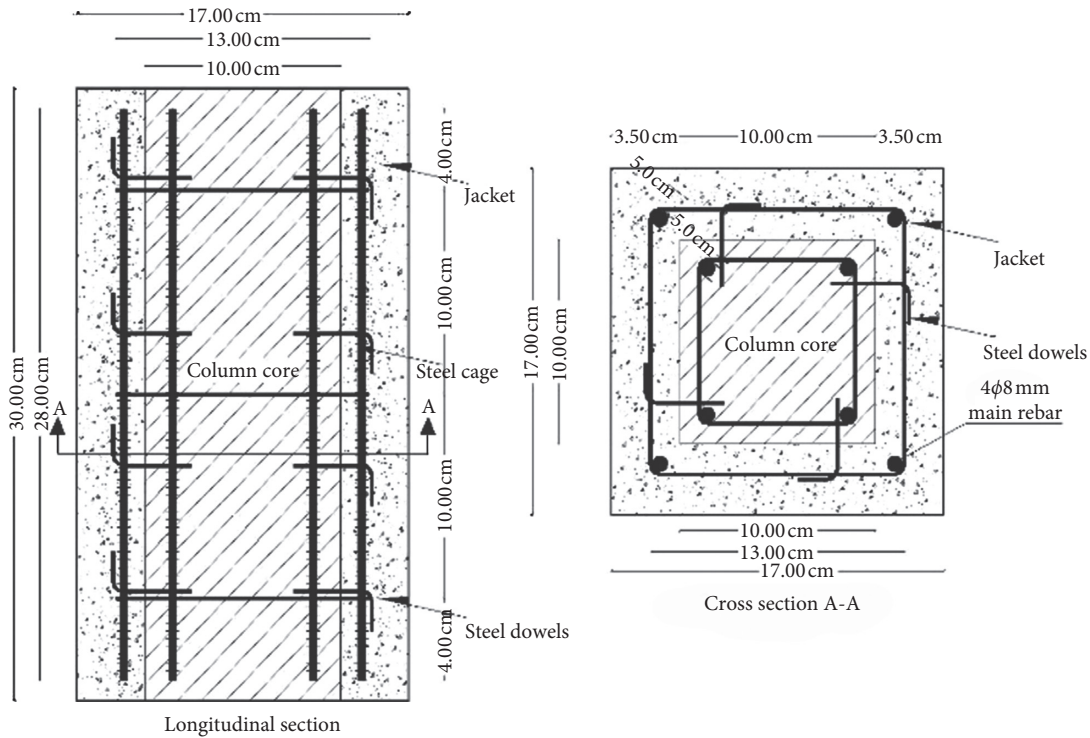


FIGURE 10: Geometry and reinforcement details of the B-S and Y-S groups.



FIGURE 11: The A-B jacketed column specimens ready for testing.



FIGURE 12: The X-Y jacketed column specimens ready for testing.

their ultimate axial strength. Strengthening the failed column restored its original capacity with similar axial stiffness and minimal ductility.

TABLE 6: Compression test results of NSC and UHPFRSCC.

Mix type	Notation	Cylinder compressive strength $S$ (MPa)
NSC	S1	27.1
	S2	25.3
	S3	26.9
	Average	26.4
UHPFRSCC	S1	103.2
	S2	106.3
	S3	107.6
	Average	105.7

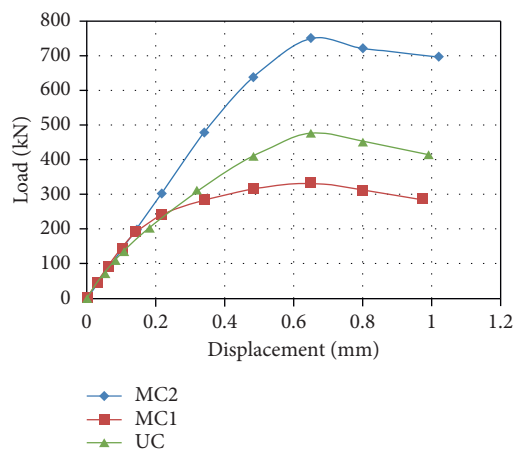


FIGURE 13: Load-displacement diagrams of UC, MC1, and MC2 reference columns.

TABLE 7: Ultimate load-carrying capacities for A-B jacketed column specimens.

Notation	$P_u$ (kN)	Column sectional area	Column core area ( $\text{cm}^2$ )	Jacket area ( $\text{cm}^2$ )
A-W	517	(15 cm $\times$ 15 cm) 225 $\text{cm}^2$		125
B-W	713	(17 cm $\times$ 17 cm) 289 $\text{cm}^2$	100	189
B-W/A-W	1.38			1.51
A-C	642	(15 cm $\times$ 15 cm) 225 $\text{cm}^2$		125
B-C	812	(17 cm $\times$ 17 cm) 289 $\text{cm}^2$	100	189
B-C/A-C	1.26			1.51
A-S	653	(15 cm $\times$ 15 cm) 225 $\text{cm}^2$		125
B-S	859	(17 cm $\times$ 17 cm) 289 $\text{cm}^2$	100	189
B-S/A-S	1.32			1.51

TABLE 8: Increases in A-B ultimate load-carrying capacity with respect to UC and MC.

A UC, $P_u$ (kN)	B		C		C/A	C/B
	MC	$P_u$ (kN)	A-B	$P_u$ (kN)		
331	MC1	478	A-W	517	1.56	1.08
	MC2	751	B-W	713	2.15	0.95
	MC1	478	A-C	642	1.94	1.34
	MC2	751	B-C	812	2.54	1.12
	MC1	478	A-S	653	1.97	1.37
	MC2	751	B-S	859	2.6	1.14

The results of the current research also indicate that the A-C and B-C jacketed column specimens show increases in ultimate load-carrying capacities of 1.94 and 2.54 times those of the UC reference columns, respectively. Table 8 also presents that A-C and B-C gain a significant increase in ultimate load-carrying capacities of 1.34 and 1.12 times those of the corresponding MC reference columns, respectively. The obtained results match those stated by Meda et al. [7] and Mourad and Shannag [16]; meanwhile, using scarification improves ultimate load-carrying capacity relative to mechanical wire brushing. The A-S and B-S jacketed column specimens show an increase in ultimate load-carrying capacities of 1.97 and 2.60 times those of the UC reference columns, respectively. Table 8 displays that A-S and B-S gain a significant increase in ultimate load-carrying capacities of 1.37 and 1.14 times those of the corresponding MC reference columns, respectively. These results are in good agreement with those obtained by Meda et al. [7] and Mourad and Shannag [16]; however, the current research indicates that using shear studs is the best method for improving ultimate load-carrying capacity.

The maximum measured axial displacements (axial displacements at rupture) of the UC and MC reference columns and A-B jacketed column specimens are compared in Table 9. The A-B-W jacketed column specimens gain a minimal increase in axial displacements at rupture relative to the UC and MC reference columns. This result is attributed to the use of NSC in jacketing, in addition to some enhancements to the concrete mix. Moreover, the A-B-C jacketed column specimens gain a minimal increase in axial displacements at rupture relative to the UC and MC reference columns. This result is attributed to the use of NSC in jacketing.

The column cores are repaired and strengthened using NSC-4.75 jacketing by applying the three jacketing methods.

A-B-W, A-B-C, and A-B-S show improved ultimate load-carrying capacities, especially when compared with the UC and MC reference columns. Figures 14 and 15 show no significant differences in the results of the ultimate load-carrying capacities of A-B-W, A-B-C, and A-B-S. The rate of increase in ultimate load-carrying capacity is almost similar to the increase in jacket thickness. The ultimate load-carrying capacities of A-B-W, A-B-C, and A-B-S increase to approximately twice those of the corresponding UC reference columns and have no significant increase relative to the MC reference columns. Figures 14 and 15 also show that A-S and B-S have the maximum axial displacement values, which indicate the best ductility.

The results of using the three methods of surface roughening for good bonding between the specimens' cores and jackets reveal that using shear studs is the best among the three methods.

**3.3. X-Y Jacketed Column Specimens (UHPFRSCC Jacket).** The overall composite cross sections of the X-Y jacketed column specimens are made of two different concrete mixes: the column cores are made of the NSC mix, whereas the outer jackets are made of the UHPFRSCC mix. Table 10 presents the average ultimate load-carrying capacity of X-Y.

The same table shows the effect of jacket thicknesses on X-Y-W's ultimate load-carrying capacity. The ratio of the jacket area of X-W/Y-W is 1.51, whereas the corresponding ratio of ultimate load-carrying capacity is 1.27. This result shows an almost direct proportional relation between jacket thickness and the ultimate load-carrying capacity of the X-Y-W jacketed column specimens. Table 10 shows the effect of jacket thicknesses on X-Y-C's ultimate load-carrying capacity. The column cores are cast using the

TABLE 9: Increases in A-B maximum axial displacement with respect to UC and MC.

A UC, axial displacement at failure (mm)	B		C		C/A	C/B
	MC	Axial displacement at failure (mm)	A-B	Axial displacement at failure (mm)		
0.972	MC1	0.99	A-W	0.99	1.02	1
	MC2	1.02	B-W	1.11	1.05	1.14
	MC1	0.99	A-C	1.02	1.05	1.03
	MC2	1.02	B-C	1.14	1.07	1.17
	MC1	0.99	A-S	1.05	1.08	1.06
	MC2	1.02	B-S	1.2	1.23	1.18

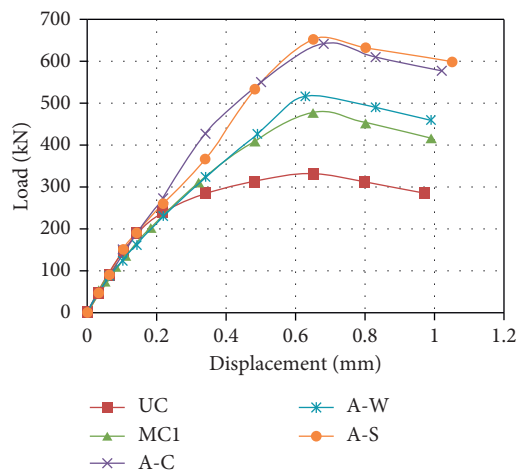


FIGURE 14: Average load-displacement diagram of A-(W-C-S) with respect to UC and MC1.

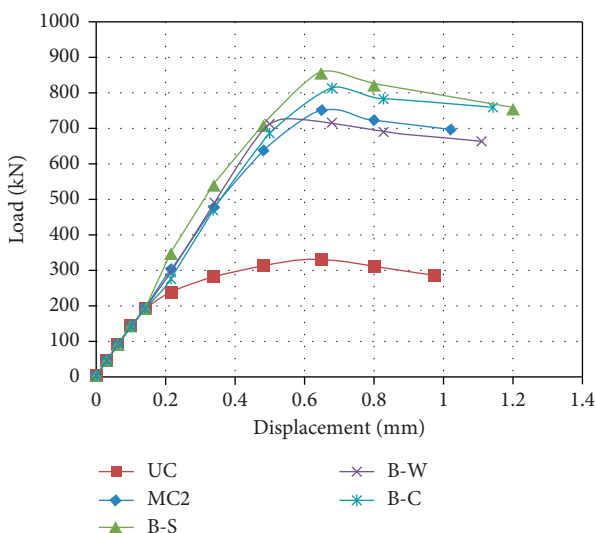


FIGURE 15: Average load-displacement diagram of B-(W-C-S) with respect to UC and MC2.

NSC mix with an unchanged cross section of 100 mm × 100 mm. Thus, the increase in cross-sectional area is obtained by applying several jacket thicknesses, almost similar to the obtained X-Y-W results. The ratio of the jacket

area of X-C/Y-C is 1.51, whereas the corresponding ratio of ultimate load-carrying capacity is 1.34. This result confirms the almost direct proportional relation between jacket thickness and the ultimate load-carrying capacity of the X-Y-C jacketed column specimens; the same results are obtained with respect to the X-Y-W jacketed column specimens. The ratio of the jacket area of X-S/Y-S is 1.51, whereas the corresponding ratio of ultimate load-carrying capacity is 1.32. This result shows the almost direct proportional relation between jacket thickness and the ultimate load-carrying capacity of the X-Y-S jacketed column specimens; the same results are obtained with respect to the X-Y-W and X-Y-C jacketed column specimens.

Table 11 indicates that the X-W and Y-W jacketed column specimens show a substantial increase in ultimate load-carrying capacities of 2.67 and 3.70 times those of the UC reference columns, respectively. Table 11 also presents that X-W and Y-W gain a significant increase in ultimate load-carrying capacities of 1.85 and 1.63 times those of the corresponding MC reference columns, respectively. These results are less than those obtained by Meda et al. [7], who strengthened a concrete column of cross section (300 mm × 300 mm) with a high-performance fibre RC jacket with 30 mm thickness. This study found that the ultimate load capacities of jacketed columns are more than four times those of unjacketed columns. In the present study, adopting a UHPFRSCC steel-reinforced jacket enhances the lateral confinement of the column specimens and thus increases the ability to sustain additional compression loads. The X-C and Y-C jacketed column specimens show considerably large increases in ultimate load-carrying capacities of 2.89 and 3.87 times those of the UC reference columns, respectively. Table 11 also shows that X-C and Y-C almost double their ultimate load-carrying capacities relative to the corresponding MC reference columns. The obtained results are less than those obtained by Meda et al. [7], who strengthened a concrete column of cross section (300 mm × 300 mm) with a high-performance fibre RC jacket with 30 mm thickness. This study found that the ultimate capacities of the jacketed columns are more than four times those of unjacketed columns. These results are primarily attributed to the use of strengthening by the jacketing method instead of the repairing and strengthening jacketing method for predamaged RC columns. Meanwhile, using scarification improves ultimate load-carrying capacity relative to mechanical wire brushing. The X-S and Y-S

TABLE 10: Ultimate load-carrying capacities for X-Y jacketed column specimens.

Notation	$P_u$ (kN)	Column sectional area	Column core area ( $\text{cm}^2$ )	Jacket area ( $\text{cm}^2$ )
X-W	883	(15 cm $\times$ 15 cm) 225 $\text{cm}^2$		125
Y-W	1224	(17 cm $\times$ 17 cm) 289 $\text{cm}^2$	100	189
Y-W/X-W	1.27			1.51
X-C	956	(15 cm $\times$ 15 cm) 225 $\text{cm}^2$		125
Y-C	1280	(17 cm $\times$ 17 cm) 289 $\text{cm}^2$	100	189
Y-C/X-C	1.34			1.51
X-S	1030	(15 cm $\times$ 15 cm) 225 $\text{cm}^2$		125
Y-S	1356	(17 cm $\times$ 17 cm) 289 $\text{cm}^2$	100	189
Y-S/X-S	1.32			1.51

TABLE 11: Increases in X-Y ultimate load-carrying capacities with respect to UC and MC.

A UC, $P_u$ (kN)	B		C		C/A	C/B
	MC	$P_u$ (kN)	X-Y	$P_u$ (kN)		
331	MC1	478	X-W	883	2.67	1.85
	MC2	751	Y-W	1224	3.7	1.63
	MC1	478	X-C	956	2.89	2
	MC2	751	Y-C	1280	3.87	1.7
	MC1	478	X-S	1030	3.11	2.15
	MC2	751	Y-S	1356	4.1	1.81

jacketed column specimens show a huge increase in ultimate load-carrying capacities of 3.11 and 4.10 times those of the UC reference columns, respectively. Table 11 also reveals that X-S and Y-S gain significant increases in ultimate load-carrying capacities that are 2.15 and 1.81 times those of the corresponding MC reference columns, respectively. The obtained results are much better than those obtained by Meda et al. [7], who strengthened a concrete column of cross section (300 mm  $\times$  300 mm) with a high-performance fibre RC jacket with 30 mm thickness. This study found that the ultimate capacities of jacketed columns are more than four times those of unjacketed columns. These results are attributed to the use of shear studs for bonding the column cores and their jacketing; this approach significantly enhances load capacity. The current research validates that using shear studs is the best method for improving ultimate load-carrying capacities.

The average load-displacement diagram is plotted for the X-Y jacketed column specimens. The maximum measured axial displacements (axial displacements at rupture) of the UC and MC reference columns and X-W and Y-W jacketed column specimens are compared in Table 12. The X-Y-W jacketed column specimens gain almost a double increase in axial displacements at rupture with respect to the UC and MC reference columns. The axial displacements of the X-W and Y-W jacketed column specimens are 1.98 and 2.04 times those of the UC reference columns, respectively. Furthermore, the axial displacements of both the X-W and Y-W jacketed column specimens are 1.94 times those of the corresponding MC reference columns. As shown in Table 12, the X-Y-C and X-Y-S jacketed column specimens gain almost a double increase in axial displacements at rupture with respect to the UC and MC reference columns.

Column cores are repaired and strengthened using UHPFRSCC jacketing by applying three jacketing types.

X-Y-W, X-Y-C, and X-Y-S show significantly improved ultimate load-carrying capacities, especially when compared with the UC and MC reference columns. Figures 16 and 17 also show no significant differences in the results of X-W, X-C, and X-S and in those of Y-W, Y-C, and Y-S in terms of ultimate load-carrying capacity. The rate of increase in ultimate load-carrying capacity is almost similar to the rate of increase in jacket thickness. The ultimate load-carrying capacities of X-Y-W, X-Y-C, and X-Y-S increase to about four and two times those of the corresponding UC and MC reference columns, respectively.

The results of using the three methods of surface roughness reveal that using shear studs is the best among the three methods.

Table 13 shows that the X-Y jacketing type significantly increases the ultimate load-carrying capacities and high ductility of the jacketed column cores because of the application of steel fibres and steel-reinforced UHPFRSCC jackets. The significant increase in the axial displacements of X-(W-C-S) and Y-(W-C-S) is attributed to the addition of 4% steel fibres in accordance with the weight of the UHPFRSCC mix; such a change results in improved material properties. The results of using the three methods of surface roughness also reveal that using shear studs is the best among the three methods.

#### 4. Conclusion

The outcomes of the experimental study can be summarised as follows:

- (i) Applying two jacket thicknesses of 25 and 35 mm with A-B and X-Y jacketing types considerably improves ultimate load-carrying capacity in almost a similar rate to the rate of increase in jacketing area.

TABLE 12: Increases in X-Y maximum axial displacements with respect to UC and MC.

A UC, axial displacement at failure (mm)	B		C		C/A	C/B
	MC	Axial displacement at failure (mm)	X-Y	Axial displacement at failure (mm)		
0.972	MC1	0.99	X-W	1.92	1.98	1.94
	MC2	1.02	Y-W	1.98	2.04	1.94
	MC1	0.99	X-C	1.92	1.98	1.94
	MC2	1.02	Y-C	2.01	2.07	1.97
	MC1	0.99	X-S	1.98	2.04	2
	MC2	1.02	Y-S	2.04	2.09	2

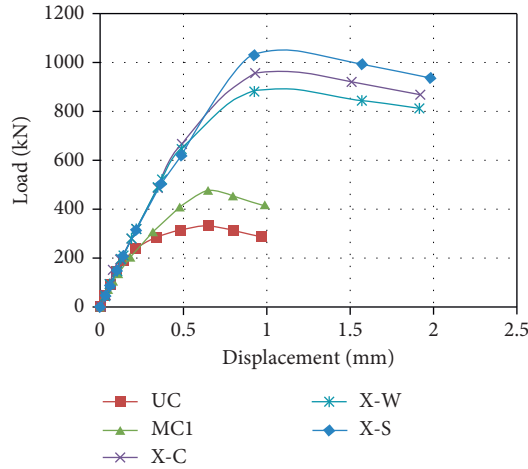


FIGURE 16: Average load-displacement diagram of X-(W-C-S) with respect to UC and MC1.

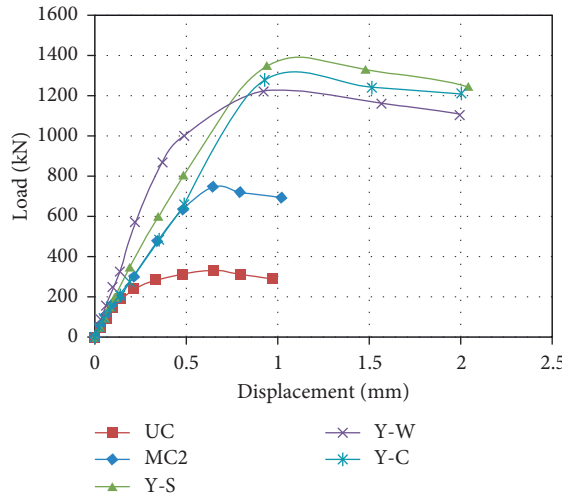


FIGURE 17: Average load-displacement diagram of Y-(W-C-S) with respect to UC and MC2.

(ii) Repairing and strengthening using UHPFRSCC and NSC-4.75 jackets significantly increases the ultimate load-carrying capacities and axial displacements of the specimens with respect to the UC and MC reference columns. The failure modes of the two jacketed column specimens are ductile and thus

provide noticeable warning signs under loading before crushing and spalling.  
(iii) Although repairing and strengthening RC columns using NSC-4.75 as a jacketing material is effective, UHPFRSCC is more effective due to the use of steel fibres. It also reduces the total strengthened column

TABLE 13: Summary of the results for all tested column specimens.

#	Description	Notation	$P_u$ (kN)	Axial displacement (mm)
1	UC unjacketed reference column	UC	331	0.972
2		MC1	478	0.99
3	MC monolithically cast reference columns	MC2	751	1.02
4		A-W	517	0.99
5	Roughening surface by mechanical wire brushing	B-W	713	1.11
6		A-C	642	1.02
7	NSC-4.75 jacket, [A-B]	B-C	812	1.14
8	Roughening surface by mechanical scarification	A-S	653	1.05
9		B-S	859	1.2
10	Bonding by using shear studs	X-W	883	1.908
11		Y-W	1224	1.989
12	UHPFRSCC jacket, [X-Y]	X-C	956	1.92
13	Roughening surface by mechanical scarification	Y-C	1280	2.001
14		X-S	1030	1.98
15	Bonding by using shear studs	Y-S	1356	2.04

sections. The UHPFRSCC can flow better than NSC-4.75 in narrow sections without segregation or honeycombing problems.

- (iv) The relationships between the applied loads and axial displacements of the tested column specimens are almost typical: a linear behaviour up to one-third of the ultimate load-carrying capacity followed by a nonlinear behaviour until failure.
- (v) The slopes of the first parts of the plotted load-displacement curves of the UC and MC reference columns are almost the same, ultimately becoming steep during repairing and strengthening with the two jacketing types. Steep slopes mean that the modulus of elasticity of strengthened columns increases.
- (vi) Applying the three methods of surface roughening, i.e., roughening by mechanical wire brushing, mechanical scarification, and using shear studs, to bond column cores and their jackets reveals that using shear studs is the best among the three methods.

## Data Availability

The experimental data used to support the findings of this study are included in the article.

## Conflicts of Interest

The authors declare that they have no conflicts of interest.

## Acknowledgments

The authors gratefully acknowledge Eng. Mohammed Abu Naja as this paper was prepared from his MSc thesis [35]. Special thanks are due to the staff of the Islamic University of Gaza (IUG) Soil and Materials Lab for their help during the sample preparation and testing.

## References

- [1] P. A. Calderón, J. M. Adam, S. Ivorra, F. J. Pallarés, and E. Giménez, "Design strength of axially loaded RC columns strengthened by steel caging," *Materials & Design*, vol. 30, no. 10, pp. 4069–4080, 2009.
- [2] K. Fukuyama, Y. Higashibata, and Y. Miyauchi, "Studies on repair and strengthening methods of damaged reinforced concrete columns," *Cement and Concrete Composites*, vol. 22, no. 1, pp. 81–88, 2000.
- [3] M. H. Allam, *Strengthening of loaded columns by R.C. jackets*, PhD thesis, Faculty of Engineering, Cairo University, Cairo, Egypt, 1995.
- [4] D. Beaupré, "Bond strength of shotcrete repair," *Shotcrete Magazine*, vol. 1, no. 2, pp. 12–15, 1999.
- [5] K. A.-D. I. Bsisu, "Retrofitting of square reinforced concrete columns subjected to concentric axial loading with steel jackets," *CEO Al-Eman Housing Company*, vol. 6, 2002.
- [6] K. G. Vandoros and S. E. Dritsos, "Concrete jacket construction detail effectiveness when strengthening RC columns," *Construction and Building Materials*, vol. 22, no. 3, pp. 264–276, 2008.
- [7] A. Meda, G. Plizzari, Z. Rinaldi, and G. Martinola, "Strengthening of R/C existing columns with high performance fiber reinforced concrete jacket," in *Proceedings of the 2nd International Conference on Concrete Repair, Rehabilitation and Retrofitting*, Cape Town, South Africa, 2009.
- [8] G. Campione, M. Fossetti, C. Giacchino, and G. Minafò, "RC columns externally strengthened with RC jackets," *Materials and Structures*, vol. 47, no. 10, pp. 1715–1728, 2014.
- [9] H. Can, "Partially jacketed (two, three, four sides) reinforced concrete column behaviour under uni-axial loading," *Teknik Dergi-Tmmob Insaat Muhendisleri Odasi*, vol. 6, pp. 337–342, 1995.
- [10] M. Frangou, K. Pilakoutas, and S. Dritsos, "Structural repair/strengthening of RC columns," *Construction and Building Materials*, vol. 9, no. 5, pp. 259–266, 1995.
- [11] S. A. Sheikh, "Performance of concrete structures retrofitted with fibre reinforced polymers," *Engineering Structures*, vol. 24, no. 7, pp. 869–879, 2002.
- [12] Y. T. Obaidat, S. Heyden, and O. Dahlblom, "The effect of CFRP and CFRP/concrete interface models when modelling

- retrofitted RC beams with FEM,” *Composite Structures*, vol. 92, no. 6, pp. 1391–1398, 2010.
- [13] M. H. Lai and J. C. M. Ho, “Confinement effect of ring-confined concrete-filled-steel-tube columns under uni-axial load,” *Engineering Structures*, vol. 67, pp. 123–141, 2014.
- [14] M. Yaqub and C. G. Bailey, “Repair of fire damaged circular reinforced concrete columns with FRP composites,” *Construction and Building Materials*, vol. 25, no. 1, pp. 359–370, 2011.
- [15] G. Campione, “Strength and ductility of R.C. columns strengthened with steel angles and battens,” *Construction and Building Materials*, vol. 35, pp. 800–807, 2012.
- [16] S. M. Mourad and M. J. Shannag, “Repair and strengthening of reinforced concrete square columns using ferrocement jackets,” *Cement and Concrete Composites*, vol. 34, no. 2, pp. 288–294, 2012.
- [17] U. Ersoy, A. T. Tankut, and R. Suleiman, “Behavior of jacketed columns,” *ACI Structural Journal*, vol. 90, no. 3, pp. 288–293, 1993.
- [18] B. Graybeal and J. Tanesi, “Durability of an ultrahigh-performance concrete,” *Journal of Materials in Civil Engineering*, vol. 19, no. 10, pp. 848–854, 2007.
- [19] B. A. Tayeh, B. H. Abu Bakar, M. A. Megat Johari, and Y. L. Voo, “Mechanical and permeability properties of the interface between normal concrete substrate and ultra high performance fiber concrete overlay,” *Construction and Building Materials*, vol. 36, pp. 538–548, 2012.
- [20] A. P. Lampropoulos, S. A. Paschalidis, O. T. Tsoulou, and S. E. Dritsos, “Strengthening of reinforced concrete beams using ultra high performance fibre reinforced concrete (UHPFRC),” *Engineering Structures*, vol. 106, pp. 370–384, 2016.
- [21] L. K. Askar, B. A. Tayeh, B. H. A. Bakar, and A. M. Zeyad, “Properties of ultra-high performance fiber concrete (UHPFC) under different curing regimes,” *International Journal of Civil Engineering and Technology (IJCIET)*, vol. 8, no. 4, pp. 965–974, 2017.
- [22] E. N. B. S. Júlio, F. A. B. Branco, and V. D. Silva, “Concrete-to-concrete bond strength. Influence of the roughness of the substrate surface,” *Construction and Building Materials*, vol. 18, no. 9, pp. 675–681, 2004.
- [23] A. A. Hallaq, B. A. Tayeh, and S. Shihada, “Investigation of the bond strength between existing concrete substrate and UHPC as a repair material,” *International Journal of Engineering and Advanced Technology (IJEAT)*, vol. 6, no. 3, pp. 210–217, 2017.
- [24] B. A. Tayeh, B. H. A. Bakar, M. A. M. Johari, and Y. L. Voo, “Evaluation of bond strength between normal concrete substrate and ultra high performance fiber concrete as a repair material,” *Procedia Engineering*, vol. 54, pp. 554–563, 2013.
- [25] A. Meda, S. Mostosi, Z. Rinaldi, and P. Riva, “Corroded RC columns repair and strengthening with high performance fiber reinforced concrete jacket,” *Materials and Structures*, vol. 49, no. 5, pp. 1967–1978, 2016.
- [26] M. Chellapandian, S. S. Prakash, and A. Sharma, “Axial compression-bending interaction behavior of severely damaged RC columns rapid repaired and strengthened using hybrid FRP composites,” *Construction and Building Materials*, vol. 195, pp. 390–404, 2019.
- [27] B. A. Tayeh, B. H. Abu Bakar, M. A. Megat Johari, and A. M. Zeyad, “Microstructural analysis of the adhesion mechanism between old concrete substrate and UHPFC,” *Journal of Adhesion Science and Technology*, vol. 28, no. 18, pp. 1846–1864, 2014.
- [28] B. A. Tayeh, B. H. Abu Bakar, M. A. Megat Johari, and M. M. Ratnam, “Existing concrete textures: their effect on adhesion with fibre concrete overlay,” *Proceedings of the Institution of Civil Engineers—Structures and Buildings*, vol. 167, no. 6, pp. 355–368, 2014.
- [29] ACI 211.1-91, *Standard Practice for Selecting Proportions for Normal, Heavyweight and Mass Concrete*, American Concrete Institute, Farmington Hills, MI, USA, 1991.
- [30] H. Rodrigues, P. Pradhan, A. Furtado, P. Rocha, and N. Vilapouca, “Structural repair and strengthening of rc elements with concrete jacketing,” *Strengthening and Retrofitting of Existing Structures*, vol. 9, pp. 181–198, 2018.
- [31] M. Arafa, S. Shihada, and A. Al Madhoun, “Mechanical properties of ultra high performance fiber reinforced self compacted concrete,” *International Journal of Engineering and Advanced Technology (IJEAT)*, vol. 3, 2013.
- [32] M. Karmout, *Mechanical Properties of Ultra High Performance Concrete Produced in Gaza Strip*, The Islamic University of Gaza, Gaza, Palestine, 2009.
- [33] K. N. Bakhsh, “Evaluation of bond strength between overlay and substrate in concrete repairs,” Master Degree thesis, Royal Institute of Technology (KTH), Stockholm, Sweden, 2010.
- [34] ASTM C192/C192M, *Standard Practice for Making and Curing Concrete Test Specimens in the Laboratory*, ASTM International, West Conshohocken, PA, USA, 2000.
- [35] M. Abu Naja, “Repair of pre-damaged (RC) columns using cementitious repair materials,” Master thesis, The Islamic University of Gaza, Gaza, Palestine, 2015.

## Research Article

# Numerical and Experimental Investigation of the Mechanical Behavior of Cable-Supported Barrel Vault Structures with Varying Temperature

Guojun Sun ,<sup>1,2</sup> Mingze Wu,<sup>3</sup> Zhihua Chen,<sup>4</sup> and Suduo Xue<sup>2,5</sup>

<sup>1</sup>Lecturer, Collage of Architecture and Civil Engineering, Beijing University of Technology, Beijing, China

<sup>2</sup>The Key Laboratory of Urban Security and Disaster Engineering, MOE, Beijing University of Technology, Beijing 100124, China

<sup>3</sup>M. A. Student, Collage of Architecture and Civil Engineering, Beijing University of Technology, Beijing, China

<sup>4</sup>Professor, Collage of Architecture and Civil Engineering, Tianjin University, Tianjin, China

<sup>5</sup>Professor, Collage of Architecture and Civil Engineering, Beijing University of Technology, Beijing, China

Correspondence should be addressed to Guojun Sun; sunny2369@163.com

Received 25 December 2018; Revised 5 May 2019; Accepted 20 May 2019; Published 10 June 2019

Academic Editor: Giosuè Boscatto

Copyright © 2019 Guojun Sun et al. This is an open access article distributed under the Creative Commons Attribution License, which permits unrestricted use, distribution, and reproduction in any medium, provided the original work is properly cited.

The cable-supported barrel vault (CSBV) structure system is a new type of hybrid spatial steel structure based on a beam string structure (or truss string structure), suspendomes, and cylindrical lattice shells. Steel cables (e.g., steel wire rope cables, steel strand cables, semiparallel steel tendons, and steel rods) are key components of CSBV structures. However, they have different elastic moduli and thermal expansion coefficients. In this study, the roof of a textile workshop (the first CSBV structure in China) was analyzed with four types of cables under the effect of varying temperature. Under half-span loading and full-span loading, the structural internal force and displacement at varying temperatures were obtained from finite element models employing four different types of steel cables. The internal force, displacement, and horizontal arch thrust changed linearly with increasing temperature. Moreover, the dynamic characteristics of CSBV with varying temperature were analyzed. The frequency of the CSBV changed linearly with increasing temperature. Based on the dynamic characteristics of CSBV with varying temperature, a seismic response time-history analysis was performed. The variation in the maximum responses of the internal force, displacement, and horizontal arch thrust was obtained. In each case, the mechanical behavior of the CSBV with semiparallel steel tendon cables was strongly affected by the temperature. Therefore, semiparallel steel tendons are not recommended as components of CSBV in cases where large temperature changes can be expected. Thereafter, a scale model of a CSBV was designed and used for experiments and corresponding finite element analyses under varying temperature. Experimental results show that the finite element method is effective for analyzing the mechanical behavior of CSBV under varying temperature.

## 1. Introduction

The static and dynamic performance of cable-supported barrel vault (CSBV) structures has been investigated using numerical and experimental methods, and superior static and dynamic performance compared to barrel vault structures has been demonstrated [2, 3]. In addition, a series of theoretical analyses and experimental studies have been carried out on the string structure, including form-finding analyses [4–6], structural optimization [7, 8], static behavior

analyses [9–11], dynamic characteristics and seismic response analyses [12], prestress design methods [13], sensitivity analyses [14], and stability studies [15–18]. As a critical load-carrying member of CSBV structures, the cables are of primary importance for guaranteeing the safety of the entire structure. Steel cables are spun helically from different types of steel wires in several layers, and as a result, the thermal expansion properties of steel cables differ from those of steel. Therefore, different cable twist qualities can also affect the value of the thermal expansion coefficient [19, 20]. The

thermal expansion coefficient of a cable member is larger than that for a common steel member. Therefore, a loss of prestress occurs in cables at higher temperatures, while an increase in the cable prestress occurs at lower temperatures. In other words, the effect of temperature on the mechanical behavior of CSBV structures is more complicated than on common steel structures. Therefore, the effect of temperature on the mechanical behavior of CSBV structures still requires further research.

In this study, four CSBV structure models were designed with different cable materials: steel rods, steel wire cables, steel stand cables, and semiparallel steel tendons. The mechanical behavior of the CSBV structures under the effect of varying temperature was investigated using numerical analyses. In addition, an experimental study of the CSBV model structure with steel strand cables was carried out. The numerical and experimental results were then compared. Finally, some conclusions have been drawn for use in practical engineering applications.

## 2. Temperature Response Analysis

**2.1. Example Analysis and Numerical Model.** The project analyzed in this study is the first CSBV structure in China: the roof of a textile workshop. The roof is 410 m long and is divided into four parts. One of these four parts with a length of 116.2 m is analyzed; its span is 50 m. According to the demand of the architecture, the rise of this CSBV structure is 4.3 m and the sag is 0.7 m. The grid pattern of the upper single-layer lattice shell is a three-way lattice grid with a grid size of approximately 4.5 m. For the rod section, three different sections are selected:  $\Phi 305 \text{ mm} \times 10 \text{ mm}$ ,  $\Phi 229 \text{ mm} \times 8 \text{ mm}$ , and  $\Phi 187 \text{ mm} \times 8 \text{ mm}$ . The sections of the struts are all  $\Phi 253 \text{ mm} \times 10 \text{ mm}$ . All cables have sections of  $\Phi 7 \text{ mm} \times 73 \text{ mm}$ , and the ultimate tensile strength of the cables is 1860 MPa. The roof dead load is  $0.80 \text{ kN/m}^2$ , and the roof live load is  $0.50 \text{ kN/m}^2$ . The building perspective, plane graph, and elevation drawing are shown in Figures 1(a), 1(b), and 1(c), respectively.

The prestress design principle of the CSBV, in which the peripheral restriction is usually a spatial pin, is that the horizontal arch thrust is zero. First, no prestress is applied, i.e., the prestress of each cable is zero. Thus, subjected to the dead weight of the structure itself, the horizontal arch thrusts can be calculated. Then, the structure is reanalyzed, and the obtained horizontal arch thrusts are applied to each cable. By performing the calculation again, a new horizontal arch thrust is obtained, changing the calculated prestress, which can then be used to recalculate the horizontal arch thrust again. This iterative process is repeated until the horizontal arch thrust is zero or close to zero, at which point the calculated prestress applied to the cables is defined as the target value. It should be noted that the geometric nonlinearity of the structure must be considered in the above calculation process. The whole process can be performed with general finite element analysis software such as ANSYS. In the ANSYS APDL finite element software package, the beam188 element was adopted to simulate the steel

members in the upper vault structure, while the struts and cables were simulated with link8 and link10 elements, respectively.

In this study, four CSBV structure models were designed with different cable materials: steel rods, steel wire cables, steel stand cables, and semiparallel steel tendons. The elastic modulus and thermal expansion coefficient of the four steel cable types are listed in Table 1. The elastic modulus and thermal expansion coefficient of the upper beam and strut were assumed to be  $2.06 \times 10^5 \text{ MPa}$  and  $1.2 \times 10^{-5}/^\circ\text{C}$ , respectively. The mechanical behavior was obtained for the temperature range of  $-40^\circ\text{C}$  to  $+40^\circ\text{C}$ . The abbreviation SR indicates the CSBV structure with cable rods, SRC represents the CSBV with steel wire rope cables, SSC represents the CSBV with the steel strand cables, and SST represents the CSBV with semiparallel steel tendons.

**2.2. Numerical Simulation of the CSBV with Full-Span Load Distribution.** Considering the practical conditions, the CSBV structure is subject to a dead load and a live load in the vertical direction. The vertical load is calculated using a load condition of  $1.2 \times \text{dead load} + 1.4 \times \text{live load}$ . Therefore, the numerical load on the whole roof is designed to be approximately  $1.2 \times 0.8 \text{ kN/m}^2 + 1.4 \times 0.5 \text{ kN/m}^2 = 1.66 \text{ kN/m}^2$ . The Surf 154 element is used to achieve full-span loading of the structure in this study. The temperature load is reduced by  $40^\circ\text{C}$  and increased by  $40^\circ\text{C}$ .

The vertical displacements of the node in the midframe and end-frame are shown in Figure 2 for Nodes 1–4. Figure 2 also shows the cable forces in the midframe and end-frame for Cables 1 and 2, the upper structural steel member (USSM) forces at the midframe and end-frame for USSM 1–4, the strut force in midframe and end-frame for Struts 1–4, and the horizontal arch thrust (HAT) in the midframe and end-frame for HAT 1 and 2.

Then, a nonlinear analysis of the CSBV structures was carried out. The results and influence of the temperature on the full-span load distribution were obtained. For example, in the full-span load distribution, the relationship between the vertical displacement of the nodes and the temperature is approximately linear.

In Figure 3, a positive sign represents an upward displacement and a negative sign represents a downward displacement. The displacements of the nodes increase with increasing temperature. The displacement trends for Node 2 and Node 4 are similar to those of Node 3, which is shown in Figure 3(b). Meanwhile, Figure 3(a) shows that the change in the displacement of the SST cables is slightly less than that of the other structures, but it can also be approximated as a linear variation.

The influence of the temperature on the cable force in the full-span load distribution is presented in Figure 4. Figure 4(a) shows the change in the cable force in the end-frame, and Figure 4(b) shows the change in the cable force in the midframe; the positive sign represents a tension force. The cable force decreases linearly with increasing temperature. The cable forces at the midframe are larger than those at the end-frame. Moreover, the SST cable force exhibits the

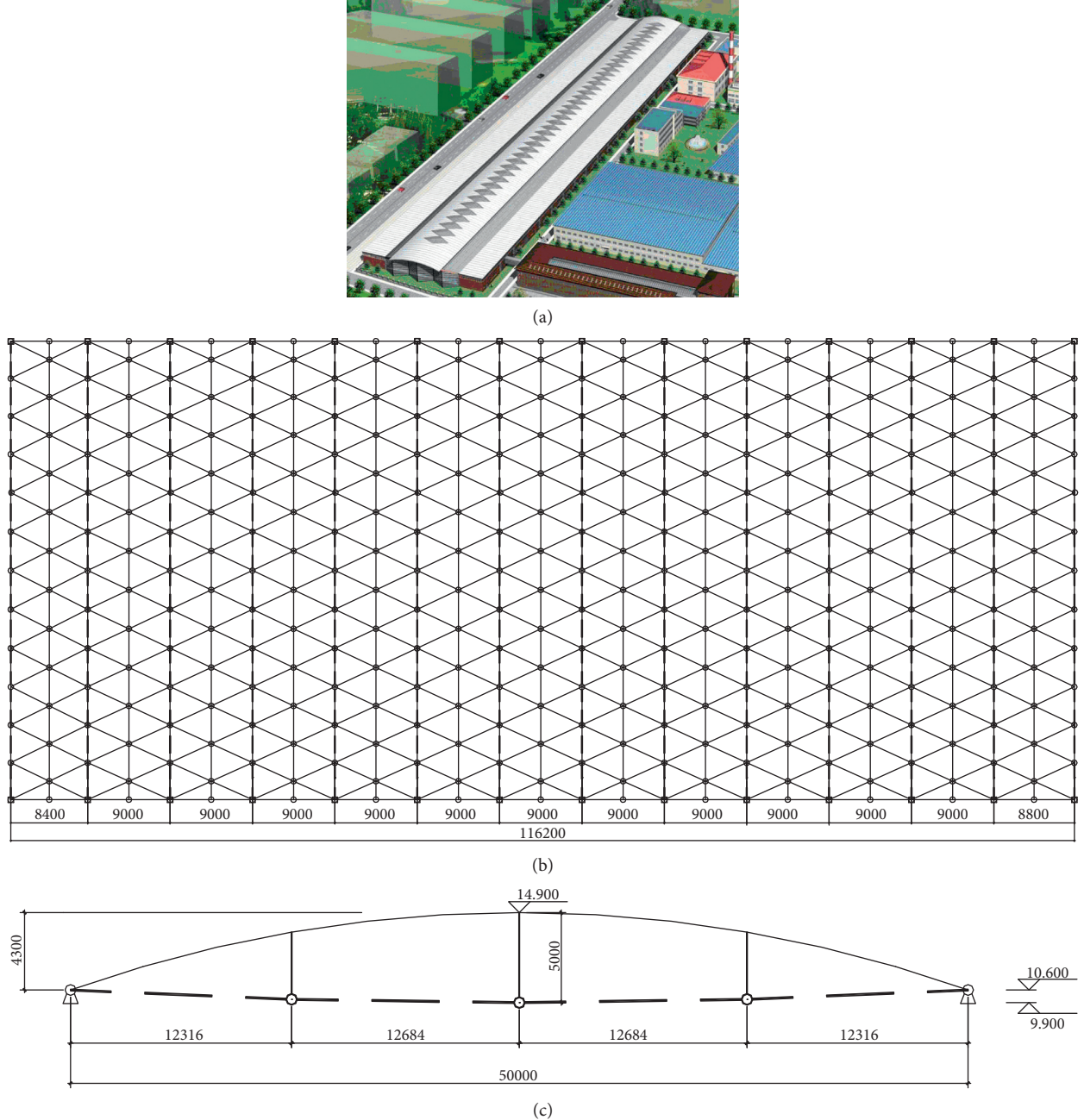


FIGURE 1: Elevation and plane graph of the CSBV structure. (a) Building perspective. (b) Plane graph of the CSBV (units: mm). (c) Elevation of the CSBV (units: mm).

TABLE 1: Modulus of elasticity and thermal expansion coefficient of the four types of cables.

Types	Steel rod	Steel wire rope cable	Steel strand cable	Semiparallel steel tendon
Elastic modulus ( $\times 10^5$ MPa)	2.06	1.4	1.95	2.05
Thermal expansion coefficient ( $\times 10^{-5}/^\circ\text{C}$ )	1.195	1.92	1.38	1.87

largest change with the temperature. Thus, the cable force of the CSBV with semiparallel steel tendons changes more than that of the CSBV with the other three types of cables owing to the large elastic modulus and thermal expansion coefficient of the SST cables.

Figure 5 shows the relationship between the strut force and the temperature under the full-span load; the negative sign represents a pressure force. The change in the strut force with temperature is approximately linear, and the strut forces decrease with increasing temperature. The strut

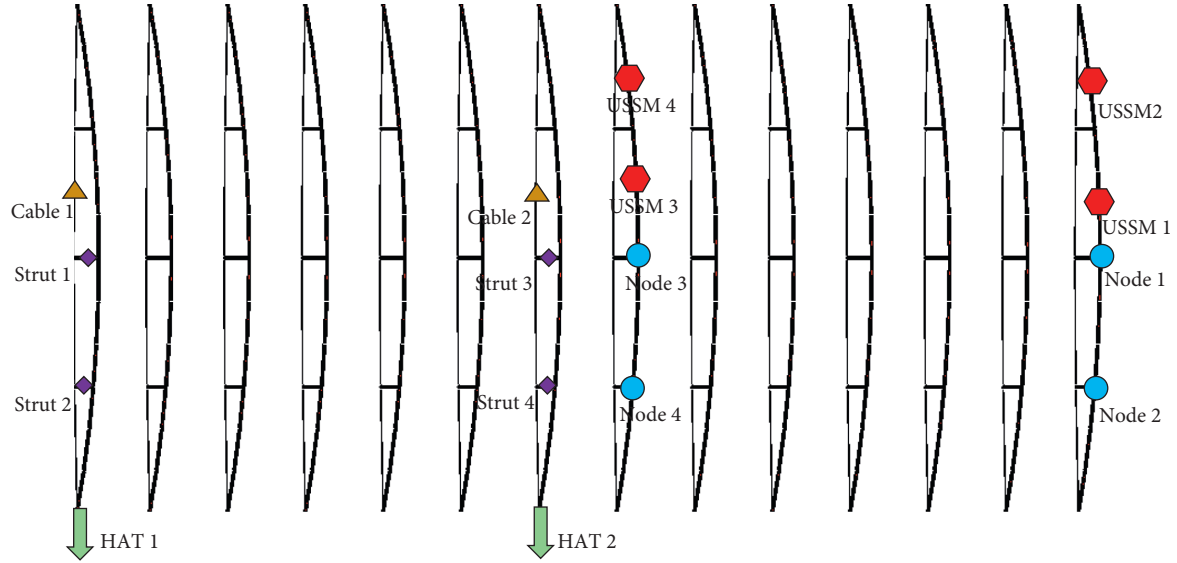


FIGURE 2: Targets of the numerical simulation analysis with a full-span load distribution.

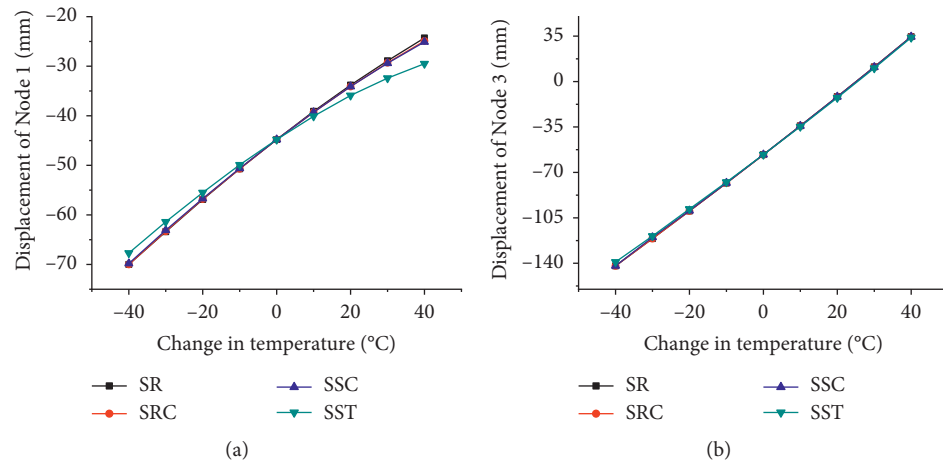


FIGURE 3: Relationship between the displacement and temperature in the full-span load distribution. Displacement of (a) Node 1 and (b) Node 3 with varying temperature.

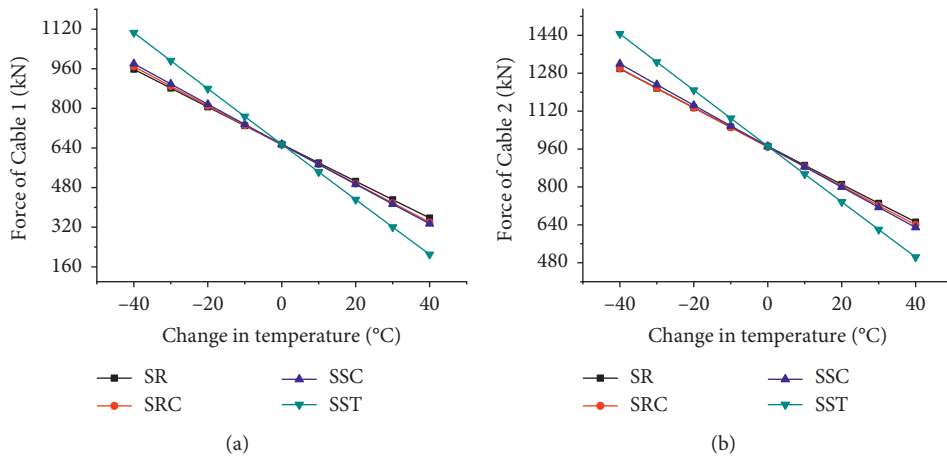


FIGURE 4: Relationship between the cable force and the temperature in the full-span load distribution. Change in the cable force of (a) Cable 1 and (b) Cable 2 with varying temperature.

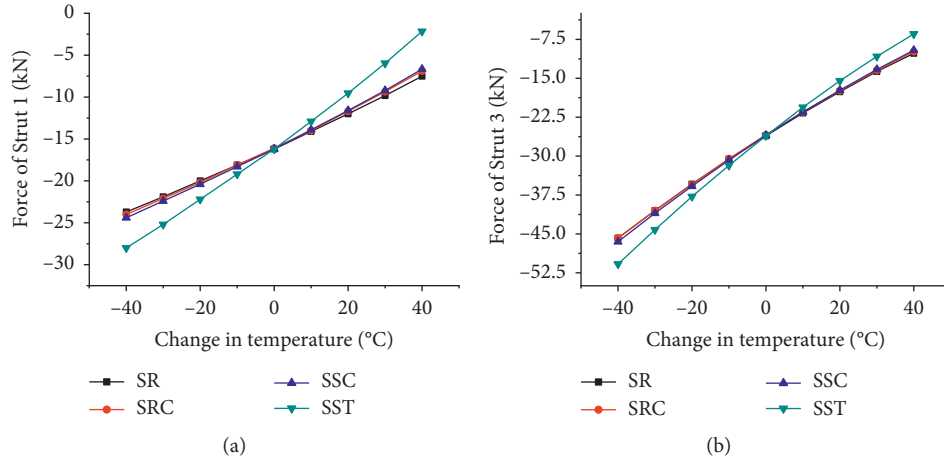


FIGURE 5: Relationship between the strut force and the temperature in the full-span load distribution. Change in the strut force of (a) Strut 1 and (b) Strut 3 with varying temperature.

pressure forces in Strut 1 and Strut 2 are lower than the strut pressure forces in Strut 3 and Strut 4. Moreover, the strut force of the CSBV with semiparallel steel tendon cables is more sensitive to the effect of temperature than the CSBV with the other cable types. This is similar to the change observed in the cable force. Therefore, the influence of temperature on the force of the vertical struts is related to the prestress of the cable. However, the influence on the force of the vertical struts is not completely in accordance with the prestress of the cable owing to the self-thermal stresses of the struts.

Figure 6 shows the influence of the temperature on the force of the USSM in the full-span load distribution; the negative sign indicates a pressure force. The relationship between the temperature and the USSM force is linear, except for in USSM 1. Moreover, the change in the force of USSM 1 under the effect of temperature is far less than its own force. Therefore, the force of USSM 1 can be considered to change linearly under the effect of temperature. The pressure force of the midframe USSM decreases with increasing temperature. In the end-frame, except for USSM 4, the USSM forces at the midspan and at the end-span decrease and increase, respectively, with increasing temperature. The force of USSM 4 in end-frame decreases under the effect of temperature. Moreover, the USSM force of the CSBV structure with semiparallel steel tendon cables is more sensitive to temperature changes. Therefore, the influence of temperature on the USSM force is related to the prestress of the cable. However, the influence of temperature on the force of the vertical struts is not completely in accordance with the prestress of the cable owing to the self-thermal stresses of the USSM.

Figure 7 shows the influence of the temperature on the horizontal arch thrust in the full-span load distribution; a negative sign represents an opposite horizontal arch thrust, i.e., the horizontal arch produces tension. The horizontal arch thrust in every structure changes linearly with the temperature. Moreover, the horizontal arch thrust increases with increasing temperature. When the semiparallel steel tendon cable is selected, the change in the horizontal arch

thrust is more pronounced under the effect of temperature. Note that the horizontal arch thrust could be negative at low temperatures. In other words, the horizontal arch thrusts could become tensile forces when the optimization goal of the cable prestress state is a zero horizontal arch thrust in the design process of the CSBV.

**2.3. Numerical Simulation of the CSBV with Half-Span Load Distribution.** Half-span loading was conducted using element surf 154, and the loading area is shown in Figure 8. The temperature change is  $\pm 40^{\circ}\text{C}$ . Figure 8 shows the vertical displacements of the nodes in the midframe and end-frame for Nodes 1–6, the cable axial force in the midframe and end-frame for Cables 1–8, the USSM force in the midframe and end-frame for USSM 1–4, the strut force in the midframe and end-frame for Struts 1–6, and the HAT in the midframe and end-frame for HAT 1–4.

Figure 9 shows the influence of the temperature on the vertical displacement of nodes in the half-span load distribution; a positive sign represents an upward displacement, and a negative sign represents a downward displacement. Node 3 and Node 6 are located in the area with the load, and their displacement evolution is complex but small. Besides Node 3 and Node 6, the displacement changes of the other nodes are similar to that of Node 1, which is shown in Figure 9(a). The displacements in these cases all increase linearly with increasing temperature. Moreover, the displacement change of the CSBV with the semiparallel cables is different than that of the CSBV with the other three cables.

The influence of the temperature on the cable force in the half-span load distribution is presented in Figure 10. Figure 10(a) shows the change in the cable force at the end-frame, and Figure 10(b) shows the change in the cable force at the midframe; the positive sign represents a tension force. The cable forces at the midframe are larger than those at the end-frame. The change in the cable force with temperature is similar to that at full load. The cable force decreases linearly with increasing temperature. Moreover, the cable force of the SST cables exhibits greater changes with the temperature,

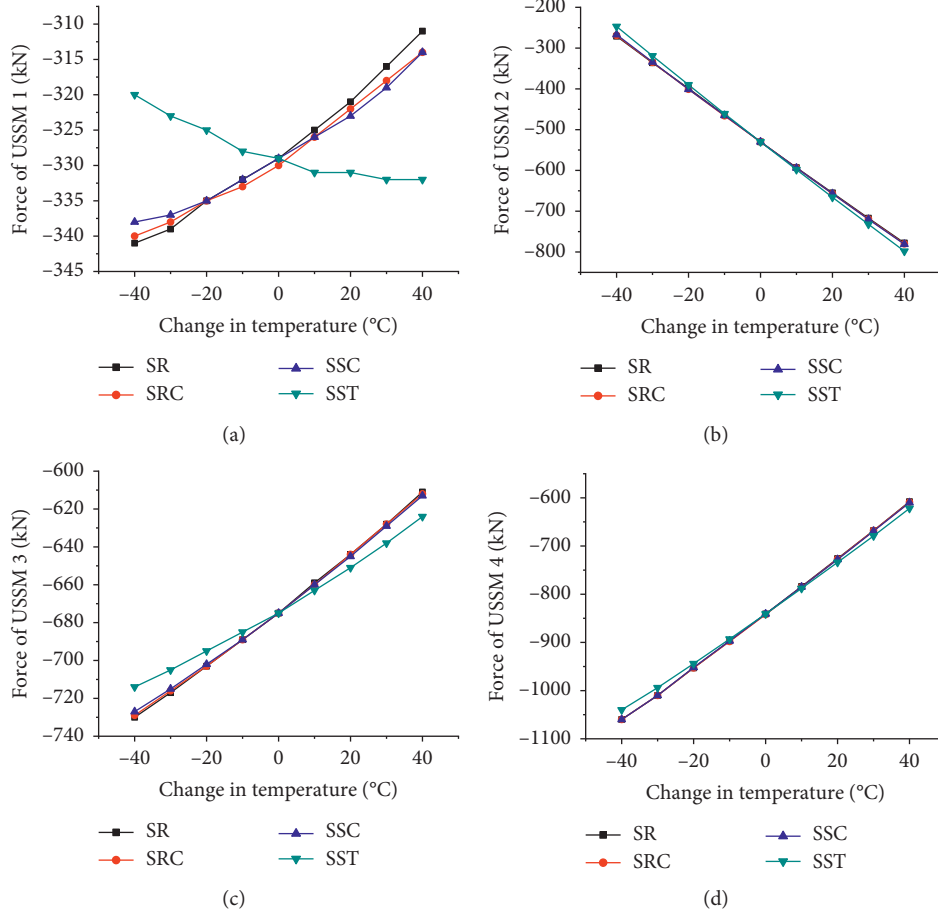


FIGURE 6: Relationship between the force at the upper structural steel members and the temperature in the full-span load distribution. Change in the force of (a) USSM 1, (b) USSM 2, (c) USSM 3, and (d) USSM 4 with varying temperature.

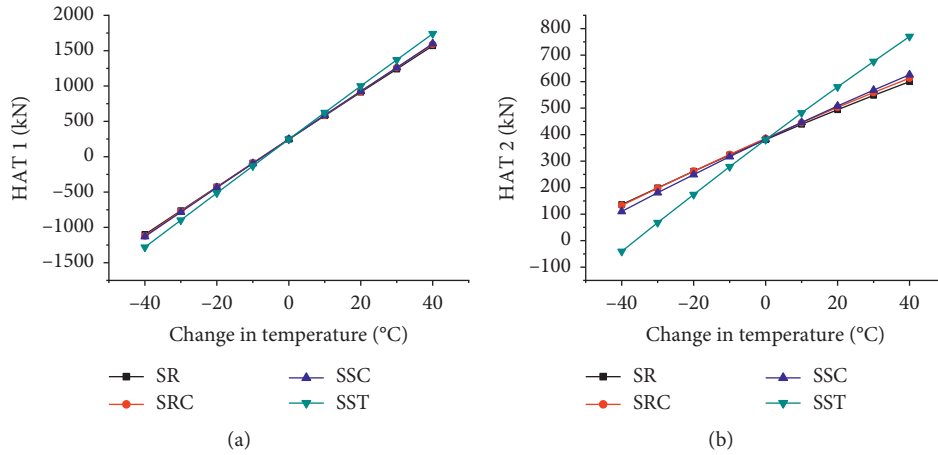


FIGURE 7: Relationship between the horizontal arch thrust and the temperature in the full-span load distribution. Change in (a) HAT 1 and (b) HAT 2 with varying temperature.

while the cable forces of the other three structures changed in a similar manner. Moreover, the cable force of the CSBV with semiparallel steel tendon cables exhibits a greater change than that of the CSBV with the other three cable

types owing to the large elastic modulus and thermal expansion coefficient of the SST cables.

Figure 11 shows the influence of the temperature on the force of the vertical struts in the half-span load distribution;

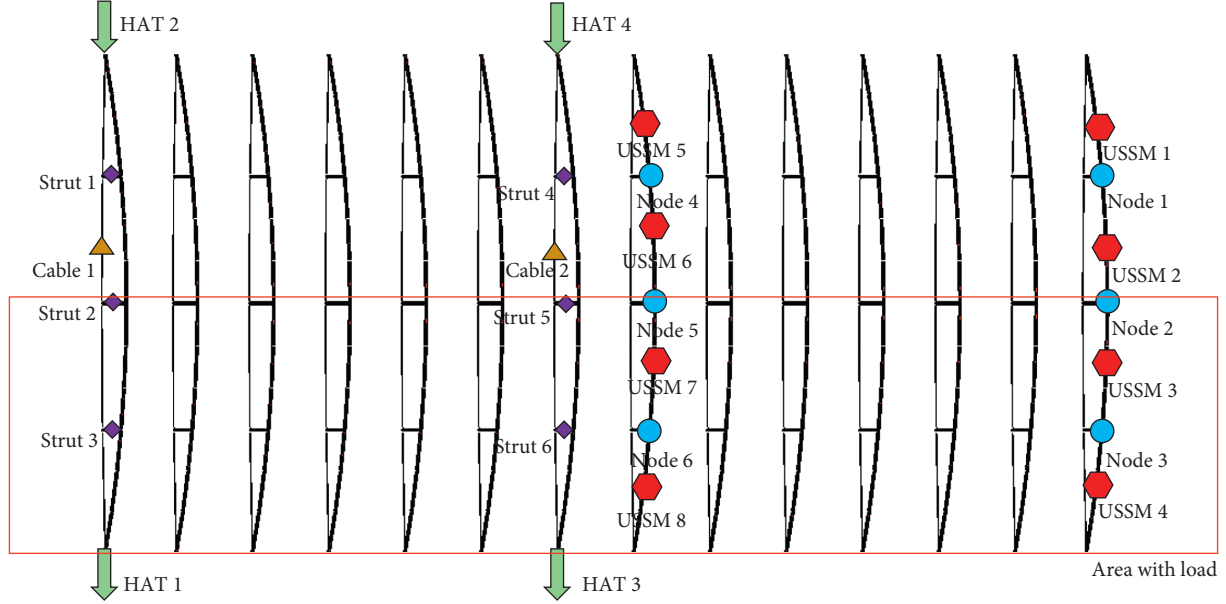


FIGURE 8: Targets in the numerical simulation analysis with a half-span load distribution.

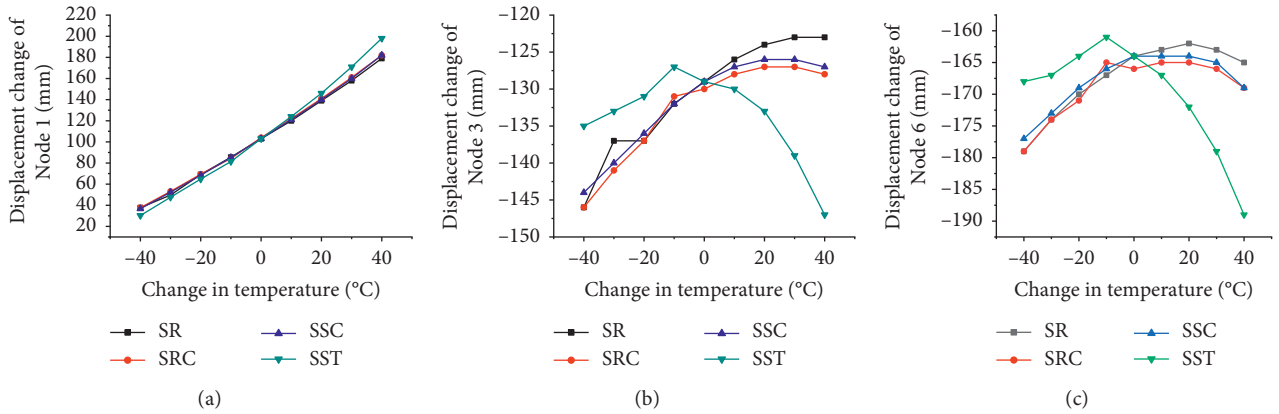


FIGURE 9: Relationship between the vertical displacement of nodes and the temperature in the half-span load distribution. Displacement of (a) Node 1, (b) Node 3, and (c) Node 6 with varying temperature.

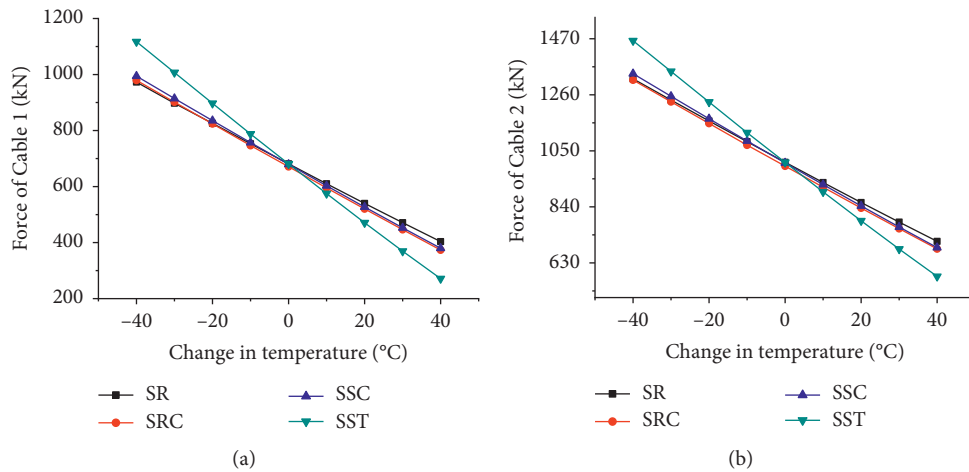


FIGURE 10: Relationship between the cable force at the end-frame and the temperature in the half-span load distribution. Change in the force of (a) Cable 1 and (b) Cable 2 with varying temperature.

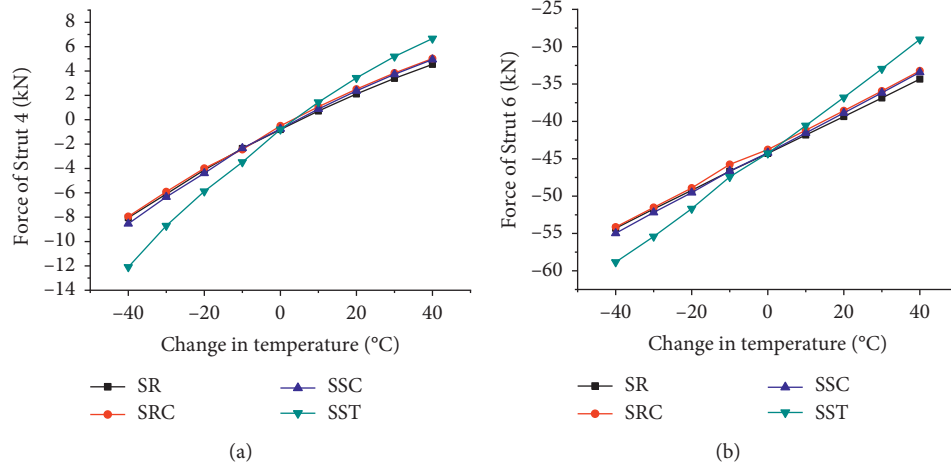


FIGURE 11: Relationship between the strut force and the temperature in the half-span load distribution. Change in the force of (a) Strut 4 and (b) Strut 6 with varying temperature.

the negative sign represents a pressure force. With increasing temperature, the strut pressure force decreases almost linearly. In the area without the load, the strut pressure force is less than that in the area with the load, as shown in Figure 11. Moreover, the strut pressure force of the CSBV with semiparallel cables exhibited a greater change than that of the CSBV with the other three cable types.

Figure 12 shows the relationship between the force of USSM and the temperature; the negative sign represents a pressure force, and the positive sign represents a tension force. Except for USSM 2, the relationship between the force of the USSM and the temperature is approximately linear. However, the change in the force of USSM 2 is smaller than that of the other members. The change in the force of USSM 4 with increasing temperature is similar to that of USSM 1; the force decreases linearly with increasing temperature, as shown in Figure 12(a). The change in the forces of USSM 5–8 is similar to that of USSM 3; the force increases with increasing temperature, as shown in Figure 12(c). Moreover, the effect of temperature on the force of the upper steel member in the CSBV with semiparallel cables is noticeably different than that of the other structures.

Figure 13 shows the relationship between the horizontal arch thrust and the temperature under the half-span load; the negative sign represents an opposite horizontal arch thrust, i.e., the horizontal arch produces tension. The horizontal arch thrust increases linearly with increasing temperature. The change in the horizontal arch thrust is larger in the end-frame than in the midframe. Moreover, the change in the horizontal thrust for the CSBV with semiparallel steel tendon cables is more obvious than that in the other three structures.

**2.4. Dynamic Characteristics of CSBV.** Considering the effect of the prestress, the first 10 vibration modes were calculated using the block Lanczos method, and the results are given in Tables 2–5. The results indicate that with increasing temperature, the frequency of the CSBV decreases linearly. Moreover, the change in the frequency of the CSBV with

semiparallel steel tendon cables is larger than that in the other structures.

**2.5. Numerical Simulation of the Seismic Response of CSBV Structures.** To investigate the effect of the temperature on the seismic response of the CSBV, a seismic wave is selected to perform a transient analysis on the structure. The roof load ( $1.0 \times 0.8 \text{ kN/m}^2 + 0.5 \times 0.5 \text{ kN/m}^2$ ) was applied to each node of the reticulated shell in the form of a concentrated mass. This transient analysis is performed using the Full method, which includes the Rayleigh damping:

$$[C] = \alpha[M] + \beta[K]. \quad (1)$$

In equation (1),  $\alpha$  and  $\beta$  have the following relationships with the viscous proportional damping coefficient,  $\xi$ :

$$\alpha = \frac{4\pi f_1 f_2 \xi}{f_1 + f_2}, \quad (2)$$

$$\beta = \frac{\xi}{\pi f_1 + \pi f_2}. \quad (3)$$

In equations (2) and (3),  $\xi$  is 0.02 and  $f_1$  and  $f_2$  are the frequencies of the first and second vibration modes, respectively, which are given in Tables 2–5. After the time-history analysis, the maximum displacement of the nodes, cable force, strut force, USSM force, and reaction force can be obtained. The test cases are similar to the simulation of the half-span load distribution shown in Figure 8. The seismic responses are shown in Figure 14, including the displacement, cable force, and horizontal arch thrust. The displacement of the nodes (Figure 14(a)), the cable force (Figure 14(b)), and the horizontal arch thrust (Figure 14(d)) changed linearly with increasing temperature. The change in the strut force with increasing temperature is not linear, but as the maximum change in the strut force is only approximately 30 kN, it can be considered to be linear. The change in the USSM force (Figure 14(e)) with increasing temperature differs from the other parameters. For the USSM

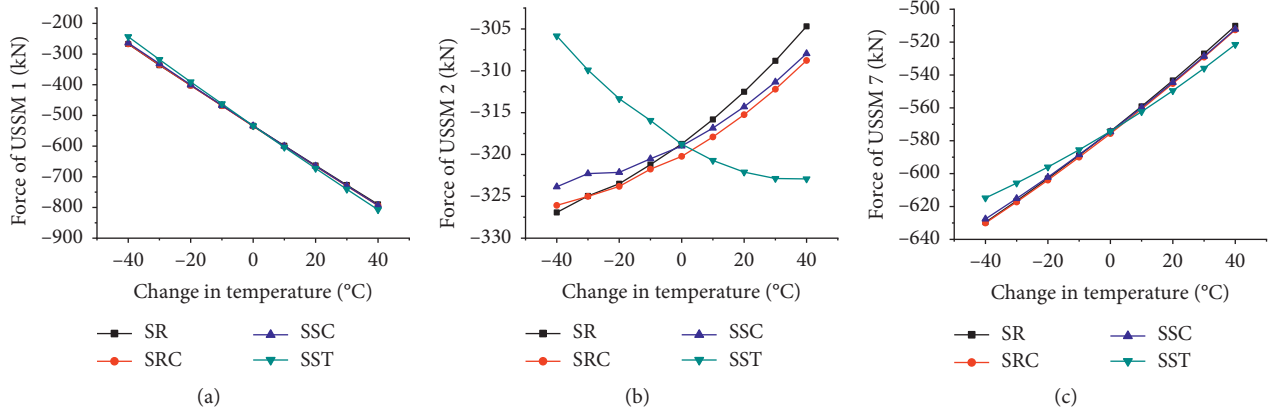


FIGURE 12: Relationship between the force of upper structural steel members and the temperature in the half-span load distribution. Change in the force of (a) USSM 1, (b) USSM 2, and (c) USSM 7 with varying temperature.

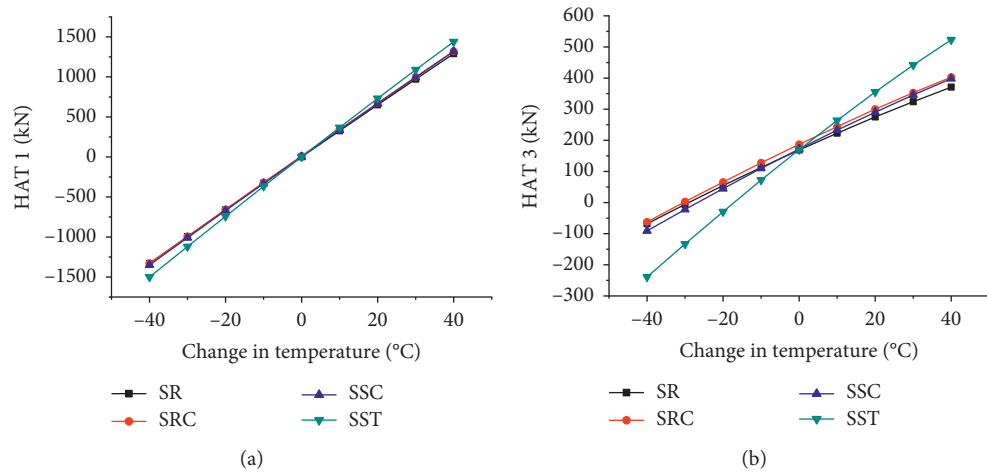


FIGURE 13: Relationship between the horizontal arch thrust and the temperature in the half-span load distribution. Change in (a) HAT 1 and (b) HAT 3 with varying temperature.

TABLE 2: Frequencies of the first 10 vibration modes of the CSBV with steel rod cables (unit: Hz).

Temperature (°C)	-40	-30	-20	-10	0	10	20	30	40
$f_1$	1.6304	1.6243	1.6181	1.612	1.6058	1.5996	1.5933	1.587	1.5807
$f_2$	1.8617	1.8533	1.8449	1.8364	1.8279	1.8193	1.8106	1.802	1.7932
$f_3$	2.3709	2.3596	2.3483	2.3368	2.3251	2.3134	2.3016	2.2896	2.2775
$f_4$	2.8177	2.8099	2.8020	2.7941	2.7861	2.7781	2.7700	2.7619	2.7537
$f_5$	2.8893	2.8807	2.8721	2.8633	2.8545	2.8456	2.8367	2.8277	2.8186
$f_6$	3.0043	2.9893	2.9740	2.9586	2.9429	2.9270	2.9110	2.8947	2.8782
$f_7$	3.0488	3.0377	3.0266	3.0153	3.0039	2.9924	2.9808	2.9691	2.9573
$f_8$	3.3223	3.3075	3.2925	3.2773	3.2619	3.2463	3.2305	3.2145	3.1983
$f_9$	3.6366	3.6168	3.5967	3.5762	3.5555	3.5344	3.5129	3.4912	3.4691
$f_{10}$	3.7133	3.694	3.6744	3.6545	3.6343	3.6138	3.5930	3.5719	3.5504

located in the side span, the USSM force changes linearly with increasing temperature. For the USSM located in the middle span, the force changes approximately linearly from  $-30^{\circ}\text{C}$  to  $+40^{\circ}\text{C}$ . Moreover, the change in the seismic responses of the CSBV having semiparallel steel tendons with temperature was larger than those in the other structures.

### 3. Experimental Verification

To verify the finite element model of the CSBV experimentally in a convenient manner, a scale model was designed. Corresponding numerical simulations and experiments were then performed.

TABLE 3: Frequency of the first 10 vibration modes of the CSBV with steel wire rope cables (unit: Hz).

Temperature (°C)	-40	-30	-20	-10	0	10	20	30	40
$f_1$	1.6296	1.6233	1.6171	1.6108	1.6045	1.5981	1.5918	1.5853	1.5789
$f_2$	1.8611	1.8526	1.8440	1.8354	1.8267	1.8180	1.8092	1.8004	1.7915
$f_3$	2.3706	2.3592	2.3477	2.3361	2.3244	2.3125	2.3006	2.2885	2.2763
$f_4$	2.8174	2.8095	2.8015	2.7934	2.7853	2.7771	2.7689	2.7606	2.7523
$f_5$	2.8891	2.8804	2.8715	2.8626	2.8537	2.8446	2.8355	2.8264	2.8171
$f_6$	3.0043	2.9891	2.9737	2.9582	2.9425	2.9265	2.9103	2.8940	2.8774
$f_7$	3.0487	3.0374	3.0261	3.0146	3.0031	2.9914	2.9797	2.9678	2.9558
$f_8$	3.3222	3.3073	3.2921	3.2768	3.2612	3.2455	3.2295	3.2133	3.1970
$f_9$	3.6367	3.6168	3.5966	3.5760	3.5552	3.5340	3.5125	3.4907	3.4685
$f_{10}$	3.7133	3.6939	3.6741	3.6541	3.6338	3.6131	3.5921	3.5708	3.5492

TABLE 4: Frequency of the first 10 vibration modes of the CSBV with steel strand cables (unit: Hz).

Temperature (°C)	-40	-30	-20	-10	0	10	20	30	40
$f_1$	1.6313	1.6250	1.6186	1.6121	1.6056	1.5991	1.5926	1.5860	1.5794
$f_2$	1.8626	1.8540	1.8453	1.8366	1.8278	1.8189	1.8100	1.8010	1.7920
$f_3$	2.3717	2.3602	2.3486	2.3369	2.3251	2.3131	2.3010	2.2888	2.2765
$f_4$	2.8190	2.8108	2.8026	2.7943	2.786	2.7777	2.7692	2.7608	2.7522
$f_5$	2.8906	2.8817	2.8727	2.8636	2.8544	2.8452	2.8359	2.8265	2.8171
$f_6$	3.0050	2.9898	2.9743	2.9587	2.9429	2.9268	2.9105	2.8941	2.8773
$f_7$	3.0501	3.0387	3.0272	3.0155	3.0038	2.9920	2.9800	2.9679	2.9557
$f_8$	3.3236	3.3084	3.2931	3.2776	3.2618	3.2459	3.2298	3.2135	3.1969
$f_9$	3.6373	3.6173	3.597	3.5764	3.5554	3.5342	3.5126	3.4906	3.4683
$f_{10}$	3.7145	3.6949	3.675	3.6548	3.6343	3.6135	3.5923	3.5709	3.5491

TABLE 5: Frequency of the first 10 vibration modes of the CSBV with semiparallel steel tendons (unit: Hz).

Temperature (°C)	-40	-30	-20	-10	0	10	20	30	40
$f_1$	1.6377	1.6298	1.6218	1.6138	1.6058	1.5977	1.5895	1.5813	1.5731
$f_2$	1.8686	1.8586	1.8484	1.8382	1.8279	1.8175	1.8071	1.7965	1.7860
$f_3$	2.3768	2.3640	2.3512	2.3382	2.3251	2.3119	2.2985	2.2850	2.2714
$f_4$	2.8266	2.8165	2.8065	2.7963	2.7861	2.7758	2.7655	2.7551	2.7446
$f_5$	2.8985	2.8876	2.8767	2.8656	2.8545	2.8433	2.8320	2.8206	2.8092
$f_6$	3.0093	2.9930	2.9765	2.9598	2.9429	2.9258	2.9084	2.8908	2.8730
$f_7$	3.0580	3.0446	3.0312	3.0176	3.0039	2.9901	2.9761	2.9620	2.9478
$f_8$	3.3310	3.3140	3.2969	3.2795	3.2619	3.2441	3.2261	3.2078	3.1893
$f_9$	3.6410	3.6201	3.5989	3.5773	3.5555	3.5332	3.5107	3.4878	3.4645
$f_{10}$	3.7212	3.7000	3.6784	3.6565	3.6343	3.6118	3.5889	3.5657	3.5421

**3.1. Scale Model.** To facilitate the experiments, a CSBV structure was designed. The span, length, rise, and sag of the prototype are 3.333 m, 3.587 m, 0.3 m, and 0.05 m, respectively. A total of seven cables are evenly spaced in the longitudinal direction, with three rods uniformly spaced in the span direction between each cable and the upper shell. The lower column height is 2.1 m.

Considering the market supply and the requirements of the welding, Q235B steel circular hollow sections with dimensions of 8 mm × 1 mm, 10 mm × 1 mm, and 12 mm × 1 mm are used. The upper barrel vault model is composed of three kinds of steel tube sections, including Φ8 mm × 1 mm, Φ10 mm × 1 mm, and Φ12 mm × 1 mm. The struts are steel tubes with sections of Φ12 mm × 1 mm. The columns are steel tube with sections of Φ50 mm × 2 mm and lengths of 2.1 m. The steel tubes are all Q235b, and the coefficient of thermal expansion is  $1.20 \times 10^{-5}/^{\circ}\text{C}$ . High-strength steel

wires with a diameter of 6 mm and tensile strength of 600 MPa are used as the cables.

**3.2. Experimental Investigation.** To verify the numerical results, an experimental investigation was carried out. According to the initial design, the experimental model is made of standard steel wire cables only. All of the bars in the upper barrel vault model are connected with welded hollow pipe joints. The ends of the upper barrel vault model are connected to the top of the column by welding. The tops of the struts are connected to the upper barrel vault model with one-way hinge bolt joints. The cable groove was used as a connection at the bottom end of the struts, while bolts were used to link the end of the cable with the top of column. By twisting these bolts, the cable forces could be adjusted to reach the design value. The cables were then fixed with cable

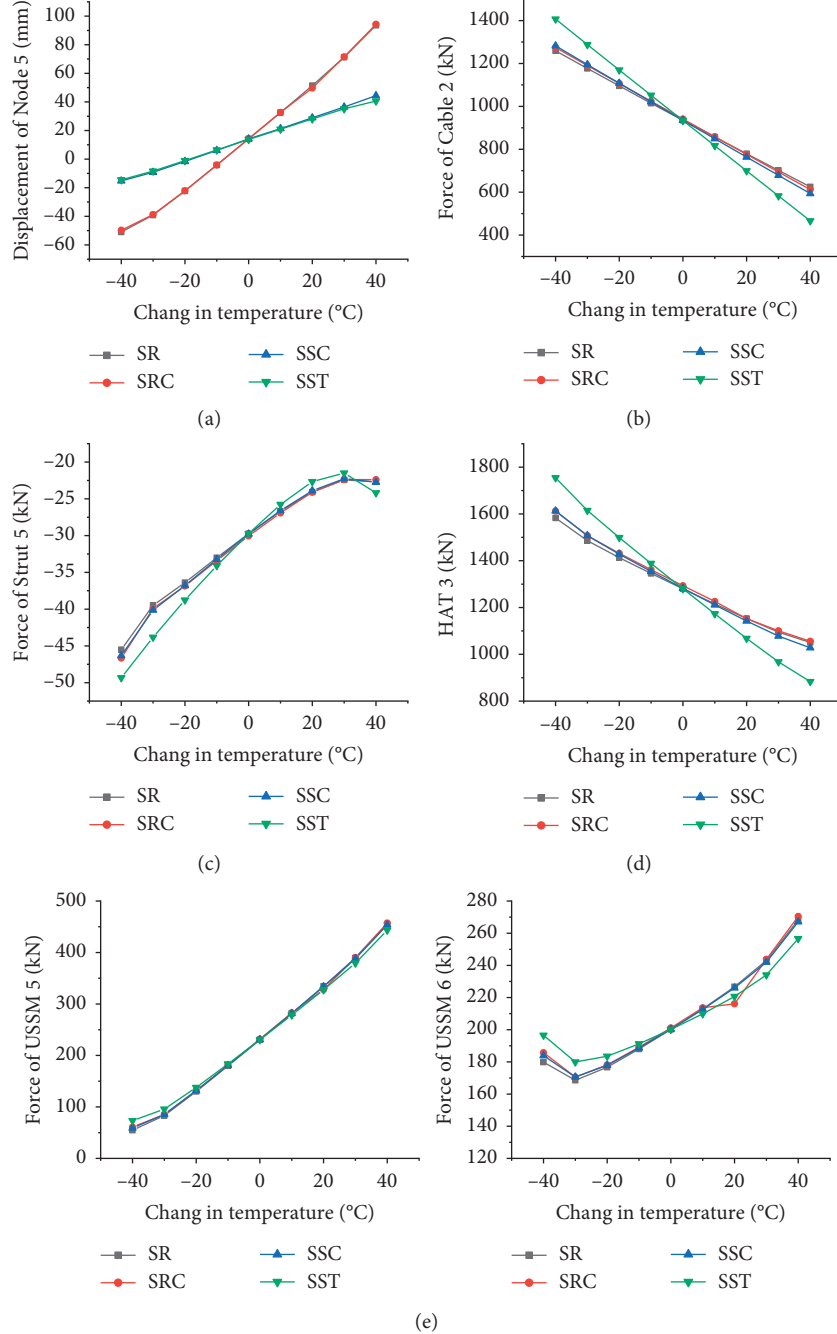


FIGURE 14: Changes in the maximum seismic response with varying temperature. (a) Change in the displacement of Node 5 with varying temperature. (b) Change in the cable force with varying temperature. (c) Change in the strut force with varying temperature. (d) Change in the horizontal arch thrust with varying temperature. (e) Change in the USSM force with varying temperature.

buttons to avoid slipping of the cables. The test model is shown in Figure 15(a).

The objective of these experiments is to measure the vertical displacement and stress of the vertical struts in the full-span load distribution and half-span load distribution. The loads were added using hanging sandbags (Figure 15(b)). To maintain consistency with the numerical analyses, 30 loading points were set in the full-span distribution, as shown in Figure 16(a), and 15 loading points were set in the half-span distribution, as shown in Figure 16(b).

During the experiments, the model was covered in a heat-retaining tent, as shown in Figure 15(c), and the lowest outdoor temperature was  $-7^{\circ}\text{C}$ . The temperature inside the tent was measured with a thermometer, and the layout of the sensors is shown in Figure 16(c). According to preliminary measurements, the temperature inside the tent was steady at approximately  $-5^{\circ}\text{C}$ . Electric stoves were used to heat the inside of the tent to a final temperature of  $35^{\circ}\text{C}$ . The layout of the displacement measuring points is shown in Figure 16(c) (D1-D3). The layout of the USSM strain measuring points is

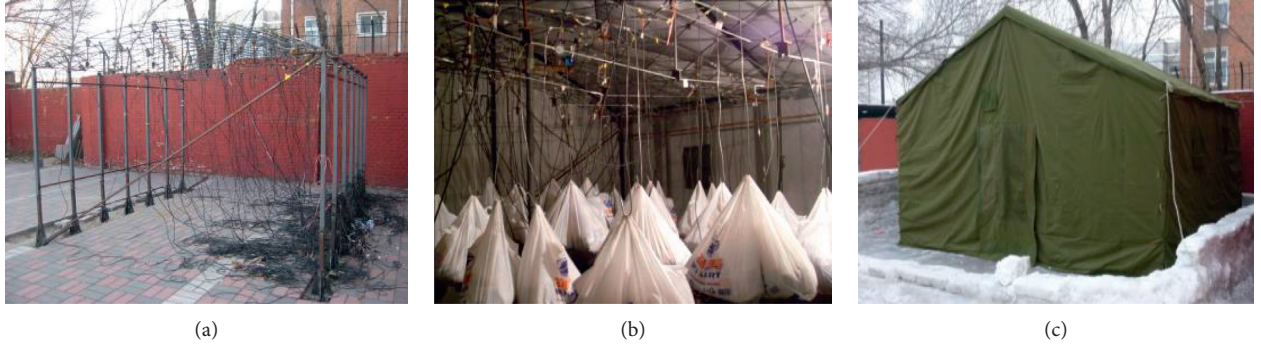


FIGURE 15: Experimental model of the CSBV structure. (a) CSBV test model. (b) Sandbags hanging on the test model. (c) Heat-retaining tent outside the CSBV model.

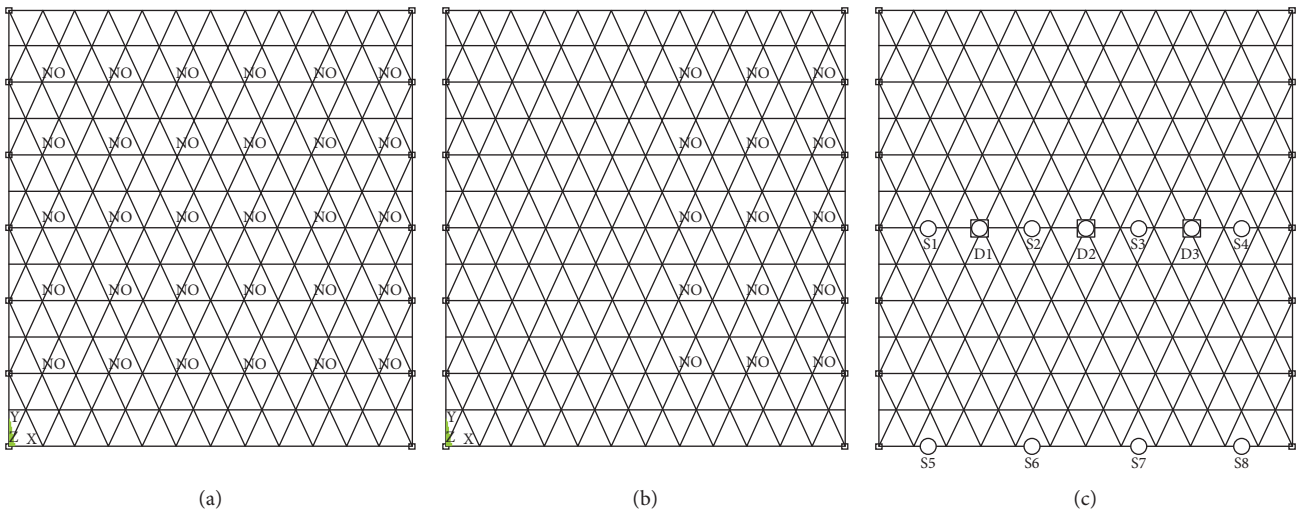


FIGURE 16: Layout of the sensors and loads on the CSBV. (a) Distribution of the hanging sandbags in the full span. (b) Distribution of the hanging sandbags in the half span. (c) Layout of the sensors on the CSBV.

also shown in Figure 16(c) (S1–S8). The USSM strains are measured with YE2539 high-speed static strain indicators, and a computer is employed as the strain measurement system. The structural displacements are measured with dial indicators.

The procedure for the experiments is as follows:

- (1) Prepare the relevant experimental equipment: set up the electric stoves, thermometers, and dial indicators in the designated locations; debug the high-speed static strain indicator; and close the tent tightly to prevent heat dissipation
- (2) Hang sandbags to load the full span according to Figure 16(a) and turn on the electric stoves to increase the temperature inside the tent from the initial  $-5^{\circ}\text{C}$ ; when the temperature in the tent reaches a stable  $35^{\circ}\text{C}$ , measure the displacements and stresses
- (3) Turn off the electric stoves and open the tent to allow the model to return to the initial temperature ( $-5^{\circ}\text{C}$ )
- (4) Hang sandbags to load the half span according to Figure 16(b) and turn on the electric stoves to increase the temperature inside the tent from the initial

$-5^{\circ}\text{C}$ ; when the temperature in the tent reaches a stable  $35^{\circ}\text{C}$ , measure the displacements and stresses.

The actual project and scale model have different rise-span ratios and proportions of the component size and model size. Therefore, their internal force changes and displacements will differ. This experiment is only intended to demonstrate the validity of the finite element model of the CSBV.

As shown in Figures 17 and 18, as the temperature increases, the trends in the experimental and simulated vertical displacements are similar, although the displacement values differ greatly. Further, the displacement change measured in the experiments is not linear. However, because the temperature in the experiments could not be stabilized at specific values between  $-5$  and  $35^{\circ}\text{C}$ , the value of the vertical displacement generated under temperatures other than  $40^{\circ}\text{C}$  will have some error. Therefore, the change in the vertical displacement in the experiments can be considered to be linear.

Figures 19 and 20 show comparisons of the change in the USSM stress in the experiments and finite element numerical simulations. Some error is introduced as a result of

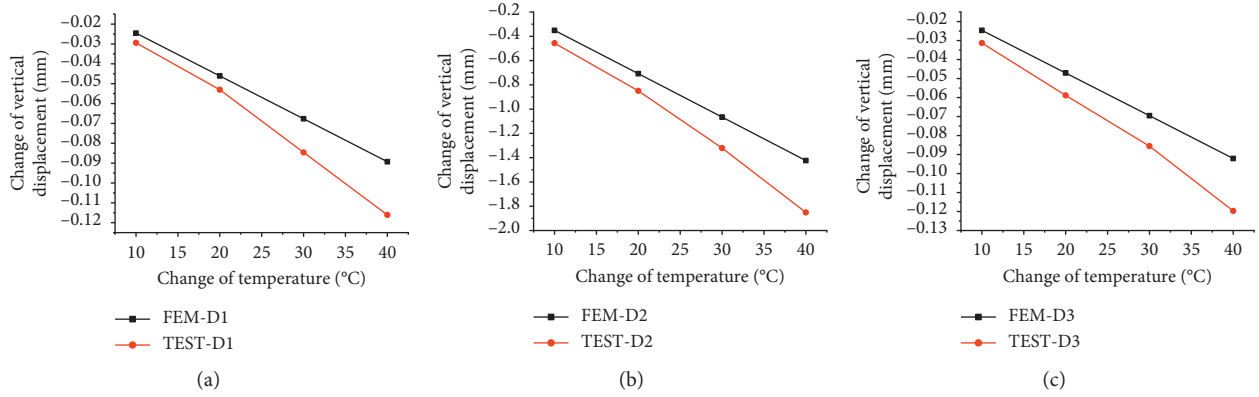


FIGURE 17: Comparison of the change in nodal displacement in the experiments and finite element numerical simulation under the full-span load. Displacement change of (a) D1, (b) D2, and (c) D3 under the full-span load.

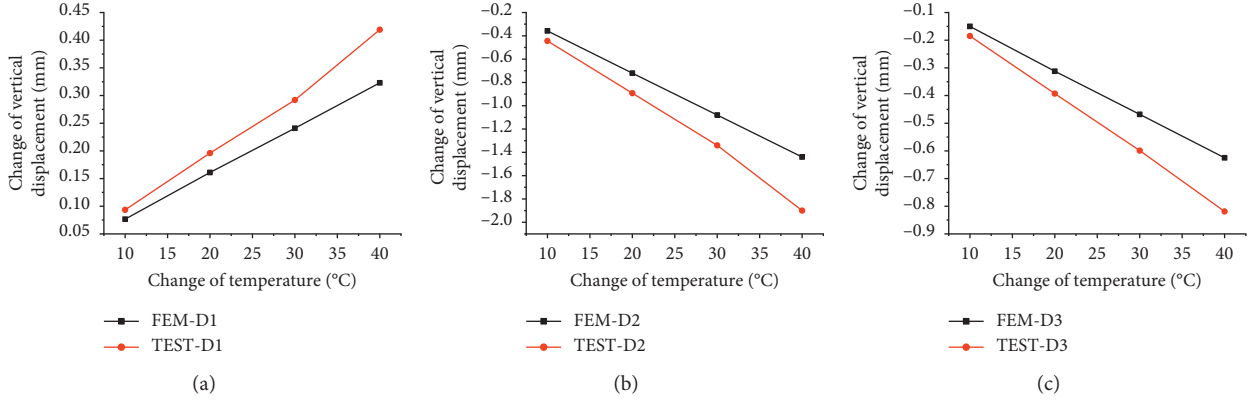


FIGURE 18: Comparison of the change in nodal displacement in the experiments and finite element numerical simulation under the half-span load. Displacement change of (a) D1, (b) D2, and (c) D3 under the half-span load.

flaws in the test model, boundary conditions, the temperature field, the precision of the measurements, etc. Except for the temperature field, these error sources are difficult to improve in the tests or numerical analysis. Owing to these errors, the values in the experiments were larger than those obtained with the finite element model. However, they have the same trends, and the change in the experimental values was approximately linear. Therefore, the finite element model of the CSBV is considered to be effective under varying temperature.

#### 4. Conclusions

CSBV structures based on beam string structures (or truss string structures) and cylindrical lattice shells are a new type of hybrid spatial steel structures. The design of the cable-supported structure is different from that of other steel structures. In this study, a finite element model of a CSBV was built with the cable force determined through iterative calculation. A numerical investigation was carried out to obtain the temperature response of the CSBV. An experimental investigation with a physical model of the CSBV was

then conducted under full-span loading and half-span loading. The following conclusions have been drawn:

- (1) The changes in the vertical displacement and USSM stress in the experiment are a little larger than those in the finite element model, but the trends are the same. Further, considering the inevitable error, the experiment verified that the finite element model of the CSBV is effective under varying temperature.
- (2) Under the full-span loading, the changes in the structure internal force and displacement can be considered linear in the CSBV design process. The cable force and strut force decrease with increasing temperature. Meanwhile, the horizontal arch thrust increases with increasing temperature. Moreover, the internal force of the CSBV with semiparallel cables exhibited a larger change than that of the CSBV with the other three cables.
- (3) Under the half-span loading, the changes in the structure internal force and displacement can be considered linear in the CSBV design process. The cable force and strut force decrease with increasing

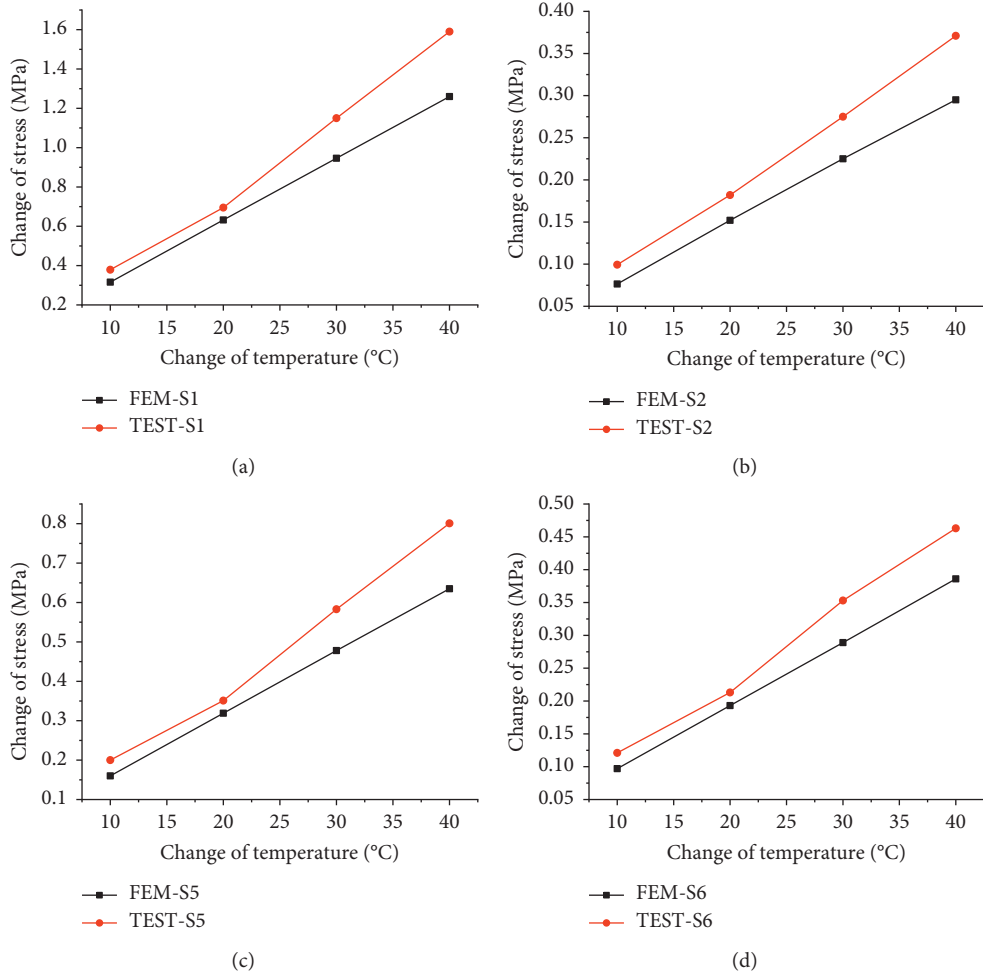


FIGURE 19: Comparison of the change in the USSM stress in the experiments and finite element numerical simulations under the full-span load. Change in the force of (a) S1, (b) S2, (c) S3, and (d) S6 under the full-span load.

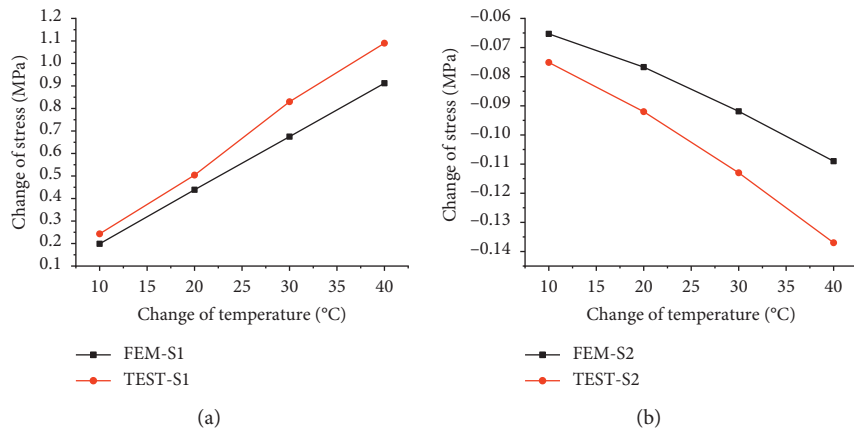


FIGURE 20: Continued.

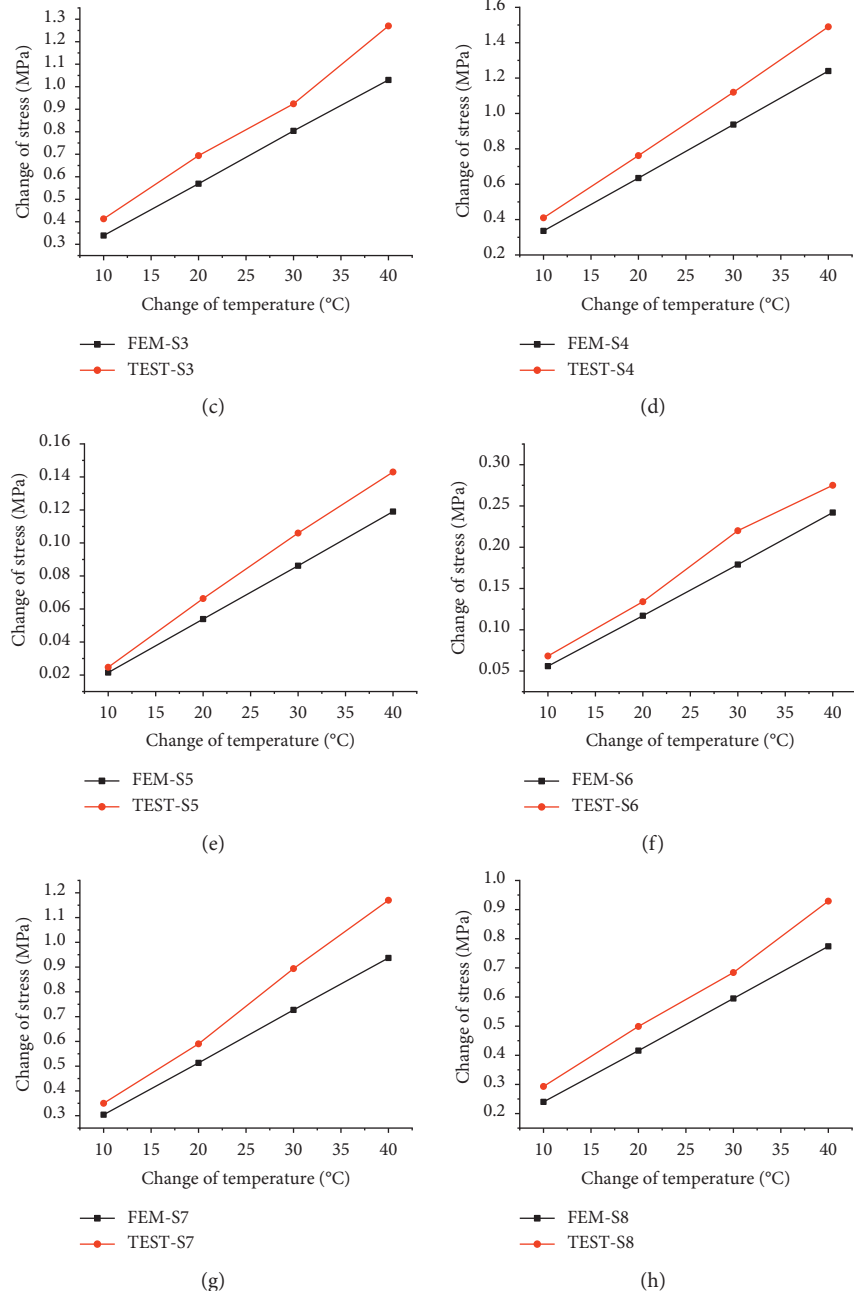


FIGURE 20: Comparison of the change in the USSM stress in the experiments and finite element numerical simulations under the half-span load. Change in the force of (a) S1, (b) S2, (c) S3, (d) S4, (e) S5, (f) S6, (g) S7, and (h) S8 under the half-span load.

temperature. Meanwhile, the horizontal arch thrust increases with increasing temperature. Moreover, the internal force of the CSBV with semiparallel cables exhibited a larger change than that of the CSBV with the other three cables.

- (4) The frequency of the CSBV decreases linearly with increasing temperature. With the seismic response,

the displacement, cable force, and horizontal arch thrust of structure change linearly with increasing temperature. The cable force decreases with increasing temperature, and the horizontal arch thrust decreases with increasing temperature.

- (5) The internal force of the CSBV with semiparallel tendon cables is more sensitive to changes in the

temperature. Therefore, in area with large temperature changes, the semiparallel cables are not recommended as components in the CSBV design process, as these can increase the loss of the cable prestress with changes in temperature. Because cables with a high elastic modulus are beneficial for the static performance of the CSBV and steel wire rope cables have a low elastic modulus, steel rod and steel strand cables are recommended as components for CSBVs considering the effect of temperature.

## Data Availability

The data used to support the findings of this study are included within the article.

## Conflicts of Interest

The authors declare that there are no conflicts of interest regarding the publishing of this paper.

## Acknowledgments

This work was sponsored by the National Nature Science Foundation of China (grant number 51408016), Natural Science Foundation of Tianjin (grant number 16JCQNJC07100), and the Scientific Research Program of Beijing Education Committee (grant number KM201710005017).

## References

- [1] Z. H. Chen, X. Y. Yan, W. T. Qiao et al., "Structure system of cable supported barrel vault structure," ZL200810053722.8, 2008, In Chinese.
- [2] W. Qiao, Z. H. Chen, and M. S. Zhao, "Test study on basic static characteristics of cable supported barrel vault structure," *International Journal of Advanced Steel Structures*, vol. 8, no. 2, pp. 199–211, 2012.
- [3] G. J. Sun, Z. H. Chen, and R. W. Longman, "Numerical and experimental investigation of the dynamic characteristics of cable supported barrel vault structure," *Journal of Mechanics of Materials and Structures*, vol. 8, no. 2, pp. 1–14, 2013.
- [4] H. Liu, W. Zhang, H. Yuan, J. Zhu, and J. Zheng, "Modified double-controlform-finding analysis for suspendomes considering the construction process and the friction of cable-strut joints," *Engineering Structures*, vol. 120, pp. 75–81, 2016.
- [5] F. Uzun, "Form-finding and analysis of an alternative tensile dome configuration," *Advances in Structural Engineering*, vol. 20, no. 11, pp. 1644–1657, 2017.
- [6] J. Lu, X. Dong, X. Zhao, X. Wu, and G. Shu, "Form-finding analysis for a new type of cable-strut tensile structures generated by semi-regular tensegrity," *Advances in Structural Engineering*, vol. 20, no. 5, pp. 772–783, 2017.
- [7] X. Liu, A. Zhang, X. Zhang, and C. Tian, "Particle swarm optimization algorithm for suspendome structure under multiple loading cases," *Engineering Computations*, vol. 33, no. 3, pp. 767–788, 2016.
- [8] L.-M. Chen and S.-L. Dong, "Optimal prestress design and construction technique of cable-strut tension structures with multi-overall selfstress modes," *Advances in Structural Engineering*, vol. 16, no. 10, pp. 1633–1644, 2013.
- [9] K. Li and D. Huang, "Static behavior of kiewitt6 suspendome," *Structural Engineering and Mechanics*, vol. 37, no. 3, pp. 309–320, 2011.
- [10] Q.-S. Cao and Z.-H. Zhang, "A simplified strategy for force finding analysis of suspendomes," *Engineering Structures*, vol. 32, no. 1, pp. 306–318, 2010.
- [11] Z. Chen, R. Z. Yan, and X. D. Wang, "Experimental researches of a suspen-dome structure with rolling cable-strut joints," *Advanced Steel Construction*, vol. 1, no. 11, pp. 15–38, 2015.
- [12] H. J. Liu, L. F. Yang, and Y. F. Luo, "Dynamic stability of large-spansuspen-domes subjected to seismic excitations," *Advanced Materials Research*, vol. 378–379, pp. 209–212, 2012.
- [13] Z. Chen, W. Qiao, and X. Yan, "Cable supported barrel vault structure system and research on mechanics feature," *Advanced Steel Construction*, vol. 6, no. 3, pp. 867–878, 2010.
- [14] J. Cai, Y. Q. Liu, and F. Jian, "Nonlinear stability analysis of a radially retractable suspen-dome," *Advanced Steel Construction*, vol. 13, no. 2, pp. 117–131, 2017.
- [15] L.-M. Chen, H. Deng, Y.-H. Cui, S.-L. Dong, and Y.-Y. Zhou, "Theoretical analysis and experimental study on sensitivity of element-length error in cable-strut tensile structures," *Advances in Structural Engineering*, vol. 19, no. 9, pp. 1463–1471, 2016.
- [16] P. Li, M. Wu, and P. Xing, "Novel cable-stiffenedsingle-layer latticed shells and their stabilities," *Journal of Constructional Steel Research*, vol. 92, pp. 114–121, 2014.
- [17] J. Guo, "Research on distribution and magnitude of initial geometrical imperfection affecting stability of suspen-dome," *Advanced Steel Construction*, vol. 7, pp. 344–358, 2011.
- [18] P. Li, M. Wu, H. Wang, and M. Shi, "Experimental and numerical analysis of cable-stiffenedsingle-layer spherical latticed shells," *Advances in Structural Engineering*, vol. 19, no. 3, pp. 488–499, 2016.
- [19] Z. Chen, Z. Liu, and G. Sun, "Thermal behavior of steel cables in prestressed steel structures," *Journal of Materials in Civil Engineering*, vol. 23, no. 9, pp. 1265–1271, 2011.
- [20] G. Sun, Z. Chen, and Z. Liu, "Analytical and experimental investigation of thermal expansion mechanism of steel cables," *Journal of Materials in Civil Engineering*, vol. 23, no. 7, pp. 1017–1027, 2011.

## Review Article

# Robustness and Resilience of Structures under Extreme Loads

Flavio Stochino ,<sup>1</sup> Chiara Bedon ,<sup>2</sup> Juan Sagaseta,<sup>3</sup> and Daniel Honfi<sup>4</sup>

<sup>1</sup>Department of Civil, Environmental Engineering and Architecture, University of Cagliari, Via Marengo 2, Building A, Cagliari, Italy

<sup>2</sup>Department of Engineering and Architecture, University of Trieste, Trieste, Italy

<sup>3</sup>Department of Civil and Environmental Engineering, University of Surrey, Guildford, UK

<sup>4</sup>RISE Research Institutes of Sweden, Gothenburg, Sweden

Correspondence should be addressed to Flavio Stochino; fstochino@unica.it

Received 21 February 2019; Accepted 30 April 2019; Published 21 May 2019

Academic Editor: Luigi Di Sarno

Copyright © 2019 Flavio Stochino et al. This is an open access article distributed under the Creative Commons Attribution License, which permits unrestricted use, distribution, and reproduction in any medium, provided the original work is properly cited.

Many of modern life activities involve the risk of fire, explosions, and impacts. In addition, natural extreme events are becoming more and more common. Thus, robustness, the ability to avoid disproportionate collapse due to an initial damage, and resilience, the ability to adapt to and recover from the effects of changing external conditions, represent two important characteristics of current structures and infrastructures. Their definitions are reviewed in this paper with the aim of sorting and describing the different approaches proposed in the literature and in the international standards. A simple example is also analysed in order to compare different methods.

## 1. Introduction

Despite advances never experienced before in technological development, catastrophic failures of structures and infrastructure systems happen from time to time as a consequence of natural or man-made extreme events. This is an effect of both a changing climate and general changes in our society with an increasing pressure in optimizing the design and management of infrastructure including a more sustainable use of materials, structures, and land. We are building taller and larger structures than ever under increasing construction pace and also within extreme environments which would not be considered possible in the past.

Absolute safety can never be achieved; therefore, it is important to consider what would happen should one or several elements of a structure fail:

- (i) Would element failure in a system lead to the collapse of the entire system or a significant part of it?
- (ii) Would the system's functionality be limited after such a failure?

(iii) What is an acceptable and tolerable performance under such circumstances?

To answer these questions, the robustness of the structure needs to be assessed and evaluated. In short, robustness is often described as the structure's ability to avoid disproportionate collapse due to an initial damage.

Besides limiting damage due to extreme events, it is important to consider how the built environment can be refurbished or rebuilt after a disaster in an efficient and timely manner. Therefore, the topic of infrastructure resilience has gained an increasing attention in the recent years. Resilience roughly refers to the ability of the infrastructure to adapt to and recover from a disturbance or damage during a disaster.

The present paper is organised as follows: in Section 2, the qualitative definitions of robustness and resilience are presented while their main quantitative measures are described in Section 3 with a representative example. Structural design considerations are stated in Section 4, and finally, in Section 5, some conclusive remarks are drawn.

## 2. Definitions of Fundamental Concepts

Robustness and resilience are two different words representing two different properties of general systems. In order to avoid confusion and to outline their respective characteristics, starting from the etymological origins of the two words, Section 2 will discuss their qualitative definition and the main historical events that led to their delineation and clarification.

**2.1. Robustness.** Most living organisms are able to survive under significantly varying conditions. Internal failures might influence overall performance; however, the most fundamental functions are maintained even under serious internal failures. This differs significantly from human designed systems, where the failure of a single element can paralyse the entire system. This natural ability to withstand failures and errors is often referred to as robustness. The word comes from the Latin word “*robus*,” which means oak and symbolises strength and long life [1].

Robustness of structures received wide attention after the 1968 Ronan Point gas explosion [2, 3] and became an even more important research topic after the 2001 World Trade Center attacks [4]. The insensitivity of a structural system to local failure has been an important and widely discussed topic since then [5–9]. During the past two decades, it has become obvious that even modern structural design codes do not sufficiently address system behaviour and focus too much on the verification of individual members and explicit consideration of system performance is required to ensure overall structural safety, i.e., to avoid consequences disproportionate to the originating cause.

Several approaches have been proposed to deal with the issue of disproportionate collapse of tall buildings [10], large span structures [11], and bridges [12, 13]. However, these papers and documents do not always use the same terminologies to describe the same phenomena or system characteristics. Therefore, various attempts had been made to define a common framework robustness assessment, such as the European COST Action TU 1406 “Structural Robustness” [14–16].

The issue of structural robustness has been recognised in structural design codes, e.g., in ISO 2394:2015 [17] and EN1991-1-7 [18], where it is defined as “*the ability of a structure to withstand events like fire, explosions, impact, or the consequences of human error, without being damaged to an extent disproportionate to the original cause.*” It is, however, not clearly defined what is considered as disproportionate.

According to ISO 2394:2015 [17], for structures “*where failure and damage can imply very serious consequences,*” the assessment of structural robustness should be based on a systematic risk-based approach. A methodology for such assessments and a categorization of structures and consequences is suggested to help decide if such a risk-based robustness assessment is needed. If a risk-based approach cannot be justified, the system’s robust behaviour should be ensured through robustness provisions, such as critical

member design, structural ties, and structural segmentation and whose effectiveness will depend on both the structural system itself and the consequences of system failure.

Starossek [6, 7], Haberland [19], and Lind [20] suggest that the general requirements for a useful definition of robustness should be as follows: expressiveness, objectivity, simplicity, calculability, and generality. It is also clear that these characteristics can be in conflict with each other. Haberland [19] proves that expressiveness cannot be developed together with calculability: often a quantitative approach tends to be very complex, and its physical meaning is easily lost. At the same time, each structure is characterized by different collapse mechanisms, so it is not easy to have a general approach that is objective and simple at the same time.

According to the Eurocode 1 [18], robustness of a structural system can be defined as the attitude of the system to survive to a given set of exposures and characterizes the entire system rather than its individual components. This definition is, however, rather broad and general. A formal, more restrictive definition of robustness has been recently suggested, e.g., by CEN/TC250/WG6 [21], referring to the ability of the system to avoid disproportionate collapse: “*Structural robustness is an attribute of a structural concept, which characterizes its ability to limit the follow-up indirect consequences caused by the direct damages (component damages and failures) associated with identifiable or unspecified hazard events (which include deviations from original design assumptions and human errors), to a level that is not disproportionate when compared to the direct consequences these events cause in isolation.*” According to this definition, robustness is seen as an indicator of the ratio between direct and indirect consequences due to certain hazards. This can be quantified in several ways as described in Section 3.1.

**2.2. Resilience.** Besides being robust, another important feature that natural systems possess is the ability of to restore their original functionality after shocks and stresses. Sometimes, the restored system even has an improved performance compared to that prior to the stressor. This ability of systems to recover and adapt is often characterized by the term resilience. The word comes from Latin as well, in which the verb “*resilire*” means to rebound or recoil [22]. In his seminal paper, Holling [23] introduced the concept of resilience to the analysis of the ecological system, which later became popular in other fields of natural and social sciences. This was then followed by technological research areas and engineering (e.g., [24]).

Various definitions of resilience exist depending on the discipline, research field, or industry sector. Resilience representing the ability of a system to recover from an extreme event has gained a wider significance in recent years. The concept is often used in earthquake engineering, and economic and social studies apply the resilience concept to communities, markets, and sociopolitical and financial systems and also to natural environments. For example,

Bhamra [25] presents an interesting classification of the resilience definitions in physical, ecological, social, engineering, and organisational systems. Rose [26] discusses an innovative economic analysis on the disaster resilience from a conceptual and operational point of view. Yumarni [27] reports on economic resilience after an earthquake.

A generic, high-level definition of disaster resilience is given by UNISDR [28]: “*The ability of a system, community or society exposed to hazards to resist, absorb, accommodate to and recover from the effects of a hazard in a timely and efficient manner, including through the preservation and restoration of its essential basic structures and functions.*”

The definition suggests that resilience has a certain temporal dimension, which needs to be considered when developing resilience measures. A convenient and simple visualization of this temporal dimension is possible through the so-called “resilience triangle” (Figure 1) typically applied for technological systems, such as the built infrastructure [29]. The triangle illustrates the abrupt performance loss and the gradual recovery over time, typical for earthquakes, impacting a larger area and a portfolio of structures.

The resilience triangle is a useful representation especially for demonstrating the resilience of technological systems. Complex systems, however, are dependent on (a) the managing organisations and (b) on other interconnected systems. The overall resilience might be influenced by attributes beyond the actual technological system, as also schematically illustrated in Figure 2.

Consider two engineering systems with the exact same performance loss and recovery characteristics for a given hazard. The two systems might use resources quite differently. In the presented case, for example, system A is more efficient during normal conditions; however, it uses resources more extensively during emergency response and recovery. System B, on the contrary, is less resource efficient during normal operation, because, for example, it has more operating personnel and stores more supplies, or has a monitoring system implemented. However, during crisis, these resources are easier to mobilise, whereas for system A, external resources need to be involved leading to additional costs. One could argue that system B is more resilient; however, it might not be straightforward to decide. A possible solution is to define a weight between, e.g., costs and performance (or several weights if more performance indicators are used) [30].

**2.3. Robustness versus Resilience.** The traditional way to mitigate the risks that structures are exposed to has been to protect them, i.e., to increase the resistance of the structural elements and enhance the robustness of the system. However, protection against all types of hazard is impossible, and improving structural robustness might not be economical after a certain level of tolerable risk. Recent research activities and incentives therefore have been focusing on ensuring resilient design concepts [31]. By doing so, Bruneau et al. [29] define four attributes of resilience:

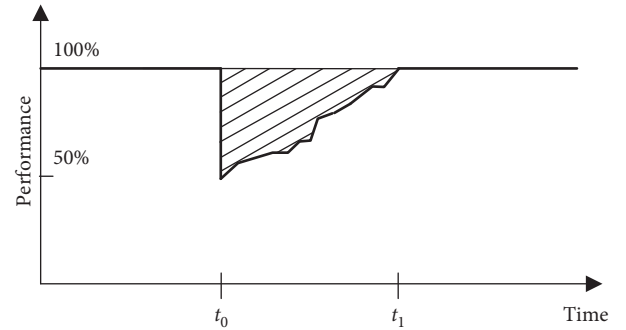


FIGURE 1: The resilience triangle (extracted from [29]).

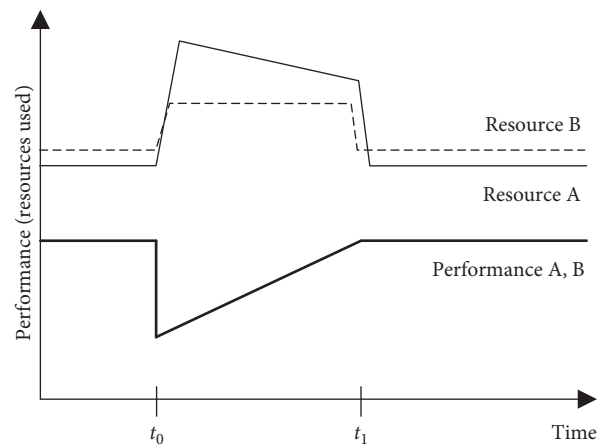


FIGURE 2: Examples of identical resilience triangle, with different use of resources A and B.

- (i) Robustness
- (ii) Redundancy
- (iii) Resourcefulness
- (iv) Rapidity

In this view, robustness is seen as part of resilience and can be associated with the drop of the performance in the resilience triangle of Figure 1.

Marjanishvili et al. [32] argues that the difference between expected and observed structural performance originates from the assumption that member-based design methods will adequately influence the global resistance from which structural robustness is derived. The authors proposed to consider robustness as a fixed property of the system as a function of topology and geometry. Topology here refers to the structure's configuration relative to the site and characterizes the expected exposure toward extreme loads. Geometry describes the layout of the structural load-bearing elements. Both attributes are fixed, i.e., cannot be changed without modifying the overall configuration of the structure, thus by defining the system's geometry, the structural robustness is defined as well.

In contrast to robustness seen as absolute system property, resilience represents a variable property which can be changed with specific design decisions. If resilience

is seen as the structure's ability of balancing between resisting, adapting to, and recovering from extreme events, then resistance represents the engineer's effort to withstand a prescribed hazard. However, structures may encounter some level of damage due to the design level of an extreme load. Even if damage is limited and members do not fail, remedial actions might be required leading to a reduced functionality of the structure for a certain period of time. Adaptation can be understood as the availability of plans for emergency situations to restore functionality after an extreme event. Recovery describes the time-varying process of restoration through remedial actions.

Then, Marjanishvili [32] propose a revised formulation of resilience and exclude adaptation and recovery, as they cannot be easily influenced and quantified by structural design. Hence, structural resilience focuses on the resistance component of generic resilience expression and is broken down into two main attributes: robustness and hazard. Structural resilience is thus associated with a specific hazard magnitude mitigated by a structural design with an assigned robustness. This definition allows the structural designer to quantify resilience and robustness and provides a basis for postevent structural assessment.

### 3. Measures of Robustness and Resilience

**3.1. Robustness Measures.** In a very general conceptual approach, robustness  $R$  can be expressed as

$$R = \frac{1}{(1 + S)}, \quad (1)$$

where  $S$  represents the variation of system properties with respect to the variation of a generic system variable. In this way, an extremely robust structure has  $R=1$ , whereas the opposite end is given by  $R=0$ .

Following the approach presented in [6, 9], it is possible to divide the robustness assessment methods into five main categories: risk-oriented models, reliability-based models, static stiffness-based models, energy-based models, and accumulative damage-based models.

**3.1.1. Risk-Oriented Models.** In case of risk-oriented strategies, the robustness definition is linked to a risk assessment. An important contribution to this approach has been produced in [33]. In his work, the consequences associated with element damage are divided into direct and indirect, or, respectively, proportional or disproportionate to the damage. Janssens [34] clearly distinguishes direct consequences, normally associated with initial damage or partial collapse of some constituent elements of the structure and indirect consequences that would extend beyond initial damage and be associated with any progressive collapse as well as loss of functionality or other negative impacts. On this basis, it is possible to introduce an index of robustness  $I_{\text{ROB}}$ :

$$I_{\text{ROB}} = \frac{R_{\text{Dir}}}{R_{\text{Dir}} + R_{\text{Ind}}}, \quad (2)$$

where  $R_{\text{Dir}}$  is the direct risk and  $R_{\text{Ind}}$  is the indirect one.  $I_{\text{ROB}}$  can also be expressed in a more general way introducing  $\bar{R}_{\text{Ind}} = R_{\text{Ind}}/R_{\text{Dir}}$  and transforming Equation (2) into

$$I_{\text{ROB}} = \frac{1}{1 + \bar{R}_{\text{Ind}}}. \quad (3)$$

The main advantage of this formulation is to calculate  $I_{\text{ROB}}$  even if there is not direct risk measure as in the case of a total loss of a structural member [9].

Faber [35] noted that Equation (2) can only be used as a rough approximation, since the hazards and direct and indirect consequences are “decoupled” from each other. In fact, a more precise formulation would be

$$I_{\text{ROB}} = E \left[ \frac{c_D(\text{DS}, H)}{c_D(\text{DS}, H) + c_{\text{ID}}(\text{SS}, \text{DS}, H)} \right], \quad (4)$$

where  $E[\cdot]$  is the expected value operator and  $c_D$  and  $c_{\text{ID}}$  are the direct and indirect consequences, respectively, originating from various scenarios of hazards  $H$ , constituent damage states DS, and system states SS.

**3.1.2. Reliability-Based Models.** A reliability-based measure of robustness  $\beta_R$ , focusing on the redundancy of the structural system, is defined by Frangopol and Curley [36]:

$$\beta_R = \frac{\beta_{\text{intact}}}{\beta_{\text{intact}} - \beta_{\text{damaged}}}, \quad (5)$$

where  $\beta_{\text{intact}}$  is the reliability index of the intact system and  $\beta_{\text{damaged}}$  is the reliability index of the damaged system. Higher values of  $\beta_R$  represent larger robustness.

**3.1.3. Static Stiffness-Based Models.** Robustness can be linked to the variation of the determinant of the stiffness matrix and the ratio between the determinant corresponding to the intact and to the damaged structure. Indeed, a structure that tends to instability has an almost singular stiffness matrix. Figure 3 shows two examples of variations in the structural system after an extreme event in a building and a bridge during World War II, as reported by Baker [37] and Thomas [38].

Nafday [39] proposes an interesting discussion about the skeletal structures safety. In particular, the link between robustness and stiffness matrix properties is investigated. The ratio between the normalized determinant of the intact structure  $|K_n|$  and the normalized determinant of the one  $|K_n^*|$  corresponding to a damaged state is proposed as the importance factor  $I$ . More critical members will have a higher importance factor [9]:

$$I = \frac{|K_n|}{|K_n^*|}. \quad (6)$$

In [7], the static stiffness properties are used to define another synthetic robustness index:

$$R_s = \min_j \frac{|K_j|}{|K_0|} \quad (7)$$

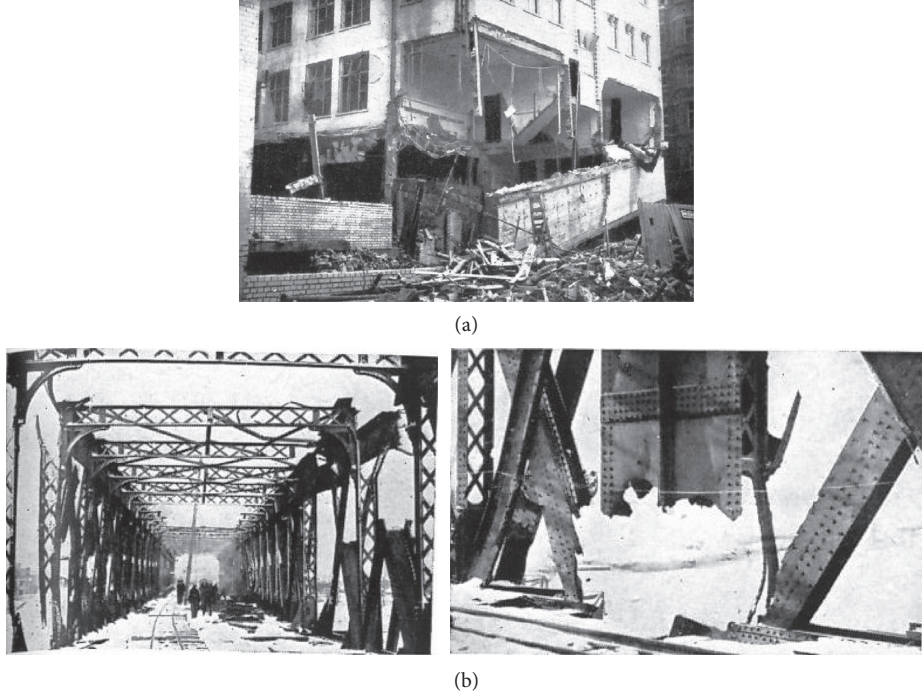


FIGURE 3: Examples of changes in structural system after local damage during extreme event (bombings during WWII): (a) seven-storey steel-framed office building reported by [37] after the main plate girder was blown down by a direct hit; (b) damage over the Oissel Bridge over the Seine reported in [38] (photographs used with the permission of the Institution of Civil Engineers, ICE).

where  $|K_0|$  is the intact structure stiffness matrix determinant, while  $|K_j|$  is the stiffness matrix determinant after removing the  $j$ -structural element. Also, in this case, robust structures present higher  $R_s$  values. Starossek [7] points out that this approach appears to be effective for structures susceptible to zipper-type collapse and less accurate for the ones susceptible to pancake-type or domino-type collapse.

A vulnerability index has been proposed by Lu [40] which is based on the form of the structure. The main concept is that poor form and connectivity yields to disproportionate consequences in damaged structure. The interested reader can also see [41].

**3.1.4. Energy-Based Models.** The principles of energy absorption and energy balance have been often applied to the assessment of robustness. Pinto [41] and Agarwal [42] present a general discussion of the main characteristics of these approaches.

A method to evaluate the collapse resistance of a structure is described in [43]. In this case, critical sequences of damage events that produce the structural collapse are analysed and the corresponding strain energy is calculated. The most critical sequences are those with the lowest energy requirement.

Starossek [7] proposed a simple approach based on the comparison of the energy released during the initial failure and the energy necessary for the failure development:

$$R_e = 1 - \max_j \frac{E_{r,j}}{E_{f,k}}, \quad (8)$$

where  $E_{r,j}$  denotes the energy released during the initial failure of a structural element  $j$  and contributing to the damage of the subsequently affected structural element  $k$ .  $E_{f,k}$  is the energy required for the collapse of the subsequently affected structural element  $k$ . Actually, Equation (8) is useful for structure that are susceptible to pancake-type or domino-type collapse. In other cases, the assessment of  $R_e$  is quite complex and requires a complete structural analysis.

Izzudin [44] proposed a ductility center robustness assessment framework based on energy balance principles for the dynamic considerations using a sudden column removal approach. In their work, they proposed the use of the pseudostatic response in combination with some ductility criteria for assessing structural robustness and acknowledged that on its own, energy absorption is not a property to quantify structural robustness.

**3.1.5. Accumulative Damage Models.** Accumulative damage models are based on the quantification of the damage progression. Starossek [7] proposes a robustness index based on damage measure:

$$R_d = 1 - \frac{p}{p_{\lim}}, \quad (9)$$

where  $p$  is the maximum total damage resulting from a certain initial damage and  $p_{\lim}$  is the corresponding acceptable total damage.  $R_d$  equal to one represents a perfect robustness condition; it means that no additional damage occurs. When  $p > p_{\lim}$ , Equation (9) yields to negative

values that highlight a not-safe condition. This formulation is mainly focused on the assessment on progressive collapse that is characterized by a huge disproportion between the magnitude of the initial damage and the resulting collapse of large part of the structure. Another version of this  $R_d$  can be defined with an integral formulation:

$$R_{d,int,lim} = 1 - \frac{2}{i_{lim} \cdot (2 - i_{lim})} \int_0^{i_{lim}} (d(i) - i) di, \quad (10)$$

where  $i_{lim}$  represents the assumable maximum extent of the initial local damage and  $d(i)$  is the maximum total damage resulting from the initial damage characterized by an extent  $i$ . These damages measures can be expressed as mass, volume, area variation of the structural element, or even by their costs. Both the damage measures  $d(i)$  and  $i$  are dimensionless values obtained by dividing the damaged value by the corresponding undamaged value. As reported in [7], the prefactor of Equation (10) is necessary to modulate the effect of disproportionate local failure. The  $i_{lim}$  value can be tuned for each case. This formulation is effective in assessing design objective in terms of robustness; more information can be found in [19].

Another robustness assessment method has been presented in [45, 46]. It is based on load-capacity evaluation and damage condition limit states. Load factors are defined as the multiplier for the load corresponding to a certain damage condition (e.g., failure of a structural element and cross section damage).

Given the load factor to reach the functionality or ultimate limit state LF and the one corresponding to critical member strength capacity  $LF_l$ , it is possible to define a system reserve factor:

$$R_f = \frac{LF}{LF_l}. \quad (11)$$

It is important to point out that  $R_f$  is dependent upon the system properties regardless of the design load level.

**3.2. Resilience Measures.** System functionality has been considered to be a key parameter for resilience measurements in [47, 48]. In particular, Henry [48] gives an interesting review of resilience metrics in different fields (psychology, infrastructure, economy, etc.) and proposes an innovative method to characterize a time-dependent resilience measure using figure-of-merit.

Royce [49] defines three resilience capacity: absorptive capacity, restorative capacity, and adaptive capacity. Absorptive capacity can be expressed as the degree to which a system can absorb the system perturbations and minimize consequences with little effort [50]. Adaptive capacity expresses the ability of a system to change in response to adverse impacts. Restorative capacity of a resilient system is the attitude to return to normal or improved performance and reliability. A new resilience factor  $\rho_i$  is proposed in [49] based on the resilience capability mentioned above and the recovery time after disaster, so that

$$\rho_i = Sp \frac{F_r F_d}{F_0^2}, \quad (12)$$

$$Sp = \begin{cases} \left(\frac{t_\delta}{t_r^*}\right) \exp[-a(t_r - t_r^*)], & \text{for } t_r \geq t_r^*, \\ \left(\frac{t_\delta}{t_r^*}\right), & \text{otherwise.} \end{cases} \quad (13)$$

In Equations (12) and (13),  $Sp$  is the speed recovery factor,  $F_0$  is the original stable system performance level,  $F_d$  denotes the performance level immediately after disruption, and  $F_r$  represents the performance level at a new stable level after recovery. In addition,  $t_r$  is the time to final recovery,  $t_r^*$  is the time to complete initial recovery actions, and  $t_\delta$  denotes the slack time. It is the maximum amount of time postdisaster that is acceptable before recovery ensues, where  $a$  is a numerical parameter. The absorptive capacity is represented by the ratio  $F_d/F_0$  that is a measure of the system performance after the disruption compared to the intact system performance. Therefore, the adaptive capacity can be expressed by the ratio  $F_r/F_0$  that assesses the degree of the system performance change at the new stable condition compared to the initial system performance. In [49], this method is enhanced in a probabilistic environment and several interesting applications are presented.

A very complete review on resilience measures is reported in [51]. The authors discuss qualitative and quantitative assessment approaches. It is interesting how the latter approaches are divided into structural based and general. Structural-based approaches examine how the structure of a system impacts its resilience; in this category, it is possible to distinguish deterministic [52] and probabilistic approaches [53]. General resilience measures evaluate system performance, regardless of the structure of system. The main idea in this approach is to quantify the system performance before and after disruption. Into this framework, it is possible to include optimization [54], fuzzy logic [55], and simulation model approaches [56].

In the literature, significant amount of research is focused on the definition of infrastructure resilience. Yi and Lence [57] present a resilience index as the ratio of the probability of failure and recovery of the system. Attoh-Okine et al. [58] enhance this method using belief functions framework, and its main applications are highway networks. Instead, a network topology approach has been proposed in [59]. In this work, the resilience factor is the ratio of the value delivery of a network after a disruption to the delivery value of the undamaged system.

Reed [60] evaluates the resilience of a networked infrastructure introducing a quality function  $Q(t)$ . Its value is 1 when the system is fully operable and 0 when is failed. An interesting contribution is given in [61], where the most advanced resilience metrics, cost- and non-cost-based ones, are described for air traffic management research. Interesting research in the field of transport network vulnerability (i.e., resilience) can be found in [62, 63] and recent publication on "The Future of National Infrastructure" [64].

For water supply systems, Todini [65] presents an interesting optimization problem of water distribution performance in which cost and resilience are the two objective functions. Surplus water is used to characterize resilience of the looped network. Indeed, it can be seen as an intrinsic capability of overcoming system collapses.

The study of direct consequences in terms of structural damage is relevant, and interesting research has been carried out on how resilient structures can reduce the damage produced by impact and explosion [66–68].

Recently, the integration of sustainability and resilience has been addressed [69, 70], but quantitative measures of resilience are not generally available for specific events such as fire and blast in concrete buildings.

Instead, in specific earthquake engineering area, the resilience metrics play an important role [67–74]. Takewaki [75] discusses the development of critical excitation methods as worst scenario analysis to upgrade the buildings earthquake resilience.

Platt [76] reports various approaches to assess recovery after seismic event. Satellite images analysis, volunteered geographic information, ground survey and observation, social audit, household surveys, insurance data, and official reports are compared and tested. The interesting conclusion of the authors is that currently it would appear to be challenging to directly measure resilience and that it is easier to analyse the recovery after disruption.

According to the community seismic resilience framework [29], resilience with respect to a specific earthquake can be calculated as the integral defined by the resilience triangle (Figure 1):

$$R = \int_{t_0}^{t_1} [100 - Q(t)] dt, \quad (14)$$

where  $t_0$  is to the time of the disruptive event and  $t_1$  is time at full recovery;  $Q$ , the quality of infrastructure, is expressed in percentage as a function of time  $t$ .

Using Equation (14) for measuring resilience might be difficult, since an increased duration of interruption could lead to an increased resilience, by integrating over a longer time period. To address this aspect, several authors proposed a fixed period of time. For example, Renschler et al. [77] define resilience as the normalized area under the functionality curve:

$$R = \int_{t_0}^{t_0+T_{LC}} \frac{Q(t)}{T_{LC}} dt, \quad (15)$$

where  $T_{LC}$  stands for control time.

Lange and Honfi [78] argue that it is important to account for anticipation and adaptation, i.e., that the performance is not 100% at hazard onset and at the end of recovery. They suggest that instead of a single resilience measure, a set of indicators is needed which provide more insights about the shape of the performance loss function and can be compared with criteria developed based on public expectations.

A generic, time-dependent resilience index  $I_{RES}(t)$  is proposed by [79], which aims to be consistent with previously mentioned risk-based measures:

$$I_{RES}(t) = E_X \left[ \frac{B_1(X, t)}{B_0(X)} \right], \quad (16)$$

where time  $t$  denotes the time after the disrupting event;  $B_0$  and  $B_1$  are the benefits of the structure before and after the event, respectively; the expectation  $E_X$  is taken over all relevant uncertainties  $X$  influencing the benefits. The resilience index thus typically falls between 0 and 1. However, for if the recovered system is improved compared to the original, the resilience can be larger than 1.

**3.3. Example.** In order to test some of the above presented robustness and resilience measures, an illustrative example is discussed as follows.

The steel frame, presented in Figure 4 with its geometrical characteristics, has been modelled in ANSYS® R18.1 [80]. The frame is fixed at the bottom of both columns, and it is characterized by an IPE 200 cross section. The material elastic longitudinal modulus is  $E = 200$  GPa and its Poisson ratio is  $\nu = 0.3$ .

As a first example, the robustness evaluation according to Starrosek and Haberland [7], Equation (7), has been developed. The ratios between the normalized stiffness matrix without the  $j$ th element and the normalized stiffness matrix of the intact system are reported in the rows of Table 1.

Thus, the minimum ratio represents a measure of structural robustness. In this case, the deletion of element 4 or 8 yields to the lower value equal to  $1.49 \cdot 10^{-7}$ . As correctly reported by [7], this is more a measure of the structural connectivity and hardly can give an accurate measure of robustness. The authors agree with this consideration given that the elimination of one column (elements 2–15 or 10–11) yields a quite high stiffness matrix ratio even if the structural damages in this condition are more important than the ones obtained after the elimination of elements 4 or 8 (Figure 4).

The energy-based measure of robustness presented in Equation (8) was applied to the same frame structure. In this case, a pancake-type collapse is considered. Thus,  $E_{r,j}$  is the energy released during the failure of the second floor beam (finite elements 5–6–7). It has been approximated by its gravitational potential energy. Instead,  $E_{f,k}$  is the energy required for the failure of the first-floor beam. For the sake of simplicity, only flexural failure has been considered and  $E_{f,k}$  has been assumed equal to the ultimate strain energy absorbed by the beam in the collapse condition. The steel constitutive behaviour is modelled by a bilinear elastoplastic curve whose yield stress is 275 MPa. The collapse mechanism considered here is characterized by 3 plastic hinges: two at beam side and one at midspan.

The bending moment  $M$ -curvature  $\theta$  relationship has been represented by

$$M = \overline{M} \tanh\left(\frac{K}{\overline{M}}\theta\right), \quad (17)$$

where  $\overline{M}$  and  $K$  are two parameters depending on the sectional and constitutive properties of the beam (see [67, 68] for more details). Thus, the ultimate strain energy can be expressed as

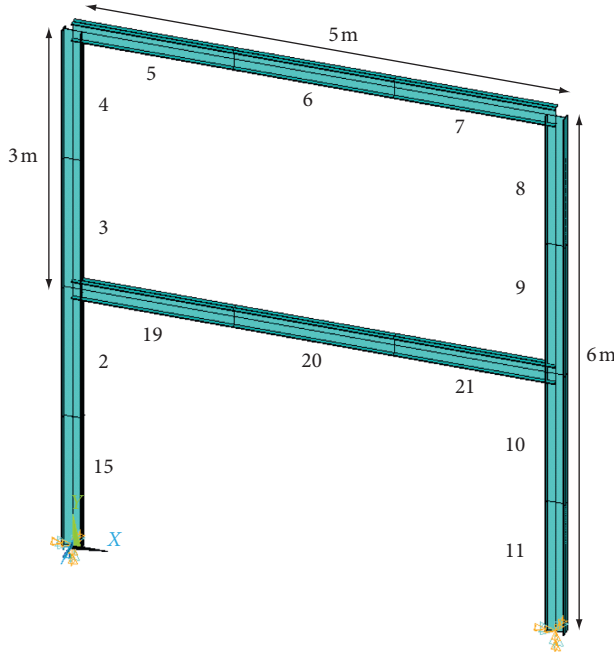


FIGURE 4: Steel frame considered in the example.

TABLE 1: Stiffness matrix determinant ratios.

Element	$R_j$
15–2	0.646588093187559
3	0.001579740685829
4	0.000000149150733
5	0.000000385626491
6	0.000231677343333
7	0.000000385626491
8	0.000000149150733
9	0.001579740685829
19	0.000002495241655
20	0.000231677343333
21	0.000002495241655
10–11	0.646588093187560

$$U = \int_0^l \int_0^\theta \bar{M} \tanh\left(\frac{K}{\bar{M}}\theta\right) d\theta dx. \quad (18)$$

In this way,  $R_e$ , see Equation (8), is equal to 0.95, which denotes a very robust structure, indeed a value equal to one denotes perfect robustness.

In order to develop an example of resilience measure, the approach proposed in [32] is applied in this case. Following this method, the resilience is seen as a function of hazard, topology, and geometry of the structure. Actually, it is necessary to define the intensity measure IM (representing the magnitude of the external event) and the C function that describes the increase of the consequences as function of the pattern of  $G(DM|IM)$ . The latter is a deterministic function of the exceedance of the engineering response parameter limit of the structure. In this specific case, it measures the damage produced by the collapse of a given structural element. Thus, C is a user-defined function capable of describing the increasing amount of structural failures associated with the location and extension of damage:

$$C(T) = \int \int CM(IM, DM) DM dIM \cdot \int \int G(DM | IM) DM (IM) dDM dIM, \quad (19)$$

where CM is the overall consequence measure obtained as the product of  $G(DM|IM)$  and IM. Now, if the rate of recovery after damage is assumed to be independent of the magnitude or type or functionality loss, the resilience can be approximated as the inverse of the consequences C defined above [32]:

$$R(T) = \frac{1}{C(T)}. \quad (20)$$

This simplified approach assumes that the consequences measured as structural loss are governed by the order and location of element failure as the intensity of the blast threat increases. Thus, resilience can be assessed and it can influence the structural system configuration since early design.

In this case, let us assume that the threat is represented by a blast load located near elements 2–15 of the steel frame (Figure 4). This load results in the failure of the first-floor left column (elements 2–15). Actually, the accurate sequence in which failure propagates from one column to the other parts of the structure can be assessed only by complex dynamic nonlinear analysis. Here, for the sake of simplicity, the damage propagation is assumed following the IM graph presented in Figure 5 and the  $G(DM|IM)$  one in Figure 6. With more details, while the former represents the engineering response parameter distribution on each structural element for the given load scenario (e.g., it can represent the Von Mises stress concentration in each element, or the maximum bending moment if the flexural failure is critical), the latter presents the cumulative number of structural elements collapsed after the sequence of progressive failures presented in the x-axis. Thus, the collapse of the left column corresponds to the failure of 1 element, the consequent failure of the top beam or of the bottom beam corresponds to 2 elements failure (one column and one beam), and finally the collapse of the right column denotes the total collapse of the 4 elements (two columns and two beams). Clearly, the magnitude of this  $G$  function distribution is arbitrary and there are many possible alternative values as there are many possible damage propagations depending on the considered scenarios.

The distribution of CM is reported in Figure 7, and after the numerical calculation of the integral presented in Equation (19), which represent the volume under the CM surface, it is possible to calculate the resilience value  $R = 26.7\%$ . Actually, this value becomes significant only when compared to other scenarios in order to find a design solution that maximizes the resilience.

#### 4. Design and Structural Considerations

Despite the large number of proposed measures for robustness and resilience discussed in previous sections, the implementation of such measures into practice is

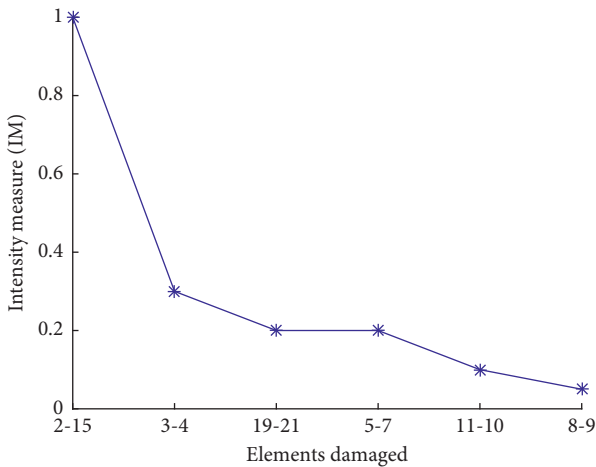


FIGURE 5: Topology plot of relative IM for all elements.

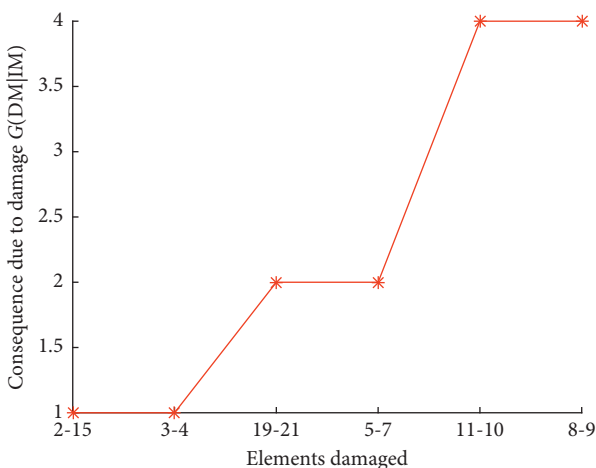


FIGURE 6: Geometry plot of consequence function for each element.

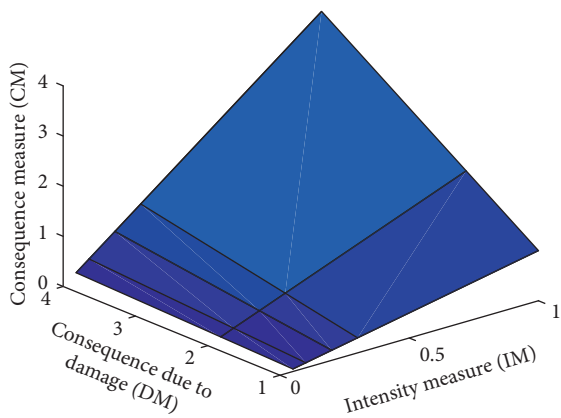


FIGURE 7: Consequence measure for the considered scenario.

cumbersome for infrastructure developers/designers and asset owners as many of the proposed approaches are still under development and they have not been yet implemented in current design standards. Perhaps, the most generally adopted design philosophy, which is now being implemented

in different codes, is the risk-based approaches in which the type, probability, and consequences of an event are compared against the cost of protection and assumed potential loss [5]. Within such frameworks, systematic risk assessment methods are being implemented in the field of structures, especially for cases of buildings with a high-risk of progressive collapse [81].

In structural engineering, the use of risk or consequence classes for buildings has been widely used in Europe and the US for some time; in this approach, the probability of failure is not directly assessed but risk is managed indirectly. For structures with a low risk of progressive collapse, robustness is not directly quantified, and generally prescriptive rules are adopted to mitigate the potential loss of one or some structural members. For higher consequence classes (i.e., Class 3 in the Eurocodes), systematic risk assessments are needed such as the one presented in [81], which suggests the identification of hazards, to eliminate (if possible) this hazard which give rises to the associated risk and for the hazard that remain to develop risk mitigation measures so far as this is possible. Such approaches are implemented with the idea that a structural design is conceived containing a level of structural robustness suitable with the level of risk to which the structure is subjected.

Another relevant issue which is affecting infrastructure designers regarding robustness and resilience considerations is the differentiation between existing and newly built infrastructure. The vulnerability and mitigating measures that can be introduced in each case can be rather different, and the use of different measures for robustness and/or resilience might not be directly applicable to the existing infrastructure. In addition, the interface between new and existing building environment can be also be problematic unless the problem is not approached as a system-of-systems.

Current structural design codes require the verification of strength and stability of structures based on the limit state concept typically associated with the failure of individual members. It is also recognised that requirements to the overall performance of the entire structural system should be set to prevent disproportionate collapse and mitigate the adverse possible effects of extraordinary situations which cannot be fully covered by prescriptive design rules.

General aspects and approaches for structural design which enhances robustness have been widely studied after World Trade Center attack in 2001, although the first principles of structural robustness were introduced in the 1970s after the Ronan Point collapse [82]. Most recently in Europe, a major work on this topic has been conducted within the COST Action TU0601 "Robustness of Structures" <http://www.cost-tu0601.ethz.ch/>. Parallel reviews took place [16, 83] raising similar limitations of existing international codes to deal with robustness. A more recent review [84] has gathered research in this field over the twenty-first century including the evolution of international codes [18, 85–93]. This work concluded that recent refinements have been introduced in international codes regarding robustness, although in many cases, the changes in the general procedures adopted are not significant.

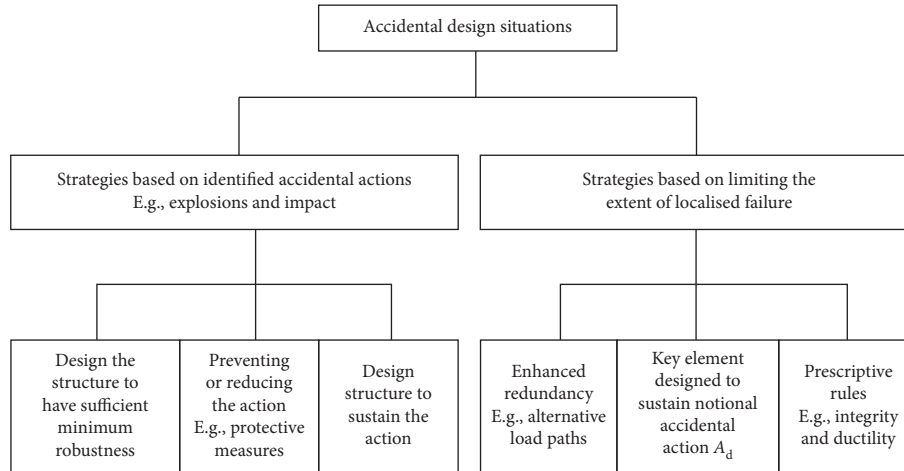


FIGURE 8: Strategies for accidental design situations according to EN1991-1-7 [18].

General recommendations to achieve a robust design include various strategies such as event control, strengthening of critical elements, provision of alternative load path, and segmentation [94]. One important strategy is to provide redundancy at various levels, i.e., at material level, member level, and system level [95, 96]. Besides improving internal redundancy, some authors argue that external redundancy could be seen as a measure to increase robustness, since if alternative means to provide the same functionality are available, the consequences of failure can be mitigated [97].

Another structural characteristic that is typically seen as beneficial for a robust behaviour is ductility especially at connections. Ductile materials and joint can accommodate larger deformations, thus allowing for redistribution of stresses and giving a warning before collapse occurs in contrast to brittle failure.

An important aspect raised by several researchers (i.e., [44]) influencing robustness is the energy absorption capacity of structures which can be considered as a useful additional property to consider in combination with redundancy and ductility.

According to EN1990 [93], “*a structure shall be designed and executed in such a way that it will not be damaged by events such as: explosion, impact, and the consequences of human errors, to an extent disproportionate to the original cause.*” In other words, the structure should be sufficiently robust. It is, however, not obvious what is a sufficient level of robustness and how it can be measured.

Regarding Eurocodes, more details on robustness are provided in EN1991-1-7 [18] concerning accidental design situations and related design strategies (Figure 8).

According to EN1991-1-7 [18] in accidental design situations, measures should be taken to mitigate the risk of accidental actions, e.g., by ensuring that the structure has sufficient robustness.

This could be done in several ways as follows:

- (1) Overdesigning and/or protecting key elements
- (2) Enhancing ductility to enable better energy absorption
- (3) Enhancing redundancy to provide alternative load paths

The informative Annex A of EN1991-1-7 [18], “*Design for consequences of localised failure in buildings from an unspecified cause,*” provides design guidance to withstand local failure from an unspecified cause without disproportionate collapse. The annex contains prescriptive rules, based on the building’s consequence class, aiming to provide sufficient robustness and decrease the chance of collapse in case of unforeseen harmful events. However, these recommendations have very limited applicability and have little use apart from multistorey RC buildings.

In general, it is widely accepted that even if a structure is extremely robust, it is impossible to resist against all kinds of hazards. Therefore, it needs to be considered what happens after failure. Performance-based design initiatives take into consideration losses due to various system damage states [98].

Many interesting papers discussed at structural and substructure level are the most important approaches to improve resilience. For example, Xilin [99] presents a structural engineering approach to the development of earthquake-resilient rocking or self-centering structures. The same self-centering approach is discussed in [100] for steel structures. Finally, also the specific bridge seismic resilience has been an interesting and wide research field [101, 102].

Resilience-based approaches, however, need to go even further [78]. A resilient design and operation of a structure should account for response, restoration of functions, and recovery. To achieve a satisfactorily high resilience, both the structure and the operating organization should have sufficient flexibility for reacting to the varying needs due to the changing circumstances. This could include adaptivity through automatized control mechanism but also well-established processes and sufficient resources, both human and materialized, in case of an emergency and in the aftermath of a disaster. Obviously, what and how this needs to be done depends on the actual structure and incident considered. General requirements and guidelines, however, can be given especially with regards to expected response and recovery times and minimum levels of functioning during and after crisis times.

## 5. Conclusions

Catastrophic failures of structures and infrastructure systems happen from time to time as a consequence of natural or man-made extreme events. Therefore, it is important to consider what would happen if one or several elements of a system fail.

The quantitative and qualitative definitions of robustness and resilience have been reviewed in this paper. If the former is simply denoted as the ability to avoid disproportionate collapse due to an initial damage, the latter is the ability to adapt and recover from a disturbance or damage due to a disaster.

Quantitative measures of robustness can be obtained with risk-oriented, energy-based, static stiffness-based, cumulative damage-based models. The effectiveness of each approach depends of the specific case because what is working well for a given structural system may became less accurate for another.

Resilience properties can be distinguished in absorptive capacity, restorative capacity, and adaptive capacity. Quantitative measures of resilience can be divided into structural based and general. Structural-based approaches examine how the structure of a system impacts its resilience while general resilience measures evaluate system performance, regardless of the structure of system.

While most resilience definition can be applied to infrastructures, very few are valid also for structures. The authors would like to underline that more research into resilient structural systems is needed, especially since adaptive and smart structures are becoming more important. In addition, current technological development requires the need of robust and resilient design even in sectors not traditionally linked to civil engineering. For example, “digital data management” affecting infrastructure development and operation of large assets can also be subject to similar principles of robustness and resilience. Data protection and security and the existence of “virtual infrastructure” will introduce new domains of research in civil engineering within the new context of Digital World and Digital Engineering.

## Conflicts of Interest

The authors declare that they have no conflicts of interest.

## Acknowledgments

The financial support of the Autonomous Region of Sardinia under grant PO-FSE 2014–2020, CCI: 2014-IT05SFOP021, through the project “Retrofitting, rehabilitation and requalification of the historical cultural architectural heritage (R3-PAS)” is acknowledged by Flavio Stochino.

## References

- [1] A. L. Barabási, *The New Science of Networks*, Perseus Books Group, New York, NY, USA, 2002.
- [2] C. Pearson and N. Delatte, “Ronan point Apartment tower collapse and its effect on building codes,” *Journal of Performance of Constructed Facilities*, vol. 19, no. 2, pp. 172–177, 2005.
- [3] M. N. Bussell and A. E. K. Jones, “Robustness and the relevance of ronan point today,” *Structural Engineer*, vol. 88, no. 23-24, pp. 20–25, 2010.
- [4] M. H. Faber, O. Kübler, and M. Fontana, “Modeling consequences due to failure of extraordinary structures,” in *Probabilistic Safety Assessment and Management*, C. Spitzer, U. Schmocke, and V. N. Dang, Eds., Springer, London, UK, 2004.
- [5] D. Cormie, G. Mays, and P. Smith, *Blast Effects on Buildings*, ICE Publishing, London, UK, 2nd edition, 2012.
- [6] U. Starossek, *Progressive Collapse of Structures*, Thomas Telford Publishing, London, UK, 2009.
- [7] U. Starossek and M. Haberland, “Approaches to measures of structural robustness,” *Structure and Infrastructure Engineering*, vol. 7, no. 7-8, pp. 625–631, 2011.
- [8] D. Asprone, R. De Risi, and G. Manfredi, “Defining structural robustness under seismic and simultaneous actions: an application to precast RC buildings,” *Bulletin of Earthquake Engineering*, vol. 14, no. 2, pp. 485–499, 2016.
- [9] C. Brett and Y. Lu, “Assessment of robustness of structures: current state of research,” *Frontiers of Structural and Civil Engineering*, vol. 7, no. 4, pp. 356–368, 2013.
- [10] M. Faber and H. Narasimhan, “COST Action TU0601-robustness of structures: a summary,” in *Robustness of Structures-Final Report of COST Action TU0601*, M. Faber, Ed., pp. A.1–A.14, CTU Publishing House, Prague, 2011.
- [11] P. Dietsch, “Robustness of large-span timber roof structures-structural aspects,” *Engineering Structures*, vol. 33, no. 11, pp. 3106–3112, 2011.
- [12] H. Stempfle and T. Vogel, *A Concept to Evaluate the Robustness of Bridges, Workshop Paper, JCSS and IABSE Workshop on Robustness of Structures*, Building Research Establishment, Garston, Watford, UK, 2005.
- [13] U. Starossek, “Progressive collapse of bridges–Aspects of analysis and design, Invited lecture,” in *Proceedings, International Symposium on Sea-Crossing Long-Span Bridges*, Mokpo, Korea, February 2006.
- [14] J. D. Sørensen, “Theoretical framework on structural robustness,” in *Robustness of Structures: Final Report of COST Action TU0601*, M. H. Faber, Ed., Czech Technical University, Prague, Czech Republic, 2011.
- [15] Arup, *Review of International Research on Structural Robustness and Disproportionate Collapse*, Department for Communities and Local Government. Arup Co, London, UK, 2011.
- [16] B. R. Ellingwood, R. Smilowitz, D. O. Dusenberry, D. Duthinh, H. S. Lew, and N. J. Carino, *Best practices for reducing the potential for progressive collapse in buildings, No. NIST Interagency/Internal Report (NISTIR)-7396*, NIST, Gaithersburg, MD, USA, 2007.
- [17] ISO 2394:2015, *General Principles on Reliability for Structures*, International Organization for Standardization, Geneva, Switzerland, 2015.
- [18] CEN EN 1991-1-7:2006, *Eurocode 1-Actions on Structures-Part 1-7: General Actions-Accidental Action*, European Committee For Standardization, Geneva, Switzerland, 2006.
- [19] M. Haberland, “Progressiver Kollaps und Robustheit (Progressive collapse and robustness),” Thesis (diploma), Hamburg University of Technology, Structural Analysis and Steel Structures Institute, Hamburg, Germany, 2007.

- [20] N. C. Lind, "A measure of vulnerability and damage tolerance," *Reliability Engineering & System Safety*, vol. 48, no. 1, pp. 1–6, 1995.
- [21] CEN/TC250/WG6 Practical definition of structural robustness vDraft, N042 WG6, PT1, 2016.
- [22] R. K. Barnhart, *The Barnhart Dictionary of Etymology*, H. W. Wilson, New York, NY, USA, 1988.
- [23] C. S. Holling, "Resilience and stability of ecological systems," *Annual Review of Ecology and Systematics*, vol. 4, no. 1, pp. 1–23, 1973.
- [24] E. Hollnagel, D. D. Woods, and N. Leveson, *Resilience engineering: Concepts and precepts*, Ashgate, Aldershot, UK, 2006.
- [25] R. Bhamra, S. Dani, and K. Burnard, "Resilience: the concept, a literature review and future directions," *International Journal of Production Research*, vol. 49, no. 18, pp. 5375–5393, 2011.
- [26] A. Rose, "Defining and measuring economic resilience to disasters," *Disaster Prevention and Management: An International Journal*, vol. 13, no. 4, pp. 307–314, 2004.
- [27] T. Yumarni, "Ten years later: economic resilience of small scale enterprise following earthquake in Bantul Yogyakarta," *Procedia Engineering*, vol. 212, pp. 309–315, 2018.
- [28] UNISDR-United Nations Office for Disaster Risk Reduction, *Terminology on Disaster Risk Reduction*, 2009, <https://www.unisdr.org/we/informterminology>.
- [29] M. Bruneau, S. E. Chang, R. T. Eguchi et al., "A framework to quantitatively assess and enhance the seismic resilience of communities," *Earthquake Spectra*, vol. 19, no. 4, pp. 733–752, 2003.
- [30] M. Nogal, A. O'Connor, B. Caulfield, and B. Martinez-Pastor, "Resilience of traffic networks: from perturbation to recovery via a dynamic restricted equilibrium model," *Reliability Engineering & System Safety*, vol. 156, pp. 84–96, 2016.
- [31] Arup, *REDi Rating System, Resilience-based Earthquake Design Initiative for the Next Generation of Buildings*, Arup Co, London, UK, 2016.
- [32] S. Marjanishvili, B. Katz, and S. Quiel, "Performance-based framework for quantifying structural resilience to blast-induced damage," in *Proceedings of the 10th International Conference of the International Institute for Infrastructure Resilience and Reconstruction (I3R2)*, Purdue University, West Lafayette, IN, USA, May 2014.
- [33] J. W. Baker, M. Schubert, and M. H. Faber, "On the assessment of robustness," *Structural Safety*, vol. 30, no. 3, pp. 253–267, 2008.
- [34] V. Janssens, D. W. O'Dwyer, and M. K. Chryssanthopoulos, "Assessing the consequences of building failures," *Structural Engineering International*, vol. 22, no. 1, pp. 99–104, 2012.
- [35] M. H. Faber, "Codified risk informed decision making for structures," in *Proceedings of the Symposium on Reliability of Engineering System*, SRES, Hangzhou, China, October 2015.
- [36] D. M. Frangopol and J. P. Curley, "Effects of damage and redundancy on structural reliability," *Journal of Structural Engineering*, vol. 113, no. 7, pp. 1533–1549, 1987.
- [37] J. F. Baker, E. L. Williams, and D. Lax, *The Design of Framed Buildings against High-Explosive Bombs. The civil engineer in war: A symposium of papers on war-time engineering problems*, Institution of Civil Engineers, London, UK, 1948.
- [38] W. N. Thomas, "The effects of impulsive forces on materials and structural members," in *The civil engineer in war: A symposium of papers on war-time engineering problems*, pp. 3–65, Thomas Telford Ltd, London, UK, 1948.
- [39] A. M. Nafday, "System safety performance metrics for skeletal structures," *Journal of Structural Engineering*, vol. 134, no. 3, pp. 499–504, 2008.
- [40] Z. Y. Lu, Y. Yu, N. J. Woodman, and D. I. Blockley, "A theory of structural vulnerability," *Structural Engineer*, vol. 77, no. 18, pp. 17–24, 1999.
- [41] J. T. Pinto, D. I. Blockley, and N. J. Woodman, "The risk of vulnerable failure," *Structural Safety*, vol. 24, no. 2–4, pp. 107–122, 2002.
- [42] J. Agarwal and J. England, "Recent developments in robustness and relation with risk," *Proceedings of the Institution of Civil Engineers-Structures and Buildings*, vol. 161, no. 8, pp. 183–188, 2008.
- [43] J. W. Smith, "Energy approach to assessing corrosion damaged structures," *Structures*, vol. 156, no. 2, pp. 121–130, 2003.
- [44] B. A. Izzudin, A. G. Vlassis, D. A. Elghazouli, and D. A. Nethercot, "Progressive collapse of multi-storey buildings due to sudden column loss – Part I: simplified assessment framework," *Engineering Structures*, vol. 30, pp. 1308–1318, 2008.
- [45] M. Ghosn and F. Moses, *NCHRP Report 406: Redundancy in Highway Bridge Superstructures*, Transportation Research Board, Washington, DC, USA, 1998.
- [46] D. Wisniewski, J. R. Casas, and M. Ghosn, "Load capacity evaluation of existing railway bridges based on robustness quantification," *Structural Engineering International*, vol. 16, no. 2, pp. 161–166, 2006.
- [47] V. Latora and M. Marchiori, "Vulnerability and protection of infrastructure networks," *Physical Review E*, vol. 71, no. 1, article 015103, 2005.
- [48] D. Henry and J. E. Ramirez-Marquez, "Generic metrics and quantitative approaches for system resilience as a function of time," *Reliability Engineering & System Safety*, vol. 99, pp. 114–122, 2012.
- [49] F. Royce and B. Bekera, "A metric and frameworks for resilience analysis of engineered and infrastructure systems," *Reliability Engineering & System Safety*, vol. 121, pp. 90–103, 2014.
- [50] E. Vugrin, E. Drake, and M. A. Ehlen, "A resilience assessment framework for infrastructure and economic systems: quantitative and qualitative resilience analysis of petrochemical supply chains to a hurricane," *Process Safety Progress*, vol. 30, no. 3, pp. 280–290, 2011.
- [51] S. Hosseini, K. Barker, and J. E. Ramirez-Marquez, "A review of definitions and measures of system resilience," *Reliability Engineering & System Safety*, vol. 145, pp. 47–61, 2016.
- [52] S. Enjalbert, F. Vanderhaegen, M. Pichon, K. A. Ouedraogo, and P. Millot, "Assessment of transportation system resilience," in *Human Modelling in Assisted Transportation*, pp. 335–341, Springer, Berlin, Germany, 2011.
- [53] B. D. Youn, C. Hu, and P. Wang, "Resilience-driven system design of complex engineered systems," *Journal of Mechanical Design*, vol. 133, no. 10, article 101011, 2011.
- [54] H. Baroud, K. Barker, and J. E. Ramirez-Marquez, "Importance measures for inland waterway network resilience," *Transportation Research Part E: Logistics and Transportation Review*, vol. 62, pp. 55–67, 2014.
- [55] S. K. Jain and P. K. Bhunya, "Reliability, resilience and vulnerability of a multipurpose storage reservoir/confiance, résilience et vulnérabilité d'un barrage multi-objectifs," *Hydrological Sciences Journal*, vol. 53, no. 2, pp. 434–447, 2008.

- [56] G. Muller, "Fuzzy architecture assessment for critical infrastructure resilience," *Procedia Computer Science*, vol. 12, pp. 367–372, 2012.
- [57] L. Yi and B. J. Lence, "Estimating resilience for water resources systems," *Water Resources Research*, vol. 43, no. 7, 2007.
- [58] N. O. Attoh-Okine, T. A. Cooper, and A. S. Mensah, "Formulation of resilience index of urban infrastructure using belief functions," *IEEE Systems Journal*, vol. 3, no. 2, pp. 147–153, 2009.
- [59] M. Omer, N. Roshanak, and A. Mostashari, "Measuring the resilience of the trans-oceanic telecommunication cable system," *IEEE Systems Journal*, vol. 3, no. 3, pp. 295–303, 2009.
- [60] D. Reed, K. C. Kapur, and R. D. Christie, "Methodology for assessing the resilience of networked infrastructure," *IEEE Systems Journal*, vol. 3, no. 2, pp. 174–180, 2009.
- [61] A. Cook, L. Delgado, G. Tanner, and S. Cristóbal, "Measuring the cost of resilience," *Journal of Air Transport Management*, vol. 56, pp. 38–47, 2016.
- [62] E. Jenelius, T. Petersen, and L. G. Mattsson, "Importance and exposure in road network vulnerability analysis," *Transportation Research Part A: Policy and Practice*, vol. 40, no. 7, pp. 537–560, 2006.
- [63] L. G. Mattsson and E. Jenelius, "Vulnerability and resilience of transport systems—a discussion of recent research," *Transportation Research Part A: Policy and Practice*, vol. 81, pp. 16–34, 2015.
- [64] J. W. Halls, M. Tran, A. J. Hickford, and R. J. Nicholls, *The Future of National Infrastructure: A System-of-Systems Approach*, Cambridge University Press, Cambridge, UK, 2016.
- [65] E. Todini, "Looped water distribution networks design using a resilience index based heuristic approach," *Urban Water*, vol. 2, no. 2, pp. 115–122, 2000.
- [66] N. Gebbeken and T. Döge, "Explosion protection—architectural design, urban planning and landscape planning," *International Journal of Protective Structures*, vol. 1, no. 1, pp. 1–21, 2010.
- [67] F. Stochino, "RC beams under blast load: reliability and sensitivity analysis," *Engineering Failure Analysis*, vol. 66, pp. 544–565, 2016.
- [68] F. Stochino and G. Carta, "SDOF models for reinforced concrete beams under impulsive loads accounting for strain rate effects," *Nuclear Engineering and Design*, vol. 276, pp. 74–86, 2014.
- [69] R. Phillips, L. Troup, D. Fannon, and M. Eckelman, "Do resilient and sustainable design strategies conflict in commercial buildings? A critical analysis of existing resilient building frameworks and their sustainability implications," *Energy and Buildings*, vol. 156, pp. 295–311, 2017.
- [70] T. Kijewski-Correa and A. A. Taflanidis, "The Haitian housing dilemma: can sustainability and hazard-resilience be achieved?," *Bulletin of Earthquake Engineering*, vol. 10, no. 3, pp. 765–771, 2012.
- [71] G. P. Cimellaro, M. A. Reinhorn, and M. Bruneau, "Quantification of seismic resilience," in *Proceedings of the 8th US National conference on Earthquake Engineering*, pp. 18–22, San Francisco, CA, USA, April 2006.
- [72] G. P. Cimellaro, M. A. Reinhorn, and M. Bruneau, "Seismic resilience of a hospital system," *Structure and Infrastructure Engineering*, vol. 6, no. 1-2, pp. 127–144, 2010.
- [73] M. Bruneau and A. Reinhorn, "Exploring the concept of seismic resilience for acute care facilities," *Earthquake Spectra*, vol. 23, no. 1, pp. 41–62, 2007.
- [74] A. Shafieezadeh and L. I. Burden, "Scenario-based resilience assessment framework for critical infrastructure systems: case study for seismic resilience of seaports," *Reliability Engineering & System Safety*, vol. 132, pp. 207–219, 2014.
- [75] I. Takewaki, "Toward greater building earthquake resilience using concept of critical excitation: a review," *Sustainable Cities and Society*, vol. 9, pp. 39–53, 2013.
- [76] S. Platt, D. Brown, and M. Hughes, "Measuring resilience and recovery," *International Journal of Disaster Risk Reduction*, vol. 19, pp. 447–460, 2016.
- [77] C. Renschler, A. Frazier, L. Arendt, G. P. Cimellaro, A. M. Reinhorn, and M. Bruneau, "Framework for defining and measuring resilience at the community scale: the PEOPLES resilience framework," MCEER Technical Report—MCEER-10-006, p. 91, University at Buffalo (SUNY), The State University of New York, Buffalo, NY, USA, 2010.
- [78] D. Lange and D. Honfi, "Resilient infrastructures for resilient communities. Safety, reliability, risk, resilience and sustainability of structures and infrastructure," in *Proceedings of the 12th International Conference on Structural Safety and Reliability (ICOSSAR 2017)*, C. Bucher, B. R. Ellingwood, and D. M. Frangopol, Eds., pp. 3155–3164, Vienna, Austria, August 2017.
- [79] M. H. Faber, "Codified risk informed decision making for structures," in *Proceedings of the Symposium on Reliability of Engineering System*, SRES, Hangzhou, China, October 2015.
- [80] Ansys R18.1 Release Notes, 2017.
- [81] Institution of Structural Engineers (IStructE), *Manual for the Systematic Risk Assessment of High-Risk Structures against Disproportionate Collapse*, Institution of Structural Engineers (IStructE), London, UK, 2013.
- [82] Minister of Housing and Local Government, *The Building (Fifth Amendment) Regulations 1970, Statutory Instruments of the UK*, S.I. 26 1970, No. 109, 1970.
- [83] M. P. Byfield, W. Mudalige, C. Morison, and E. Stoddart, "A review of progressive collapse research and regulations," *Proceedings of the ICE-Structures and Buildings*, vol. 167, no. 8, pp. 447–456, 2014.
- [84] J. M. Adam, F. Parisi, J. Sagaseta, and X. Lu, "Research and practice on progressive collapse and robustness of building structure in the 21st century," *Engineering Structures*, vol. 173, pp. 122–149, 2018.
- [85] Australian Building Codes Board (ABC), *National Construction Code (NCC): Volumes 1 & 2*, Council of Australian Governments, Australia, 2016.
- [86] China Association for Engineering Construction Standardization (CECS), *Code for Anti-Collapse Design of Building Structures*, CECS, Beijing, China, 2014.
- [87] Department of Defence (DoD), *Design of Buildings to Resist Progressive Collapse (UFC 4-023-03)*, Unified Facilities Criteria, Washington, DC, USA, 2009.
- [88] Department of Communities and Local Government, *The Building Regulations 2010-Structure: Approved Document A*, HM Government, UK, 2010.
- [89] General Services Administration (GSA), *Alternative Path Analysis and Design Guidelines for Progressive Collapse Resistance*, Office of Chief Architects, Washington, DC, USA, 2013.
- [90] International Code Council, *International Building Code (IBC 2009)*, International Code Council, Washington, DC, USA, 2009.

- [91] National Research Council of Canada, *National Building Code of Canada*, Canadian Commission on Building and Fire Codes, Canada, 1995.
- [92] NYC Department of Buildings, *Building Code (Chapter 16—Structural Design)*, NYC Construction Codes, New York, NY, USA, 2014.
- [93] CEN EN 1990, *Eurocode—Basis of Structural Design*, European Committee For Standardization, Geneva, Switzerland, 2005.
- [94] G. T. D. Canisius, *Structural Robustness Design For Practicing Engineers*, COST Action TU0601—Robustness of Structures, European Cooperation in Science and Technology, Brussels, Belgium, 2011.
- [95] F. P. Bos, *Safety Concepts in Structural Glass Engineering—Towards an Integrated Approach*, PhD Thesis, TU Delft, Delft, Netherlands, 2009.
- [96] D. Honfi and M. Overend, “Glass structures—learning from experts,” in *Proceedings of COST Action TU0905 Mid-Term Conference on Structural Glass*, J. Belis, C. Louter, and D. Mocibob, Eds., pp. 527–536, Poreč, Croatia, April 2013.
- [97] D. Honfi, D. Lange, C. Pursiainen, and B. Rød, *On the Contribution of Technological Concepts to the Resilience of Bridges as Critical Infrastructure Assets*, pp. 962–969, 19th IABSE Congress, Stockholm, Sweden, 2016.
- [98] K. A. Porter, “An overview of PEER’s performance-based earthquake engineering methodology,” in *Ninth International Conference on Applications of Statistics and Probability in Civil Engineering*, ICASP9, San Francisco, CA, USA, 2003.
- [99] L. Xilin, Y. Mao, Y. Chen, J. Liu, and Y. Zhou, “New structural system for earthquake resilient design,” *Journal of Earthquake and Tsunami*, vol. 7, no. 3, article 1350013, 2013.
- [100] A. L. Zhang, Y. X. Zhang, and X. C. Liu, “Research outlook of earthquake resilient prestressed steel structures,” *Beijing Gongye Daxue Xuebao, Journal of Beijing University of Technology*, vol. 39, no. 4, pp. 507–515, 2013.
- [101] A. Venkittaraman and B. Swagata, “Enhancing resilience of highway bridges through seismic retrofit,” *Earthquake Engineering & Structural Dynamics*, vol. 43, no. 8, pp. 1173–1191, 2014.
- [102] S. Chandrasekaran and B. Swagata, “Retrofit optimization for resilience enhancement of bridges under multihazard scenario,” *Journal of Structural Engineering*, vol. 142, no. 8, article C4015012, 2016.

## Research Article

# Comparison of Uplift Capacity and Nonlinear Failure Surfaces of Single-Belled Anchor in Homogeneous and Layered Sand Deposits

Tanaya Deb<sup>1</sup> and Sujit Kumar Pal<sup>2</sup>

<sup>1</sup>Research Scholar, Department of Civil Engineering, NIT Agartala, Agartala, Tripura, India

<sup>2</sup>Associate Professor, Department of Civil Engineering, NIT Agartala, Agartala, Tripura, India

Correspondence should be addressed to Tanaya Deb; debtanaya88@gmail.com

Received 10 October 2018; Accepted 11 March 2019; Published 16 May 2019

Guest Editor: Michel Arrigoni

Copyright © 2019 Tanaya Deb and Sujit Kumar Pal. This is an open access article distributed under the Creative Commons Attribution License, which permits unrestricted use, distribution, and reproduction in any medium, provided the original work is properly cited.

This experimental study explains the contribution of embedment ratios, diameter ratios, and bell angles to uplift capacities of single-belled anchors and formation of nonlinear failure surfaces in homogeneous and layered sand deposits. Uplift capacities in both types of sand deposits are increased with higher embedment ratios, lesser diameter ratios, and bell angles. Uplift capacities are higher in layered sand deposit in comparison with homogeneous sand deposit for the same model. Analytical uplift capacities are predicted by the horizontal slice method based on observed failure surfaces. A comparative discussion is made on nonlinear failure surfaces as well as analytical uplift capacities in reference to aforementioned parameters for the variation in sand deposits. The 45° and 63° belled anchors are more effective as uplift-resistant structures than 72° anchors in both types of sand deposits. Out of 36 analytical data on homogeneous sand and 33 analytical data on layered sand, 94.45% data are within the range of +08.51 to -10.70% and 100% data are within the range of +10.47 to -10.72%, respectively, with respect to the experimental uplift capacities. Four numbers of multiple linear regression models have been developed by observed breakout factors to eliminate the size effect, so the newly developed models are suitable for actual engineering to compare with prototype tests within the suggested imitation of values of variable parameters.

## 1. Introduction

For radar tower, television line tower, power pole, roadside sign posts, and outdoor sign pools, imbalance horizontal forces mainly due to severe wind velocity and resultant uplift load are more than their self-weight. Peck et al. [1] reported that piles are often used specially to resist tensile forces beneath several common types of structures such as towers, gas storage tanks, and tall stacks; beneath such structures, the tensile forces are always caused by the moment due to wind. In such structures, the expected uplift load and overturning moments are basic design considerations to ascertain their types, shapes, and sizes. Bellied anchor piles may be attractive and economy-friendly alternative to resist resultant pull-out forces in foundation design, but its uplift capacity has yet not been fully investigated. The uplift capacity is influenced by embedment

depths, sizes of diameter, and bell angles as observed by Dickin et al. [2–8], but these studies are carried out on homogeneous sand only. Few field tests on belled anchors were reported by Adams and Radhakrishna [9] and Ismael and Kylm [10]. The experimental, numerical, and mathematical studies were also been conducted on embedment depth and different sizes of plate anchors by Meyerhof et al. [11–20].

The behaviour of anchors in layered sand was experimentally investigated by Bouazza and Finlay [21] on laboratory models. Kumar [22] conducted a numerical study on uplift resistance of circular and strip anchor where failure mechanism was explained by velocity hydrograph. Sakai and Tanaka [23] presented pictorial view of failure mechanism in two-layered sand, where medium dense and loose sands were overlying dense sand and vice versa. But these studies are performed on plate anchors only. Till the

date, studies on the uplift behaviour as well as nonlinear failure behaviour on belled anchors in higher-dense sand overlying lesser-dense sand have yet been lacking.

In all the available studies conducted on plate anchors in homogeneous sand, it had been well documented that uplift capacity is derived by the combination of weight of breakout sand wedge and mobilized shear along failure surfaces [12, 24–28]. The study on analytical net uplift capacity of belled anchor in layered sand is still lacking.

Linear failure surface having slip surface at angle  $\phi/2$  with vertical [13, 15, 29],  $\phi$  with vertical [18], and  $\psi$  with vertical [29] were documented. Meyerhof and Adams [11] suggested that slip surface was pyramidal shaped and initiates from circular anchor base, making angle within the range of  $\phi/2$  to  $\phi/4$  in dense sand and cylindrical shaped failure in loose sand. Ghaly et al. [30] in their analysis investigated that the failure wedge had the shape of truncated cone around shallow and transition anchor, and the cone angle made with vertical was up to  $(2/3)\phi$ . Balla [12] first introduced nonlinear failure surface initiated tangentially from edge of horizontal plate anchor which terminated at ground surface making angle of  $(45^\circ - \phi/2)$  in dense sand, and Chattopadhyay and Pise [26] used the same boundary condition as established by Balla [12]. Saran et al. [31] used hyperbolic stress-strain relationship of soil element and predicted that formation of breakout wedge was linear in shape. Ilamparuthi and Muthukrisnaiah [32] and Ilamparuthi et al. [33] experimentally reported that, around plate anchor (half-cut flat and curved circular models which were semicylindrical in shape), the failure surface originated making an angle of  $(\phi/2 \pm 2)^\circ$  with edge of anchor base. But these studies are performed on plate anchors in homogeneous sand media only, and studies on the nonlinear failure pattern around belled anchors have yet been very limited.

The existing literatures are having dearth of data on uplift capacity as well as predictive mathematical models are insufficient to provide a clear understanding on the comparison of uplift behaviour and actual pattern of failure surface around belled anchors due to changes in sand strata and different parameters.

## 2. Failure Mechanism under Uplift Loading

At the initial stage with the application of uplift loading, the total stress beneath the anchor base starts to gradually decrease and simultaneously there is gradual increase of total stress just above the anchor base with upward movement of anchor; this phenomenon continues and lasts long up to failure. In this present study, it is observed that, at the first stage of pulling, the sand at the most neighbouring zone of anchor base move along with the anchor and simultaneously there is initiation of cavity below the anchor base. Saeedy [27] explained that sand above the anchor started to be compressed with initial uplift and degree of compression of locked up sand above the anchor base was dependent on state of stress that helps in mobilization of shear strength and continues to be compressed up to the verge of failure. Within the compressed zone for locking up of sands, the significant

factors are dilatancy of sand [14] and higher interlocking among the sand particles within the failure zone [32].

With continuous pulling, the shear stress level in sand near the anchor base increased gradually to reach shear strength and simultaneously the cavity is expanded. The slip surfaces have started from the anchor base and progressively migrate above the anchor base towards sand surface with more lateral spreading. Kumar [22] stated that failure wedge development occurred at that velocity as that of the upward velocity of anchor.

At the collapsed stage, it is noticed that, when the displaced sand around the base begin to flow downward to fill the cavity, simultaneously emerging failure surface reaches the sand surface following a nonlinear path, and it is due to the fact that (i) at plastic stage, shear strength is fully mobilized along failure surface and (ii) on the verge of failure, tension cracks are produced in disturbed soil around the base. In the present study, it has been observed that the failure wedge once generated remains unchanged even after further pulling and the domain outside of failure surface remains in rest position. The pulling is sustained after the failure indicated by the proving ring till the sand particles around the base of models move downward to fill up the cavity which is a fully collapsed stage. Matsuo [24] reported that, due to uplift of anchor, earth pressure within the wedge altered from semiactive condition to passive condition. Failure surface mechanism in homogeneous sand deposit was reported by Dickin et al. [3, 8] by using semicylindrical modelling. Sakai and Tanaka [23] explained that development of shear band indicated the localized deformation in layered sand. In this study, similar type of failure mechanism is observed for both the types of sand deposits.

## 3. Objectives of the Present Study

The present study aims to explore the comparison in the uplift behaviour of 3D belled anchor models and formation of respective failure surfaces on both the sides of 2D panels in homogeneous and layered buried sand with variation in several embedment ratios and anchor characteristics on the basis of experimental study. The present study has anticipated analytical uplift capacity, i.e., combination of dead weight of breakout wedge and mobilized shear based on horizontal slice method using observed failure surfaces. The comparison in nonlinear failure surfaces as well as analytical uplift capacities are correlated with comparison of experimental uplift capacity values in same model based on sand types. The analytical uplift capacities are compared with the experimental values, and predicted errors are reported based on experimental data. To predict breakout factors in both homogeneous and layered sand deposits, multiple linear regression models are developed and these are compared with breakout factor of present study and very few previous data.

## 4. Materials, Models, and Testing Procedure

**4.1. Sand, Model Anchors, and Testing Tank.** Two different types of dry sands collected from the local market are used to

represent the layered foundation media in the present study, and these are designated as sand I ( $S_I$ ) and sand II ( $S_{II}$ ). In layered sand deposit,  $S_{II}$  is overlying  $S_I$ , hence it is designated as  $S_{II}/S_I$ . Figure 1 shows the grain size distribution curve of sand samples. The physical and engineering properties are presented in Table 1. In Table 1, it is observed that  $\gamma$  and  $\phi$  values of  $S_{II}$  are higher than those of  $S_I$ , so  $S_{II}$  is stronger than  $S_I$  in the present test condition.

The shaft and bell portion of the bell anchor is fabricated from solid rounded bar, and these two parts are welded internally. The diameter of shaft is kept constant at 26 mm. The hollow 2D panel anchors are fabricated from 1 mm thick steel plates, and shaft and bell thickness are same as shaft and bell diameter of 3D models. The heights of both types of models are fixed at 650 mm. The 2D panels are  $590 \pm 2.5$  mm in length. The identifications of 3D model and 2D panel along with their detail geometric dimensions are presented in Table 2 (column (i) to (vi)). At the top of all 3D models and the centre of the length of 2D panels, a small hollow cylindrical arrangement is welded with internal grooving to hold the proving ring gently. Near to the top of cylindrical arrangement, two numbers of horizontally projected short steel strips are welded at  $180^\circ$  to each other to hold the couple of dial gauges gently.

The inner dimensions of testing tank is  $700 \text{ mm (l)} \times 600 \text{ (w)}$  mm in plan area and 700 mm in height and supported by steel frame. Its four sides are enclosed by pieces of plaxi-glass of 12 mm thick, and these are frictionless. Vertical steel stiffeners are joined with frame by welding, and sheets of plaxi-glass are bolted with stiffeners and a frame to prevent outward deflection. The testing tank size is sufficient to be free from boundary effects.

**4.2. Sand Bed Preparation for 3D Models and 2D Panels.** Prior to the preparation of foundation media  $S_I$  and  $S_{II}/S_I$ , first a 10 mm thick compacted sand bed is properly finished with horizontal surface to avoid eccentricity prior to install 3D model and 2D panel over the bed. The values of  $L$  and  $L/L_b$  are explained in details in Table 2 (column (vii) and (viii)) for models installed in homogeneous sand deposit ( $S_I$ ). In layered sand deposit,  $S_I$  of constant thickness ( $L_I$ ) of 168 mm is underlying  $S_{II}$ . Over  $S_I$ ,  $S_{II}$  is poured for rest of the predetermined height ( $L_{II}$ ) to attain desired embedment ratio. The ratios of  $L_{II}/L$  and  $L_I/L$  are presented in Table 3 (column (v) and (vi)). The placement density of  $S_I$  and  $S_{II}$  is achieved by raining technique [2, 21], and height of free fall is fixed to be 700 mm in both the cases, and a soil tray is used manually to fill the testing tank. The plot of reproduced density vs. calibrated height of fall is presented in Figure 2. The regularity of sand density is checked by placing few wooden cubes of 80 cc in the corners of model tank within both deposits and deviation in density observed to be  $\pm 1\%$  only.

To study the failure surfaces on both the sides of 2D panels in  $S_{II}/S_I$  media, successive layers of 3 mm thick dyed (i.e., red colour) and 18 mm thick nondyed (i.e., natural colour) sand  $S_I$  is poured up to height of 168 mm, and overlying deposit of  $S_{II}$  is similarly prepared by using dyed (i.e., green colour) and non-dyed sand (i.e., natural colour) maintaining the same thickness. The homogeneous sand bed on both the sides of 2D

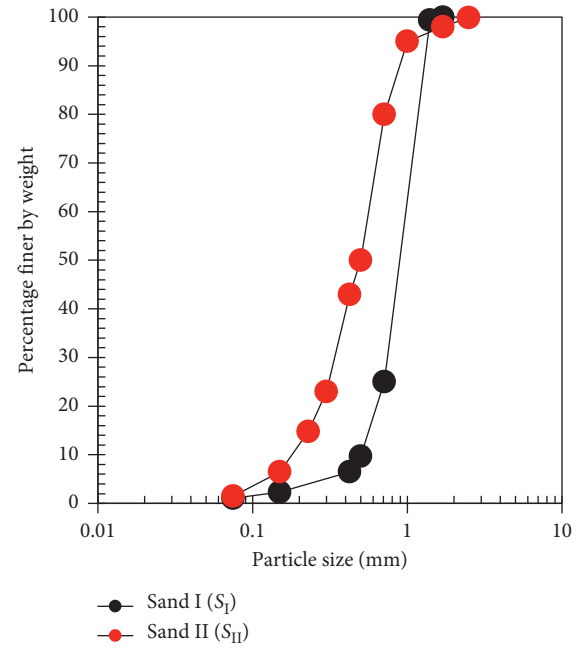


FIGURE 1: Grain size distribution for sand I ( $S_I$ ) and sand II ( $S_{II}$ ).

TABLE 1: Properties of sand I ( $S_I$ ) and sand II ( $S_{II}$ ).

Physical properties	Test results	
	$S_I$	$S_{II}$
Medium sand, 2 to 0.425 mm (%)	93.50	77.50
Fine sand, 0.425 to 0.075 mm (%)	6.50	23.00
Silt and clay, 0.075 to 0.002 mm (%)	1.05	1.50
Effective grain size, $D_{10}$ (mm)	0.71	0.23
Average grain size, $D_{50}$ (mm)	0.93	0.65
Coefficient of curvature, $C_c$	0.91	1.33
Coefficient of uniformity, $C_u$	1.00	3.26
Sand classification as per USCS	SP	SW
Specific gravity, $G_s$	2.67	2.69
Minimum void ratio, $e_{min}$	0.63	0.49
Maximum void ratio, $e_{max}$	0.88	0.79
Void ratio at placement density, $e_{exptl}$	0.71	0.58
Minimum dry density, $\gamma_{min}$ (kN/m <sup>3</sup> )	14.20	15.00
Maximum dry density, $\gamma_{max}$ (kN/m <sup>3</sup> )	16.50	18.20
Placement dry density, $\gamma$ (kN/m <sup>3</sup> )	15.60	16.90
Relative density, $D_r$ (%)	64.38	63.94
<i>Engineering properties</i>		
Undrained cohesion, $c$ (kN/m <sup>2</sup> )	0.00	0.00
Soil internal friction angle, $\phi$ (°)	33.50	39.00
Coefficient of hydraulic conductivity, $k$ (m/sec)	$1.83 \times 10^{-4}$	$7.83 \times 10^{-5}$
Modulus of elasticity, $E_s$ (kPa)	31,600	46,000
Dilatancy angle, $\psi$ (°)	3.50	9.00

panel is prepared by successive layers of 3 mm thick dyed (i.e., red colour) and 18 mm thick nondyed sand  $S_I$ . The number of layers is dependent on the height above the anchor base, and the thickness of top most layer which is less than 3 mm is finished with continuing colour of sand. The thickness of dyed and nondyed layers is conveniently determined to maintain the placement densities of sand.

TABLE 2: Detail geometry of the 3D model and 2D panel and their designations in homogeneous sand deposit ( $S_I$ ).

$\alpha$ (°) (i)	$D_s$ or $T_s$ (ii)	$D_b$ or $T_b$ (iii)	$D_b/D_s$ or $T_b/T_s$ (iv)	3D model identifications (v)	2D panel identifications (vi)	$L/D_b$ or $L/T_s$ (vii)	$L$ (mm) (viii)	3D model designations in $S_I$ (ix)	2D panel designations in $S_{II}/S_I$ (x)
45	26	92	0.28	3D:45-0.28	2D:45-0.28	276	3	3D:45-0.28-3-( $S_I$ )	2D:45-0.28-3-( $S_I$ )
						368	4	3D:45-0.28-4-( $S_I$ )	2D:45-0.28-4-( $S_I$ )
						460	5	3D:45-0.28-5-( $S_I$ )	2D:45-0.28-5-( $S_I$ )
45	26	80	0.33	3D:45-0.33	2D:45-0.33	240	3	3D:45-0.33-3-( $S_I$ )	2D:45-0.33-3-( $S_I$ )
						320	4	3D:45-0.33-4-( $S_I$ )	2D:45-0.33-4-( $S_I$ )
						400	5	3D:45-0.33-5-( $S_I$ )	2D:45-0.33-5-( $S_I$ )
45	26	68	0.38	3D:45-0.38	2D:45-0.38	204	3	3D:45-0.38-3-( $S_I$ )	2D:45-0.38-3-( $S_I$ )
						272	4	3D:45-0.38-4-( $S_I$ )	2D:45-0.38-4-( $S_I$ )
						340	5	3D:45-0.38-5-( $S_I$ )	2D:45-0.38-5-( $S_I$ )
45	26	56	0.46	3D:45-0.46	2D:45-0.46	168	3	3D:45-0.46-3-( $S_I$ )	2D:45-0.46-3-( $S_I$ )
						224	4	3D:45-0.46-4-( $S_I$ )	2D:45-0.46-4-( $S_I$ )
						280	5	3D:45-0.46-5-( $S_I$ )	2D:45-0.46-5-( $S_I$ )
63	26	92	0.28	3D:63-0.28	2D:63-0.28	276	3	3D:63-0.28-3-( $S_I$ )	2D:63-0.28-3-( $S_I$ )
						368	4	3D:63-0.28-4-( $S_I$ )	2D:63-0.28-4-( $S_I$ )
						460	5	3D:63-0.28-5-( $S_I$ )	2D:63-0.28-5-( $S_I$ )
63	26	80	0.33	3D:63-0.33	2D:63-0.33	240	3	3D:63-0.33-3-( $S_I$ )	2D:63-0.33-3-( $S_I$ )
						320	4	3D:63-0.33-4-( $S_I$ )	2D:63-0.33-4-( $S_I$ )
						400	5	3D:63-0.33-5-( $S_I$ )	2D:63-0.33-5-( $S_I$ )
63	26	68	0.38	3D:63-0.38	2D:63-0.38	204	3	3D:63-0.38-3-( $S_I$ )	2D:63-0.38-3-( $S_I$ )
						272	4	3D:63-0.38-4-( $S_I$ )	2D:63-0.38-4-( $S_I$ )
						340	5	3D:63-0.38-5-( $S_I$ )	2D:63-0.38-5-( $S_I$ )
63	26	56	0.46	3D:63-0.46	2D:63-0.46	168	3	3D:63-0.46-3-( $S_I$ )	2D:63-0.46-3-( $S_I$ )
						224	4	3D:63-0.46-4-( $S_I$ )	2D:63-0.46-4-( $S_I$ )
						280	5	3D:63-0.46-5-( $S_I$ )	2D:63-0.46-5-( $S_I$ )
72	26	92	0.28	3D:72-0.28	2D:72-0.28	276	3	3D:72-0.28-3-( $S_I$ )	2D:72-0.28-3-( $S_I$ )
						368	4	3D:72-0.28-4-( $S_I$ )	2D:72-0.28-4-( $S_I$ )
						460	5	3D:72-0.28-5-( $S_I$ )	2D:72-0.28-5-( $S_I$ )
72	26	80	0.33	3D:72-0.33	2D:72-0.3	240	3	3D:72-0.33-3-( $S_I$ )	2D:72-0.33-3-( $S_I$ )
						320	4	3D:72-0.33-4-( $S_I$ )	2D:72-0.33-4-( $S_I$ )
						400	5	3D:72-0.33-5-( $S_I$ )	2D:72-0.33-5-( $S_I$ )
72	26	68	0.38	3D:72-0.38	2D:72-0.38	204	3	3D:72-0.38-3-( $S_I$ )	2D:72-0.38-3-( $S_I$ )
						272	4	3D:72-0.38-4-( $S_I$ )	2D:72-0.38-4-( $S_I$ )
						340	5	3D:72-0.38-5-( $S_I$ )	2D:72-0.38-5-( $S_I$ )
72	26	56	0.46	3D:72-0.46	2D:72-0.46	168	3	3D:72-0.46-3-( $S_I$ )	2D:72-0.46-3-( $S_I$ )
						224	4	3D:72-0.46-4-( $S_I$ )	2D:72-0.46-4-( $S_I$ )
						280	5	3D:72-0.46-5-( $S_I$ )	2D:72-0.46-5-( $S_I$ )

**4.3. Experimental Programme.** To carry out experimental investigations on the uplift behaviour of single-belled anchors and failure surfaces in buried sand, conditions are explained below:

**4.3.1. Series A (Experimental Investigation on Uplift Capacity of 3D Models).** Each model is installed at  $L/D_b$  of 3, 4, and 5, having  $D_s/D_b = 0.28, 0.33, 0.38$ , and 0.46 and  $\beta$  of 45, 63, and 72° in  $S_I$  and  $S_{II}/S_I$  deposits. In this series, total 69 tests are performed.

**4.3.2. Series B (Failure Mechanism Study on Both the Sides of 2D Panels).** Each model is installed at  $L/T_b = 3, 4$ , and 5,  $T_s/T_b = 0.28, 0.33, 0.38$ , and 0.46, and  $\alpha = 45, 63$ , and 72° in  $S_I$

and  $S_{II}/S_I$  deposits. In this series also, total 69 tests are performed.

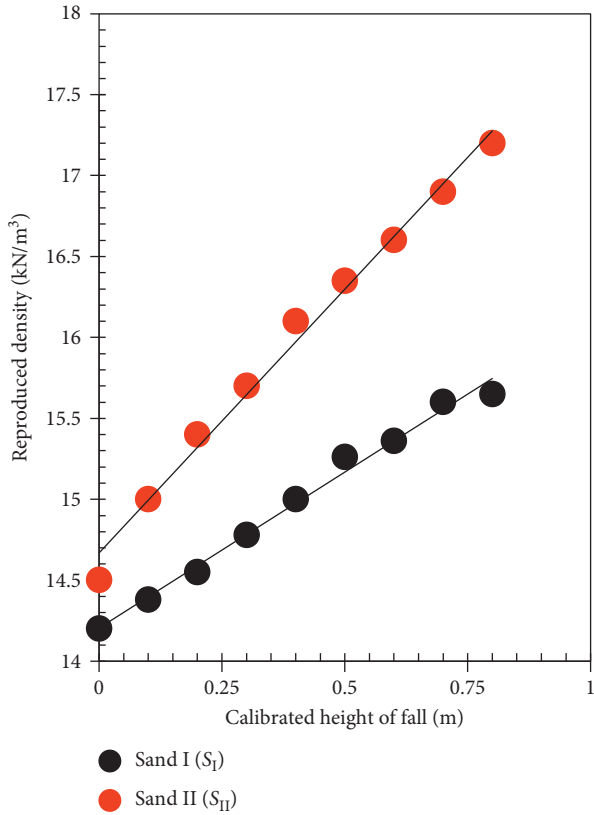
**4.4. Experimental Setup, Test Procedures, and Observations.** Figure 3 shows the schematic diagram of the experimental setup consisting of a loading frame, anchor installed inside the model tank, connected proving ring, position of dial gauges, and other accessories. The loading frame of steel channels having horizontal beam (reaction frame) consisting of ball-bearing arrangement and the base is bolted in concrete for stability. A pulling shaft as screw jack passes through ball-bearing system by nut and screw motion. The bottom of pulling shaft is connected with top of the model along with the proving ring. Vertical movement of shaft is controlled by a manually operated

TABLE 3: Detail thickness of sand I ( $S_I$ ) and sand II ( $S_{II}$ ) in layered sand deposit ( $S_{II}/S_I$ ) and 3D model and 2D panel and their designations in  $S_{II}/S_I$ .

3D model identifications (i)	2D panel identifications (ii)	$L$ (iii)	$L/D_b$ or $L/T_s$ (iv)	$L_{II}/L$ (v)	$L_I/L$ (vi)	3D anchor designations in $S_I$ (vii)	2D panel designations in $S_{II}/S_I$ (viii)
3D:45-0.28	2D:45-0.28	276	3	0.39	0.61	3D:45-0.28-3-(0.39 $S_{II}$ / 0.61 $S_I$ )	2D:45-0.28-3-(0.39 $S_{II}$ / 0.61 $S_I$ )
		368	4	0.54	0.46	3D:45-0.28-4-(0.54 $S_{II}$ / 0.46 $S_I$ )	2D:45-0.28-4-(0.54 $S_{II}$ / 0.46 $S_I$ )
		460	5	0.63	0.37	3D:45-0.28-5-(0.63 $S_{II}$ / 0.37 $S_I$ )	2D:45-0.28-5-(0.63 $S_{II}$ / 0.37 $S_I$ )
3D:45-0.33	2D:45-0.33	240	3	0.30	0.70	3D:45-0.33-3-(0.30 $S_{II}$ / 0.70 $S_I$ )	2D:45-0.33-3-(0.30 $S_{II}$ / 0.70 $S_I$ )
		320	4	0.47	0.53	3D:45-0.33-4-(0.47 $S_{II}$ / 0.53 $S_I$ )	2D:45-0.33-4-(0.47 $S_{II}$ / 0.53 $S_I$ )
		400	5	0.58	0.42	3D:45-0.33-5-(0.58 $S_{II}$ / 0.42 $S_I$ )	2D:45-0.33-5-(0.58 $S_{II}$ / 0.42 $S_I$ )
3D:45-0.38	2D:45-0.38	204	3	0.18	0.82	3D:45-0.38-3-(0.18 $S_{II}$ / 0.82 $S_I$ )	2D:45-0.38-3-(0.18 $S_{II}$ / 0.82 $S_I$ )
		272	4	0.38	0.62	3D:45-0.38-4-(0.38 $S_{II}$ / 0.62 $S_I$ )	2D:45-0.38-4-(0.38 $S_{II}$ / 0.62 $S_I$ )
		340	5	0.51	0.49	3D:45-0.38-5-(0.51 $S_{II}$ / 0.49 $S_I$ )	2D:45-0.38-5-(0.51 $S_{II}$ / 0.49 $S_I$ )
3D:45-0.46	2D:45-0.46	168	3	1.00	1.00	3D:45-0.46-3-( $S_I$ )	2D:45-0.46-3-( $S_I$ )
		224	4	0.25	0.75	3D:45-0.46-4-(0.25 $S_{II}$ / 0.75 $S_I$ )	2D:45-0.46-4-(0.25 $S_{II}$ / 0.75 $S_I$ )
		280	5	0.40	0.60	3D:45-0.46-5-(0.40 $S_{II}$ / 0.60 $S_I$ )	2D:45-0.46-5-(0.40 $S_{II}$ / 0.60 $S_I$ )
3D:63-0.28	2D:63-0.28	276	3	0.39	0.61	3D:63-0.28-3-(0.39 $S_{II}$ / 0.61 $S_I$ )	2D:63-0.28-3-(0.39 $S_{II}$ / 0.61 $S_I$ )
		368	4	0.54	0.46	3D:63-0.28-4-(0.54 $S_{II}$ / 0.46 $S_I$ )	2D:63-0.28-4-(0.54 $S_{II}$ / 0.46 $S_I$ )
		460	5	0.63	0.37	3D:63-0.28-5-(0.63 $S_{II}$ / 0.37 $S_I$ )	2D:63-0.28-5-(0.63 $S_{II}$ / 0.37 $S_I$ )
3D:63-0.33	2D:63-0.33	240	3	0.30	0.70	3D:63-0.33-3-(0.30 $S_{II}$ / 0.70 $S_I$ )	2D:63-0.33-3-(0.30 $S_{II}$ / 0.70 $S_I$ )
		320	4	0.47	0.53	3D:63-0.33-4-(0.47 $S_{II}$ / 0.53 $S_I$ )	2D:63-0.33-4-(0.47 $S_{II}$ / 0.53 $S_I$ )
		400	5	0.58	0.42	3D:63-0.33-5-(0.58 $S_{II}$ / 0.42 $S_I$ )	2D:63-0.33-5-(0.58 $S_{II}$ / 0.42 $S_I$ )
3D:63-0.38	2D:63-0.38	204	3	0.18	0.82	3D:63-0.38-3-(0.18 $S_{II}$ / 0.82 $S_I$ )	2D:63-0.38-3-(0.18 $S_{II}$ / 0.82 $S_I$ )
		272	4	0.38	0.62	3D:63-0.38-4-(0.38 $S_{II}$ / 0.62 $S_I$ )	2D:63-0.38-4-(0.38 $S_{II}$ / 0.62 $S_I$ )
		340	5	0.51	0.49	3D:63-0.38-5-(0.51 $S_{II}$ / 0.49 $S_I$ )	2D:63-0.38-5-(0.51 $S_{II}$ / 0.49 $S_I$ )
3D:63-0.46	2D:63-0.46	168	3	1.00	1.00	3D:63-0.46-3-( $S_I$ )	2D:63-0.46-3-( $S_I$ )
		224	4	0.25	0.75	3D:63-0.46-4-(0.25 $S_{II}$ / 0.75 $S_I$ )	2D:63-0.46-4-(0.25 $S_{II}$ / 0.75 $S_I$ )
		280	5	0.40	0.60	3D:63-0.46-5-(0.40 $S_{II}$ / 0.60 $S_I$ )	2D:63-0.46-5-(0.40 $S_{II}$ / 0.60 $S_I$ )
3D:72-0.28	2D:72-0.28	276	3	0.39	0.61	3D:72-0.28-3-(0.39 $S_{II}$ / 0.61 $S_I$ )	2D:72-0.28-3-(0.39 $S_{II}$ / 0.61 $S_I$ )
		368	4	0.54	0.46	3D:72-0.28-4-(0.54 $S_{II}$ / 0.46 $S_I$ )	2D:72-0.28-4-(0.54 $S_{II}$ / 0.46 $S_I$ )
		460	5	0.63	0.37	3D:72-0.28-5-(0.63 $S_{II}$ / 0.37 $S_I$ )	2D:72-0.28-5-(0.63 $S_{II}$ / 0.37 $S_I$ )

TABLE 3: Continued.

3D model identifications (i)	2D panel identifications (ii)	$L$ (iii)	$L/D_b$ or $L/T_s$ (iv)	$L_{II}/L$ (v)	$L_I/L$ (vi)	3D anchor designations in $S_I$ (vii)	2D panel designations in $S_{II}/S_I$ (viii)
3D:72-0.33	2D:72-0.33	240	3	0.30	0.70	3D:72-0.33-3-(0.30 $S_{II}$ / 0.70 $S_I$ )	2D:72-0.33-3-(0.30 $S_{II}$ / 0.70 $S_I$ )
		320	4	0.47	0.53	3D:72-0.33-4-(0.47 $S_{II}$ / 0.53 $S_I$ )	2D:72-0.33-4-(0.47 $S_{II}$ / 0.53 $S_I$ )
		400	5	0.58	0.42	3D:72-0.33-5-(0.58 $S_{II}$ / 0.42 $S_I$ )	2D:72-0.33-5-(0.58 $S_{II}$ / 0.42 $S_I$ )
3D:72-0.38	2D:72-0.38	204	3	0.18	0.82	3D:72-0.38-3-(0.18 $S_{II}$ / 0.82 $S_I$ )	2D:72-0.38-3-(0.18 $S_{II}$ / 0.82 $S_I$ )
		272	4	0.38	0.62	3D:72-0.38-4-(0.38 $S_{II}$ / 0.62 $S_I$ )	2D:72-0.38-4-(0.38 $S_{II}$ / 0.62 $S_I$ )
		340	5	0.51	0.49	3D:72-0.38-5-(0.51 $S_{II}$ / 0.49 $S_I$ )	2D:72-0.38-5-(0.51 $S_{II}$ / 0.49 $S_I$ )
3D:72-0.46	2D:72-0.46	168	3	1.00	1.00	3D:72-0.46-3-( $S_I$ )	2D:72-0.46-3-( $S_I$ )
		224	4	0.25	0.75	3D:72-0.46-4-(0.25 $S_{II}$ / 0.75 $S_I$ )	2D:72-0.46-4-(0.25 $S_{II}$ / 0.75 $S_I$ )
		280	5	0.40	0.60	3D:72-0.46-5-(0.40 $S_{II}$ / 0.60 $S_I$ )	2D:72-0.46-5-(0.40 $S_{II}$ / 0.60 $S_I$ )

FIGURE 2: Reproduced density vs. calibrated height of fall relation of sand I ( $S_I$ ) and sand II ( $S_{II}$ ).

rotating circular wheel fixed with nut arrangement supported on the ball-bearing system. The clockwise motion of wheel helps the model anchors to move upward. The dial gauges of 0.01 mm accuracy are attached properly with magnetic bases which are fitted on steel bars running over the top of model tank. The proving ring of 1.0 kN

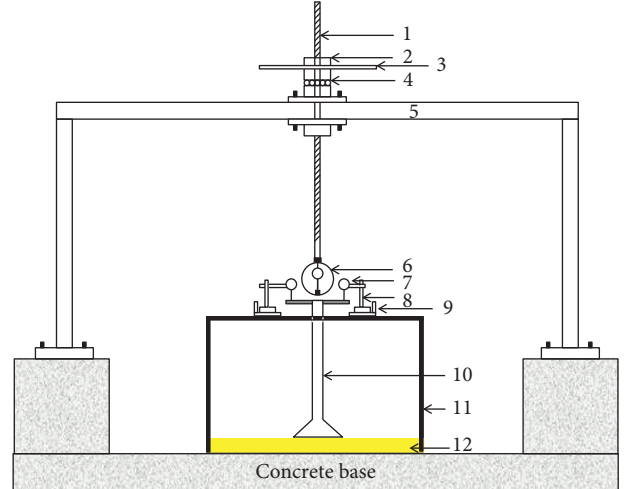


FIGURE 3: Schematic diagram of the experimental setup (front view): (1) long screw, (2) nut, (3) rotating wheel, (4) ball-bearing arrangement, (5) reaction frame, (6) proving ring, (7) dial gauge, (8) magnetic base, (9) magnetic base fixture, (10) model anchor, (11) model tank, and (12) sand bed.

capacity records the gross uplift capacity of model anchors, and corresponding displacement of the anchors are recorded from deflection in dial gauges.

## 5. Model Designations

In Table 2 (column (ix) and (x)), the detail designation of 3D models and 2D panels is represented as they are installed in  $S_I$  deposit. In Table 3, (column (vii) and (viii)), the detail designation of 3D models and 2D panels is presented as they are installed in  $S_{II}/S_I$  deposit. In order to represent any model, a common coding system is maintained, consisting of five sections. The first, second, third, fourth, and fifth sections specify the size (either 3D or 2D),  $\beta$ ,  $D_s/D_b$  (in case of 3D model) or  $T_s/T_b$  (in case of 2D panel),  $L$ /

$D_b$ , and type of sand deposit (either  $S_I$  or  $S_{II}/S_I$ ), respectively. When a 3D model is having  $\beta = 45^\circ$ ,  $D_s/D_b = 0.28$  at  $L/D_b = 5$ , and its 37% and 63% of total embedment depth are in  $S_I$  (bottom layer) and  $S_{II}$  (top layer), respectively, then it is designated as 3D:45-0.28-5-(0.63 $S_{II}/0.37S_I$ ); and the identical panel is represented as 2D:45-0.28-5-(0.63 $S_{II}/0.37S_I$ ). The symbol 3D:63-0.33-4-( $S_I$ ) implies that a 3D model has  $\beta = 63^\circ$ ,  $D_s/D_b = 0.33$ , and  $L/D_b = 4$  and it is embedded fully in  $S_I$  and identical 2D panel is represented as 2D:63-0.28-4-( $S_I$ ).

## 6. Test Results of 3D Models and Discussions

All the experimental data of  $Q_u(S_I)$  and  $Q_u(S_{II}/S_I)$  for each 3D models are shown in Table 4 (column (ii) and (vi), respectively) facilitate to compare uplift behaviour of belled anchors in  $S_I$  and  $S_{II}/S_I$  deposits in reference to variation in  $L/D_b$ ,  $L/D_b$ , and  $\beta$ . On the basis of experimental data, the effect of embedment ratios, diameter ratios, and bell angles on different uplift capacities of belled anchors in homogeneous and layered sand deposits is discussed herein.

**6.1. Comparison of Uplift Capacities of 3D Belled Anchor in Homogeneous ( $S_I$ ) and Layered ( $S_{II}/S_I$ ) Sand Deposits in reference to Embedment Ratios, Diameter Ratios, and Bell Angles.** Figures 4(a) and 4(b) represent the comparison of net uplift capacity vs. model displacement for models 3D:45-0.46 and 3D:72-0.28, respectively, both in  $S_I$  and  $S_{II}/S_I$  deposits, installed at  $L/D_b = 3, 4$ , and 5. The patterns of net uplift capacity vs. model displacement curves are not similar for both  $S_I$  as well as  $S_{II}/S_I$  deposits. In  $S_I$ , initially, the curve is linear representing true elastic response in very early stage and at that stage rate of increment in uplift, resistance is higher than the vertical displacement. Thereafter, the curve takes the shape of pseudoelastic pattern resembling curvilinear and finally produces elastoplastic response with rapid growth of plastic region as well as highest rate of deformation. The behaviour of curves is similar in nature as demonstrated by Rowe and Davis [14] and Deb and Pal [34].

In general, in  $S_{II}/S_I$ , more or less curvilinear shape is noticed in net uplift capacity vs. anchor displacement curve up to bottom layer of sand ( $S_I$ ). After that, in all curves, there is a sudden higher rate of increment in uplift capacity at very lower rate of upward displacement. This type of net uplift capacity vs. anchor displacement behaviour is dominated by the strength differences in top and bottom layers of sand. A similar pattern of relationship in net uplift capacity vs. anchor displacement curves was reported by Stewart [35] for plate anchors installed in soft clay underlying comparatively dense sand. In layered sand, for same model, the net uplift capacity vs. anchor displacement curves show more upward movement than that of homogeneous sand as the thickness of  $S_{II}$  gradually increases with higher value of embedment ratio. In both cases, at collapsed stage strength mobilization is lower than the rate of increment in vertical displacement. Net ultimate uplift capacity ( $Q_u(S_I)$  and  $Q_u(S_{II}/S_I)$ ) from experimental observation is presented as

$$\begin{aligned} Q_u(S_I) &= Q_g(S_I) - W_M, \\ Q_u\left(\frac{S_{II}}{S_I}\right) &= Q_g\left(\frac{S_{II}}{S_I}\right) - W_M. \end{aligned} \quad (1)$$

In case of  $S_{II}/S_I$  deposit,  $Q_u(S_{II}/S_I)$  values for 3D:45-0.33-3-(0.30 $S_{II}/0.70S_I$ ), 3D:45-0.38-3-(0.18 $S_{II}/0.82S_I$ ), 3D:45-0.46-4-(0.25 $S_{II}/0.75S_I$ ), 3D:63-0.33-3-(0.30 $S_{II}/0.70S_I$ ), 3D:63-0.38-3-(0.18 $S_{II}/0.82S_I$ ), 3D:63-0.46-4-(0.25 $S_{II}/0.75S_I$ ), 3D:72-0.33-3-(0.30 $S_{II}/0.70S_I$ ), 3D:72-0.38-3-(0.18 $S_{II}/0.82S_I$ ), and 3D:672-0.46-4-(0.25 $S_{II}/0.75S_I$ ) are found to be higher than  $Q_u(S_I)$  by maximum 10%. For other models of the present study, the values of  $Q_u(S_{II}/S_I)$  are within 20 to 50% higher than  $Q_u(S_I)$ .

It has been explored from the experimental data presented in Table 4 (column (ii) and (vi)) that, due to increase in the values of  $L/D_b$ , both the values of  $Q_u(S_I)$  and  $Q_u(S_{II}/S_I)$  are gradually increased irrespective of  $D_s/D_b$  and  $\beta$ . For example,  $Q_u(S_I)$  values in 3D:63-0.38-3-( $S_I$ ), 3D:63-0.38-4-( $S_I$ ), and 3D:63-0.38-5-( $S_I$ ) are 43.83, 85.20, and 121.18 N, respectively, and  $Q_u(S_{II}/S_I)$  values in 3D:63-0.38-3-(0.18 $S_{II}/0.82S_I$ ), 3D:63-0.38-4-(0.38 $S_{II}/0.62S_I$ ), and 3D:63-0.38-5-(0.51 $S_{II}/0.49S_I$ ) are 47.04, 103.81, and 166.85 N, respectively. Dickin et al. [2, 29, 36] in case of plate anchors [7, 8, 34] for belled anchors had noticed that uplift capacity was significantly increased by higher embedment ratios in homogeneous sand deposit. Higher embedment ratio involves larger overburden pressure on same anchor base irrespective of the type of sand deposit. The overburden pressure becomes significantly larger when stronger sand of increasing thickness is overlying comparatively weaker sand of fixed thickness, so  $Q_u(S_{II}/S_I)$  is higher than  $Q_u(S_I)$  for the same model.

There has been a general trend to gradually decrease in both  $Q_u(S_I)$  and  $Q_u(S_{II}/S_I)$  with increase in values of  $D_s/D_b$  irrespective of  $L/D_b$ ,  $\beta$ ,  $S_I$  and  $S_{II}/S_I$ . It has been revealed from the data reported in Table 4 (column (ii) and (vi)) that  $Q_u(S_I)$  values in 3D:45-0.28-5-( $S_I$ ), 3D:45-0.33-5-( $S_I$ ), 3D:45-0.38-5-( $S_I$ ), and 3D:45-0.46-5-( $S_I$ ) are 347.56, 235.75, 134.35, and 71.56 N, respectively, and  $Q_u(S_{II}/S_I)$  values in 3D:45-0.28-5-(0.63 $S_{II}/0.37S_I$ ), 3D:45-0.33-5-(0.58 $S_{II}/0.42S_I$ ), 3D:45-0.38-5-(0.51 $S_{II}/0.49S_I$ ), and 3D:45-0.46-5-(0.40 $S_{II}/0.60S_I$ ) are 523.51, 294.28, 179.73, and 85.16 N, respectively. Dickin et al. [2, 4, 7, 8, 34, 36] in dry sand observed that uplift capacity was considerably decreased by higher diameter ratios in homogeneous sand deposit. In the present study, increasing thickness of overlying stronger sand in layered sand deposit is responsible for higher value of  $Q_u(S_{II}/S_I)$  than  $Q_u(S_I)$  in the same model.

It has been noticed from the experimental data reported in Table 4 (column (ii) and (vi)) that there has been a general trend for gradually decrease in  $Q_u(S_I)$  and  $Q_u(S_{II}/S_I)$  with increase in  $\beta$ , regardless  $L/D_b$ ,  $D_s/D_b$ ,  $S_I$ , and  $S_{II}/S_I$ . In the present study, it is observed that, when  $\beta$  increased from 45 to 63° and from 63 to 72°, almost all the values of uplift capacities decreased by maximum 10% and by 17 to 22%, respectively, in both the types of sand deposits. The similar pattern in behaviour of uplift capacity was noticed by Nazir et al. [8, 34] for small bell angles up to 60° installed in homogeneous dry cohesionless soil in conventional test by

TABLE 4: Values of experimental uplift capacities in  $S_I$  and  $S_{II}/S_I$  ( $Q_u(S_I)$  and  $Q_u(S_{II}/S_I)$ ), analytical uplift capacities in  $S_I$  and  $S_{II}/S_I$  ( $Q_{u,anlyl.}(S_I)$  and  $Q_{u,anlyl.}(S_{II}/S_I)$ ), error (%) on  $Q_{u,anlyl.}(S_I)$  based on  $Q_u(S_I)$ , and error (%) on  $Q_{u,anlyl.}(S_{II}/S_I)$  based on  $Q_u(S_{II}/S_I)$ .

3D model designations in $S_I$ (i)	$Q_u(S_I)$ (N) (ii)	$Q_{u,anlyl.}(S_I)$ (N) (iii)	Error (%) in (iii) based on (ii) (iv)	3D model designations in $S_{II}/S_I$ (v)	$Q_u(S_{II}/S_I)$ (N) (vi)	$Q_{u,anlyl.}(S_{II}/S_I)$ (N) (vii)	Error (%) in (vii) based on (vi) (viii)
3D:45-0.28-3-( $S_I$ )	123.98	125.28	-01.05	3D:45-0.28-3- ( $0.39S_{II}/0.61S_I$ )	151.15	149.60	+01.03
3D:45-0.28-4-( $S_I$ )	234.84	226.65	+03.50	3D:45-0.28-4- ( $0.54S_{II}/0.46S_I$ )	297.90	276.30	+07.25
3D:45-0.28-5-( $S_I$ )	347.56	383.70	-10.40	3D:45-0.28-5- ( $0.63S_{II}/0.37S_I$ )	523.51	481.68	+08.00
3D:45-0.33-3-( $S_I$ )	82.30	80.85	+01.76	3D:45-0.33-3- ( $0.30S_{II}/0.70S_I$ )	89.76	95.97	-06.92
3D:45-0.33-4-( $S_I$ )	154.75	154.75	-00.00	3D:45-0.33-4- ( $0.47S_{II}/0.53S_I$ )	189.53	187.57	+01.03
3D:45-0.33-5-( $S_I$ )	235.75	251.07	-06.50	3D:45-0.33-5- ( $0.58S_{II}/0.42S_I$ )	294.28	325.84	-10.72
3D:45-0.38-3-( $S_I$ )	48.10	50.63	-05.30	3D:45-0.38-3- ( $0.18S_{II}/0.82S_I$ )	50.71	52.34	-03.22
3D:45-0.38-4-( $S_I$ )	93.38	95.23	-01.98	3D:45-0.38-4- ( $0.38S_{II}/0.62S_I$ )	112.92	115.80	-02.54
3D:45-0.38-5-( $S_I$ )	134.35	147.90	-10.08	3D:45-0.38-5- ( $0.51S_{II}/0.49S_I$ )	179.73	188.64	-04.96
3D:45-0.46-3-( $S_I$ )	25.70	28.45	-10.70	3D:45-0.46-3-( $S_I$ )	25.70	28.45	-10.70
3D:45-0.46-4-( $S_I$ )	47.11	47.24	-00.28	3D:45-0.46-4- ( $0.25S_{II}/0.75S_I$ )	50.54	54.50	-07.82
3D:45-0.46-5-( $S_I$ )	71.56	71.77	-00.30	3D:45-0.46-5- ( $0.40S_{II}/0.60S_I$ )	85.16	84.44	+00.85
3D:63-0.28-3-( $S_I$ )	115.17	106.51	+07.52	$Q_{u,63-0.28-3-}$ ( $0.39S_{II}/0.61S_I$ )	138.05	128.56	+06.88
3D:63-0.28-4-( $S_I$ )	204.65	199.90	+02.33	$Q_{u,63-0.28-4-}$ ( $0.54S_{II}/0.46S_I$ )	271.30	247.51	+08.77
3D:63-0.28-5-( $S_I$ )	313.90	321.46	-02.41	3D: 63-0.28-5- ( $0.63S_{II}/0.37S_I$ )	480.16	447.44	+06.82
3D:63-0.33-3-( $S_I$ )	74.54	73.83	+00.95	3D:63-0.33-3- ( $0.30S_{II}/0.70S_I$ )	81.30	84.66	-04.13
3D:63-0.33-4-( $S_I$ )	142.40	136.42	+04.20	3D:63-0.33-4- ( $0.47S_{II}/0.53S_I$ )	170.71	167.42	+01.93
3D:63-0.33-5-( $S_I$ )	218.68	213.21	+02.50	3D:63-0.33-5- ( $0.58S_{II}/0.42S_I$ )	273.15	269.43	+01.36
3D:63-0.38-3-( $S_I$ )	43.83	43.82	+00.02	3D:63-0.38-3- ( $0.18S_{II}/0.82S_I$ )	47.04	48.21	-02.48
3D:63-0.38-4-( $S_I$ )	85.20	79.26	+06.96	3D:63-0.38-4- ( $0.38S_{II}/0.62S_I$ )	103.81	100.80	+02.91
3D:63-0.38-5-( $S_I$ )	121.18	117.97	+02.65	3D:63-0.38-5- ( $0.51S_{II}/0.49S_I$ )	166.48	166.85	-00.22
3D:63-0.46-3-( $S_I$ )	21.71	25.77	-18.72	3D:63-0.46-3-( $S_I$ )	21.71	25.77	-18.72
3D:63-0.46-4-( $S_I$ )	42.53	41.42	+02.60	3D:63-0.46-4- ( $0.25S_{II}/0.75S_I$ )	45.77	48.71	-06.43
3D:63-0.46-5-( $S_I$ )	64.33	63.38	+01.48	3D:63-0.46-5- ( $0.40S_{II}/0.60S_I$ )	78.02	74.10	+05.02
3D:72-0.28-3-( $S_I$ )	95.14	89.81	+05.61	3D:72-0.28-3- ( $0.39S_{II}/0.61S_I$ )	112.38	104.71	+06.82
3D:72-0.28-4-( $S_I$ )	177.06	166.48	+05.98	3D:72-0.28-4- ( $0.54S_{II}/0.46S_I$ )	221.14	191.08	+13.60
3D:72-0.28-5-( $S_I$ )	257.56	251.10	+02.51	$Q_{u,72-0.28-5-}$ ( $0.63S_{II}/0.37S_I$ )	370.34	347.20	+06.25
3D:72-0.33-3-( $S_I$ )	60.86	63.00	-03.52	3D:72-0.33-3- ( $0.30S_{II}/0.70S_I$ )	66.61	68.52	-02.87
3D:72-0.33-4-( $S_I$ )	112.20	105.46	+06.00	3D:72-0.33-4- ( $0.47S_{II}/0.53S_I$ )	136.13	122.74	+09.83

TABLE 4: Continued.

3D model designations in $S_I$ (i)	$Q_u(S_I)$ (N) (ii)	$Q_{u,\text{anlyl.}}(S_I)$ (N) (iii)	Error (%) in (iii) based on (ii) (iv)	3D model designations in $S_{II}/S_I$ (v)	$Q_u(S_{II})/S_I$ (N) (vi)	$Q_{u,\text{anlyl.}}(S_{II})/S_I$ (N) (vii)	Error (%) in (vii) based on (vi) (viii)
3D:72-0.33-5-( $S_I$ )	170.15	155.67	+08.51	3D:72-0.33-5- ( $0.58S_{II}/0.42S_I$ )	219.37	198.94	+09.31
3D:72-0.38-3-( $S_I$ )	36.93	40.00	-08.32	3D:72-0.38-3- ( $0.18S_{II}/0.82S_I$ )	38.91	42.40	-08.97
3D:72-0.38-4-( $S_I$ )	70.76	66.95	+05.39	3D:72-0.38-4- ( $0.38S_{II}/0.62S_I$ )	84.14	78.70	+06.46
3D:72-0.38-5-( $S_I$ )	98.94	99.40	-00.46	3D:72-0.38-5- ( $0.51S_{II}/0.49S_I$ )	132.12	118.74	+10.12
3D:72-0.46-3-( $S_I$ )	19.65	22.88	-16.46	3D:72-0.46-3-( $S_I$ )	19.65	22.88	-16.46
3D:72-0.46-4-( $S_I$ )	33.60	36.01	-07.18	3D:72-0.46-4- ( $0.25S_{II}/0.75S_I$ )	37.57	39.48	-05.08
3D:72-0.46-5-( $S_I$ )	51.16	52.70	-03.01	3D:72-0.46-5- ( $0.40S_{II}/0.60S_I$ )	63.76	60.88	+04.52

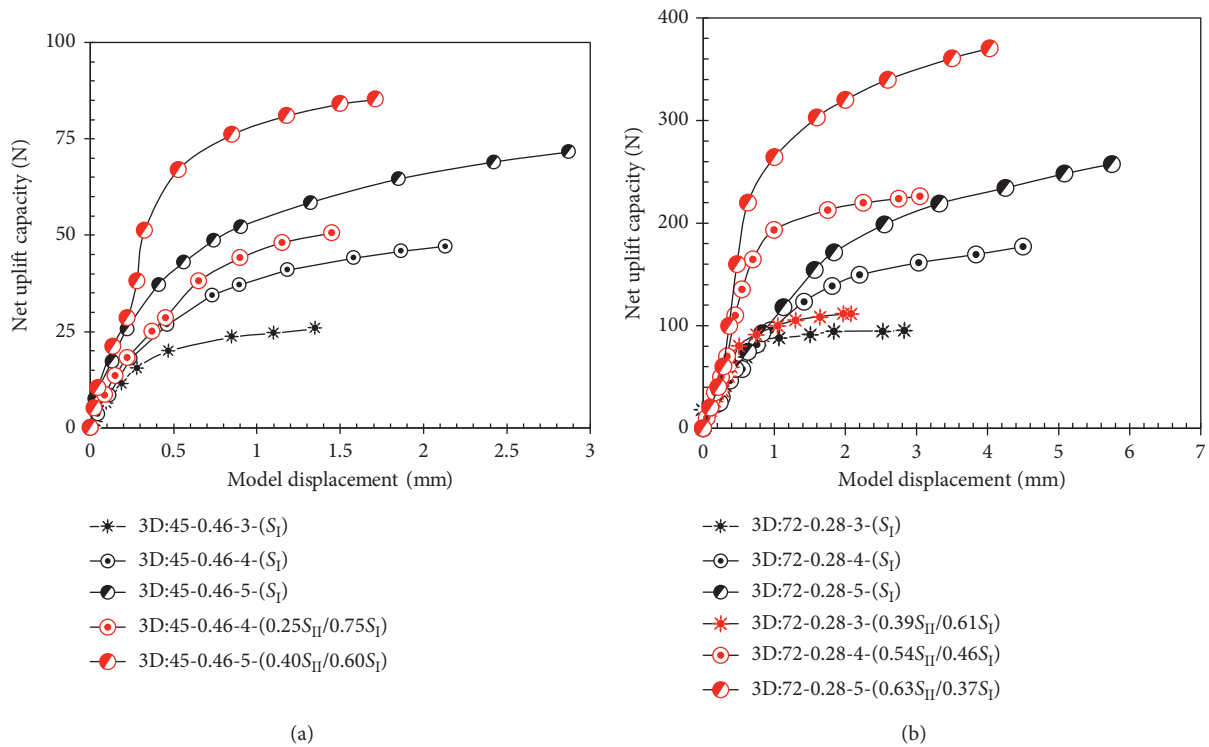


FIGURE 4: Comparison of net uplift capacity vs. model displacement (a) for model 3D:45-0.46 and (b) for model 3D:72-0.28, both in homogeneous ( $S_I$ ) and layered ( $S_{II}/S_I$ ) sand deposits at  $L/D_b = 3, 4$ , and 5.

physical modelling. Dickin and Leung [3] reported the variation in uplift behaviour of anchors having bell angle within a range of 22 to 72° in centrifugal modelling test and noticed that, when bell angle was 72°, there was a rapid decrease in uplift capacity in comparison to those found for 62° belled anchor. In case of each model,  $Q_u(S_{II}/S_I)$  is relatively higher than  $Q_u(S_I)$ , as more tensile load necessitates for developing and lifting larger breakout wedge in  $S_{II}/S_I$ .

## 7. Observations on Nonlinear Failure Surfaces

Before installation of 2D panels inside the testing tank, due to symmetry about vertical axis, a vertical centre-line is

marked along the thickness of each model. This centre line is detectable from outside of plaxi-glass. In this study, applied forces are acting along the vertical plane of 2D panels.

Figures 5(a)–5(c) show the typical pictorial failure surfaces on both the sides of 2D:45-0.46-4-( $S_I$ ), 2D:63-0.33-5-( $S_I$ ), and 2D:72-0.46-4-( $S_I$ ), respectively. Figures 6(a)–6(c) represent the typical pictorial failure surfaces on both the sides of 2D:45-0.28-3-(0.39 $S_{II}$ /0.61 $S_I$ ), 2D:63-0.33-4-(0.47 $S_{II}$ /0.53 $S_I$ ), and 2D:72-0.38-3-(0.18 $S_{II}$ /0.82 $S_I$ ), respectively. The midpoint of panel base is taken as origin (0, 0), and failure points are presented in co-ordinate system in semi-infinite sand mass. At the collapsed stage, at every 21 mm vertical interval, the corresponding horizontal distance between

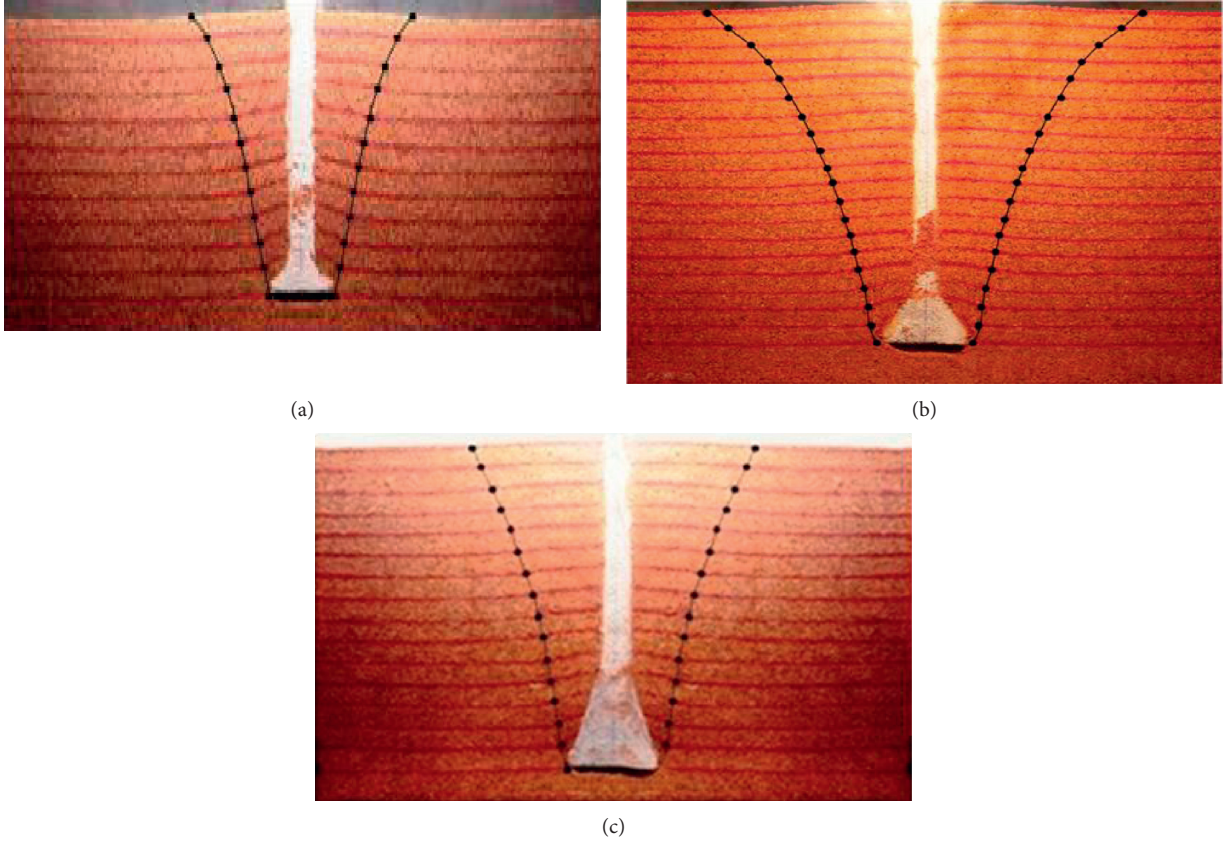


FIGURE 5: Pictorial view of nonlinear failure surfaces on both the sides of (a) panel 2D:45-0.46-4-( $S_I$ ), (b) panel 2D:63-0.33-5-( $S_I$ ), and (c) panel 2D:72-0.33-4-( $S_I$ ).

centre line and deformed dyed sand layers of breakout wedge is measured.

In typical Figures 7–13, plots of failure surfaces are presented to explore the comparison of the behaviour of failure surfaces and uplift capacities in  $S_I$  and  $S_{II}/S_I$  deposits in reference to embedment ratios, diameter ratios, and bell angles. In these plots, failure surface is symbolized by “FS.” It is observed that, for all the 45 and 63° anchors,  $\beta_a(S_I)$  and  $\beta_a(S_{II}/S_I)$  values are very close, and these are within the range of 12.09 to 15.95°. For the 72° anchors, almost all the  $\beta_a(S_I)$  and  $\beta_a(S_{II}/S_I)$  values are within the range of 8.13 to 10.78°. The  $\beta_f(S_I)$  and  $\beta_f(S_{II}/S_I)$  values for the 45 and 63° anchors are within the range of 32.74 to 50.19°. For the 72° anchors, all the  $\beta_f(S_I)$  and  $\beta_f(S_{II}/S_I)$  values are within the range of 19.98 to 27.76° and 24.62 to 34.22°, respectively. In general, for all models, the difference between the values of  $\beta_a(S_I)$  and  $\beta_f(S_I)$ , and  $\beta_a(S_{II}/S_I)$  and  $\beta_f(S_{II}/S_I)$  are at least 10°, which supports the nonlinearity of the failure surfaces.

## 8. Analysis of Failure Surfaces Based on Horizontal Slice Method

The horizontal failure points obtained from both the sides of 2D panels can be identically replicated around the 3D model anchors as a three-dimensional axisymmetric solid body of breakout sand. From the known coordinates of failure points, a number of horizontal slices are found having 21 mm ( $\Delta z$ ) thickness. Each slice of breakout sand is

acting as a truncated cone in the axisymmetric model, and elemental forces acting on the slice wedge are presented by the free body diagram, as shown in Figures 14 and 15 for  $S_I$  and  $S_{II}/S_I$  deposits, respectively. All the mathematical terms and expressions used to establish the method of plastic analysis is explained in Sections 8.1 and 8.2.

**8.1. Analysis of Breakout Wedge in Homogeneous Sand Deposit ( $S_I$ ).** Similar procedure is followed to analyze net ultimate uplift capacity in layered buried sand ( $S_{II}/S_I$ ) and presented elaborately in next Section 8.2.

Analytical gross ultimate uplift capacity for whole wedge is found by summing up gross uplift capacities for  $n$  number of slices:

$$Q_{g.anlyl}(S_I) = \sum_{j=1}^m Q_{j,g.anlyl}(S_I), \quad (2)$$

and analytical net ultimate uplift capacity is

$$Q_{u.anlyl}(S_I) = Q_{g.anlyl}(S_I) - W_{anlyl}(S_I), \quad (3)$$

where  $m$  = total numbers of slices in the wedge;  $j$  = any slice within the failure wedge (value: 1 to  $m$ );  $Q_{j,g.anlyl}(S_I)$  = gross ultimate uplift capacity of  $j^{th}$  wedge in  $S_I$  deposit;  $Q_{g.anlyl}(S_I)$  = gross ultimate uplift capacity of wedge in  $S_I$  deposit;  $Q_{u.anlyl}(S_I)$  = net ultimate uplift capacity of wedge in  $S_I$  deposit; and  $W_{anlyl}(S_I)$  = weight of sand equal to the same

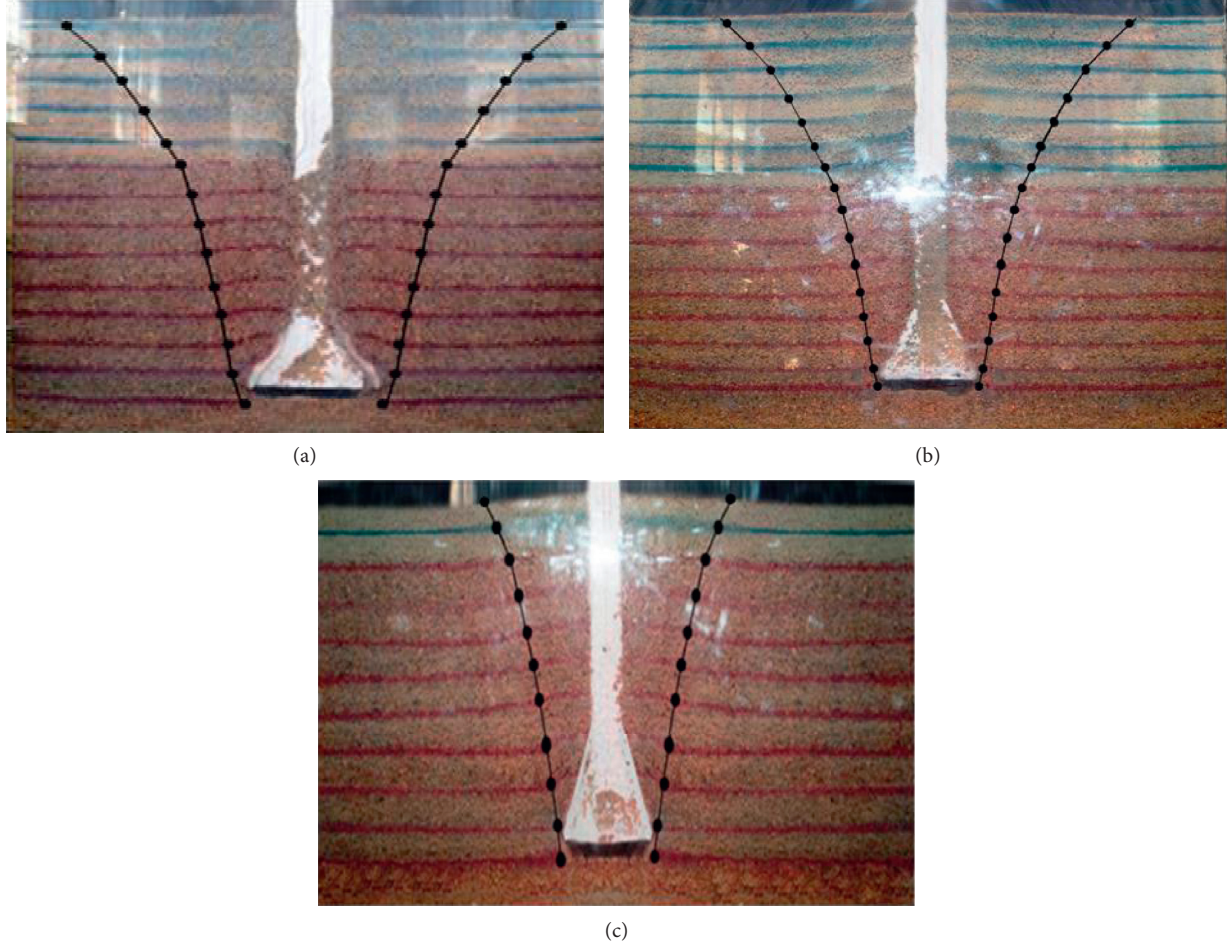


FIGURE 6: Pictorial view of nonlinear failure surfaces on both the sides of (a) panel 2D:45-0.28-3-(0.39 $S_{II}$ /0.61 $S_I$ ), (b) panel 2D:63-0.33-4-(0.47 $S_{II}$ /0.53 $S_I$ ), and (c) panel 2D:72-0.38-3-(0.18 $S_{II}$ /0.82 $S_I$ ).

volume of the respective anchor model inside the breakout wedge in  $S_I$  deposit.

**8.2. Analysis of Breakout Wedge in Layered Sand Deposit ( $S_{II}$ / $S_I$ ).** The interference of  $d$  was ignored by Dickin et al. [2, 26] on failure mechanism of plate and semicylindrical belled piles, so the same is followed in this study also. Moreover, Dickin and Leung [3] presented that artificially roughened belled shaft contribute to only 10% hike in uplift capacity.

Soil reaction on failure plane of  $j^{\text{th}}$  slice:

$$\Delta F_j = \Delta R_j \Delta L_j = \left[ \gamma_I \{(y_j + \Delta y) - y_j\} \cdot \{k_0 \cos \beta_j + \sin \beta_j\} \frac{\Delta y}{\cos \beta_j} \right]. \quad (4)$$

Soil reaction on failure plane of  $i^{\text{th}}$  slice:

$$\Delta F_i = \Delta R_i \Delta L_i = \left[ \gamma_{II} \{(y_i + \Delta y) - y_i\} \cdot \{k_0 \cos \beta_i + \sin \beta_i\} \frac{\Delta y}{\cos \beta_i} \right]. \quad (5)$$

At the collapsed stage, in state of limit equilibrium of soil, Mohr–Coulomb failure criteria can be considered. In accordance with Chattopadhyay and Pise [26], the vertical component of downward acting resultant mobilized shear resistance for  $j^{\text{th}}$  and  $i^{\text{th}}$  slice surface is calculated as follows:

$$\Delta T_{vj} = \left[ 2\gamma_I \pi \Delta y \left( r_j + \frac{\Delta r_j}{2} \right) \{(y_j + \Delta y) - y_j\} \cdot \{k_0 \cos \beta_j + \sin \beta_j\} \tan \phi \right], \quad (6)$$

$$\Delta T_{vi} = \left[ 2\gamma_{II} \pi \Delta y \left( r_i + \frac{\Delta r_i}{2} \right) \{(y_i + \Delta y) - y_i\} \cdot \{k_0 \cos \beta_i + \sin \beta_i\} \tan \phi \right].$$

Resultant surcharge intensity for  $j^{\text{th}}$  slice:

$$= \left[ \pi \left\{ (q_{rj} + \Delta q_{rj}) (r_j + \Delta r_j)^2 - (q_{rj} r_j^2) \right\} \right]. \quad (7)$$

Resultant surcharge intensity for  $i^{\text{th}}$  slice:

$$= \left[ \pi \left\{ (q_{ri} + \Delta q_{ri}) (r_i + \Delta r_i)^2 - (q_{ri} r_i^2) \right\} \right]. \quad (8)$$

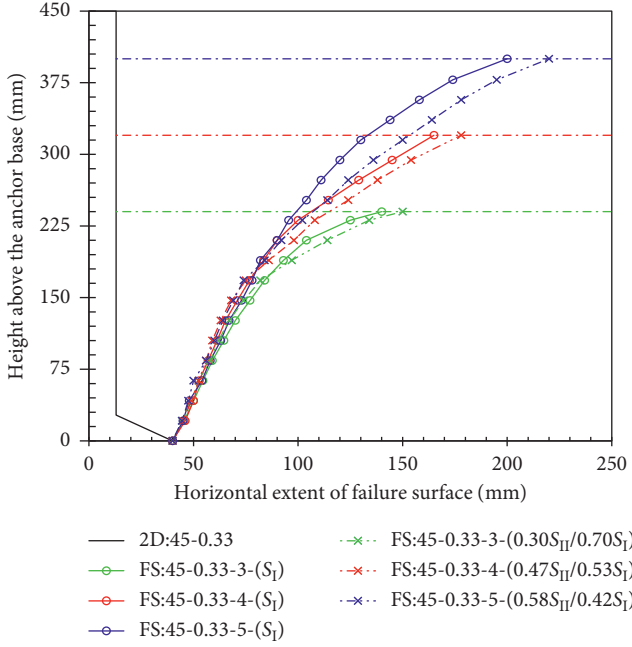


FIGURE 7: Comparison of FS:45-0.33-3-(S<sub>I</sub>) and FS:45-0.33-3-(0.30S<sub>II</sub>/0.70S<sub>I</sub>), FS:45-0.33-4-(S<sub>I</sub>) and FS:45-0.33-4-(0.47S<sub>II</sub>/0.53S<sub>I</sub>), and FS:45-0.33-5-(S<sub>I</sub>) and FS:45-0.33-5-(0.58S<sub>II</sub>/0.42S<sub>I</sub>).

Self-weight of the  $j^{\text{th}}$  slice:

$$= \left[ \pi \gamma_1 \frac{\Delta y}{3} \left\{ r_j^2 + (r_j + \Delta r_j)^2 + r_j(r_j + \Delta r_j) \right\} \right]. \quad (9)$$

Self-weight of the  $i^{\text{th}}$  slice:

$$= \left[ \pi \gamma_{II} \frac{\Delta y}{3} \left\{ r_i^2 + (r_i + \Delta r_i)^2 + r_i(r_i + \Delta r_i) \right\} \right]. \quad (10)$$

Considering vertical equilibrium for all elementary forces of  $j^{\text{th}}$  and  $i^{\text{th}}$  slice, gross ultimate uplift capacity is

$$\begin{aligned} Q_{j,g,\text{anly}} \left( \frac{S_{II}}{S_I} \right) &= \left[ 2\gamma_1 \pi \Delta y \left( r_j + \frac{\Delta r_j}{2} \right) \{ (y_j + \Delta y) - y_j \} \right. \\ &\quad \cdot \{ k_0 \cos \beta_j + \sin \beta_j \} \tan \phi \Big] \\ &\quad + \left[ \pi \{ (q_{rj} + \Delta q_{rj})(r_j + \Delta r_j)^2 - (q_{rj} r_j^2) \} \right] \\ &\quad + \left[ \pi \gamma_1 \frac{\Delta y}{3} \left\{ r_j^2 + (r_j + \Delta r_j)^2 + r_j(r_j + \Delta r_j) \right\} \right], \end{aligned}$$

$$\begin{aligned} Q_{i,g,\text{anly}} \left( \frac{S_{II}}{S_I} \right) &= \left[ 2\gamma_{II} \pi \Delta y \left( r_i + \frac{\Delta r_i}{2} \right) \{ (y_i + \Delta y) - y_i \} \right. \\ &\quad \cdot \{ k_0 \cos \beta_i + \sin \beta_i \} \tan \phi \Big] \\ &\quad + \left[ \pi \{ (q_{ri} + \Delta q_{ri})(r_i + \Delta r_i)^2 - (q_{ri} r_i^2) \} \right] \\ &\quad + \left[ \pi \gamma_{II} \frac{\Delta y}{3} \left\{ r_i^2 + (r_i + \Delta r_i)^2 + r_i(r_i + \Delta r_i) \right\} \right]. \end{aligned} \quad (11)$$

Analytical gross ultimate uplift capacity ( $Q_{g,\text{anly}}(S_{II}/S_I)$ ) for whole wedge may be computed by summing up gross uplift capacities for total  $m$  number of slices in lower as well as upper layer:

$$Q_{g,\text{anly}} \left( \frac{S_{II}}{S_I} \right) = \sum_{j=1}^5 Q_{j,g,\text{anly}} \left( \frac{S_{II}}{S_I} \right) + \sum_{i=6}^m Q_{i,g,\text{anly}} \left( \frac{S_{II}}{S_I} \right). \quad (12)$$

Analytical net ultimate uplift capacity:

$$Q_{u,\text{anly}} \left( \frac{S_{II}}{S_I} \right) = Q_{g,\text{anly}} \left( \frac{S_{II}}{S_I} \right) - W_{\text{anly}} \left( \frac{S_{II}}{S_I} \right), \quad (13)$$

where  $i = \text{any slice within the failure wedge in top layer (value: 6 to } m\text{)}$ ;  $j = \text{any slice within the failure wedge in bottom layer (value: 1 to } 5\text{)}$ ;  $m = \text{total numbers of slices in breakout wedge}$ ;  $Q_{rj+\Delta rj} = q\pi(r_j + \Delta r_j)^2$ , surcharge load acting downward in  $j^{\text{th}}$  slice;  $QQ_{rj} = q\pi r_j^2$ , surcharge load acting upward in  $j^{\text{th}}$  slice;  $Q_{ri+\Delta ri} = q\pi(r_i + \Delta r_i)^2$ , acting downward in  $i^{\text{th}}$  slice;  $QQ_{ri} = q\pi r_i^2$ , acting upward in  $i^{\text{th}}$  slice;  $r_i + \Delta r_i = \text{larger radius of } i^{\text{th}}$  slice at the height of  $y_i + \Delta y$ ;  $r_i = \text{smaller radius of } i^{\text{th}}$  slice;  $r_j + \Delta r_j = \text{larger radius of } j^{\text{th}}$  slice at the height of  $y_j + \Delta y$ ;  $r_j = \text{smaller radius of } j^{\text{th}}$  slice at height of  $z_j$  from anchor base;  $\beta_i = \text{failure angle made with vertical by elemental } i^{\text{th}}$  slice;  $\beta_j = \text{failure angle made with vertical by elemental } j^{\text{th}}$  slice;  $\gamma_{II}(y_i + \Delta y) = \text{vertical pressure from } i^{\text{th}}$  slice acting downward;  $\gamma_1(y_j + \Delta y) = \text{vertical pressure from } j^{\text{th}}$  slice acting downward;  $\gamma_{II}y_i = \text{vertical reaction within } i^{\text{th}}$  slice acting upward;  $\gamma_1y_j = \text{vertical reaction within } j^{\text{th}}$  slice acting upward; and  $k_0 = (1 - \sin \phi)$ , used by Chattopadhyay and Pise [26].

## 9. Discussions

Based on failure surface study, the analytical data of net ultimate uplift capacity are found out for both homogeneous ( $Q_{u,\text{anly}}(S_I)$ ) and layered ( $Q_{u,\text{anly}}(S_{II}/S_I)$ ) buried sand, and results are summarized in Table 4 (column (iii) and (vii)). On the basis of these data comparison of  $Q_{u,\text{anly}}(S_I)$  and  $Q_{u,\text{anly}}(S_{II}/S_I)$  in reference to embedment ratios, diameter ratios and bell angles are discussed herein. The variation in the values of maximum extent of failure in both the types of sand deposits has also been discussed in this section.

**9.1. Comparison of Nonlinear Failure Surface around 2D Panels and Analytical Uplift Capacities of 3D Bellied Anchor in Homogeneous and Layered Sand in reference to Embedment Ratios, Diameter Ratios, and Bell Angles.** From the mentioned Figures 7–13, it is observed that all the curves of failure surface are similar in pattern. The migration of curves started from the edge of anchor base and terminated in sand-surface. At anchor base and sand-surface, the values of horizontal distance of breakout points are minimum and maximum, respectively. The influence of overburden pressure and confinement of sand is maximum near to anchor base and minimum towards the sand-surface; hence, radial expansion of failure points near anchor base is minimum, gradually extensive in horizontal direction, and ultimately maximum at sand-surface ( $r_{\max}(S_I)$  in  $S_I$  deposit and  $r_{\max}(S_{II}/S_I)$  in  $S_{II}/S_I$  deposit). Higher the confining pressure

effects on lesser dilation of sand, subsequently lesser sliding and more interlocking.

The typical Figures 7–9 present that at higher embedment depth, near to the anchor base, failure points are relatively closer to each other, but the failure points towards the sand-surfaces have propensity to move more in horizontal direction, and thus  $r_{\max}(S_I)$  or  $r_{\max}(S_{II}/S_I)$  values are larger in deep embedment depth compared to those wedges formed due to shallow embedment depth. Hence, larger volumes of wedges are generated for more embedment depth in comparison to those wedges generated due to smaller embedment depth in both the types of sand deposits. It has been noticed that, in  $S_{II}/S_I$  deposit, in upper layer, comparatively wider zone of failure is developed than those observed in  $S_I$  deposit. Matsuo et al. [24, 34] presented the pattern of failure surfaces in homogeneous sand deposit from the experimental study, Kumar [22] in collapse mechanism and velocity hydrograph, and Sakai and Tanaka [23] in shear bend propagation for layered sand and presented that linear failure surfaces in denser overlying sand extended horizontally more than underlying lesser dense sand. The typical Figures 7–9 reflect that, in FS:45-0.33-3-(0.30 $S_{II}/0.70S_I$ ), FS:72-0.38-3-(0.18 $S_{II}/0.82S_I$ ), and FS:63-0.46-4-(0.25 $S_{II}/0.75S_I$ ), there is a little hike in expansion of wedge than FS:45-0.33-3-( $S_I$ ), FS:72-0.38-3-( $S_I$ ), and FS:63-0.46-4-( $S_I$ ), respectively. In case of Figure 7, in FS:45-0.33-4-(0.47 $S_{II}/0.53S_I$ ) and FS:45-0.33-5-(0.58 $S_{II}/0.42S_I$ ), the lateral expansion of wedge is higher in upper layer of sand than in FS:45-0.33-4-( $S_I$ ) and FS:45-0.33-5-( $S_I$ ), respectively. The same trend is also observed for FS:72-0.38-4-(0.38 $S_{II}/0.62S_I$ ) and FS:72-0.38-5-(0.51 $S_{II}/0.49S_I$ ) (in Figure 8) and FS:63-0.46-5-(0.40 $S_{II}/0.60S_I$ ) (in Figure 9) resulting in larger volume of wedges with higher values of  $r_{\max}(S_{II}/S_I)$  than  $r_{\max}(S_I)$ . As a result, more volume of sand is contained inside, providing higher dead-weight of breakout sand and exposing more lateral surface area to develop frictional shear (as  $\gamma$  and  $\phi$  values are higher for top layer than bottom layer). Data analysis from Table 4 (column (iii) and (vii)) reveals that, for 3D:63-0.28-3-(0.39 $S_{II}/0.61S_I$ ), 3D:63-0.28-4-(0.54 $S_{II}/0.46S_I$ ), and 3D:63-0.28-5-(0.63 $S_{II}/0.37S_I$ ),  $Q_{u,\text{anly.}}(S_{II}/S_I)$  values are 128.56, 247.51, and 447.44 N, respectively, whereas in the same model,  $Q_{u,\text{anly.}}(S_I)$  values 106.51, 199.90, and 321.46 N at  $L/D_b = 3, 4$ , and 5, respectively.

The typical graphical illustration of horizontal extent of failure points vs. embedment ratios for panels possessing  $T_s/T_b$  of 0.28, 0.33, 0.38, and, 0.46 and each panel belonging to  $\beta$  of 45°, at  $L/T_b$  of 5 are presented in Figures 10(a) and 10(b) for both homogeneous and layered sand deposits. From the Figure 9, it is observed that volume of wedge inside the FS:45-0.28-5-( $S_I$ ), FS:45-0.33-5-( $S_I$ ), FS:45-0.38-5-( $S_I$ ), and FS:45-0.46-5-( $S_I$ ) are in the descending order, so among these four wedges,  $Q_u:45-0.46-5-(S_I)$  is minimum and  $Q_u:45-0.28-5-(S_I)$  is maximum. Similarly in Figure 9, it is noticed that volume of wedge inside the FS:45-0.28-5-(0.63 $S_{II}/0.37S_I$ ), FS:45-0.33-5-(0.58 $S_{II}/0.42S_I$ ), FS:45-0.38-5-(0.51 $S_{II}/0.49S_I$ ), and FS:45-0.46-5-(0.40 $S_{II}/0.60S_I$ ) is in descending order; hence, among these four wedges  $Q_u:45-0.46-5-(0.40S_{II}/0.60S_I)$  is minimum and  $Q_u:45-0.28-5-(0.63S_{II}/0.37S_I)$  is maximum.

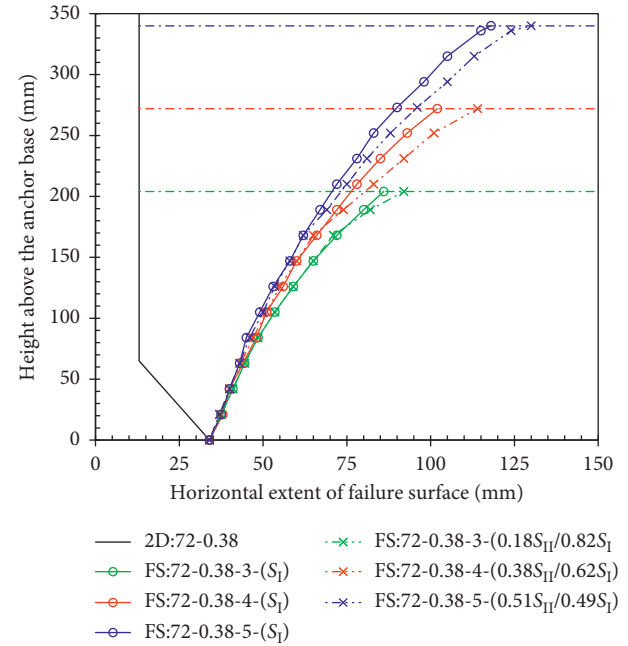


FIGURE 8: Comparison of FS:72-0.38-3-( $S_I$ ) and FS:72-0.38-3-(0.18 $S_{II}/0.82S_I$ ), FS:72-0.38-4-( $S_I$ ) and FS:72-0.38-4-(0.38 $S_{II}/0.62S_I$ ), and FS:72-0.38-5-( $S_I$ ) and FS:72-0.38-5-(0.51 $S_{II}/0.49S_I$ ).

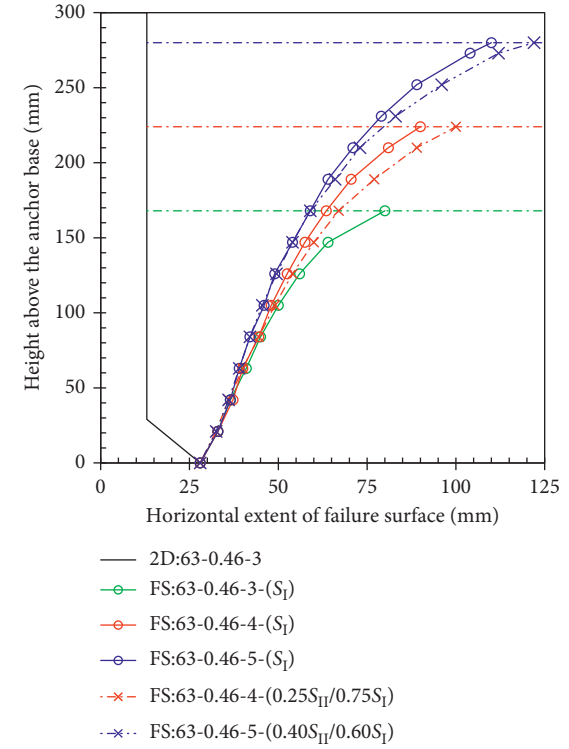


FIGURE 9: Failure surface around panel 2D:63-0.46-3-( $S_I$ ), in comparison to FS:63-0.46-4-( $S_I$ ) and FS:63-0.46-4-(0.25 $S_{II}/0.75S_I$ ) and FS:63-0.46-5-( $S_I$ ) and FS:63-0.46-5-(0.40 $S_{II}/0.60S_I$ ).

The abovementioned failure surfaces as developed in  $S_I$  and  $S_{II}/S_I$  around their respective panels are presented in Figures 11(a)–11(d). These figures reveal that the integrated volume of wedge as well as dead weight of sand inside the

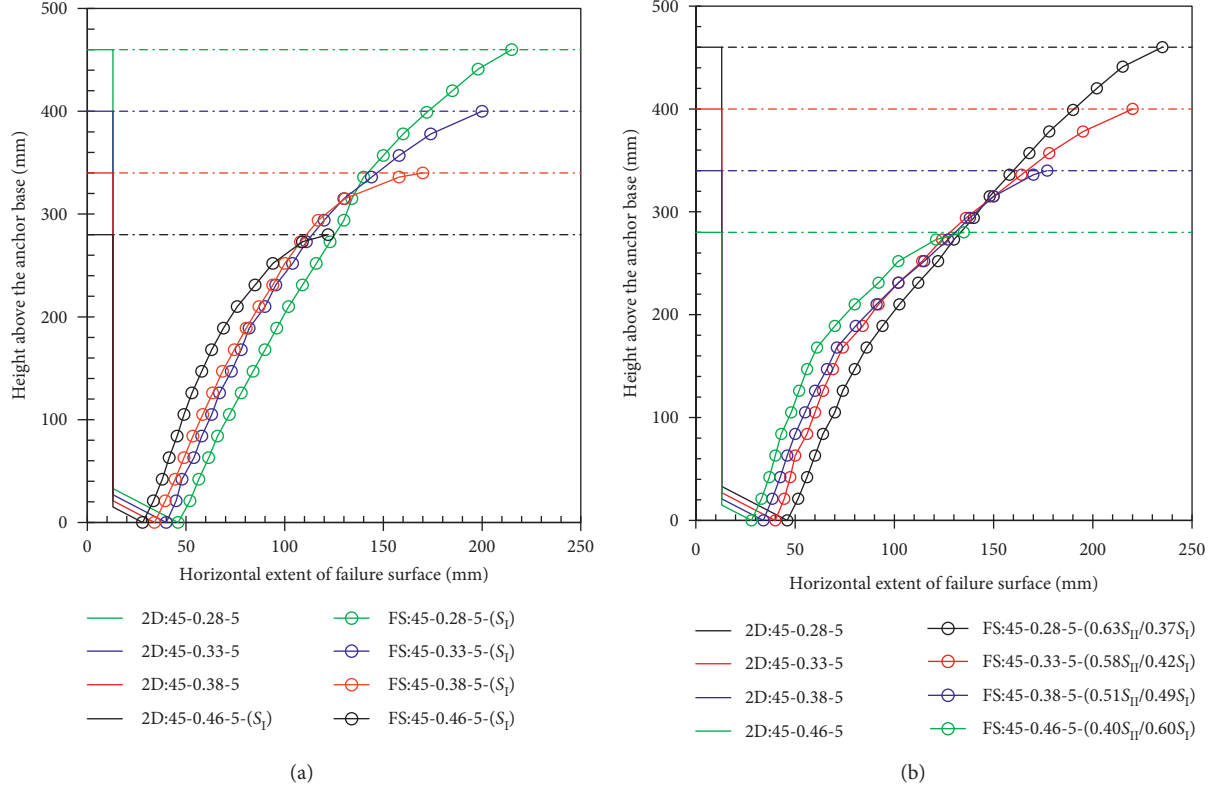


FIGURE 10: Height above the anchor base vs. horizontal extent of failure surface besides (a) panels having  $a = 45^\circ$ ,  $L/T_b = 5$ , and  $T_s/T_b = 0.28$ , 0.33, 0.38, and 0.46 in homogeneous sand deposit ( $S_I$ ) and (b) panels having  $a = 45^\circ$  and  $L/T_b = 0.28$ , 0.33, 0.38, and 0.46 in layered sand deposit ( $S_{II}/S_I$ ).

wedge and frictional area is higher in  $S_{II}/S_I$  compared to  $S_I$ . Data analysis from Table 4 (column (iii) and (vii)) shows that the values of  $Q_u:63-0.28-4-(S_I)$ ,  $Q_u:63-0.33-4-(S_I)$ ,  $Q_u:63-0.38-4-(S_I)$ , and  $Q_u:63-0.46-4-(S_I)$  are 199.90, 136.42, 79.26, and 41.42 N, respectively, and for same models, the values of  $Q_u:63-0.28-4-(0.54S_{II}/0.46S_I)$ ,  $Q_u:63-0.33-4-(0.47S_{II}/0.53S_I)$ ,  $Q_u:63-0.38-4-(0.38S_{II}/0.62S_I)$ , and  $Q_u:63-0.46-4-(0.25S_{II}/0.75S_I)$  are 247.51, 167.42, 100.80, and 48.71 N, respectively.

The typical graphical illustration of failure surfaces around panels having different values of  $\beta$  for 2D panels at  $L/T_b = 4$ ,  $T_s/T_b$  of 0.33 and 2D panels at  $L/T_b = 5$ ,  $T_s/T_b$  of 0.28 is represented in Figures 12 and 13 in homogeneous and layered sand deposits, respectively. In general, it is observed that the failure surfaces for 45 and 63° anchors are very close to each other than 72° anchors in both  $S_I$  and  $S_{II}/S_I$  deposits. Larger bell angle stands for steeper tapered bell base; so the base of sand column contains sand of comparatively lesser stability as well as potential to mobility than that of vertically standing sand column above the tapered portion of bell base possessing lesser bell angle. In case of 72° belled anchor, the sand close to anchor base possesses noticeably lesser potential to mobility, and obviously lesser sand dilatancy may hinder the radial movement of wedge near about anchor base as well as further radial extension of wedge upward up to sand surface. Due to this similar phenomenon in both  $S_I$  and  $S_{II}/S_I$ , lesser volume of wedge is generated for 72° belled anchor

and yields smaller dead-weight of breakout wedge as well as shear strength mobilization at collapsed stage. Matsuo et al. [24, 34] reported the similar behaviour of failure surfaces in sand for different belled angles. In Figure 12, it is observed that FS:45-0.33-5-( $0.58S_{II}/0.42S_I$ ), FS:63-0.33-5-( $0.58S_{II}/0.42S_I$ ), and FS:72-0.33-5-( $0.58S_{II}/0.42S_I$ ) are comparatively extensive in nature than FS:45-0.33-5( $S_I$ ), FS:63-0.33-5( $S_I$ ), and FS:72-0.33-5( $S_I$ ). In Figure 13, similar type of observation can be made as FS:45-0.28-5-( $0.63S_{II}/0.37S_I$ ), FS:63-0.33-5-( $0.63S_{II}/0.37S_I$ ), and FS:72-0.33-5-( $0.63S_{II}/0.37S_I$ ) are comparatively extensive in nature than FS:45-0.25-5( $S_I$ ), FS:63-0.28-5( $S_I$ ), and FS:72-0.28-5( $S_I$ ). Data analysis from Table 4 (column (iii) and (vii)) presents that  $Q_u(S_I)$  values are 147.90, 117.97, and 99.40 N for 3D:45-0.38-5( $S_I$ ), 3D:63-0.38-5( $S_I$ ), and 3D:72-0.38-5( $S_I$ ), respectively, and for the same models 3D:45-0.38-5-( $0.51S_{II}/0.49S_I$ ), 3D:63-0.38-5-( $0.51S_{II}/0.49S_I$ ), and 3D:72-0.38-5-( $0.51S_{II}/0.49S_I$ )  $Q_u(S_{II}/S_I)$  values are 188.64, 166.85, and 118.74 N, respectively.

**9.2. Comparison of  $r_{max}(S_I)$  and  $r_{max}(S_{II}/S_I)$  Values of Failure Surface at Sand Surface in Homogeneous ( $S_I$ ) and Layered ( $S_{II}/S_I$ ) Sand Deposits.** The  $r_{max}(S_I)$  and  $r_{max}(S_{II}/S_I)$  values are increased with higher  $L/T_b$  irrespective of  $T_s/T_b$ ,  $\beta$ , and types of sand deposits (i.e.,  $S_I$  and  $S_{II}/S_I$ ), but the values of  $r_{max}(S_{II}/S_I)$  are higher than  $r_{max}(S_I)$ , as observed from Figures 7–9.

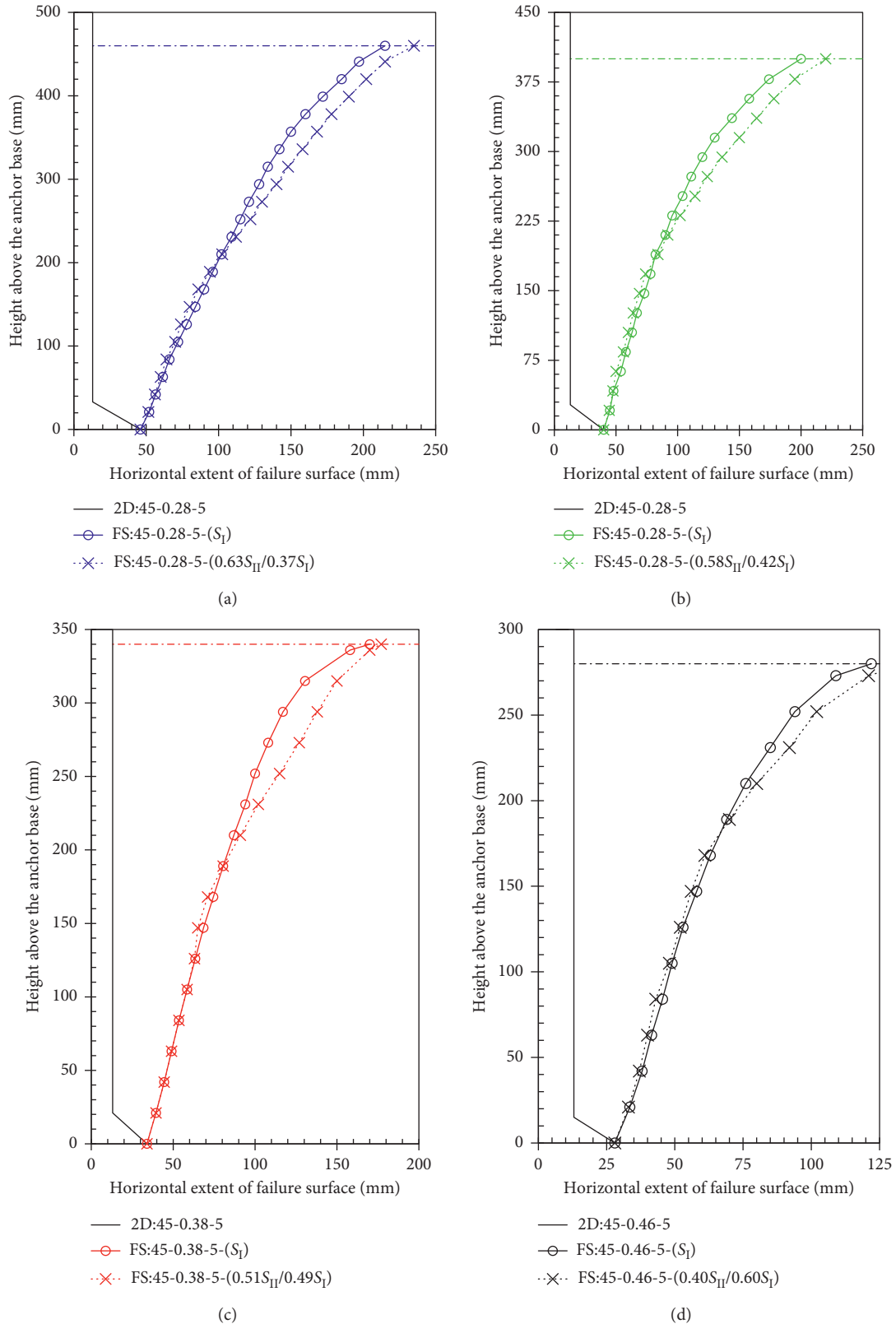


FIGURE 11: Comparison of (a) FS:45-0.28-5-( $S_I$ ) and FS:45-0.28-5-( $0.63S_{II}/0.37S_I$ ), (b) FS:45-0.33-5-( $S_I$ ) and FS:45-0.33-5-( $0.58S_{II}/0.42S_I$ ), (c) FS:45-0.38-5-( $S_I$ ) and FS:45-0.38-5-( $0.51S_{II}/0.49S_I$ ), and (d) FS:45-0.46-5-( $S_I$ ) and FS:45-0.46-5-( $0.40S_{II}/0.60S_I$ ).

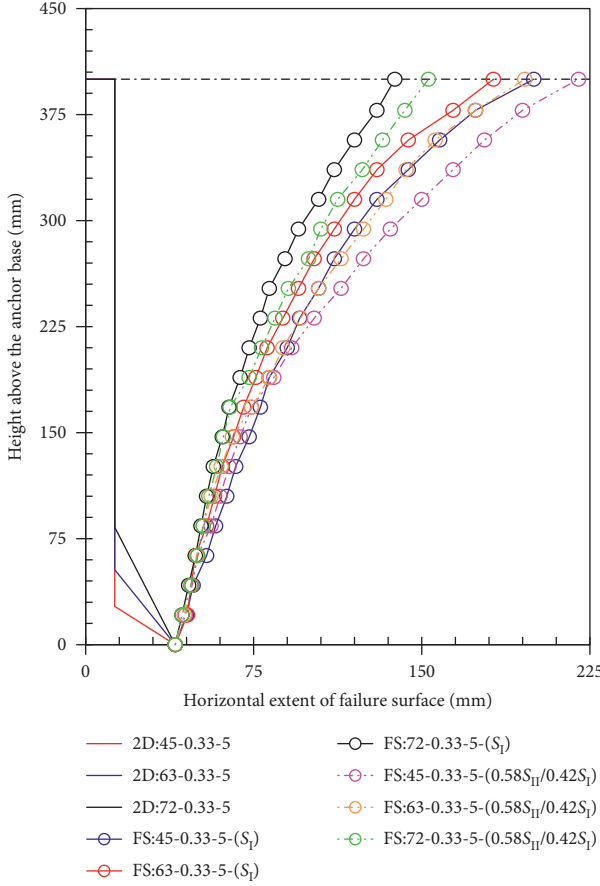


FIGURE 12: Comparison of FS:45-0.33-5-( $S_I$ ) and FS:45-0.33-5-( $0.58S_{II}/0.42S_I$ ), FS:463-0.33-5-( $S_I$ ) and FS:63-0.33-5-( $0.58S_{II}/0.42S_I$ ), and FS:72-0.33-5-( $S_I$ ) and FS:72-0.33-5-( $0.58S_{II}/0.42S_I$ ).

For FS:72-0.33-3-( $S_I$ ), FS:72-0.33-4-( $S_I$ ), and FS:72-0.33-5-( $S_I$ ), the values of  $r_{\max}(S_I)$  are 100, 124, and 138 mm, respectively, and for FS:72-0.33-3-( $0.30S_{II}/0.70S_I$ ), FS:7-0.33-4-( $0.47S_{II}/0.53S_I$ ), and FS:72-0.33-5-( $0.58S_{II}/0.42S_I$ ), the values of  $r_{\max}(S_{II}/S_I)$  are 109, 130, and 153 mm, respectively. Deb et al. [34, 36] reported that, as the values of embedment ratio increases, lateral heave at sand surface gradually increases in homogeneous buried sand.

The  $r_{\max}(S_I)$  and  $r_{\max}(S_{II}/S_I)$  values are progressively increased with lesser  $T_s/T_b$ , regardless  $L/T_b$ ,  $\beta$ ,  $S_I$ , and  $S_{II}/S_I$  deposits, but the values of  $r_{\max}(S_{II}/S_I)$  are higher than  $r_{\max}(S_I)$ , as noticed from Figures 10 and 11. For FS:45-0.28-4-( $S_I$ ), FS:45-0.33-4-( $S_I$ ), FS:45-0.38-4-( $S_I$ ), and FS:45-0.46-4-( $S_I$ ), the values of  $r_{\max}(S_I)$  are 150, 140, 100, and 82 mm, respectively, and for FS:45-0.28-4-( $0.54S_{II}/0.46S_I$ ), FS:45-0.33-4-( $0.47S_{II}/0.53S_I$ ), FS:45-0.38-4-( $0.3S_{II}/0.62S_I$ ), and FS:45-0.46-4-( $0.25S_{II}/0.75S_I$ ), the values of  $r_{\max}(S_{II}/S_I)$  are 198, 178, 158, and 109 mm, respectively.

The  $r_{\max}(S_I)$  and  $r_{\max}(S_{II}/S_I)$  values at sand surface are gradually decreased with higher values of  $\beta$  despite of  $L/T_b$ ,  $T_s/T_b$ ,  $S_I$ , and  $S_{II}/S_I$  deposit, but the values of  $r_{\max}(S_{II}/S_I)$  are higher than  $r_{\max}(S_I)$ , as observed from Figures 12 and 13. For FS:45-0.33-4-( $S_I$ ), FS:63-0.33-4-( $S_I$ ), and FS:72-0.33-5-( $S_I$ ), the values of  $r_{\max}(S_I)$  are 165, 152, and 124 mm,

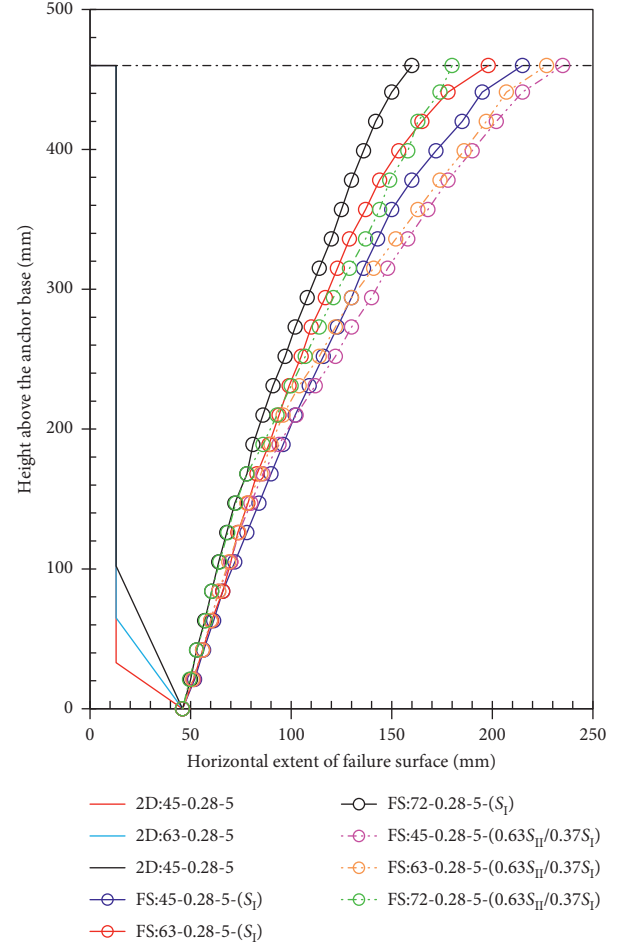


FIGURE 13: Comparison of FS:45-0.28-5-( $S_I$ ) and FS:45-0.28-5-( $0.63S_{II}/0.37S_I$ ), FS:63-0.28-5-( $S_I$ ) and FS:63-0.28-5-( $0.63S_{II}/0.37S_I$ ), and FS:72-0.28-5-( $S_I$ ) and FS:72-0.28-5-( $0.63S_{II}/0.37S_I$ ).

respectively, and for FS:45-0.33-4-( $0.47S_{II}/0.53S_I$ ), FS:63-0.33-4-( $0.47S_{II}/0.53S_I$ ), and FS:72-0.33-4-( $0.47S_{II}/0.53S_I$ ), the values of  $r_{\max}(S_{II}/S_I)$  are 178, 170, and 130 mm, respectively. Deb and Pal [34] have made similar observation on the variation in horizontal extent of failure points at sand surface for variation in  $L/T_b$  and  $\beta$ .

## 10. Breakout Factor

Net ultimate uplift capacities ( $Q_u(S_I)$  and  $Q_u(S_I/S_{II})$ ) are presented as breakout factor, nondimensionalized by density ( $\gamma_I$  or both  $\gamma_I$  and  $\gamma_{II}$ ), embedment depth ( $L$  or both  $L_I$  and  $L_{II}$ ), and belled base area ( $A_b$ ). The breakout factors ignore the size effect. For similar anchor characteristics, breakout factors are similar, rather for small-scale or full-scale models. For homogeneous sand deposit, breakout factors ( $N_{u,obs.}(S_I)$ ) are calculated as follows:

$$N_{u,obs.}(S_I) = \frac{Q_u(S_I)}{\gamma A_b L}. \quad (14)$$

For layered sand deposit, breakout factors ( $N_{u,obs.}(S_I/S_{II})$ ) are calculated as

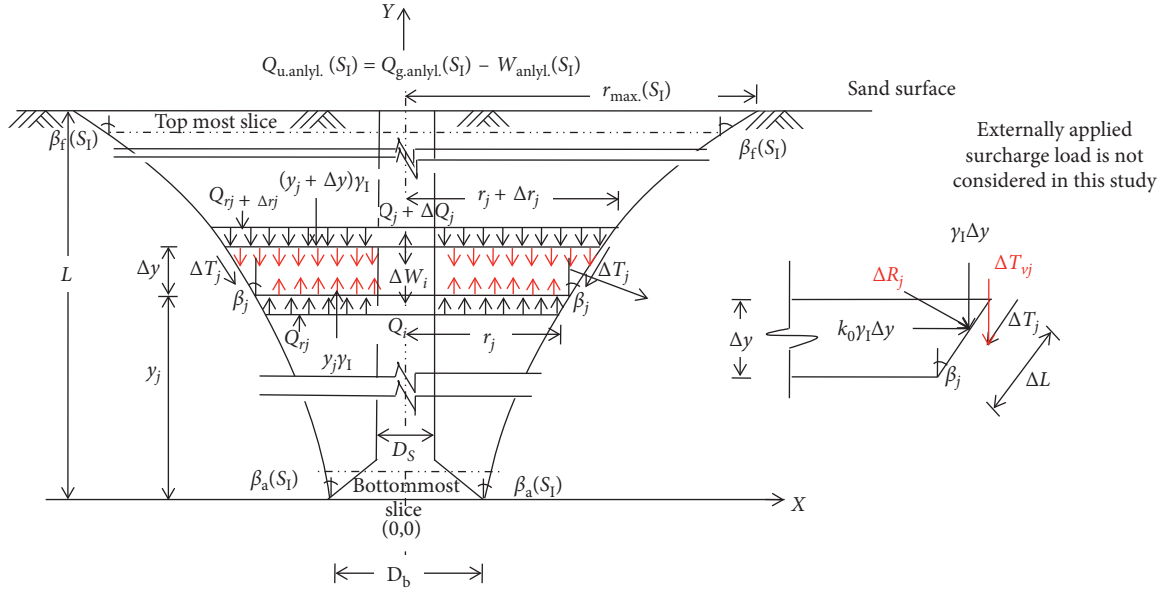


FIGURE 14: Free body diagram of a three-dimensional elemental slice wedge as per the horizontal slice method, in homogeneous sand deposit ( $S_I$ ).

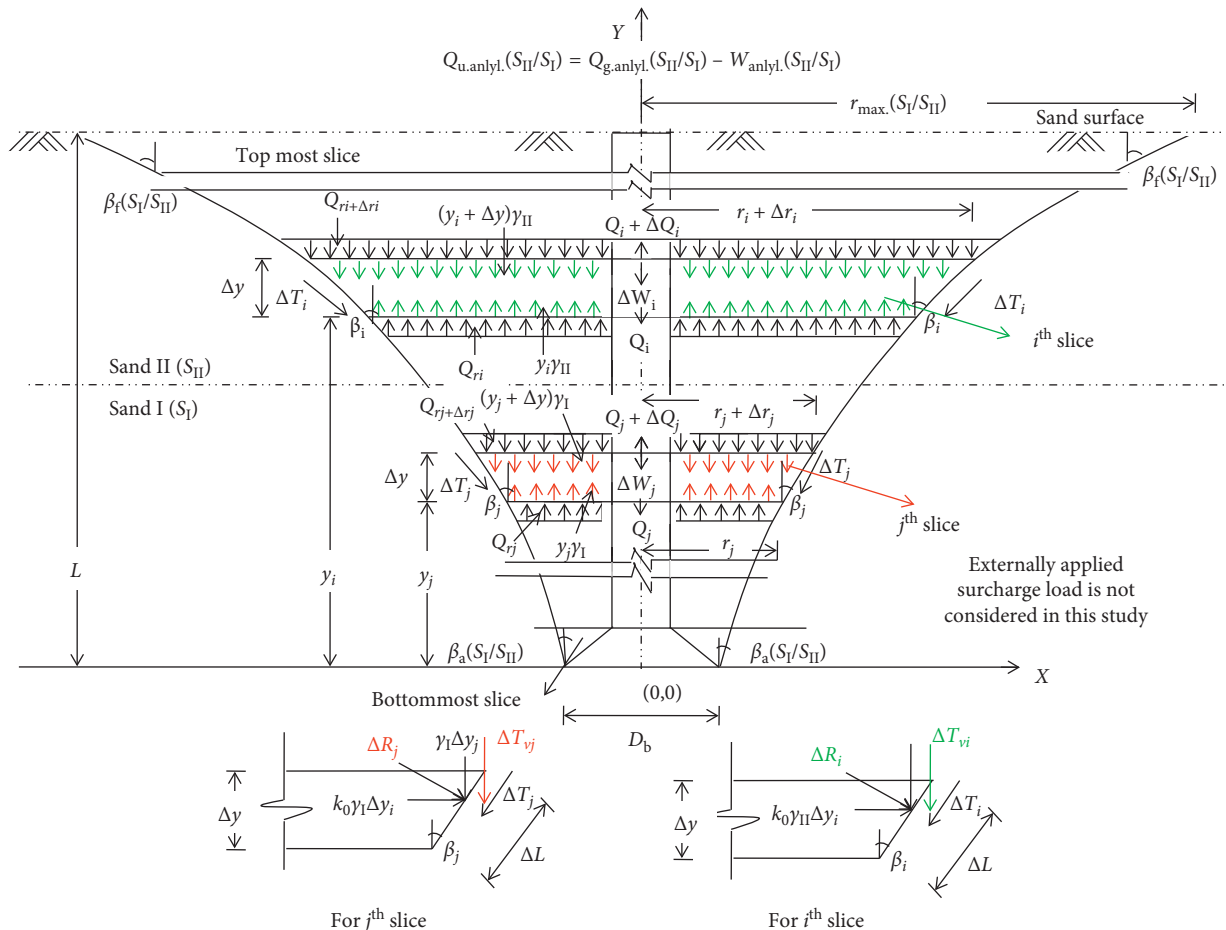


FIGURE 15: Free body diagram of a three-dimensional elemental slice wedge as per the horizontal slice method, in layered sand deposit ( $S_{II}/S_I$ ).

$$N_{u,(\text{obs.}(S_{II}/S_I))} = \frac{Q_u(S_{II}/S_I)}{A_b(\gamma_{II}L_{II} + \gamma_I L_I)}. \quad (15)$$

To develop the regression models with observed breakout factors (i.e.,  $N_{u,(\text{obs.}S_I)}$  and  $N_{u,(\text{obs.}SI/SII)}$ ) for  $45^\circ$ ,  $63^\circ$  and  $72^\circ$  belled anchors, these are identified as  $N_{u,(\text{obs.}45^\circ)}$ ,  $N_{u,(\text{obs.}63^\circ)}$ , and  $N_{u,(\text{obs.}72^\circ)}$ , respectively. Similarly, for all the  $45^\circ$ ,  $63^\circ$ , and  $72^\circ$  belled anchors, the breakout factors are identified as  $N_{u,(\text{obs.}45^\circ, 63^\circ, 72^\circ)}$ .

## 11. Multiple Linear Regression Models

**11.1. Significance of Multiple Regression Coefficients as a Whole Multiple Regression Coefficient and Partial Multiple Regression Coefficients.** The multiple linear regression is a predictive analysis to explain the relationship between one dependent parameter and two or more independent parameters, and the judgment of regression equations can be done through estimation of  $R^2$ ,  $R_{\text{adj}}^2$ , and  $E_s$  (as explained by Draper and Smith [37]). The significance of multiple regression coefficients as a whole and in part separately can be evaluated through ‘‘F’’ test and ‘‘t’’ test, respectively. This study is made for the level of significance ( $\alpha$ ) of requisite hypothesis = 0.05.

The ‘‘F’’ test can evaluate all multiple coefficients, simultaneously, whereas ‘‘t’’ test that can evaluate only one regression coefficient at a time. These two tests imply the probability of acceptance of the assumed model to predict data. In accordance with the null hypothesis, there is no statistical significance among the variables, i.e.,  $H_0: \xi_1 = \xi_2 = \dots = \xi_p = 0$ . According to the alternative hypothesis ( $H_a$ ), at least one of the values of  $\xi$  is nonzero.

The decision rule for ‘‘F’’ test is

$$\begin{aligned} &\text{reject } H_0, \text{ if } F_{\text{cal}} > F_{(1-\alpha, p-1, n-p)}, \\ &\text{accept } H_0, \text{ if } F_{\text{cal}} \leq F_{(1-\alpha, p-1, n-p)}, \end{aligned} \quad (16)$$

where  $F_{(1-\alpha, p-1, n-p)}$  is chosen from the  $F$  table for the level of significance  $\alpha = 0.05$ .

If the null hypothesis is not accepted in case of ‘‘F’’ test, then ‘‘t’’ test should be performed to assess the contribution of each independent variables to explain the dependent variable. From the ‘‘t’’ statistics, if any regression coefficient is defined as insignificant, then a new regression model should be proposed by eliminating the previous data in the set of independent variables.

The decision rule for ‘‘t’’ test is

$$\begin{aligned} &\text{reject } H_0, \text{ if } t_{\text{cal}} > t_{(1-\alpha/2, n-p)} \text{ or } t_{\text{cal}} < -t_{(1-\alpha/2, n-p)}, \\ &\text{accept } H_0, \text{ if } -t_{(1-\alpha/2, n-p)} \leq t_{\text{cal}} \leq t_{(1-\alpha/2, n-p)}, \end{aligned} \quad (17)$$

where  $t_{(1-\alpha/2, n-p)}$  is chosen from the  $t$  table for the level of significance  $\alpha = 0.05$ .

**11.2. Possible Multiple Regression Models Proposed by Using the Values of  $N_{u,(\text{obs.}45^\circ)}$ ,  $N_{u,(\text{obs.}63^\circ)}$ ,  $N_{u,(\text{obs.}72^\circ)}$ , and  $N_{u,(\text{obs.}45^\circ, 63^\circ, 72^\circ)}$ .** Based on each 19 set of observed scattered values of  $N_{u,(\text{obs.}45^\circ)}$ ,  $N_{u,(\text{obs.}63^\circ)}$ , and  $N_{u,(\text{obs.}72^\circ)}$ , the regression

models (18), (19), and (20) have been established to predict  $N_{u,(\text{pred.}45^\circ)}$ ,  $N_{u,(\text{pred.}63^\circ)}$ , and  $N_{u,(\text{pred.}72^\circ)}$ , respectively, as a function of  $L/D_b$ ,  $D_s/D_b$ , and  $i$ :

$$N_{u,(\text{pred.}45^\circ)} = 3.54 + 1.67 \left( \frac{L}{D_b} \right) - 4.19 \left( \frac{D_s}{D_b} \right) - 2.96(a), \quad (18)$$

$$N_{u,(\text{pred.}63^\circ)} = 3.87 + 1.48 \left( \frac{L}{D_b} \right) - 4.61 \left( \frac{D_s}{D_b} \right) - 2.97(a), \quad (19)$$

$$N_{u,(\text{pred.}72^\circ)} = 2.75 + 1.17 \left( \frac{L}{D_b} \right) - 2.70 \left( \frac{D_s}{D_b} \right) - 2.26(a). \quad (20)$$

The use of 63 sets of scattered data of  $N_{u,(\text{obs.}45^\circ, 63^\circ, 72^\circ)}$  has assisted in developing model (21) to predict  $N_{u,(\text{pred.}(45^\circ, 63^\circ, 72^\circ))}$ , where  $L/D_b$ ,  $D_s/D_b$ ,  $\beta$ , and  $i$  are the independent variables:

$$\begin{aligned} N_{u,(\text{pred.}(45^\circ, 63^\circ, 72^\circ))} = & 6.79 + 1.43 \frac{L}{D_b} - 3.12 \frac{D_s}{D_b} \\ & - 0.06(\beta) - 2.71(a). \end{aligned} \quad (21)$$

These models (18), (19), and (20) are developed to predict breakout factors for  $45^\circ$ ,  $63^\circ$ , and  $72^\circ$  anchors, respectively, and each model is valid for the values of  $L/D_b$  and  $D_s/D_b$  within the ranges of 3 to 5 and 0.28 to 0.46, respectively; the values of  $a$  is 1 in homogeneous sand deposit and within the ranges of 0.37 to 0.82 when  $S_I$  ( $\gamma_I = 15.60 \text{ kN/m}^3$ ) is underlying. In the model (21), the additional parameter  $\beta$  lies within the ranges of 45 to 72°.

In the model (18), the values of  $R^2$ ,  $R_{\text{adj}}^2$ , and  $E_s$  have been found out, and these are 0.961, 0.953, and 0.392, respectively. The values of  $R^2$ ,  $R_{\text{adj}}^2$ , and  $E_s$  are calculated as 0.968, 0.961, and 0.339, respectively for model (19). In the model (20), the values of  $R^2$ ,  $R_{\text{adj}}^2$ , and  $E_s$  are 0.961, 0.952, and 0.262, respectively. The values of  $R^2$ ,  $R_{\text{adj}}^2$ , and  $E_s$  are 0.934, 0.929, and 0.458, respectively, in model (21). The calculated value of  $F_{\text{cal}(45^\circ)}$ ,  $F_{\text{cal}(63^\circ)}$ , and  $F_{\text{cal}(72^\circ)}$  are 123.57, 150.38, and 115.57, respectively; these three values of  $F_{\text{cal}(45^\circ)}$ ,  $F_{\text{cal}(63^\circ)}$ , and  $F_{\text{cal}(72^\circ)}$  are greater than tabulated  $F_{(0.95, 2, 54)} = 3.168$ . The calculated value of  $F_{\text{cal}(45^\circ, 63^\circ, 72^\circ)} = 203.85$ , and this is greater than tabulated  $F_{(0.95, 3, 248)} = 2.631$ . The independent variables, coefficients, standard error, and  $t$  statistics of all the parameters and values of  $t_{\text{critical}}$  for models (18) to (21) have been presented in Table 5.

The models (18) to (21) of the present study may be followed for full-scale models of identical anchor characteristics as used in this study. This particular study may be directly used for the densities, values of  $L/D_b$ ,  $D_s/D_b$ , and  $\beta$  and  $a$  as used in this study. Due to the paucity of data in the relevant literature, these equations cannot be verified with previous data in homogeneous as well as layered sand deposits. These multiple regression equations are verified by other data of the present study, which are not used for development of these correlations. These equations may be

TABLE 5: Independent variables, coefficients, standard error,  $t_{\text{statistics}}$ , and  $t_{\text{critical}}$  of all the parameters from models (18) to (21).

Parameters	Coefficients	Standard error	$t$ statistics	$t_{\text{critical}} = t_{(0.975,54)}$
In accordance with model (18)				
$L/D_b$	+1.67	0.11	14.54	2.01
$D_s/D_b$	-4.19	1.43	2.93	
$a$	-2.96	0.41	7.13	
In accordance with model (19)				
$L/D_b$	+1.48	0.10	14.62	2.01
$D_s/D_b$	-4.61	1.21	3.80	
$a$	-2.97	0.36	8.16	
In accordance with model (20)				
$L/D_b$	+1.17	0.08	15.27	2.01
$D_s/D_b$	-2.70	1.00	2.69	
$a$	-2.26	0.29	7.84	
Parameters	Coefficients	Standard error	$t$ statistics	$t_{\text{critical}} = t_{(0.975,248)}$
In accordance with model (21)				
$L/D_b$	+1.43	0.74	19.47	1.979
$D_s/D_b$	-3.62	0.94	3.85	
$\beta$	-0.06	0.01	11.23	
$a$	-2.71	0.26	10.27	

checked before application due to a wide range of prevailing variations in-field soil properties.

## 12. Validation of Experimental Results

The values of  $Q_u(S_I)$ ,  $Q_{u,\text{anlyl.}}(S_I)$ , and predicted errors (%) on  $Q_{u,\text{anlyl.}}(S_I)$  are presented in Table 4 column (ii), (iii), and (iv), respectively. The values of  $Q_u(S_I)$  and  $Q_{u,\text{anlyl.}}(S_I)$  are compared and errors in 94.45% data are within the range of +08.51 to -10.70%. The values of  $Q_u(S_{II}/S_I)$ ,  $Q_{u,\text{anlyl.}}(S_{II}/S_I)$  as well as predicted errors (%) on  $Q_{u,\text{anlyl.}}(S_{II}/S_I)$  are presented in Table 4 column (vi), (vii), and (viii), respectively. The results of  $Q_u(S_{II}/S_I)$  and  $Q_{u,\text{anlyl.}}(S_{II}/S_I)$  are compared, and errors in all the data are within the range of +10.47 to -10.72%. In absence of field test data on uplift resistance, an ideal knowledge regarding soil profile, simulation of strata in laboratory, and failure study on both the sides of 2D panels may be helpful for the practicing engineers to rationally predict the most probable failure pattern and to evaluate net uplift capacity by execution of horizontal slice method in failure surface.

Table 6 presents that the errors are within the ranges of +3.72 to -14.11% to predict  $N_{u,\text{(pred.}45^\circ)}$  based on  $N_{u,\text{(obs.}45^\circ)}$ , +8.35 to -11.87% to predict  $N_{u,\text{(pred.}63^\circ)}$  based on  $N_{u,\text{(obs.}63^\circ)}$ , +6.77 to -4.75% to predict  $N_{u,\text{(pred.}72^\circ)}$  based on  $N_{u,\text{(obs.}72^\circ)}$ , and -10.45 to +16.01% to predict  $N_{u,\text{(pred.}45^\circ,63^\circ,72^\circ)}$  based on  $N_{u,\text{(obs.}45^\circ,63^\circ,72^\circ)}$  in accordance with the models (18), (19), (20), and (21), respectively.

## 13. Practical Applications

Two different types of sands are used in this study, because the existing buried soil (in low lying areas) and newly filled material may not be identical by geotechnical properties. In fact, the homogeneity of soil in whole depth of foundation and frictional soil in huge quantity may not prevail in the construction site. For anchors, soil having high density and frictional angle is useful as filling material. For this study, it may be assumed that

the foundation soil is either dry cohesionless single-layered soil or layered soil (denser sand overlying comparatively lesser dense sand). It may also be assumed that usually ground water table is adequately below the anchor base or has been lowered down below the anchor base for a short time during the construction period. Wenbai et al. [38] described the installation and uplift capacity of belled pile in drought loess having  $w$  calcium gluing property. Chae et al. [39] reported the field test on belled pile in weathered sand stone of Abu Dhabi. Experimental studies on the numbers of 2D panels and 3D models are conducted in laboratories in sand only. It should be checked and modify accordingly when different soil profiles of wide range of variation will be encountered at site. So, prior to direct implementation, these equations, and analytical method, it should be checked as per site soil conditions.

Experimental investigations on the model anchors are performed in laboratory in the sand only. In future, in a similar type of problem by formation of regression models for any other set of sand densities,  $L/D_b$ ,  $D_s/D_b$ ,  $\beta$ , and  $a$ , it is possible to find out the predicted  $N_u$ . The present regression models should be checked and revised accordingly when different soil profiles of a wide range of geotechnical properties will be encountered in construction field.

## 14. Concluding Remarks

Based on experimental results, analytical study, and discussions, following concluding remarks may be highlighted.

### 14.1. Uplift Capacities of 3D Models in Homogeneous ( $S_I$ ) and Layered ( $S_{II}/S_I$ ) Sand Deposits

- (i) The uplift capacities of belled anchors in layered sand ( $Q_u(S_{II}/S_I)$ ) are higher than homogeneous sand ( $Q_u(S_I)$ ) deposit. The model 3D:45-0.33-3-(0.30S<sub>II</sub>/0.7S<sub>I</sub>), 3D:45-0.38-3-(0.18S<sub>II</sub>/0.82S<sub>I</sub>), 3D:45-0.46-4-(0.25S<sub>II</sub>/0.75S<sub>I</sub>), 3D:63-0.33-3-(0.30S<sub>II</sub>/

TABLE 6: Comparison of the observed breakout factor and predicted breakout factor by using models (18) to (21).

Comparison of $N_{u,(\text{obs},45^\circ)}$ and $N_{u,(\text{pre},45^\circ)}$ by using model (18)						
Source	$L/D_b$	$D_s/D_b$	a	$N_{u,(\text{obs},45^\circ)}$	$N_{u,(\text{pre},45^\circ)}$	Errors (%)
Present study	3	0.33	1.00	4.37	4.21	+03.72
	4	0.46	0.75	5.75	6.07	-05.61
	4	0.28	0.46	7.47	7.69	+02.88
	5	0.38	1.00	6.97	7.34	-05.28
Bera and Banerjee [6]	3	0.4	1.00	3.43	3.91	-14.11
Comparison of $N_{u,(\text{obs},63^\circ)}$ and $N_{u,(\text{pre},63^\circ)}$ by using model (19)						
Source	$L/D_b$	$D_s/D_b$	a	$N_{u,(\text{obs},63^\circ)}$	$N_{u,(\text{pre},63^\circ)}$	Errors (%)
Present study	5	0.46	1.00	5.98	6.18	-03.33
	4	0.38	1.00	5.53	5.07	+08.35
	3	0.33	0.70	4.21	4.71	-11.87
	4	0.28	0.46	6.80	7.13	-04.90
Comparison of $N_{u,(\text{obs},72^\circ)}$ and $N_{u,(\text{pre},72^\circ)}$ by using model (20)						
Source	$L/D_b$	$D_s/D_b$	a	$N_{u,(\text{obs},72^\circ)}$	$N_{u,(\text{pre},72^\circ)}$	Errors (%)
Present study	3	0.38	1.00	3.19	2.97	+06.77
	4	0.28	1.00	4.64	4.41	+04.87
	5	0.46	0.60	5.73	6.00	-04.75
	5	0.33	0.42	6.67	6.78	-01.35
Comparison of $N_{u,(\text{obs},45^\circ,63^\circ,72^\circ)}$ and $N_{u,(\text{pre},45^\circ,63^\circ,72^\circ)}$ by using model (21)						
Source	$L/D_b$	$D_s/D_b$	$\beta$	a	$N_{u,(\text{obs},45^\circ,63^\circ,72^\circ)}$	$N_{u,(\text{pre},45^\circ,63^\circ,72^\circ)}$
Present study	3	0.33	45	1.00	4.37	4.48
	4	0.46	45	0.75	5.75	6.11
	4	0.38	63	1.00	5.53	4.64
	3	0.33	63	0.70	4.21	4.21
	4	0.28	72	1.00	4.64	4.47
	5	0.46	72	0.60	5.73	6.33

$0.70S_I$ , 3D:63-0.38-3-(0.18 $S_{II}/0.82S_I$ ), 3D:63-0.46-4-(0.25 $S_{II}/0.75S_I$ ), 3D:7-0.33-3-(0.30 $S_{II}/0.70S_I$ ), 3D:72-0.38-3-(0.18 $S_{II}/0.82S_I$ ), and 3D:672-0.46-4-(0.25 $S_{II}/0.75S_I$ ) are found to be less effective to gain higher  $Q_u(S_{II}/S_I)$  compared to  $Q_u(S_I)$  in homogeneous sand deposit.

- (ii) Uplift capacities of belled anchors are gradually higher for deeper embedment in both homogeneous ( $S_I$ ) and layered ( $S_{II}/S_I$ ) sand deposits. With increase in the values of  $L/D_b$ , the rate of increase in uplift capacities of belled anchors in layered sand ( $Q_u(S_{II}/S_I)$ ) is comparatively higher than  $Q_u(S_I)$  for the same model, regardless the particular values of  $D_s/D_b$  and  $\beta$ .
- (iii) Uplift capacities of belled anchors are gradually higher for lesser diameter ratios in both homogeneous ( $S_I$ ) and layered ( $S_{II}/S_I$ ) sand deposits. With decrease in the values of  $D_s/D_b$  from 0.46 to 0.28, the increase in  $Q_u(S_{II}/S_I)$  is comparatively higher than  $Q_u(S_I)$  for the same model, irrespective of particular values of  $L/D_b$  and  $\beta$ .
- (iv) The 45 and 63° belled anchors are more efficient uplift-protective structures than 72° anchors capacities in both types of sand deposits. For the change of  $\beta$  value from 63 to 72°,  $Q_u(S_I)$  and  $Q_u(S_{II}/S_I)$  are decreased at higher rate than those rates of decrement as observed for the change in  $\beta$  value from 45 to 63°. The increase in  $Q_u(S_{II}/S_I)$  is

comparatively higher than  $Q_u(S_I)$  for the same model, irrespective of particular values of  $L/D_b$  and  $D_s/D_b$ .

#### 14.2. Nonlinear Failure Surfaces around 2D Panels in Homogeneous ( $S_I$ ) and Layered ( $S_{II}/S_I$ ) Sand Deposits and Analytical Approach

- (i) All the nonlinear failure curves are similar in pattern; they are formed from edge of anchor base and terminated at sand-surface irrespective of type of sand deposits, values of embedment ratios, thickness ratios, and bell angles.
- (ii) The nonlinear failure surfaces of belled anchors in layered sand are larger than homogeneous sand deposit. The models FS:45-0.33-3-(0.30 $S_{II}/0.70S_I$ ), FS:45-0.38-3-(0.18 $S_{II}/0.82S_I$ ), FS:45-0.46-4-(0.25 $S_{II}/0.75S_I$ ), FS:63-0.33-3-(0.30 $S_{II}/0.70S_I$ ), FS:63-0.38-3-(0.18 $S_{II}/0.82S_I$ ), FS:63-0.46-4-(0.25 $S_{II}/0.75S_I$ ), FS:72-0.33-3-(0.30 $S_{II}/0.70S_I$ ), FS:72-0.38-3-(0.18 $S_{II}/0.82S_I$ ), and FS:672-0.46-4-(0.25 $S_{II}/0.75S_I$ ) are found to be slightly wider than corresponding failure surfaces in homogeneous sand deposit.
- (iii) At higher values of embedment ratio, larger volume of failure wedge is formed than those formed due to smaller embedment ratio in both the type of sand deposits, in models possessing certain value of thickness ratio (or diameter ratio) and bell angle.

The values of  $Q_{u,\text{anlyl.}}(S_{II}/S_I)$  are progressively larger for higher embedment ratios than  $Q_{u,\text{anlyl.}}(S_I)$  values for the same model in reference of embedment ratios.

- (iv) With larger values of thickness ratio (or diameter ratio), smaller volume of breakout wedge is generated in both the type of sand deposits, in models having certain value of embedment ratio and bell angle. The values of  $Q_{u,\text{anlyl.}}(S_{II}/S_I)$  are higher than  $Q_{u,\text{anlyl.}}(S_I)$  values for the same model in reference of thickness ratios (or diameter ratios).
- (v) For anchor having steeper bell, angle volume of breakout wedge is gradually reduced and for 72° belled anchor of the reduction rate is higher in both the types of sand deposits, in models belonging to certain value of embedment ratio and thickness ratio (or diameter ratio). The values of  $Q_{u,\text{anlyl.}}(S_{II}/S_I)$  are higher than  $Q_{u,\text{anlyl.}}(S_I)$  values for the same model in reference of bell angles.
- (vi) The  $r_{\max}(S_I)$  and  $r_{\max}(S_{II}/S_I)$  values show increasing trend when the failure surfaces are developed for higher values of embedment ratio, lesser thickness ratio, and bell angle of 2D panels in both the types of sand deposits. But  $r_{\max}(S_{II}/S_I)$  values are comparatively higher than  $r_{\max}(S_I)$  in reference of embedment ratios, thickness ratios (or diameter ratios), and bell angles.
- (vii) Out of 36 analytical data in homogeneous sand, 94.45% data are within the range of +08.51 to -10.70% and all 33 analytical data in layered sand are within the range of +10.47 to -10.72%, with respect to the experimental uplift capacities.
- (viii) Four numbers of multiple regression models have been developed by  $N_{u,\text{(obs.}45^{\circ}\text{)}}$ ,  $N_{u,\text{(obs.}63^{\circ}\text{)}}$ ,  $N_{u,\text{(obs.}72^{\circ}\text{)}}$ , and  $N_{u,\text{(obs.}45^{\circ},63^{\circ},72^{\circ}\text{)}}$ . The errors on 84.20% values of  $N_{u,\text{(pred.}45^{\circ}\text{)}}$ ,  $N_{u,\text{(pred.}63^{\circ}\text{)}}$ , and  $N_{u,\text{(pred.}72^{\circ}\text{)}}$  are within the range of +08.35 to -10.45% based on  $N_{u,\text{(obs.}45^{\circ}\text{)}}$ ,  $N_{u,\text{(obs.}63^{\circ}\text{)}}$ ,  $N_{u,\text{(obs.}72^{\circ}\text{)}}$ , and  $N_{u,\text{(obs.}45^{\circ},63^{\circ},72^{\circ}\text{)}}$ . Breakout factors eliminate the size effect, so the newly developed multiple linear regression models are appropriate for actual engineering to compare with prototype tests within the proposed limitation of values of variable parameters.

## Notations

$a:$	Portions of embedment depth of anchor in the lower layer
$D_b:$	Base diameter of 3D belled anchor
$D_s:$	Shaft diameter of 3D belled anchor
$D_s/D_b:$	Diameter ratio of 3D belled anchor
$E_s:$	Estimated standard error of regression statistics

$F_{\text{cal}(45^{\circ})}$ ,  $F_{\text{cal}(63^{\circ})}$ ,  $F_{\text{cal}(72^{\circ})}$ , Calculated values of  $F$  statistics in regression model prepared by  $N_{u,\text{(obs.}45^{\circ}\text{)}}$ ,  $N_{u,\text{(obs.}63^{\circ}\text{)}}$  and  $N_{u,\text{(obs.}72^{\circ}\text{)}}$  and  $N_{u,\text{obs.}(45^{\circ},54^{\circ},63^{\circ})}$ , respectively

$L:$  Embedment depth of belled anchor

$L/D_b:$  Embedment ratio in 3D belled anchor

$L/T_b:$  Embedment ratio in 2D panel anchor

$n:$  Total number of observations in all groups

$N_{u,\text{(obs.}45^{\circ}\text{)}}$ ,  $N_{u,\text{(obs.}63^{\circ}\text{)}}$ , and  $N_{u,\text{(obs.}72^{\circ}\text{)}}$ : Observed values of breakout factor for 45°, 63°, and 72° anchors, respectively

$N_{u,\text{(pre.}45^{\circ})}$ ,  $N_{u,\text{(pre.}63^{\circ})}$ , and  $N_{u,\text{(pre.}72^{\circ}\text{)}}$ : Predicted values of breakout factor for 45°, 63°, and 72° anchors, respectively

$N_{u,\text{(pre.}45^{\circ},63^{\circ},72^{\circ}\text{)}}$ : Predicted values of breakout factor for 45°, 63°, and 72° anchors

$N_{u,\text{obs.}(45^{\circ},63^{\circ},72^{\circ})}$ : Observed values of breakout factor for 45°, 63°, and 72° anchors

$p:$  Number of independent groups

$Q_g(S_I)$ : Gross ultimate uplift capacity of 3D models installed in  $S_I$  from experimental observation

$Q_g(S_{II}/S_I)$ : Gross ultimate uplift capacity of 3D models installed in  $S_{II}/S_I$  from experimental observation

$Q_{g,\text{anlyl.}}(S_I)$ : Analytical gross ultimate uplift capacity of 3D models installed in  $S_I$  deposit

$Q_{g,\text{anlyl.}}(S_{II}/S_I)$ : Analytical gross ultimate uplift capacity of 3D models installed in  $S_{II}/S_I$  deposit

$R^2:$  Coefficient of determination

$R_{\text{adj}}^2:$  Adjusted multiple coefficients of determination

$r_{\max}(S_I)$ : Maximum horizontal extent of failure point at sand surface of  $S_I$  deposit

$r_{\max}(S_{II}/S_I)$ : Maximum horizontal extent of failure point at sand surface of  $S_{II}/S_I$  deposit

$T_b:$  Bell thickness in 2D panel anchor

$T_s:$  Shaft thickness in 2D panel anchor

$T_s/T_b:$  Thickness ratio in 2D panel anchor

$\text{USCS:}$  Unified soil classification system

$W_{\text{anlyl.}}(S_I)$ : Weight of sand equal to the volume of belled anchor inside the wedge of  $S_I$

$W_{\text{anlyl.}}(S_{II}/S_I)$ : Weight of sand equal to the volume of belled anchor inside the wedge of  $S_{II}/S_I$

$W_M$ :	Self-weight of 3D model
$\beta$ :	Bell angle of anchor
$\beta_a(S_I)$ :	Initial failure angle with vertical in bottom most slice in $S_I$ deposit
$\beta_a(S_{II}/S_I)$ :	Initial failure angle with vertical in bottom most slice in $S_{II}/S_I$ deposit
$\beta_f(S_I)$ :	Final angle of failure with vertical in top most slice in $S_I$ deposit
$\beta_f(S_{II}/S_I)$ :	Final angle of failure with vertical in top most slice in $S_{II}/S_I$ deposit
$\xi_1, \xi_2, \dots, \xi_p$ :	Regression coefficients.

## Data Availability

The data used to support the findings of this study are available from the corresponding author upon request.

## Disclosure

The authors are solely involved in the manuscript writing, editing, approval, or decision to publish.

## Conflicts of Interest

The authors declare that there are no conflicts of interest.

## Acknowledgments

The authors are grateful to the Department of Civil Engineering, National Institute of Technology, Agartala, for providing all necessary facilities for this investigation. The research work presented here was supported by the Institute Fellowship to the first author from the Ministry of Human Resource and Development, Government of India. The experimental setup and models are fabricated from the financial assistantship of the Departmental Promotional Fund of Civil Engineering Department.

## References

- [1] R. B. Peck, W. E. Hanson, and T. H. Thornburn, *Foundation Engineering*, John Wiley and Sons, Inc., New York, NY, USA, 2nd edition, 1974.
- [2] E. A. Dickin and C. F. Leung, "Performance of piles with enlarged bases subject to uplift forces," *Canadian Geotechnical Journal*, vol. 27, no. 5, pp. 546–556, 1990.
- [3] E. A. Dickin and C. F. Leung, "The influence of foundation geometry on the uplift behaviour of piles with enlarged bases," *Canadian Geotechnical Journal*, vol. 29, no. 3, pp. 498–505, 1992.
- [4] S. K. Pal, "Uplift capacity of shallow and deep belled anchors tied geofabric strips," M.Tech. dissertation, IIT Kharagpur, West Bengal, India, 1992.
- [5] A. Ghosh and A. K. Bera, "Effect of geotextile ties on uplift capacity of anchors embedded in sand," *Geotechnical and Geological Engineering*, vol. 28, no. 5, pp. 567–577, 2010.
- [6] A. K. Bera and U. Banerjee, "Uplift capacity of model bell shaped anchor embedded in sand," *International Journal of Geotechnical Engineering*, vol. 7, no. 1, pp. 84–90, 2013.
- [7] A. K. Bera, "Parametric study on uplift capacity of anchor with tie in sand," *KSCE Journal of Civil Engineering*, vol. 18, no. 4, pp. 1028–1035, 2014.
- [8] R. Nazir, H. Moayedi, A. Pratikso, and M. Mosallanezhad, "The uplift load capacity of an enlarged base pier embedded in dry sand," *Saudi Society for Geosciences*, vol. 8, no. 9, pp. 7285–7296, 2014.
- [9] J. I. Adams and H. S. Radhakrishna, "Uplift resistance of augered footings in fissured clay," *Canadian Geotechnical Journal*, vol. 8, no. 3, pp. 452–462, 1971.
- [10] N. F. Ismael and T. W. Klym, "Behavior of rigid piers in layered cohesive soils," *Journal of Geotechnical Engineering*, vol. 104, pp. 1061–1074, 1978.
- [11] G. G. Meyerhof and J. I. Adams, "The ultimate uplift capacity of foundation," *Canadian Geotechnical Journal*, vol. 5, no. 4, pp. 225–244, 1968.
- [12] A. Balla, "The resistance to breaking-out of mushroom foundations for pylons," in *Proceedings of the 5th International Conference on Soil Mechanics and Foundation Engineering*, vol. 1, pp. 569–576, Paris, France, July 1961.
- [13] S. P. Clemence and C. J. Veesaert, "Dynamic uplift resistance of anchors in sand," in *Proceedings of the International Conference on Soil-Structure Interaction*, pp. 389–397, Roorkee, India, January 1977.
- [14] R. K. Rowe and E. H. Davis, "The behaviour of anchor plates in sand," *Géotechnique*, vol. 32, no. 1, pp. 25–41, 1982.
- [15] E. J. Murray and J. D. Geddes, "Uplift of anchor plates in sand," *Journal of Geotechnical Engineering*, vol. 113, no. 3, pp. 202–215, 1987.
- [16] N. R. Krishnaswamy and S. P. Parashar, "Uplift behaviour of plate anchors with geosynthetics," *Geotextiles and Geomembranes*, vol. 13, no. 2, pp. 67–89, 1994.
- [17] E. A. Dickin and M. Laman, "Uplift response of strip anchors in cohesionless soil," *Advances in engineering software*, vol. 38, no. 8-9, pp. 618–625, 2007.
- [18] L. Vanitha, N. R. Patra, and S. Chandra, "Uplift capacity of pile group anchors," *Geotechnical and Geological Engineering*, vol. 25, no. 3, pp. 339–347, 2007.
- [19] S. Mittal and S. Mukherjee, "Vertical uplift capacity of a group of helical screw anchors in sand," *Indian Geotechnical Journal*, vol. 43, no. 3, pp. 238–250, 2013.
- [20] E. R. Sujatha and R. Balamuruga, "Pullout behaviour of circular plate anchor in sand: a small scale investigation," *Asian Journal of Applied Sciences*, vol. 7, no. 6, pp. 424–432, 2014.
- [21] A. Bouazza and T. W. Finlay, "Uplift capacity of plate anchors buried in a two-layered sand," *Géotechnique*, vol. 40, no. 2, pp. 293–297, 1990.
- [22] J. Kumar, "Uplift resistance of strip and circular anchors in a two layered sand," *Soils and Foundations*, vol. 43, no. 1, pp. 101–107, 2003.
- [23] T. Sakai and T. Tanaka, "Experimental and numerical study of uplift behaviour of shallow circular anchor in two layered sand," *Journal of Geotechnical and Geoenvironmental Engineering*, vol. 133, no. 4, pp. 469–477, 1985.
- [24] M. Matsuo, "Study on the uplift resistance of footing (I)," *Soils and Foundations*, vol. 7, no. 4, pp. 1–37, 1967.
- [25] K. S. S. Rao and J. Kumar, "Vertical uplift capacity of horizontal anchors," *Journal of Geotechnical Engineering*, vol. 120, no. 7, pp. 1134–1147, 1994.
- [26] B. C. Chottapadhyay and P. J. Pise, "Breakout resistance of horizontal anchors in sand," *Japanese Society of Soil Mechanics and Foundation Engineering*, vol. 26, no. 4, pp. 16–26, 1986.
- [27] H. S. Saeedy, "Stability of circular vertical earth anchors," *Canadian Geotechnical Journal*, vol. 24, no. 3, pp. 452–456, 1987.

- [28] B. Sutherland, W. Flnlay, and M. O. Fadl, "Uplift capacity of embedded anchors in sand," in *Proceedings of the 3rd International Conference on the Behaviour of Offshore Structures*, vol. 2, pp. 451–463, Cambridge, MA, USA, 1889.
- [29] P. A. Vermeer and W. Sutjiadi, "The uplift resistance of shallow embedded anchors," in *Proceedings of the 11th International Conference on Soil Mechanics and Foundation Engineering*, vol. 4, pp. 1635–1638, San Francisco, CA, USA, 1985.
- [30] A. Ghaly, A. Hanna, and M. Hanna, "Uplift behavior of screw anchors in sand. I: dry sand," *Journal of Geotechnical Engineering*, vol. 117, no. 5, pp. 773–793, 1991.
- [31] S. Saran, G. Ranjan, and A. S. Nene, "Soil anchors and constitutive laws," *Journal of Geotechnical Engineering*, vol. 112, no. 12, pp. 1084–1100, 1986.
- [32] K. Ilamparuthi and K. Muthukrishnaiah, "Anchors in sand bed: delineation of rupture surface," *Ocean Engineering*, vol. 26, no. 12, pp. 1249–1273, 1999.
- [33] K. Ilamparuthi, E. A. Dickin, and K. Muthukrisnaiah, "Experimental investigation of the uplift behaviour of circular plate anchors embedded in sand," *Canadian Geotechnical Journal*, vol. 39, no. 3, pp. 648–664, 2002.
- [34] T. Deb and S. K. Pal, "Study on the uplift behaviour and failure pattern of single belled anchor with 3D and 2D models in cohesionless soil bed," *Iranian Journal of Science and Technology Transaction in Civil Engineering*, 2018.
- [35] W. Stewart, "Uplift capacity of circular plate anchors in layered soil," *Canadian Geotechnical Journal*, vol. 22, no. 4, pp. 589–592, 1985.
- [36] K. Ilamparuthi and E. A. Dickin, "Predictions of the uplift response of model belled piles in geogrid-cell-reinforced sand," *Geotextiles and Geomembranes*, vol. 19, no. 2, pp. 89–109, 2001.
- [37] N. R. Draper and H. Smith, *Applied Regression Analysis*, John Wiley and Sons, New York, NY, USA, 1998.
- [38] L. Wenbai, Z. Jian, and M. T. Mohr, "Uplift bearing tests and calculations of belled piles in loess of arid regions," in *Proceedings of Fifth International Conference on Case Histories in Geotechnical Engineering*, pp. 13–17, New York, NY, USA, April 2004.
- [39] D. Chae, W. Cho, and Y. H. Na, "Uplift capacity of belled pile in weathered sandstones," *International Society of Offshore and Polar Engineers*, vol. 22, no. 4, pp. 297–305, 2012.

## Research Article

# Effect of Selected Nanospheres on the Mechanical Strength of Lime-Stabilized High-Plasticity Clay Soils

Ali Ghorbani ,<sup>1</sup> Hadi Hasanzadehshooili ,<sup>1</sup> Mostafa Mohammadi,<sup>1</sup> Fariborz Sianati,<sup>2</sup> Mahdi Salimi,<sup>1</sup> Lukasz Sadowski ,<sup>3</sup> and Jacek Szymanowski<sup>3</sup>

<sup>1</sup>Department of Civil Engineering, Faculty of Engineering, University of Guilan, Rasht, Guilan, Iran

<sup>2</sup>Pardis Branch, University of Guilan, Rasht, Guilan, Iran

<sup>3</sup>Faculty of Civil Engineering, Wroclaw University of Science and Technology, Wybrzeze Wyspianskiego 37, 50-370 Wroclaw, Poland

Correspondence should be addressed to Ali Ghorbani; ghorbani@guilan.ac.ir

Received 20 December 2018; Revised 26 February 2019; Accepted 24 March 2019; Published 30 April 2019

Academic Editor: Chiara Bedon

Copyright © 2019 Ali Ghorbani et al. This is an open access article distributed under the Creative Commons Attribution License, which permits unrestricted use, distribution, and reproduction in any medium, provided the original work is properly cited.

The proper design of protective structures may start from improving the characteristics of soils. In order to obtain reasonable safety criteria, several research studies have recently been dedicated to enhancing complex civil engineering structural systems with the use of nanotechnology. Thus, the following paper investigates the effect of nanospheres, including nanosilica (nano-SiO<sub>2</sub>) and nano zinc oxide (nano-ZnO), on lime-stabilized high-plasticity clay soil. For this purpose, unconfined compressive strength (UCS) and California bearing ratio (CBR) tests were performed on samples. The results showed that the use of the selected nanospheres greatly increased the UCS of the samples compared to untreated soil. The UCS value of samples containing 6% lime and 1.5% nano-ZnO after 28 days of treatment increased by 5-fold compared to the UCS of untreated samples. In addition, the samples containing 6% lime and 2% nano-SiO<sub>2</sub>, with similar curing conditions, experienced a 5.3-fold increase in their UCS value compared to the untreated samples. These compounds were considered as the optimal amounts and showed the highest mechanical strength in both UCS and CBR tests. The same trend was achieved in the CBR test, in which the CBR value for the optimal mixtures containing nano-ZnO and nano-SiO<sub>2</sub> was 14.8 and 16.6 times higher than that of high-plasticity clay soil, respectively. Finally, the results obtained from scanning electron microscopy (SEM) analysis revealed that the nanospheres caused a dense and compact matrix to form in the soil, which led to the enhancement of the mechanical strength of the treated samples.

## 1. Introduction

When designing protective structures, high-plasticity clay soils, which are widely scattered throughout the world, are very problematic. This is mainly due to the fact that they are highly sensitive after being exposed to moisture. The presence of these soils in construction projects should be specifically addressed and treated if necessary due to their undesirable behaviour such as swelling, shrinkage, dispersion, low mechanical strength, and high level of settlement [1–3]. To overcome such problems, several approaches are available to treat them, including the use of geosynthetics, piles, electroosmosis techniques, and stabilization [4–14]. These methods can lead to increased mechanical strength,

reduced settlement, and controlled swelling or shrinking of soils, as well as providing a suitable site for the construction of structures. Among these methods, stabilization with the use of chemical additives, most notably lime and cement, is considered as one of the most effective techniques to improve the characteristics of soil [15–18].

In the past few decades, many studies have been conducted on the chemical stabilization of soils using these traditional materials [19–26]. The use of such stabilizers increases the soil pH up to about 12, which in turn provides long-term reactions. Khemissa and Mahamedi [27] determined the physicochemical and mechanical parameters of high-plasticity clay stabilized with a mixture of Portland cement and extinct lime. They found that the geotechnical

parameters are consistent and confirmed the enhancement of the bearing capacity of high-plasticity clay soil, which is interpreted by a substantial increase in its mechanical strength and durability. A summary of recent studies on soil stabilization by other researchers is presented in Table 1. Despite ongoing research on soil stabilization with traditional materials, there is a need to find new and better performing materials to replace conventional additives.

In order to obtain reasonable safety criteria, several research studies have recently been dedicated to enhancing complex civil engineering structural systems using nanotechnology. Nanodimension stabilizers are highly effective in soil stabilization from both physical and chemical viewpoints. Nanospheres have a particularly high specific surface area and are therefore more involved in chemical reactions [31]. Moreover, the very fine particles of nanospheres may improve the characteristics of soil [37].

Nano-SiO<sub>2</sub> and nano-ZnO are two types of additives that have very good properties in combination with soil. In recent years, these nanospheres have attracted great research interest because of their high pozzolanic activity in cement-based systems. According to Mostafa et al. [38], the addition of nano- and micro-SiO<sub>2</sub> to lime-stabilized soil improved its mechanical strength values and its compressive strength increased with a lower nano-SiO<sub>2</sub> content compared to silica fume. Saleh et al. [39] showed that the addition of nano-SiO<sub>2</sub> and nano-ZnO improves soil behaviour. Similar results have been reported by other researchers when using these materials, as can be seen in Table 1. Despite the numerous studies on the use of these materials in soil stabilization, less attention has been paid to their combination with lime. In addition, it should be noted that the application of these effective additives on the mechanical properties of high-plasticity clay soils has not yet been investigated.

The high-plasticity clay soil in the present study does not have a sufficient mechanical strength and causes severe damage to a construction built on it due to the weak structure of soil particles. Therefore, finding a reliable and practical technique was the main goal of this research. In this study, the effect of nano-SiO<sub>2</sub> and nano-ZnO on the mechanical strength parameters of high-plasticity clay soil stabilized with lime was investigated and their microstructural changes were carefully considered. For this purpose, unconfined compressive strength (UCS) and California bearing ratio (CBR) tests were performed on samples. In addition, scanning electron microscopy (SEM) analysis was applied to observe the microstructural properties.

## 2. Materials and Methods

**2.1. Properties of High-Plasticity Clay Soil.** The high-plasticity clay soil that was used in this study was collected from a depth of 1 m at an excavation site within the University of Guilan (5th kilometer of the Rasht-Tehran road). Based on the UCS value obtained from the studied clay (174.55 kPa), it was stated that the soil of this region exhibits very low strength and consequently would not withstand the loads imposed upon it. Moreover, the poor particle-size distribution shown in Figure 1 indicates the lack of mechanical

strength of the soil and the necessity of soil stabilization before any further operations. Due to the low mechanical strength and high compressibility of soil in this region, the soil is considered to be problematic. Since the soil in this area is subjected to heavy loads during the construction of high-rise buildings, it is important to improve its mechanical strength properties. Figure 1 shows the particle-size distribution of the studied high-plasticity clay soil according to ASTM D2487-11 [40]. Some of the properties of the studied soil, determined based on ASTM D4318 [41], are presented in Table 2. Moreover, the standard compaction test was carried out according to ASTM D698 [42]; and the maximum dry density (MDD) and optimum moisture content (OMC) of the samples were 1470 kg/m<sup>3</sup> and 23%, respectively. The results of the chemical analysis obtained from X-ray fluorescence analysis are presented in Table 3.

**2.2. Properties of Hydrated Lime.** The hydrated lime used in this study was obtained from Qom Limestone Factory and contained about 51% quick lime (CaO) with particles finer than sieve No. 60 (0.250 mm). Table 4 shows the chemical properties of the lime, which were provided by the manufacturer.

**2.2.1. Properties of the Studied Nanospheres.** In this study, lime was replaced by 1, 1.5, and 2% of nanospheres including nano-SiO<sub>2</sub> and nano-ZnO with average sizes of 20–30 and 30–50 nm and surface areas of 220 m<sup>2</sup>/g and 50 m<sup>2</sup>/g, respectively. In this research, regardless of the specifications given by the nanomaterial manufacturer, the specific surface area of the nanospheres was measured by nitrogen adsorption at 77 K by using the Brunauer–Emmett–Teller (BET) method. The nanospheres were obtained from the Iranian Pishgaman Nanomaterial Company. In this study, particle-size distribution was calculated for each nanosphere sample from the SEM images by using ImageJ software. Then, the number of pixels occupied by the number of particles was counted. It should be noted that ImageJ software has been used for postprocessing and particle analysis by many researchers. Figure 2 shows the SEM microstructure and the particle size of nano-SiO<sub>2</sub> and nano-ZnO. The properties of both nanospheres are given in Table 5.

## 2.3. Description of Conducted Laboratory Tests

**2.3.1. Sample Preparation Process.** The results of previous studies have shown that the characteristics of soil improve to a certain extent, with the use of additives, and that higher amounts of them can have adverse effects on soil strength. In order to obtain the most favourable mixture of lime-nanospheres, the ratio of cementitious materials should be strongly considered due to the fact that the replacement of larger amounts of lime-nanospheres can lead to a poor mixture with lower strength. Therefore, the optimum amount of nanospheres as a substitute for lime can only be determined by trial and error. By and large, based on the results of previous studies, the optimum amount of lime in

TABLE 1: Examples of recent soil stabilization research.

Reference	Soil type	Stabilizer type	Curing time (days)	Tests
Yi et al. [28]	Soft high-plasticity clay	Lime, GGBS	7, 28, 90	UCS, MIP
Ghorbani et al. [22]	Sulfate silty sand	Lime, micro-SiO <sub>2</sub>	7, 28	UCS, CBR
Choobbasti et al. [29]	Sandy soil	Cement, nano-SiO <sub>2</sub>	7	UCS
Bahmani et al. [30]	High-plasticity clay soil	Cement, nano-SiO <sub>2</sub>	7, 14, 28	UCS
Ghasabkolaei et al. [31]	High-plasticity clay soil	Cement, nano-SiO <sub>2</sub>	7, 14, 28	UCS, CBR
Yoobanpot et al. [32]	Soft high-plasticity clay	Cement, fly ash residue	3, 7, 28, 90	UCS
Alnahhal et al. [33]	Sand	OPC, CKD, nano-CKD	7, 28, 56	UCS
García et al. [34]	Soft high-plasticity clay	Nano-SiO <sub>2</sub>	—	UCS
Sharma et al. [25]	High-plasticity clayey sand	Lime, cement	1, 3, 7, 14, 21, 28	UCS, shear strength
Abbasi et al. [35]	Dispersive high-plasticity clayey soils	Nano-high-plasticity clay	1, 3, 7	Pinhole
Choobbasti et al. [36]	Sand	Cement, nano-SiO <sub>2</sub>	7	UCS, triaxial

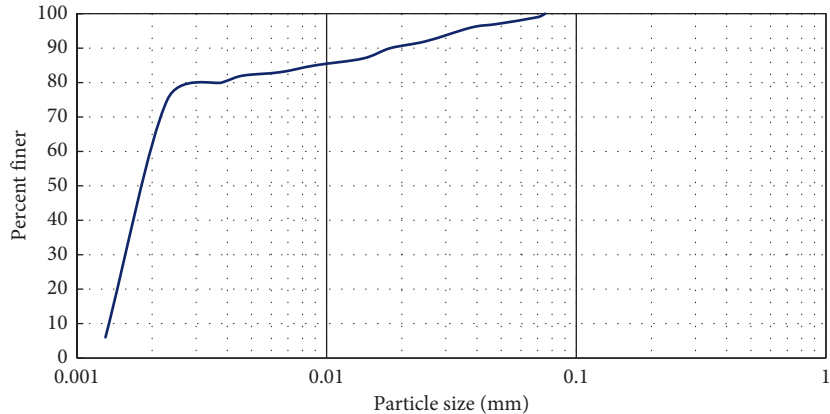


FIGURE 1: Particle-size distribution of the studied high-plasticity clay soil (obtained according to ASTM D2487-11 [40]).

TABLE 2: Physical properties and Atterberg limits of the studied high-plasticity clay soil.

Parameter	Value
$G_s$	2.7
Liquid limit (LL) (%)	62.5
Plastic limit (PL) (%)	30.11
Plasticity index (PI) (%)	32.39
Maximum dry density (MDD) (kg/m <sup>3</sup> )	1470
Optimum moisture content (OMC) (%)	23
Unconfined compressive strength (UCS) (kPa)	174.55
Unsoaked California bearing ratio (CBR) (%)	4.9

TABLE 3: Chemical compositions of the studied high-plasticity clay soil (obtained from X-ray fluorescence analysis).

Formula	Content (%)
SiO <sub>2</sub>	53.9
Al <sub>2</sub> O <sub>3</sub>	16.4
CaO	3.14
Fe <sub>2</sub> O <sub>3</sub>	8.8
MgO	2.0
K <sub>2</sub> O	5.2
Na <sub>2</sub> O	0.57
P <sub>2</sub> O <sub>5</sub>	0.1
TiO <sub>2</sub>	0.79
Other particles	0.2
L.O.I	8.9

TABLE 4: Chemical compositions of hydrated lime (provided by the manufacturer).

Formula	Content (%)
K <sub>2</sub> O	4
SO <sub>3</sub>	0.8
MgO	2.65
CaO	51.64
Fe <sub>2</sub> O <sub>3</sub>	0.13
Al <sub>2</sub> O <sub>3</sub>	0.24
SiO <sub>2</sub>	1.36
L.O.I	39.18

clay soil stabilization has been reported to be between 4 and 8 [23, 43–45], which is consistent with the specified values in this study. Thus, the amounts of 3, 6, and 9% by weight of lime were added to the soil to determine the optimum amount of lime. Based on the results, 6% lime content had the highest mechanical strength and was considered as the optimum value. Then, the amounts of 1, 1.5, and 2% by weight of nano-SiO<sub>2</sub> or nano-ZnO with the optimum amount of lime (6%) were added to the soil, as presented in Table 6. The dry soil and additives (lime and nanospheres) were stirred with about 50% of the total amount of water needed to obtain the optimum moisture content. After that, the soil and admixture were mixed manually and the remaining water was added to bring the sample to the

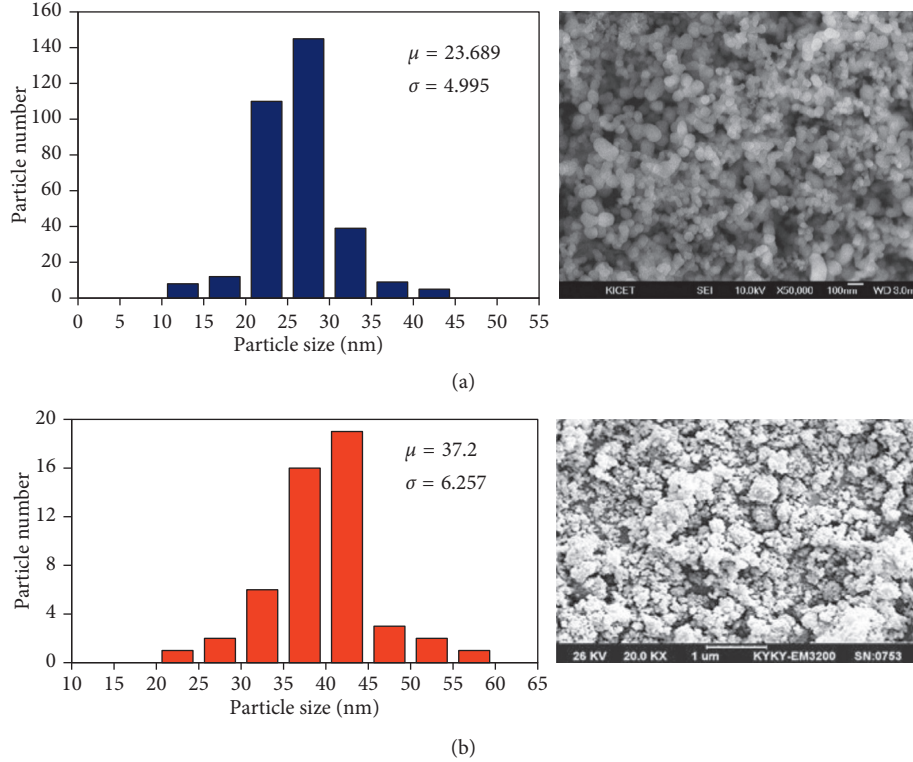


FIGURE 2: SEM microstructure and particle size of nanospheres: (a) nano- $\text{SiO}_2$  and (b) nano-ZnO.

TABLE 5: Selected properties of studied nanospheres.

Name of the property	Nano- $\text{SiO}_2$	Nano-ZnO
Color	White	White
Average particle sizes (nm)	20–30	30–50
pH	7	6
Specific surface area (SSA) ( $\text{m}^2/\text{kg}$ )	220000	50000
Purity (%)	98.31	99.14

TABLE 6: Mixture proportions of used materials.

Test no.	Lime (%)	Nano- $\text{SiO}_2$ (%)	Nano-ZnO (%)
1	3	0	0
2	6	0	0
3	9	0	0
4	6	1	0
5	6	1.5	0
6	6	2	0
7	6	0	1
8	6	0	1.5
9	6	0	2

Each test was performed three times.

desired moisture content. It should be noted that all the samples were prepared at maximum dry density and optimum moisture content. Finally, SEM analysis (model VEGA/TESCAN) was applied to the samples in order to observe changes in soil microstructure and to investigate the interaction between the soil and additives. For SEM observation, the samples were mounted on stubs with

aluminum tape and then coated in a sputter coater with 20 nm of gold at an accelerating voltage of 10–15 kV.

**2.3.2. Unconfined Compressive Strength.** To carry out the unconfined compressive strength test according to ASTM D2166-91 [46], the soil, additives, and water were mixed with different proportions and then compacted into a mould in three layers with 25 blows/layer. The mould had a height and diameter of 9.8 and 4.9 cm, respectively. The samples were packed into airtight containers and stored at 25°C with respect to the curing time of 7, 14, and 28 days. The unconfined compressive strength (UCS) loading was carried out with a fixed displacement rate of 1 mm/min and continued until the initial failure of the samples. Figure 3 shows the cylindrical mould, the prepared samples, and the sample under loading in the UCS test.

**2.3.3. California Bearing Ratio Tests.** To carry out the unsoaked California bearing ratio (CBR) test according to ASTM D1883-16 [47], the dry soil and additives were mixed for each sample individually and then water was added to them to achieve the optimum moisture content. After that, they were thoroughly mixed to obtain uniform samples. A cylindrical mould with a diameter of 6 inches and a height of 4.8 inches was used to perform the tests. The compounds were placed into the mould in 5 layers so that each layer was packed with 56 blows of a 4.5 kg hammer dropped from a height of 457 mm, according to ASTM D1557 [48]. Then, the



FIGURE 3: Unconfined compressive strength test: (a) mould, (b) prepared samples, and (c) sample under loading.

mould containing the materials was placed in an airtight plastic bag to ensure that no moisture was lost. Finally, the mould was placed inside the CBR apparatus, and the test was conducted with a penetration rate of 1.27 mm/min after 7 days of treatment. According to Spanish legislation, the CBR index has been referred to as the only way of evaluating the bearing capacity of treated soil with chemical additives, and the minimum CBR index is considered to be higher than or equal to 20 after 7 days [49]. Therefore, a 7-day treatment was conducted in order to evaluate and compare the CBR results. Figure 4 shows the mould, the prepared samples after 7 days of curing, and the CBR apparatus used in the study.

### 3. Results and Discussion

**3.1. Effect of Nanospheres on Unconfined Compressive Strength.** Figure 5 illustrates the effect of lime on the unconfined compressive strength (UCS) of high-plasticity clay soil over curing time. As can be seen, the UCS increased and reached its maximum resistance with the addition of lime of

up to 6%, whereas the UCS value was reduced for higher amounts of lime. The presence of lime in the samples increased the pH value of the soil and provided the conditions for long-term pozzolanic reactions. Moreover, the increase in curing time also resulted in an improved mechanical strength in all the samples, which was due to the completion of chemical reactions. The maximum strength was recorded as 876 kPa after 28 days of treatment for the sample containing 6% lime. Higher amounts of lime, however, reduce the UCS of the soil due to the lack of significant friction and low cohesion [50]. Moreover, the MDD and OMC values of untreated soil change as soon as additives are added to the soil. This may also affect the optimum lime content, and as a result, the UCS values reduce for a higher lime content. Finally, it can be concluded that the optimum amount of lime for pozzolanic reactions in the soil samples was determined to be 6%, and this amount was selected for subsequent experiments with nanospheres.

Figures 6 and 7 show the variations of soil UCS for various combinations of lime with nano-zinc and nano-SiO<sub>2</sub>



FIGURE 4: California bearing ratio test: (a) mould, (b) samples after 7 days of curing, and (c) California bearing ratio test apparatus.

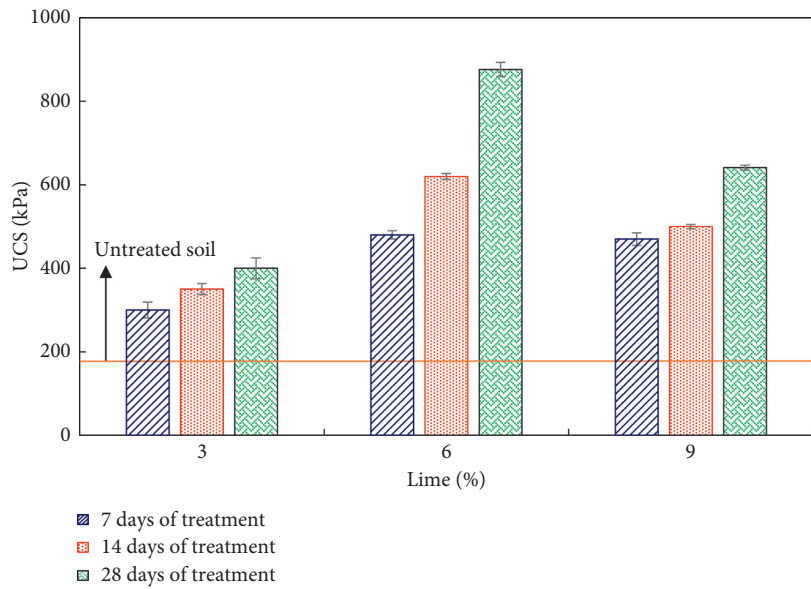


FIGURE 5: Effect of lime on the UCS of soil after a curing time of up to 28 days.

during different treatment periods, respectively. The UCS value increased in all the samples with the increase of curing time, and therefore, the sample containing 6% lime with 1% nano-ZnO had a strength equal to 867 and 500 kPa after 7 and 28 days of treatment, respectively. These values were equal to 881 and 598 kPa for the same samples of nano-SiO<sub>2</sub>, respectively. Based on Figure 6, the addition of 1.5% of nano-ZnO to the samples increased the UCS to a maximum value. By adding further amounts of nano-ZnO, the strength decreased slightly. Therefore, the optimum amount of nano-ZnO in combination with 6% lime was reported as 1.5%, which resulted in a 5-fold increase after 28 days of treatment compared to the untreated soil. Moreover, the UCS increased by adding up to 2% of nano-SiO<sub>2</sub> to the optimum lime content (6%) so that it reached the highest level of 1000 kPa after 28 days of treatment,

which is equivalent to an increase of about 5.3 times compared to that of untreated soil.

In general, the increase of UCS by adding different compounds can be attributed to short- and long-term reactions. Pozzolanic reactions lead to the formation of calcium silicate hydrate (CSH) and calcium aluminate hydrate (CAH) gels that fill the voids and thus increase the UCS of the samples [51, 52]. Based on the Figures 6 and 7, the optimum value of nano-ZnO and nano-SiO<sub>2</sub> in combination with 6% lime was reported at 1.5 and 2%, respectively. Moreover, the results indicated a better performance of nano-SiO<sub>2</sub> than nano-ZnO.

**3.2. Effect of Additives on CBR.** In this study, the CBR test was performed after 7 days of treatment in order to more

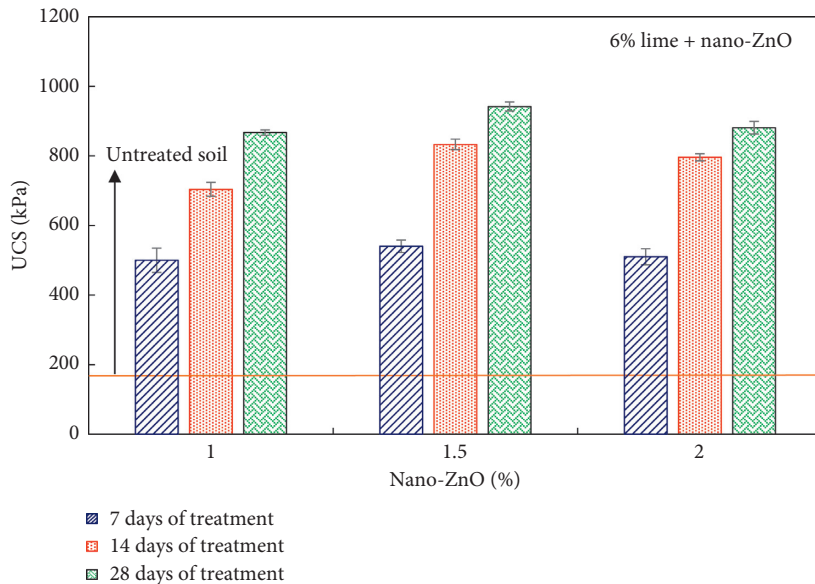


FIGURE 6: Effect of nano-ZnO on the UCS of lime-stabilized soil after a curing time of up to 28 days.

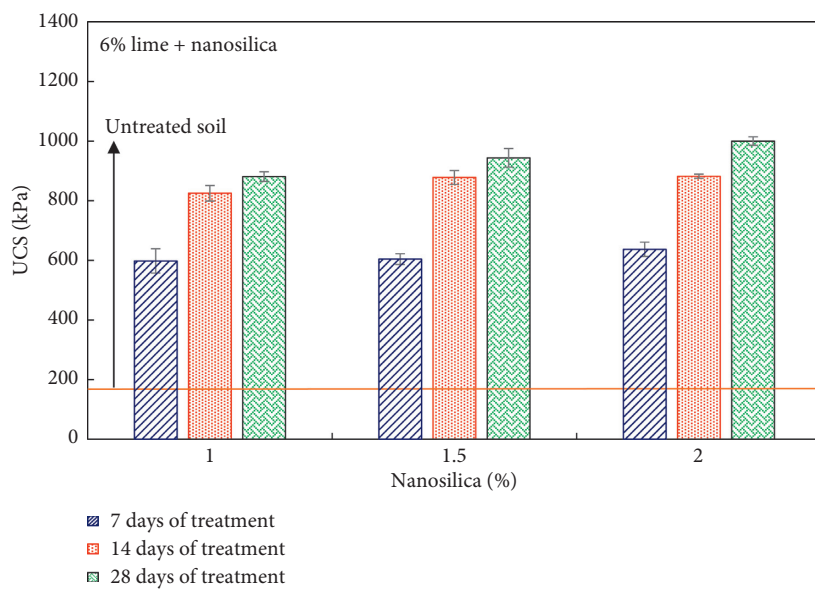


FIGURE 7: Effect of nano-SiO<sub>2</sub> on the UCS of lime-stabilized soil after a curing time of up to 28 days.

accurately evaluate the mechanical strength behaviour in all the samples. Figure 8 shows the results of the CBR for the lime-stabilized samples, and it can be seen that adding the lime increased the CBR, which demonstrated a peak for the lime content of 6%. The CBR value for this optimum amount of lime was reported at about 56.9%. Afterwards, the CBR value was reduced by adding more lime, which was similar to the trend of UCS values. A CBR of about 50% was obtained for the sample containing 9% lime, which was about 10 times higher than that of untreated soil.

For samples containing nano-ZnO, the CBR value increased with an increasing amount of nanospheres, as shown in Figure 9. The sample containing 1.5% of nano-ZnO exhibited the highest CBR (about 72.6%), which was

consistent with the UCS test. Increasing the nano-ZnO content by more than 1.5% resulted in a decrease in the CBR value to about 62.8%. However, in the samples containing up to 2% nano-SiO<sub>2</sub> content, the amount of CBR continued to increase, reaching a peak of about 81.4%, as illustrated in Figure 10. This amount was reported to be about 74.3% and 77.9% for the content of 1% and 1.5% of nano-SiO<sub>2</sub>, respectively, which showed a significant increase compared to the untreated soil. Similar to what was observed for the UCS, the performance of nano-SiO<sub>2</sub> was also slightly better than that of nano-ZnO.

**3.3. Effect of Nanospheres on the Microstructure.** In this study, the SEM technique was applied to monitor structural

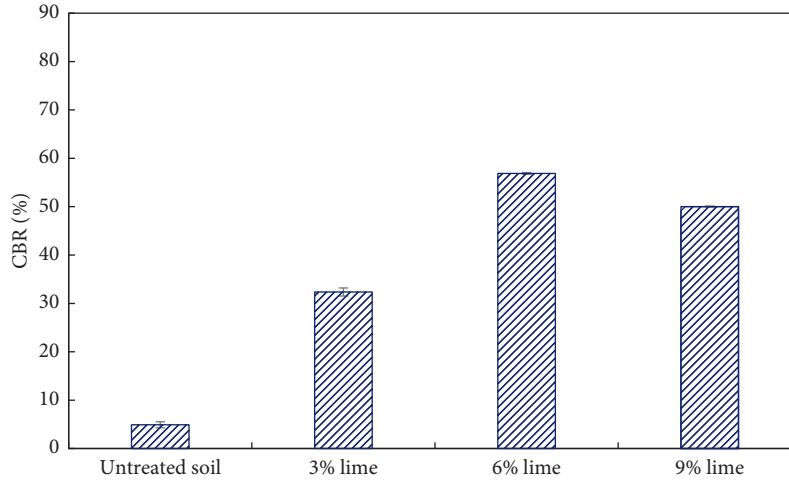


FIGURE 8: Effect of lime on the CBR of soil after 7 days of treatment.

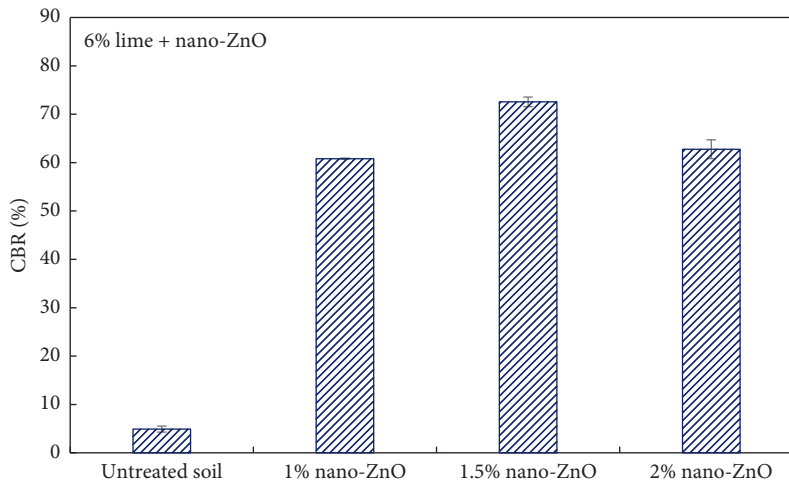


FIGURE 9: Effect of nano-ZnO on the CBR of lime-stabilized soil after 7 days of treatment.

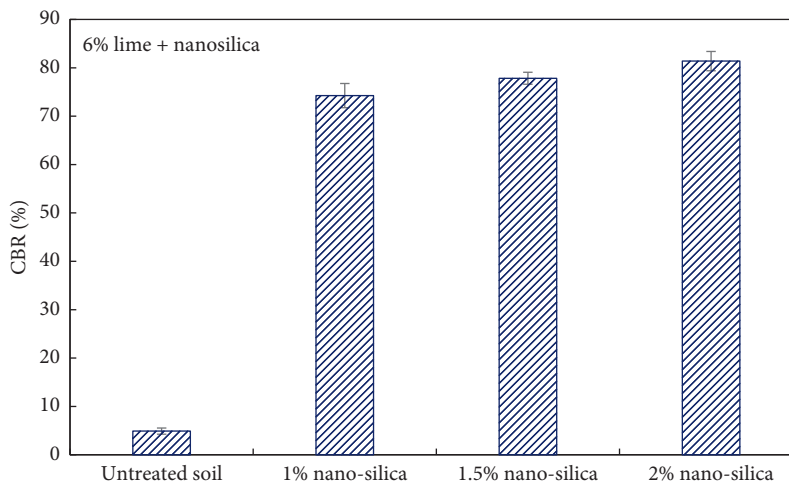


FIGURE 10: Effect of nano-SiO<sub>2</sub> on the CBR of lime-stabilized soil after 7 days of treatment.

changes and to better understand the interactions between the soil and additives. For this purpose, in addition to the untreated soil sample, two samples treated with additives

that provided the highest mechanical strength (6% lime + 1.5% nano-ZnO and 6% lime + 2% nano-SiO<sub>2</sub>) were analyzed. The SEM images of these three samples are shown

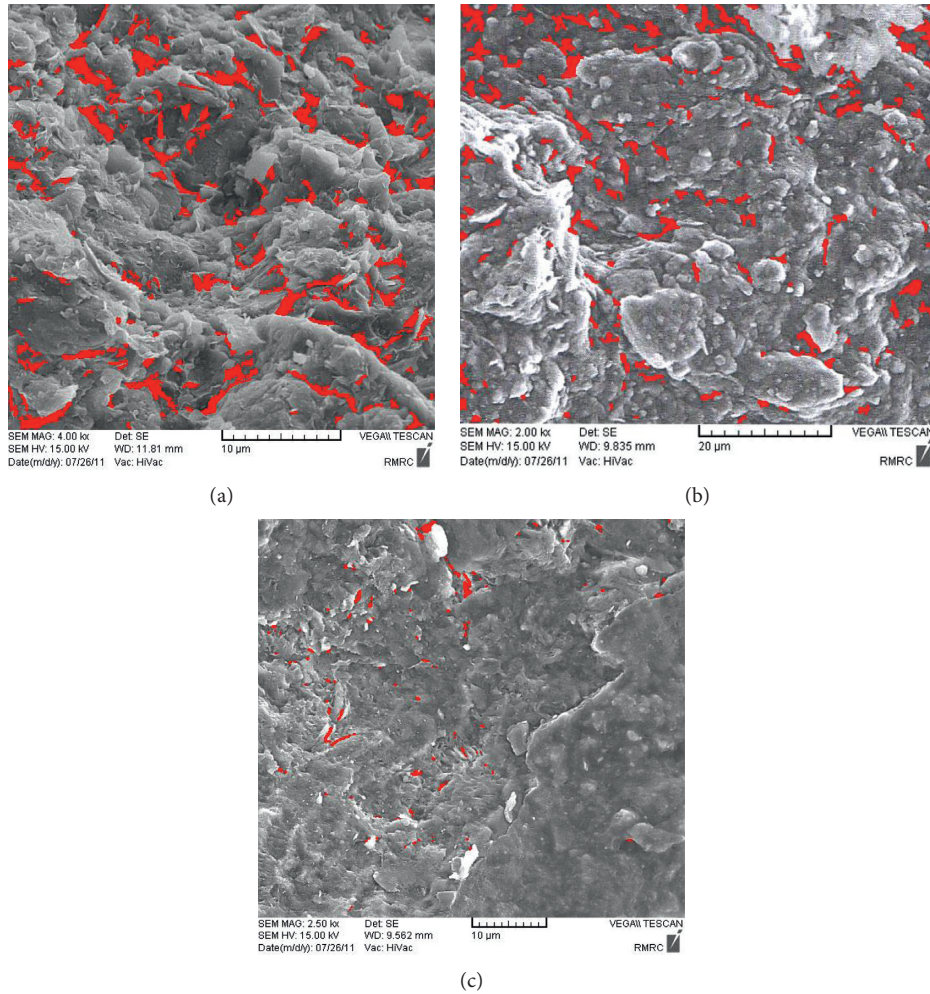


FIGURE 11: SEM micrographs: (a) the high-plasticity clay soil, (b) 6% lime + 1.5 nano-ZnO, and (c) 6% lime + 2% nano-SiO<sub>2</sub>.

in Figure 11 in such a way that the porosity is shown as red particles. As seen in Figure 11(a), the untreated soil texture is completely porous (about 9.03%), which leads to very poor results in UCS and CBR tests. Figure 11(b) shows that the increase of additive containing nano-ZnO to the untreated soil led to a decrease in porosity from 9.03% to 5.73%. This causes more friction between particles, resulting in much greater mechanical strength compared to the pure soil. Figure 11(c) shows the sample containing nano-SiO<sub>2</sub>, which had the highest strength and the minimum porosity of approximately 0.82%. In this sample, the soil particles form a dense and compact matrix and are easily detected in the cementitious gel that covers the particles. On the one hand, nano-SiO<sub>2</sub> serves as a filler, and on the other hand, it acts as a very effective pozzolan with lime and improves the bond between particles [53, 54].

#### 4. Conclusions

The purpose of this study was to evaluate the effect of nanoscale materials, including nano-ZnO and nano-SiO<sub>2</sub>, on lime-stabilized high-plasticity clay soils. For this purpose, a series of UCS and CBR tests were performed on samples, and later, based on SEM images, soil

microstructure changes before and after treatment were investigated. Nanospheres have a much higher surface area because of their very small size, and they therefore participate in the reactions and accelerate the formation of cementitious products. Moreover, these materials are placed between lime and soil particles and fill voids, which increases the mechanical strength of the samples. Based on the tests performed on various compounds, the following results were obtained:

- (i) The addition of nano-ZnO and lime to soil increased UCS in such a way that the optimum nano-ZnO value in a mixture with 6% lime was reported to be 1.5%, which led to a 5-fold increment after 28 days of curing compared to that of untreated soil.
- (ii) The addition of nano-SiO<sub>2</sub> to lime-stabilized soil resulted in an increased mechanical strength, meaning that a UCS value of about 1000 kPa was measured in the sample containing 6% lime + 2% nano-SiO<sub>2</sub> after 28 days of curing, which is equivalent to about 5.3 times that of the untreated soil.
- (iii) In all the samples, an increased curing time resulted in an increased UCS, which can be attributed to the completion of long-term pozzolanic reactions and

- the formation of calcium silicate hydrate and calcium hydrate aluminate gels.
- (iv) Based on the results obtained from the CBR test, it was found that the performance of nano-SiO<sub>2</sub> was slightly better than that of nano-ZnO. The CBR value was reported to be about 81.1% for the sample containing nano-SiO<sub>2</sub>, while the highest CBR value for the nano-ZnO samples was about 72.6%. This increased performance was significant compared to untreated soil (4.9%).
- ## Data Availability
- No data were used to support this study.
- ## Conflicts of Interest
- The authors declare that they have no conflicts of interest.
- ## References
- [1] F. Darikandeh and B. V. S. Viswanadham, "Swell behavior of expansive soils with stabilized fly ash columns," in *Ground Improvement Techniques and Geosynthetics*, pp. 399–406, Springer, Singapore, 2019.
  - [2] A. K. Jha and P. V. Sivapullaiah, "Mechanism of improvement in the strength and volume change behavior of lime stabilized soil," *Engineering Geology*, vol. 198, pp. 53–64, 2015.
  - [3] A. Soltani, A. Taheri, M. Khatibi, and A. R. Estabragh, "Swelling potential of a stabilized expansive soil: a comparative experimental study," *Geotechnical and Geological Engineering*, vol. 35, no. 4, pp. 1717–1744, 2017.
  - [4] A. Afrasiabian, M. Salimi, M. Movahedrad, and A. H. Vakili, "Assessing the impact of GBFS on mechanical behaviour and microstructure of soft clay," *International Journal of Geotechnical Engineering*, pp. 1–11, 2019.
  - [5] A. R. Goodarzi and M. Salimi, "Stabilization treatment of a dispersive clayey soil using granulated blast furnace slag and basic oxygen furnace slag," *Applied Clay Science*, vol. 108, pp. 61–69, 2015.
  - [6] A. R. Goodarzi and M. Salimi, "Effect of iron industry slags on the geotechnical properties and mineralogy characteristics of expansive clayey soils," *Modares Journal of Civil Engineering*, vol. 15, no. 2, pp. 161–170, 2015.
  - [7] A. Ghorbani, M. Salimzadehshooiili, J. Medzvieckas, and R. Kliukas, "Strength characteristics of cement-rice husk ash stabilised sand-clay mixture reinforced with polypropylene fibers," *Baltic Journal of Road and Bridge Engineering*, vol. 13, no. 4, pp. 447–474, 2018.
  - [8] A. Ghorbani and H. Hasanzadehshooiili, "Prediction of UCS and CBR of microsilica-lime stabilized sulfate silty sand using ANN and EPR models: application to the deep soil mixing," *Soils and Foundations*, vol. 58, no. 1, pp. 34–49, 2018.
  - [9] B. Ghosh, B. Fatahi, H. Khabbaz, and J.-H. Yin, "Analytical study for double-layer geosynthetic reinforced load transfer platform on column improved soft soil," *Geotextiles and Geomembranes*, vol. 45, no. 5, pp. 508–536, 2017.
  - [10] E. B. Khoshbakht, A. H. Vakili, M. S. Farhadi, and M. Salimi, "Reducing the negative impact of freezing and thawing cycles on marl by means of the electrokinetical injection of calcium chloride," *Cold Regions Science and Technology*, vol. 157, pp. 196–205, 2019.
  - [11] A. Soltani, A. Deng, A. Taheri, and M. Mirzababaei, "Rubber powder-polymer combined stabilization of South Australian expansive soils," *Geosynthetics International*, vol. 25, no. 3, pp. 304–321, 2018.
  - [12] A. H. Vakili, M. Kaedi, M. Mokhberi, M. R. b. Selamat, and M. Salimi, "Treatment of highly dispersive clay by lignosulfonate addition and electroosmosis application," *Applied Clay Science*, vol. 152, pp. 1–8, 2018.
  - [13] A. H. Vakili, J. Ghasemi, M. R. bin Selamat, M. Salimi, and M. S. Farhadi, "Internal erosional behaviour of dispersive clay stabilized with lignosulfonate and reinforced with polypropylene fiber," *Construction and Building Materials*, vol. 193, pp. 405–415, 2018.
  - [14] M. M. Yamin, M. F. Attom, and R. Y. Liang, "Solutions for soil-pile-soil forces in pile stabilized slopes," *Geotechnical and Geological Engineering*, vol. 35, no. 4, pp. 1859–1869, 2017.
  - [15] A. H. Vakili, M. R. B. Selamat, M. Salimi, and S. G. Gararei, "Evaluation of pozzolanic Portland cement as geotechnical stabilizer of a dispersive clay," *International Journal of Geotechnical Engineering*, pp. 1–8, 2019.
  - [16] A. Behnood, "Soil and clay stabilization with calcium- and non-calcium-based additives: a state-of-the-art review of challenges, approaches and techniques," *Transportation Geotechnics*, vol. 17, pp. 14–32, 2018.
  - [17] A. R. Goodarzi, H. R. Akbari, and M. Salimi, "Enhanced stabilization of highly expansive clays by mixing cement and silica fume," *Applied Clay Science*, vol. 132–133, pp. 675–684, 2016.
  - [18] Ł. Sadowski, M. Nikoo, and M. Nikoo, "Hybrid metaheuristic-neural assessment of the adhesion in existing cement composites," *Coatings*, vol. 7, no. 4, p. 49, 2017.
  - [19] M. Al-Mukhtar, A. Lasledj, and J.-F. Alcover, "Behaviour and mineralogy changes in lime-treated expansive soil at 20°C," *Applied Clay Science*, vol. 50, no. 2, pp. 191–198, 2010.
  - [20] H. Chen and Q. Wang, "The behaviour of organic matter in the process of soft soil stabilization using cement," *Bulletin of Engineering Geology and the Environment*, vol. 65, no. 4, pp. 445–448, 2006.
  - [21] M. Cong, C. Longzhu, and C. Bing, "Analysis of strength development in soft clay stabilized with cement-based stabilizer," *Construction and Building Materials*, vol. 71, pp. 354–362, 2014.
  - [22] A. Ghorbani, H. Hadi, K. Masoud, D. Younes, and M. Jurgis, "Stabilization of problematic silty sands using microsilica and lime," *Baltic Journal of Road & Bridge Engineering*, vol. 10, no. 1, pp. 61–70, 2015.
  - [23] H. B. Nagaraj, M. V. Sravan, T. G. Arun, and K. S. Jagadish, "Role of lime with cement in long-term strength of compressed stabilized earth blocks," *International Journal of Sustainable Built Environment*, vol. 3, no. 1, pp. 54–61, 2014.
  - [24] M. Salimi, M. Ilkhani, and A. H. Vakili, "Stabilization treatment of Na-montmorillonite with binary mixtures of lime and steelmaking slag," *International Journal of Geotechnical Engineering*, pp. 1–7, 2018.
  - [25] L. K. Sharma, N. N. Sirdesai, K. M. Sharma, and T. N. Singh, "Experimental study to examine the independent roles of lime and cement on the stabilization of a mountain soil: a comparative study," *Applied Clay Science*, vol. 152, pp. 183–195, 2018.
  - [26] R. N. Yong and V. R. Ouhadi, "Experimental study on instability of bases on natural and lime/cement-stabilized clayey soils," *Applied Clay Science*, vol. 35, no. 3–4, pp. 238–249, 2007.

- [27] M. Khemissa and A. Mahamedi, "Cement and lime mixture stabilization of an expansive overconsolidated clay," *Applied Clay Science*, vol. 95, pp. 104–110, 2014.
- [28] Y. Yi, L. Gu, and S. Liu, "Microstructural and mechanical properties of marine soft clay stabilized by lime-activated ground granulated blastfurnace slag," *Applied Clay Science*, vol. 103, pp. 71–76, 2015.
- [29] A. J. Choobbasti, A. Vafaei, and S. S. Kutanaei, "Mechanical properties of sandy soil improved with cement and nanosilica," *Open Engineering*, vol. 5, no. 1, 2015.
- [30] S. H. Bahmani, N. Farzadnia, A. Asadi, and B. B. K. Huat, "The effect of size and replacement content of nanosilica on strength development of cement treated residual soil," *Construction and Building Materials*, vol. 118, pp. 294–306, 2016.
- [31] N. Ghasabkolaei, A. Janalizadeh, M. Jahanshahi, N. Roshan, and S. E. Ghasemi, "Physical and geotechnical properties of cement-treated clayey soil using silica nanoparticles: an experimental study," *European Physical Journal Plus*, vol. 131, no. 5, p. 134, 2016.
- [32] N. Yoobanpot, P. Jamsawang, and S. Horpibulsuk, "Strength behavior and microstructural characteristics of soft clay stabilized with cement kiln dust and fly ash residue," *Applied Clay Science*, vol. 141, pp. 146–156, 2017.
- [33] W. Alnahhal, R. Taha, H. Al-Nasseri, and S. Nishad, "Effect of using Cement Kiln Dust as a nano-material on the strength of cement mortars," *KSCE Journal of Civil Engineering*, vol. 22, no. 4, pp. 1361–1368, 2018.
- [34] S. García, P. Trejo, O. Ramírez, J. López-Molina, and N. Hernández, "Influence of nanosilica on compressive strength of lacustrine soft clays," in *Proceedings of the 19th International Conference on Soil Mechanics and Geotechnical Engineering*, pp. 369–372, Seoul, Korea, September 2017.
- [35] N. Abbasi, A. Farjad, and S. Sepehri, "The use of nanoclay particles for stabilization of dispersive clayey soils," *Geotechnical and Geological Engineering*, vol. 36, no. 1, pp. 327–335, 2018.
- [36] A. J. Choobbasti, A. Vafaei, and S. Soleimani Kutanaei, "Static and cyclic triaxial behavior of cemented sand with nanosilica," *Journal of Materials in Civil Engineering*, vol. 30, no. 10, article 04018269, 2018.
- [37] S. Bahri, H. B. Mahmud, and P. Shafiq, "Effect of utilizing unground and ground normal and black rice husk ash on the mechanical and durability properties of high-strength concrete," *Sādhanā*, vol. 43, no. 2, p. 22, 2018.
- [38] A. Mostafa, M. S. Ouf, and M. Elgendi, "Stabilization of subgrade pavement layer using silica fume and nano silica," *International Journal of Scientific & Engineering Research*, vol. 7, no. 3, 2016.
- [39] H. M. Saleh, F. A. El-Saied, T. A. Salaheldin, and A. A. Hezo, "Macro-and nanomaterials for improvement of mechanical and physical properties of cement kiln dust-based composite materials," *Journal of Cleaner Production*, vol. 204, pp. 532–541, 2018.
- [40] ASTM D2487-11, *Standard Practice for Classification of Soils for Engineering Purposes (Unified Soil Classification System)*, ASTM International, West Conshohocken, PA, USA, 2011.
- [41] ASTM D4318-10, *Standard Test Methods for Liquid Limit, Plastic Limit, and Plasticity Index of Soils*, ASTM International, West Conshohocken, PA, USA, 2010.
- [42] ASTM D698-12, *Standard Test Methods for Laboratory Compaction Characteristics of Soil Using Standard Effort*, ASTM International, West Conshohocken, PA, USA, 2012.
- [43] J. L. Eades and R. E. Grim, "Reaction of hydrated lime with pure clay minerals in soil stabilization," *Highway Research Board Bulletin*, vol. 262, pp. 51–53, 1996.
- [44] F. G. Bell, "Lime stabilization of clay minerals and soils," *Engineering Geology*, vol. 42, no. 4, pp. 223–237, 1996.
- [45] J. P. Sahoo and P. K. Pradhan, "Effect of lime stabilized soil cushion on strength behaviour of expansive soil," *Geotechnical and Geological Engineering*, vol. 28, no. 6, pp. 889–897, 2010.
- [46] ASTM D2166-91, "Standard test method for unconfined compressive strength of cohesive soil," *Designation D 2166-91: Annual book of ASTM Standards*, American Society for Testing and Materials, Vol. 4, Philadelphia, PA, USA, 1995.
- [47] ASTM D1883-16, *Standard Test Method for California Bearing Ratio (CBR) of Laboratory-Compacted Soils*, ASTM International, West Conshohocken, PA, USA, 2016.
- [48] ASTM D1557-12, *Standard Test Methods for Laboratory Compaction Characteristics of Soil Using Modified Effort*, ASTM International, West Conshohocken, PA, USA, 2012.
- [49] A. Seco, F. Ramírez, L. Miqueleiz, B. García, and E. Prieto, "The use of non-conventional additives in Marls stabilization," *Applied Clay Science*, vol. 51, no. 4, pp. 419–423, 2011.
- [50] M. Mavroulidou, X. Zhang, M. J. Gunn, and Z. Cabarkapa, "Water retention and compressibility of a lime-treated, high plasticity clay," *Geotechnical and Geological Engineering*, vol. 31, no. 4, pp. 1171–1185, 2013.
- [51] A. P. Furlan, A. Razakamanantsoa, H. Ranaivomanana, D. Levacher, and T. Katsumi, "Shear strength performance of marine sediments stabilized using cement, lime and fly ash," *Construction and Building Materials*, vol. 184, pp. 454–463, 2018.
- [52] B. T. Vu, V. Q. Tran, Q. D. Nguyen et al., "A geochemical model for analyzing the mechanism of stabilized soil incorporating natural pozzolan, cement and lime," in *Proceedings of the China-Europe Conference on Geotechnical Engineering*, pp. 852–857, Springer, Vienna, Austria, August 2018.
- [53] A. J. Choobbasti and S. S. Kutanaei, "Microstructure characteristics of cement-stabilized sandy soil using nanosilica," *Journal of Rock Mechanics and Geotechnical Engineering*, vol. 9, no. 5, pp. 981–988, 2017.
- [54] H. Cui, Z. Jin, X. Bao, W. Tang, and B. Dong, "Effect of carbon fiber and nanosilica on shear properties of silty soil and the mechanisms," *Construction and Building Materials*, vol. 189, pp. 286–295, 2018.

## Research Article

# Mechanical Properties of High-Strength High-Performance Reinforced Concrete Shaft Lining Structures in Deep Freezing Wells

Shilong Peng,<sup>1</sup> Chuanxin Rong<sup>1</sup>, Hua Cheng<sup>1,2</sup>, Xiaojian Wang,<sup>1</sup> Mingjing Li,<sup>1</sup> Bin Tang,<sup>1</sup> and Xuemei Li<sup>1</sup>

<sup>1</sup>School of Civil Engineering and Architecture, Anhui University of Science and Technology, 168 Taifeng St, Huainan 232001, China

<sup>2</sup>School of Resources and Environmental Engineering, Anhui University, 111 Jiulong Rd, Hefei 230601, China

Correspondence should be addressed to Chuanxin Rong; chxrong@aust.edu.cn

Received 9 November 2018; Revised 2 March 2019; Accepted 18 March 2019; Published 8 April 2019

Academic Editor: Chiara Bedon

Copyright © 2019 Shilong Peng et al. This is an open access article distributed under the Creative Commons Attribution License, which permits unrestricted use, distribution, and reproduction in any medium, provided the original work is properly cited.

As coal resources must be mined from ever deeper seams, high-strength, high-performance concrete shaft linings are required to resist the load of the soil surrounding the deep freezing well. In order to determine the optimal concrete mix for the unique conditions experienced by such high-strength high-performance reinforced concrete shaft lining (HSHPRCSL) structures in deep freezing wells, an experimental evaluation of scaled HSHPRCSL models was conducted using hydraulic pressure load tests. It was observed that as the specimens ruptured, plastic bending of the circumferential reinforcement occurred along the failure surface, generated by compression-shear failure. These tests determined that HSHPRCSL capacity was most affected by the ultimate concrete uniaxial compressive strength and the thickness-diameter ratio and least affected by the reinforcement ratio. The experimental results were then used to derive fitting equations, which were compared with the results of theoretical expressions derived using the three-parameter strength criterion for the ultimate bearing capacity, stress, radius, and load in the elastic and plastic zones. The proposed theoretical equations yielded results within 8% of the experimentally fitted results. Finally, the finite element analysis method is used to verify the abovementioned results, and all errors are less than 12%, demonstrating reliability for use as a theoretical design basis for deep HSHPRCSL structures.

## 1. Introduction

As the more accessible portions of coal resources near the surface are gradually depleted in large coal producing Chinese provinces such as Hebei, Henan, Shandong, and Anhui, it is necessary to mine deeper coal seams. As mines are constructed deeper, the alluvium traversed by the shaft lining becomes thicker and thicker. For example, the Wanfu Mine, currently under construction at the Juye Coalfield in Shandong, and the Kouzixi Mine, being planned for the Zhangou Coalfield in Anhui, will traverse 600–800 m of overlying ground. This, naturally, results in an increase in the ground pressure acting on the shaft lining. To resist strong frost heave pressure and permanent load acting on the freezing shaft lining in such deep alluvium, it is necessary

to provide a high-strength shaft lining structure [1, 2]. According to the theory of shaft lining structural design, the primary method of improving the ultimate bearing capacity of a freezing shaft lining is to increase the thickness of the shaft lining, use steel plate on the inside face of the lining as a concrete restraint structure, or cast the shaft using high-strength concrete. Among these options, the most effective measure is to increase the concrete strength in the shaft lining by using high-strength, high-performance concrete (HSHPC) [3], such as grades C60 to C80, in the design of the deep freezing shaft lining structure.

Although C60–C80 grade HSHPC has been used in China in bridge, water conservation, and high-rise building projects, the construction environment and performance requirements of these HSHPCs are quite different from those

required of deep-alluvium freezing shaft lining concrete. Because the thickness of the inner and outer shaft lining increases from about 0.7 m in shallow strata to about 1.2 m in deep strata, the use of HSHPC in these deep structures is classified as a mass concrete project, and accordingly the control of cracking is a significant challenge during the construction process. To ensure the safety of the wellbore as it is sunk to such depths, the average design temperature of the freezing wall is reduced from about  $-10^{\circ}\text{C}$  to about  $-15^{\circ}\text{C}$ . As the temperature of the freezing wellbore is decreased, the difference between the internal and external temperature of the shaft lining concrete increases, resulting in a deterioration of the concrete curing environment. Generally, when constructing a shaft lining in deep alluvium using a freezing wellbore, the concrete should have high strength, high impermeability, and good workability [4]. Therefore, to ensure that the HSHPC mix ratio used in shaft construction is economical, reasonable, and reliable, it is essential to conduct research on the preparation and behaviour of HSHPC in deep freezing wells.

Domestic and foreign scholars alike have conducted a great deal of research into concrete shaft linings [5–10], but there has been little research into the mechanical properties of a high-strength, high-performance reinforced concrete shaft lining (HSHPRCSL) structure, and most of this existing research has been mainly experimental [3, 11–14]. Yang derived a practical equation for the radial and vertical bearing capacity of a concrete shaft lining using the results of a destructive testing program of concrete shaft lining models and expressed the concrete strength criterion for the inner face of the shaft lining in a form similar to the Coulomb shear strength criterion equation [7]. Rong et al. obtained an experimental regression equation for the ultimate bearing capacity of a shaft lining using the experimental results of shaft lining model tests and analysed the mechanical properties of the shaft lining structure using the Mohr–Coulomb strength criterion [14]. Assuming that the external load is not too large, it is often more practical to analyse the mechanical properties of shaft lining concrete using the Mohr–Coulomb criterion, but it has been found that the mechanical properties of concrete under multiaxial stress should be considered under large external loads [15]. Indeed, the vertical shaft lining of a coal mine shaft constructed using the freezing method in deep alluvium generally adopts a double-layer shaft lining structure type in which the concrete of the inner shaft lining of the freezing well is generally in a bi- or tridirectional stress state [16–18]. Because the three-parameter strength criterion [19–22] considers the influence of multiaxial stress, it is better equipped to reflect the mechanical properties of an HSHPRCSL under multiaxial stress.

In view of the current state of HSHPRCSL research and according to the special curing environment and construction conditions of deep freezing shaft linings, in this study, the qualities of different mix ratios are evaluated in preparation tests of C60–C80 HSHPC to obtain an optimal mix. According to the stress characteristics of the inner shaft lining of a deep freezing well, the mechanical properties and failure characteristics of the HSHPRCSL structure are then

studied using model tests and theoretical calculations. A three-parameter strength criterion conforming to the strength characteristics of the concrete is then adopted to derive an analytical expression for the ultimate bearing capacity and stress distribution in the elastic and plastic zones of an HSHPRCSL structure. Finally, the finite element analysis method is used to verify the abovementioned results. The resulting conclusions provide a design basis for the engineering application of HSHPC in deep freezing shaft lining structures.

## 2. Evaluation of HSHPC Mixes

**2.1. Objectives of HSHPC Preparation.** High-strength, high-performance concrete possesses excellent properties before and after hardening that are provided by mixing a fine active admixture and high-efficiency compound water-reducing agent under conditions of low cement content and low water-cement ratio. These properties generally include high workability, high impermeability, high volume stability (no cracking during hardening and smaller shrinkage and creep), high strength (above C30 grade), the maintenance of continuous growth in long-term strength, and ultimately excellent durability when subjected to a harsh environment. In view of the special curing environment and construction conditions of the inner shaft lining of a freezing shaft in deep alluvium, the inner shaft lining concrete should possess high strength, crack resistance, seepage prevention, and high early strength to prevent leakage of the shaft lining after the thawing of the frozen wall. Therefore, the preparation of HSHPC for an inner shaft lining should address the following principle qualities:

- (i) Ultrahigh early strength with which concrete can be demoulded 10 hours after pouring
- (ii) Simple preparation process
- (iii) Good workability and a slump greater than 180 mm, which is convenient for transportation and pouring
- (iv) Low hydration heat and high durability
- (v) High volume stability and high impermeability

**2.2. Preparation of HSHPC.** Various factors affecting the strength, fluidity, and durability of HSHPC include the variety and dosage of cement, the mix ratio of the concrete, the variety and dosage of admixtures and externally mixed active materials, the aggregate gradation, the construction process, and the environmental conditions at the site. In general, the common mix for grade C60 HSHPC and above consists of a high-grade cement, superplasticiser (with a water reduction rate greater than or equal to 35%), mineral admixture, high quality aggregate, and controlled sand content.

### 2.3. Selection of Raw Materials for HSHPC

**2.3.1. Cement.** The C60–C80 HSHPC evaluated in this study used Conch brand P.O. 42.5R and P.O. 52.5R early strength ordinary Portland cement with lower relative hydration heats, produced by Ningguo Cement Factory. The early

strength and low heat of hydration properties of this cement make it especially suitable for the preparation of HSHPC for use in freezing shaft linings in deep alluvium.

**2.3.2. Aggregate.** The fine aggregate used in this study was Huaibin medium sand from Henan Province with a fineness modulus of 2.9, a bulk density of  $1540 \text{ kg/m}^3$ , and a mud content of 1.6%. The coarse aggregate used was Shangyao limestone gravel from Huainan City and Mingguang basalt from Chuzhou City, both in Anhui Province, which have a crushing index of 8.3% and 3.3%, respectively, and a continuous grain size grade of 5–31.5 mm.

**2.3.3. Water Reducing Agent.** In consideration of the special use environment of HSHPC in shaft linings, it is critical that an admixture be selected that provides excellent performance with the raw materials in the mix. A compatibility test was accordingly conducted by evaluating eight types of high-efficiency composite water-reducing agents (superplasticisers). In the end, an NF naphthalene-based superplasticiser produced by Huainan Mining Group Synthetic Material Co., Ltd., was selected for use in the experiments due to its good compatibility with the other materials in the mix.

**2.3.4. Mineral Admixture.** The mineral admixtures used in the experiments were a silicon powder produced by Shanxi Dongyi Ferroalloy Factory, a ground slag produced by Hefei Iron and Steel Group of Jinjiang Building Materials Co., Ltd., and a Grade I fly ash produced by Huainan Pingwei Power Plant. The main chemical components of the silicon powder and ground slag are provided in Table 1.

The type of silicon powder used in this study contained extremely fine particles consistent with an ultrafine solid material with ultrafine characteristics. The  $\text{SiO}_2$  content of the silicon powder was greater than 90%, its average particle size was  $0.1\text{--}0.15 \mu\text{m}$ , its minimum particle size was  $0.01 \mu\text{m}$ , and particles of less than  $1 \mu\text{m}$  accounted for more than 80% of the powder. The specific surface area was  $250\ 000\text{--}350\ 000 \text{ cm}^2/\text{g}$ , which is 70–90 times that of cement. The specific gravity was  $2.1\text{--}3.0 \text{ g/cm}^3$ , and the bulk density was  $200\text{--}250 \text{ kg/m}^3$ . The specific surface area of the ground slag was  $3800 \text{ cm}^2/\text{g}$ . The water demand ratio of the fly ash was 89%, its loss on ignition was 0.95%, its  $\text{SO}_3$  content was 0.29%, and its fineness was 4%.

**2.4. Compressive Strength Test Results for HSHPC Mixes.** According to the specification for the design of concrete mixes, the mixing strengths of C60, C65, C70, C75, and C80 concrete are 69.8, 74.8, 79.8, 84.8, and 89.8 MPa, respectively. Using the orthogonal testing method, the C60–C80 concrete mix proportions shown in Table 2 were evaluated for application in freezing shaft linings.

Compressive strength tests were conducted on the mixes detailed in Table 2 with the results shown in Table 3, in which it can be seen that the three-day compressive strengths of the mixes reached 80% of the design value, the seven-day compressive strengths reached 90% of the design value, and

TABLE 1: Chemical composition of silicon powder and ground slag (%).

Component	$\text{SiO}_2$	$\text{Al}_2\text{O}_3$	$\text{Fe}_2\text{O}_3$	$\text{CaO}$	$\text{MgO}$	$\text{SO}_3$
Silicon powder	92.6	0.78	0.59	0.8	1.0	0.81
Ground slag	35.3	8.93	1.26	42.2	6.9	2.0

the twenty-eight-day compressive strengths met or exceeded the design strength. These results indicate that that proposed mixes are able to fully meet the strength and performance requirements of the HSHPGCSL.

### 3. HSHPGCSL Model Test Method

**3.1. Similarity Principle of Model Test.** Given the high-strength and large size of an HSHPGCSL structure, destructive tests on a prototype shaft lining were determined to be prohibitively difficult to implement. As a result, scale models of a shaft lining structure were tested in this study.

The objective of the model tests was not only to determine the stress distribution within the shaft lining section but also to measure the failure load of the shaft lining. Therefore, the shaft lining model design must not only be subjected to scaled stress and deformation but also to a scaled load via a similarity index. Using similarity theory and the basic equations of elasticity, this study applied the equation analysis method [23] to determine the similarity index of the shaft lining model.

The similarity conditions of the stress and deformation in the shaft lining model can be obtained from the geometric equations, boundary equations, and physical equations as follows:

$$\left\{ \begin{array}{l} \frac{C_\varepsilon C_l}{C_\delta} = 1, \\ \frac{C_p}{C_\sigma} = 1, \\ \frac{C_E C_\varepsilon}{C_\sigma} = 1, \\ C_\nu = 1, \end{array} \right. \quad (1)$$

where  $C_\varepsilon$  is the strain similarity constant;  $C_l$  is the geometric similarity constant;  $C_\delta$  is the displacement similarity constant;  $C_p$  is the load (surface force) similarity constant;  $C_E$  is the elastic modulus similarity constant;  $C_\sigma$  is the stress similarity constant; and  $C_\nu$  is Poisson's ratio similarity constant.

The HSHPGCSL is a composite structure composed of two materials, steel and concrete, so in order to ensure that the stress and deformation of each component of the model and the prototype are strictly comparable, it is necessary to maintain geometric similarity between the model and prototype of shaft lining before, throughout, and after loading and deformation; accordingly,  $C_l = C_\delta$  and  $C_\varepsilon = 1$ . Therefore, the stress and strain conditions in the shaft lining can be written as

TABLE 2: Mix ratios of C60, C65, C70, C75, and C80 HSHPC.

Specimen number	Strength grade	Cement : sand : stone : water : mineral admixture (kg)	Cementitious materials (kg)	Water-binder ratio	Sand ratio (%)	Admixture dosage (%)
1	C60	410 : 628.0 : 1166.3 : 151.2 : 130	540	0.280	35	NF1.8
2	C65	410 : 625.5 : 1161.6 : 152.6 : 145	555	0.275	35	NF1.8
3	C70	410 : 620.0 : 1151.4 : 145.6 : 150	560	0.260	35	NF1.9
4	C75	420 : 622.5 : 1156.1 : 144.1 : 145	565	0.255	35	NF2.0
5	C80	430 : 616.6 : 1145.1 : 146.3 : 155	585	0.250	35	NF2.0

TABLE 3: HSHPC strength test results.

Specimen number	Design strength grade	Slump (mm)	Compressive strength of cube specimen (MPa)		
			3 d	7 d	28 d
1	C60	206	57.6	63.7	70.4
2	C65	213	60.7	69.8	75.8
3	C70	195	64.2	72.7	79.5
4	C75	210	69.5	78.2	85.3
5	C80	205	73.2	81.4	90.1

$$\begin{cases} \frac{C_l}{C_\delta} = 1, \\ \frac{C_p}{C_\sigma} = 1, \\ \frac{C_E C_\varepsilon}{C_\sigma} = 1. \end{cases} \quad (2)$$

In order to ensure that the load and shape of the shaft lining model are identical to those of the prototype at the time of failure, the stress-strain behaviour of the model in the elastic state must be similar to that of the prototype in the elastic state. Accordingly, the following strength requirements should be met:

- (i) The stress-strain curves of the shaft lining model and prototype should be similar throughout the loading process
- (ii) The strength of the materials in each part of the shaft lining should be similar to each other
- (iii) The strength criteria for the damage of the model and prototype shaft lining should be similar

To fully meet the required conditions of similarity, it is preferable that the materials proposed for the prototype shaft lining structure be used in the model test. Therefore, the structural material of the shaft lining model was adjusted in the experiment as follows:

$$\begin{cases} C_E = C_\sigma = C_p = C_R = 1, \\ C_\varepsilon = 1, \\ C_\mu = 1, \end{cases} \quad (3)$$

where  $C_R$  is the strength similarity constant and  $C_\mu$  is the reinforcement ratio similarity constant.

In this case, the appropriate geometric similarity constant is the only variable that needs to be determined. In order to make the study results universal, instead of using a specific shaft lining as the simulation object, the simulation was concerned with the effects of the thickness-diameter ratio  $\lambda$ , a dimensionless quantity with a similarity constant equal to 1. Model tests of three different shaft lining thicknesses were accordingly conducted with  $\lambda$  values of 0.219, 0.216, and 0.201. In consideration of the size of the test loading device and the characteristics of the shaft lining structure of the main shaft of the Jixi Shengjian coal mine in Shandong and the auxiliary shaft of the Huainan Dingji coal mine in Anhui, the shaft lining model parameters were obtained from an orthogonal design table [24] and are shown in Table 4. The geometry of the shaft lining model is shown in Figure 1, in which the outer diameter and height of the model are 925.0 mm and 562.5 mm, respectively, and the thickness is varied by changing the inner diameter.

**3.2. Model Loading.** To ensure good quality, the shaft lining models were cast using professional formwork. To provide consistent boundary conditions under load, the top and bottom faces of the model were processed using a lathe to obtain a high finish after pouring. The shaft lining model loading tests were conducted using a high-load hydraulic loading device, shown in Figure 2, to maintain a constant load simulating the uniform ground pressure, as shown in the schematic in Figure 3. The load test was conducted by first applying a preload two to three times before increasing the load in stable pressure increments, each held for 5–10 minutes while measured data were recorded, until the model exhibited damage.

**3.3. Measurement Method.** The compressive strengths of the HSHPC mixes were determined by three standard cube compression tests for each model mix, with the average values reported in Table 4. The load applied to the

TABLE 4: Model parameters.

Model	$a$ (mm)	$b$ (mm)	$\lambda$	$\mu$ (%)	$\sigma_{cm}$ (MPa)
A-1	380.5	462.5	0.216	0.9	65.3
A-2	380.5	462.5	0.216	1.2	72.2
A-3	380.5	462.5	0.216	0.6	76.8
A-4	385	462.5	0.201	1.38	67.9
A-5	385	462.5	0.201	1.38	74.2
A-6	385	462.5	0.201	1.38	79.3
A-7	379.5	462.5	0.219	0.7	62.2
A-8	379.5	462.5	0.219	0.7	78.3

Note:  $a$  is the inner radius;  $b$  is the outer radius;  $\lambda$  is the thickness-diameter ratio, where  $\lambda = (b - a)/a$ ;  $\mu$  is the reinforcement ratio; and  $\sigma_{cm}$  is the average cube compressive strength.

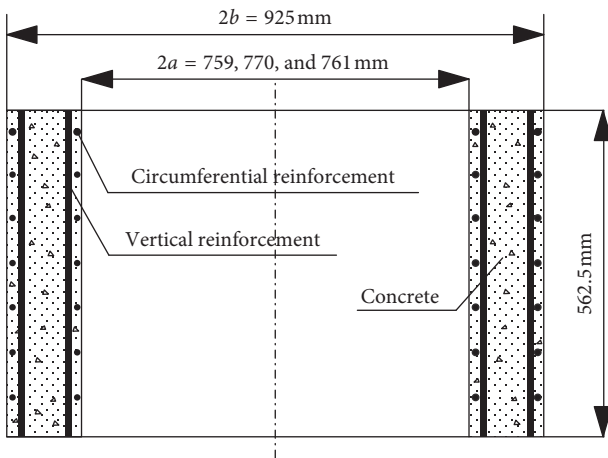


FIGURE 1: Shaft lining structure model (unit: mm).



FIGURE 2: Shaft lining model loading device.

HSHPRCSL model was measured using the standard pressure gauge installed on the high-pressure loading device and a BPR oil pressure sensor. Measurements of the strain in the shaft lining model were conducted using resistance strain gages arranged on the inner and outer surfaces of the concrete models and on the inner and outer rows of reinforcing bars, as shown in Figures 4 and 5. Two levels of gages were located vertically along the shaft lining model, and each layer contained four measurement points arranged in the circumferential direction. The load and strain in the shaft lining were collected and processed in real time by the test system. During the test, the system used the oil pressure

sensor to determine the load in order to ensure that the load cell voltage regulation error was within the allowable range.

### 3.4. Concrete Strength Data Processing

**3.4.1. Standard Value of Cube Compressive Strength.** According to the Code for the Design of Concrete Structures [25], the concrete strength grade should be determined according to the standard 150-mm cube compressive strength,  $\sigma_c$ , obtained by testing using the standard test method at an age of 28 days or whatever age is required by the design. After statistical analysis, the compressive strength of the concrete can be approximately taken as a normal distribution, as shown in Figure 6, such that the average cube compressive strength provides 95% accuracy.

If the total area under the curve in Figure 6 is taken as 1 and the area on both sides of the average value  $\kappa$  is 50%, using  $\kappa - 1.645\delta = (1 - 1.645\delta)\kappa$  as the line of demarcation, the area to the left and right should be 5% and 95%, respectively. Using these statistical characteristics, the relationship between the standard cube compressive strength  $\sigma_c$  and the average compressive strength  $\sigma_{cm}$  can be obtained as follows:

$$\sigma_c = (1 - 1.645\delta)\sigma_{cm}, \quad (4)$$

where  $\delta$  is the coefficient of variation of the concrete strength according to the statistics of the test results and can be determined by interpolation from the numerical values provided in Table 5.

**3.4.2. Axial Compressive Strength.** Considering the difference between the actual strength of the HSHPRCSL and the concrete strength determined by the cube test, past experience, and test data analysis and in reference to the relevant design code provisions of other countries [26], the strength of the concrete structure design should be corrected based on the concrete strength of the specimen. In this study, the correction coefficient was set to 0.88.

The ratio of prism compressive strength to axial compressive strength,  $\alpha_{cl}$ , for ordinary concrete (less than or equal to C50) is  $\alpha_{cl} = 0.76$ , while for high-strength concrete (C80), it is  $\alpha_{cl} = 0.82$ . When the concrete strength grade is between C50 and C80, linear interpolation is used to determine the appropriate ratio.

Because high-strength concrete is more brittle than conventional concrete, in order to ensure the safety of the structure, a brittleness reduction factor,  $\alpha_{c2}$ , has been introduced in the specification. For ordinary concrete (less than or equal to C40),  $\alpha_{c2} = 10$ , while for high-strength concrete (C80),  $\alpha_{c2} = 0.87$ . When the concrete strength grade is between C40 and C80, linear interpolation is used to determine the ratio.

According to these provisions, the standard value of the concrete axial compressive strength can be obtained as follows, with the results shown in Table 6:

$$\sigma_y = 0.88\alpha_{cl}\alpha_{c2}\sigma_c = 0.88\alpha_{cl}\alpha_{c2}(1 - 1.645\delta)\sigma_{cm}. \quad (5)$$

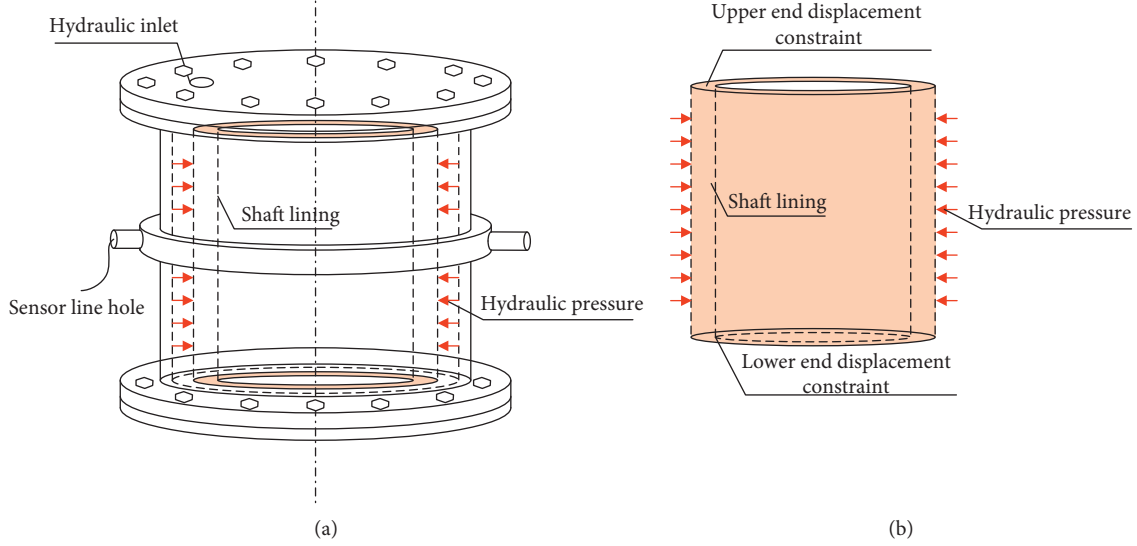


FIGURE 3: Schematic diagram of shaft lining model loading device.

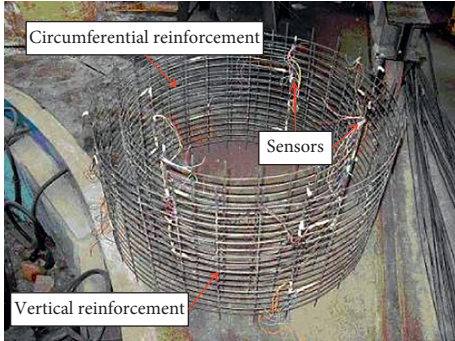


FIGURE 4: Layout of reinforcing mesh and measurement points of shaft lining model.

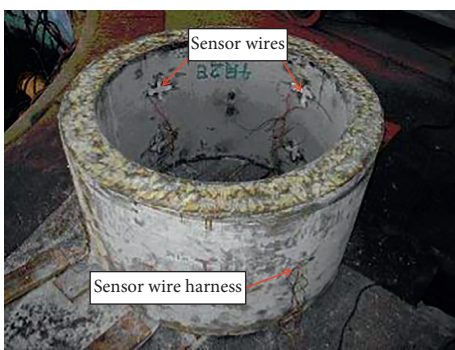


FIGURE 5: Shaft lining model and concrete surface measurement points.

**3.4.3. Axial Tensile Strength.** The standard axial tensile strength  $\sigma_t$  is calculated as follows, with the results shown in Table 7:

$$\sigma_t = 0.88 \times 0.395 \sigma_c^{0.55} (1 - 1.645\delta)^{0.45} \times \alpha_{c2}, \quad (6)$$

where the coefficient of 0.395 and the exponent of 0.55 represent the relationship of axial tensile strength to the cube

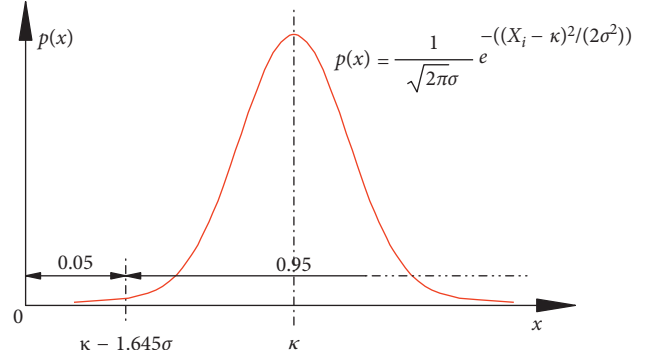


FIGURE 6: Normal distribution of concrete compressive strength.

compressive strength, determined by statistical analysis of the test data.

**3.4.4. Biaxial Compressive Strength.** The biaxial strength envelope of the concrete is a closed curve composed of four segments, shown in Figure 7, each of which expresses tensile stress as negative and compressive stress as positive, determined according to the quadrant in which the segment is located. The strength envelope curve can be described by the following equations:

$$\left\{ \begin{array}{l} L_1 : f_1^2 + f_2^2 - 2\nu f_1 f_2 = \sigma_1^2, \\ L_2 : \sqrt{f_1^2 + f_2^2 - f_1 f_2} - \alpha_s (f_1 + f_2) = (1 - \alpha_s) \sigma_y, \\ L_3 : \frac{f_2}{\sigma_y} - \frac{f_1}{\sigma_1} = 1, \\ L_4 : \frac{f_1}{\sigma_y} - \frac{f_2}{\sigma_1} = 1, \end{array} \right. \quad (7)$$

TABLE 5: Coefficient of variation of concrete strength (%) [25].

Strength grade	C15	C20	C25	C30	C35	C40	C45	C50	C55	C60–C80
$\delta$	23.3	20.6	18.9	17.2	16.4	15.6	15.6	14.9	14.9	14.1

TABLE 6: Standard value of axial concrete compressive strength (MPa) [25].

Strength grade	C15	C20	C25	C30	C35	C40	C45	C50	C55	C60	C65	C70	C75	C80
$\sigma_y$	10.0	13.4	16.7	20.1	23.4	26.8	29.6	32.4	35.5	38.5	41.5	44.5	47.4	50.2

TABLE 7: Standard value of axial concrete tensile strength (MPa) [25].

Strength grade	C15	C20	C25	C30	C35	C40	C45	C50	C55	C60	C65	C70	C75	C80
$\sigma_l$	1.27	1.54	1.78	2.01	2.20	2.39	2.51	2.64	2.74	2.85	2.93	2.99	3.05	3.11

where  $\alpha_s$  is the shear yield parameter, determined by  $\alpha_s = (r - 1)/(2r - 1)$ ;  $r$  is the increase coefficient of biaxial compressive strength, ranging from 1.13 to 1.15, determined by experimental data and taken as 1.2 in the absence of experimental data;  $f_i$  is the representative value of the multiaxis concrete strength;  $f_1 \geq f_2 \geq f_3$ ; and  $\nu$  is Poisson's ratio of the concrete, taken in the range of 0.18–0.22.

For convenience of calculation, the biaxial compressive strengths indicated in Figure 7 can be interpolated according to the data in Table 8.

#### 4. Results of HSHPRCSL Model Tests

**4.1. Ultimate Bearing Capacity of HSHPRCSL.** The experimentally determined ultimate bearing capacities ( $P_b$ ) of the shaft lining models are provided in Table 9, in which it can be seen that, under the action of a uniformly distributed load, the HSHPRCSL models exhibit a high bearing capacity, providing a reasonable solution to the issues of supporting shafts in deep alluvium. Through a regression analysis of the test results in Table 9, the regression formula for the ultimate bearing capacity of HSHPRCSL structures can be obtained as follows:

$$P_b = 0.557\sigma_c^{1.272}\lambda^{0.917}\mu^{0.0302}, \quad (8)$$

which indicates that the ultimate bearing capacity ( $P_b$ ) of the shaft lining is mainly related to the standard concrete cube compressive strength ( $\sigma_c$ ), thickness-diameter ratio ( $\lambda$ ), and the reinforcement ratio ( $\mu$ ).

In order to provide a reasonable and economic shaft lining design, the relationships between bearing capacity and reinforcement ratio and between bearing capacity and concrete compressive strength (Figures 8 and 9, respectively) were determined using empirical equation (8). Under the action of a uniformly distributed load, the power exponent of the reinforcement ratio ( $\mu$ ) was accordingly determined to be 0.0302, very close to 0, indicating that an increase in the reinforcement ratio has only a very small effect on the ultimate bearing capacity of the HSHPRCSL models. As shown in Figure 8, for the same concrete strength grade, an increase in the reinforcement ratio from 0.3% to 0.8% results

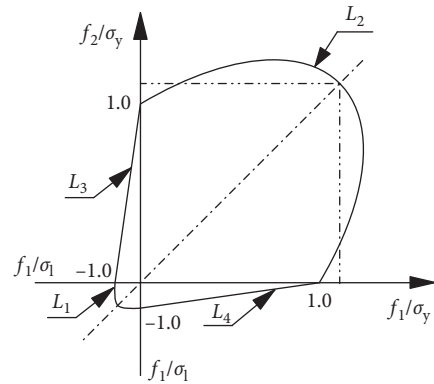


FIGURE 7: Strength envelope diagram of biaxial stress in concrete.

in only an approximately 0.85 MPa improvement in the ultimate bearing capacity while requiring a significant increase in the quantity of reinforcing bars. This not only increases the project cost but also makes underground concrete vibration very difficult, adversely affecting the quality of the poured concrete. Therefore, improving the ultimate bearing capacity of the shaft lining by increasing the reinforcement ratio is unreasonable. Due to the insignificant influence of the reinforcement ratio on the ultimate bearing capacity of the models, the contribution of the reinforcement ratio to the ultimate bearing capacity of the reinforced concrete shaft lining is not considered in the following theoretical analysis of the ultimate bearing capacity.

The ultimate bearing capacity of the HSHPRCSL model was found to be significantly influenced by the strength grade of the concrete. Figure 9 indicates that an increase of 10 MPa in the concrete strength grade raised the ultimate bearing capacity of the model by about 6.29 MPa. An increase in the thickness-diameter ratio was also observed to improve the ultimate bearing capacity of the model: at C60, an increase in the thickness-diameter ratio from 0.2 to 0.3 raised the ultimate bearing capacity of the model by about 8.87 MPa. Combined with an increase in concrete strength grade, the effect of an increase in the thickness-diameter

TABLE 8: Compressive strength of concrete under biaxial compression [25].

$f_1/\sigma_y$	1.0	1.05	1.10	1.15	1.20	1.25	1.29	1.25	1.20	1.16
$f_2/\sigma_l$	0	0.07	0.16	0.25	0.36	0.50	0.88	1.03	1.11	1.16

TABLE 9: Comparison of theoretically, experimentally, and numerically determined HSHPRCSL plastic ultimate bearing capacity.

Model	$\sigma_{cm}$ (MPa)	$\sigma_c$ (MPa)	$\sigma_y$ (MPa)	$\sigma_l$ (MPa)	$\sigma_{2y}$ (MPa)	$P_{b1}$ (MPa)	$P_{b2}$ (MPa)	$P_{b3}$ (MPa)
A-1	65.3	49.19	31.85	2.62	40.26	17.0	17.51	18.72
A-2	72.2	54.98	35.44	2.74	44.79	19.5	20.25	21.82
A-3	76.8	58.87	37.82	2.83	47.80	21.0	22.08	22.40
A-4	67.9	51.38	33.21	2.67	41.98	16.8	16.99	17.50
A-5	74.2	56.67	36.48	2.78	46.11	19.0	19.29	20.87
A-6	79.3	61.01	39.12	2.87	49.45	21.0	21.21	23.01
A-7	62.2	46.45	30.13	2.55	38.08	15.5	16.58	16.95
A-8	78.3	60.14	38.59	2.85	48.78	21.5	23.13	23.88

Note:  $\sigma_{cm}$  is the average cube compressive strength;  $\sigma_c$  is the standard cube compressive strength;  $\sigma_y$  is the prismatic axial compressive strength;  $\sigma_l$  is the prismatic axial tensile strength;  $\sigma_{2y}$  is the biaxial compressive strength;  $P_{b1}$  is the experimentally determined ultimate bearing capacity;  $P_{b2}$  is the theoretically determined ultimate bearing capacity; and  $P_{b3}$  is the numerically determined ultimate bearing capacity.

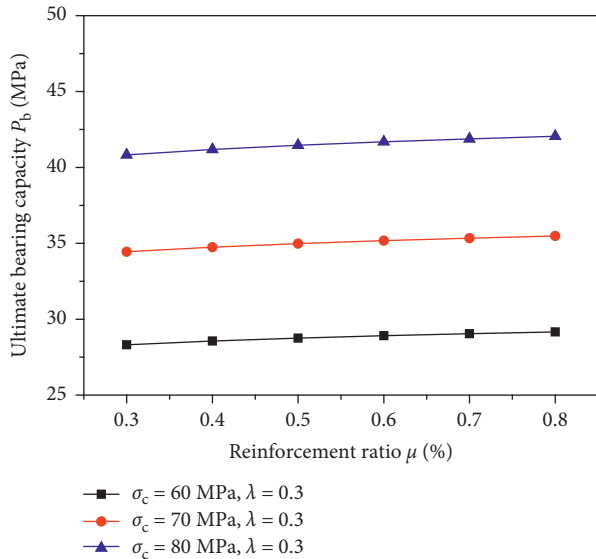


FIGURE 8: Relationship curve between ultimate bearing capacity and reinforcement ratio.

ratio on the increase in bearing capacity would be even more noticeable. For C80 concrete, an increase in the thickness-diameter ratio from 0.2 to 0.3 raises the ultimate bearing capacity of the HSHPRCSL model by about 12.79 MPa. However, in reality, increasing the thickness-diameter ratio is often limited by engineering conditions; therefore, the ultimate bearing capacity of HSHPRCSL is most effectively improved by increasing the strength of the concrete during the design stage.

**4.2. HSHPRCSL Model Failure Modes.** Figure 10 depicts the typical observed failure mode of the HSHPRCSL models. When the external load on the shaft lining was fairly large, the circumferential stress in the interior face of the shaft

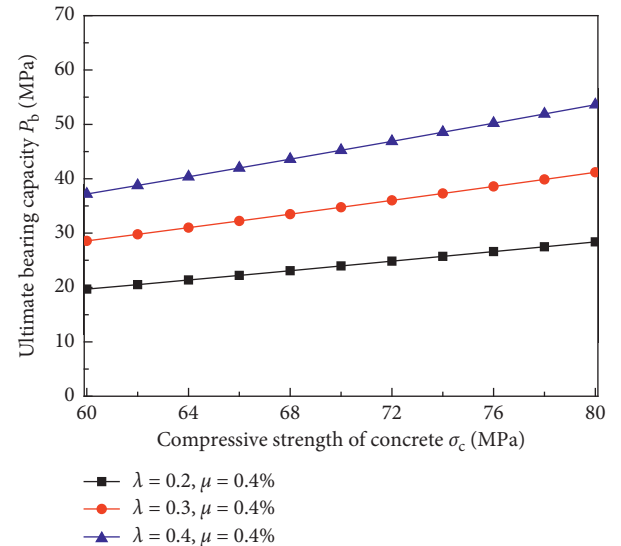


FIGURE 9: Relationship between ultimate bearing capacity and concrete compressive strength.

concrete reached its ultimate strength first. As the direction of free deformation is normal to the inner face, these surfaces of the models exhibited very small inclined cracks and local peeling at this time. As the applied load was increased, the high stress area in which the ultimate strength had been exceeded rapidly spread from the inner face to the outer face of the model, and compression and shear failure eventually occurred in the portion of the shaft lining in which the concrete was the weakest, forming a failure surface running through the entire thickness of the shaft lining model. When failure occurred, large chunks of concrete were observed to fall, inclined broken cracks appeared, and the circumferential bars bent plastically along the failure surface. The angle between the failure surface and the maximum principle stress was between 25 and 30°, suggesting a compressive shear failure.



FIGURE 10: Shaft lining model failure mode.

## 5. Theoretical Analysis of HSHPRCSL Based on the Three-Parameter Strength Criterion

**5.1. Three-Parameter HSHPC Strength Criterion.** The failure surface of the three-parameter strength criterion, shown in Figure 11, is smooth as its meridian is a parabola, a significant improvement over conventional strength criteria. The three-parameter strength criterion is usually expressed in terms of uniaxial tensile strength, uniaxial compressive strength, and biaxial compressive strength, represented by  $\sigma_1$ ,  $\sigma_y$ , and  $\sigma_{2y}$ , respectively [19], using as a combination of stresses  $\rho$ ,  $\xi$ , and  $\theta$ , defined by

$$\begin{cases} \rho = \sqrt{2J_2}, \\ \xi = \frac{1}{\sqrt{3}}I_1, \\ \cos 3\theta = \frac{3\sqrt{3}J_3}{2\sqrt{J_2^3}}, \quad 0 \leq \theta \leq 60^\circ, \end{cases} \quad (9)$$

where  $I_1 = \sigma_1 + \sigma_2 + \sigma_3 = 3\sigma_m$ ,  $J_2 = 1/6[(\sigma_1 - \sigma_2)^2 + (\sigma_2 - \sigma_3)^2 + (\sigma_3 - \sigma_1)^2]$ , and  $J_3 = s_1s_2s_3 = (\sigma_1 - \sigma_m)(\sigma_2 - \sigma_m)(\sigma_3 - \sigma_m)$ .

For the yield plane of the three-parameter strength criterion shown in Figure 11, any point  $M(\rho, \xi, \theta)$  on the failure plane can be defined by

$$M(\rho, \xi, \theta) = \rho^2 + A_1(\theta)\rho + A_2(\theta)\xi + A_3(\theta) = 0, \quad (10)$$

where  $A_1(\theta) = 1/2(a_1 + a_2) + 1/2(a_2 - a_1)\cos 3\theta$ ,  $A_2(\theta) = 1/2(b_1 + b_2) + 1/2(b_2 - b_1)\cos 3\theta$ ,  $A_3(\theta) = -\sqrt{3}[1/2(b_1 + b_2) + 1/2(b_2 - b_1)\cos 3\theta]\sigma_1$ ,  $a_1 = (\sqrt{6}/9)(K_y^2 - K_{2y}^2 - 3)\sigma_1$ ,  $a_2 = (\sqrt{6}/9)(2K_{2y}^2 - 2K_{2y} - 3)\sigma_1$ ,  $b_1 = (2\sqrt{3}/9)K_y(K_y - 1)\sigma_1$ ,  $b_2 = (2\sqrt{3}/9)K_{2y}(K_{2y} - 1)\sigma_1$ , and  $K_y = \sigma_y/\sigma_1$ ,  $K_{2y} = \sigma_{2y}/\sigma_1$ .

**5.2. Mechanical Model.** Because the shaft lining is under external pressure, the principle stress components  $\sigma_r$ ,  $\sigma_\theta$ , and  $\sigma_z$ , defined as the radial stress, hoop stress, and vertical stress, respectively, are all negative as they are compressive such that  $0 > \sigma_r > \sigma_z > \sigma_\theta$ . Supposing that  $a$  and  $b$  are the inner and outer radii of the shaft lining, respectively, under

the action of external pressure, the shaft lining is in a state of elastic-plastic behaviour, where  $r_p$ , determined and applied later in this section, denotes the radius of the elastic-plastic boundary (as illustrated in Figure 12).

**5.3. Analysis of Elastic-Plastic Behaviour and Ultimate Bearing Capacity of HSHPRCSL Structures.** Mine shaft lining can be analysed as a plane axially symmetric problem in which the radial stress  $\sigma_r$  and hoop stress  $\sigma_\theta$  are only a function of  $r$ , having nothing to do with  $\theta$  such that  $\sigma_r = \sigma_r(r)$  and  $\sigma_\theta = \sigma_\theta(r)$ . The intermediate principal stress is thus determined by  $\sigma_z = \beta/2(\sigma_r + \sigma_\theta)$ , where the intermediate principal stress coefficient  $\beta$  is defined as  $0 \leq \beta \leq 1$ . In the plastic zone,  $\beta = 1$ , making  $\sigma_1 = \sigma_r$ ,  $\sigma_3 = \sigma_\theta$ , and  $\sigma_2 = (\sigma_r + \sigma_\theta)/2$ . Previously published work [27] has demonstrated that when the externally applied load  $p$  is very small, the shaft is in the elastic stage, with the stress components being defined as

$$\begin{cases} \sigma_r = -\frac{b^2 p}{b^2 - a^2} \left( 1 - \frac{a^2}{r^2} \right), \\ \sigma_\theta = -\frac{b^2 p}{b^2 - a^2} \left( 1 + \frac{a^2}{r^2} \right). \end{cases} \quad (11)$$

As  $p$  gradually increases, the stress in the inner shaft lining ( $r = a$ ) reaches the concrete strength first, entering the plastic zone. This external load is defined as the elastic limit stress, denoted as  $p_e$  and determined as follows:

$$p_e = \frac{(b^2 - a^2)}{4b^2} \left[ -(\sqrt{2}A_1 - \sqrt{3}A_2) + \sqrt{(\sqrt{2}A_1 - \sqrt{3}A_2)^2 - 8A_3} \right]. \quad (12)$$

When the external load  $p > p_e$ , the shaft lining enters the elastic-plastic stage, the plastic zone ( $a \leq r \leq r_p$ ) begins to appear on the inner face of the shaft lining, and as  $p$  continues to increase, the plastic zone gradually extends outward. Because of axial symmetry, there is only the load  $q$  on the interface between the elastic and plastic zones, where  $\sigma_r|_{r=r_p} = -q$ , and  $r_p$  is the radius of the elastic-plastic boundary, shown in Figure 12. In the plastic zone, the stress component is satisfied by

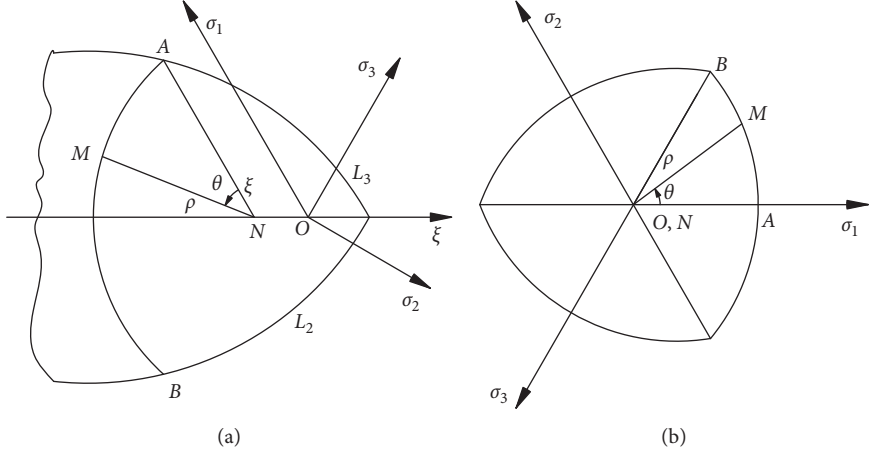


FIGURE 11: Parabolic three-parameter strength criterion.

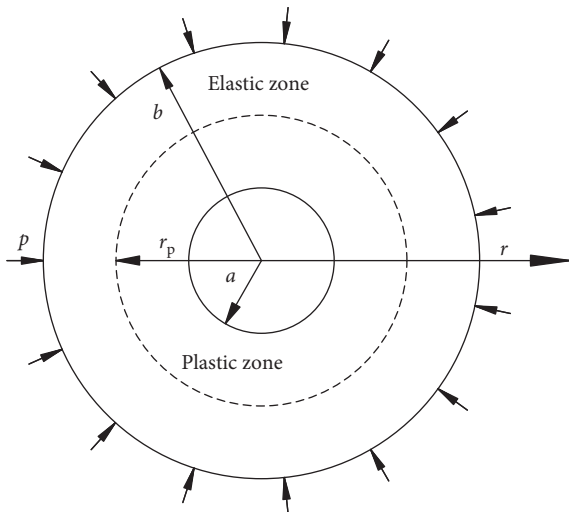


FIGURE 12: Mechanical model of concrete shaft lining.

$$\left\{ \begin{array}{l} \sigma_r = -\frac{1}{\sqrt{3} A_2} \rho^2(r) + \left( \frac{1}{\sqrt{2}} - \frac{A_1}{\sqrt{3} A_2} \right) \rho(r) - \frac{A_3}{\sqrt{3} A_2}, \\ \sigma_\theta = -\frac{1}{\sqrt{3} A_2} \rho^2(r) - \left( \frac{1}{\sqrt{2}} + \frac{A_1}{\sqrt{3} A_2} \right) \rho(r) - \frac{A_3}{\sqrt{3} A_2}, \end{array} \right. \quad (13)$$

where  $\rho(r)$  can be obtained in MATLAB using  $\rho(r) - \rho(a) + (1/2)(A_1 - \sqrt{3/2} A_2)\ln(\rho(r)/\rho(a)) - \sqrt{3/2} A_2 \ln(r/a) = 0$ , the known material parameters, and  $\rho(a) = (1/2)[-(A_1 - \sqrt{3/2} A_2) + \sqrt{(C_1 - \sqrt{3/2} A_2)^2 - 4A_3}]$ .

When the plastic zone ( $a \leq r \leq r_p$ ) begins to appear in the shaft lining, the shaft lining in the elastic zone ( $r_p \leq r \leq b$ ) can be treated as a new elastic shaft lining subjected to an inner load  $q$  (where  $r = r_p$ ) and an external load  $p$  (where

$r = b$ ). The components of stress due to these loads can be expressed as

$$\left\{ \begin{array}{l} \sigma_r = \frac{b^2 r_p^2 (p - q)}{(b^2 - r_p^2) r^2} + \frac{r_p^2 q - b^2 p}{b^2 - r_p^2}, \\ \sigma_\theta = -\frac{b^2 r_p^2 (p - q)}{(b^2 - r_p^2) r^2} + \frac{r_p^2 q - b^2 p}{b^2 - r_p^2}. \end{array} \right. \quad (14)$$

The relationship between the ultimate bearing capacity of the HSHPRCSL,  $P_b$ , and the radius of the plastic zone of the shaft wall,  $r_p$ , can be obtained using the three-parameter strength criterion, and the radial stress at the interface between the elastic and plastic zones as follows

$$P_b = \frac{\sqrt{\left[4b^2q - (b^2 - r_p^2)\alpha\right]^2 - 8\left[2b^4q^2 - (b^2 - r_p^2)(\sqrt{2}b^2A_1 - \sqrt{3}r_p^2A_2)q + A_3(b^2 - r_p^2)^2\right]} + \left[4b^2q - (b^2 - r_p^2)\alpha\right]}{4b^2}, \quad (15)$$

where  $\alpha = \sqrt{2}A_1 - \sqrt{3}A_2$ .

## 6. Analysis of Results

**6.1. Theoretical Analysis of Ultimate Bearing Capacity of HSHPRCSL.** According to the Code for the Design of Concrete Structures [25, 26] with reference to Tables 6 and 7, when the concrete strength grade is between C40 and C80,  $K_y = \sigma_y/\sigma_1 = 11.21\text{--}16.14$ , the exact value of which can be calculated by interpolation according to the measured strength grade of the concrete. Because the failure of the shaft lining first occurred on the inner face at the edge of the lining,  $f_1 = \sigma_\theta$ ,  $f_2 = \sigma_\theta/2$ ,  $f_1/f_2 = (\sigma_\theta)/(\sigma_\theta/2) = 2$ , and  $\sigma_{2y}/\sigma_y = f_1/\sigma_y = 1.264$  can be obtained by interpolating the information in Table 8, so  $K_{2y} = \sigma_{2y}/\sigma_1 = 14.17\text{--}20.40$ . According to equation (15), if the strength grade of the concrete and the geometry of the shaft lining have already been determined, the relationship between the ultimate bearing capacity  $P_b$  of the HSHPRCSL and its plastic zone radius  $r_p$  can be determined. Accordingly, the ultimate bearing capacity of each specimen in the model experiment was analysed using the three-parameter strength criterion with the resulting ultimate bearing capacities shown in Table 9. Clearly, the differences between the calculated and experimental results are very small, all less than 8%, indicating that the proposed theoretical equation derived from the three-parameter strength criterion, which has fewer parameters and a simpler functional form than the more complex multiaxial strength theory, can accurately reflect the mechanical properties of an HSHPRCSL structure.

According to the analysis of model test results, the ultimate bearing capacities of the HSHPRCSL models were found to be significantly influenced by the concrete strength to the extent that the ultimate bearing capacity of a HSHPRCSL is most effectively improved by increasing the strength of the concrete during the design stage. To analyse the degree of correlation between the experimentally derived fitted equation and the theoretically derived equation based on the three-parameter strength criterion for the ultimate bearing capacity of the shaft lining, specimens with thickness-diameter ratios of  $\lambda = 0.216$  and 0.201 for A-1-A-3 and A-4-A-6, respectively, were compared separately. The ultimate bearing capacities of the HSHPRCSL specimens constructed of C60-C80 concrete for thickness-diameter ratios of  $\lambda = 0.216$  and 0.201 were then obtained as shown in Figures 13 and 14, respectively.

From Figures 13 and 14, it can be seen that the trend law of the ultimate bearing capacity with the change in concrete compressive strength as determined by the three-parameter strength criterion is the nearly the same as that of the fitted curve, with both approximating a linear distribution. Figure 13 shows that when the inner radius of the shaft lining  $a = 380.5$  mm, the outer radius  $b = 462.5$  mm and the thickness-diameter ratio  $\lambda = 0.216$ , as the concrete strength grade increases by 5 MPa within the range of C60-C80, the ultimate bearing capacity of the shaft lining obtained by the fitted curve increases by approximately 2.4 MPa, while the ultimate bearing capacity based on the three-parameter

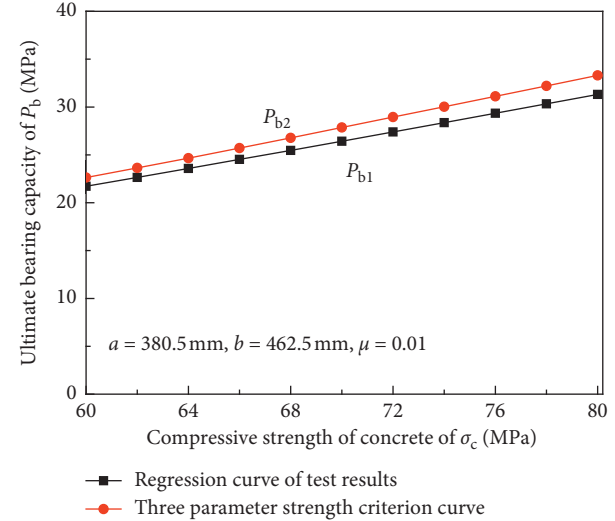


FIGURE 13: The relationship between ultimate bearing capacity and compressive strength when  $\lambda = 0.216$ .

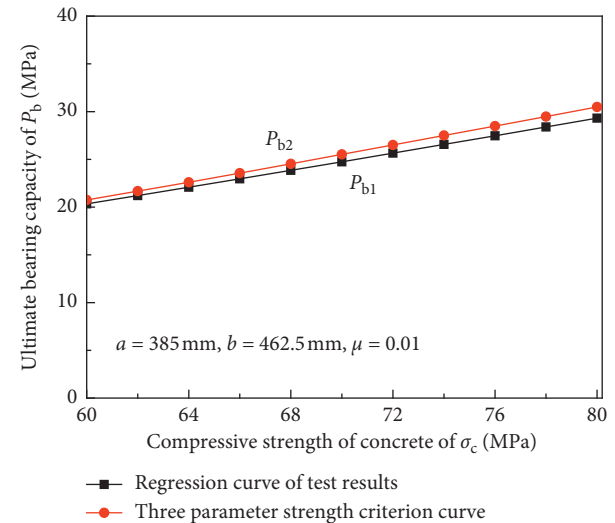


FIGURE 14: The relationship between ultimate bearing capacity and compressive strength when  $\lambda = 0.201$ .

strength criterion increases about 2.67 MPa. Figure 14 shows that when the inner radius of the shaft lining  $a = 385$  mm, the outer radius  $b = 462.5$  mm and the thickness-diameter ratio  $\lambda = 0.201$ , as the concrete strength grade increases by 5 MPa within the range of C60-C80, the ultimate bearing capacity of the shaft lining obtained by the fitted curve increases by approximately 2.25 MPa, while the ultimate bearing capacity based on the three-parameter strength criterion increases by about 2.44 MPa.

The above analysis demonstrates that the difference between the ultimate bearing capacity of the HSHPRCSL calculated using the proposed equation based on the three-parameter strength criterion and calculated using the fitting equation based on experimental results is very small, with errors around about  $\pm 5\%$ . Thus, the calculation of the ultimate bearing capacity of HSHPRCSL by equations (8)

and (15) is reliable, providing a basis for the design of HSHPRCSL structures.

**6.2. Finite Element Analysis of Ultimate Bearing Capacity of HSHPRCSL.** It is well known that reasonable and accurate numerical approach could be implemented as an alternative to costly and time-consuming full-scale experimental tests, allowing an extensive parametric investigation of composite joints and possible design optimizations [28]. In order to understand the actual ultimate bearing capacity of the shaft lining with the same strength under the boundary conditions of engineering practices, the finite element numerical simulation method is used to further analyse the ultimate bearing capacity of the shaft lining.

In the finite element model, the concrete is simulated by SOLID65 three-dimensional solid element, the steel bar is simulated by LINK8 bar element, and the reinforced-concrete separated model is adopted. Displacement coordination is achieved by sharing joint between concrete elements and steel elements. The constitutive relationship of concrete is determined by the multilinear kinematic hardening model (bilinear kinematic), as well as the uniaxial compressive test results of HSHPC blocks. The failure criterion of concrete is Willam and Warnke's five-parameter failure criterion [29]. The bilinear kinematic hardening model is adopted for steel bars, and Mises criterion is used for its yield. Vertical constraints are applied to the upper and lower surfaces of the model, and uniform surface loads are applied to the outer surface of the model according to the loading history of the test. The network partition of the finite element model is shown in Figure 15. Specific physical and mechanical parameters of concrete and steel bar are shown in Tables 10 and 11.

Through finite element calculation, the ultimate bearing capacity of 8 HSHPRCSLs is obtained. From Table 9, it can be seen that the finite element calculation results of ultimate bearing capacity of HSHPRCSL are slightly higher than those of model tests and theoretical formulas. The reason is that the constraints of the finite element model fully reflect the three-dimensional compressive state of the shaft lining, and the ultimate compressive strength of concrete will be greatly improved under the three-dimensional compressive state, which cannot be truly reflected in the test. Generally speaking, the errors are all less than 12%, which verifies the rationality of the finite element model. It is further explained that the research carried out in this paper can provide a basis for the design of high-strength and high-performance concrete shaft lining.

## 7. Conclusions

In this study, a series of high-strength, high-performance concrete (HSHPRC) mix tests were first conducted to determine the optimal mix ratio for use in deep freezing shaft linings. Then, a series of high-strength, high-performance reinforced concrete shaft lining (HSHPRCSL) models were tested to determine their mechanical properties and failure characteristics. And then, a theoretical analysis based on the

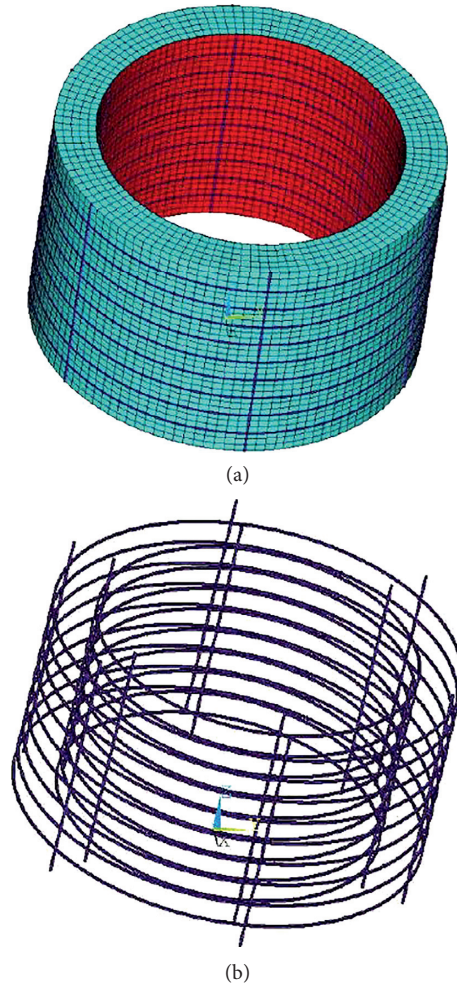


FIGURE 15: Finite element model of HSHPRCSL.

three-parameter strength criterion was undertaken to determine the ultimate bearing capacity of the HSHPRCSL models, providing analytical expressions for elastic and plastic zone radii, stress, and load. Finally, the finite element analysis method is used to verify the abovementioned results. The following conclusions were obtained:

- (1) According to the special curing environment and construction conditions to which deep freezing shaft linings are subjected, an optimised concrete mix was proposed for concrete strengths in the range of C60 to C80, providing important information to promote improved design and construction of deep alluvium freezing shaft linings.
- (2) When the HSHPRCSL models ruptured, large chunks of concrete were observed to fall, inclined broken cracks appeared, plastic bending of the circumferential reinforcement occurred along the failure surface, and compressive-shear failure occurred with an angle between the failure surface and the maximum principle stress of 25–30°.
- (3) Results of the HSHPRCSL model tests indicated a high ultimate bearing capacity. The factors that

TABLE 10: The force parameter table of concrete.

Model	$E$ ( $\times 10^4$ MPa)	Poisson ratio	$\sigma_f$ (MPa)	$\sigma_{cm}$ (MPa)	$\sigma_t$ (MPa)	$\beta_t$	$\beta_c$
A-1	3.66	0.2	39.2	65.3	7.18	0.45	0.9
A-2	3.72	0.2	43.3	72.2	8.10	0.45	0.9
A-3	3.77	0.2	46.1	76.8	8.35	0.45	0.9
A-4	3.59	0.2	40.7	67.9	7.45	0.45	0.9
A-5	3.67	0.2	44.5	74.2	8.21	0.45	0.9
A-6	3.75	0.2	47.6	79.3	8.42	0.45	0.9
A-7	3.62	0.2	37.3	62.2	6.71	0.45	0.9
A-8	3.78	0.2	47.0	78.3	8.39	0.45	0.9

Note:  $E$  is the modulus of elasticity;  $\sigma_f$  is the yield stress;  $\sigma_t$  is the uniaxial tensile strength of concrete;  $\beta_t$  is the shear transfer coefficient when cracks open; and  $\beta_c$  is the shear transfer coefficient when the crack closes.

TABLE 11: The force parameter table of rebar.

$E$ ( $\times 10^5$ MPa)	Poisson ratio	$\sigma_f$ (MPa)
2.1	0.3	340

influenced the ultimate bearing capacity were, in order of decreasing influence, the ultimate uniaxial compressive strength of the concrete, the thickness-diameter ratio, and the reinforcement ratio. Under a uniform externally applied load, when the concrete strength grade was increased by 10 MPa, the ultimate bearing capacity of the model increased by 6.29 MPa. For the same concrete strength grade, an increase in the reinforcement ratio from 0.3% to 0.8% only improved the ultimate bearing capacity of the shaft lining by about 0.85 MPa.

- (4) The theoretical HSHPRCSL ultimate bearing capacities, calculated based on the three-parameter strength criterion, were basically consistent with the experimental results, showing an error of less than 8%. Clearly, the proposed method for the theoretical calculation of the ultimate bearing capacity of HSHPRCSL structures is reliable, providing a theoretical basis for the design of HSHPRCSL structures in deep alluvium freezing wells.
- (5) Due to the constraints of the finite element model fully reflecting the three-dimensional compression state of the borehole lining, the finite element calculation results of the ultimate bearing capacity of HSHPRCSL are slightly higher than those of the model test and theoretical formula. However, the errors are less than 12%, which verifies the rationality of the finite element model.

## Data Availability

The data used to support the findings of this study are available from the corresponding author upon request.

## Conflicts of Interest

The authors declare that there are no conflicts of interest regarding the publication of this paper.

## Acknowledgments

This work was financially supported by the National Natural Science Foundation of China (Grant nos. 51374010, 51474004, 51874005, 51878005, and 51804006) and The Key project of Anhui Provincial Natural Science Research in Colleges and Universities (Grant nos. KJ2010A094 and KJ2011A093).

## References

- [1] Y. Yao, H. Cheng, C. Rong et al., "Analysis and prediction of vertical shaft freezing pressure in deep alluvium based on RBF fuzzy neural network model," *Journal of Mining & Safety Engineering*, vol. 33, pp. 70–76, 2016, in Chinese.
- [2] G. Spagnoli, P. Oreste, and L. Lo Bianco, "New equations for estimating radial loads on deep shaft linings in weak rocks," *International Journal of Geomechanics*, vol. 16, no. 6, article 06016006, 2016.
- [3] Z. Yao, H. Cheng, and J. Yang, "Experimental study on mechanical properties of high strength reinforced concrete shaft lining in deep alluvium," *Journal of China Coal Society*, vol. 29, pp. 167–171, 2004, in Chinese.
- [4] H. Song, H. Cheng, and Z. Yao, "An experimental research of large volume high-strength and high-performance concrete in deep frozen shaft lining and its application," *West, China Exploration Engineering*, vol. 18, pp. 154–156, 2006, in Chinese.
- [5] H. Lü and G. Cui, "Mechanical mechanism of shaft lining structure fracture in thick alluvium," *Journal of China University of Mining and Technology*, vol. 28, pp. 539–543, 1999, in Chinese.
- [6] X. Chen and W. Yang, "Curing monolayer freezing shaft lining," *Journal of China University of Mining and Technology*, vol. 39, pp. 201–207, 2010, in Chinese.
- [7] J. Yang, "Failure and strength characteristics of the concrete shaft lining," *Journal of China Coal Society*, vol. 23, pp. 246–251, 1998, in Chinese.
- [8] L. Liao, A. de la Fuente, S. Cavalaro, and A. Aguado, "Design procedure and experimental study on fibre reinforced concrete segmental rings for vertical shafts," *Materials & Design*, vol. 92, pp. 590–601, 2016.
- [9] T. Majcherczyk, Z. Niedbalski, and D. Wałach, "Variations in mechanical parameters of rock mass affecting shaft lining/zmiany parametrów mechanicznych górotworu I ich wpływ na obudowę szybową," *Archives of Mining Sciences*, vol. 58, no. 3, pp. 629–642, 2013.
- [10] G. Tiberti, F. Minelli, and G. Plizzari, "Reinforcement optimization of fiber reinforced concrete linings for conventional

- tunnels," *Composites Part B: Engineering*, vol. 58, pp. 199–207, 2014.
- [11] Y. Wang, J. Huang, J. Li et al., "Early-stage strength growth of high-strength concrete in outer freezing shaft walls," *Journal of China University of Mining and Technology*, vol. 37, pp. 595–598, 2008, in Chinese.
- [12] Z. Yao, H. Cheng, and W. Sun, "Testing studies on the structure of high strength composite shaft wall in deep soil layer," *Rock and Soil Mechanics*, vol. 24, pp. 739–743, 2003, in Chinese.
- [13] Z. Yao, H. Cheng, and C. Rong, "Experimental study on composite shaft Lining of inner steel plate cylinder and high strength reinforced concrete in deep frozen shaft," *Chinese Journal of Rock Mechanics and Engineering*, vol. 27, pp. 153–158, 2008, in Chinese.
- [14] C. Rong, X. Wang, and H. Cheng, "Research on mechanical characteristics of high-strength reinforced concrete shaft lining in deep alluvium," *Chinese Journal of Rock Mechanics and Engineering*, vol. 27, pp. 2841–2847, 2008, in Chinese.
- [15] Z. Guo and C. Wang, "Investigation of strength and failure criterion of concrete under multi-axial stresses," *China Civil Engineering Journal*, vol. 24, pp. 1–13, 1991, in Chinese.
- [16] Z.-s. Yao, H. Chang, and C.-x. Rong, "Research on stress and strength of high strength reinforced concrete drilling shaft lining in thick top soils," *Journal of China University of Mining and Technology*, vol. 17, no. 3, pp. 432–435, 2007.
- [17] R. Ritter and M. Curbach, "Material behavior of ultra-high-strength concrete under multiaxial stress states," *ACI Materials Journal*, vol. 112, no. 5, pp. 641–651, 2015.
- [18] K. Speck and M. Curbach, "Ein einheitliches dreiaxiales Bruchkriterium für alle Betone," *Beton und Stahlbetonbau*, vol. 105, no. 4, pp. 233–243, 2010.
- [19] B. Xu and X. Liu, *Applied Elastic-Plastic Mechanics*, Tsinghua University Press, Beijing, China, 1995, in Chinese.
- [20] Y. Zhang and M. Lu, "Three-parameter failure criterion for plain concrete," *Journal of Shanghai Jiaotong University*, vol. 24, pp. 62–88, 1990, in Chinese.
- [21] P. V. Lade, "Three-parameter failure criterion for concrete," *Journal of the Engineering Mechanics Division*, vol. 108, pp. 850–863, 1982.
- [22] S. A. B. da Fontoura, "Lade and modified lade 3D rock strength criteria," in *The ISRM Suggested Methods for Rock Characterization, Testing and Monitoring: 2007-2014*, R. Ulusay, Ed., Springer International Publishing, Cham, Switzerland, 2015.
- [23] L. I. Sedov, M. Friedman, and R. E. Street, *Similarity and Dimensional Methods in Mechanics*, Mir Publishing, Moscow, Russia, 1982.
- [24] J. Dong, J. Yang, G. Yang et al., "Research on similar material proportioning test of model test based on orthogonal design," *Journal of China Coal Society*, vol. 37, pp. 44–49, 2012, in Chinese.
- [25] The National Standards Compilation Group of the People's Republic of China, *GB50010-2010 Code for Design of Concrete Structures*, China Architecture and Building Press, Beijing, China, 2010, in Chinese.
- [26] American Concrete Institute, *Building Code Requirements for Structural Concrete and Commentary*, ACI 318R-11, American Concrete Institute, Farmington Hills, MI, USA, 2011.
- [27] X. Li, C. Rong, and H. Cheng, "Mechanical properties of high-strength concrete shaft lining based on three-parameter strength criterion," *Journal of Guangxi University (Natural Science Edition)*, vol. 41, pp. 308–316, 2016, in Chinese.
- [28] C. Amadio, C. Bedon, M. Fasan, and M. R. Pecce, "Refined numerical modelling for the structural assessment of steel-concrete composite beam-to-column joints under seismic loads," *Engineering Structures*, vol. 138, pp. 394–409, 2017.
- [29] C. Rong and H. Cheng, "Study on mechanical characteristics of reinforced concrete arc shaft wall in frozen shaft," *Rock and Soil Mechanics*, vol. 27, pp. 193–198, 2006, in Chinese.

## Research Article

# Research on Improved Equivalent Diagonal Strut Model for Masonry-Infilled RC Frame with Flexible Connection

Guang Yang ,<sup>1,2,3</sup> Erfeng Zhao ,<sup>1,2</sup> Xiaoya Li,<sup>4</sup> Emad Norouzzadeh Tochaei,<sup>5</sup> Kan Kan ,<sup>2</sup> and Wei Zhang ,<sup>2,6</sup>

<sup>1</sup>State Key Laboratory of Hydrology-Water Resources and Hydraulic Engineering, Hohai University, Nanjing 210098, China

<sup>2</sup>College of Water Conservancy and Hydropower Engineering, Hohai University, Nanjing 210098, China

<sup>3</sup>National Engineering Research Center of Water Resources Efficient Utilization and Engineering Safety, Hohai University, Nanjing 210098, China

<sup>4</sup>Melbourne Business School, The University of Melbourne, Parkville, VIC 3010, Australia

<sup>5</sup>Civil and Materials Engineering, University of Illinois at Chicago, 842 W Taylor St., Chicago, IL 60607, USA

<sup>6</sup>The Water Conservancy Bureau of Yangzhou, Yangzhou 225000, China

Correspondence should be addressed to Guang Yang; 920764311@qq.com and Erfeng Zhao; zhaoerfeng@hhu.edu.cn

Received 25 October 2018; Revised 6 January 2019; Accepted 4 February 2019; Published 4 March 2019

Academic Editor: Chiara Bedon

Copyright © 2019 Guang Yang et al. This is an open access article distributed under the Creative Commons Attribution License, which permits unrestricted use, distribution, and reproduction in any medium, provided the original work is properly cited.

The reinforced concrete (RC) frame with masonry infill wall is one of the most common structural systems in many countries. It has been widely recognized that the infill wall has significant effects on the seismic performance of RC frame structure. During the Wenchuan earthquake (China 2008), a lot of infilled RC frame structures suffered serious damages due to the detrimental effects brought about by the infill wall rigidly connected to the surrounding frame. In order to solve this problem, flexible connection, introduced by Chinese designers, is recommended by the updated Chinese seismic design code, because of its effect to reduce the unfavorable interaction between infill wall and frame. Although infilled RC frame structure with flexible connection has a lot of advantages, but because of the lack of research, this structure type is seldom used in practical engineering. Therefore, it is of great significance to scientifically investigate and analyze the effects of flexible connection on structure behaviors of infilled RC frame. In this study, a macrofinite element numerical simulation method for infilled RC frame with flexible connection was investigated. Firstly, the effects of connection between infill wall and surrounding frame on in-plane behaviors of infilled RC frame were discussed. Secondly, based on deeply studying the equivalent diagonal strut models for infilled RC frame with rigid connection, an improved equivalent diagonal strut model for infilled RC frame with flexible connection was proposed. Employed with inversion analysis theory, the parameter in the proposed model was estimated through artificial fish swarm algorithm. Finally, applied with the existing experiment results, a case study was conducted to verify the effectiveness and feasibility of the proposed model.

## 1. Introduction and Literature Review

Infilled reinforced concrete (RC) frame structure is a commonly used structural system around the world. Usually, the infill wall is considered as a nonstructural component, and the interaction between infill wall and surrounding frame is ignored. However, numerous studies have shown that infill wall has significant effects on the seismic performance of RC frame structure. With the deepening of research and complexity, some scholars

believed that the connection between infill wall and surrounding frame also has considerable influences on the seismic performance of infilled RC frame. Generally speaking, applied with some construction measures, such as concrete structural column, core columns, binding steel bar, and so on, the infill wall close connects with the surrounding frame. This kind of connection is called rigid connection, as shown in Figure 1(a). However, during the 2008 Wenchuan earthquake, a lot of masonry-infilled RC frame structures suffered severe damages (Figure 2), due to the detrimental

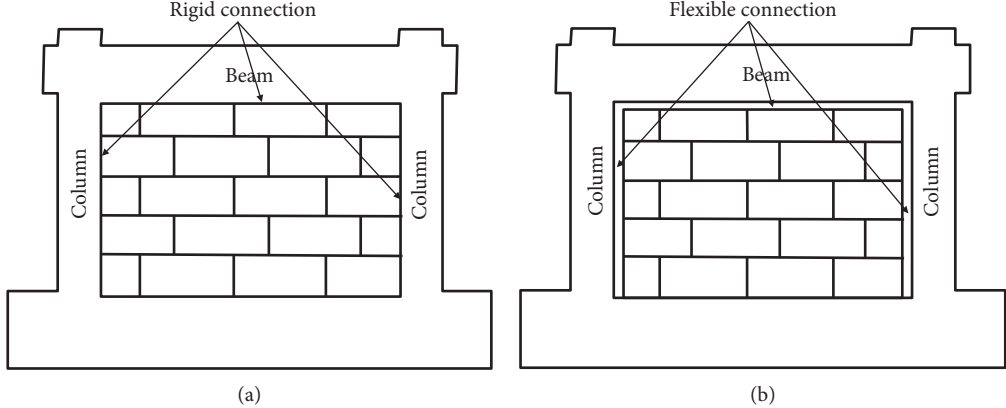


FIGURE 1: Connection types between infill wall and surrounding frame.



FIGURE 2: Damages of infilled RC frames after the 2008 Wenchuan earthquake.

effects brought about by the infill wall rigidly connected to the surrounding frame. In order to solve this problem, a preset crack is set between the infill wall and the surrounding frame, and the width of preset crack is in the range of 20 mm~30 mm. Moreover, the preset crack is filled with vibration-absorptive material, such as polystyrene foam board and flexible foaming agent. Therefore, the infill wall is separated from the surrounding frame, and this kind of connection is called flexible connection (Figure 1(b)) by Chinese designers. According to the updated Chinese seismic design code [1], the flexible connection is recommended, because of its ability to reduce the unfavorable interaction between infill wall and surrounding frame as well as to improve the seismic performance of infilled RC frame structure [2]. Therefore, it is of great significance to scientifically investigate and analyze the effects of flexible connection on behaviors of infilled RC frame.

To date, in general, many researchers have experimentally and numerically investigated the structure behaviors of infilled RC frame. Following, an overview of research findings were investigated. Since the first attempt completed by Thomas [3], a large number of experiment researches on infilled RC frame have been concluded. Mehrabi et al. [4] completed an experiment research on twelve RC frames infilled with brick masonry and concluded that the maximum force capacity of infilled RC frame is about 1.5~2.3 times than that of bare frame. Stylianidis [5] introduced three successive experiment studies on RC frame which were infilled with perforated clay brick block masonry. Tests results showed that the effects of infill wall on the strength, stiffness, and energy dissipation capacity of RC frame are significant. The data from Kakaletsis and Karayannidis [6] indicated that RC frames with strong infills showed higher initial stiffness and

higher ductility than those with weak infills, but infill strength did not substantially influence strength or energy dissipation. Cavalieri and Trapani [7] reported that the frames infilled with lightweight concrete masonry and calcarenite masonry can improve the dissipative properties compared to the RC frames infilled with clay masonry. Regarding the effects of opening on the performance of infilled RC frame, Kakaletsis and Karayannis [8] investigated single-story, single-bay scaled specimens under cyclic horizontal loading. Research results showed that for low lateral displacement, the energy dissipation of specimens with openings was higher than that of bare frame; for high lateral displacement, the energy dissipation of specimens with openings was reduced and that of the bare frame remained constant. Mallick and Garg [9] investigated the effect of opening positions on the behavior of infilled RC frames with or without shear connectors. They found that an opening at either end of the loaded diagonal of an infilled frame without connectors reduces its lateral strength about 75%, and its lateral stiffness about 85–90% as compared to that of a similar infilled frame with solid infill wall (without opening). For infilled RC frames with shear connectors, the presence of an opening on either end of the loaded diagonal reduces its stiffness by 60%–70% as compared to that of similar infilled RC frame with a solid infill wall. For both types of frames, the loss of strength and stiffness due to a centrally loaded square opening having side dimensions one fifth those of the panel is about 25%–50% compared to similar frames without openings. In recent years, some Chinese researchers considered the effects of connection between infill wall and surrounding frame. Jiang et al. [10] completed an experimental research on five RC frame specimens with masonry infill wall and flexible connection. The results showed that flexible connections can retard the stiffness degradation and improve the energy dissipation ability of frame structure. Zhou et al. [11] and Peng et al. [12] investigated the failure mechanism and seismic behaviors of the infilled RC frames with different connections. The experimental results showed that the specimens with flexible connection have lower bearing capacity than those with rigid connections, but the other performance indexes are better.

In recent years, there have been achieved great successes in nonlinear finite element modeling methods for masonry-infilled RC frame structures [13–19]. From a general point of view, there are two different approaches [20–23]: microfinite element approach and macrofinite element approach, as shown in Figure 3. According to Lourenco [21], the micromodelling approach for masonry infill wall can be summarized in two different ways: simplified micromodelling method and detailed micromodelling method. For the first one (Figure 4(a)), the expanded units are represented by continuum elements and the properties of mortar and brick-mortar interface are lumped into a common element. For the second one (Figure 4(b)), brick units and mortar are represented by continuum elements, and brick units-mortar interaction are represented by different continuum elements, which leads to accurate results and intensive computational

requirement. Zhou et al. [24] proposed a microfinite element simulation method for infilled RC frame with flexible connection. The plane stress element was utilized to simulate the infill wall, and the spring element was utilized to simulate the connection between filled wall and surrounding frame. The simulation results showed that the proposed method can reflect the characteristics of wall-frame interactions effectively. Applied with the quasistatic test results, a finite element analysis research was conducted by Peng et al. [12]. Research results showed that the influence of connection type and constructional details of infill wall are significant. Till now, the microfinite element methods for infilled RC frame have achieved a lot of achievements, and extensive and in-depth state-of-the-art reports can be found in [23]. However, studies on the microfinite element methods for infilled RC frame with flexible connection are relatively few.

For macrofinite element method, it is on the basis of replacing the infill wall by one (or more) equivalent strut. This method is usually frequently employed in order to perform nonlinear static or dynamic analyses because of its simplicity, and most technical codes also suggest the macromodel method. Holmes [25] replaced the infill wall with an equivalent diagonal strut, and the cross-section width ( $w$ ) equal to 1/3 of the diagonal length ( $d$ ). Afterwards, based on modifying the equivalent width, several researchers put forward a series of detailed methods [26–28]. With the deepening of research and complexity, some researchers took into account the local shear stresses transferred by the infill wall to the surrounding frame and proposed a series of multiple-strut macrofinite element models. Crisafulli [29] investigated the influence of different multiple-strut configurations in structural response. Crisafulli and Carr [30] developed a multiple-strut macrofinite element model including classical truss elements and a special shear spring to simulate the influence of the vertical load on the overall strength of the infill wall (Figure 5(a)). Chrysostomou et al. [31] proposed a six-strut model, which take into account both stiffness and strength degradation of infill walls (Figure 5(b)). El-Dakhakhni et al. [32] proposed a three-strut model having one concentric and two eccentric struts (Figure 5(c)). For infill walls with openings, some researchers have proposed the use of conventional equivalent diagonal struts with a reduction factor, the value of which is derived from some geometrical properties of opening and masonry infill wall [33, 34]. Another approach to model a masonry infill wall with opening is to use a series of horizontal springs, where each spring represents a subpanel of infill wall [35]. Till now, the macrofinite simulation methods for infilled RC frame have achieved considerable success; extensive and in-depth state-of-the-art reports can be found in [36, 37].

Judging from the existing research findings, studies on experiments and numerical simulation methods for infilled RC frame with flexible connection are few, and there is no systematic study. In this study, a macrofinite element numerical simulation method for infilled RC frame with flexible connection was proposed. Firstly, the effects of connection between infill wall and surrounding frame on in-plane

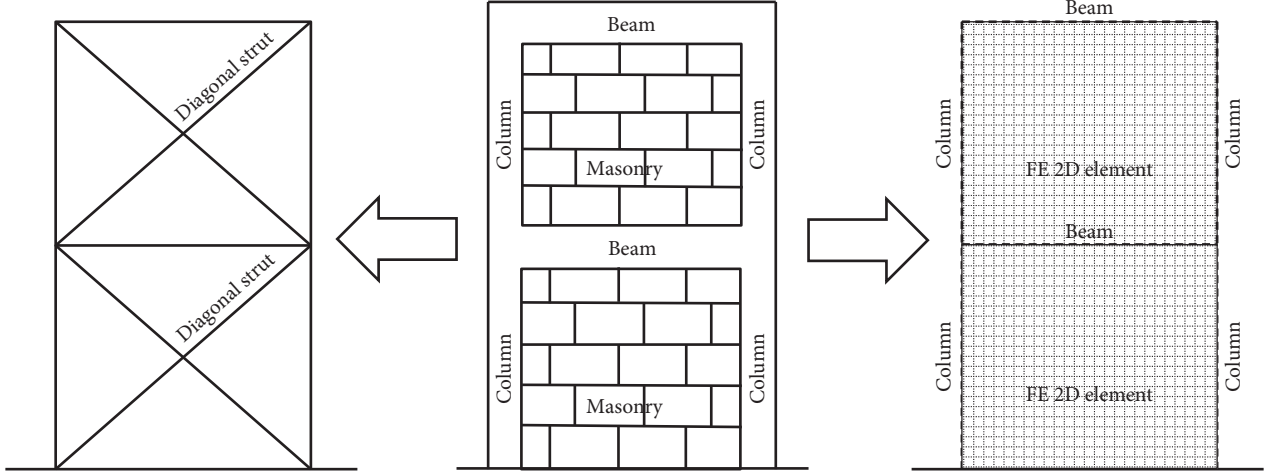


FIGURE 3: Macrofinite element approach and microfinite element approach.

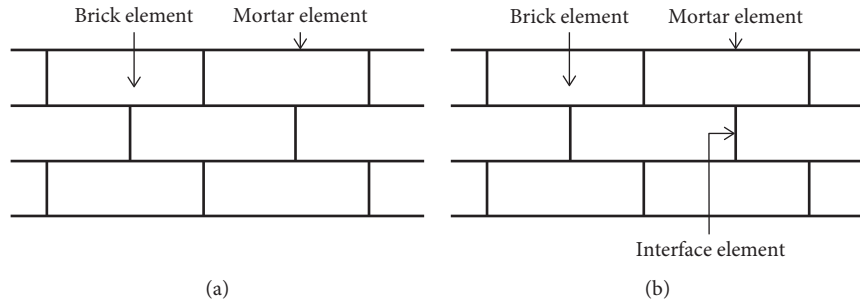


FIGURE 4: Micromodeling method: (a) simplified micromodeling; (b) detailed micromodeling.

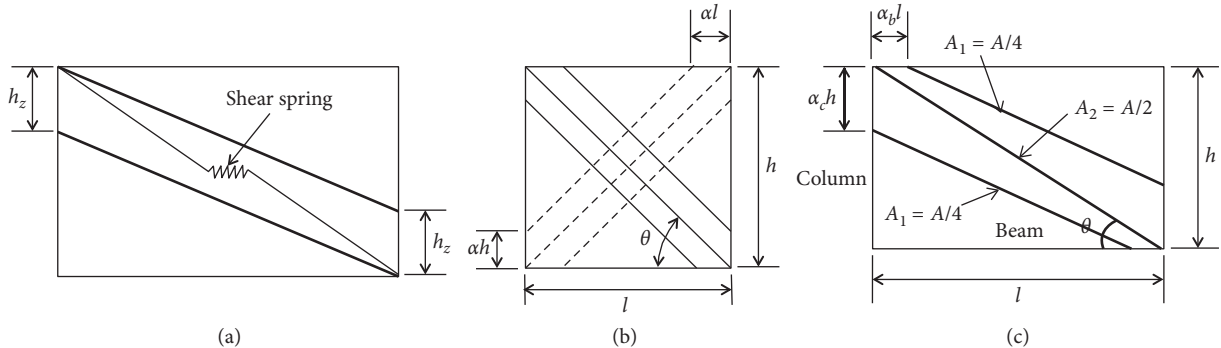


FIGURE 5: Multiple-strut macrofinite element models: (a) double-strut model with shear spring [30]; (b) six-strut model [31]; (c) three-strut model [32].

behaviors of infilled RC frame were discussed. Secondly, based on deeply studying the equivalent diagonal strut models for infilled RC frame with rigid connection, an improved equivalent diagonal strut model for infilled RC frame with flexible connection was proposed, and the parameter in the proposed model was estimated through artificial fish swarm algorithm. Finally, based on the existing experiment results, a case study was conducted to verify the effectiveness and feasibility of proposed model. Simulation results showed that the proposed model is effective.

## 2. Effects of Connection on In-Plane Behaviors of Infilled RC Frame

In this section, combined with existing research achievements, the effects of connection between infill wall and surrounding frame on in-plane behaviors of infilled RC frame were deeply discussed, which lays a solid foundation for the subsequent research.

Generally speaking, under the action of horizontal lateral force, the in-plane failure process of infilled RC

frame consists of four stages, and the characteristics in each stage can be characterized as follows. In stage 1, infill wall and surrounding frame are in elastic state and work together to bare the horizontal lateral force. In stage 2, with the increase of lateral load, cracks occur at the contact area of surrounding frame and infill wall, and the diagonal areas of infill wall are crushed. In this stage, the frame structure is still in elastic state, but because of the propagation of concrete cracks and crushed zone, infill wall and surrounding frame cannot work together to bare the horizontal lateral force. In stage 3, with the continuous increase of load, cracks occur at beams and columns, and due to the oversize crushed zone, the infill wall loses its bearing capacity. In stage 4, the horizontal lateral force is mainly borne by beams and columns. When the horizontal lateral force reaches a threshold, the frame structure will be destroyed. From the point of view of lateral deformation, the above-mentioned failure process can be simplified as a deformation process as shown in Figure 6(a). Figure 6(b) shows the stiffness degradation of two specimens performed by Huang [38], one specimen is a bare frame and another one is an infilled RC frame with rigid connection. Figure 6(c) shows the deformation failure processes of above-mentioned two specimens under the action of horizontal lateral forces, and the following conclusions can be obtained. Firstly, the initial lateral stiffness of infilled RC frame with rigid connection is about 2.69 times than that of bare frame. During the experimental process, the stiffness degradation of infilled RC frame with rigid connection is faster than that of bare RC frame. At the end of experiment, the lateral stiffness of infilled RC frame with rigid connection is approximately equal to that of rare frame, which indicates that the infill wall has basically been destroyed in the later stage, and the lateral stiffness of frame structure are mainly provided by frame. Secondly, for the specimen with rigid connection, the yield displacement and yield load are about 7.12 mm~8.03 mm and 169 KN~272 KN, respectively; and for the rare frame, the yield displacement and yield load are about 9.13 mm and 145 KN, respectively. So, the infilled RC frame with rigid connection yielded earlier than the rare frame in the experiment process. Thirdly, the horizontal bearing capacity of infilled RC frame with rigid connection is 271 KN, about 1.6 times that of the bare frame (191 KN). Therefore, infill wall with rigid connection can significantly enhance both the initial lateral stiffness and strength of frame structure, but due to the effects brought about by infill wall rigidly connected to surrounding frame, the infill wall is easy to be damaged under the action of horizontal lateral forces.

In order to investigate the effects of flexible connection on in-plane behaviors of infilled RC frame, a quasistatic experiment was performed by Zhou et al. [11]. Figure 7(a) shows the stiffness degradation of three specimens, one specimen is a rare frame, one is an infilled RC frame with rigid connection, and another one is an infilled RC frame with flexible connection; Figure 7(b) shows the deformation failure processes of above-mentioned specimens; Figure 8 shows the failure modes of above-mentioned specimens; and the following conclusions can

be obtained. Firstly, the initial lateral stiffness of infilled RC frame with rigid connection is about 4.28 times that of bare frame, and the initial lateral stiffness of specimen with flexible connection is about 1.96 times that of bare frame. During the experimental process, the stiffness degradation processes of specimens with rigid connection and flexible connection are all faster than that of bare frame, but flexible connection can retard the stiffness degradation of frame structure. Secondly, for the specimen with rigid connection, the yield displacement and yield load are about 6.84 mm and 373.88 KN, respectively; for the specimen with flexible connection, the yield displacement and yield load are about 7.08 mm and 251.0 KN, respectively; and for the rare frame, the yield displacement and yield load are about 9.59 mm and 166.3 KN, respectively. Thirdly, the horizontal bearing capacity of specimen with rigid connection is 421.1 KN, about 1.48 times than that of bare frame (284.5 KN), and the horizontal bearing capacity of specimen with flexible connection is 331.2 KN, about 1.16 times that of the bare frame. According to the above analysis, although the effects of flexible connection on lateral stiffness and bearing capacity of frame structure are inferior to that of rigid connection, it can reduce the unfavorable interaction between infill wall and surrounding frame, retard the stiffness degradation, and effectively improve the seismic performance of frame structure.

### 3. Improved Equivalent Diagonal Strut Model

According to Section 2, there exist significant differences in effects of connection on in-plane behaviors of infilled RC frame. On this basis, based on discussing the action pattern of flexible connection, an improved equivalent diagonal strut model for simulating the in-plane behavior of infilled RC frame with flexible connection was proposed in this section.

**3.1. Action Pattern of Flexible Connection.** The infilled RC frame with flexible connection is one kind of new structure types, so there are great differences between the action pattern of flexible connection and that of rigid connection. Generally speaking, the action pattern of rigid connection can be characterized by contact model, as shown in Figure 9(a). Specifically, in normal direction, if contact pressure is less than or equal to 0, two contact surfaces will separate from each other, and if contact pressure is greater than 0, load will transfer between infill wall and surrounding frame. For flexible connection, the preset crack between infill wall and surrounding frame is filled with vibration-absorptive materials, so its action pattern is much more complicated than that of rigid connection. Based on deeply studying the properties of vibration-absorptive materials [39, 40], the compression behavior of filling material can be characterized by the Kelvin model [41, 42] and the tensile behavior of filling material can be characterized by failure element model [42], as shown in Figure 9(b). Therefore, if the microfinite element analysis approach is adopted, the

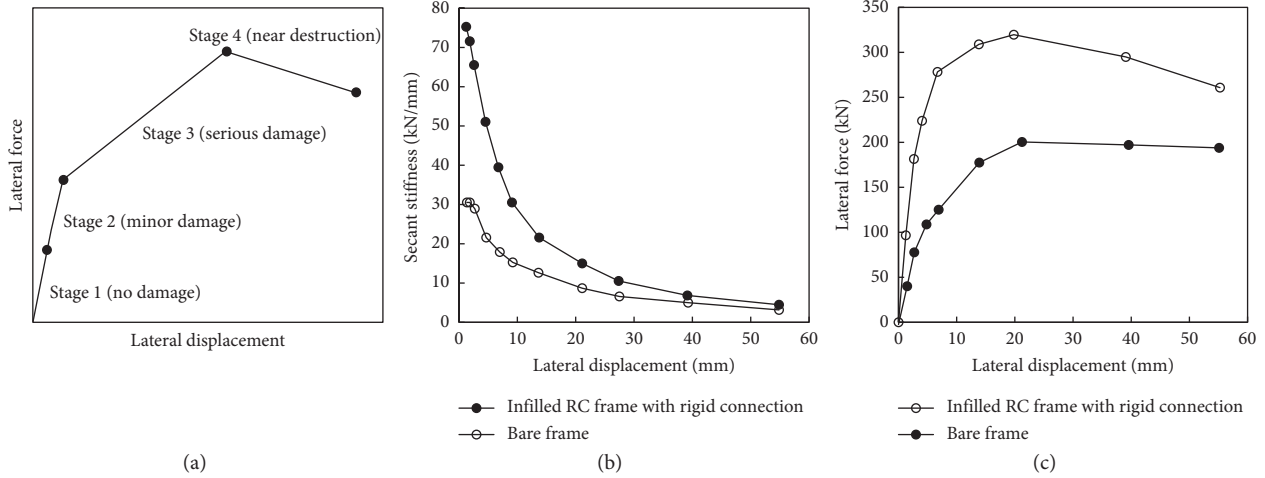


FIGURE 6: (a) Deformation failure processes; (b) stiffness degradation of two specimens provided by reference [38]; (c) deformation failure processes of two specimens provided by reference [38].

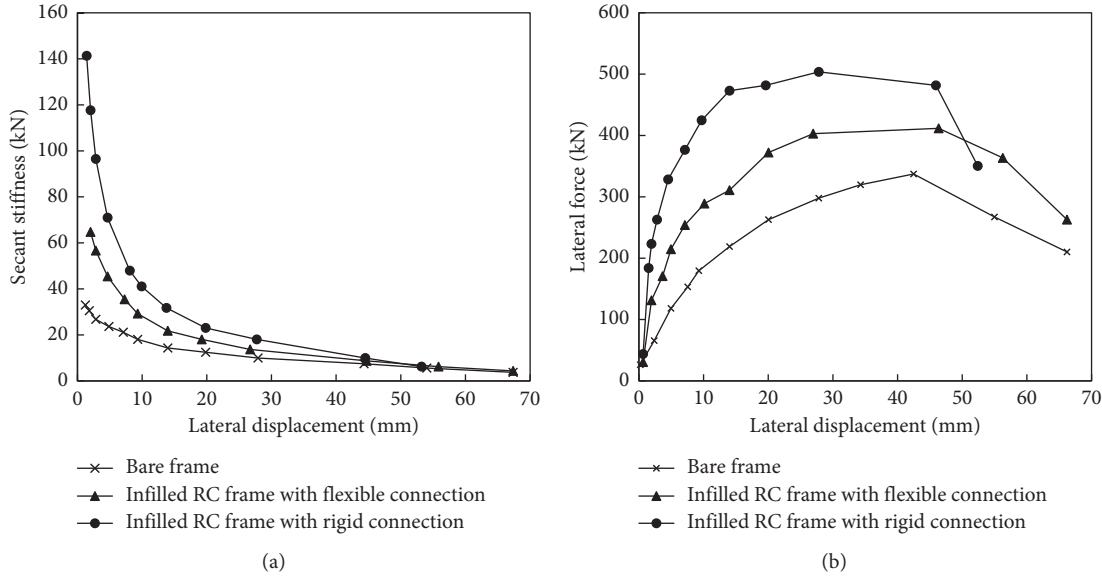


FIGURE 7: (a) Stiffness degradation of two specimens provided by reference [11]; (b) deformation failure processes of three specimens provided by reference [11].

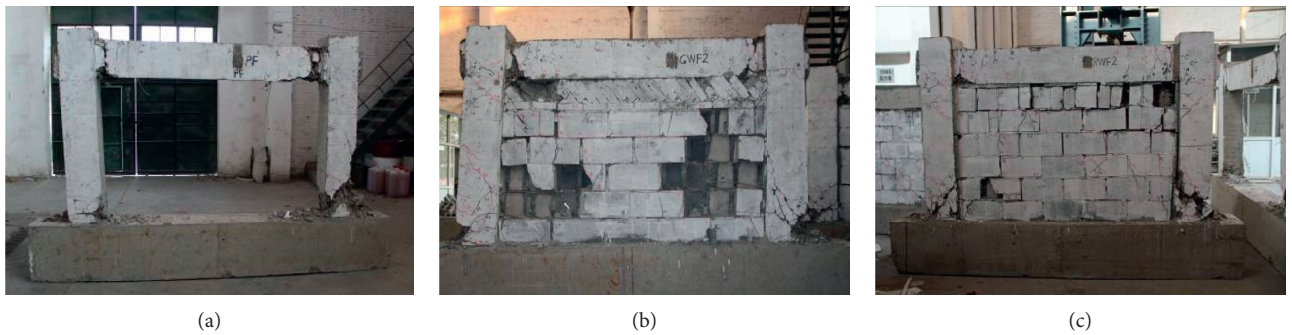


FIGURE 8: Final failure modes of three specimens provided by reference [11]: (a) bare frame; (b) infilled RC frame with rigid connection; (c) infilled RC frame with flexible connection.

behavior of flexible connection can be accurately simulated. For macrofinite element analysis approach, some simplifications must be adopted.

The effects of flexible connection on lateral stiffness of infilled RC frame are similar to that of opening. So in this study, combined with the macrofinite element simulation methods for infilled RC frame with opening, a simplified analysis method for simulating the effects of flexible connection on infilled RC frame was proposed. The effects of opening on the lateral stiffness of infilled RC frames were deeply investigated by references [33, 34], and the stiffness reduction factor  $\lambda$ , defined as the stiffness of the infill wall with opening to that of the infill wall without opening, was introduced to characterize the effects of opening. According to the research findings provided by references [33, 34], the parameter  $\lambda$  is related to the opening percentage (opening area/infill wall area) and opening position. Figure 10 shows three typical opening positions, named Case A, Case B, and Case C. Figure 11 shows the relationship between stiffness reduction factor and opening percentage (0%~25%) of the above-mentioned cases, and the following findings can be obtained. Firstly, if the opening position is fixed, the increase of opening percentage led to the stiffness degradation of infilled RC frame. Secondly, if the opening percentage is fixed, the opening positions have great influences on the stiffness reduction factor. For above-mentioned cases, the stiffness reduction factor of Case A is the maximum, the second one is Case B, and the stiffness reduction factor of Case C is the minimum. It has been proved that the stiffness reduction factor  $\lambda$  of Case B can be expressed as follows:

$$\lambda = 1 - 2\alpha_w^{0.54} + \alpha_w^{1.14}. \quad (1)$$

In equation (1),  $\alpha_w$  denotes the opening percentage of infill wall. On this basis, the single-strut model for Case B was proposed by reference [33], and the effectiveness of proposed model was verified through a study case.

For the infilled RC frame with flexible connection, as shown in Figure 1(b), it can be considered as the infilled RC frame with opening, and its location is at the joint area between infill wall and surrounding frame. So in this study, the effects of flexible connection on infilled RC frame are also characterized by stiffness reduction factor  $\lambda$ . According to Section 1, the width of preset crack is in the range of 20 mm~30 mm, so the opening area is much less than the area of infill wall. Therefore, the opening position and opening percentage are approximately fixed, so the stiffness reduction factor  $\lambda$  of flexible connection can be approximately considered as a constant value.

**3.2. Model Constructing.** Judging from the existing research results, a lot of researchers have studied the macrofinite element numerical simulation methods for infilled RC frame with rigid connection, summarized as single-strut macrofinite element models and multiple-strut macrofinite element models. In this section, based on deeply studying the

existing single-strut models for infilled RC frame with rigid connection, an improved single-strut model for infilled RC frame with flexible connection was proposed.

According to references [25, 43, 44], the width ( $w$ ) of equivalent compressed diagonal strut can be expressed as equations (2)–(4). The above equations were accepted by the majority of researchers dealing with the analysis of infilled RC frame with rigid connection and also recommended by many existing seismic design codes [45–47].

$$\frac{w}{d} = 0.175 \cdot \lambda_h^{-0.4}, \quad (2)$$

$$\lambda_h = \sqrt[4]{\frac{E_w t_w \sin(2\theta)}{4E_c I_c H_{in}}}, \quad (3)$$

$$\theta = \tan^{-1}\left(\frac{h_w}{L_w}\right). \quad (4)$$

In above equations,  $d$  denotes the diagonal length of the infill wall,  $E_w$  denotes the modulus of elasticity of the infill wall,  $E_c I_c$  denotes the flexural rigidity of the columns,  $t_w$  denotes the thickness of the infill wall and equivalent strut,  $h$  denotes the column height between centerlines of beams,  $L_w$  denotes the length of infill wall, and  $h_w$  denotes the height of infill wall. The meanings of the above-mentioned parameters are shown in Figure 12.

According to section 3.1, the effect of flexible connection on the lateral stiffness of infilled RC frame is similar to that of opening. Therefore, the stiffness reduction factor  $\lambda$  was introduced to improve equation (2), which can be expressed as follows:

$$\frac{w}{d} = 0.175 \cdot \lambda \cdot \lambda_h^{-0.4}. \quad (5)$$

Therefore, the key problem is to determine the value of stiffness reduction factor ( $\lambda$ ). In this study, inversion analysis theory [48, 49] was introduced to solve this problem. Generally speaking, a lot of monitoring instruments are installed in the specimens, such as LVDT, optical fiber, and so on, and during the experimental process, the measured values of effect quantities, such as displacement, force, stress, and so on, will be acquired. The principle of inversion analysis is to make measured values and calculated values as near as possible and, on this basis, seek the optimal values of undetermined parameters. So based on the principle of minimum residual sum of squares, a constrained optimization problem, for estimating the value of stiffness reduction factor, can be constructed:

$$\begin{cases} \min & Q(\lambda) = \sum_{i=1}^n \sum_{j=1}^m (\delta_{ij} - \delta'_{ij})^2, \\ \text{s.t.} & \underline{\lambda} \leq \lambda \leq \bar{\lambda}. \end{cases} \quad (6)$$

In equation (6),  $m$  denotes the total number of measured values,  $n$  denotes the number of monitoring instruments,  $\delta_{ij}$  denotes the experimental values,  $\delta'_{ij}$  denotes the calculated value,  $\lambda$  denotes the stiffness reduction factor,  $\bar{\lambda}$  denotes the upper limit of parameter  $\lambda$ , and  $\underline{\lambda}$  denotes the lower limit of

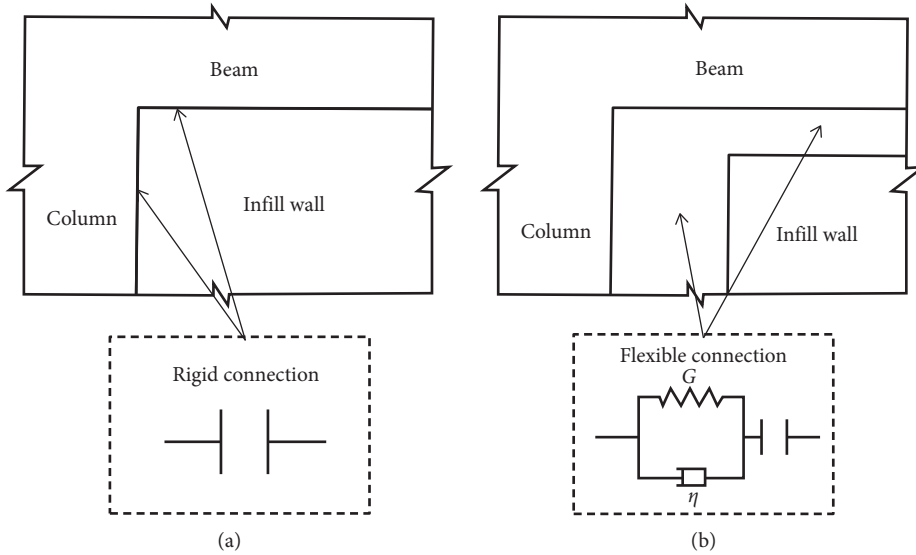


FIGURE 9: Action patterns of flexible connection and rigid connection.

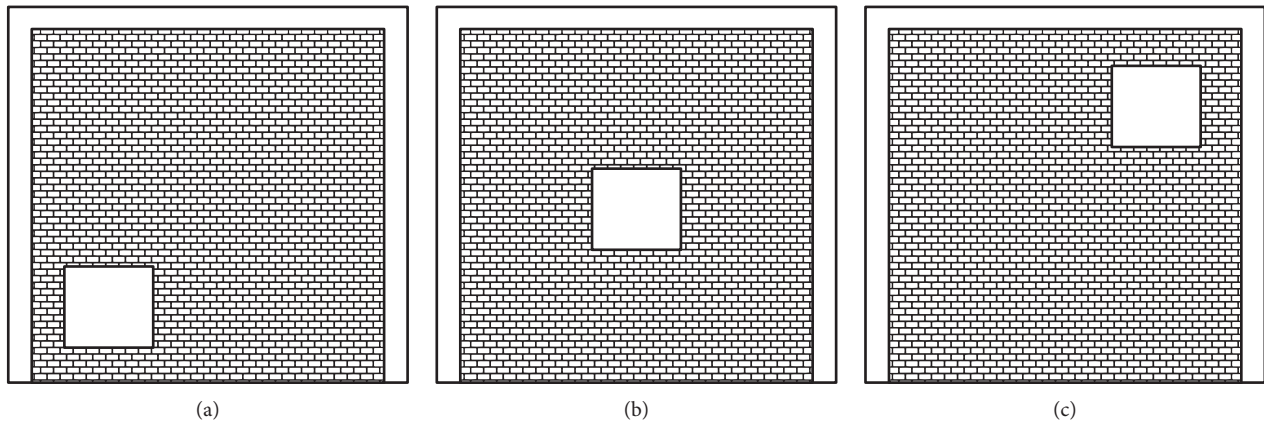


FIGURE 10: Opening positions. (a) Case A, (b) Case B, (c) Case C.

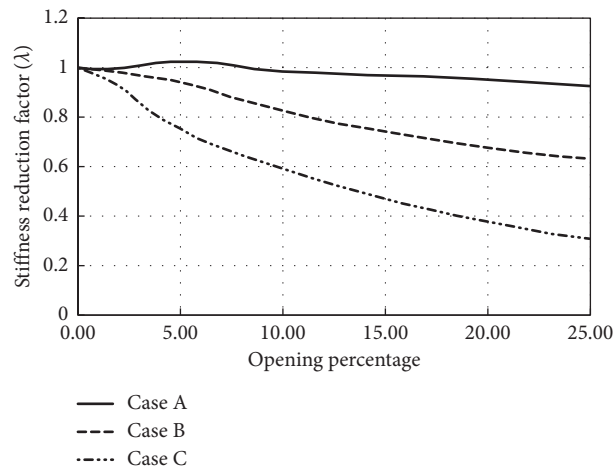


FIGURE 11: The relationship between the stiffness reduction factor and the opening percentage.

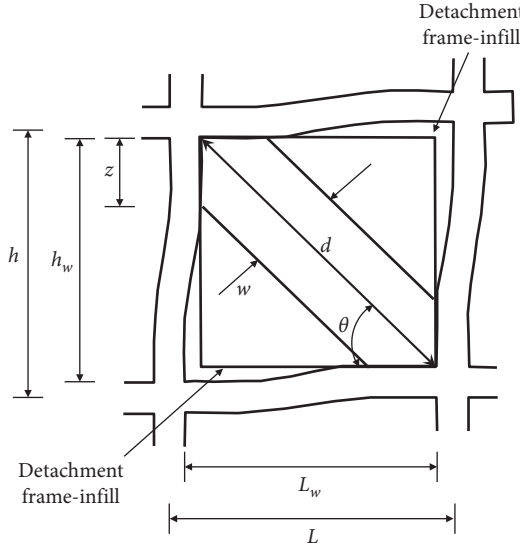


FIGURE 12: Equivalent diagonal strut model.

parameter  $\lambda$ . Therefore, the estimation problems of parameters in proposed models are transformed into a constrained optimization problem. In this study, the global optimum solution of objective function (6) was searched by artificial fish swarm algorithm (AFSA).

**3.3. Parameters Estimation.** In nature, a fish moves to the region with more food by vision or sense, and this behavior is called preying. Also, in order to guarantee their existence and avoid danger, nature fish assemble and move in groups, and this behavior is called swarming. What's more, if a fish researches a region with more food, the other fish will trail and reach this region, and this behavior is called chasing. On the basis of above-mentioned behaviors, artificial fish swarm algorithm (AFSA) [50–52] possesses a high search speed and global search capability.

If a minimization problem having D-dimensional search space,  $N$  denotes the population quantity of artificial fish swarm.  $X_i = (x_{i1}, x_{i2}, \dots, x_{iD})$  denotes the position of artificial fish  $i$ . The food concentration at position  $X_i$  is denoted by  $Q(X_i)$ . The distance between  $X_i$  and  $X_j$  is denoted by  $d_{ij} = X_i - X_j$ . The parameter  $Step$  denotes the largest allowed space step of an artificial fish.  $\delta$  denotes the crowded degree of artificial fish swarm.  $Visual$  denotes the visible range of an artificial fish.  $t$  denotes the iteration number.  $Num$  denotes the maximum number of iterations. If the number of iterations is greater than  $Num$ , the iteration will be suspended; otherwise, continue iterating.

The preying behavior of artificial fish swarm has been described below. Suppose the initial state of artificial fish  $i$  is denoted by  $X_i$ , this artificial fish randomly chooses a new state within its visual, and the new state  $X'_i$  can be expressed as follows [50]:

$$X'_i = X_i + \text{rand}(0, 1) \times \text{visual}. \quad (7)$$

If  $f(X_j) < f(X'_i)$ , the artificial fish  $i$  moves toward to  $X_i^{(t+1)}$ , based on the equations (8) and (9) [51, 52]:

$$X_i^{(t+1)} = X_i^{(t)} + \text{rand}(0.1) \times \text{step} \times \frac{X_j^{(t)} - X_i^{(t)}}{\|X_j^{(t)} - X_i^{(t)}\|}, \quad (8)$$

$$\|X_j^{(t)} - X_i^{(t)}\| = \sqrt{(X_j^{(t)})^2 - (X_i^{(t)})^2}. \quad (9)$$

If  $f(X_j) > f(X'_i)$ , the artificial fish  $i$  selects another state randomly. If the artificial fish  $i$  fails to find a feasible solution within the given time, under this circumstance, it moves one step randomly, based on equation (10) [53, 54]:

$$X_i^{(t+1)} = X_i^{(t)} + \text{rand}(0, 1) \times \text{step}. \quad (10)$$

The swarming behavior of artificial fish swarm has been described below. Suppose the present position of an artificial fish is denoted by  $X_i$ ,  $nf$  denotes the number of artificial fish within a particular visual,  $X_c$  denotes the center position of artificial fish swarm, and  $Y_c$  denotes the food concentration of  $X_c$ .  $X_c$  and  $Y_c$  can be expressed as follows:

$$X_c = \sum_j \frac{X_j}{nf}, \quad (11)$$

$$Y_c = Q(X_c).$$

If  $(Y_c/nf) < \delta Y_i$ , then this is not a crowded area. Otherwise, the artificial fish  $i$  moves toward  $X_i^{(t+1)}$  in the following direction [55]:

$$X_i^{(t+1)} = X_i^{(t)} + \text{rand}(0.1) \times \text{Step} \times \frac{X_c^{(t)} - X_i^{(t)}}{\|X_c^{(t)} - X_i^{(t)}\|}. \quad (12)$$

If swarming is not advantageous, AFSA executes the preying behavior.

The chasing behavior of artificial fish swarm was described below. Suppose the present position of an artificial fish is denoted by  $X_i$ ,  $X_m$  denotes the best position with highest food consistence within artificial fish  $i$ 's visual, and  $nf$  denotes the number of artificial fish within a particular visual. If  $(Y_m/nf) > \delta Y_i$ , the artificial fish  $i$  moves one step toward  $X_i^{(t+1)}$ , which can be expressed as follows [54, 56]:

$$X_i^{(t+1)} = X_i^{(t)} + \text{rand}(0.1) \times \text{step} \times \frac{X_m^{(t)} - X_i^{(t)}}{\|X_m^{(t)} - X_i^{(t)}\|}, \quad (13)$$

If this is not advantageous, AFSA also executes the preying behavior.

## 4. Simulation and Analysis

The Open System for Earthquake Engineering Simulation (OpenSEES) is a software framework for simulating the seismic response of structural and geotechnical systems. It provides a wide range of element types and material models for nonlinear finite element analysis [56–59]. According to the quasistatic experiment performed by Zhou et al. [11, 24], three specimens were tested under the action of horizontal lateral cyclic force, one specimen is a bare frame (PF), one is an infilled RC frame with rigid connection (GWF1), and

another one is an infilled RC frame with flexible connection (RWF1). In this section, based on the experiment results provided by references [11, 24], OpenSEES was applied to the numerical simulation analysis, and then a case study was conducted to verify the effectiveness and feasibility of proposed model.

**4.1. Modeling Details.** The dimensions and reinforcements of beams and columns are shown in Figure 13. The lateral loading protocol is shown in Figure 14. In the computational model, beams and columns were represented by displacement-based beam-column element, and cross sections were defined using fiber discretization with distinct layers for longitudinal reinforcement [60]. Equivalent diagonal struts were represented by truss element.

For material model used in this paper, the longitudinal steel bar was modeled by Steel01 (Figure 15(a)), masonry was modeled by Concrete01 (Figure 15(b)), and concrete was modeled by Concrete02 (Figure 15(c)). The material parameters of concrete, rebar, and masonry are shown in Tables 1–3, respectively. Confining effect due to the prescribed transverse reinforcement is accounted for using confined concrete properties for core concrete material as suggested by Mander et al. [61, 62].

The model proposed by Zhao and Sridharan [63] was used to characterize the stress and end slip response of steel rebar. This model imitates the strain penetration effects using the zero-length section element [60]. A zero-length section element includes one section corresponding to one integration point, which determines the force-deformation response of the element. The function embodied in Figure 16 depicts the envelope of the bar stress versus the slip response at the end of the flexural member. The slip at the point that the bar stress reaches the yield ( $s_y$ ) and ultimate strengths ( $s_u$ ) are obtained from the equations (14) and (15), respectively:

$$s_y = 0.1 \left[ \frac{d_b}{4} \frac{f_y}{\sqrt{f'_c}} (2\alpha + 1) \right]^{1/\alpha} + 0.0134, \quad (14)$$

$$s_u = 35s_y. \quad (15)$$

In equations (14) and (15),  $d_b$  (in) denotes the diameter of rebar,  $f_y$  (ksi) and  $f'_c$  (ksi) denote the yield strength of rebar and compressive strength of concrete, respectively, and the parameter  $\alpha$  is set to 0.4.

**4.2. Simulation Results of PF and GWF1.** In this section, nonlinear pushover analysis and nonlinear hysteretic analysis for PF and GWF1 were conducted, respectively. Based on the equations (2)–(4), the parameters of equivalent diagonal strut model for GWF1 can be determined, as listed in Table 4. Figure 17 shows the comparison between nonlinear pushover analysis results and corresponding experiment results of PF and GWF1. According to the calculation results, in the stage of linear deformation, the simulation results approach to the measured values. Due to measurement errors, limitations of material models, and so on, there

exist some deviations between the simulation results and the experiment results in the stage of nonlinear deformation. However, these deviations are permissible in engineering practice. The comparison between nonlinear hysteretic analysis result and corresponding experiment result of for GWF1 is shown in Figure 18(a), and the comparison between simulation result and experiment result of stiffness degradation of GWF1 during the process of pushover is shown in Figure 18(b). According to the calculation results, the equivalent diagonal strut model for infilled RC frame with rigid connection is effective and can reflect the characteristics of wall-frame interaction.

**4.3. Simulation Results of RWF1.** According to the lateral loading protocol as shown in Figure 14, the objective function (6) can be written as follows:

$$\begin{cases} \min & Q(\lambda) = \sum_{j=1}^m (F_j - F'_j)^2, \\ \text{s.t.} & \underline{\lambda} \leq \lambda \leq \bar{\lambda}. \end{cases} \quad (16)$$

In equation (16),  $F_i$  denotes the measured value of lateral force at the control displacement  $i$ ,  $F'_i$  denotes the calculated value of lateral force at the control displacement  $i$ ,  $\lambda$  denotes the stiffness reduction factor,  $\bar{\lambda}$  denotes the upper limit of parameter  $\lambda$ , and  $\underline{\lambda}$  denotes the lower limit of parameter  $\lambda$ . Figure 19 shows the comparison between pushover analysis results and corresponding experiment results under different stiffness reduction conditions. According to the calculation results, the decrease of stiffness reduction factor leads to the decrease of initial lateral stiffness and bearing capacity of FEM model for RWF1. Moreover, due to measurement errors, limitations of material models, and so on, there exist some deviations between the simulation results and experiment results in the nonlinear stage. Therefore, based on the principle of inversion analysis introduced in Section 3.2, the experiment values of linear stage were applied to determine the stiffness reduction factor of flexible connection.

Generally speaking, the stiffness reduction factor  $\lambda$  is in the range of [0, 1]. The parameters of AFSA were listed as follows:  $N$  was set to 20,  $Visual$  was set to 1,  $\delta$  was set to 0.618,  $Step$  was set to 0.5,  $Num$  was set to 200, and the convergence threshold  $\epsilon$  was set to  $1 \times 10^{-4}$ . The optimization process of AFSA is shown in Figure 20. According to the optimization results, AFSA converged with 70 iterations, and the convergence value of stiffness reduction factor was equal to 0.52. Therefore, the strut width  $w$  of improved equivalent diagonal strut for infilled RC frame with flexible connection can be expressed as follows:

$$w = 0.091 \cdot \lambda_h^{-0.4} \cdot d, \quad (17)$$

$$\lambda_h = \sqrt[4]{\frac{E_w t_w \sin(2\theta)}{4E_c I_c H_{in}}}. \quad (18)$$

Employed with the equations (17) and (18), the parameters of the equivalent diagonal strut model for RWF1 are

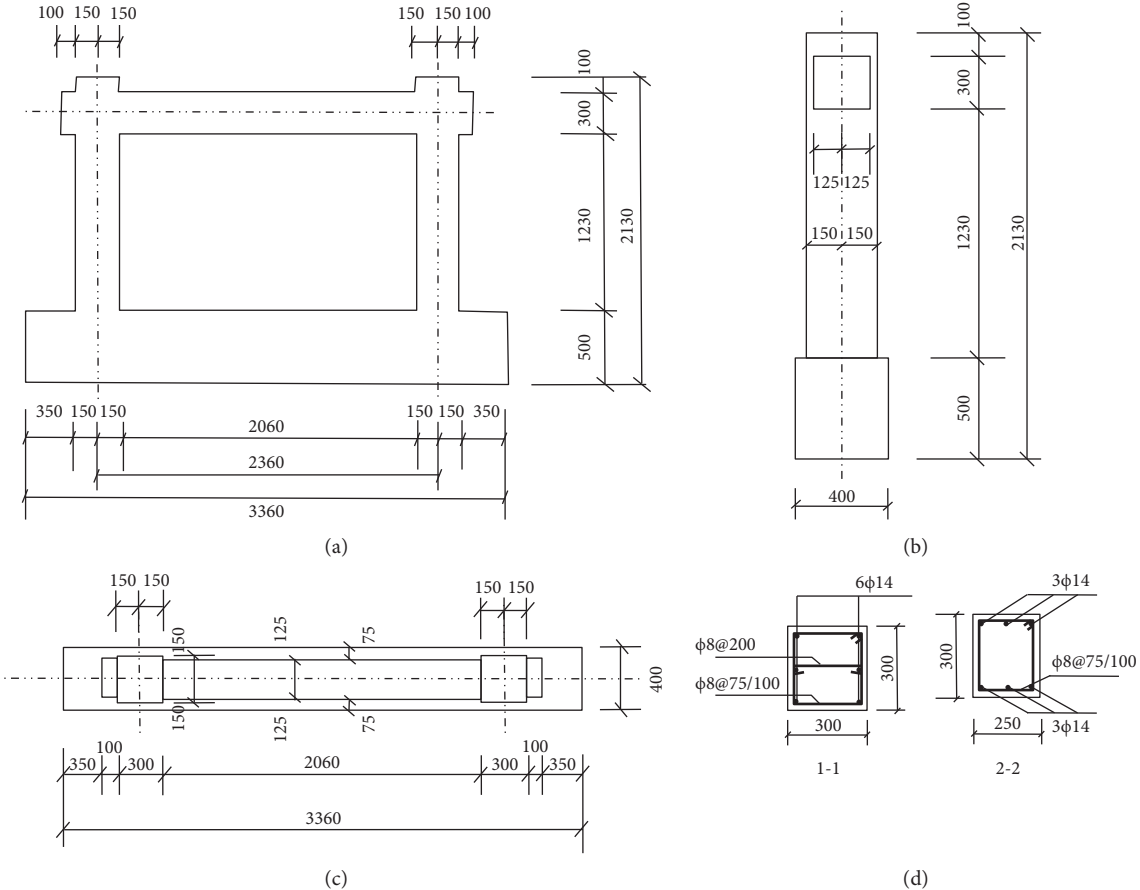


FIGURE 13: Dimensions and reinforcements of RC frame.

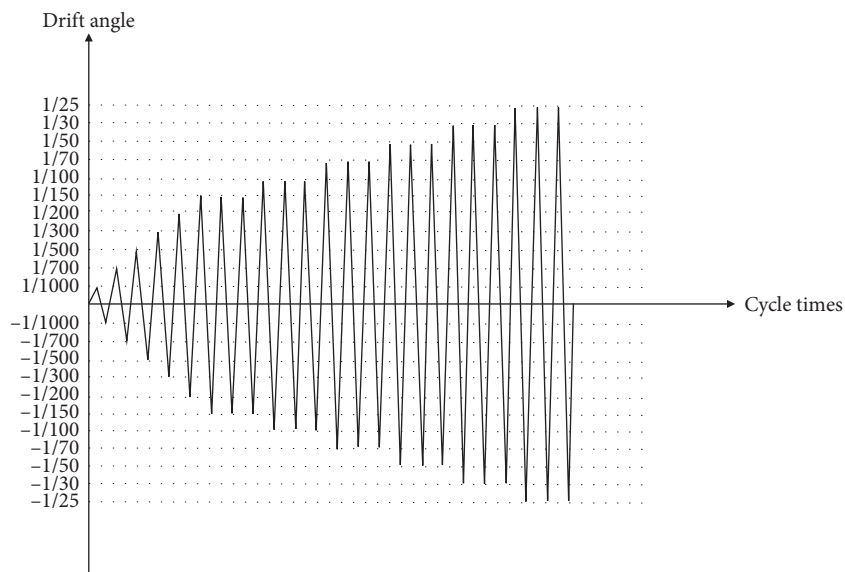


FIGURE 14: Lateral loading protocol.

shown in Table 5. The comparison between nonlinear hysteretic analysis result and corresponding experiment result is shown in Figure 21(a), and the comparison between simulation result and experiment result of stiffness degradation of

GWF1 during the process of pushover is shown in Figure 21(b). According to the calculation results, the model proposed in this study can reflect the in-plane behavior of infilled RC frame with flexible connection effectively.

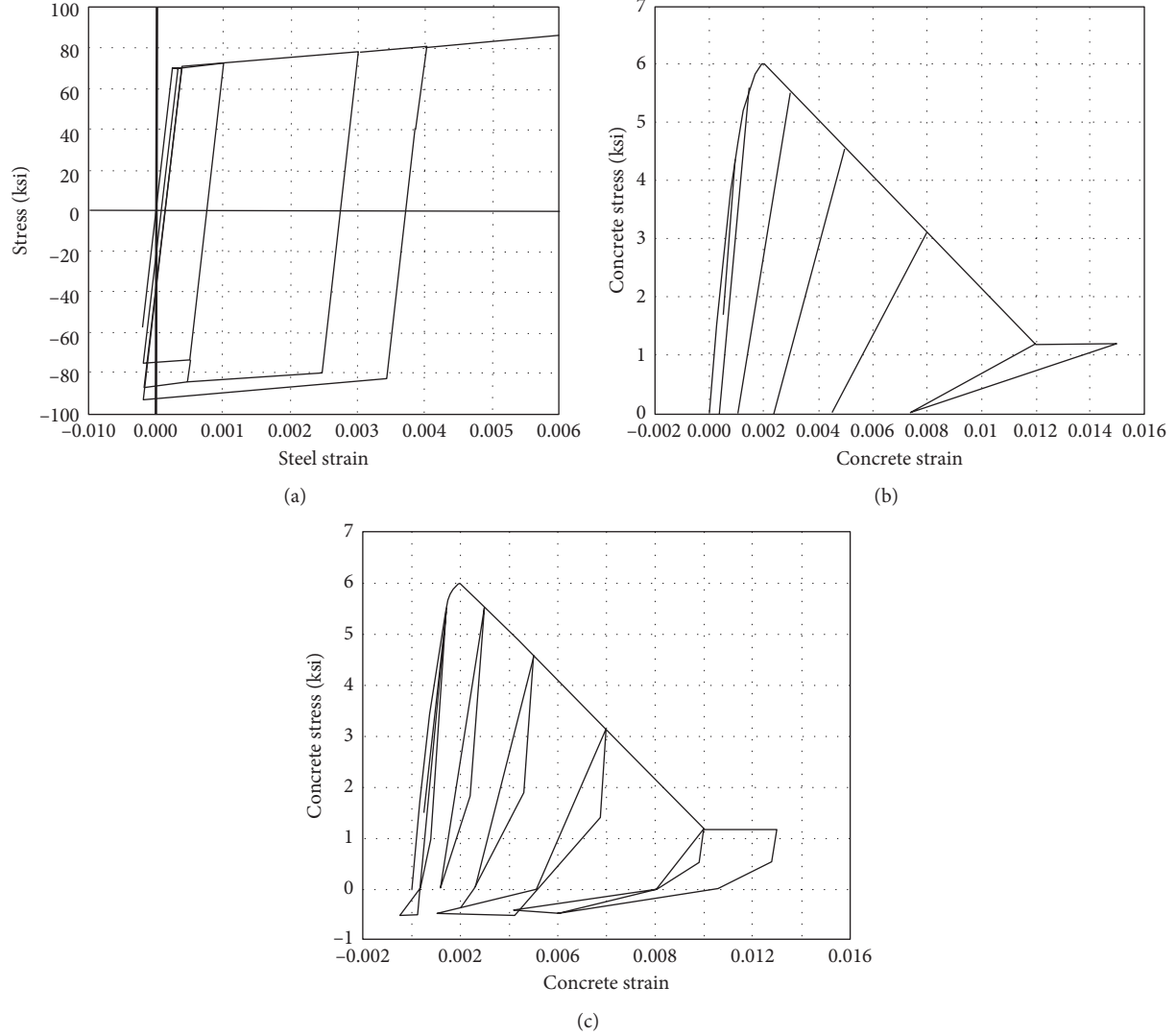


FIGURE 15: Material models [60].

TABLE 1: Parameters of concrete material [24].

Parameters	Beams	Columns
Concrete compressive strength (MPa)	23.6	25.6
Concrete strain at maximum strength	0.0035	0.00447
Concrete crushing strength (MPa)	20.06	21.76
Concrete strain at crushing strength	0.0129	0.018
Ratio between unloading slope (ultimate compression strain) and initial slope	0.5	0.5
Tensile strength (MPa)	2.26	2.26
Tension softening stiffness (MPa)	$2.26 \times 10^3$	$2.26 \times 10^3$

## 5. Conclusion

During the 2008 Wenchuan earthquake, a lot of masonry-infilled RC frame structures suffered serious damages due to the detrimental effects brought about by infill wall rigidly connected to surrounding frame. In order to solve this problem, the flexible connection, introduced by Chinese designers, is recommended by the updated Chinese seismic design code. Although infilled RC frame structure with

TABLE 2: Parameters of steel material [24].

Parameters	Beams	Columns
Initial modulus of elasticity (MPa)	$2 \times 10^5$	$2 \times 10^5$
Yield strength (MPa)	483.8	483.8
Strain-hardening ratio	0.01	0.01

TABLE 3: Parameters of masonry material [24].

Parameters	Columns
Concrete compressive strength (MPa)	1.02
Concrete strain at maximum strength	0.0023
Concrete crushing strength (MPa)	0.5377
Concrete strain at crushing strength	0.0046

flexible connection has a lot of advantages, but because of the lack of research, this structure type is seldom used in practical engineering. Therefore, it is of great significance to scientifically analyze and investigate the effects of flexible connection on structure behaviors of infilled RC frame. So in this study,

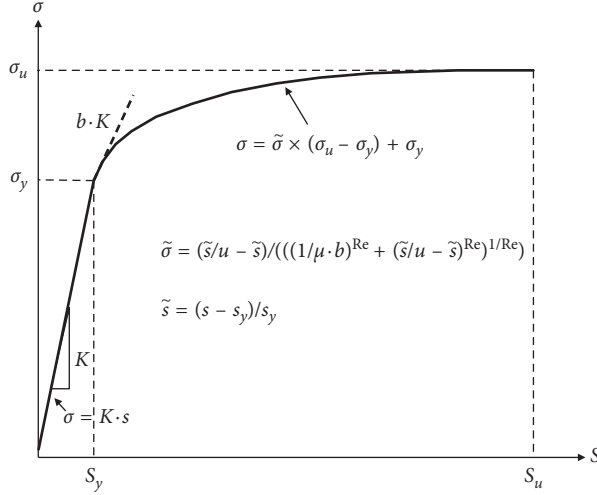


FIGURE 16: Steel bar stress versus slip for completely anchored reinforcing bars into footings.

TABLE 4: Parameters of equivalent diagonal strut model for GWF1.

$E_w$ (MPa)	$E_c$ (MPa)	$a$ (mm)	$b$ (mm)	$I_c$ ( $\text{mm}^4$ )	$t_w$ (mm)	$\sin \theta$
443	5727.07	300	300	$6.75 \times 10^8$	240	0.513
$\cos \theta$	$d$ (mm)	$h$ (mm)	$l_b$	$H_{in}$ (mm)	$\lambda_h$	$w$ (mm)
0.859	2399.27	1380	2360	1230	0.00149	533.439

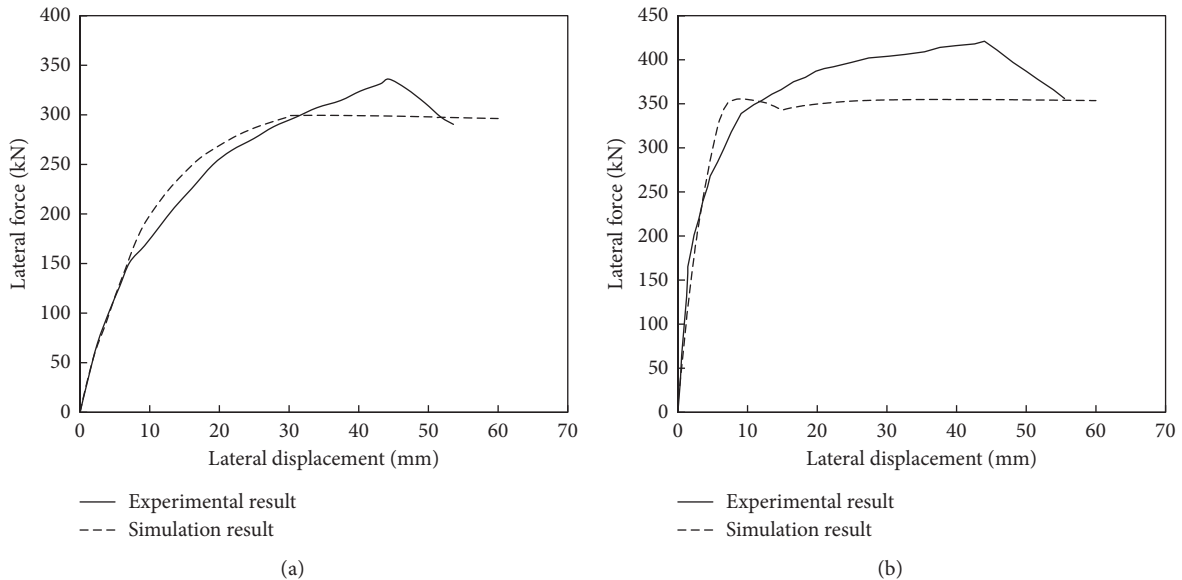


FIGURE 17: Comparison between pushover analysis results and experiment results: (a) PF; (b) GWF1.

an improved equivalent diagonal strut model for masonry-infilled RC frame with flexible connection was developed. Accordingly, the following conclusions are drawn:

- (1) Based on deeply studying and analyzing the existing research achievements, the effects of connection on in-plane behaviors of infilled RC frame were discussed. Although the effects of flexible connection on initial lateral stiffness and bearing capacity of frame structure are inferior to that of rigid connection, it

can reduce the unfavorable interaction between infill wall and surrounding frame, retard the stiffness degradation, and effectively improve the seismic performance of frame structure. Especially for the effect of flexible connection on the initial lateral stiffness of infilled RC frame, its effects are similar to that of opening.

- (2) Based on discussing the action pattern of flexible connection and applied with the macrofinite element

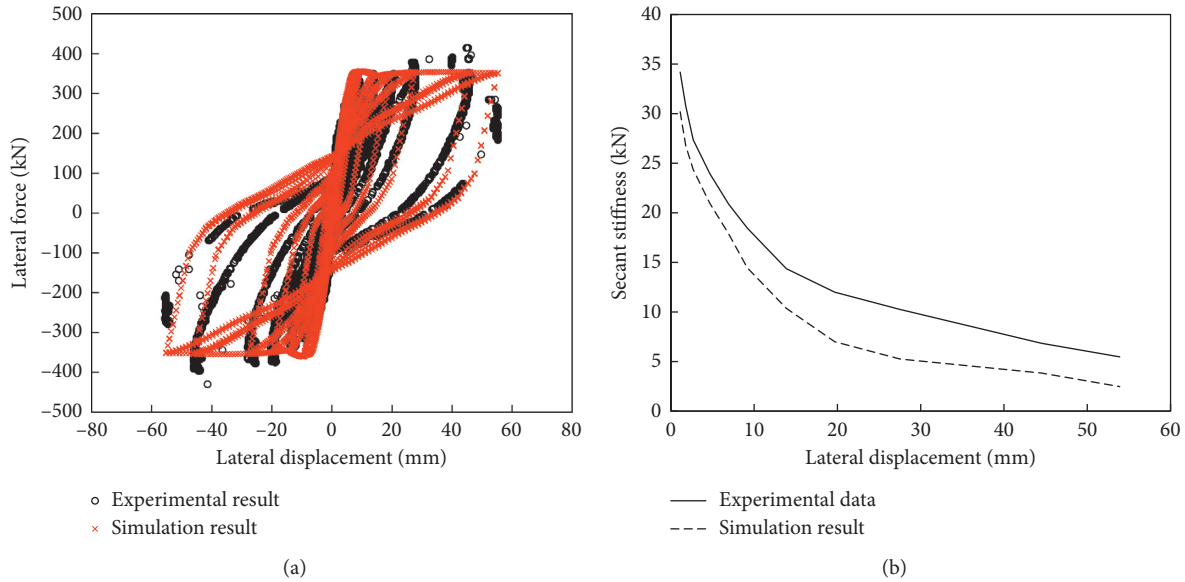


FIGURE 18: Comparison between simulation results and experiment results of GWF1: (a) hysteresis loop; (b) stiffness degradation.

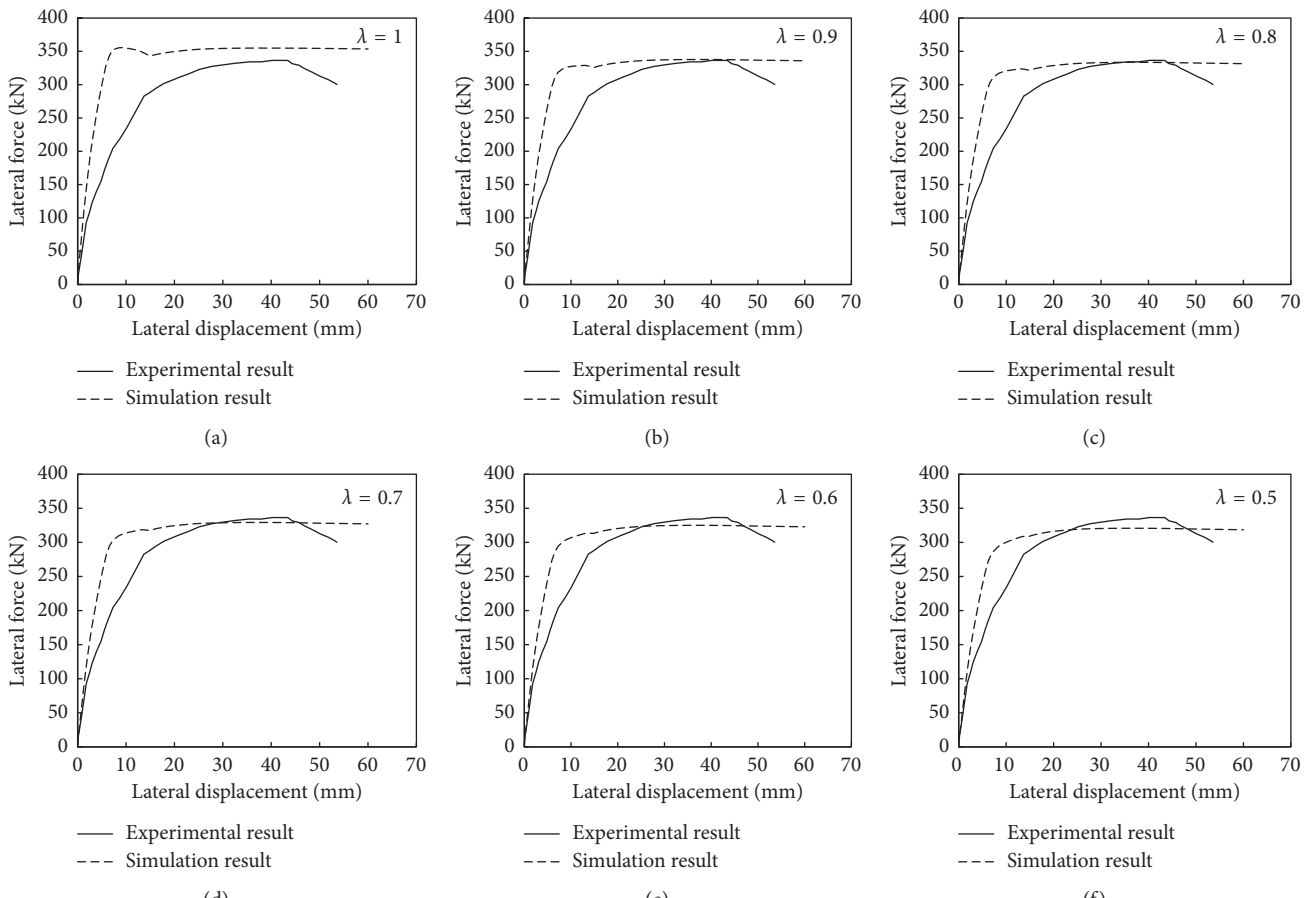


FIGURE 19: Continued.

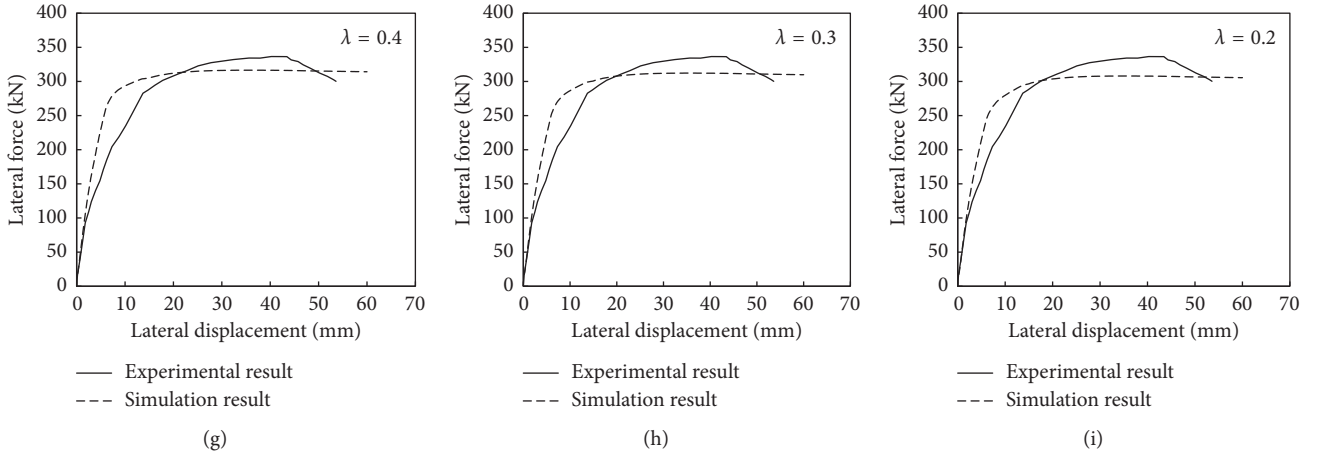


FIGURE 19: Comparison between pushover analysis results and experiment results under different stiffness reduction conditions.

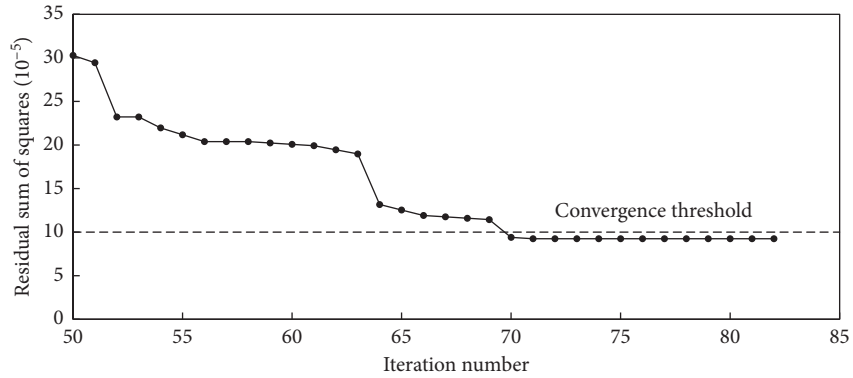


FIGURE 20: Optimization process of AFSA.

TABLE 5: Parameters of improved equivalent diagonal strut model for RWF1.

$E_w$ (MPa)	$E_c$ (MPa)	$a$ (mm)	$b$ (mm)	$I_c$ ( $\text{mm}^4$ )	$t_w$ (mm)	$\sin \theta$
443	5727.07	300	300	$6.75 \times 10^8$	240	0.513
$\cos \theta$	$d$ (mm)	$h$ (mm)	$l_b$	$H_{\text{in}}$ (mm)	$\lambda_h$	$w$ (mm)
0.859	2399.27	1380	2360	1230	0.00149	277.388

simulation methods for infilled RC frame with opening, the stiffness reduction factor  $\lambda$  was introduced to characterize the effects of flexible connection on lateral stiffness of infilled RC frame. Moreover, on the basis of analyzing the structure characteristics of infilled RC frame with flexible connection, the conclusion that the stiffness reduction factor of flexible connection is approximately a constant value was drawn. Then, combined with the existing equivalent diagonal strut models for infilled RC frames with rigid connection, an improved equivalent diagonal strut model for infilled RC frame with flexible connection was proposed.

- (3) Inversion theory was introduced to determine the value of stiffness reduction factor, and the principle is to make measured values and calculated values as near as possible. Based on minimum residual sum of

squares, a constrained optimization problem, for estimating stiffness reduction factor, was constructed, and then artificial fish swarm algorithm (AFSA) was applied to search the global optimum solution of objective function through preying behavior, swarming behavior, and chasing behavior.

- (4) Up to now, relevant experimental and numerical researches about infilled RC frame with flexible connection are very less and need to be further urgently. In this study, only applied with the experiment results provided by reference [11, 24], the stiffness reduction factor  $\lambda$  was determined through AFSA, and on this basis, an improved equivalent diagonal strut model for infilled RC frame with flexible connection was proposed. Therefore, the effectiveness and feasibility of the proposed model need to be further verified based on more experiment results. Moreover,

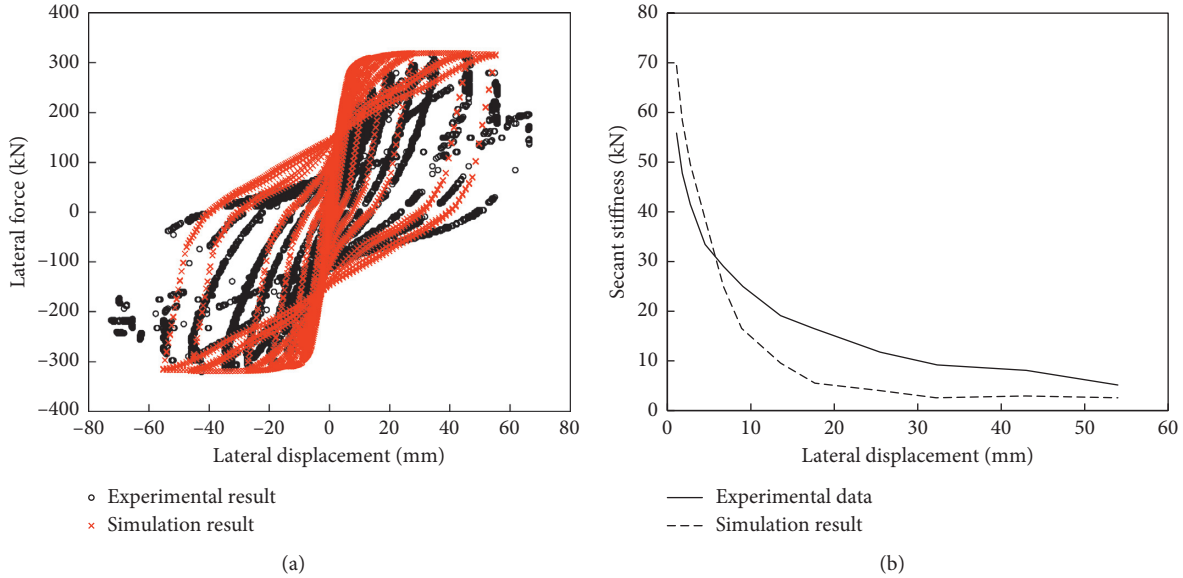


FIGURE 21: The result of hysteretic analysis and nonlinear pushover analysis (RWF1).

it is worthwhile pointing out that the analysis method based on inversion theory can be extended to build more accurate models for infilled RC frame with flexible connection, such as multiple-struts models.

## Data Availability

The data used to support the findings of this study are available from the corresponding author upon request.

## Conflicts of Interest

The authors declare no conflicts of interest.

## Authors' Contributions

Y. G. conceptualized the study; Y. G. and L. X. Y. performed data curation; Y. G. and Z. E. F. supervised the study; Y. G., L. X. Y., Z. E. F., E. N. T., K. K., and Z. W. performed formal analysis; Y. G. and L. X. Y. wrote the original draft; Y. G., Z. E. F., L. X. Y., E. N. T., K. K., and Z. W. reviewed and edited the article.

## Acknowledgments

This study was supported by the Central University Basic Research Project (grant no. 2017B40214), National Key R&D Program of China (2016YFC0401601 and 2017YFC0804607), National Natural Science Foundation of China (grant nos. 51739003, 51479054, 51779086, 51579086, 51379068, 51579083, 51579085, and 51609074), Project Funded by the Priority Academic Program Development of Jiangsu Higher Education Institutions (YS11001), Jiangsu Natural Science Foundation (grant no. BK20160872), Special Project Funded of National Key Laboratory (20145027612 and 20165042112), and Key R&D Program of Guangxi (AB17195074).

## References

- [1] China Architecture and Building Press, *Technical specification for concrete small-sized hollow block masonry buildings (JGJ/T 14-2011)*, China Architecture and Building Press, Beijing, China, 2011, in Chinese.
- [2] Z. F. Yuan, L. Yuan, and B. Liu, "Discussion on design and application of masonry filled walls separated from frame columns," *Building Structure*, vol. 40, no. 5, pp. 112–116, 2010, in Chinese.
- [3] F. G. Thomas, "The strength of brickwork," *Journal of Structural Engineering*, vol. 31, pp. 35–46, 1953.
- [4] A. B. Mehrabi, P. Benson Shing, M. P. Schuller, and J. L. Noland, "Experimental evaluation of masonry-infilled RC frames," *Journal of Structural Engineering*, vol. 122, no. 3, pp. 228–237, 1996.
- [5] K. C. Stylianidis, "Experimental investigation of masonry infilled RC frames," *Open Construction and Building Technology Journal*, vol. 6, no. 1, pp. 194–212, 2012.
- [6] D. J. Kakaletsis and C. G. Karayannis, "Influence of masonry strength and openings on infilled R/C frames under cycling loading," *Journal of Earthquake Engineering*, vol. 12, no. 2, pp. 197–221, 2008.
- [7] L. Cavalieri and F. Di Trapani, "Cyclic response of masonry infilled RC frames: experimental results and simplified modeling," *Soil Dynamics and Earthquake Engineering*, vol. 65, pp. 224–242, 2014.
- [8] D. J. Kakaletsis and C. G. Karayannis, "Experimental investigation of infilled reinforced concrete frames with openings," *ACI Structural Journal*, vol. 106, no. 2, pp. 132–41, 2009.
- [9] D. Mallick and R. Garg, "Effect of openings on the lateral stiffness of infilled frames," *Proceedings of the Institution of Civil Engineers*, vol. 49, no. 2, pp. 193–209, 1971.
- [10] H. Jiang, X. Liu, and J. Mao, "Full-scale experimental study on masonry infilled RC moment-resisting frames under cyclic loads," *Engineering Structures*, vol. 91, pp. 70–84, 2015.
- [11] X. J. Zhou, X. L. Jiang, D. D. Xu, J. K. Song, and C. H. Yang, "Experimental research on seismic behavior of flexible

- connection frame structure infilled with new masonry," *Word earthquake engineering*, vol. 31, no. 1, pp. 58–67, 2015, in Chinese.
- [12] Q. Peng, X. Zhou, and C. Yang, "Influence of connection and constructional details on masonry-infilled RC frames under cyclic loading," *Soil Dynamics and Earthquake Engineering*, vol. 108, pp. 96–110, 2018.
  - [13] H. R. Lotfi, *Finite element analysis of fracture of concrete and masonry structures*, Ph.D. Thesis, University of Colorado Boulder, Boulder, Colorado, 1992.
  - [14] P. B. Lourenco, *Computational strategies for masonry structures*, Ph.D. Thesis, Delft University of Technology, Delft, Netherlands, 1996.
  - [15] A. B. Mehrabi and P. B. Shing, "Finite element modeling of masonry-infilled RC frames," *Journal of Structural Engineering*, vol. 123, no. 5, pp. 604–613, 1997.
  - [16] Y.-J. Chiou, J.-C. Tzeng, and Y.-W. Liou, "Experimental and analytical study of masonry infilled frames," *Journal of Structural Engineering*, vol. 125, no. 10, pp. 1109–1117, 1999.
  - [17] M. M. Attard, A. Nappi, and F. Tin-Loi, "Modeling fracture in masonry," *Journal of Structural Engineering*, vol. 133, no. 10, pp. 1385–1392, 2007.
  - [18] G. Al-Chaar, A. B. Mehrabi, and T. Manzouri, "Finite element interface modeling and experimental verification of masonry-infilled R/C frames," *Masonry Society Journal*, vol. 26, no. 1, pp. 47–65, 2008.
  - [19] A. Stavridis and P. B. Shing, "Finite-element modeling of nonlinear behavior of masonry-infilled RC frames," *Journal of Structural Engineering*, vol. 136, no. 3, pp. 285–296, 2010.
  - [20] D. Mallick and R. Seven, "Dynamic characteristics of infilled frames," *Proceedings of the Institution of Civil Engineers*, vol. 39, no. 2, pp. 261–287, 1968.
  - [21] P. B. Lourenço, "Computations on historic masonry structures," *Progress in Structural Engineering and Materials*, vol. 4, no. 3, pp. 301–319, 2002.
  - [22] D. M. Cotovos, N. D. Stathopoulos, and C. A. Zeris, "Behavior of RC beams subjected to high rates of concentrated loading," *Journal of Structural Engineering*, vol. 134, no. 12, pp. 1839–1851, 2008.
  - [23] W. J. Wu, "Study on the seismic performance of the infilled RC frames with openings," M.S. Thesis, Chang'an University, Xi'an, China, 2018.
  - [24] X. J. Zhou, P. Q. Chen, and Y. L. Wang, "Finite element calculation and experiment comparison about masonry-infilled frame structure considering and connection ways between infill wall and frame," *Word Earthquake Engineering*, vol. 31, no. 2, pp. 188–195, 2015, in Chinese.
  - [25] M. Holmes, "Steel frames with brickwork and concrete infilling," *Proceedings of the Institution of Civil Engineers*, vol. 19, no. 4, pp. 473–478, 1961.
  - [26] J. L. Dawe and C. K. Seah, "Analysis of concrete masonry infilled steel frames subjected to in-plane loads," in *Proceedings of the 5th Canadian Masonry Symposium*, pp. 329–340, Vancouver, BC, Canada, June 1989.
  - [27] A. J. Durrani and Y. H. Luo, "Seismic retrofit offlat-slab buildings with masonry infill," in *Proceedings of the NCEER Workshop on Seismic Response of Masonry Infills*, Report NCEER-94-0004, San Francisco, CA, USA, February 1994.
  - [28] R. J. Mainstone, "On the stiffness and strength of infilled frames," *Proceedings of Institute of Civil Engineers*, vol. 7360S, pp. 57–89, 1971.
  - [29] F. J. Crisafulli, *Seismic Behaviour of Reinforced Concrete Structures with Masonry Infills*, University of Canterbury, Christchurch, New Zealand, 1997.
  - [30] F. J. Crisafulli and A. J. Carr, "Proposed macro-model for the analysis of infilled frame structures," *Bulletin of the New Zealand Society of Earthquake Engineering*, vol. 40, pp. 69–77, 2007.
  - [31] C. Z. Chrysostomou, P. Gergely, and J. F. Abel, "A six-strut model for nonlinear dynamic analysis of steel infilled frames," *International Journal of Structural Stability and Dynamics*, vol. 2, pp. 335–353, 2003.
  - [32] W. W. El-Dakhakhni, M. Elgaaly, and A. A. Hamid, "Three-strut model for concrete masonry-infilled steel frames," *Journal of Structural Engineering*, vol. 129, no. 2, pp. 177–185, 2003.
  - [33] J. C. Kong, *Seismic performance of masonry infilled rc frame structures with openings*, Ph.D. Thesis, Harbin Institute of Technology, Harbin, China, 2017, in Chinese.
  - [34] A. Giannakas, D. Patronis, and M. Fardis, "The influence of the position and the size of openings to the elastic rigidity of infill walls," *Proc. 8th Hellenic Concrete Conf.*, pp. 49–56, 1987.
  - [35] H. Mostafaei and T. Kabeyasawa, "Effect of infill masonry walls on the seismic response of reinforced concrete buildings subjected to the 2003 Bam earthquake strong motion: a case study of Bam telephone center," *Bulletin of the Earthquake Research Institute*, vol. 79, pp. 133–156, 2004.
  - [36] Q. Q. Zhang, "Study on earthquake resistance behavior impact of infill walls on reinforced concrete frame structure," M.S. Thesis, Harbin Institute of Technology, Harbin, China, 2013, in Chinese.
  - [37] L. Cavalieri, F. Di Trapani, P. G. Asteris, and V. Sarhosis, "Influence of column shear failure on pushover based assessment of masonry infilled reinforced concrete framed structures: a case study," *Soil Dynamics and Earthquake Engineering*, vol. 100, pp. 98–112, 2017.
  - [38] Q. X. Huang, *Study on seismic behavior and elastic-plastic analysis method for seismic responses of RC frame infilled with new masonry*, Ph.D. Thesis, Huaqiao University, Xiamen, China, 2011, in Chinese.
  - [39] S. Gómez-Fernández, M. Günther, B. Schartel, M. A. Corcuer, and A. Eceiza, "Impact of the combined use of layered double hydroxides, lignin and phosphorous polyol on the fire behavior of flexible polyurethane foams," *Industrial Crops and Products*, vol. 125, pp. 346–359, 2018.
  - [40] X. Wang, S. He, G. Wang et al., "Characterization of PBDD/F emissions from simulated polystyrene insulation foam via lab-scale programmed thermal treatment testing," *Chemosphere*, vol. 211, pp. 926–933, 2018.
  - [41] C. Li, G. Chen, W. Wang et al., "Grain boundary passivation by CdCl<sub>2</sub> treatment in CdTe solar cells revealed by Kelvin probe force microscopy," *Journal of Materials Science: Materials in Electronics*, vol. 29, no. 24, pp. 20718–20725, 2018.
  - [42] H. G. Jin, H. J. Li, and G. G. Sun, "Analysis of interaction between reinforced concrete frame and infilled wall subject to earthquake-induced ground motion," *Earthquake Engineering And Engineering Dynamics*, vol. 37, no. 4, pp. 31–41, 2017, in Chinese.
  - [43] B. S. Smith, "Behavior of square infilled frames," *American Society of Civil Engineers*, vol. 92, no. 1, pp. 381–403, 1966.
  - [44] B. S. Smith and C. Carter, "A method of analysis for infilled frames," *Proceedings of the Institution of Civil Engineers*, vol. 44, pp. 31–48, 1969.
  - [45] R. J. Mainstone and G. A. Weeks, "The influence of a bounding frame on the racking stiffness and strength of brick walls," in *Proceedings of the 2nd International Brick Masonry Conference*, pp. 165–171, Stoke-on-Trent, UK, April 1970.

- [46] FEMA-274, *NEHRP Commentary on the Guidelines for the Seismic Rehabilitation of Buildings*, Federal Emergency Management Agency, Washington DC, USA, 1997.
- [47] FEMA-306, *Evaluation of Earthquake Damaged Concrete and Masonry Wall Buildings: Basic Procedures Manual*, Federal Emergency Management Agency, Washington DC, USA, 1998.
- [48] G. Yang, H. Z. Liu, K. Zhu, and D. S. Liu, "The inversion analysis for mechanical parameters of dam based on the artificial fish swarm algorithm," *Applied Mechanics and Materials*, vol. 416-417, pp. 1786–1790, 2013.
- [49] C. G. Liu, C. S. Gu, and B. Chen, "Zoned elasticity modulus inversion analysis method of a high arch dam based on unconstrained Lagrange support vector regression (support vector regression arch dam)," *Engineering with Computers*, vol. 33, no. 3, pp. 1–14, 2016.
- [50] S. A. El-said, A. Osamaa, and A. E. Hassanien, "Optimized hierarchical routing technique for wireless sensors networks," *Soft Computing*, vol. 20, no. 11, pp. 4549–4564, 2015.
- [51] E. Hussein, A. I. Hafez, A. E. Hassanien, and A. A. Fahmy, "Nature inspired algorithms for solving the community detection problem," *Logic Journal of the IGPL*, vol. 25, no. 6, pp. 902–914, 2017.
- [52] X. Jin, S. Xie, J. He, Y. Lin, Y. Wang, and N. Wang, "Optimization of tuned mass damper parameters for floating wind turbines by using the artificial fish swarm algorithm," *Ocean engineering*, vol. 167, pp. 130–141, 2018.
- [53] X. Li, K. Tang, M. N. Omidvar, Z. Yang, and K. Qin, "Benchmark functions for the CEC 2013 special session and competition on large-scale global optimization, CEC 2013," *Gene*, vol. 7, pp. 1–23, 2013.
- [54] Y. Wu, X. L. Huang, X. Z. Gao, and K. Zenger, "Cultural artificial fish-swarm optimization algorithm and application in the parameters identification of rotor system," *Electric Machines and Control*, vol. 16, pp. 102–108, 2012.
- [55] M. B. Mu'azu, A. T. Salawudeen, T. H. Sikiru, A. Muhammad, and A. I. Abdu, "Weighted artificial fish swarm algorithm with adaptive behavior based linear controller design for nonlinear inverted pendulum," *Journal of Engineering Research*, vol. 20, pp. 1–12, 2015.
- [56] E. T. Norouzzadeh, M. Khanmohammadi, and M. Arabpanahan, "Prediction of nonlinear behavior of steel coupling beams under seismic loads based on experimental results," in *Proceedings of 15th World Conference on Earthquake Engineering (15'WCEE)*, vol. 18, Lisbon, Portugal, September 2012.
- [57] L. Wang, W. Xuan, N. N. Feng, S. P. Cong, F. Liu, and Q. M. Gao, "Research on seismic performance of reinforced concrete frame with unequal span under low cyclic reversed loading," *The Open Civil Engineering Journal*, vol. 10, no. 1, pp. 373–383, 2016.
- [58] C. Corrado and C. Be, "Multi-objective optimization of FRP jackets for improving the seismic response of reinforced concrete frames," *American Journal of Engineering and Applied Sciences*, vol. 9, no. 3, pp. 669–679, 2016.
- [59] R. M. Oinam, R. Sugumar, and D. R. Sahoo, "A comparative study of seismic performance of RC frames with masonry infills," *Procedia Engineering*, vol. 173, pp. 1784–1791, 2017.
- [60] S. Mazzoni, F. McKenna, M. H. Scott, and G. L. Fenves, *OpenSEES Command Language Manual*, University of California, Berkeley, CA, USA, 2007.
- [61] J. B. Mander, M. J. N. Priestley, and R. Park, "Observed stress-strain behavior of confined concrete," *Journal of Structural Engineering*, vol. 114, no. 8, pp. 1827–1849, 1988.
- [62] J. B. Mander, M. J. N. Priestley, and R. Park, "Theoretical stress-strain model for confined concrete," *Journal of Structural Engineering*, vol. 114, no. 8, pp. 1804–1826, 1988.
- [63] J. Zhao and S. Sritharan, "Modeling of strain penetration effects in fiber-based analysis of reinforced concrete structures," *ACI Structural Journal*, vol. 104, no. 2, pp. 133–141, 2007.

## Research Article

# Buckling Analysis of Sandwich Plate Systems with Stiffening Ribs: Theoretical, Numerical, and Experimental Approaches

Guangping Zou ,<sup>1</sup> Yuyang Wang,<sup>1</sup> Qichao Xue ,<sup>1,2</sup> and Chunwei Zhang<sup>2</sup>

<sup>1</sup>College of Aerospace and Civil Engineering, Harbin Engineering University, Harbin 150001, China

<sup>2</sup>Department of Civil Engineering, Qingdao University of Technology, Qingdao, China

Correspondence should be addressed to Qichao Xue; [xueqichao@hrbeu.edu.cn](mailto:xueqichao@hrbeu.edu.cn)

Received 21 November 2018; Revised 9 January 2019; Accepted 4 February 2019; Published 4 March 2019

Academic Editor: Chiara Bedon

Copyright © 2019 Guangping Zou et al. This is an open access article distributed under the Creative Commons Attribution License, which permits unrestricted use, distribution, and reproduction in any medium, provided the original work is properly cited.

This paper discusses a global buckling analysis approach for sandwich plates with stiffening ribs. The approach is based on theoretical study and is implemented by the finite element method (FEM). The equilibrium equation corresponding to critical global buckling of the sandwich plate with stiffening ribs under simple supported boundary condition is established by the energy method. The critical buckling solutions for a typical rectangular sandwich plate system (SPS) with a single stiffening rib in the longitudinal direction are then investigated while varying the potential influencing factors. The shear rigidity within the inner core exerts little effect on global buckling and can be neglected. An FEM study on elastic buckling was then conducted via ANSYS software. The advantages of the SPS were highlighted via its elastic eigenvalue buckling numerical analysis with multiple stiffeners. The ultimate buckling loads were computed similarly for different influential factors. Finally, an SPS specimen was tested in a compression test. The results showed that when the rib spacing is large, the local buckling of the plates in the grillage is controllable and the SPS is more resistant to both local and global buckling. The results based on our theoretical method agreed well with those of the FEM and experimental results.

## 1. Introduction

Steel sandwich panels comprise two solid faceplates and one low-density core. Initially installed in aerospace equipment, they are now increasingly used in shipbuilding. A new type of sandwich plate, called the sandwich plate system (SPS), comprises two metal faceplates sandwiching a continuous polyurethane (PU) elastomer core. SPSs are important for weight reduction, rapid reparation, and impact resistance in bridge engineering [1] and the shipbuilding fields [2]. Figure 1 shows the application of SPS in different fields and differentiates the shapes of the SPS from those of conventional structures.

PU elastomer is significantly viscoelastic with high damping characteristics. Therefore, a PU elastomer core can potentially raise the noise isolation and damping behaviors of the whole SPS structure [3]. In shipbuilding, stiffeners are usually bonded with steel plates or sandwich plates to increase the stiffness of the whole structure under variable loads. SPSs with stiffening ribs have several advantages over conventional steel plates; in particular, they increase the

corrosion resistance and reduce the processing cost by diminishing the space requirements of the discrete stiffeners [4].

In recent years, applications and simulations of SPS have been extensively researched. Martin [5] conducted static and fatigue tests of an SPS bridge deck. Chunlei et al. [6] calculated the stress distribution in an orthotropic steel bridge deck that was stiffened by SPSs. The lateral load-distribution characteristics of SPS bridges were delineated via numerical simulations by Harris et al. [7]. Based on the finite element method (FEM), Feng et al. [8] developed a new numerical simulation with shell elements for studying SPS structures. Shang [9] studied the typical failure mode and ultimate strength of an SPS in a model test under combined biaxial compression and lateral pressure. Liu et al. [10] analyzed the crashworthiness of a ship with an SPS hull using FEM software. They demonstrated the superior collision resistance and energy-absorbing capacity of the SPS-incorporated structure over the conventional structure. Zou et al. [11] analyzed the effect of adhesive in an equivalent modelling of SPS.

Rib-stiffened plates are the most common engineering applications of SPSs. As analysis approaches and

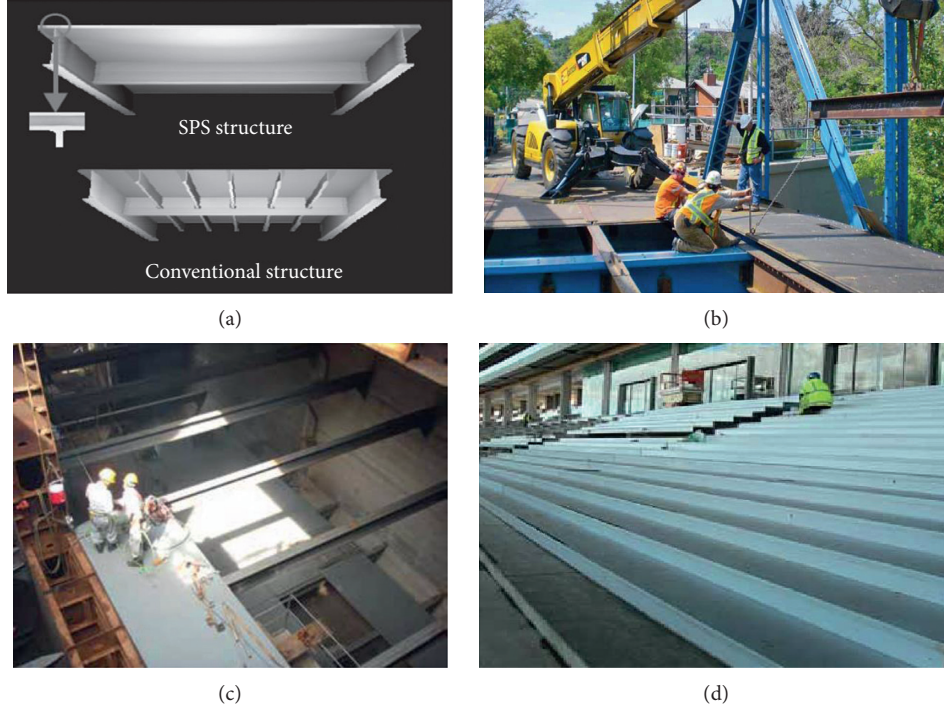


FIGURE 1: Comparison SPS versus conventional structure: (a) comparison between conventional structure and SPS structure; (b) SPS application as bridge deck; (c) SPS applied as partition board in superstructure of ship; (d) SPS stairs in stadium.

manufacturing techniques of sandwich materials continue to develop, different kinds of sandwich plates are being considered for engineering practice. Two popular examples in the literature are stiffened sandwich plates and plates with viscoelastic properties. Liu and Hollaway [12] presented an optimization procedure for composite panel structures with stiffening ribs under multiple loading cases. Wang and Zhao [13] presented an FEM for vibrating stiffened sandwich plates with moderately thick viscoelastic cores. Gara et al. [14] developed a series of experimental tests and a numerical model for wall sandwich panels. John and Li [15] proposed a new sandwich design with an orthogrid-stiffened syntactic foam core based on shape-memory polymer. Xin and Lu [16] analytically modeled the wave propagation in orthogonally rib-stiffened sandwich structures. Briscoe et al. [17] presented a model of shear buckling and local bearing failure in web-core sandwich panels and validated it in experiments. Goel et al. [18] presented a model and numerical simulation of foam sandwich panels subjected to impulsive loading. Adopting a virtual testing approach, Wadee et al. [19] characterized the mechanical behavior of folded core structures for advanced sandwich composites under flatwise compression loads. Yuan and Dawe [20] numerically analyzed the free vibrations and buckling of sandwich plates using a B-spline finite strip method.

Buckling failure is an important failure mode of plates with stiffening ribs under various conditions. Global buckling of plates with stiffeners was first studied by Timoshenko and Gere [21]. Heder [22] approximated the buckling load of a simply supported stiffened sandwich panel using an energy-based method. Zhao et al. [23] introduced an equivalent laminate modelling method that analyzes the global buckling

of stiffened panels with different sectional shapes and stringer distribution forms. Al-Qablan [24] developed a semianalytical buck analysis of stiffened sandwich plates based on first-order shear deformation plate theory (SDPT).

Amadio and Bedon [25–28] studied the effect of variable factors, including multiple mechanical and geometrical aspects, on the buckling behavior of laminated glass elements by combining theoretical methods, numerical simulations, and experiments. In their paper, the normalized resistant domain was proposed for the assessment of the proposed stability check. It was proved that the method was very effective for evaluating buckling behavior of laminated structures through comparing the critical buckling load derived by different analytical interaction formulations. The study was also beneficial to provide us a new theoretical approach to the research of buckling of sandwich panel with ribs.

The present paper theoretically analyzes global buckling in SPSs with stiffening ribs and compares the buckling properties of SPS and conventional rib-stiffened structures. Global buckling is then analyzed via FEM. Finally, an SPS panel stiffened by inner ribs is fabricated and tested in a compression testing facility. Parts of this paper have been published in conference proceedings by the corresponding author [29, 30].

## 2. Theoretical Buckling Analysis of Sandwich Plates with Stiffening Ribs

**2.1. Derivation of Buckling Equation for Ribbed SPSs.** SPS is a typical sandwich structure with a PU elastomer core and steel faceplates (Figure 2(a)). The thicknesses of the core and faceplates are denoted by  $t$  and  $t_f$ , respectively. The system

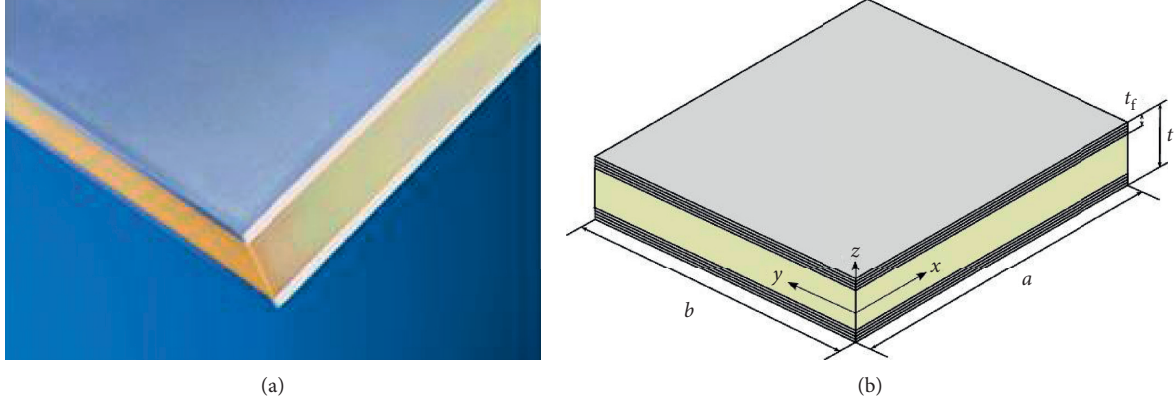


FIGURE 2: SPS structure: (a) system sandwich plate system; (b) schematic view of SPS structure.

was set up in Cartesian coordinates with the  $x$ - $y$  plane parallel to the in-plane of the sandwich plate, and the  $z$ -axis perpendicular to the plane (Figure 2(b)). In engineering practice, SPSs are usually stiffened by ribs inside the core as well as on the cross wall (Figure 3(a)) and plate exterior (Figure 1(a)).

The global theoretical buckling analysis for sandwich plates with stiffener ribs can be combined with the bending theory of sandwich plates and conventional stiffened plates. The analysis was simplified by the following assumptions:

- (1) The sandwich plate is modeled by traditional SDPT sandwich plate theory (Hoff's theory), in which only the core bears shear effects under transverse loads. The bending rigidity of the faceplates is also considered.
- (2) The SPS stiffeners are perfectly connected with the sandwich plate, and they deform along with the plate at all times. The torsional effect of the stiffeners during buckling is ignored when calculating the critical buckling loads.

As shown in Figure 3, the sandwich plate with rectangular stiffening ribs experiences in-plane pressure under the simply supported boundary conditions. The buckling shape of the global stiffened sandwich plate was expressed as the following bitrigonometric series:

$$w = \sum_{m=1}^{\infty} \sum_{n=1}^{\infty} a_{mn} \sin \frac{m\pi x}{a} \sin \frac{n\pi y}{b}, \quad (1)$$

where  $w$  is the out-of-plane deflection function and  $a$  and  $b$  are the plate length and width, respectively.  $a_{mn}$  are the polynomial parameters of the bitrigonometric series, where  $m$  is the number of semiwaves and  $n$  is the number of ribs. Ignoring the bending stiffness of the core (justified under the above assumptions), the total deformation energy of the global sandwich structure was divided into two parts: the bending deformation energy of the faceplates and the shear deformation energy of the PU elastomer core. The total energy is thus calculated as

$$\Delta U = \Delta U_{bf} + \Delta U_{tc}, \quad (2)$$

where  $\Delta U_{bf}$  and  $\Delta U_{tc}$  are the bending and shearing deformation energy of the sandwich plate, respectively.

Based on traditional sandwich plate theory, the deformation of the sandwich plate was considered as the deformation of a homogeneous plate with the same bending stiffness under external loads plus the shear deformation of the core:

$$w = w_0 - \frac{D_h}{C} \nabla^2 w, \quad (3)$$

where  $C = G_c(h+t)$  and  $G_c$  is the torsional modulus of the core;  $D_h$  is the equivalent stiffness of the whole Sandwich plate; and  $w_0$  denotes the deformation corresponding to the bending effect, which is similar (in form) to the whole deformation of the sandwich plate:

$$w_0 = \sum_{m=1}^{\infty} \sum_{n=1}^{\infty} b_{mn} \sin \frac{m\pi x}{a} \sin \frac{n\pi y}{b}. \quad (4)$$

Substituting equations (1) and (4) into equation (3), the relation between  $a_{mn}$  and  $b_{mn}$  is given as

$$b_{mn} = a_{mn} \left( 1 - \frac{D_h}{C} \left( \frac{m^2}{a^2} + \frac{n^2}{b^2} \right) \pi^2 \right). \quad (5)$$

Setting the parameter  $B_{mn} = (1 - (D_h/C)((m^2/a^2) + (n^2/b^2))\pi^2)$ , the bending deformation energy becomes

$$\Delta U_{bf} = \frac{\pi^4 D_h}{2} \frac{ab}{4} \sum_{m=1}^{\infty} \sum_{n=1}^{\infty} B_{mn}^2 a_{mn}^2 \left( \frac{m^2}{a^2} + \frac{n^2}{b^2} \right)^2, \quad (6)$$

where  $D_h$  defines the bending stiffness of a single face of the panel. Similarly, the bending deformation energy of core was determined as

$$\Delta U_{bc} = \frac{\pi^4 D_c}{2} \frac{ab}{4} \sum_{m=1}^{\infty} \sum_{n=1}^{\infty} B_{mn}^2 a_{mn}^2 \left( \frac{m^2}{a^2} + \frac{n^2}{b^2} \right)^2, \quad (7)$$

where  $D_c$  is the bending stiffness of the core. These quantities are, respectively, calculated as follows:

$$D_h = D_0 + 2D_f = \frac{E_f(h+t)^2 t}{2(1-v_f^2)} + 2 \frac{E_f t^3}{12(1-v_f^2)}, \quad (8)$$

where  $D_0$  is the bending stiffness of the whole sandwich plate (ignoring the stiffness of the faceplates).  $\Delta U_{tc}$  is expressed as

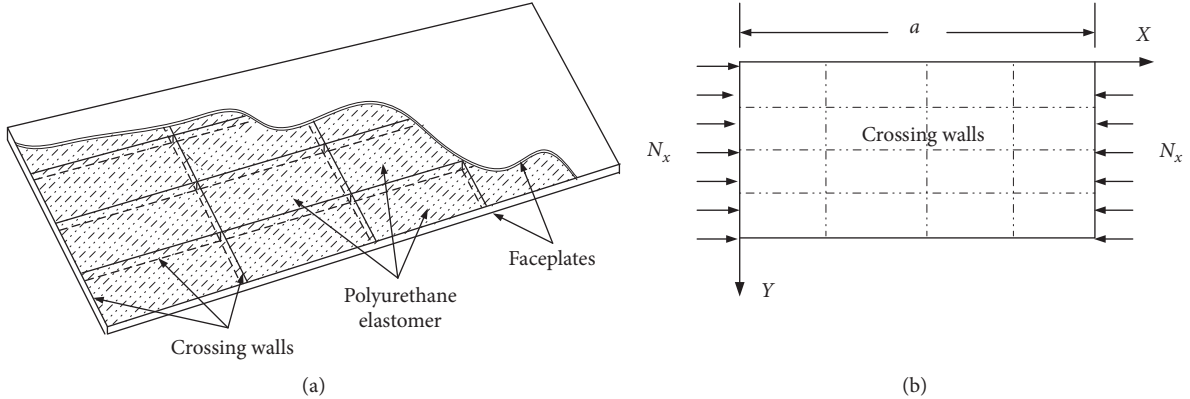


FIGURE 3: Section of sandwich plate and SPS with stiffeners. (a) Structure sketch of SPS reinforced by cross wall. (b) Simplified loading schematic diagram.

$$\begin{aligned}\Delta U_{tc} &= \frac{1}{2} \iint_s (\tau_{xz} \gamma_{xz} + \tau_{yz} \gamma_{yz}) dx dy \\ &= \frac{h+t}{2G_c} \iint_s (\tau_{xz}^2 + \tau_{yz}^2) dx dy.\end{aligned}\quad (9)$$

Under the assumptions of Hoff's plate theory, shear stress is uniformly distributed along the core section. Following the arguments in [31], the shear stress is calculated as

$$\begin{aligned}\tau_{xz} &= \frac{Q_{cx}}{h+t}, \\ \tau_{yz} &= \frac{Q_{cy}}{h+t}.\end{aligned}\quad (10)$$

The external shear loads  $Q_{cx}$  and  $Q_{cy}$  are assumed to be uniformly distributed along the section. Using the equilibrium equation of thin-plate bending theory, they are, respectively, expressed as follows:

$$\begin{aligned}Q_{cx} &= Q_{xh} - Q_{xf} = -D_h \frac{\partial}{\partial x} \nabla^2 w + 2D_f \frac{\partial}{\partial x} \nabla^2 w, \\ Q_{cy} &= Q_{yh} - Q_{yf} = -D_h \frac{\partial}{\partial y} \nabla^2 w + 2D_f \frac{\partial}{\partial y} \nabla^2 w,\end{aligned}\quad (11)$$

where  $E_f$  and  $v_f$  are Young's modulus and Poisson's ratio of the faceplates, respectively. The subscript c, f, and h represent the core, faceplates, and the whole sandwich plate, respectively. Substituting equations (10) and (11) into equation (9) gives

$$\Delta U_c = \frac{D_0^2}{(h+t)^2} \frac{ab\pi^6}{8G_c} \sum_{m=1}^{\infty} \sum_{n=1}^{\infty} a_{mn}^2 \left( \frac{m^2}{a^2} + \frac{n^2}{b^2} \right)^3. \quad (12)$$

As the stiffeners are bonded to the structure, the ribs deform along with the plate; thus, the bending deformation energy  $\Delta U_i$  is given by

$$\begin{aligned}\Delta U_i &= \frac{EI_i}{2} \int_0^a \left( \frac{\partial^2 w}{\partial x^2} \right)^2_{y=c_i} dx \\ &= \frac{\pi^4 EI_i}{4a^3} \sum_{m=1}^{\infty} m^4 \left( a_{m_1} \sin \frac{\pi c_i}{b} + a_{m_2} \sin \frac{2\pi c_i}{b} + \dots \right)^2,\end{aligned}\quad (13)$$

where  $EI_i$  is the bending stiffness of the rib at distance  $c_i$  from the side of the panel ( $y=0$ ).

When the sandwich panel is buckling, the work  $\Delta T$  done by the in-plane pressure  $N_x$  is given by

$$\Delta T = \frac{N_x}{2} \frac{ab}{4} \sum_{m=1}^{\infty} \sum_{n=1}^{\infty} \frac{m^2 \pi^2}{a^2} a_{mn}^2, \quad (14)$$

and the work done by the force  $P_i$  acting on each rib is

$$\begin{aligned}\Delta T_i &= \frac{P_i}{2} \int_0^a \left( \frac{\partial w}{\partial x} \right)^2_{y=c_i} dx \Delta U_{bf} \\ &= \frac{\pi^4 D_h}{2} \frac{ab}{4} \sum_{m=1}^{\infty} \sum_{n=1}^{\infty} B_{mn}^2 a_{mn}^2 \left( \frac{m^2}{a^2} + \frac{n^2}{b^2} \right)^2 \\ &= \frac{\pi^2 P_i}{4a} \sum_{m=1}^{\infty} m^2 \left( a_{m_1} \sin \frac{\pi c_i}{b} + a_{m_2} \sin \frac{2\pi c_i}{b} + \dots \right)^2.\end{aligned}\quad (15)$$

Neglecting the torsional deformation energy of the ribs, the total potential energy is computed as

$$\prod = \Delta U_{bf} + \Delta U_{bc} + \Delta U_{tc} + \Delta \sum_i U_i - \left( \Delta T + \Delta \sum_i T_i \right), \quad (16)$$

adopting the following symbols:

$$\begin{aligned}\beta &= \frac{a}{b}, \\ \frac{EI_i}{bD_h} &= \gamma_i, \\ \frac{P_i}{bN_x} &= \frac{A_i}{b(h+2t)} = \delta_i, \\ \sigma_{cr} &= \frac{N_x}{A},\end{aligned}\quad (17)$$

where  $A_i$  is the section area of the rib. Substituting equations (12)–(15) and equation (17) into equation (16), the total potential energy becomes

$$\prod = \frac{(D_h + D_c) \sum_{m=1}^{\infty} \sum_{n=1}^{\infty} B_{mn}^2 a_{mn}^2 (m^2 + n^2 \beta^2)^2 + (\pi^2 D_0^2 / G_c (h+t)^2) \sum_{n=1}^{\infty} a_{mn}^2 (m^2 + n^2 \beta^2)^3}{\sum_{m=1}^{\infty} \sum_{n=1}^{\infty} a_{mn}^2 m^2 + 2 \sum_i \delta_i \sum_{m=1}^{\infty} m^2 (\sum_{n=1}^{\infty} a_{mn} \sin(n\pi c_i/b))^2} \\ + \frac{2 \sum_i D_h \gamma_i \sum_{m=1}^{\infty} m^4 (\sum_{n=1}^{\infty} a_{mn} \sin(n\pi c_i/b))}{\sum_{m=1}^{\infty} \sum_{n=1}^{\infty} a_{mn}^2 m^2 + 2 \sum_i \delta_i \sum_{m=1}^{\infty} m^2 (\sum_{n=1}^{\infty} a_{mn} \sin(n\pi c_i/b))^2} - \frac{b^2 (h+2t) \beta^2}{\pi^2} \sigma_{cr}. \quad (18)$$

Equating  $\Pi$  to 0 in equation (18), we obtain

$$0 = \frac{\pi^2}{b^2 \beta^2 (h+2t)} \times \left[ (D_h + D_c) \sum_{m=1}^{\infty} \sum_{n=1}^{\infty} B_{mn}^2 a_{mn}^2 (m^2 + n^2 \beta^2)^2 + \frac{\pi^2 D_0^2}{b^2 \beta^2 G_c (h+t)} \sum_{m=1}^{\infty} \sum_{n=1}^{\infty} a_{mn}^2 (m^2 + n^2 \beta^2)^3 \right. \\ \left. + 2 \sum_i D_h \gamma_i \sin \frac{n\pi c_i}{b} m^4 \left( \sum_{p=1}^{\infty} a_{mp} \sin \frac{p\pi c_i}{b} \right) \right] \\ - \sigma_{cr} \left[ a_{mn} m^2 + 2 \sum_i \delta_i \sin \frac{n\pi c_i}{b} m^2 \left( \sum_{p=1}^{\infty} a_{mp} \sin \frac{p\pi c_i}{b} \right) \right]. \quad (19)$$

Equation (18) computes the critical buckling load for different numbers of ribs.

**2.2. Global Buckling Calculation for a Sandwich Plate with One Rib.** To verify the effectiveness of previous analyses and investigate the differences between sandwich plates and conventional stiffening plates, we first explored the influences of various parameters on a single-ribbed sandwich plate. As shown in Figure 4, the sandwich plate is arranged with only one rib in the center of the plate, and the width of the plate is divided into equal intervals, meaning that  $c_i$  equaled to  $b/2$ . Assuming one buckling wave along the  $y$ -axis (i.e.,  $n = 1$ ) and half a wave along the  $x$ -axis (i.e.,  $m = 1$ ) as a typical example, equation (18) can be written as follows:

$$0 = \frac{\pi^2}{b^2 \beta^2 (h+2t)} \left[ (D_h + D_c) a_1 B_{mn}^2 (1 + \beta^2)^2 + \frac{\pi^2 D_0^2}{G_c \beta^2 b^2 (h+t)} a_1 (1 + \beta^2)^3 \right] + \left[ \frac{2\pi^2 D_h \gamma}{b^2 \beta^2 (h+2t)} - 2\delta \sigma_{cr} \right] \\ \cdot (a_1 - a_3 + a_5 - \dots) - a_1 \sigma_{cr}, \\ 0 = \frac{\pi^2}{b^2 \beta^2 (h+2t)} \left[ (D_h + D_c) a_2 B_{mn}^2 (1 + 4\beta^2)^2 + \frac{\pi^2 D_0^2}{G_c \beta^2 b^2 (h+t)} a_2 (1 + 4\beta^2)^3 \right] - a_2 \sigma_{cr}, \\ 0 = \frac{\pi^2}{b^2 \beta^2 (h+2t)} \left[ (D_h + D_c) a_3 B_{mn}^2 (1 + 9\beta^2)^2 + \frac{\pi^2 D_0^2}{G_c \beta^2 b^2 (h+t)} a_3 (1 + 9\beta^2)^3 \right] + \left[ \frac{2\pi^2 D_h \gamma}{b^2 \beta^2 (h+2t)} + 2\delta \sigma_{cr} \right] \\ \cdot (a_1 - a_3 + a_5 - \dots) - a_3 \sigma_{cr}, \\ 0 = \frac{\pi^2}{b^2 \beta^2 (h+2t)} \left[ (D_h + D_c) a_4 B_{mn}^2 (1 + 16\beta^2)^2 + \frac{\pi^2 D_0^2}{G_c \beta^2 b^2 (h+t)} a_4 (1 + 16\beta^2)^3 \right] - a_4 \sigma_{cr} \dots \quad (20)$$

In thin-plate bending theory with stiffeners, the first-order critical buckling loads are approximated by equation (20). All terms  $a_{mn}$  are equaled to 0 except  $a_1$ , the first term of the double triangular series. Introducing the parameter  $\varphi$ ,

$$\varphi = \frac{\pi^2 D_0^2}{G_c \beta^2 b^2 D_h (h+t)^2} (1 + \beta^2)^3, \quad (21)$$

$\sigma_{cr}$  can be written as

$$\sigma_{cr} = \frac{\pi^2 D_h}{b^2 (h+2t)} \frac{B_{mn}^2 (1 + \beta^2)^2 + \varphi + 2\gamma}{\beta^2 (1 + 2\delta)}. \quad (22)$$

The parameter  $\varphi$  relates to the shear deformation work done by the core. Introducing the coefficient of critical buckling  $k$ ,

$$k = \frac{B_{mn}^2 (1 + \beta^2)^2 + \varphi + 2\gamma}{\beta^2 (1 + 2\delta)}, \quad (23)$$

$\sigma_{cr}$  finally becomes

$$\sigma_{cr} = k \frac{\pi^2 D_h}{b^2 (h+2t)}. \quad (24)$$

When  $n$  is even, the parameter  $a_{mn}$  in equation (20) takes a single value, and equation (20) expresses the deflection of the internode line. When the sandwich panel is uniformly buckled to generate an even number of semiwaves along the  $y$  direction, the internode line remains straight, meaning that the ribs arranged along the center of the plate are nonfunctional.

As  $\beta$  increases, multiple semiwaves may appear in the compression loading direction ( $m \neq 1$ ). Therefore, substituting  $m$  in equation (20), we obtained the total potential energy. The potential energy of a sandwich plate with  $n$  ribs is calculated by substituting  $c_i = b/(n+1)$  in equation (19). The first-order critical buckling loads are approximately given by

$$\sigma_{cr} = \frac{\pi^2 D_h}{b^2 (h+2t)} \frac{B_{mn}^2 (1 + \beta^2)^2 + \varphi + 2 \sum_i \gamma_i \sin^2(\pi c_i/b)}{\beta^2 (1 + 2 \sum_i \delta_i \sin^2(\pi c_i/b))}. \quad (25)$$

**2.3. Examples of Solutions to Buckling Theory.** Stiffeners influence sandwich plates with single and multiple ribs in a similar manner. Therefore, as an example, we analyzed a simple supported rectangular sandwich panel with a single rib (Figure 4). The length  $b$  is 2030 mm, and the width  $a$  is calculated from  $\beta$ . The faceplate and core thicknesses are  $t = 2$  mm and  $h = 13.6$  mm, respectively. For steel faceplates,

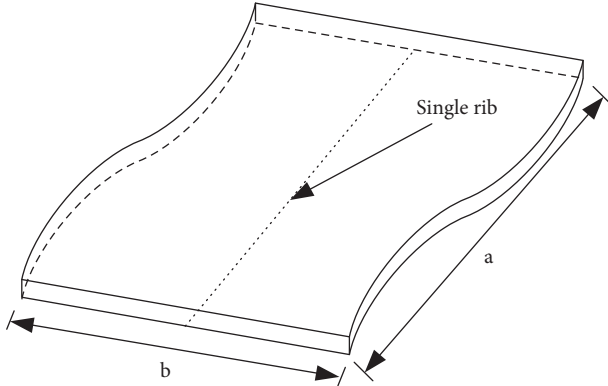


FIGURE 4: Straight rib when the plate is buckling.

Young's modulus is  $E = 2.1 \times 10^5$  MPa and Poisson's ratio is 0.3. The shear modulus  $G_c$  of the core is taken as 308 MPa.

According to equation (22), the critical stress is governed by the bending stiffness of the components in the sandwich plates. The critical stresses for different stiffness (equation (8)) in the above example are listed in Table 1.

As shown in Table 1, the total bending stiffness of the sandwich plate is 0.55% higher when considering the bending stiffness of the faceplate than when not considering the stiffness factor. Moreover, the bending stiffness of the core is approximately 0.32% of the overall bending of the bending rigidity of the sandwich plate. Therefore, we concluded that the bending stiffness of the faceplates can be ignored when calculating the bending stiffness.

In engineering practice, the cross-sectional area of the ribs is 2%–10% of the section area of the plates. In the present example, the stiffener is considered to cover 5% of the cross-sectional area of the plate. The effect of the inertia moment of the stiffening rib is then investigated under critical buckling loads.

When the faceplate thickness is fixed, increasing the core thickness will increase the bending stiffness of the whole structure. Figure 5 plots the effect of core thickness on the critical buckling load for different  $\beta$ . The faceplate thickness and inertia moment are fixed at 2 mm and  $(418 \times 10^4)$  mm<sup>4</sup>, respectively. Increasing the core thickness increased the bending stiffness of the SPS. Here, we considered only the first buckling semiwave. Lowering the  $\beta$  value reduced the influence of the core thickness: at low  $\beta$ , the corresponding curve changed gently; at higher  $\beta$ , it increased more sharply.

Figure 6 shows the critical buckling loads in the case of multiple semiwave buckling, corresponding to different core thicknesses. The inertia moment of the rib is fixed at  $418 \times 10^4$  mm<sup>4</sup>.

As shown in Figure 6, the critical buckling load changed slowly with the thickness of the core in sandwich plates. Increasing the core thickness from 5 to 50 mm significantly increased the critical buckling load from approximately 5000 N/mm to 11000 N/mm. This result can be explained by the sharp increase in bending stiffness of the SPS as the core thickness increased.

Figure 7 relates the critical buckling coefficient to the inertia moment of the rib for different numbers of

TABLE 1: Different rigidities of the sandwich plate.

Bending stiffness	$D_0$	$D_f$	$D_h$	$D_c$
Value	56.162 N/mm	0.153 N/mm	56.474 N/mm	0.184 N/mm

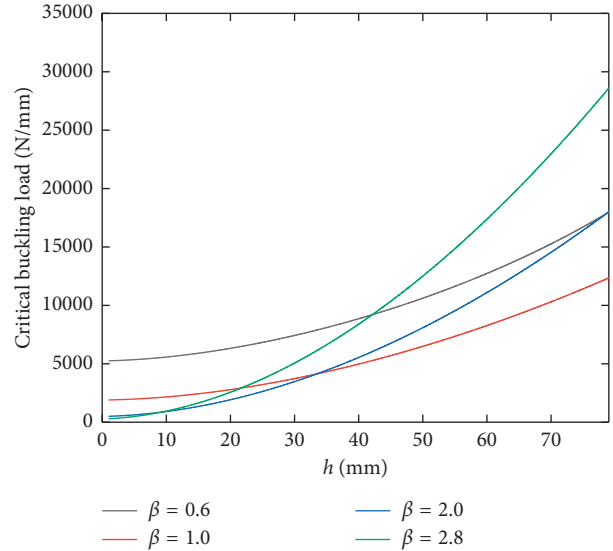


FIGURE 5: Relation between critical buckling load and core thickness for different  $\beta$ .

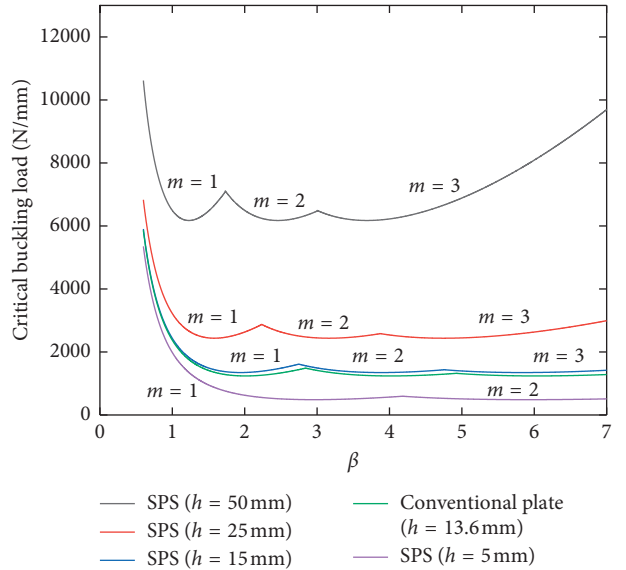


FIGURE 6: Relation between critical buckling load and  $\beta$  for different core thicknesses.

semiwaves, where the section area of the ribs is 2% of the total section area. The critical buckling coefficient is quite sensitive to the inertia moment of the stiffening ribs. When the bending stiffness of the ribs is ignored, the critical coefficient is minimized when the SPS panel buckled into two semiwaves ( $n = 1, m = 2$ ); as the bending stiffness of the ribs increased above  $81.7$  cm<sup>4</sup>, the critical coefficient appeared at

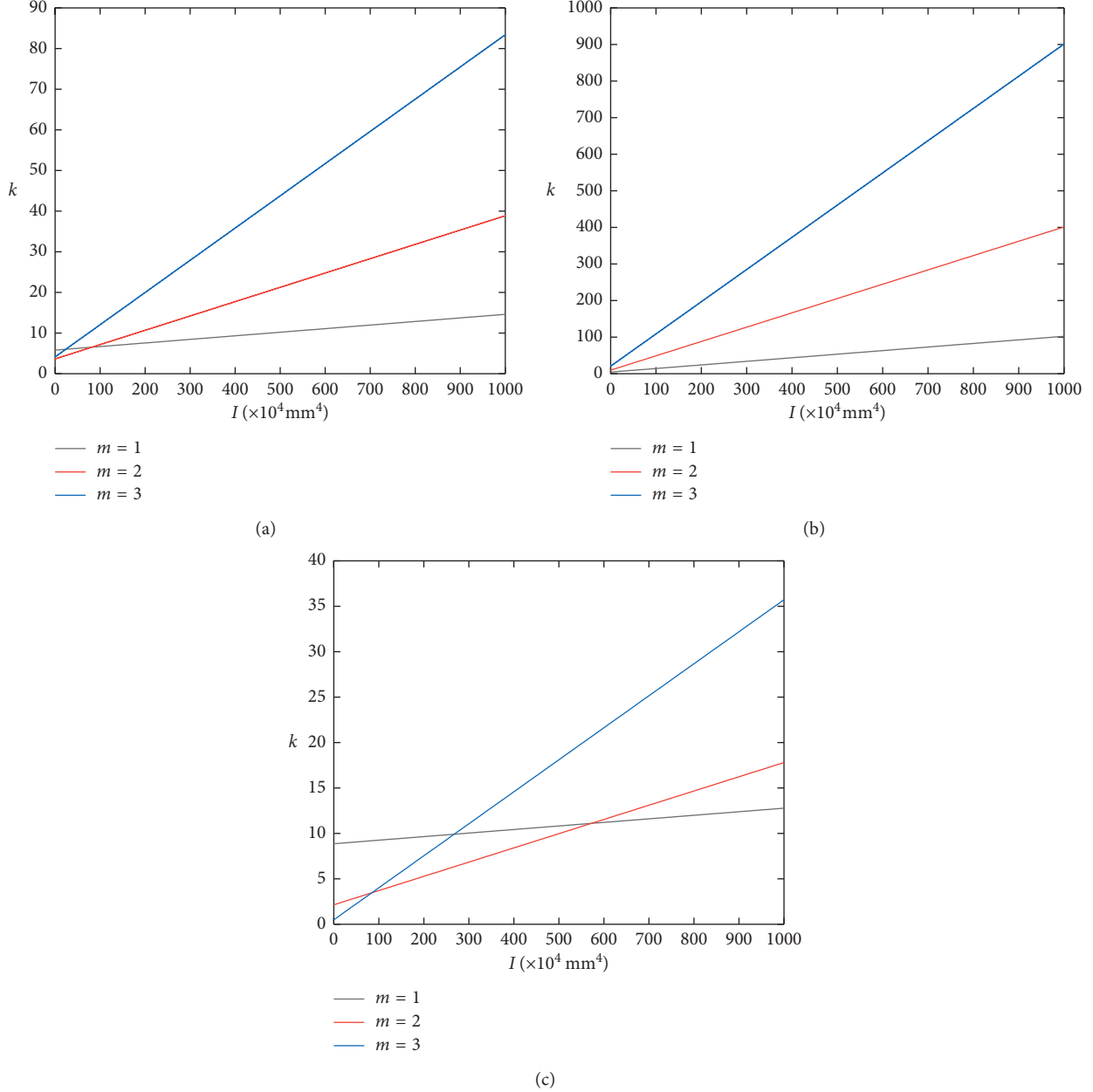


FIGURE 7: Relation between critical buckling load coefficient  $k$  and rib inertia moment for (a)  $\beta = 2$ , (b)  $\beta = 0.6$ , and (c)  $\beta = 3$ .

lower values in the curve with the hollow circles. This result indicates a change in the buckling of the SPS structure from two semiwaves to one semiwave ( $m=1$ ) along the  $x$  direction.

As the three curves in Figure 7(b) do not intersect, changing the inertia moment of the stiffening rib did not affect the buckling wave number, and the corresponding buckling waveform remained as one semiwave. As seen in Figure 7(c), when the stiffening rib is not installed on the sandwich panel, the buckling waveform is three half-waves. For small inertia moments of the stiffening rib, the buckling form exhibited two semiwaves. As the inertia moment of the stiffening rib increased, the sandwich panel buckled into one semiwave, indicating a major role of the stiffening rib in the

buckling of the overall structure. The critical buckling stress in a conventional plate with ribs is given by

$$\sigma_{\text{cr}} = \frac{\pi^2 D_h}{b^2 (h + 2t)} \frac{D_h B_{mn}^2 (1 + \beta^2)^2 + \varphi + 2\gamma}{\beta^2 (1 + 2\delta)}. \quad (26)$$

The  $\beta$  values at the critical buckling load for different inertia moments of a single rib on the SPS and steel plates are displayed in Figure 8. According to these curves, the inertia moment significantly affects the critical buckling load. A low critical buckling load always accompanies a small inertia moment but cannot fall below the critical buckling load of the structure without the rib. The critical buckling load tended to increase with increasing inertia moment of the

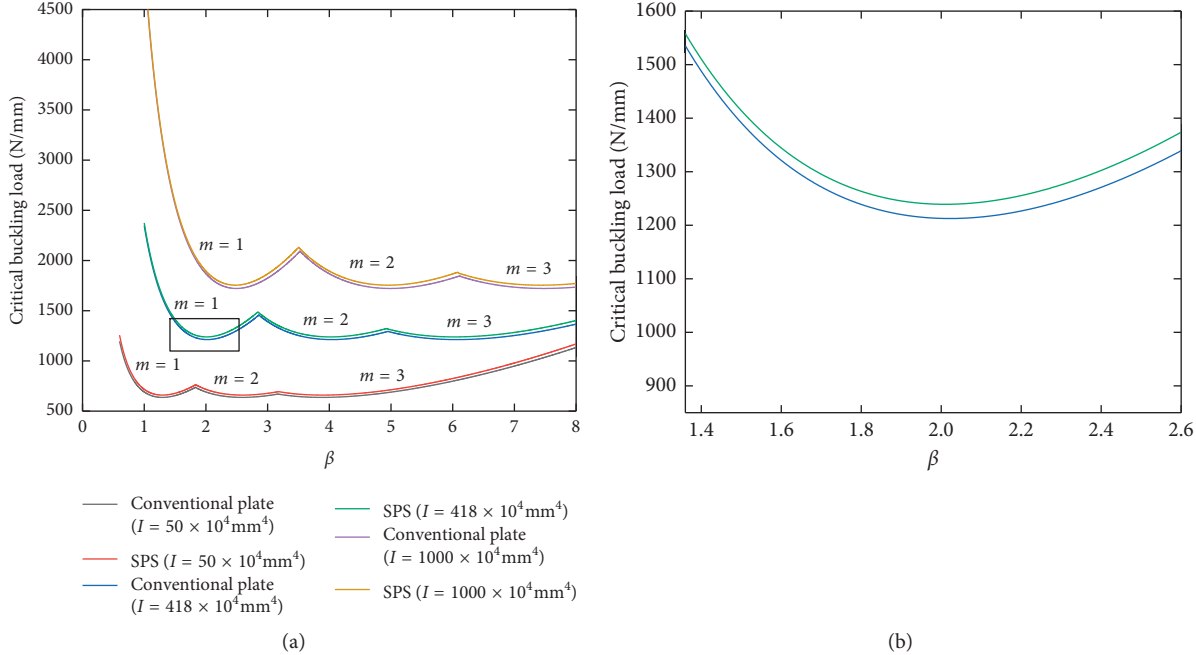


FIGURE 8: Relation between  $\beta$  and critical buckling load for different inertia moments of a single rib on the SPS and steel plates. (a) Original relations between  $\beta$  and critical buckling loads. (b) Local enlargement of the curves in (a).

ribs, but the growth trend of critical buckling stress gradually slows down. Meanwhile, the inertia moment is positively correlated with the buckling wavelength.

Clearly, when the inertia moment of the rib is small, the critical buckling load is also small but is lower-limited by the load without the ribs. After decreasing by a certain degree, the load grew slowly with increasing inertia moment. Increasing the inertia moment also increased the buckling wavelength.

Figure 8(b) in a zoom-in of the area delineated by the rectangular frame in Figure 8(a). The upper and lower curves are the results of SPS considering the shearing deformation energy and the equivalent conventional steel structure, respectively. The small gap between the two curves implies that the shearing deformation energy can be neglected.

Figure 9 plots the critical buckling stresses as functions of  $\beta$  for different inertia moments of a single rib on the SPS and conventional steel plate. The critical buckling stress significantly differed between the two curves. Moreover, the absolute value of this difference increased roughly proportionally to the critical buckling stress. The reasons are explained as follows: as the critical buckling loads are similar for the SPS and conventional plates, the larger cross-sectional area of the sandwich plates in comparison with the conventional plates reduces the critical stress in the former relative to the latter. The ratio of the critical buckling stresses in the sandwich and homogeneous plates is computed from equations (24) and (26) as

$$B_{mn} \frac{h_0}{h + 2t} = B_{mn} \frac{\sqrt[3]{12((h + t)^2 t)/2} + (t^3/6)}{h + 2t}. \quad (27)$$

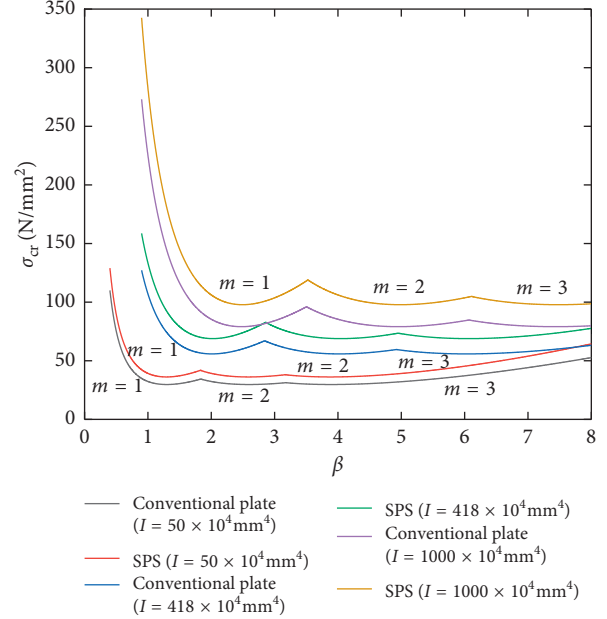


FIGURE 9: Relation between  $\beta$  and critical buckling stress for different inertia moments of a single rib in the SPS and steel plate.

With their large Young's modulus, the faceplates in the sandwich structure are the main load-bearing components under in-plane compression stress. For the same compression load and cross-sectional area, the compressive stress under a critical buckling load will be higher in the faceplates of SPS than in a conventional steel plate because the faceplates take most of compression load in SPS. The multiplication factor is  $(1 + (h/2t))$ . At this time, the ratio of the critical buckling stresses in the sandwich and homogeneous plates is given by

$$B_{mn} \frac{h_0}{2t} = B_{mn} \frac{\sqrt[3]{12(12((h+t)^2 t)/2) + (t^3/6))}}{2t}. \quad (28)$$

Figure 10 relates the critical buckling stress to  $\beta$  for different inertia moments of the SPS and steel plates. The critical buckling load under in-plane pressure, at which buckling first appears, is larger in the SPS than in the conventional plate, implying higher internal stresses in the SPS than in the conventional plate.

In typical applications, the ratio  $\delta$  of the faceplate thickness to the core thickness lied between 1:5 and 1:10. Substituting  $\delta$  in equation (28), the ratio of the critical buckling loads of the faceplate and core ranges from 3 to 4.5. For the common beam-plate composite structures in engineering practice, the stress in the plate component is far from the yield strength when overall buckling occurs. Therefore, when the steel plate is made into a sandwich structure, buckling occurs under large inner stress, which improves the utilization of the material.

### 3. FEM Analyses of SPS and Conventional Plates with Stiffening Ribs

**3.1. FEM Eigenvalue Buckling Analysis.** The calculations in Section 2 cannot determine the local buckling in SPSs. The critical buckling stress in ribbed sandwich plates is sometimes controlled by local buckling in a single grid. FEM analysis can estimate both the global and local buckling in SPSs and can assess the influences of different factors on the critical buckling loads of conventional plates and SPSs with stiffening ribs.

In this analysis, the material properties are unchanged from those in Section 2, and the stiffening ribs are simulated as beam elements. The conventional steel plates and SPSs are constructed from shell elements. Figure 11 shows the FEM model with  $\beta = 2$  and  $\beta = 5$ .

**3.2. Analysis of SPS with a Single Stiffened Rib.** To verify the accuracy of the above analysis, the above theoretical calculations are compared with the FEM results of an eigenvalue analysis. The theoretical and FEM results of an SPS with a single stiffening rib for different  $\beta$  values and inertia moments are shown in Figure 12. Here, the inertia moment of the single rib is varied from  $5 \times 10^4$  to  $1000 \times 10^4 \text{ mm}^4$ , and  $\beta$  is set to 1.0 (critical buckling load  $\sim 450\text{--}3000 \text{ N/mm}$ ) and 2.0 (critical buckling load  $\sim 450\text{--}1500 \text{ N/mm}$ ).

The results of both methods are highly consistent and exhibited the same general trends. At some points, the difference between the results is increased by local buckling in certain grids. The error is larger for  $\beta < 2$ , reflecting the higher inertia of the stiffener rib in this case. When global buckling occurred, the calculation and numerical results are relatively close.

**3.3. Result Comparisons for Steel Grillage and SPS with Stiffening Ribs.** This subsection first investigates the influence of  $\beta$  on the critical buckling load. In the FEM, the

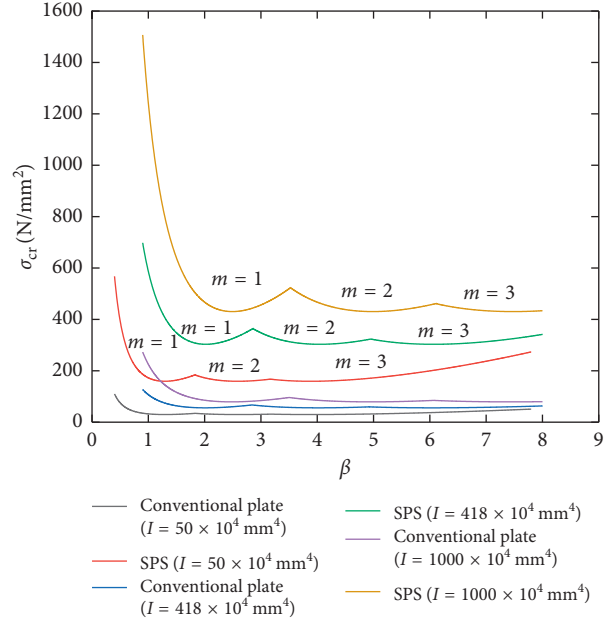


FIGURE 10: Relation between  $\beta$  and critical buckling stresses (actual) for different inertia moments of the single rib in the SPS and steel plates.

conventional plate is 2000 mm wide and 4 mm thick. Meanwhile, the core and faceplate thicknesses of the SPS are set to 16 mm and 2 mm, respectively. The sandwich panel is stiffened by four ribs with rectangular cross sections. The inertia moment of each rib is  $22500 \text{ mm}^4$ .

The critical buckling loads for the different  $\beta$  values are shown in Figure 13. The critical buckling loads are approximately three times higher in the ribbed SPS than in the conventional plates, confirming that the core in SPS enhances the bending stiffness of the whole structure. The small bump in both curves indicated a transformation of the buckling shape from one half-wave to two half-waves.

Figure 14 plots the critical buckling load versus inertia moment of the ribs. The critical buckling load is an approximately linear function of number of ribs. However, in the conventional plates, the critical buckling loads tended to remain steady after the inertia moment of the ribs reached a certain threshold. At this time, first-order buckling is not global buckling but in fact local buckling in a single cell of the grillage. Therefore, when the number of ribs in the plates is fixed, enlarging the stiffeners can significantly improve the stability until the appearance of local buckling in one cell of the grillage.

Figure 15 plots the critical buckling loads in the  $x$  and  $y$  directions in conventional and SPS plates with different numbers of ribs. For a given number of stiffeners, the critical buckling loads are larger in the  $x$  direction than in the  $y$  direction because the compressive loads are applied in the  $x$  direction. Moreover, the critical buckling load along the  $y$  direction (Figure 15(b)) increased slightly more rapidly with rib number than the critical buckling load along the  $x$  direction (Figure 15(a)), implying that transverse stiffeners exert little influence on the critical buckling loads. Finally,

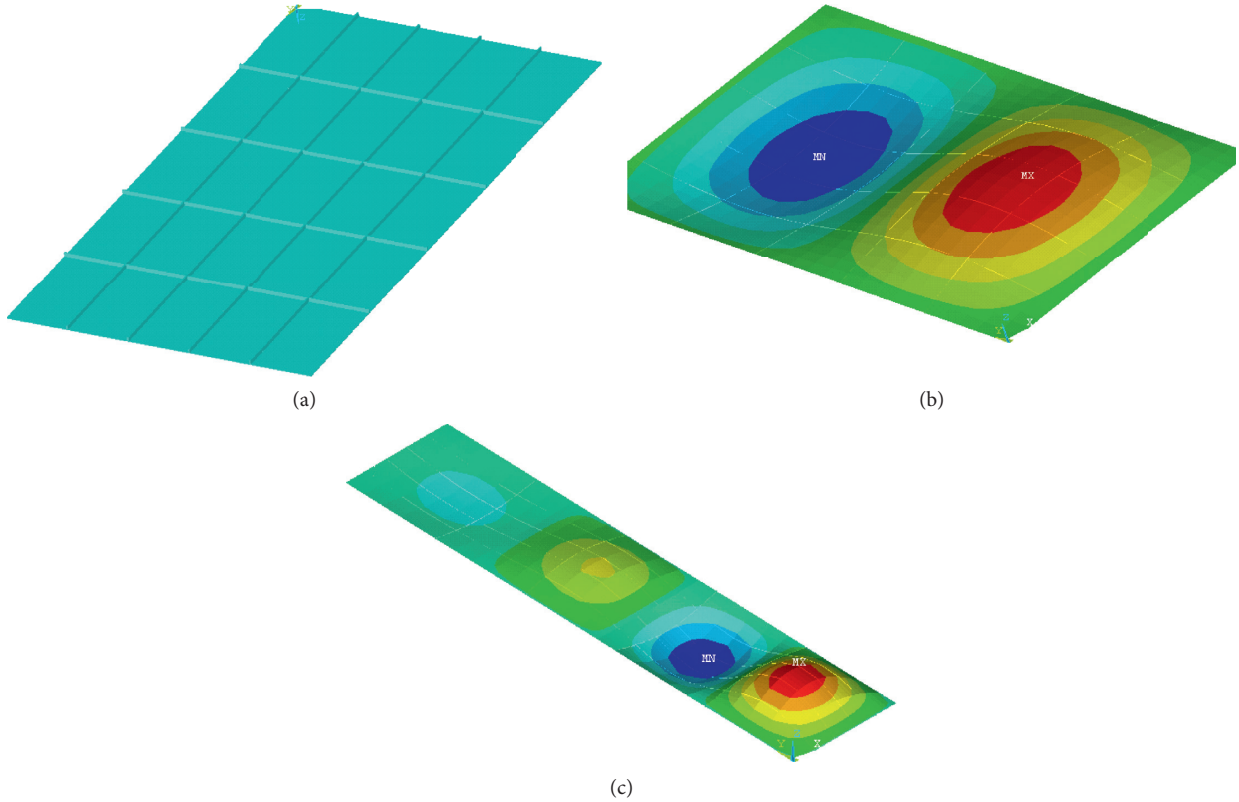


FIGURE 11: Finite element analysis of plates with stiffeners and the first-order buckling model: (a) ribbed SPS structure in the FEM model, (b) FEM model with  $\beta = 2$ , and (c) FEM model with  $\beta = 5$ .

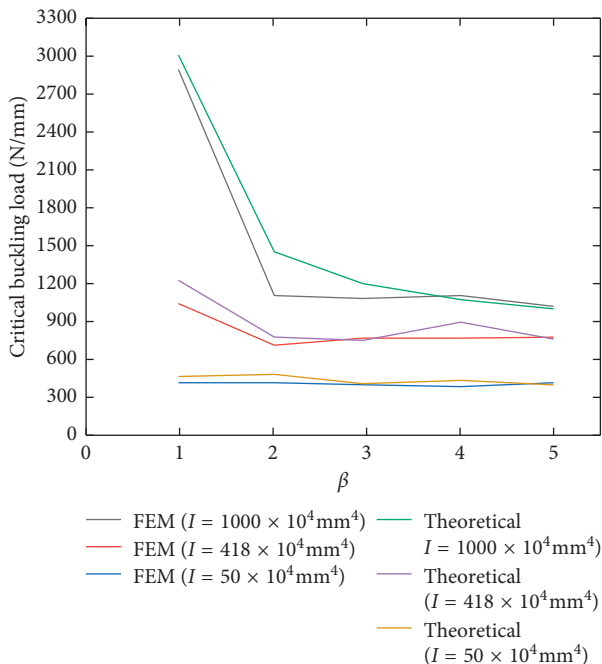


FIGURE 12: Comparisons between theoretical and FEM results.

the SPS structure can withstand higher critical buckling loads than conventional plates with the same number of stiffeners.

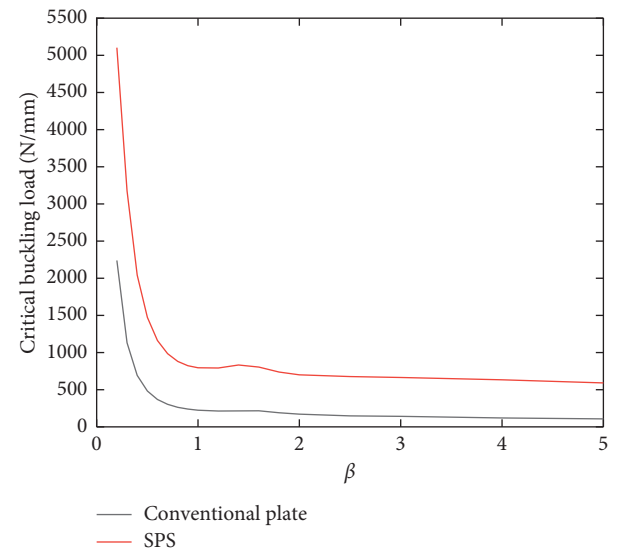


FIGURE 13: Critical buckling loads in ribbed SPS and conventional plates with different length-to-width ratios.

## 4. Buckling Experiment for SPS with Stiffening Ribs

**4.1. Design and Preparation of the Test Specimen.** To verify the calculation result, a typical SPS model test is conducted in a compression testing machine. The shape and sizes of the

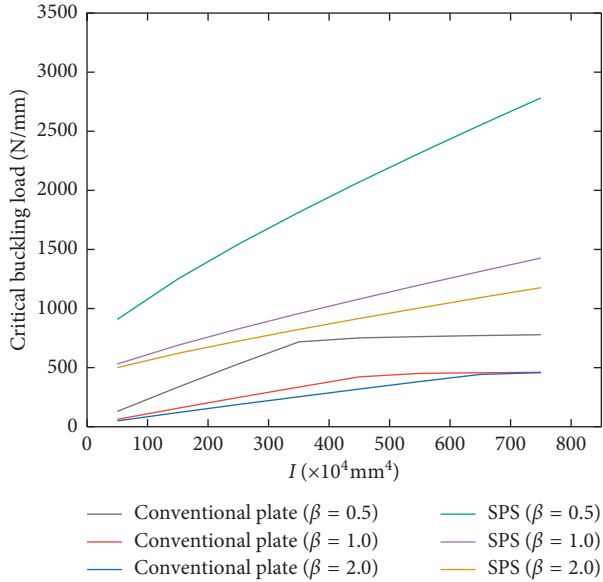
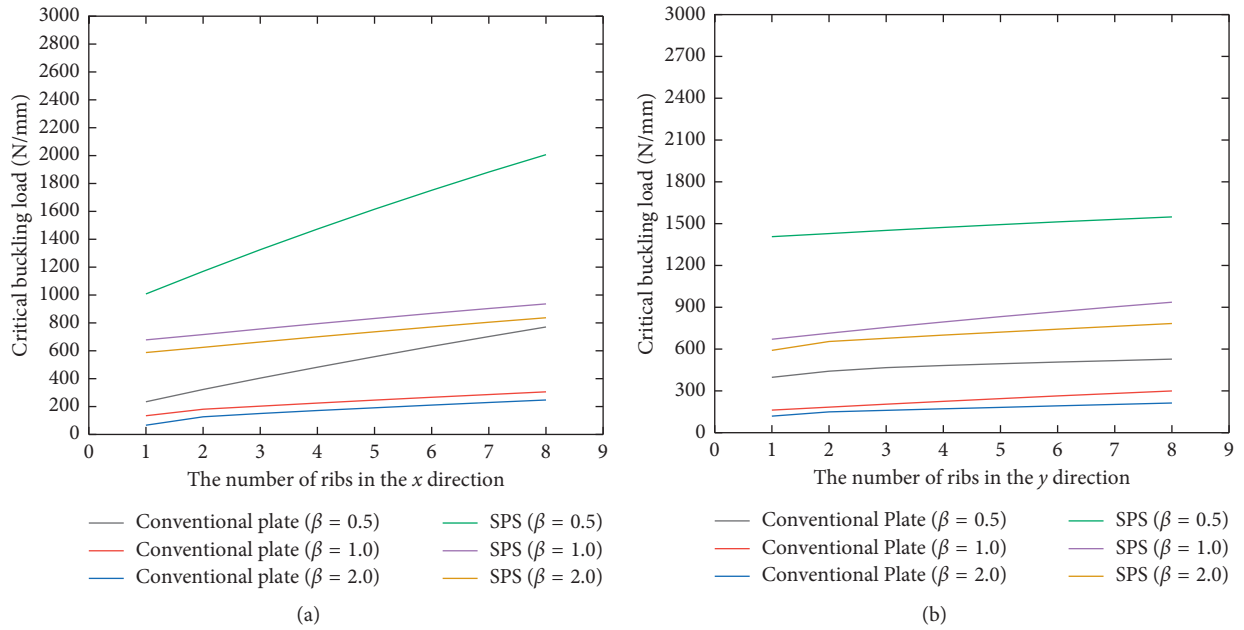


FIGURE 14: Critical buckling loads in ribbed SPSs and conventional plates with different inertia moments of stiffeners.

FIGURE 15: Critical buckling loads in the conventional plates and SPSs with different numbers of ribs: (a)  $x$  direction and (b)  $y$  direction.

specimens under the available experimental conditions are shown in Figure 16. The faceplates and ribs are constructed from steel with the same thickness (2 mm). The faceplates and reinforcement crossing walls are joined by argon arc welding, forming a closed box. Two holes in the top of the specimen (each of diameter of 20 mm) are formed for filling the polyurethane elastomer. Other holes in the inner walls are manufactured to form a tunnel for pouring the materials (mixed polymer and curing agent) into the full interior of the specimen.

The specimen is prepared as shown in Figure 17. First, the mixed liquid of polymer and curing agent is poured into

a closed container. Under air pressure applied by an air compressor, the compound liquid flowed to the opening hole beneath the specimen. Twenty minutes later, the polyurethane elastomer had solidified. The specimen is laid aside for two weeks to fully solidify the elastomer; then, it is tested for its buckling behavior.

Although the stiffeners in the sandwich structure mentioned in the previous calculations have different shapes, the buckling analysis therein is unchanged. To ensure the same constraint conditions in the experiment and the previous analysis, a steel constraining device with V-shaped grooves is designed and installed. This device

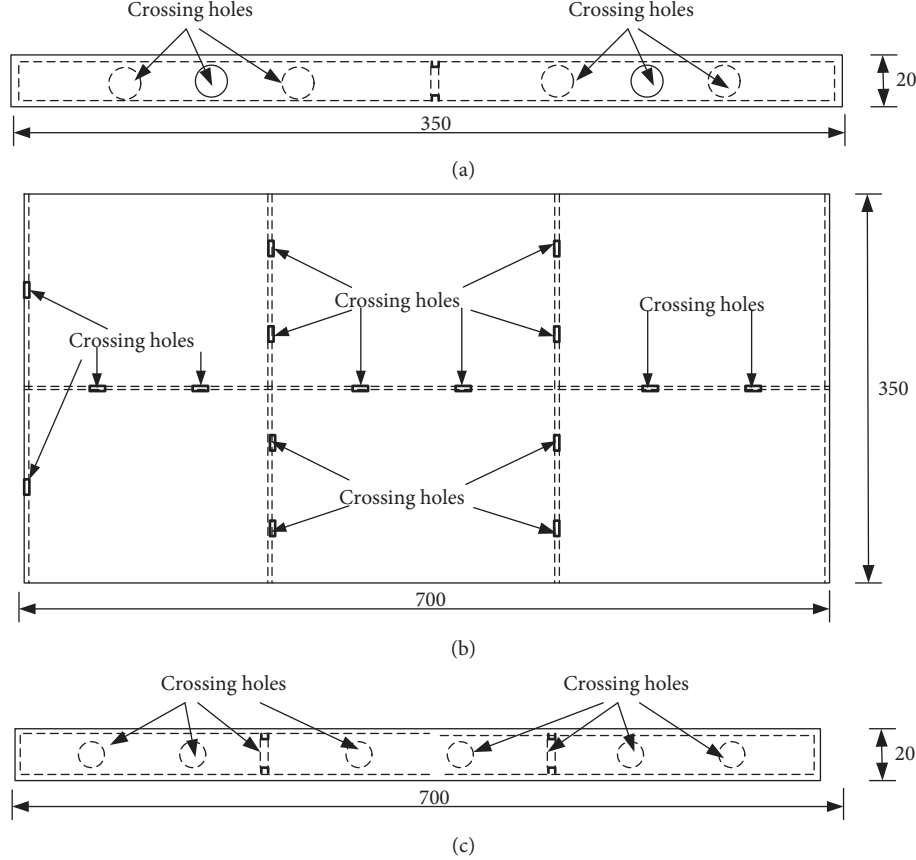


FIGURE 16: Shape and sizes of the test specimens. (a) Side view of specimen. (b) Top view of specimen. (c) Front view of specimen.

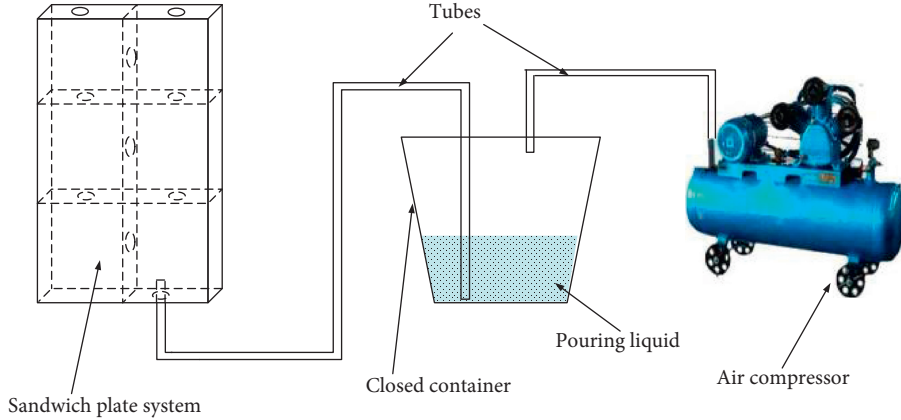


FIGURE 17: Preparation process of the SPS specimen.

constrained the deflections in the out-of-plane direction only.

**4.2. Experimental Results and Discussion.** Buckling experiments in a compression test machine are conducted on an SPS model with and without the injected PU elastomer (Figure 18).

The out-of-plane displacements of the SPS experimental model with the stiffeners are constrained by the V-shape

grooves installed at all sides, but the boundary deflections in the vertical direction are unrestrained. The pressure is applied by the compression testing machine. The loading speed is 2 mm/min, and the experiments are terminated when the total vertical displacement reached 20 mm. The critical buckling loads obtained in different ways are given in Table 2.

Figure 19 shows the load-displacement curve obtained in the compression experiment. The theoretical and FEM results differed by 5.2% and 3.9%, respectively, from those of



FIGURE 18: SPS buckling experiment.

TABLE 2: Critical buckling loads of the test specimens.

Methods	With PU core	Error (with PU core)	Without PU core	Error (no PU core)
Experiment	557.1	N/A	420.3	N/A
Theoretical	585.9	5.2%	544.7	29.6%
FEM	579.0	3.9%	403.4	4.0%

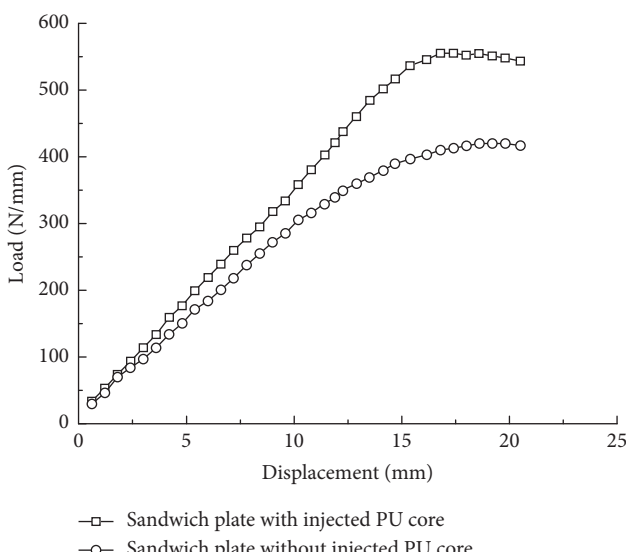


FIGURE 19: Load-displacement curve obtained in the experiment.

the sandwich plate with a PU core (Table 2 and Figure 19). The difference can be explained by the nonideal boundary constraints in the experiment. In the real case, the boundary constraints are affected by initial bending during welding of the SPS product, which creates a slight gap between the boundary and the fixture device. The results of the sandwich plate without the PU core specimen differed from the FEM and calculation results by almost the same amount (4.0%). However, in the specimen with the PU core, the theoretical and experimental results differed by 29.6%, and the curve change at the position of buckling is less obvious in the experimental specimen. This discrepancy is attributed to local buckling in the corner grids and the assumption of the first-order buckling model, meaning that local buckling appears before the whole structure buckling. In the real case, the PU core can prevent local buckling and raise the buckling strength.

## 5. Conclusions

A global buckling analysis approach for sandwich plate with stiffening ribs and PU core is discussed here based on theoretical, FEM, and experiments, the following conclusions can be obtained:

- (1) The theoretical method present here can forecast the critical global buckling loads and has little error with FEM
- (2) SPS can reduce the number of stiffeners and get larger critical buckling loads than conventional steel grilage structure
- (3) Inertia moments of ribs influence resistance of buckling failure are limited, because local buckling is appeared before global buckling
- (4) The theoretical, FEM, and experiments results show that the existence of PU core in SPS can rise the buckling strength tremendously, about 36.6% in the experiments

## Data Availability

The data used to support the findings of this study are included within the article.

## Conflicts of Interest

The authors declare that there are no conflicts of interest regarding the publication of this paper.

## Acknowledgments

This research was funded by the Natural Science Foundation of Heilongjiang Province (grant number G023017001), the Fundamental Research Funds for the Central Universities (grant number HEUCF180204), the National Natural Science Foundation of China (grant numbers 51409056 and 51678322), and the Taishan Scholar Priority Discipline Talent Group program funded by the Shan Dong Province.

## References

- [1] D. K. Harris, T. Cousins, T. M. Murray, and E. D. Sotelino, "Field investigation of a sandwich plate system bridge deck," *Journal of Performance of Constructed Facilities*, vol. 22, no. 5, pp. 305–315, 2008.
- [2] S. J. Kennedy, J. Bond, D. Braun, P. G. Noble, and J. D. Forsyth, "An innovative "no hot work" approach to hull repair on in-service FPSOs using sandwich plate system overlay," in *Proceedings of Offshore Technology Conference*, Houston, TX, USA, May 2003.
- [3] M. Shariyat, "A double-superposition global-local theory for vibration and dynamic buckling analyses of viscoelastic composite/sandwich plates: a complex modulus approach," *Archive of Applied Mechanics*, vol. 81, no. 9, pp. 1253–1268, 2011.
- [4] M. Brooking, "The performance, safety and production benefits of SPS structures for double hull tankers," in *Proceedings of RINA Conference on Double Hull Tankers*, London, UK, February 2004.
- [5] J. D. Martin, *Sandwich Plate System Bridge Deck Tests*, Virginia Polytechnic Institute and State University, Blacksburg, VA, USA, 2005.
- [6] C. Chunlei, L. Yunsheng, and W. Yuanqing, "Behavior analysis of orthotropic steel bridge decks strengthened by SPS," *Journal of Shijiazhuang Tiedao University (Natural Science)*, vol. 3, p. 5, 2010.
- [7] D. K. Harris, T. Cousins, E. D. Sotelino, and T. M. Murray, "Flexural lateral load distribution characteristics of sandwich plate system bridges: parametric investigation," *Journal of Bridge Engineering*, vol. 15, no. 6, pp. 684–694, 2010.
- [8] G.-q. Feng, G. Li, Z.-h. Liu, H.-l. Niu, and C.-f. Li, "Numerically simulating the sandwich plate system structures," *Journal of Marine Science and Application*, vol. 9, no. 3, pp. 286–291, 2010.
- [9] G. Shang, *Ultimate strength study for light weight ship structure*, Ph.D. thesis, Shipbuilding Research Institute of China, Beijing, China, 2011.
- [10] K. Liu, Z. L. Wang, Y. C. Zhang, and W. Y. Tang, "Research on the design of hull crashworthiness structure based on sandwich plate system," *Journal of Ship Mechanics*, vol. 18, no. 12, pp. 1505–1514, 2014.
- [11] G. Zou, Y. Wu, and Y. Hou, "Study of sandwich plate system in three-point bending considering effect of adhesive," *Materials Research Innovations*, vol. 19, no. 5, pp. 486–489, 2016.
- [12] J.-S. Liu and L. Hollaway, "Design optimisation of composite panel structures with stiffening ribs under multiple loading cases," *Computers & Structures*, vol. 78, no. 4, pp. 637–647, 2000.
- [13] H.-y. Wang and D.-y. Zhao, "Free vibration analysis of stiffened sandwich plates," *Shipbuilding of China*, vol. 1, p. 14, 2010.
- [14] F. Gara, L. Ragni, D. Roia, and L. Dezi, "Experimental tests and numerical modelling of wall sandwich panels," *Engineering Structures*, vol. 37, pp. 193–204, 2012.
- [15] M. John and G. Li, "Self-healing of sandwich structures with a grid stiffened shape memory polymer syntactic foam core," *Smart Materials and Structures*, vol. 19, no. 7, article 075013, 2010.
- [16] F. Xin and T. Lu, "Analytical modeling of wave propagation in orthogonally rib-stiffened sandwich structures: sound radiation," *Computers & Structures*, vol. 89, no. 5-6, pp. 507–516, 2011.
- [17] C. R. Briscoe, S. C. Mantell, T. Okazaki, and J. H. Davidson, "Local shear buckling and bearing strength in web core sandwich panels: model and experimental validation," *Engineering Structures*, vol. 35, pp. 114–119, 2012.
- [18] M. D. Goel, V. A. Matsagar, S. Marburg, and A. K. Gupta, "Comparative performance of stiffened sandwich foam panels under impulsive loading," *Journal of Performance of Constructed Facilities*, vol. 27, no. 5, pp. 540–549, 2012.
- [19] M. A. Wadee, S. Yiatros, and M. Theofanous, "Comparative studies of localized buckling in sandwich struts with different core bending models," *International Journal of Non-Linear Mechanics*, vol. 45, no. 2, pp. 111–120, 2010.
- [20] W. X. Yuan and D. J. Dawe, "Free vibration and stability analysis of stiffened sandwich plates," *Composite Structures*, vol. 63, no. 1, pp. 123–137, 2004.
- [21] S. P. Timoshenko and J. M. Gere, *Theory of Elastic Stability*, McGraw-Hill, New York, NY, USA, 1961.
- [22] M. Heder, "A simple method to estimate the buckling stress of stiffened sandwich panels," *Composite structures*, vol. 26, no. 1-2, pp. 95–107, 1993.
- [23] Q. Zhao, H. Jin, Y. Ding, and P. Chi, "Equivalent laminates model for stiffened panel global buckling analysis," *Acta Materiae Compositae Sinica*, vol. 3, p. 033, 2009.
- [24] H. Al-Qablan, "Semi-analytical buckling analysis of stiffened sandwich plates," *Journal of Applied Sciences*, vol. 10, no. 23, pp. 2978–2988, 2010.
- [25] C. Amadio and C. Bedon, "Buckling of laminated glass elements in out-of-plane bending," *Engineering Structures*, vol. 32, no. 11, pp. 3780–3788, 2010.
- [26] C. Bedon and C. Amadio, "Buckling of flat laminated glass panels under in-plane compression or shear," *Engineering Structures*, vol. 36, pp. 185–197, 2012.
- [27] C. Amadio and C. Bedon, "A buckling verification approach for monolithic and laminated glass elements under combined in-plane compression and bending," *Engineering Structures*, vol. 52, pp. 220–229, 2013.
- [28] C. Bedon and C. Amadio, "Buckling analysis of simply supported flat glass panels subjected to combined in-plane uniaxial compressive and edgewise shear loads," *Engineering Structures*, vol. 59, pp. 127–140, 2014.
- [29] Q. C. Xue, G. P. Zou, Y. Wu, J. Li, and L. Shang, "A comparative study between steel grillage and SPS stiffening plate based on FEA eigen value analysis," *Key Engineering Materials*, vol. 525–526, pp. 337–340, 2013.
- [30] Q. C. Xue, G. P. Zou, Y. Wu, H. L. Xiong, and M. Chai, "Calculation for elastic global buckling of sandwich plates with ribs," *Applied Mechanics and Materials*, vol. 188, pp. 25–30, 2012.
- [31] N. J. Hoff, "Bending and buckling of rectangular sandwich plates," *Technical Report Archive & Image Library*, vol. 18, no. 2225, p. 330, 1950.

## Research Article

# Improved SDOF Approach to Incorporate the Effects of Axial Loads on the Dynamic Responses of Steel Columns Subjected to Blast Loads

Junbo Yan , Yan Liu , and Fenglei Huang 

State Key Laboratory of Explosion Science and Technology, Beijing Institute of Technology, Beijing 100081, China

Correspondence should be addressed to Yan Liu; liuyan@bit.edu.cn

Received 19 September 2018; Revised 15 October 2018; Accepted 15 January 2019; Published 12 February 2019

Academic Editor: Chiara Bedon

Copyright © 2019 Junbo Yan et al. This is an open access article distributed under the Creative Commons Attribution License, which permits unrestricted use, distribution, and reproduction in any medium, provided the original work is properly cited.

In this paper, a complicated single-degree-of-freedom (SDOF) approach was developed to determine the global response of steel columns under combined axial and blast-induced transverse loads. Nonlinear section and member analyses were incorporated into the suggested SDOF method to account for the complex features of the material behavior, the high strain rate effect, and the column geometry. The SDOF technique was validated through comparisons with available finite element and experimental data, and a good consistency was obtained. Then, the validated SDOF approach was utilized to derive the pressure-impulse curves under various levels of axial loading. The level of the axial load was shown to have a significant influence on the dynamic behavior of a steel column subjected to a blast load.

## 1. Introduction

Recently, increasingly frequent terrorist activities have made blast protection essential for engineering communities [1]. The failure of load-bearing columns can result in the progressive collapse of structures. Therefore, it is important to improve the reliability of vulnerable columns under blasts to ensure the safety of structures [2, 3].

One of the most widely used approaches to assess the effects of blasts on structures is the equivalent single-degree-of-freedom (SDOF) approach. In addition, the efficient SDOF method has proven to be a powerful tool for deriving iso-damage pressure-impulse (P-I) diagrams, which can predict structural damage. For example, several technical manuals such as the unified facilities criteria (UFC) [4] based on linear resistance curves are used to design protective structures subjected to blast loads, and idealized load-deformation characteristics are given in the form of design charts. Dragos and Wu [5] proposed a simplified SDOF approach based on the new concept of a reduced resistance-deflection function to derive the P-I diagram for steel columns. Fallah and Louca [6] proposed analytical formulas for obtaining a

normalized P-I diagram based on a simple SDOF method incorporating the linear resistance. Further, Nassr et al. [7] demonstrated the SDOF method's ability to study the response of steel beams subjected to blast loads, and Nassr et al. [8] later employed the SDOF approach to study the axial load effects on steel columns under blast loads. In addition, Wang et al. [9] studied the SDOF approach to evaluate the concrete structural members under close-in nonuniform blast loads, and a comparison with test results indicated that the SDOF method can give reasonable predictions. Bedon et al. [10] carried out the analytical calculations by means of SDOF formulations derived from structural dynamics theories and proposed a design approach for practical estimation of buckling strength of glass elements in the analyzed loading and boundary conditions. Liu et al. [11] performed the field tests to investigate the blast response of steel-reinforced concrete (RC) beams and validate the nonlinear SDOF approach to predict the maximum displacements of RC beams subjected to blast loading. However, the axial load effect was neglected.

Currently, structural elements are typically simplified as having perfectly elastic-plastic force-deformation relationships [7, 8]. However, this idealized member resistance has inherent

limitations for capturing the gradual effect of plastic behavior on the dynamic properties of the system [9, 12]. Therefore, employing this force-deformation characteristic causes some uncertainty in the calculations.

Further, in reality, when subjected to a lateral blast pressure, an axial load tends to induce additional lateral deformation and magnify bending within a column. Thus, a structural response to blast loads that ignores axial load effects may not very accurately reflect the true behavior of a structure [13].

In this paper, a more accurate and sophisticated flexural behavior (featuring both the moment-curvature relationship and the force-deformation relationship) that considers the complex features of the slab geometry and the material's behavior under high strain rate loading is incorporated into a nonlinear SDOF approach for the dynamic analysis of columns subjected to blast-induced shock waves under various levels of axial compressive loads.

This approach also has the capability to generate iso-contour P-I diagrams of blast-loaded columns. To validate the suggested SDOF approach, the structural load-deformation characteristics, predicted maximum displacements, and iso-displacement P-I diagrams in this paper were compared against experimental and finite element model (FEM) results from [5, 14], respectively.

## 2. Theoretical Analyses of the Response of a Steel Column

**2.1. Sectional Analysis.** Assuming that plane sections remain planar under purely flexural behavior, a sectional analysis is performed to compute the moment-curvature characteristics for use in member analysis [15] as shown in Figure 1.

A solution procedure to generate the moment-curvature is outlined below, as shown in Figure 2.

- (1) The cross section of the column is divided into a desirable number of slices  $n$  parallel to the column axis.
- (2) Strain values  $\varepsilon_{\text{top}}$  are specified for the extreme steel compression fiber, and a corresponding depth  $x_n$  for the neutral axis is selected. The strain profile within the section is then generated:

$$\varepsilon_i = \frac{x_i}{x_n} \varepsilon_{\text{top}}, \quad (1)$$

where  $x_i$  is the distance between the corresponding layer and the neutral axis.

- (3) After the strain profile within the section is generated, the internal forces on the cross section are generated by employing the material's stress-strain relationships:

$$N_i = b h_i \sigma_i, \quad (2)$$

where  $b$  is the width of the section,  $\sigma_i$  is the stress on the  $i$ -th layer of the steel, and  $h_i$  is height of the  $i$ -th layer of the section.

- (4) The depth of the neutral axis is revised until the difference between the applied axial load  $N$  and the resultant internal force is within a convergence criterion:

$$\sum_i^n \sigma_i \Delta A_i = N, \quad (3)$$

where  $\Delta A_i$  is the area of the  $i$ -th layer of the section.

- (5) The resulting moments and curvatures are then calculated using these internal forces and strain profiles:

$$M = \sum_i^n \sigma_i \Delta A_i x_i, \quad (4)$$

$$\phi = \frac{\varepsilon_{\text{top}}}{x_n}.$$

- (6) Another incremental extreme compression fiber strain is selected, and the procedure is repeated until the extreme compression of concrete up to its ultimate compressive strain is reached for a given axial load.

**2.2. Material Modeling.** The stress-strain relationships of the member's material are incorporated into a member analysis to relate the member's deformation to the developed internal forces. The stress-strain curve is identical to the material properties described in [15], which have been thoroughly validated.

**2.2.1. Steel.** Compressive stress-strain relationships are assumed to be the same as tensile stress-strain relationships. The stress-strain relationship for reinforcing steel in tension consists of two linear segments, as shown in Figure 3.

**2.2.2. High Strain Rate Effect on Steel.** Accounting for the effects of high strain rates is critical in the analysis and design of members subjected to blast loads, as materials experience an increase in strength under high strain rates. The dynamic increase factor, DIF, is defined as the ratio of the dynamic material strength to the static material strength. Based on the relationship proposed by Malvar and Crawford [16], the dynamic material increase factors for both the yield strength and the ultimate strength are given by the following:

$$\text{DIF} = \left( \frac{\dot{\varepsilon}_s}{10^{-4}} \right)^\alpha, \quad (5)$$

where the DIF for the yield strength of steel may be determined by substituting  $\alpha = \alpha_{f_y}$  into equation (5) as follows:

$$\alpha_{f_y} = 0.074 - \frac{0.040 f_y}{414}, \quad (6)$$

where  $f_y$  is the static yield strength of steel (in MPa). Similarly, the DIF for the ultimate strength of steel may be determined by substituting  $\alpha = \alpha_{f_u}$  in equation (5) as follows:

$$\alpha_{f_u} = 0.019 - \frac{0.009 f_u}{414}. \quad (7)$$

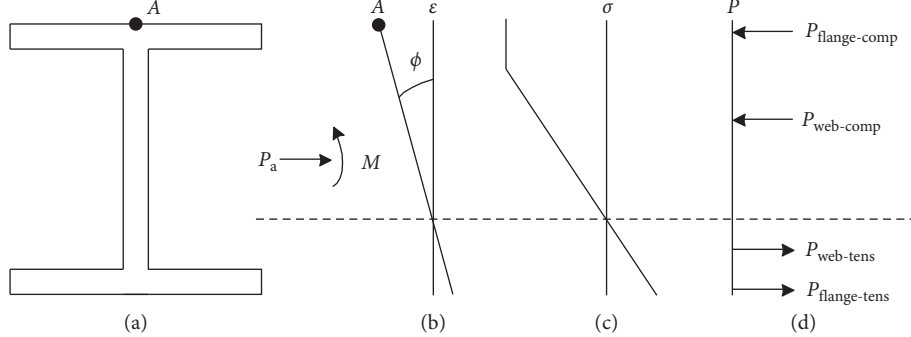


FIGURE 1: Moment-curvature analysis for a section. (a) Cross section. (b) Strain. (c) Stress. (d) Force.

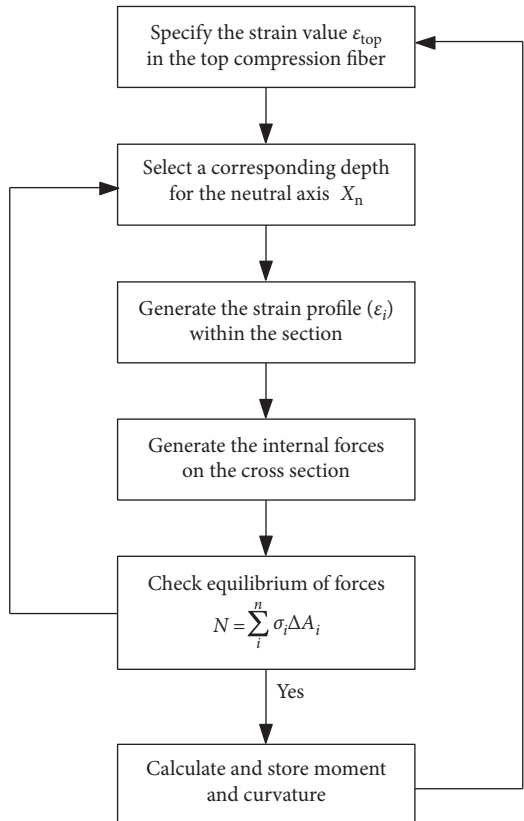


FIGURE 2: Flow chart of the numerical procedure for section analysis.

**2.3. Member Analysis.** To capture the full time history response of a steel-reinforced concrete column subjected to dynamic loading, the complete force-displacement relationship rather than the ultimate resistance is needed. The moment-curvature curve generated by sectional analysis is used to perform the member analysis of the steel-reinforced columns.

The following discussion outlines a procedure for obtaining the complete nonlinear resistance functions for steel concrete columns, which is also shown in Figure 4:

- Establish the moment-curvature relationship for the section. A column with a length  $l$  is divided equally into a desirable number of segments (equal to  $m$ ), each of which has a length  $\Delta l$ , as shown in Figure 5. Assume

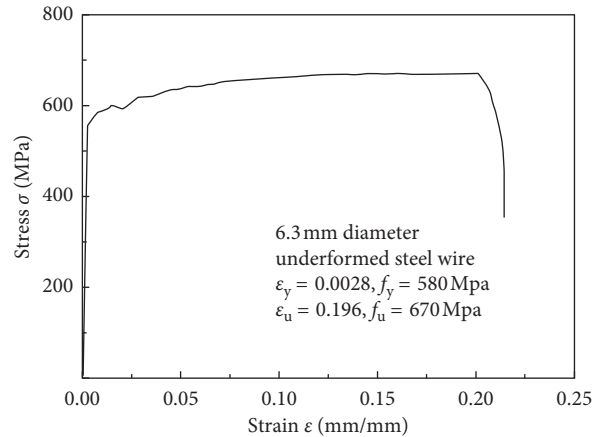


FIGURE 3: Tensile stress-strain relationship of steel.

a curvature on the midspan of the column  $\varphi_m$ ; the initial  $\varphi_m$  is zero, and at every step,  $\varphi_m = \varphi_m + \Delta\varphi$ . The moment  $M_m$  on the midspan is then computed based on the moment-curvature relationships.

$m = 500$  was used for the analysis. Convergence study shows that further decrease of mesh size only has little effect on the numerical results but leads to a much longer calculation time.

- Assume an initial incremental distributed deflection  $\delta_{i,k}$  ( $i = 0, 1, \dots, m$ ).
- The assumed horizontal load  $P$  is calculated by the axial load  $P_a$ ,  $M_m$ , and  $\delta_{i,0}$ :

$$P = \frac{2(M_m - P_a \delta_{i,k})}{l} \quad (8)$$

- The incremental distributed moment  $M_i$  is calculated by  $P$ ,  $P_a$ , and  $\delta_{i,k}$ . Then, the distributed curvature  $\varphi_i$  is determined based on the moment-curvature relationship:

$$M_i = P \cdot x_i + P_a \cdot \delta_{i,k}. \quad (9)$$

- In the conjugate column method, each segment divided above is considered a small imaginary column having the same length as the original segment. The midspan displacement of the segment can be calculated by the following expression:

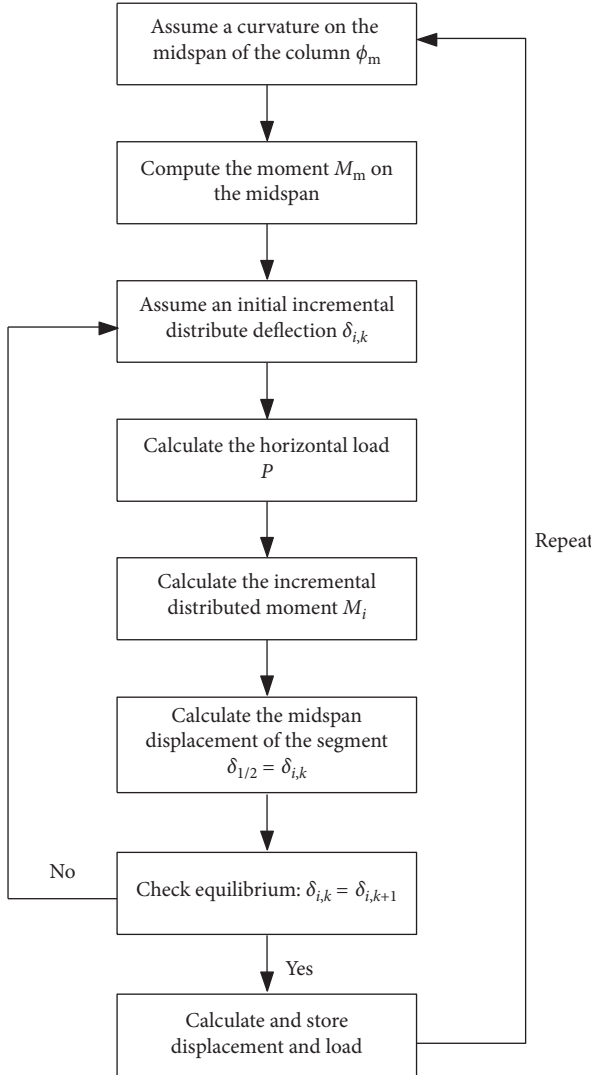


FIGURE 4: Flow chart of the numerical procedure for calculating the resistance function.

$$\delta_{l/2} = \delta_{i,k} = \sum_{i=1}^{m/2} \varphi_i \Delta x \left( \frac{l}{2} - x_i \right). \quad (10)$$

- (6) Assume the new incremental distributed deflection is  $\delta_{i,k+1}$ , repeat steps (4)-(6), and then determine  $\delta_{i,2}, \delta_{i,3}, \dots, \delta_{i,k}, \delta_{i,k+1}$ . If  $\delta_{i,(k+1)}$  and  $\delta_{i,k}$  are close enough (where the difference is less than an allowable value), then enter the next cycle. Finally, the whole load-deflection curve is determined [1].

**2.4. Dynamic SDOF Analysis.** The dynamic response of the columns was predicted using dynamic inelastic single-degree-of-freedom (SDOF) analysis after defining the nonlinear resistance curve for the structure [11]. The SDOF system is shown in Figure 6.

The idealized SDOF system is described by the following equation of motion:

$$K_M M \ddot{x}(t) + K_L R(x(t)) = K_L F_c(t), \quad (11)$$

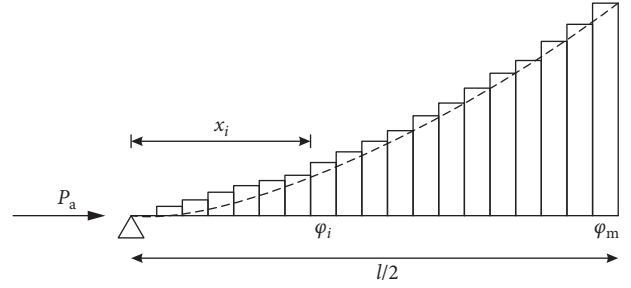


FIGURE 5: Member analysis.

where  $x(t)$  and  $\dot{x}(t)$  represent the displacement and acceleration, respectively, of the column at the midspan,  $M$  is the mass of the column,  $R(x)$  is the resistance as a function of the displacement, and  $F_c(t)$  is the loading as a function of time.

$K_M$  is the mass factor required to transfer a system with a distributed mass into an equivalent SDOF system and is computed by the following equation:

$$K_M = \frac{\int_0^L \bar{m} \varphi(x)^2 dx}{\bar{x} L}, \quad (12)$$

where  $\bar{m}$  is the mass per unit length of the member and  $\Phi(x)$  is the shape function of the member.

$K_L$  is the load factor used to transform the distributed force and stiffness into a single point load and is defined as follows:

$$K_L = \frac{\int_0^L F \varphi(x) dx}{FL}. \quad (13)$$

It is convenient to define a load mass factor [2],  $K_{LM}$ , as a ratio of the mass factor to the load factor:

$$K_{LM} = \frac{K_M}{K_L}. \quad (14)$$

Moreover, the response of the system may be written as follows by incorporating the axial load effect:

$$K_{LM} M \ddot{x}(t) + R(x) = F_c(t) + \frac{8P_a}{L} x, \quad (15)$$

where  $P_a$  is the axial load. The load mass transformation factor,  $K_{LM}$ , is defined based on the Biggs analysis [17].

Newmark proposed the following numerical solution technique for this equation [18]:

- (1) Assume that  $y$ ,  $\dot{y}$ , and  $\ddot{y}$  are known at the time  $t = t_i$  and assign them the subscript  $i$ .
- (2)  $t_{i+1} = t_i + \Delta t$  and assume a value  $\ddot{y}_{i+1}$  for the acceleration at time  $t_{i+1}$ ,  $\dot{y}_{i+1} = \dot{y}_i + (\ddot{y}_i + \ddot{y}_{i+1})(\Delta t/2)$ .
- (3) Compute a velocity at  $t_{i+1}$ ,  $\dot{y}_{i+1} = \dot{y}_i + (\ddot{y}_i + \ddot{y}_{i+1})(\Delta t/2)$ . Compute a displacement at  $t_{i+1}$ ,  $y_{i+1} = y_i + \dot{y}_i \Delta t + ((1/2) - \beta) \ddot{y}_i (\Delta t)^2 + \beta \ddot{y}_{i+1} (\Delta t)^2$ .
- (4) Substitute  $y_{i+1}$  and  $\dot{y}_{i+1}$  into the above equation and compute a new value for  $\ddot{y}_{i+1}$ .
- (5) Check whether  $\ddot{y}_{i+1}$  from step 2 is sufficiently close to  $\ddot{y}_{i+1}$  from step 5. If they are sufficiently close, the

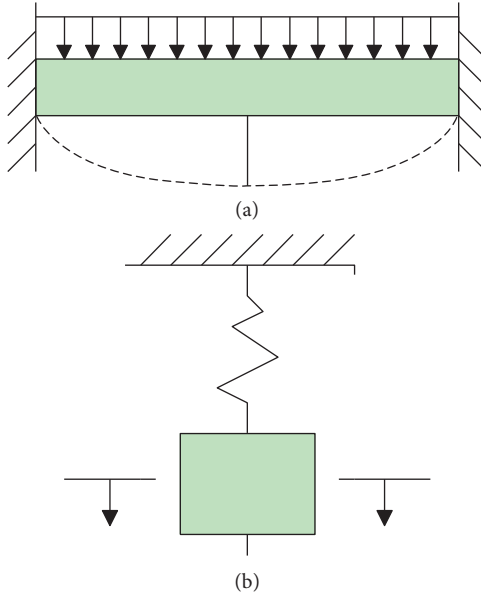


FIGURE 6: SDOF system. (a) Real structure. (b) Equivalent SDOF system.

solution is achieved. If they are not close, repeat steps 2 through 6 until convergence is attained. Since one needs to assume a new value for  $\ddot{y}_{i+1}$  in step 2, it is quite efficient to select the value obtained in step 5 for this purpose.

The  $\beta$  factor determines how the acceleration changes within a time step. In step 2, it is assumed that  $\ddot{y}$  varies linearly over  $\Delta t$ . Thus, the default value for  $\beta$  is 1/6 [19].

**2.5. P-I Diagram.** A P-I diagram as an iso-response curve is typically employed to assess the dynamic response of a structure subjected to a blast load. P-I curves consist of combinations of the peak reflected overpressure and the impulse that cause the same damage level based on a pre-defined failure mode.

For this study, the midspan displacement of the column is considered the damage criterion. One point on the P-I diagram is generated by specifying an initial positive load duration and iterating a reflected overpressure until the maximum midspan displacement predicted by the SDOF analysis reaches the predetermined damage value.

### 3. Analysis of Blast-Loaded Steel Columns

**3.1. Validation of the SDOF Method Using FEM Results Available in [1].** Dragos and Wu [5] performed an FE analysis of two steel columns under blast loads. One of the two steel columns presented in [5] was also utilized in this study to validate the present SDOF approach. The span of the abovementioned steel column was 4 m, and the width and thickness of the flanges were 102 mm and 10.3 mm, respectively. The columns were simply

supported. The total depth of the section was 160 mm, and the thickness of the web was 6.6 mm. The yield strength and Young modulus of the steel specimens were 470 MPa and 180 GPa, respectively.

A 359 kPa reflected pressure and 23.88 ms positive blast duration for the blast conditions were chosen for the calculation. The maximum displacements of the steel column specimens under an axial load of 350 kN were calculated by employing the proposed SDOF analysis.

Figure 7 shows a comparison of the deflection time history between the calculated and FEM results [5]. The calculated and FEM midspan maximum displacements of the steel column are 208.3 mm and 207.7 mm, respectively. However, a significant discrepancy occurs in the initial portions of the midspan deflection histories by both analyses. The negligence of membrane action and damping effects is a possible reason for the significant discrepancies in the initial portions of the midspan deflection histories by both analyses.

P-I diagrams for the maximum midspan displacement of 208.8 mm calculated above using the proposed SDOF approach were generated under an axial load of 350 kN. Figure 8 compares the P-I diagram of a column obtained by the proposed method with the FEM results available in [5]. As the figure illustrates, the P-I combination in the present SDOF analysis is very close to the FEM results from [5]. This result indicates that the present SDOF model gives a reliable prediction of the P-I diagram of a steel column subjected to blast loads.

**3.2. Validation of the SDOF Method Using the Experimental Results in [14].** To further validate the accuracy of the abovementioned SDOF approach, maximum midspan displacements generated from the proposed SDOF analysis were compared with the results of the test reported by Nassr et al. [14].

Thirteen typical wide-flange steel columns with two different section sizes, W150 × 24 and W200 × 71, were chosen by Nassr et al. [14] to investigate the dynamic responses of the steel columns to blast loads. Only the steel columns with a section size of W150 × 24 and a height of 2413 mm under the blast conditions in shot 1 and shot 3 are analyzed herein. All of the steel columns were pinned at the top and supported by rollers at the bottom. Therefore, the load mass factor,  $K_{LM}$ , was taken as being equal to 0.78 and 0.66 before and after yielding, respectively. The axial load in the experiment was 270 kN for the two specimens.

Figure 9 shows the layouts of the steel column's sections [14]. The static nominal yield strength and ultimate strength of the test specimens were 393 and 537 MPa, respectively. In shot 1, a charge size of 50 kg at a stand-off distance of 10.3 m was used to generate the blast environment. The average of the measured reflected pressures was 307 kPa, and the positive phase duration had an average value of 7.3 ms. In shot 3, a pressure time history was obtained by a charge size of 150 kg at a stand-off distance of 9 m. The peak pressure and positive phase

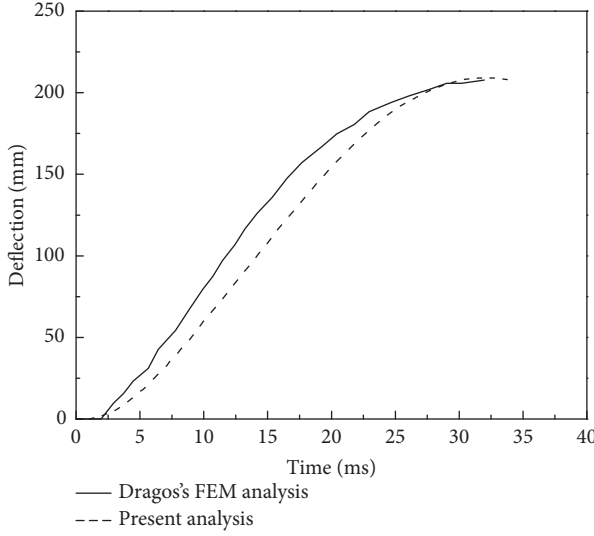


FIGURE 7: Comparison of the midspan displacements for blast no. 1.

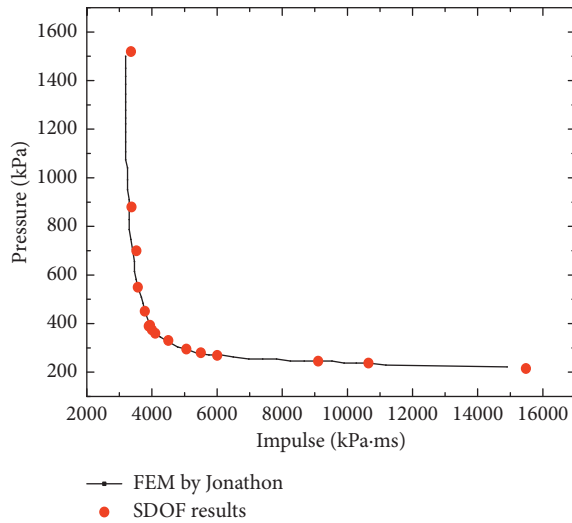


FIGURE 8: Comparison of P-I diagrams.

duration were 1560 kPa and 6.2 ms, respectively. A typical reflected pressure time history obtained in shot 1 is shown in Figure 10.

Comparisons of the calculated and test deflection time histories at the middle of the column are shown in Figure 11. The differences in the maximum deflections between the present analysis and experiments are 2.5% and 2.6% for shot 1 and shot 3, respectively. This result indicates that the SDOF model also gives reliable predictions of the responses of steel columns to blast loads. However, significant discrepancies occur in the initial portions of the midspan deflection histories by both analyses. The difference in the load-time histories under the real blast load and the SDOF analysis represents one possible reason for the reduced accuracy. The reflected pressure as a function of time was modeled using an equivalent triangular blast load having the same peak reflected pressure and impulse found

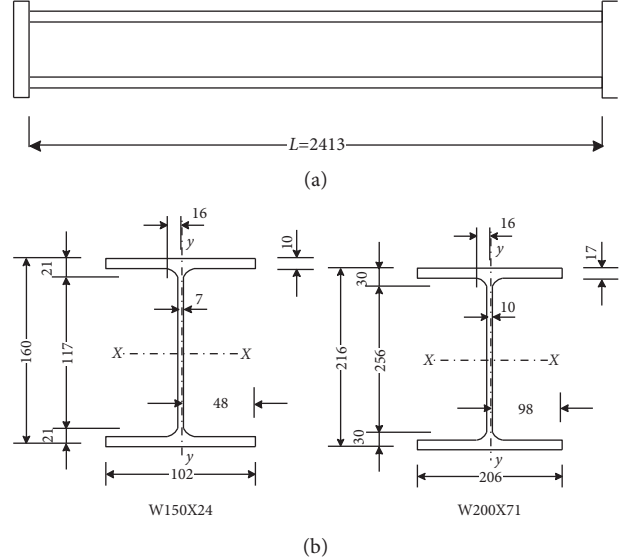


FIGURE 9: (a) Test specimens and (b) cross sections of the test specimens.

in the experiments. Thus, more accurate load-time histories should be employed. In addition, the shear damage mode is not considered in the present study; accordingly, a more accurate SDOF model considering other damage modes should be analyzed in further research.

**3.3. Effects of Axial Loads.** When a column is subjected to blast loads, the static compressive axial load induced by the gravity load affects the dynamic response of the column. The specimen analyzed above ( $W150 \times 24$ ) and the blast conditions (shot 1 and shot 3) available in [14] were employed here to investigate the effects of axial loads on the dynamic responses of steel columns. The effects of axial loads were investigated by applying three different axial loads, namely, 0 kN, 270 kN, and 400 kN.

**3.3.1. Effects of Axial Loads on the Maximum Displacements.** Figure 12 illustrates the effects of different axial loads on the displacement responses of columns under various load conditions. When the impulsive loading and corresponding deformation are small, the midspan displacement decreases with an increase in the axial load because the axial load amplifies the moment capacity of the column. However, when the column experiences large deformation, an increasing axial load results in a greater midspan displacement. This is caused by the  $P-\Delta$  effect, which is that when a column is subjected to both lateral and axial loading, the axial load creates an additional bending moment and thus enhances the lateral deflection of the column. The blast load induces lateral deformation in the column, causing the applied and resisting axial forces to form a couple, as they are no longer collinear. This couple causes additional lateral deformation and bending in the column, thereby inducing a greater mid-span displacement.

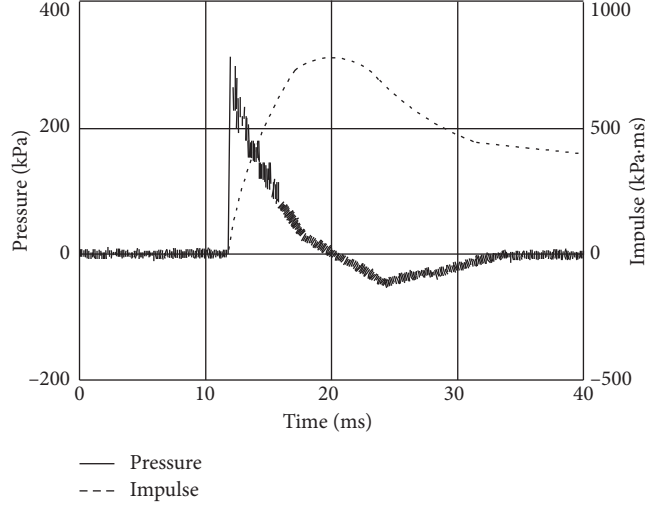


FIGURE 10: A typical reflected pressure time history obtained in shot 1.

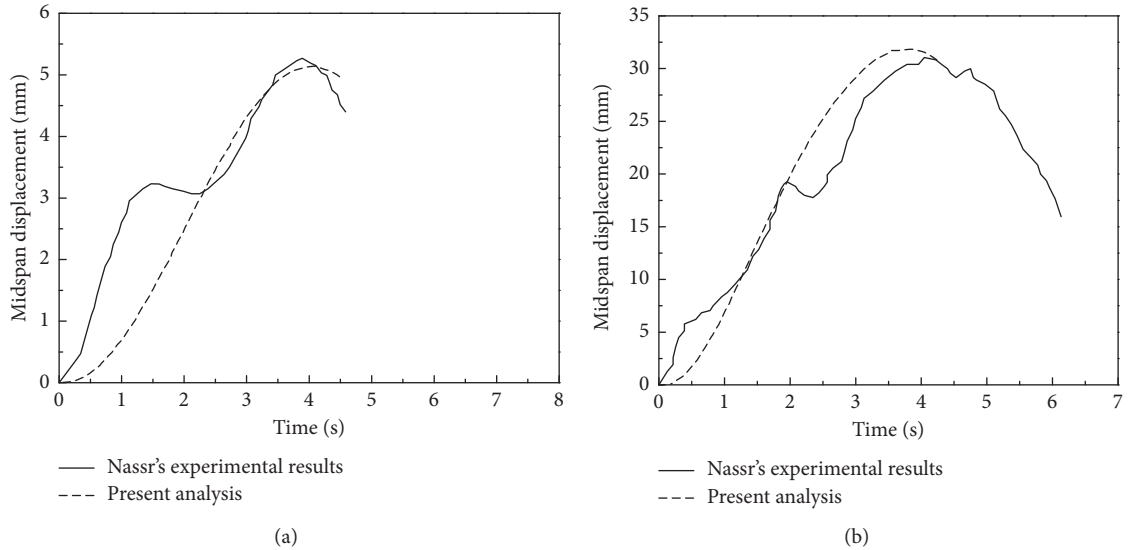


FIGURE 11: Experimental midspan displacements plotted against those predicted by SDOF analysis. (a) Comparison of the midspan displacements for shot 1. (b) Comparison of the midspan displacements for shot 3.

**3.3.2. Effects of Axial Loads on P-I Diagrams.** To investigate the effects of axial loads on the P-I diagram of a steel column, P-I diagrams were generated under the abovementioned axial loads. The maximum midspan displacements of 10 mm and 90 mm were determined as damage criteria.

Both P-I diagrams are shown in Figure 13. As seen from Figure 13(a), with a decrease in the axial load applied to the columns, the P-I diagram shifts to the left. This result indicates that an increase in the axial load can increase the ability of a column to resist blast loads. However, Figure 13(b) indicates that a larger axial load can decrease the ability of a steel column to resist blast loads when the maximum midspan displacement is large because of the P- $\Delta$  effect.

#### 4. Conclusion

In this paper, an SDOF model was developed to determine the global response of blast-loaded steel columns. The model also incorporates nonlinear moment-curvature and force-deformation relationships instead of a perfectly linear elastic-plastic force-deformation relationship. The proposed member analysis accounted for the material constitutive model, the strain rate effects, the gradual effect of the formation and progression of plastic behavior, and the effects of various axial loads. To validate the SDOF method, the theoretical SDOF maximum displacements were compared with the FEM and experimental results in [5, 14], respectively. The results

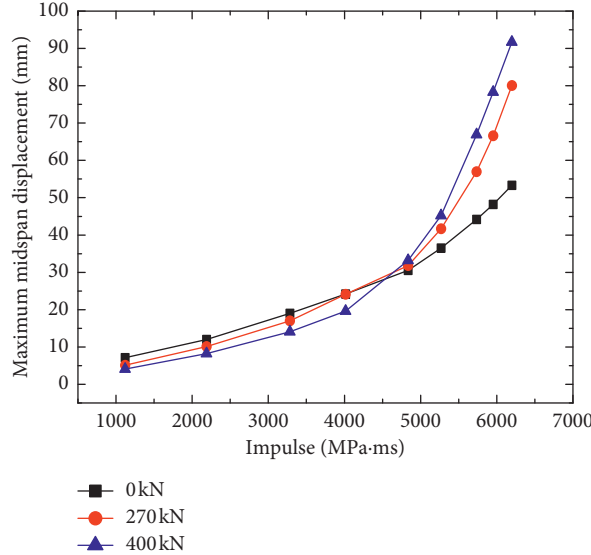


FIGURE 12: Effects of axial loads on the displacement responses of columns under various load conditions.

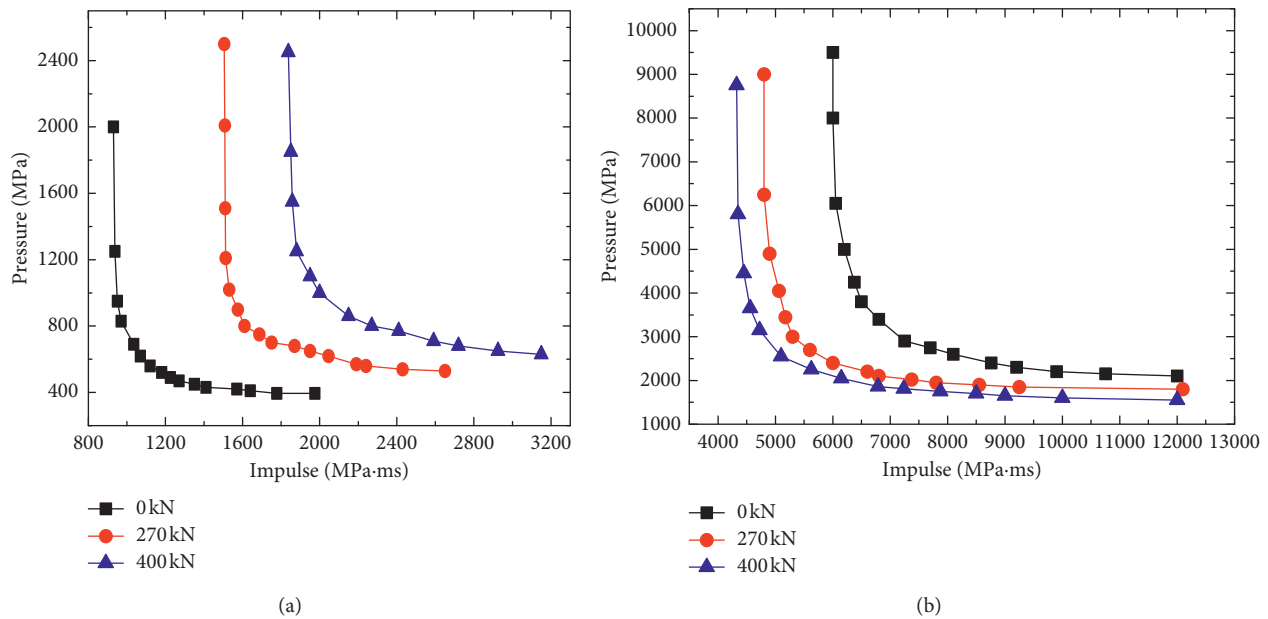


FIGURE 13: P-I curves for varying axial loads. (a) P-I curves for a 10 mm midspan displacement. (b) P-I curves for a 90 mm midspan displacement.

agreed well, indicating that the proposed SDOF model can accurately predict the deflection and P-I diagram of a blast-loaded column.

The maximum midspan displacements and P-I diagrams for steel columns under various axial loads were generated based on the proposed SDOF approach. The level of the axial compressive load was found to have a significant effect on the response of a steel column. When the level of the blast load is small, an increase in the axial load can reduce the maximum displacement and enhance the ability of the column to resist the blast load, which is caused by the enhanced moment capacity induced by the axial load. However, when the level of the

blast load is sufficiently large, an increase in the axial load can increase the maximum displacement and reduce the ability to resist the blast load, which is caused by the P-D effect.

## Data Availability

The origin data used to support the findings of this study are included within the article. The Matlab code data used to support the findings of this study were supplied by Junbo Yan under license and thus cannot be made freely available. Requests for access to these data should be made to Junbo Yan (e-mail address: 3120140060@bit.edu.cn).

## Conflicts of Interest

The authors declare that there are no conflicts of interest regarding the publication of this paper.

## Acknowledgments

This paper was supported by the National Natural Science Foundation of China under grant nos. 11390362 and 11221202.

## References

- [1] J. Dragos, C. Wu, M. Haskett, and D. Oehlers, "Derivation of normalized pressure impulse curves for flexural ultra high performance concrete slabs," *Journal of Structural Engineering*, vol. 139, no. 6, pp. 875–885, 2012.
- [2] S. Astarlioglu, T. Krauthammer, D. Morency, and T. P. Tran, "Behavior of reinforced concrete columns under combined effects of axial and blast-induced transverse loads," *Engineering Structures*, vol. 55, pp. 26–34, 2013.
- [3] A. Echevarria, A. E. Zaghi, V. Chiarito, R. Christenson, and S. Woodson, "Experimental comparison of the performance and residual capacity of CFFT and RC bridge columns subjected to blasts," *Journal of Bridge Engineering*, vol. 21, no. 1, article 04015026, 2015.
- [4] United States Department of Defense, "Unified facilities criteria: design of buildings to resist progressive collapse," in *UFC 4-023-03*, United States Department of Defense, Washington, DC, USA, 2009.
- [5] J. Dragos and C. Wu, "Single-degree-of-freedom approach to incorporate axial load effects on pressure impulse curves for steel columns," *Journal of Engineering Mechanics*, vol. 141, no. 1, article 04014098, 2014.
- [6] A. S. Fallah and L. A. Louca, "Pressure-impulse diagrams for elastic-plastic-hardening and softening single-degree-of-freedom models subjected to blast loading," *International Journal of Impact Engineering*, vol. 34, no. 4, pp. 823–842, 2007.
- [7] A. A. Nassr, A. G. Razaqpur, M. J. Tait, M. Campidelli, and S. Foo, "Strength and stability of steel beam columns under blast load," *International Journal of Impact Engineering*, vol. 55, pp. 34–48, 2013.
- [8] A. A. Nassr, A. G. Razaqpur, M. J. Tait, M. Campidelli, and S. Foo, "Dynamic response of steel columns subjected to blast loading," *Journal of structural engineering*, vol. 140, no. 7, article 04014036, 2013.
- [9] W. Wang, D. Zhang, F. Lu, S.-C. Wang, and F. Tang, "Experimental study on scaling the explosion resistance of a one-way square reinforced concrete slab under a close-in blast loading," *International Journal of Impact Engineering*, vol. 49, pp. 158–164, 2012.
- [10] C. Bedon, C. Amadio, and A. Sinico, "Numerical and analytical investigation on the dynamic buckling behavior of glass columns under blast," *Engineering Structures*, vol. 79, pp. 322–340, 2014.
- [11] Y. Liu, J.-b. Yan, and F.-l. Huang, "Behavior of reinforced concrete beams and columns subjected to blast loading," *Defence Technology*, vol. 14, no. 5, pp. 550–559, 2018.
- [12] E. Jacques, A. Lloyd, and M. Saatcioglu, "Predicting reinforced concrete response to blast loads," *Canadian Journal of Civil Engineering*, vol. 40, no. 5, pp. 427–444, 2012.
- [13] M. Colombo and P. Martinelli, "SDOF models for RC and FRC circular plates under blast loads," *Applied Mechanics and Materials*, vol. 82, pp. 440–445, 2011.
- [14] A. A. Nassr, A. G. Razaqpur, M. J. Tait, M. Campidelli, and S. Foo, "Experimental performance of steel beams under blast loading," *Journal of Performance of Constructed Facilities*, vol. 26, no. 5, pp. 600–619, 2011.
- [15] E. Jacques, *Blast Retrofit of Reinforced Concrete Walls and Slabs*, University of Ottawa, Ottawa, Canada, 2011.
- [16] L. J. Malvar and J. E. Crawford, "Dynamic increase factors for concrete," in *Naval Facilities Engineering Service Center Port Hueneme CA*, 1998.
- [17] J. M. Biggs and B. Testa, *Introduction to Structural Dynamics*, McGraw-Hill, New York, NY, USA, 1964.
- [18] N. M. Newmark, "A method of computation for structural dynamics," *Journal of the engineering mechanics division*, vol. 85, pp. 67–94, 1959.
- [19] T. Krauthammer, *Modern Protective Structures*, CRC Press, Boca Raton, FL, USA, 2008.

## Research Article

# Shear Storage Capacity of Vertical Stiffener Joints between Concrete-Filled Double Steel Tubular Columns and Steel Beams

Zhijun Zhou<sup>1</sup>, Yufen Zhang<sup>1</sup>, Miao Wang<sup>3</sup>, and Krushar Demoha<sup>4</sup>

<sup>1</sup>School of Highway, Chang'an University, Xi'an 710064, Shaanxi Province, China

<sup>2</sup>School of Civil and Transportation Engineering, Hebei University of Technology, Tianjin 300401, China

<sup>3</sup>School of Civil Engineering, North China University of Technology, Beijing 100144, China

<sup>4</sup>Department of Mechanical Engineering, University of Auckland, Auckland, New Zealand

Correspondence should be addressed to Yufen Zhang; [yufenzh@gmail.com](mailto:yufenzh@gmail.com)

Received 18 October 2018; Revised 27 November 2018; Accepted 26 December 2018; Published 3 February 2019

Academic Editor: Chiara Bedon

Copyright © 2019 Zhijun Zhou et al. This is an open access article distributed under the Creative Commons Attribution License, which permits unrestricted use, distribution, and reproduction in any medium, provided the original work is properly cited.

Based on the low cyclic loading test results of vertical stiffener joints between concrete-filled double steel tubular (CFDST) columns and steel beams, the shear transfer mechanism and shear resistance were analyzed in this paper. A conceptual model formulated was presented in terms of equilibrium and stress-strain relationships. The results calculated by the theoretical model and the available experimental data were compared, and then one new concept of shear storage coefficient was proposed for the determination of the shear storage capacity of the joint, which quantitatively explained the ductility failure progression of the joint specimens in the seismic performance test. It was concluded that the vertical stiffener joint had sufficient shear resistance, which met the seismic design principle of strong shear and weak bending. Results show that the ribbed joints have greater shear resistance than unribbed ones; lengthening the overhang of the vertical stiffener can both increase shear resistance and shear storage capacity of the joint; axial compression ratio can reduce the shear storage capacity. The paper also suggests that the joint design should ensure enough safety storage of shear resistance to improve the seismic performance.

## 1. Introduction

With the development of concrete-filled steel tubular (CFST) column, concrete-filled double steel tubular (CFDST) column emerged in the form of circular internally and square externally, fully filled with concrete. CFDST column can make full use of circular steel tube for its good confinement performance and square steel tube for its good ductility advantages, so the new type of column can be applied to high-rise buildings and bridge engineering [1–3]. CFDST column has been firstly applied in the construction of city hall in Wuppertal, Germany. The vertical stiffener joint between a CFDST column and an H-type beam has been verified that it has the good hysteretic behavior, bearing capacity, and ductility [4–6], but the shear behavior of the joint core has not been studied including the shear resistance. It is well known that strength calculation mainly includes bending strength and shear strength in joint design. To ensure a proper failure progression and ductility, the

joint panel zone should typically be stronger than the neighboring beam and column. So, many calculation procedures for joint shear strength have been proposed. Koester [7] conducted a series of experiments on the panel zone shear strength of rectangular steel girder-to-CFST composite connections. Various shear strength for CFST joint panels has been analyzed to date [8–11]. And a simplified trilinear model to predict the shear strength versus the shear deformation response in panel zone was presented for vertical stiffener connections between L-shaped columns composed of concrete-filled steel tubes and steel beams [12]. The superposition method was also applied to estimate the beam-column joint shear strength [13–18], and the applicability and accuracy of the strength superposition method for the estimation of joint shear strength were verified explicitly. However, these studies have been limited in scope to ordinary CFST or composite concrete structures. The vertical stiffener joint of CFDST structure has very different configurations, which provide different shear components.

The shear failure of beam-column joint may cause the immediate collapse of a building, and strengthening such joints can have a significant influence upon the earthquake resistance of structures. Therefore, it is necessary to develop an effective rehabilitation strategy to strengthen such joints in order to avoid or delay their shear failure. According to the principle of structure design “strong shear and weak bending,” shear strength becomes the control condition of the strength calculation. When shear strength calculation was not estimated accurately, the structure would lead to the lack of shear capacity even the shear failure [19–23], so shear storage capacity was analyzed in this paper based on the low cyclic loading test results of vertical stiffener joints between CFDST columns and steel beams. A conceptual model is presented for assessing the cracked vertical stiffener joints with shear failure. The model is entirely formulated in terms of equilibrium and stress-strain relationships and can be used to assess the shear capacity of a series of components including steel tubes, vertical stiffener, anchorage web, and joint core concrete. The calculated results were compared to the experimental ones at the state of both yielding and damage. Then, one new concept of shear storage coefficient was proposed for the determination of the joint’s shear storage capacity. In order to better evaluate the seismic design principles of strong joints, the joint’s safety reserve of shear capacity was quantitatively explained to ensure proper failure progression and ductility, which can provide reference for engineering design of CFDST structure.

## 2. The Shear Model and Force Transfer Mechanism

Vertical stiffener joints were tested by quasistatic cyclic loading at the both ends of the steel beam [6], i.e., the fixed vertical force  $N$  was applied on the column top, and two 500 kN MTS servo actuators were placed at east and west beam ends to achieve the reciprocating load by pushing and pulling at the same time. The joint specimens were intended to simulate the connection between an interior column and the two adjacent steel beams in a frame structure. Table 1 lists the details of the six specimens tested in this investigation, where  $l_E$  is the overhang length of vertical stiffener;  $n$  is the axial compressive force ratio; and two kinds of configuration of anchorage webs are unribbed and ribbed. The outer steel tube is square with the section type of  $B \times t$ , and the inner steel tube is circular with the section type of  $\Phi 2r_i \times t_i$  as shown in Table 1. The section of H-shaped steel beam is  $244 \times 175 \times 7 \times 11 \text{ mm}^4$ .

Force diagram in panel zone is shown in Figure 1, where  $V_j$  represents the experimental shear force in panel zone;  $P$  is the actual load value on the beam end;  $H_b$  and  $H_c$  are the height of steel beam and column, respectively;  $L_b$  is the distance from the beam end to the surface of CFDST column; and  $H$  is the distance from the top to the bottom hinge of the column. According to the equilibrium condition, the shear force in the panel zone can be determined according to the load of the beam end in the actual experiment.

$$V_j = \frac{2PL_b}{H_b - t_b} - V_c = \frac{2PL_b}{H_b - t_b} - \frac{PL}{H}, \quad (1)$$

where  $V_c$  represents the horizontal reactive force at the column end when the beam end force is  $P$  and  $t_b$  represents the thickness of the steel beam flange.

In this joint system, anchorage web, vertical stiffeners, and horizontal end plate play the main force-transferring role. The transverse profile of the vertical stiffener joint is shown in Figure 2(a). Anchorage web is groove-welded vertically on the inner steel tube, going outside the outer steel tube, and then it connects with the steel beam web by bolts. Meanwhile vertical stiffener is groove-welded on the column surface, and its overhangs weld with the end plate at right angles. In order to solve the stress concentration problem, the radius-cut section is used for the end plate. The other side of end plate as wide as the beam is butt welded to the beam flange. In addition, the application of anchorage web embedded in the concrete between inner tube and outer tube can improve work ability and globality of the joint. And the embedded anchorage web is higher than the steel beam, so anchorage web can be chosen as two types including unribbed and ribbed joints as shown in the longitudinal profile in Figure 2(b).

The compressive strength of the concrete  $f_{cu}$  is 59.5 MPa. The material properties of the steel plates obtained through the standard material test method are given in Table 2. The steel of anchorage plate and vertical stiffener is the same steel as the square tube. The bolts were tightened with a special torque wrench according to design requirements, and the friction-type high-strength bolt M20 belongs to the level 10.9. According to the suggestion of ATC-24 [24], a displacement control with three cycles at each displacement amplitude was used after the specimen yielded. The cantilever-displacement increments between each cycle were 3 mm one time before yielding and 6 mm three times after yielding until failure occurred.

The main function of the vertical stiffener is to protect the outer steel tube web from shearing. On the other hand, together with the horizontal end plates, vertical stiffeners can transmit tension or compression of the steel beam flange, so the vertical stiffeners can bear shear force from the panel zone and horizontal pulling or pushing force from beam flanges. The anchorage web is mainly subjected to shearing force of the beam web, and the ribs can help transmit part of the pulling force from beam flanges to the joint core. The force-transferring path of the vertical stiffener joint is basically included: (1) horizontal shear force of column end is transferred to vertical stiffeners and outer steel tube by welds and then to joint core concrete; (2) vertical shear force of beam end is transferred to vertical stiffeners and anchorage webs and then to the panel zone. The calculation formula in the AIJ specification [25] proposed by the Architectural Institute of Japan takes into account the shear strength of both the steel tube cross section and the core concrete cross section. So, the shear model of the vertical stiffener joints is composed as a series of components. The shear capacity in panel zone includes the contributions from steel tubes, the vertical stiffeners, anchorage webs, and the joint core concrete. Among them, the core concrete contributes the shear capacity in the way of plane shearing and pressure lever

TABLE 1: Summary of the joint specimens and analysis results.

Specimens	$B \times t$ (mm $^2$ )	$\Phi 2r_i \times t_i$ (mm $^2$ )	$l_E$ (mm)	$n$	Anchorage web	$V_{yE}$ (kN)	$V_{uE}$ (kN)	$V_{yC}$ (kN)	$V_{uC}$ (kN)	$R_y$	$R_u$
SBJ1-1	$250 \times 8$	$\Phi 133 \times 6$	80	0.23	Unribbed	1248.9	1703.9	2433.3	4070.9	1.95	2.39
SBJ1-2	$250 \times 8$	$\Phi 133 \times 6$	120	0.23	Unribbed	1373.6	1774.2	2722.9	4544.6	1.98	2.56
SBJ2-1	$250 \times 8$	$\Phi 133 \times 6$	80	0.23	Ribbed	1392.4	1959.5	2974.4	4841.8	2.14	2.47
SBJ2-2	$250 \times 8$	$\Phi 133 \times 6$	120	0.23	Ribbed	1548.3	2126.1	3264.0	5315.5	2.11	2.50
SBJ3-1	$250 \times 8$	$\Phi 133 \times 6$	80	0.40	Unribbed	1326.7	1669.5	2433.3	4070.9	1.83	2.44
SBJ3-2	$250 \times 5$	$\Phi 133 \times 6$	80	0.23	Ribbed	1325.5	1856.6	2830.2	4544.2	2.14	2.45

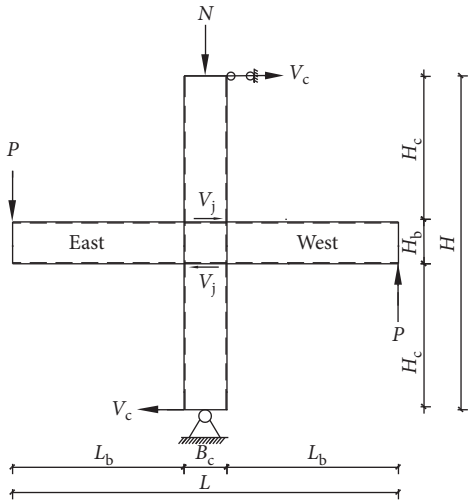


FIGURE 1: Force diagram in panel zone.

model, respectively. Shear capacity of each component can be calculated using different stress states based on the different deformation mechanism, and finally the ultimate shear capacity of the joint will be obtained on the principle of limit equilibrium superposition.

### 3. Calculation of the Theoretical Shear Resistance

**3.1. Basic Assumptions.** For the double steel tubes and core concrete, the effect of axial compressive stress is considered to calculate the shear capacity, while for the force-transmitting members' vertical stiffeners and anchorage webs, pure shear stress state is used without considering the effect of axial stress since they are considered as main connecting part to the beam-column connections. In order to simplify the calculation and analysis, the following basic assumptions are also introduced:

- (1) There is no relative slip between steel tubes and concrete, and the axial deformation is consistent
- (2) After the steel tube has yielded, the cross-sectional shape does not change, and bending deformation and local buckling of inner and outer steel tubes are ignored [26]
- (3) Shear force transferring of vertical stiffener joints is through vertical stiffener and anchorage web to the outer square and inner circular steel tubes, and concrete baroclinic force transmission mode [20] is considered because there is no inner diaphragm

**3.2. Outer Square Steel Tube.** The circumferential tensile stress of the steel tube wall has a weakening effect on the shear capacity of the joint, so it should be considered into the calculation of the shear capacity. As the confinement of square steel tube on the concrete is not uniform, concrete-filled square tubular column can be equivalent to concrete-filled circular tube column according to the principle of equal area [27]. The shear force-shear deformation skeleton curve of outer steel tube webs is taken as trilinear model of shear [28, 29] shown in Figure 3, where  $V_{oy}$ ,  $V_{ou}$ , respectively, represent the yield and ultimate shear stress of the outer steel tube web.

Figure 4 is the stress state of the outer steel tube web, where  $\sigma_{oz}$  is the compressive stress produced by the vertical steel tube web under the action of vertical axial compression,  $\sigma_{o\theta}$  is the lateral tensile stress of the outer steel tube web,  $\tau_o$  stands for the shear stress of the outer steel tube. In the following subscripts, the subscripts s and c represent steel and concrete, respectively; subscripts i and o represent inner and outer steel tube, respectively; and subscripts z, r, and  $\theta$  represent longitudinal, radial, and circumferential directions, respectively. It can be seen from Figure 4 that the stress state of outer steel tube web can be expressed as  $\sigma_x = \sigma_{o\theta}$ ,  $\sigma_y = \sigma_{oz}$ ,  $\tau_{xy} = \tau_o$ , so the principal stresses of the outer steel tube are

$$\begin{aligned}\sigma_1 &= \frac{\sigma_{oz} + \sigma_{o\theta}}{2} + \sqrt{\left(\frac{\sigma_{oz} - \sigma_{o\theta}}{2}\right)^2 + \tau_o^2}, \\ \sigma_2 &= 0, \\ \sigma_3 &= \frac{\sigma_{oz} + \sigma_{o\theta}}{2} - \sqrt{\left(\frac{\sigma_{oz} - \sigma_{o\theta}}{2}\right)^2 + \tau_o^2}.\end{aligned}\quad (2)$$

According to von Mises yield criterion, the yield stress of the outer steel tube is

$$f_{oy} = \sqrt{\frac{[(\sigma_1 - \sigma_2)^2 + (\sigma_2 - \sigma_3)^2 + (\sigma_3 - \sigma_1)^2]}{2}}, \quad (3)$$

where  $f_{oy}$  is the yield strength of the outer steel tube web. By substituting equation (2) into equation (3), we have

$$f_{oy} = \sqrt{\sigma_{oz}^2 + \sigma_{o\theta}^2 - \sigma_{oo}\sigma_{o\theta} + 3\tau_o^2}. \quad (4)$$

So, the shear stress of the outer steel tube under axial compression is

$$\tau_{oy} = \frac{1}{\sqrt{3}} \sqrt{f_{oy}^2 - \sigma_{oz}^2 - \sigma_{o\theta}^2 + \sigma_{oz}\sigma_{o\theta}}. \quad (5)$$

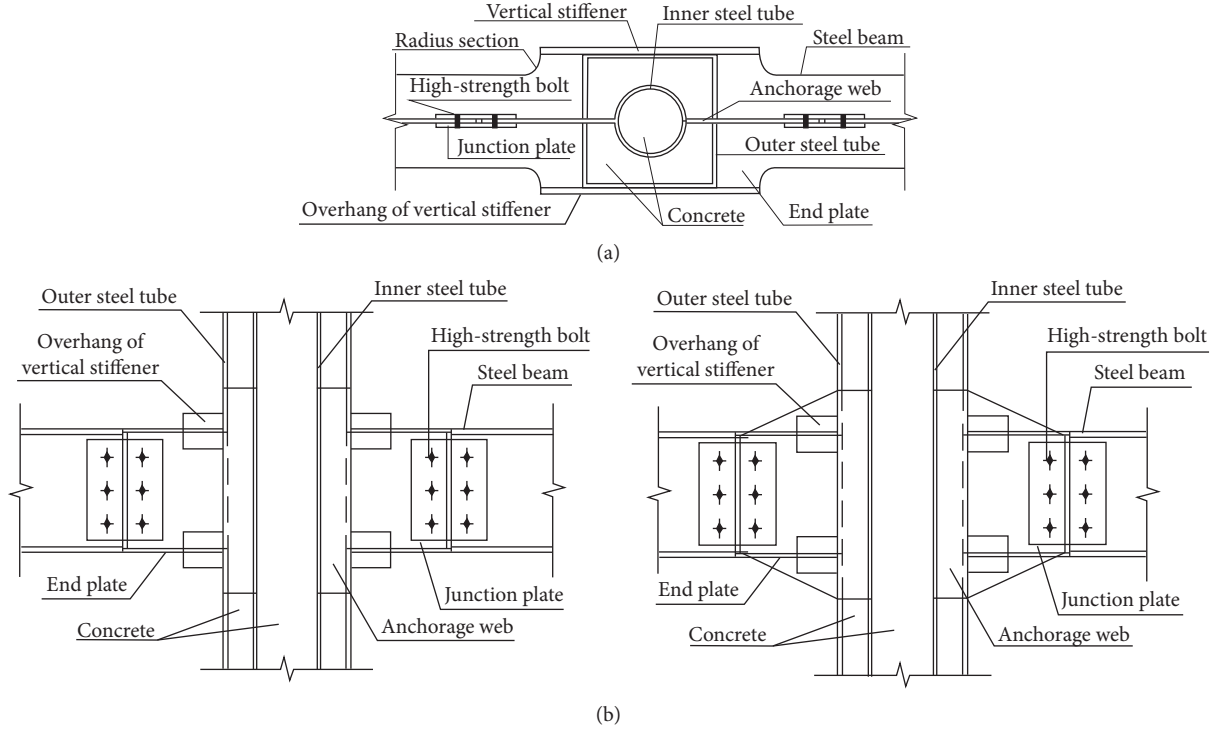


FIGURE 2: Details of vertical stiffener joints. (a) Transverse profile. (b) Longitudinal profile.

TABLE 2: Material properties of the steel.

Steel material	Square tube	Circle tube	End plate	Beam flange	Beam web
Average thickness (mm)	7.6	6.4	11.5	10.6	6.6
Yield strength (MPa)	338.12	323.08	272.61	272.41	291.00
Ultimate strength (MPa)	481.70	491.39	445.86	447.40	457.23
Elastic modulus ( $10^5$ MPa)	2.257	2.152	2.132	2.213	2.157

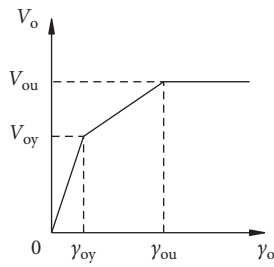


FIGURE 3: Trilinear shear force-deformation model.

Then, the yield shear resistance of the outer steel tube web is

$$V_{oy} = A_o \tau_{oy} = \frac{A_o}{\sqrt{3}} \sqrt{f_{oy}^2 - \sigma_{oz}^2 - \sigma_{o\theta}^2 + \sigma_{oz}\sigma_{o\theta}}, \quad (6)$$

where  $A_o$  represents the cross-sectional area of outer steel tube and  $V_{oy}$  represents the yield shear resistance of outer steel tube. The ultimate shear resistance of outer steel tube based on the trilinear shear model is

$$V_{ou} = \frac{A_o}{\sqrt{3}} \sqrt{f_{ou}^2 - \sigma_{oz}^2 - \sigma_{o\theta}^2 + \sigma_{oz}\sigma_{o\theta}}. \quad (7)$$

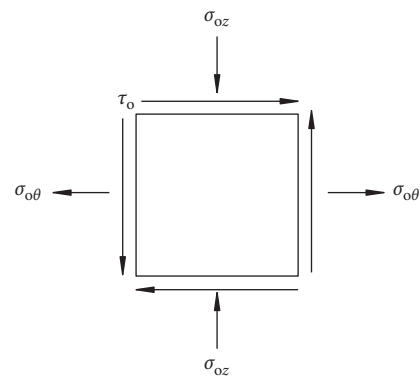


FIGURE 4: Stress state of steel plate of outer steel tube.

**3.3. Inner Circular Steel Tube.** Similar with the outer steel tube, the inner steel tube has the same stress state as shown in Figure 4. Its shear stress is  $\tau_{iy} = (1/\sqrt{3}) \sqrt{f_{iy}^2 - \sigma_{iz}^2 - \sigma_{i\theta}^2 + \sigma_{iz}\sigma_{i\theta}}$ ; the yield shear resistance of the inner circular steel tube is

$$V_{iy} = A_i \tau_{iy} = \frac{A_i}{\sqrt{3}} \sqrt{f_{iy}^2 - \sigma_{iz}^2 - \sigma_{i\theta}^2 + \sigma_{iz}\sigma_{i\theta}} \quad (8)$$

Then, the ultimate shear resistance of the inner circular steel tube is described as

$$V_{iu} = \frac{A_i}{\sqrt{3}} \sqrt{f_{iu}^2 - \sigma_{iz}^2 - \sigma_{i\theta}^2 + \sigma_{iz}\sigma_{i\theta}}, \quad (9)$$

where  $V_{iy}$  denotes the yield shear resistance of the inner circular steel tube and  $V_{iu}$  denotes the ultimate shear resistance of the inner circular steel tube. The shearing area of the inner circular steel tube is  $A_i$ . In literature [30],  $A_i = \pi R \times t_i$  was obtained when shear strength was analyzed by the method of elastic mechanics, where  $R$  is the radius of the inner circular tube. In this paper, the inner round steel tube is wrapped in the concrete of the CFDST column, so the shear capacity has been improved absolutely. Taking into account the simplified method of material mechanics, the projection area of round tube diameter is taken as shearing area, that is,  $A_i = 2 d \times t_i = 4R \times t_i$ , where  $d$  represents the diameter of the inner circular pipe and  $t_i$  represents the wall thickness of the inner circular steel tube.

**3.4. Vertical Stiffeners.** The vertical stiffeners are taken in pure shear stress state without considering the effect of axial stress since they are considered as main connecting part to the beam-column connections. Stress state of vertical stiffeners is  $\sigma_x = 0$ ,  $\sigma_y = 0$ ,  $\tau_{xy} = -\tau_v$ ; therefore, the principal stresses are  $\sigma_1 = \tau_v$ ;  $\sigma_2 = 0$ ;  $\sigma_3 = -\tau_v$ . According to von Mises yield criterion, the shear stress of the vertical stiffeners is obtained:  $\tau_{vy} = f_{vy}/\sqrt{3}$ , where  $f_{vy}$  is the yield strength of the vertical stiffeners. So, the yield shear resistance and the ultimate shear resistance of the vertical stiffener are listed, respectively, as follows:

$$V_{vy} = A_v \tau_{vy} = \frac{f_{vy} A_v}{\sqrt{3}}, \quad (10)$$

$$V_{vu} = \frac{f_{vu} A_v}{\sqrt{3}}, \quad (11)$$

where  $A_v$  is the horizontal cross-sectional area of the whole vertical stiffeners,  $f_{vu}$  is the ultimate strength of the vertical stiffeners,  $V_{vy}$  represents the yield shear resistance of the vertical stiffener, and  $V_{vu}$  represents the ultimate shear resistance of the vertical stiffener.

**3.5. Anchorage Web.** An anchored web is welded to the inner steel tube, and its extended part out of the outer steel tube is connected to the steel beam web. The yield shear stress of the anchored web is known from the foregoing conclusions as  $\tau_{ay} = f_{ay}/\sqrt{3}$ , where  $f_{ay}$  is the yield strength of the anchorage web, so yield shear resistance and ultimate shear resistance of the anchored web are, respectively, expressed as follows:

$$V_{ay} = A_a \tau_{ay} = \frac{f_{ay} A_a}{\sqrt{3}}, \quad (12)$$

$$V_{au} = \frac{f_{au} A_a}{\sqrt{3}}, \quad (13)$$

where  $A_a$  denotes shearing area of the anchorage web. The anchorage web has two types including ribbed and unribbed ones. For the unribbed anchorage web, shearing area is calculated as its horizontal cross-sectional area between inner and outer steel tubes, while for the ribbed anchorage web, shearing area is calculated as its full horizontal cross-sectional area.  $f_{au}$  is ultimate strength of the anchorage web.  $V_{ay}$  is yield shear resistance of the anchorage web, and  $V_{au}$  is ultimate shear resistance of the anchorage web.

**3.6. Outer and Inner Concrete.** The inner and outer concrete are constrained by steel tubes, and due to the presence of axial pressure, the core concrete is under three-dimensional compression state, so the shear strength of concrete can maintain a constant value without a decline when it reaches the ultimate shear strength. Therefore, the shear stress-strain curve of core concrete is simplified as the ascending and horizontal segments as shown in Figure 5.

The shear strength and shear deformation of concrete are studied in 1992 [31]. According to those experimental results, the ascending curve of shear stress-shear strain is obtained as follows:

$$\begin{aligned} y &= 0.8x^4 - 1.7x^3 + 1.9x, \\ x &= \frac{\gamma}{\gamma_p}, \\ y &= \frac{\tau}{\tau_p}, \end{aligned} \quad (14)$$

where  $\gamma_p$  and  $\tau_p$  represent the peak shear strain and stress, respectively,  $\tau_p = 0.42 f_{cu}^{0.55}$  and  $\gamma_p = (176.80 + 83.56\tau_p) \times 10^{-6}$ ; then, the shear resistance of inner and outer concrete is considered as

$$V_c = \tau (A_{co} + A_{ci}), \quad (15)$$

where  $A_{co}$  and  $A_{ci}$ , respectively, represent the cross-sectional area of outer and inner concrete.

#### 4. Test Results and Shear Storage Capacity

Figure 6 reveals beam end load ( $P$ ) versus displacement ( $\Delta$ ) envelope curves of the six joint specimens on west (W) and east (E) beam ends. For the convenience of presentation, the loading force is considered as positive when the actuators push and negative when the actuators pull, while the push displacement of the west end is considered as

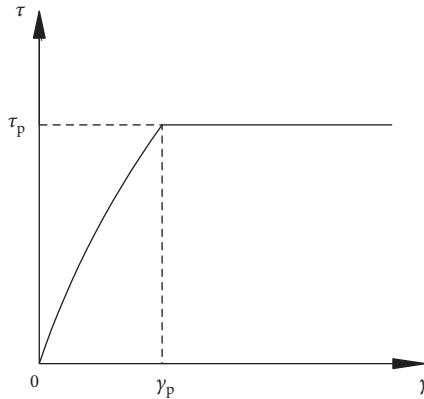


FIGURE 5: Shear stress-strain curve of the core concrete.

positive and the push displacement of the east end as negative. The yield load  $P_y$  of joints is determined according to Figure 7. The yield load and ultimate load in the test are taken as the average value of push and pull force on both west and east beam ends. Then, the corresponding magnitude of shear forces in the test can be obtained by equation (1). The shear force in the panel zone at the state of yield load and ultimate load in the test is listed in Table 1, where  $V_{yE}$  represents the shear force corresponding to the average yield load of east and west beams and  $V_{uE}$  represents the shear force corresponding to the average ultimate load of east and west beams.

The theoretical shear resistance of the vertical stiffener joints is calculated by the principle of superposition according to the limit equilibrium theory. Based on the aforementioned equations of the shear capacity of the joint components, the calculated shear capacity is listed in Table 1.  $V_{yC}$  is the calculated theoretical yield shear resistance obtained from Equations (6), (8), (10), (12), and (15);  $V_{uC}$  is the calculated theoretical ultimate shear resistance obtained from Equations (7), (9), (11), (13), and (15). In the calculations, ribbed anchorage web and vertical stiffener plate provide a large amount contribution to the joint's shear resistance. Therefore, the ribbed joints have greater shear capacity than unribbed ones, and shear resistance improves with the increase of overhang length of vertical stiffener. By comparison of specimens SBJ2-1 and SBJ3-2, the thickness of square steel tube has a slight influence on the joint's shear capacity. It can be concluded that the force-transferring connectors including vertical stiffeners and anchorage webs play a dominant role in the shear bearing capacity of the joint.

As can be seen in Table 1, compared with the experimental data of six joint specimens in the seismic performance test, the calculated results of yield shear resistance and ultimate shear resistance are much larger than the experimental shear force corresponding to the cracked vertical stiffener joint. It indicates that the joint has enough shear storage ability to avoid the shear failure of the panel zone. The main reason is that the vertical stiffener joints in the experiment belong to the “strong column and weak beam” type, so the failure modes of the specimens are

roughly the similar damage caused by the bending failure at beam ends. The plastic hinge occurred away from the curvature of the horizontal end plate in the test as shown in Figure 8. Strain measured in the test also showed the panel zone was in elastic state basically. So, the steel tubes, connectors (including anchorage web and vertical stiffeners), and core concrete worked in good mechanical performance to guarantee the strong shear capacity and stiffness, indicating that such joint design is in line with “strong shear and weak bending” principle of the seismic design.

In fact,  $V_{uC}$  is the calculated ultimate shear resistance for cracked vertical stiffener joints with shear failure, while  $V_{uE}$  is the shear force corresponding to the cracked experimental joints with bending failure, so the theoretical resistance proposed cannot be checked via full strength joints since the beam resistant bending moment is limiting the maximum shear strength. However, it indicates that the configuration of vertical stiffener joints can guarantee an effective rehabilitation strategy to strengthen such joints in order to avoid or delay their shear failure. This storage ability can be reflected by shear storage coefficient. The so-called shear storage coefficient is the ratio between the theoretical shear resistance and the actual shear force in experiments, which is described as

$$R_y = \frac{V_{yC}}{V_{yE}}, \quad (16)$$

$$R_u = \frac{V_{uC}}{V_{uE}}, \quad (17)$$

where  $R_y$  is the shear storage coefficient at the yield state and  $R_u$  is the shear storage coefficient at the ultimate load state. In fact, the shear storage coefficient in equations (16) and (17) is not a new concept of shear reserve. In the verification of seismic ability in some structure, the ratio of shear capacity and the actual shear force in earthquake must be greater than 1 [32, 33]. The paper puts forward this ratio for the vertical stiffener joint to quantify its shear safety reserves. Shear storage coefficient of the joint mainly takes the quantitative relationship between its shear bearing capacity and shear failure into account, so as to better evaluate the seismic design principle of strong joints and provide reference for the improvement of joint seismic design codes. The shear storage coefficient determines the safe storage capacity to ensure a proper failure progression and ductility of these joints, and increasing the shear storage coefficient can improve the seismic performance of the joint as well. The calculations of shear storage coefficient are shown in Table 1, where  $R_y$  is obtained as 2.02 at average and  $R_u$  is 2.47. The shear storage coefficient  $R_y$  and  $R_u$  of SBJ3-1 with the higher axial compression ratio is the smallest as shown in Table 1, so axial compression ratio can reduce the shear storage capacity of the joint. By comparison of specimens SBJ1-1, SBJ1-2, SBJ2-1, and SBJ2-2, it can also be concluded that lengthening the overhang of the vertical stiffener can increase the joint's shear storage capacity, while the influence of ribs is not evident.

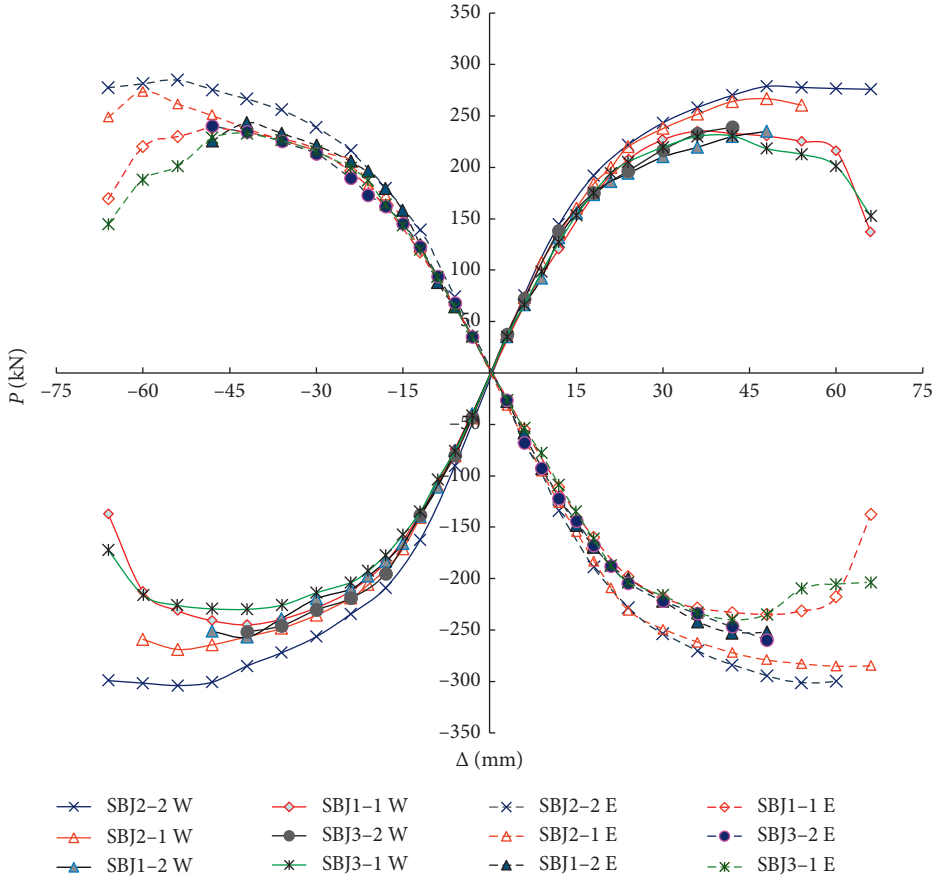
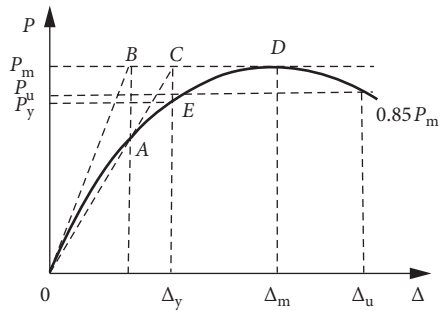
FIGURE 6: Skeleton curves of  $P$ - $\Delta$  on beam ends.

FIGURE 7: Determination for the yield load in test.

## 5. Conclusions

On the basis of the low cyclic loading test results of vertical stiffener joints between concrete-filled double steel tubular (CFDST) columns and steel beams, the shear storage capacity was analyzed in this paper. A conceptual model was presented for assessing the cracked vertical stiffener joint. The shear performance and force transfer mechanism were reasonably assumed. The model was entirely formulated in terms of equilibrium and stress-strain relationships and could be used to effectively assess the shear capacity of a series of components including steel tubes, vertical stiffener, anchorage web, and joint core concrete. The shear capacity

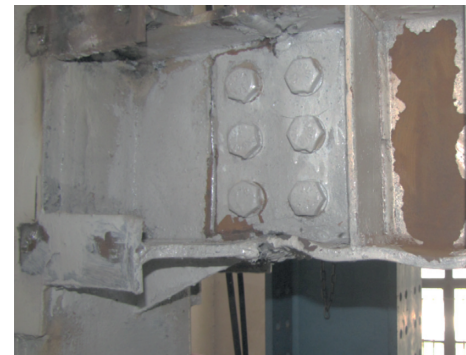


FIGURE 8: The failure mode in the test.

equation of the joints provided a simplified calculation method and corresponding reference for the engineering design of CFDST structure.

The yield and ultimate shear resistance of the vertical stiffener joints of CFDST were calculated and compared with the experimental results, and one new index of shear storage coefficient was put forward in order to quantitatively explain the safe reserve of ductile failure. Shear storage coefficient determined the safe storage capacity of the joint to avoid its shear failure mode, and improving the reserve coefficient can ensure proper failure progression and ductility. The results show that the ribbed joints have greater shear resistance than

unribbed ones, while the influence on shear storage capacity is not evident; lengthening the overhang of the vertical stiffener can increase both the shear resistance and joint's shear storage capacity; axial compression ratio can reduce the joint's shear storage capacity. Therefore, the vertical stiffener joint has enough safety storage to meet the seismic design principle of "strong shear and weak bending."

## Data Availability

The data used to support the findings of this study are available from the corresponding author upon request.

## Conflicts of Interest

The authors declare that there are no conflicts of interest regarding the publication of this article.

## Acknowledgments

The authors would like to acknowledge the support provided by the Chinese National Science Foundation (grant no. 51478004). The financial support from Hebei University of Technology is also appreciated.

## References

- [1] S. H. Cai, *Modern Steel Tube Concrete Structure*, People's Communications Press, Beijing, China, 2003, in Chinese.
- [2] Y.-F. Zhang and Z.-Q. Zhang, "Study on equivalent confinement coefficient of composite CFST column based on unified theory," *Mechanics of Advanced Materials and Structures*, vol. 23, no. 1, pp. 22–27, 2015.
- [3] G. Du, A. Andjelic, Z. Li, Z. Lei, and X. Bie, "Residual axial bearing capacity of concrete-filled circular steel tubular columns (CFCSTCs) after transverse impact," *Applied Sciences*, vol. 8, no. 5, p. 793, 2018.
- [4] D. F. Zhang, J. H. Zhao, Y. F. Zhang et al., "Finite element analysis of seismic performance of composite concrete-filled steel tube column-steel beam connection," *World Earthquake Engineering*, vol. 29, no. 1, pp. 49–59, 2013, in Chinese.
- [5] Y. F. Zhang and Z. Q. Zhang, "Connection design of concrete-filled twin steel tubes column," in *Proceedings of 2014 Structural and Civil Engineering Workshop (SCEW 2014)*, pp. 365–370, Tokyo, Japan, November 2014.
- [6] Y. F. Zhang and D. F. Zhang, "Experimental study on the seismic behaviour of the connection between concrete-filled twin steel tubes column and steel beam," *European Journal of Environmental and Civil Engineering*, vol. 19, no. 3, pp. 347–365, 2014.
- [7] B. D. Koester, "Panel zone behavior of moment connections between rectangular concrete-filled steel tubes and wide flange beams," Ph.D. dissertation, University of Texas, Austin, Texas, USA, 2000.
- [8] L. Jian, "Shear strength of connections between concrete filled steel tubes and beams," *Applied Mechanics and Materials*, vol. 351–352, pp. 75–79, 2013.
- [9] L. Kang, R. T. Leon, X. Lu, and X. L. Lu, "Shear strength analyses of internal diaphragm connections to CFT columns," *Steel and Composite Structures*, vol. 18, no. 5, pp. 1083–1101, 2015.
- [10] G. Parra-Montesinos and J. K. Wight, "Modeling shear behavior of hybrid RCS beam-column connections," *Journal of Structural Engineering*, vol. 127, no. 1, pp. 3–11, 2001.
- [11] M. H. Jones and Y. C. Wang, "Experimental studies and numerical analysis of the shear behavior of fin plates to tubular columns at ambient and elevated temperatures," *Steel and Composite Structures*, vol. 8, no. 3, pp. 179–200, 2008.
- [12] W. Zhang, Z. Chen, Q. Xiong, and T. Zhou, "Calculation method of shear strength of vertical stiffener connections to L-CFST columns," *Advances in Structural Engineering*, vol. 21, no. 6, pp. 795–808, 2017.
- [13] A. Soler, A. Barroso, and V. Mantić, "Failure initiation criterion in bonded joints with composites based on singularity parameters and practical procedure for design purposes," *Composite Interfaces*, vol. 22, no. 8, pp. 743–755, 2015.
- [14] H. París, S. Z. Li, and Z. Li, "Shear behavior of composite frame inner joints of SRRC column-steel beam subjected to cyclic loading," *Steel and Composite Structures*, vol. 27, no. 4, pp. 495–508, 2018.
- [15] A. P. Ramos, V. J. G. Lúcio, and D. M. V. Faria, "The effect of the vertical component of prestress forces on the punching strength of flat slabs," *Engineering Structures*, vol. 76, pp. 90–98, 2014.
- [16] A. Oinonen and G. Marquis, "Shear damage simulation of adhesive reinforced bolted lap-connection interfaces," *Engineering Fracture Mechanics*, vol. 109, pp. 341–352, 2013.
- [17] C.-C. Chen, B. Suswanto, and Y.-J. Lin, "Behavior and strength of steel reinforced concrete beam-column joints with single-side force inputs," *Journal of Constructional Steel Research*, vol. 65, pp. 1569–1581, 2009.
- [18] C.-C. Chen and K.-T. Lin, "Behavior and strength of steel reinforced concrete beam-column joints with two-side force inputs," *Journal of Constructional Steel Research*, vol. 65, pp. 641–649, 2009.
- [19] T. Wu, X. Liu, D. Y. Li, G. H. Xing, and B. Q. Liu, "Study on the shear strength of interior joints of reinforced concrete frames based on the Bayesian theory," *Engineering Mechanics*, vol. 32, no. 3, pp. 167–174, 2015.
- [20] J. G. Nie and G. G. Xu, "Shear stress analysis of concrete filled square steel tubular joints," *Journal of Tsinghua University*, vol. 49, no. 6, pp. 782–786, 2009, in Chinese.
- [21] C. Amadio, C. Bedon, M. Fasan, and M. R. Pecce, "Refined numerical modelling for the structural assessment of steel-concrete composite beam-to-column joints under seismic loads," *Engineering Structures*, vol. 138, no. 5, pp. 394–409, 2017.
- [22] L. Xiao, X. Z. Li, and Z. G. John Ma, "Behavior of perforated shear connectors in steel-concrete composite joints of hybrid bridges," *Journal of Bridge Engineering*, vol. 22, no. 4, article 04016135, 2017.
- [23] N. E. Shanmugam, C. H. Yu, J. Y. R. Liew, and T. H. Teo, "Modelling of steel-concrete composite joints," *Journal of Constructional Steel Research*, vol. 46, no. 1–3, pp. 247–249, 1998.
- [24] ATC-24, *Guidelines for Cyclic Seismic Testing of Components of Steel Structures*, Applied Technology Council, Redwood City, CA, USA, 1992.
- [25] Architectural Institute of Japan (AIJ), *AIJ Standard for Structural Calculation of Steel Reinforced Concrete Structures*, AIJ, Tokyo, Japan, 1987.
- [26] M. Pop, O. Corbu, and P. Pernes, "Steel-concrete materials performance in composite joints configuration," *IOP Conference Series: Materials Science and Engineering*, vol. 209, no. 1, article 012103, 2017.

- [27] Y. F. Zhang, J. H. Zhao, and W. F. Yuan, "Study on compressive bearing capacity of concrete filled square steel tube column reinforced by circular steel tube inside," *Journal of Civil Engineering and Management*, vol. 19, no. 6, pp. 787–795, 2013.
- [28] I. Nishiyama, T. Fujimoto, T. Fukumoto, and K. Yoshioka, "Inelastic force-deformation response of joint shear panels in beam-column moment connections to concrete-filled tubes," *Journal of Structural Engineering*, vol. 130, no. 2, pp. 244–252, 2004.
- [29] T. Fukumoto and K. Morita, "Elastoplastic behavior of panel zone in steel beam-to-concrete filled steel tube column (CFT) column connections," in *Proceedings of the 6th ASCCS Conference Vol. 1: Composite and Hybrid Structures, Los Angeles*, pp. 565–572, CA, USA, March 2000.
- [30] D. X. Zhang and S. M. Zhang, "Shear strength of concrete filled steel tubular column and beam joint," *Journal of Harbin University of Civil Engineering and Architecture*, vol. 34, no. 3, pp. 35–39, 2001, in Chinese.
- [31] Q. Zhang and Z. H. Guo, "Study on shear strength and shear deformation of concrete," *Journal of Building Structures*, vol. 13, no. 5, pp. 17–24, 1992, in Chinese.
- [32] S. C. Zhao, Y. H. Liu, J. A. Kou et al., "Preliminary research on seismic capacity reserve for ductile and brittle structures," *Journal of Southwest Jiaotong University*, vol. 44, no. 3, pp. 327–335, 2009, in Chinese.
- [33] B. R. Ding, "Analysis of typical seismic damage of two categories of structures," Master's Degree Thesis, Institute of Engineering Mechanics, China Earthquake Administration, Harbin, China, 2011.

## Research Article

# Generation of Uniform Hazard Spectrum Based on the Stochastic Method of Simulating Ground Motion and Its Use in Nuclear Power Plants

Xueming Zhang ,<sup>1</sup> Weiming Yan,<sup>1</sup> Haoxiang He ,<sup>1</sup> Yunlun Sun,<sup>2</sup> and Shicai Chen <sup>1</sup>

<sup>1</sup>Beijing Key Laboratory of Earthquake Engineering and Structural Retrofit, Beijing University of Technology, Beijing 100124, China

<sup>2</sup>Chinergy Co., Ltd., Beijing 100193, China

Correspondence should be addressed to Haoxiang He; hhx7856@163.com

Received 26 September 2018; Accepted 19 November 2018; Published 20 December 2018

Guest Editor: Filipe Santos

Copyright © 2018 Xueming Zhang et al. This is an open access article distributed under the Creative Commons Attribution License, which permits unrestricted use, distribution, and reproduction in any medium, provided the original work is properly cited.

To obtain an accurate uniform hazard spectrum (UHS), this paper proposes combining a stochastic simulation with probabilistic seismic hazard analysis. The stochastic method fully accounts for the effect of the source mechanism, path, and site effect. Historical ground motions in the site specific to the nuclear power plant (NPP) are simulated, and a UHS with an equal exceeding probability is proposed. To compare the seismic performance of the NPP under different ground motions generated by the existing site spectrum (SL-2), the UHS generated by the safety evaluation report, and the US RG1.60 spectrum, respectively, a three-dimensional finite element model is established, and dynamic analysis is performed. Results show that the structural responses to different spectra varied; the UHS response was slightly larger than that of RG1.60. This finding is relatively more reasonable than prior research results. The UHS generated using the stochastic simulation method can provide a reference for the seismic design of NPPs.

## 1. Introduction

In recent years, nuclear power plant (NPP) construction in China entered a stage of mass development. By the end of 2016, China was operating 14 NPPs, and 27 are scheduled to be built. However, given the large-scale construction and operation of NPPs, associated safety problems have become prominent. Once an accident occurs in an NPP, the core can melt and radioactive substances can leak out, causing potentially disastrous consequences. To ensure the NPP safety, various sudden disasters (e.g., tsunamis, earthquakes, debris flows, landslides, and aircraft crashes) are considered possibilities during operation, with earthquakes being the most probable one. The Fukushima nuclear accident and its catastrophic consequences raised global awareness of the gravity of seismic safety problems in NPPs. Strong earthquakes occur frequently in China and can lead to secondary

disasters. Therefore, improving the safety of NPPs and ensuring their seismic performance is very important.

The aseismic design spectrum is the foundation of the design of NPPs and associated facilities. Throughout the last few decades, the United States Regulatory Guide 1.60 (RG1.60) spectrum [1] was used in the seismic design of NPPs, but the RG1.60 spectrum contains no site-specific conditions. Therefore, probabilistic seismic hazard analysis (PSHA) with such conditions has attracted increasing attention. PSHA is a methodology used to estimate the probability of various extents of earthquake-cause ground motion being exceeded at a given location in the future [2]. The main goal of PSHA is to provide a design response spectrum for structural analysis. This generated spectrum is called the uniform hazard spectrum (UHS) because every ordinate has an equal exceeding probability. United States Regulatory Guide 1.208 [3] provides a method to obtain the

UHS, the purpose of which is to provide guidance for the establishment of a site-specific ground motion response spectrum. Choi et al. [4] developed the UHS using available seismic hazard data for four Korean NPP sites. Desai and Choudhury [5] analysed site-specific seismic hazards and one-dimensional equivalent linear ground responses of important sites in Mumbai, and a designed UHS with 5% damping was obtained from the PSHA at each site.

However, many countries such as China do not maintain sufficient strong motion and seismological information; most strong earthquake data in historical records are simply described narratively. Thus, seismic hazard curves remain highly uncertain. For major projects such as NPPs and projects in which serious secondary disasters may occur, earthquake-safe requirements should be determined based on the results of an earthquake safety evaluation report (SER). Current Chinese NPP earthquake safety assessments are based on the maximum construction method, maximum historical earthquake method, and integrated probability method for response spectrum design. The response spectrum obtained by SER is called the SL-2 spectrum, but this spectrum does not represent the same exceeding probability over the entire frequency range of interest. Additionally, the UHS obtained from the probability method only accounts for the attenuation of bedrock ground motion. Hence, a new method should be applied to generate a new spectrum that fully considers factors such as the source mechanism, path, and site effect.

The stochastic method has mainly been used to compute ground motion at frequencies of engineering interest [6]. Since its introduction by Hanks and McGuire [7] and subsequent enhancements by Boore [8], the method has been extended to analyse stochastic finite-fault effects [9, 10] and equivalent linear site response [11, 12]. These applications rely on point-source formulation in the stochastic method, which has changed little in the last few years. In this paper, a method of simulating ground motion using the stochastic method to determine UHS is proposed. To analyse reaction characteristics, a high-temperature gas-cooled reactor plant is selected, and a three-dimensional finite element model of the NPP is established to analyse the dynamic response of the NPP under UHS excitation. The NPP is approximately 23 kilometers south of Rongcheng City, 14 kilometers northwest of Shidao, and 68 kilometers southeast of Weihai City, Shandong Province, China, as shown in Figure 1.

## 2. Generation of Regional Historical Ground Motion

In this study, the stochastic method was used to simulate ground motion [13]. The point-source stochastic model, implemented with the software package Stochastic-Method SIMulation (SMSIM) [14], was used to generate regional historical ground motion. By separating the spectrum of ground motion into source, path, and site components, models based on the stochastic method can be easily modified to account for specific situations.



FIGURE 1: NPP location.

**2.1. Source.** The simplest and most commonly used source is the classic single-corner-frequency model [15]. The Fourier acceleration amplitude spectrum (abbreviated here as  $A$ ) is given by

$$A \propto \frac{M_0 f^2}{1 + (f/f_c)^2}, \quad (1)$$

where  $M_0$  is the seismic moment and  $f_c$  is the corner frequency [13]. The high-frequency level  $A_{HF}$  is given by

$$A_{HF} \propto M_0 f_c^2. \quad (2)$$

The corner frequency is related to seismic moment  $M_0$  and stress drop  $\Delta\sigma$ , with the corresponding formula given by

$$f_c = 4.906 \times 10^6 \beta \left( \frac{\Delta\sigma}{M_0} \right)^{1/3}, \quad (3)$$

where  $\beta$  is the shear-wave velocity in the source vicinity.

This paper uses the generalized additive double-corner-frequency (ADCF) model [16] in which the acceleration source spectrum is proportional to

$$A \propto \frac{M_0 f^2 (1 - \varepsilon)}{\left[ 1 + (f/f_a)^{pf_a} \right]^{pd_a}} + \frac{M_0 f^2 \varepsilon}{\left[ 1 + (f/f_a)^{pf_a} \right]^{pd_a}}, \quad (4)$$

where  $f_a$  and  $f_b$  are the double-corner frequencies;  $\varepsilon$  is the weighting parameter; and  $pf$  and  $pd$  denote the frequency power and denominator power, respectively. The subscripts a and b refer to quantities appearing in the two parts of the double-corner-frequency source model. For high frequencies ( $f \gg f_a$  and  $f \gg f_b$ ), the formula becomes

$$A_{HF} \propto \left( \frac{M_0 f^2}{f^{pf_a \times pd_a}} \right) (1 - \varepsilon) f_a^{pf_a \times pd_a} + \left( \frac{M_0 f^2}{f^{pf_b \times pd_b}} \right) \varepsilon f_b^{pf_b \times pd_b}. \quad (5)$$

The constancy of the high-frequency acceleration spectral level requires that the following constraint be satisfied:

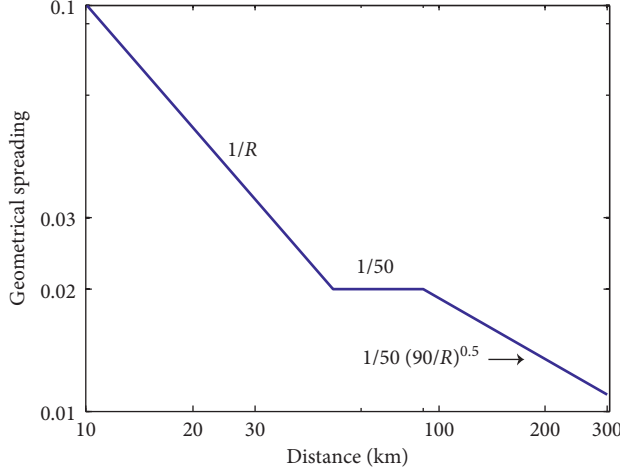


FIGURE 2: Geometrical spreading function.

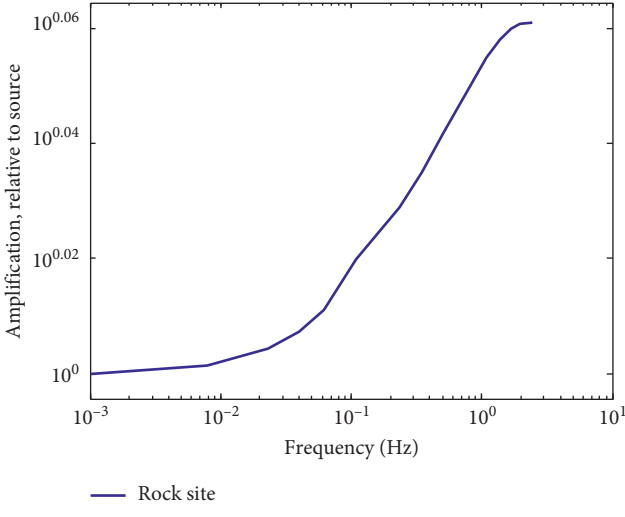


FIGURE 3: Amplification vs. frequency.

$$pf_a \cdot fd_a = pf_b \cdot pd_b = 2. \quad (6)$$

The high-frequency level is

$$A_{HF} \propto M_0 (1 - \varepsilon) f_a^2 + M_0 \varepsilon f_b^2. \quad (7)$$

Atkinson and Silva's [17] correlation between  $f_a$  and  $M$  is used in this paper.  $pf_a = pf_b = 2.0$  and  $pd_a = pd_b = 1$  are from the study of Boore et al. [16]. According to observational data from Shandong [18], the density and shear-wave velocity at the source were  $2.7 \text{ g/cm}^3$  and  $3.2 \text{ km/s}$ , respectively.

**2.2. Path Effect.** The simplified path effect  $P$  is given by the multiplication of the geometrical spreading and  $Q$  functions,

$$P(R, f) = Z(R) \exp \left[ \frac{-\pi f R}{Q(f) c_Q} \right], \quad (8)$$

where  $c_Q$  is the seismic velocity, and the geometrical spreading function  $Z(R)$  is given by a piecewise continuous three-segment straight line as follows:

$$Z(R) = \begin{cases} \frac{R_0}{R}, & R \leq R_1, \\ Z(R_1) \left( \frac{R_1}{R} \right)^{p_1}, & R_1 \leq R \leq R_2, \\ Z(R_2) \left( \frac{R_2}{R} \right)^{p_2}, & R_2 \leq R, \end{cases} \quad (9)$$

where  $R$  is the closest distance to the rupture surface. Based on the crust thickness in Shandong and references in the literature from the Shandong Seismic Network [19],  $R_0 = 1$ ,  $R_1 = 50$ ,  $R_2 = 90$ ,  $p_1 = 0.0$ , and  $p_2 = 0.5$ , as shown in Figure 2.

The NPP is at the bedrock site; therefore, the quality factor  $Q$  can be obtained using the rock site in eastern North America [20].

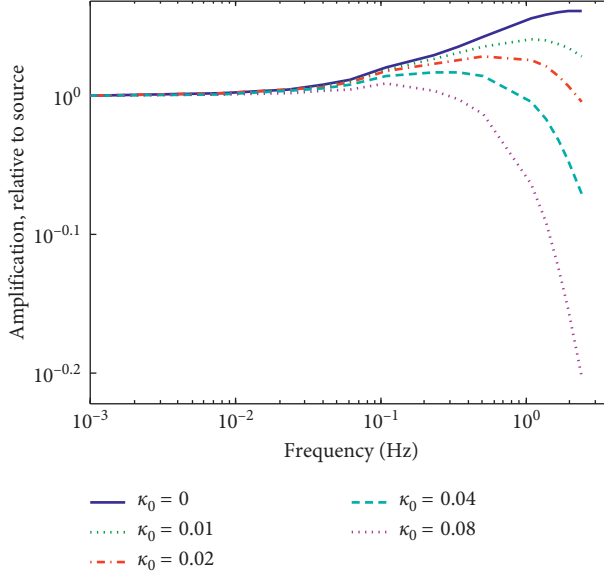


FIGURE 4: Site amplification combined effect of path-independent diminution.

TABLE 1: Historical earthquake records near the NPP site ( $M_s \geq 4.7$ ; \* represents lack of information).

No.	Earthquake time Year-month-day	Epicenter location		Magnitude	Distance (km)	Accuracy
		Longitude	Latitude			
1	BC70.06.01	36.3	119.2	7	306.46	4
2	495.04.01	37.6	120.9	5.25	160.25	5
3	1046.04.24	36.9	121.4	5	100.6341	4
4	1346.03	37.5	119.5	5	274.6924	5
5	1408.02.28	37.6	121.1	4.75	144.5236	4
6	1409.02.13	37.6	121.1	4.75	144.5236	4
7	1506.09.07	36.3	120.7	4.75	179.5199	1
8	1509.04.21	35.4	119.7	4.75	308.3935	3
9	1517.10.01	37.6	119.2	5.5	302.8976	4
10	1543.05.08	35.2	118.5	5	412.4283	3
11	1548.09.22	38.0	120.7	7	197.9331	5
12	1584.03	37.5	119.2	5	300.7126	3
13	1588.07.02	37.5	118.5	5	361.7426	5
14	1597.10.06	38.5	120.0	7	280.1267	5
15	1597.12	37.7	121.6	5.25	115.4321	4
16	1598.02.13	37.4	121.3	5.75	118.8754	3
17	1621.11.22	37.9	121.2	5.25	156.405	4
18	1642.08.11	37.2	120.6	4.75	173.0536	4
19	1668.07.26	36.4	119.2	6.75	303.7531	3
20	1668.08.24	36.5	118.5	5.75	363.078	—
21	1672.06.17	35.6	118.8	6	367.6132	*
22	1686.01.18	37.7	121.8	4.75	103.5937	4
23	1687.11.20	37.6	121.5	4.75	114.8229	4
24	1736.12.25	37.8	121.6	5	123.4755	4
25	1796.03	36.0	119.4	5	300.0419	3
26	1829.11.19	36.6	118.5	6.25	361.4066	2
27	1852.11.17	36.0	118.8	5	350.6615	3
28	1854.06.04	36.3	118.7	4.75	349.9403	3
29	1888.06.13	38.5	119.0	7.5	354.0953	4
30	1910.01.08	35.0	122.0	6.75	224.4953	5
31	1910.01.09	35.0	122.0	4.9	224.4953	2
32	1924.02.19	35.0	120.0	5	316.16	*
33	1932.08.22	36.1	121.6	6.3	127.6046	2

TABLE 1: Continued.

No.	Earthquake time Year-month-day	Epicenter location		Magnitude	Distance (km)	Accuracy
		Longitude	Latitude			
34	1939.01.08	37.1	121.6	5.2	83.661	*
35	1948.05.23	37.6	121.9	6	89.3951	4
36	1969.07.18	38.2	119.4	7.4	307.9253	2
37	1969.07.18	38.1	119.3	4.8	311.368	3
38	1969.07.18	38.1	119.3	4.9	311.368	2
39	1969.07.18	38.0	119.0	5.1	331.954	2
40	1969.07.19	38.2	119.4	4.7	307.9253	2
41	1992.01.23	35.3	121.13	5.2	224.464	1
42	1992.11.04	35.33	123.33	4.7	196.3993	1
43	2002.07.23	35.53	122.21	4.8	184.8908	3

2.3. Site. The site and path effect are each considered. The amplification and attenuation can be conveniently separated as follows:

$$S(f) = A(f) \cdot D(f), \quad (10)$$

where the amplification function  $A(f)$  is usually relative to the source and the diminution function  $D(f)$  is used to model the path-independent loss of energy. Applications must specify reference conditions for the  $A$  and  $D$  functions. The square-root-impedance approach [21] is applied to the crustal amplification function in this case, as presented in Figure 3.

The attenuation operator  $D(f)$  in equation (10) accounts for the path-independent loss of high frequency in ground motion. Two filters are commonly applied that involve the  $f_{\max}$  filter [8]

$$D(f) = \left[ 1 + \left( \frac{f}{f_{\max}} \right)^8 \right]^{-1/2}, \quad (11)$$

and the  $\kappa_0$  filter [22]

$$D(f) = \exp(-\pi\kappa_0 f). \quad (12)$$

The  $\kappa_0$  filter is applied in this paper. The combined effect of amplification and attenuation for a series of diminution parameters  $\kappa_0$  is displayed in Figure 4 for the hard rock site.

2.4. Generation of Regional Historical Ground Motion. A total of 43 earthquakes of  $M_s \geq 4.7$  were recorded in the NPP site region from 70 BC to May 2006 (Table 1), in which five were 7.0–7.9 earthquakes; six were 6.0–6.9 earthquakes; 17 were 5.0–5.9 earthquakes; and 15 were 4.7–4.9 earthquakes. The distribution of earthquakes is shown in Figure 5. The 17<sup>th</sup> earthquake record, with a magnitude of 5.25 and distance of 156 km, was selected as an example.

SMSIM was used to obtain typical time-series earthquake data (Figure 6) and the pseudoabsolute response spectral acceleration (PSA) of all historical regional ground motion. Assuming all sources involve a point-source model, the 5% damped PSA of all earthquakes is shown in Figure 7.

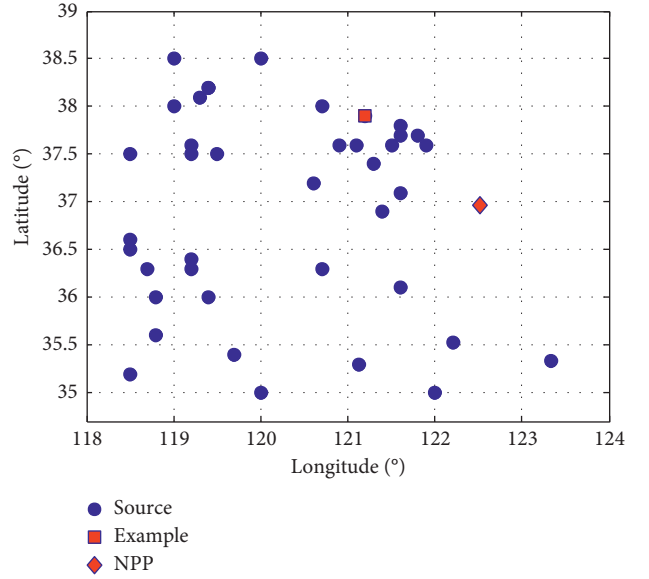


FIGURE 5: Earthquake distribution (regional scope: 118.5°–124° east longitude and 35.0°–38.5° north latitude; time range: 70 BC–May 2006; magnitude range:  $M_s \geq 4.7$ ).

### 3. UHS Generation

The natural logarithm of PSA appeared normally distributed for each period; as such, the probability of exceeding any PSA level can be computed using knowledge of the mean ln PSA and standard deviation  $\sigma_{\ln \text{PSA}}$ :

$$P(\text{PSA} > x) = 1 - \Phi\left(\frac{\ln x - \bar{\ln \text{PSA}}}{\sigma_{\ln \text{PSA}}}\right), \quad (13)$$

where  $\Phi()$  is the standard normal cumulative distribution function. Two thousand years of earthquake records were counted; hence, the return period of every earthquake was equal to 2000. The annual rate of recurrence was  $1/2000 = 0.0005$ . The annual rate of exceedance in each period was calculated by combining the probability of exceedance and recurrence. Figure 8 shows the hazard curve at individual periods of 0.2 s and 1 s, after which an annual rate exceeding  $10^{-4}$  was selected. The UHS with a  $10^{-4}$  exceedance rate for the NPP site was plotted by combining the PSAs from all periods, as depicted in Figure 9.

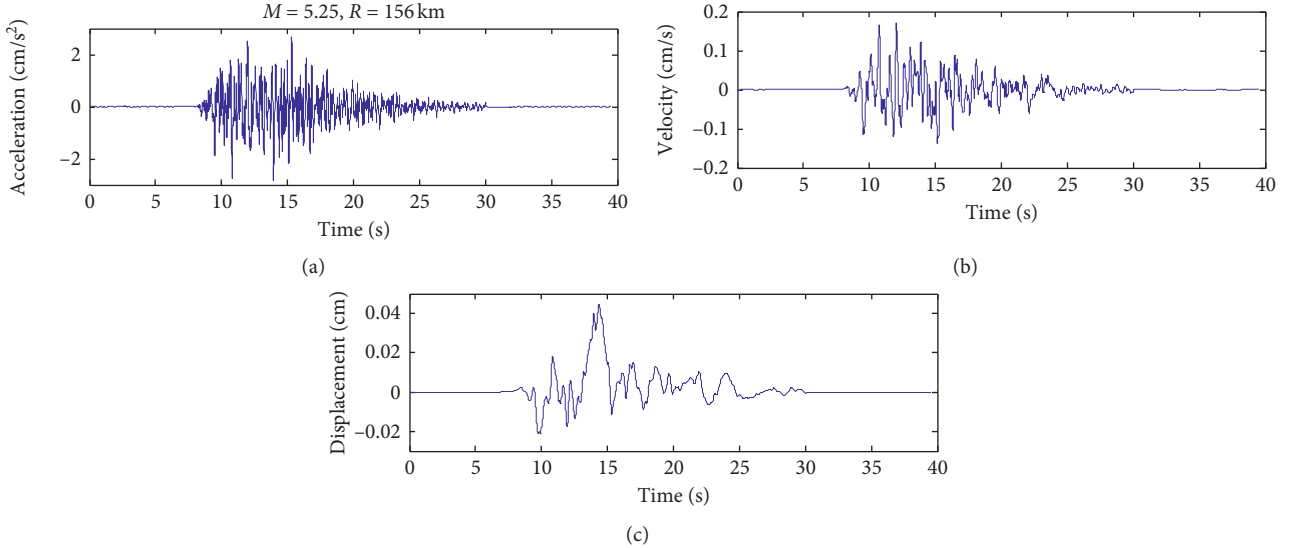
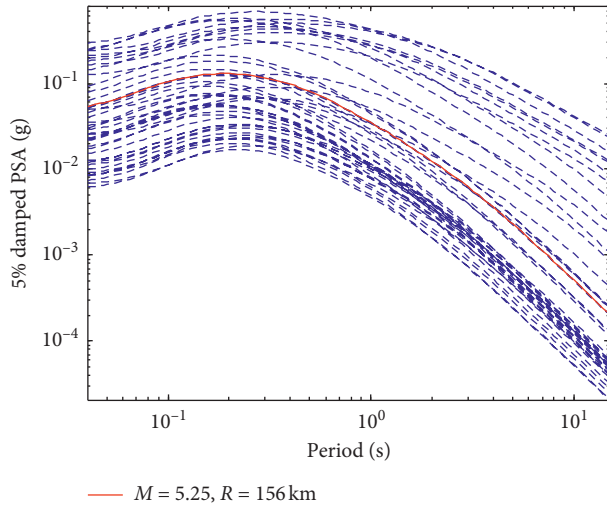


FIGURE 6: Time series for the example.

FIGURE 7: PSA for all point sources ( $M_s \geq 4.7$ ; from 70 BC to May 2006).

The UHS (obtained from the SER generated using the probability method), SL-2 spectrum (from SER, enveloped by the probabilistic and deterministic methods at a zero-period acceleration of 0.12 g), and RG1.60 spectrum (zero-period acceleration equal to SL-2 spectrum) were compared with the UHS generated by the stochastic method (hereafter referred to as the new UHS; Figure 10). The RG1.60 spectrum was largest before 0.15 s, and the SL-2 spectrum was largest at 0.16 s only. After 0.16 s, the SL-2 spectrum began to exhibit a downward trend with an amplitude below that of the RG1.60 spectrum and UHS. The amplitude of UHS was larger than that of RG1.60, except at 0.4 s.

#### 4. Finite Element Model Analysis of NPP

**4.1. Establishment and Calculation of FEM.** To verify the dynamic response of UHS for the NPP, FEM was established

in SAP2000. The base elevation was -15.55 m, the roof elevation of the reactor building was 44.1 m, and there were eight floors in total. The roof elevation of the spent fuel plant and auxiliary plant was 36.08 and 21.6 m, respectively. The layout is depicted in Figure 11. The main components of the plant were shear walls and floors that were quite thick. A thick shell element was therefore adopted to simulate the linear state of the NPP. According to the response spectrum in Figure 9, the artificial acceleration time-history curves of each response spectrum were generated, as shown in Figure 12. Two-directional horizontal earthquakes were used as dynamic excitations in the NPP.

**4.2. Result Analysis.** The simulation results indicate that the natural period of NPP was 0.22 s. Due to space limitations, this paper only analyses the results in the X direction. Figure 13 presents the interlayer drift angle of

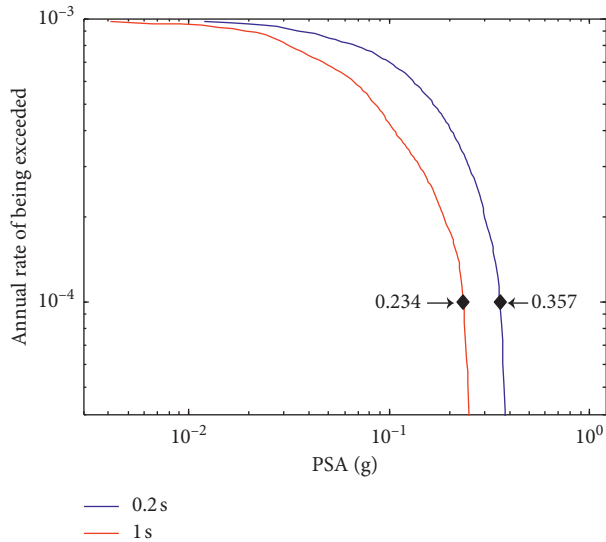


FIGURE 8: Hazard curves at 0.2 s and 1 s.

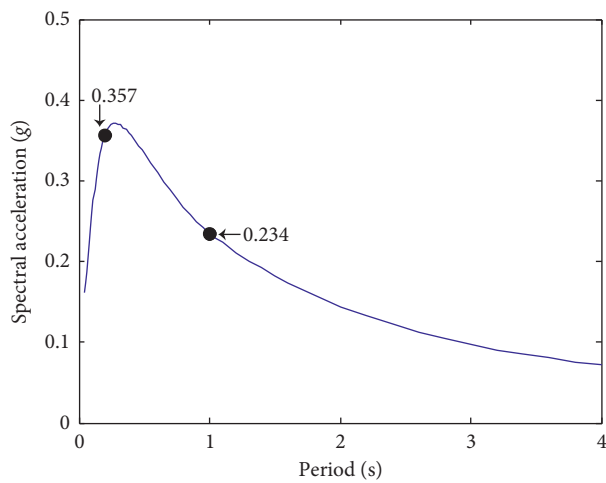
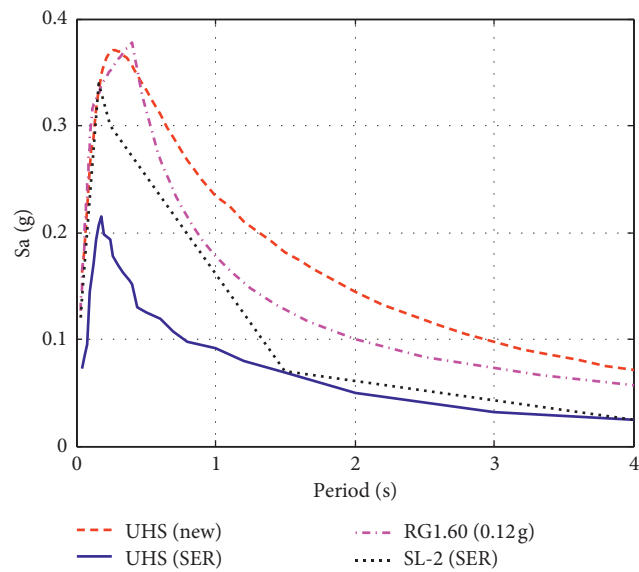
FIGURE 9: UHS.  $1 \times 10^{-4}$  rate of exceedance.

FIGURE 10: Comparison of the new UHS with other spectra.

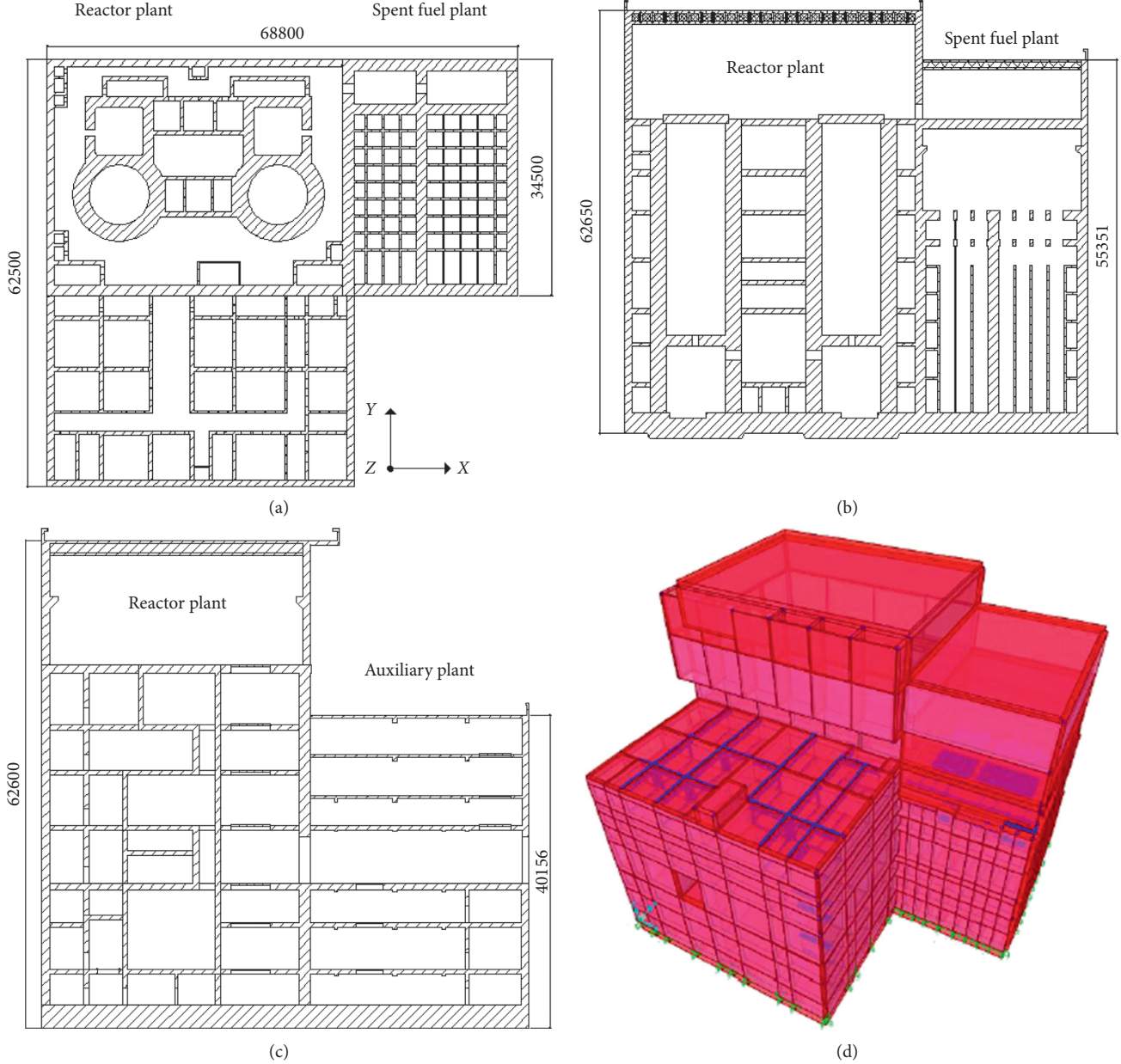


FIGURE 11: NPP layout. (a) Plan graph. (b) Reactor and spent fuel direction profile. (c) Reactor and auxiliary direction profile. (d) 3D FEM.

the NPP at different heights. The height of the maximum interlayer drift angle varied for seismic waves generated by different response spectra. The maximum of RG1.60 was in the third layer, whereas others were in the 6<sup>th</sup> layer. The angles of the 1<sup>st</sup> to 3<sup>rd</sup> layers increased gradually and reduced in the 4<sup>th</sup> layer; a clear inflection occurred in the 3<sup>rd</sup> layer. The angle demonstrated a slight increase from the 5<sup>th</sup> to 6<sup>th</sup> layer, and the 6<sup>th</sup> layer to the top declined gradually. The UHS (SER) angle was smallest. The SL-2 angle was less than that of new UHS and RG1.60. The new UHS and RG1.60 angles were close, but the new UHS angle was larger at the top; the amplitude of the two response spectra was quite small for the natural vibration period, and the NPP response was therefore similar in each.

Figure 14 presents the peak displacement at different elevations. The peak increased along with the elevation. At the same height, the maximum displacement was the peak of the new UHS. Comparing the elevation at 44.1 m, the peak of the new UHS was 5.19 mm, and the peak value of RG1.60 was close to that of SL-2.

Figures 15 and 16 depict the interlayer shear force and bending moment, respectively. The shear force showed a minor change within the first three layers and then decreased from the 3<sup>rd</sup> layer to the top. The bending moment declined from the bottom to the top, but a slight inflection point appeared in the 5<sup>th</sup> layer. The force and moment values of UHS and RG1.60 were close and larger than that those of SL-2.

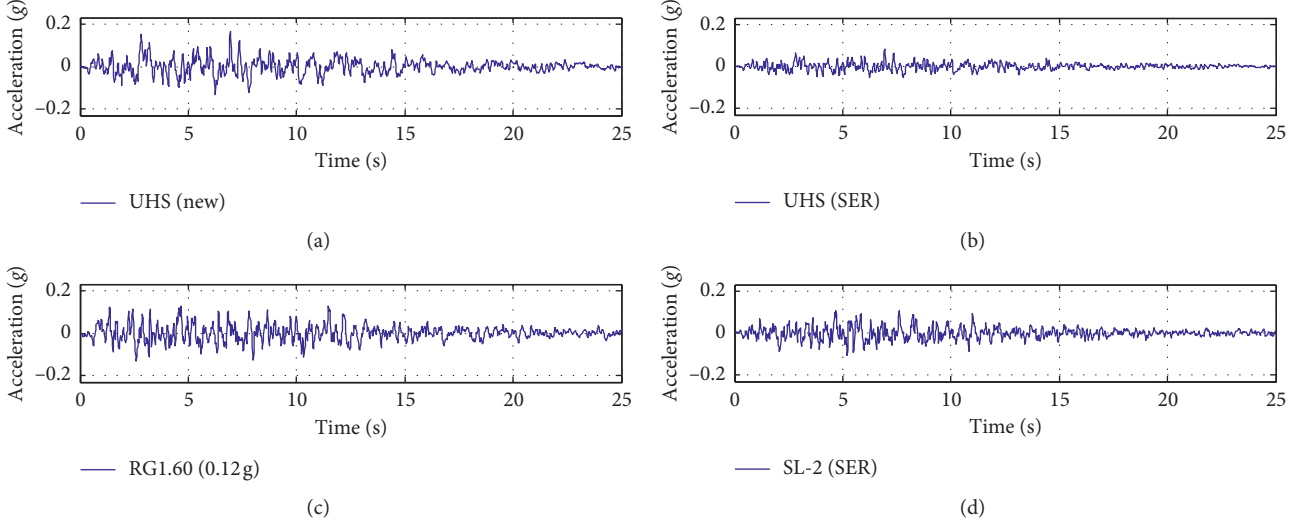


FIGURE 12: Acceleration time-history curve in the X direction. Each response generated two artificial seismic waves; the number of cross-correlation coefficients was less than 0.3.

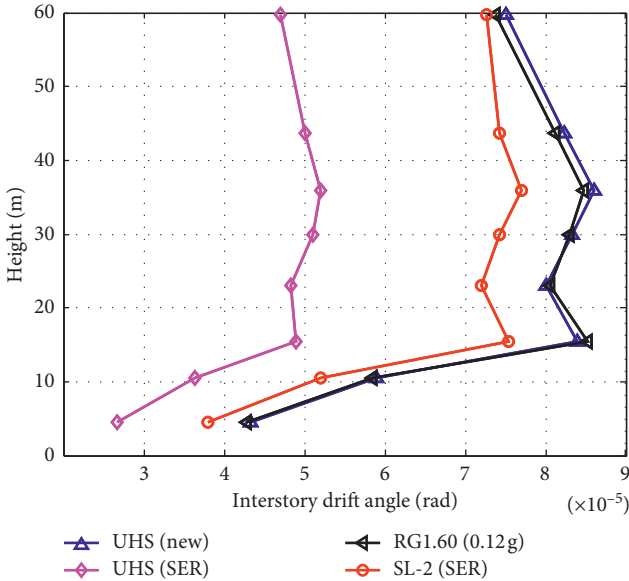


FIGURE 13: Interlayer drift angle of NPP.

The acceleration time-history and Fourier spectrum of the first-loop pressure release and the bottom plate (elevation 7.5 m) of the absorbing ball shutdown system were analysed as shown in Figures 17 and 18. The peak value of the RG1.60 spectrum acceleration was largest, nearly 0.26 g, and that of SER UHS was smallest with a peak value of 0.14 g. For the Fourier spectrum, RG1.60 and the new UHS each had a widely distributed range within 7 Hz. The Fourier spectrum of the new UHS was more homogeneous than that of SL-2. These results indicate that the response of different spectra to the NPP varied. The dynamic response of the new UHS to NPP was larger than that of others.

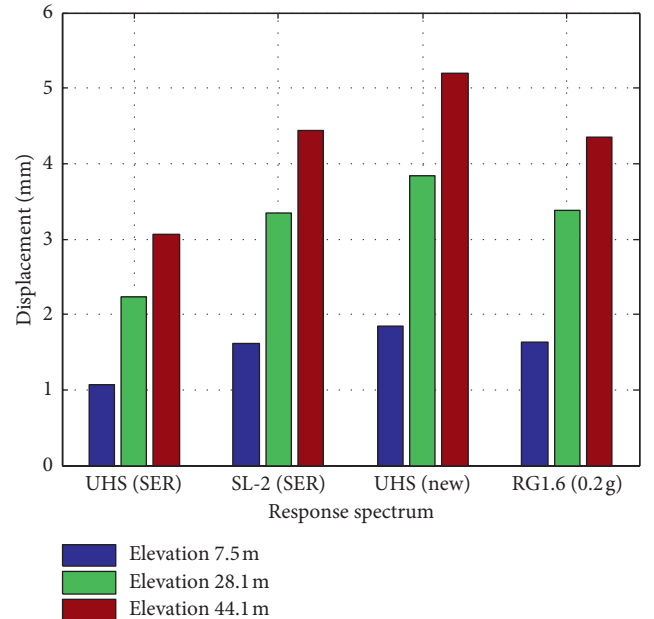


FIGURE 14: Displacement peaks in different layers.

## 5. Conclusion

This paper combines stochastic simulation ground motion and a probabilistic method to generate a UHS with an annual exceedance probability of  $10^{-4}$ . Compared with previous studies, the effects of various parameters were fully accounted for when generating the response spectrum, including the source mechanism, propagation path, and site effect. Key parameters were discussed with regard to site-specific conditions of the selected NPP. The new UHS was compared with the SL-2 spectrum, SER UHS, and RG1.60 spectrum, revealing that the new UHS and the SER UHS

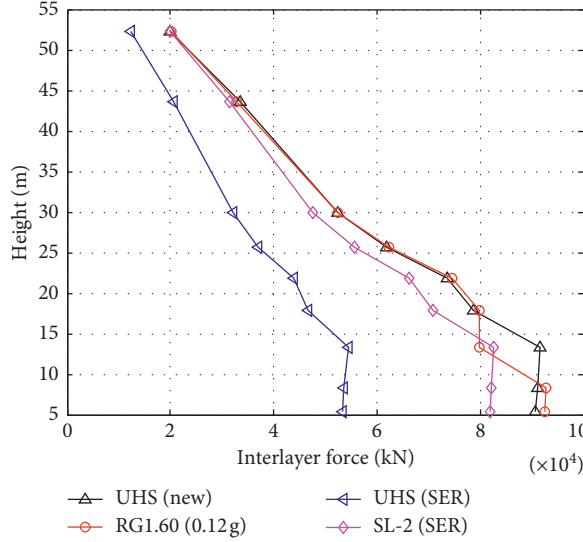


FIGURE 15: Interlayer shear force.

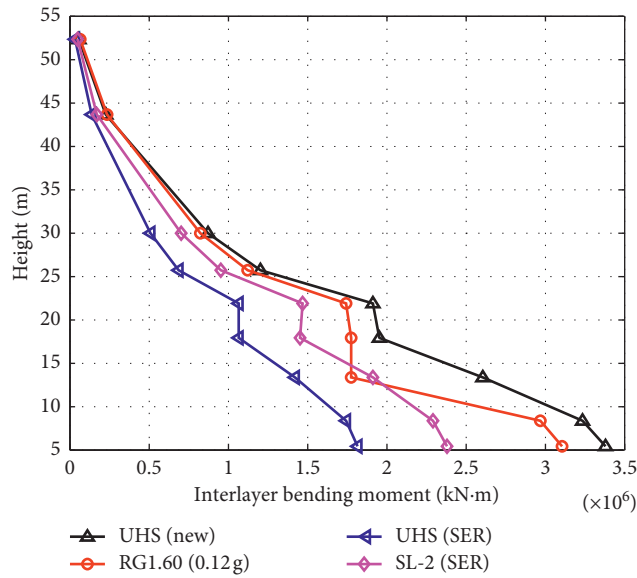


FIGURE 16: Interlayer bending moment.

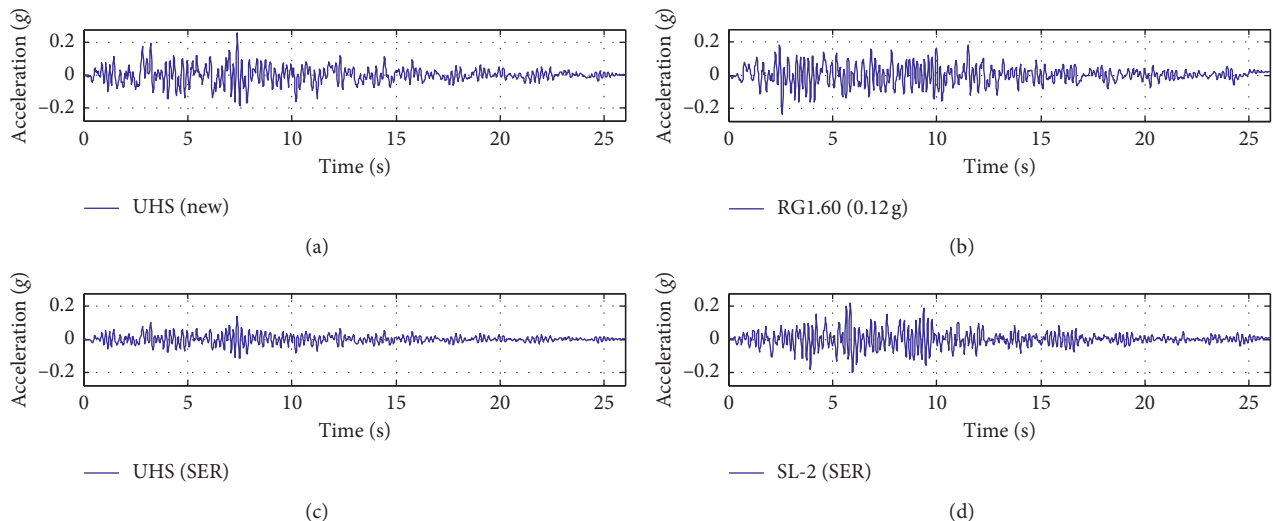


FIGURE 17: Acceleration time-history curve at 7.5 m.

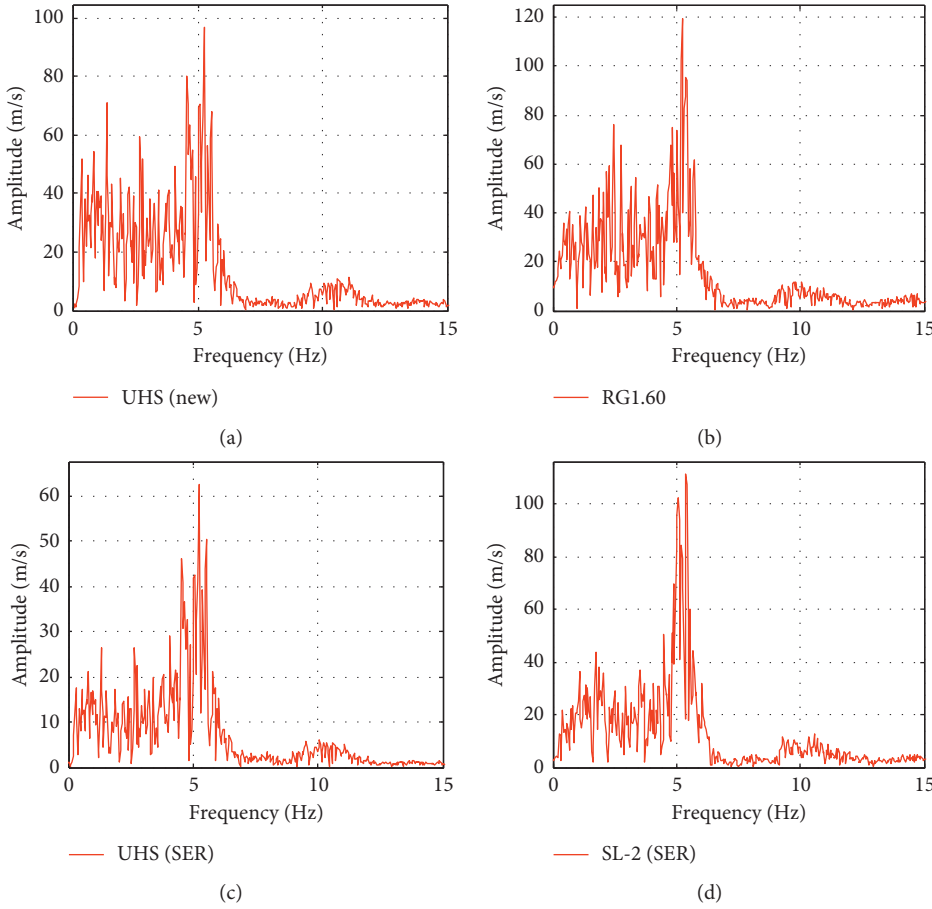


FIGURE 18: Fourier spectrum at 7.5 m.

obtained using the simplified attenuation relation differed substantially in spectrum shape and amplitude. The amplitude of the new UHS and RG1.60 was close to the short period and slightly larger than the SL-2 spectrum. Then, the three-dimensional FEM of the NPP was established, and its dynamic time-history analysis was implemented in SAP2000. The simulation results indicate that different response spectra presented unique dynamic responses to the NPP. UHS exhibited a large response; as such, the UHS generated using the stochastic simulation method can provide a necessary reference for design and aseismic checking of NPPs.

## Data Availability

The data used to support the findings of this study are available from the corresponding author upon request.

## Conflicts of Interest

The authors declare no conflicts of interest.

## Acknowledgments

This work was supported by the National Key R&D Program of China (2017YFC1500604).

## References

- [1] U.S. Nuclear Regulatory Commission, *Regulatory Guide 1.60, Design Response Spectra for Seismic Design of Nuclear Power Plants*, U.S. Nuclear Regulatory Commission, Washington, DC, USA, 1973.
- [2] United States Nuclear Regulatory Commission (USNRC), *Guidance for Performing Probabilistic Seismic Hazard Analysis for a Nuclear Plant Site: Example Application to the Southeastern United States (NUREG/CR-6607)*, United States Nuclear Regulatory Commission (USNRC), Washington, DC, USA, 2002.
- [3] U.S. Nuclear Regulatory Commission, *Regulatory Guide 1.208, a Performance-Based Approach to Define the Site-Specific Earthquake Ground Motion*, U.S. Nuclear Regulatory Commission, Washington, DC, USA, 2007.
- [4] I.-K. Choi, M. Nakajima, Y.-S. Choun, and Y. Ohtori, “Development of the site-specific uniform hazard spectra for Korean nuclear power plant sites,” *Nuclear Engineering and Design*, vol. 239, no. 4, pp. 790–799, 2009.
- [5] S. S. Desai and D. Choudhury, “Site-specific seismic ground response study for nuclear power plants and ports in Mumbai,” *Natural Hazards Review*, vol. 16, no. 4, article 04015002, 2015.
- [6] D. M. Boore and E. M. Thompson, “Revisions to some parameters used in stochastic-method simulations of ground motion,” *Bulletin of the Seismological Society of America*, vol. 105, no. 2A, pp. 1029–1041, 2015.

- [7] T. C. Hanks and R. K. McGuire, "The character of high-frequency strong ground motion," *Bulletin of the Seismological Society of America*, vol. 71, no. 6, pp. 2071–2095, 1981.
- [8] D. M. Boore, "Stochastic simulation of high-frequency ground motions based on seismological models of the radiated spectra," *Bulletin of the Seismological Society of America*, vol. 73, no. 6A, pp. 1865–1894, 1983.
- [9] I. A. Beresnev and G. M. Atkinson, "FINSIM-a FORTRAN program for simulating stochastic acceleration time histories from finite faults," *Seismological Research Letters*, vol. 69, no. 1, pp. 27–32, 1998.
- [10] D. Motazedian and G. M. Atkinson, "Stochastic finite-fault modeling based on a dynamic corner frequency," *Bulletin of the Seismological Society of America*, vol. 95, no. 3, pp. 995–1010, 2005.
- [11] E. M. Rathje and M. C. Ozbay, "Site-specific validation of random vibration theory-based seismic site response analysis," *Journal of Geotechnical and Geoenvironmental Engineering*, vol. 132, no. 7, pp. 911–922, 2006.
- [12] A. R. Kottke and E. M. Rathje, "Technical manual for strata," PEER Rep. 2008/10, p. 84, Pacific Earthquake Engineering Research Center, University of California, Berkeley, CA, USA, 2008.
- [13] D. M. Boore, "Simulation of ground motion using the stochastic method," *Pure and Applied Geophysics*, vol. 160, no. 3, pp. 635–676, 2003.
- [14] D. M. Boore, *SMSIM-Fortran Programs for Simulating Ground Motion from Earthquakes: Version 6.20-A Revision of OFR 96-80-A*, U. S. Geol. Surv. Open-file Rept. 00-509, 2014.
- [15] J. N. Brune, "Tectonic stress and spectra of seismic shear waves from earthquakes," *Journal of Geophysical Research*, vol. 75, no. 26, pp. 4997–5009, 1970.
- [16] D. M. Boore, C. D. Alessandro, and N. A. Abrahamson, "A generalization of the double-corner-frequency source spectral model and its use in the SCEC BBP validation exercise," *Bulletin of the Seismological Society of America*, vol. 104, no. 5, pp. 2378–2398, 2004.
- [17] G. M. Atkinson and W. Silva, "Stochastic modeling of California ground motions," *Bulletin of the Seismological Society of America*, vol. 90, no. 2, pp. 255–274, 2000.
- [18] A. Ji, Y. Zhao, J. Zheng, J. H. Zhao, B. Li, and D. Wu, "Determination of the focus parameters of the moderate and small earthquakes in Shandong and its adjacent areas," *Journal of Catastrophology*, vol. 23, pp. 113–117, 2008, in Chinese.
- [19] C. Yin, X. Lin, J. Mu, and B. Qu, "Calculation of site response of digital seismic station in Shandong province, Seismol," *Seismological and Geomagnetic Observation and Research*, vol. 34, pp. 98–103, 2013, in Chinese.
- [20] G. M. Atkinson and D. M. Boore, "The attenuation of fourier amplitudes for rock sites in Eastern North America," *Bulletin of the Seismological Society of America*, vol. 104, no. 1, pp. 513–528, 2014.
- [21] D. M. Boore, "The uses and limitations of the square-root-impedance method for computing site amplification," *Bulletin of the Seismological Society of America*, vol. 103, no. 4, pp. 2356–2368, 2013.
- [22] J. G. Anderson and Y. Lei, "Nonparametric description of peak acceleration as a function of magnitude, distance, and site in Guerrero, Mexico, B," *Bulletin of the Seismological Society of America*, vol. 84, no. 4, pp. 1003–1017, 1994.